

**The Application of Resonance
Ionisation Mass Spectrometry to
Trace Analysis in Solids.**

**Ian Stewart Borthwick
Department of Physics and Astronomy
University of Glasgow**

**Presented as a thesis for the degree of Doctor of Philosophy
in the University of Glasgow**

© Ian S Borthwick, August 1993.

ProQuest Number: 11007696

All rights reserved

INFORMATION TO ALL USERS

The quality of this reproduction is dependent upon the quality of the copy submitted.

In the unlikely event that the author did not send a complete manuscript and there are missing pages, these will be noted. Also, if material had to be removed, a note will indicate the deletion.



ProQuest 11007696

Published by ProQuest LLC (2018). Copyright of the Dissertation is held by the Author.

All rights reserved.

This work is protected against unauthorized copying under Title 17, United States Code
Microform Edition © ProQuest LLC.

ProQuest LLC.
789 East Eisenhower Parkway
P.O. Box 1346
Ann Arbor, MI 48106 – 1346

Thesis
9590
copy 1

GLASGOW
UNIVERSITY
LIBRARY

***This thesis is dedicated to the memory of my dad,
William Borthwick,
whose help and encouragement was
instrumental in both its commencement
and its completion.***

Summary

Resonant ionisation mass spectrometry (RIMS) is a laser based technique which can detect gas phase atoms with a very high degree of selectivity and sensitivity. The basic concepts of the technique are detailed. For RIMS to be applied to the detection of trace quantities of elements in solid samples the sample must be atomised. If small areas of a surface are to be analysed then the atomisation technique must be able to be applied selectively to these areas. There are two suitable atomisation techniques which have been investigated; laser ablation and ion beam sputtering. Laser ablation is the less well characterised technique and the basic physical processes involved are detailed. This discussion then develops to detail the models which have been applied to the description of the velocity distribution of neutral atoms liberated by laser ablation. A brief review of the experimental investigations of laser ablation pertinent to the work discussed in this thesis is included.

A detailed experimental study of laser ablation was undertaken by the author. After a discussion of the experimental arrangement involved this work is discussed in depth. The velocity distributions of neutral atoms liberated from solid samples by laser ablation have been studied as functions of laser wavelength for a variety of metal and non-metal samples. The effect of changing the ablation laser power on the velocity distribution has also been investigated. The results obtained from gold and lead foils indicate that a thermal mechanism can be applied to describe the laser ablation of these metals. This was also the case for the various elements ablated from a certified steel standard. It is shown that the relative sensitivity factors determined from this analysis are superior to those previously reported. The energy distribution of atoms liberated by the laser ablation of aluminium samples were in some instances unexpectedly high, and this is explained as being due to the contribution from an oxide film on the sample surface. Several methods which have been investigated in an attempt to reduce the interference from ions created by the ablation laser on the RIMS signal are detailed.

A more efficient method of utilising the sample by laser ablation has been

developed, this involves tuning the ablation laser wavelength to an atomic resonance of the atom being detected. This technique, called Resonant Laser Ablation, which can result in enhancements in the ion yield of three orders of magnitude, is discussed in detail. The results from other researchers, and workers in Glasgow are given to illustrate the important contribution that atomic collisions have in this process. The discussion also details the work of the author in applying the technique to the detection of small quantities of aluminium in a solid sample.

The interfacing of an ion gun with a high current density to the RIMS system, by the author, is also discussed. The processes occurring during ion sputtering are understood more quantitatively than is the case for laser ablation. The essential results from sputtering theory are reported. Ion sputtering has been used to allow the quantification of the amount of material liberated by the laser ablation of a pure metal target. The two atomisation techniques are compared for trace analysis applications by undertaking a study of aluminium samples which each contain various concentrations of Mg and Mn.

Acknowledgements

A great number of people have give me help and encouragement during the course of my project. I would like to thank them all, especially:

- my supervisor, Dr. K. W. D. Ledingham for his enthusiasm and encouragement throughout the period of my studies.
- Dr. R. P. Singhal for helping me to understand many theoretical concepts.
- Mr. C. T. J. Scott for his assistance in some of the experiments.
- Dr. P. T. McCombes for his guidance in areas of data acquisition and computing.
- Dr. C. J. McLean for his assistance with electron microscopy.
- Dr. Wang Li for his advice in the area of resonant laser ablation.
- Dr. A. Clark for his advice in the experimental and theoretical aspects of laser spectroscopy and for his diligent proof-reading of this volume.
- Dr. A. Marshall, Dr. M. Campbell, Dr. R. Jennings, Dr A. P. Land and Ms. R. Zheng for many helpful discussions on various aspects of my work.
- Mr. T. McCanny and Mr. R. Maxwell for their technical assistance.
- Mr. T. Neil and his staff in the mechanical workshop for constructing numerous pieces of equipment.
- Mr. R. Pallester and his colleagues for manufacturing and maintaining electronic equipment.
- Miss C. McIntyre for her secretarial assistance.
- Alusuisse-Lonza Services, Neuhausen, Switzerland, for kindly providing samples.
- The S.E.R.C. for financial support.
- My family, for their encouragement, support and considerable financial help.

Publications List

McCombes P T, Borthwick I S, Jennings R, Land A P, Ledingham K W D, Singhal R P, Towrie M, (1990)

Characterisation of the energy and spatial distribution of neutrals produced by laser ablation

SPIE Proceedings Series, 1208 pp88-98

Wang Li, Borthwick I S, Jennings R, McCombes P T, Ledingham K W D, Singhal R P and McLean C J, (1991)

The detailed characteristics of resonant laser ablation

Resonance Ionization Spectroscopy 1990. Inst. Phys. Conf. Ser. 114, pp455-458

McCombes P T, Borthwick I S, Jennings R, Ledingham K W D, Singhal R P, (1991)

Resonance ionization mass spectrometry applied to the trace analysis of gold

Inst. Phys. Conf. Ser. 113, pp163-168

Wang Li, Borthwick I S, Jennings R, McCombes P T, Ledingham K W D, Singhal R P and McLean C J, (1991)

Observations and analysis of resonant laser ablation of GaAs

Appl. Phys. B, 53 pp34-38

Borthwick I S, Ledingham K W D and Singhal R P, (1992)

Resonant Laser Ablation - a novel surface analytic technique

Spectrochimica Acta, 47B pp1259-1265.

Ledingham K W D, Borthwick I S and Singhal R P, (1992)

Trace analysis using laser ablation resonant ionisation mass spectrometry

“SERC Central Laser Facility Annual Report 1992”. Rutherford Appleton Laboratory Report RAL-92-020, pp206-207

Ledingham K W D, Borthwick I S and Singhal R P, (1992)
The characteristics of resonant laser ablation for surface analysis
Surf. Interface. Anal., 18 pp576-578

Campbell M, Javaud S, Zheng R, Ledingham K W D, Singhal R P,
Borthwick I, Clark A, Marshall A, Sander J, (1992)
Attenuation Characteristics of an all-silica u.v. fibre
SPIE Proceedings Series, 1712 pp150-159

Borthwick I S, Ledingham K W D, Scott C T J and Singhal R P, (1992)
*Laser ablation as a sample atomisation technique for resonant ionisation
mass spectrometry*
"Resonance Ionization Spectroscopy 1992."Inst. Phys. Conf. Ser. No128
pp279-282

Borthwick I S, Scott C. T J, Ledingham K W D and Singhal R P, (1993)
*Non-Thermal Velocity Distributions Of Aluminium Atoms
Ablated From Aluminium Metal.*
To be published in the proceeding of COLA'93, AIP Publishing

Borthwick I S, Clark A, Ledingham K W D and Singhal R P, (1993)
*The Characteristics Of Q-Switched Laser Ablation For Several Elements
From A Low Alloy Steel.*
To be published in the proceeding of COLA'93, AIP Publishing

Contents

<i>Frontispiece</i>	(i)
<i>Summary</i>	(iii)
<i>Acknowledgements</i>	(v)
<i>Publications</i>	(vi)
<i>Contents</i>	(viii)

Chapter 1: Introduction.

§1.1 Introduction	1
§1.2 What is trace analysis?	1
§1.3 What is RIS?	2
§1.4 Different RIS schemes	3
§1.5 What is RIMS?	6
§1.6 High energy ion microprobe techniques	8
§1.7 Secondary Ion Mass Spectrometry	9
§1.7.1 Static SIMS	10
§1.7.2 Dynamic SIMS	11
§1.8 Laser ablation based techniques	12
§1.8.1 Mass spectrometry	13
§1.8.2 Inductively coupled plasma techniques	14
§1.8.3 Atomic emission spectroscopy	14

Chapter 2: Laser Ablation for Sample Atomisation.

§2.1 Introduction	16
§2.2 Absorption of laser light	16
§2.3 Laser induced heating	18
§2.4 Vaporisation	20
§2.5 Velocity distribution of the vaporised material	21
§2.6 Hydrodynamic velocity	23
§2.7 Knudsen layer formation	24
§2.8 Adiabatic expansion	28
§2.9 Plasma formation	28
§2.10 Experimental measurements of laser induced neutral particle emission	30
§2.10.1 Metals	31

§2.10.2 Compound semiconductors	33
§2.10.2.1 Photons below the bandgap energy	34
§2.10.2.2 Photons above the bandgap energy	36
§2.10.3 Elemental semiconductors	44
§2.10.4 High temperature superconductors	46
§2.10.5 Insulators	47
§2.10.6 Polymers	49
Chapter 3: Instrumentation.	
§3.1 Introduction	51
§3.2 Mass spectrometer and vacuum system	51
§3.3 Laser system and optics	55
§3.3.1 Ionising lasers	56
§3.3.2 Ablation lasers	58
§3.4 Data Acquisition electronics and software	59
§3.5 Previous studies with the RIMS system	62
Chapter 4: Experimental Investigation of Laser Induced Atomisation.	
§4.1 Introduction	65
§4.2 Aluminium	65
§4.2.1 RIMS studies of 532nm wavelength laser ablation of aluminium	66
§4.2.2 Effect of increasing laser power	72
§4.2.3 Effect of changing the ablation laser wavelength	75
§4.2.4 Surface modification resulting from the laser ablation of aluminium	77
§4.3 Gold	80
§4.4 Lead	82
§4.5 Low alloy steel	83
§4.6 AlGaAs	90
§4.7 Sapphire	92
§4.8 Stability of the PAI signal	93
§4.9 Stage current	94
§4.10 Methods for eliminating interference from ions created by the ablation laser	96
§4.10.1 Pulsing the deflector plates	96
§4.10.2 Pulsed extraction voltages	97

§4.10.3 Static fields	99
§4.11 Conclusions	100
Chapter 5: Resonant Laser Ablation.	
§5.1 Introduction	104
§5.2 RLA experiments performed by other researchers	105
§5.3 Broadening mechanisms	107
§5.3.1 Natural radiative linewidth	108
§5.3.2 Doppler broadening	108
§5.3.3 Power broadening	109
§5.3.4 Collisional broadening	110
§5.4 Initial RLA experiments performed in Glasgow	112
§5.5 Collisional mechanisms in RLA	114
§5.6 The application of RLA to trace analysis	119
Chapter 6: A comparison of ion sputtering and laser ablation for sample atomisation for RIMS	
§6.1 Introduction	123
§6.2 The Profiling Ion Gun	123
§6.3 Initial studies of ion bombardment with RIMS	127
§6.4 Neutral yields	128
§6.5 Trace analysis of metals using RIMS	134
Chapter 7: Conclusions	142
References	145

Chapter 1

Introduction

§1.1 Introduction

As technological advances it is becoming increasingly necessary to be able to monitor and control the quality of many aspects of the world around us. This may involve, for example, pollutants in the environment or impurities in advanced materials, which are present in very small concentration but have a significant effect. There is a need for a technique which can detect a single atom or molecule of a particular species in the presence of a much higher concentration of another species. Such a technique has existed for more than a decade, it is called resonance ionisation spectroscopy (RIS). The reason that RIS has not provided the answer to all of the problems of trace analysis is due to the difficulties of applying the laboratory technique to practical problems. The Laser Ionisation Studies Group in the Department of Physics and Astronomy has been striving to apply RIS to practical problems. These problems include the monitoring of pollutants in the atmosphere, the detection of sensitive materials including explosives and narcotics, the analysis of the composition of advance semiconductor materials and the detection of trace elements in solids. The work of the author has been in this final area, where RIS has been combined with mass spectrometry in the hybrid technique resonant ionisation mass spectrometry (RIMS). RIS and RIMS are techniques which are applied to atoms in the gas phase. An important aspect of applying RIMS to trace analysis in solids is sample atomisation. There are two techniques which can be used to atomise specific areas of a solid: laser ablation and ion bombardment. In this thesis the development of both of these techniques for atomising samples with subsequent analysis by RIMS will be described. In this chapter the basic concepts of RIS and RIMS will be detailed together with a brief account of the other techniques which can be employed for the trace microanalysis of solids.

§1.2 What is trace analysis ?

The term trace analysis describes an analysis which measures a very

small concentration of atoms or molecules that are present in a much larger concentration of another substance (the matrix). Before detailing the techniques that have the sensitivity to perform trace analysis a short account of the typical quantities involved will be given. The standard convention for describing the level of a trace element is to give its concentration in the matrix. The abbreviation ppm is used to denote a concentration in parts-per-million. This can denote either an atomic number concentration, where the subscript at can be used, e.g. ppm_{at}, or a weight concentration, where the subscript wt is used. In practice these concentrations are not significantly different, except for the case of an especially light element in a heavy matrix, or conversely a heavy element in a light matrix. If the elemental concentration is significantly below 1ppm this can be termed ultra-trace analysis and the terms parts-per-billion (1 in 10⁹) and parts per trillion (1 in 10¹²) are employed. The abbreviations ppb and ppt are used. However the trace element concentration is not the only significant parameter, the absolute quantity of the trace element detected should also be reported. This quantity is usually given in nanograms, picograms, femtograms or even attograms. It is useful to appreciate that 10¹³ atoms of nickel has a mass of 1ng and would form an atomic layer ~700µm square. In this case a femtogram would contain 10⁷ atoms (while a femtomole contains ~6*10⁸ atoms or molecules.) The quantification of the amount of material is required because often it is the case that both the concentration and absolute quantity of the element of interest are small.

§1.3 What is RIS?

The principle of resonance ionisation spectroscopy (RIS) is very straightforward. A laser beam with a wavelength tuned to be in resonance with a strong electronic transition of the element under investigation, illuminates the sample volume. This can cause excitation and subsequently ionisation of the element under study, as shown in Fig.1.1. The cross sections for excitation from the ground state to an excited state are of the order of 10⁻¹²cm⁻². In order to saturate these transitions, that is to excite every atom of the element of interest in the laser beam, requires a photon density easily obtainable with commercial dye laser systems. The cross section for the ionising step, that is the transition from the excited state into the ionisation continuum, has a cross section approximately six

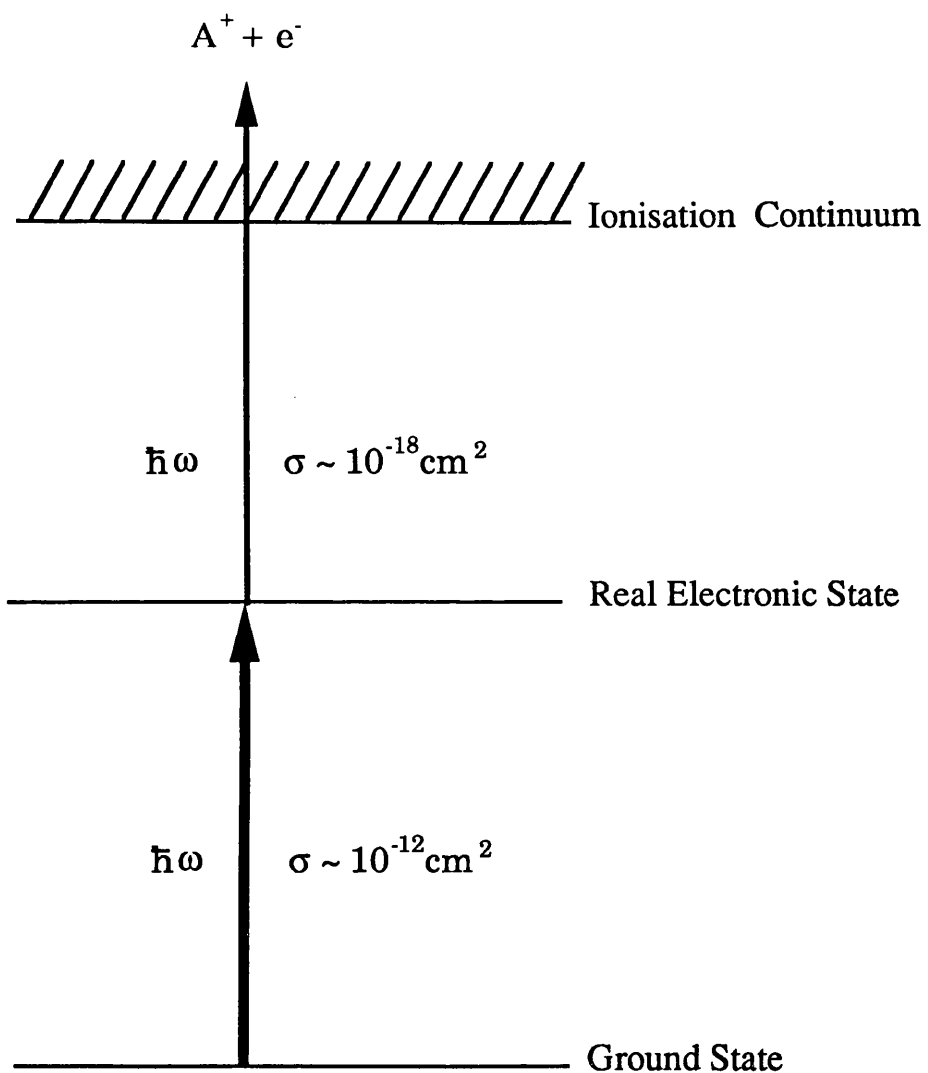


Fig.1.1 The basic concept of resonant ionisation spectroscopy

orders of magnitude smaller than that of the excitation step. However, in a seminal paper Hurst *et al* (1979) illustrated that with the powers achievable from pulsed dye lasers it is possible to saturate the ionisation step in the majority of elements in the periodic table. Hence RIS is a highly sensitive technique with the potential of ionising all of the atoms of interest in the laser beam volume. The technique is also highly selective, since the energy levels of each element are unique. It is therefore possible to excite and ionise one species without affecting any of the other elements in the illuminated volume. Although conceptually straightforward RIS was not observed until tuneable dye lasers were developed. Many of the initial experiments involved the alkali metals because these elements have the lowest first ionisation potentials. The first demonstration of RIS was for rubidium (Ambartzumian and Letokhov, 1972). Single atom detection was first achieved for caesium (Hurst *et al*, 1977). The caesium atoms were thermally liberated into a proportional counter that was operated with a pressure of 100 torr of argon-methane counter gas. In a recently published book Hurst and Payne (1988) discuss this work in detail, together with the theoretical framework for RIS and its many applications. Letokhov (1987) covered similar areas with particular reference to work performed in the former Soviet Union.

§1.4 Different RIS schemes

The scheme shown in Fig.1.1 is the simplest possible application of RIS. However, the excited state in most elements have energies which require ultra-violet photons to promote electrons from the ground state to the excited state. In experimental systems the tuneable photons are produced by dye lasers and the wavelengths available are limited, essentially to the visible range. Ultra-violet photons can be produced by exploiting non-linear effects in crystals to double the frequency of the dye laser photons, as will be discussed in §3.3.1. Hurst *et al* (1979) showed that five basic RIS schemes could be used to ionise all of the elements in the periodic table, with the exception of helium and neon. These five schemes require only one or two tuneable lasers and are shown in Fig.1.2.(1)-(5). Scheme (1) is the simplest possible RIS scheme, involving the absorption of one photon to promote the electron to an excited state and ionisation is due to the absorption of a second photon of the same frequency. Scheme (2) requires a frequency doubled photon to promote the electron to an excited state with

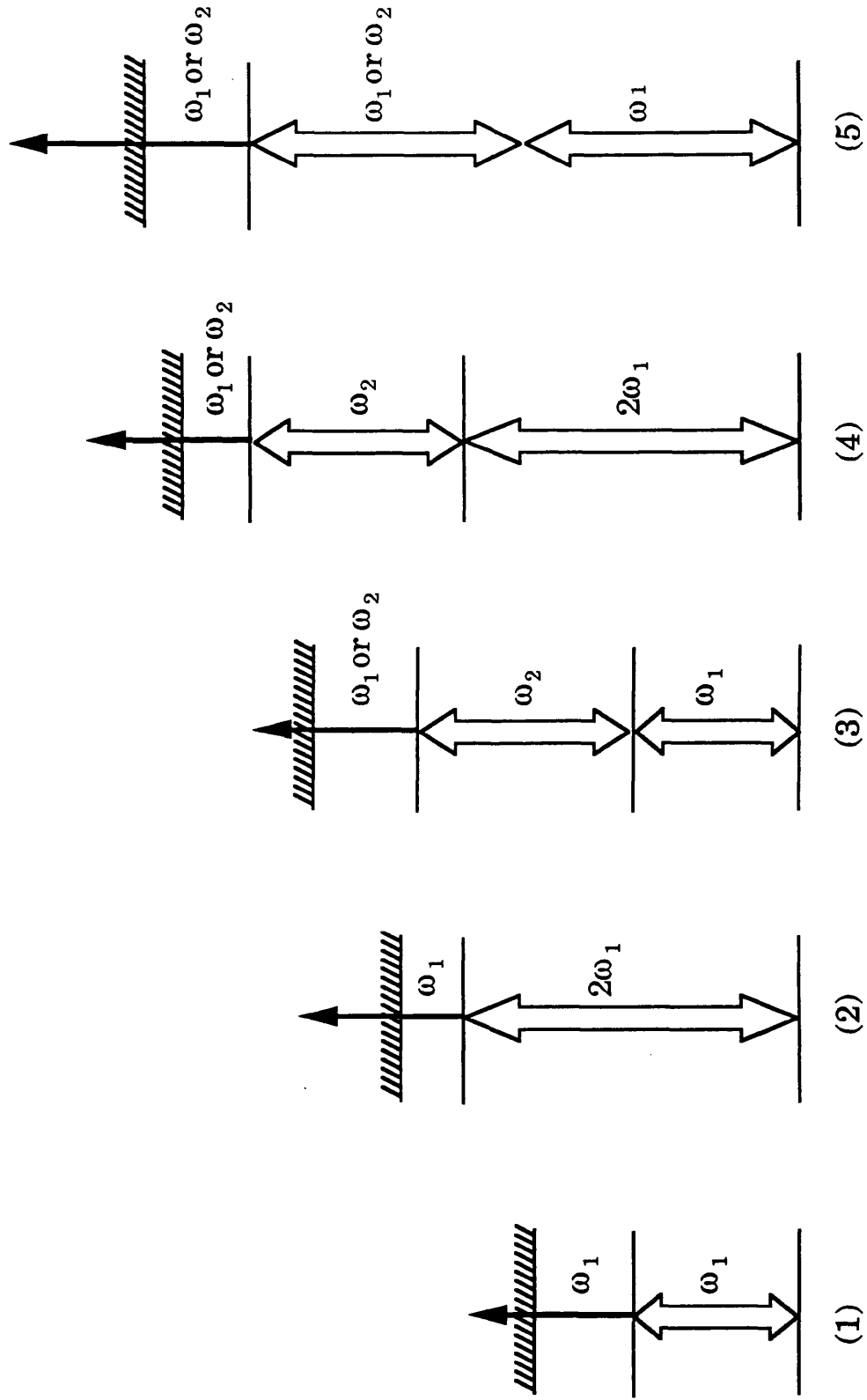


Fig.1.2 The five basic RIS schemes

ionisation affected by a photon of the fundamental wavelength. This is the scheme employed for most of the RIS experiments described in this thesis. Scheme (3) requires two tuneable lasers and is called a two-colour scheme. Photons of the first colour excite the electron to one bound state and absorption of a photon of the second colour causes excitation to a higher energy bound state. The absorption of a photon of either colour promotes the electron into the ionisation continuum. An advantage of a two-colour scheme is that the selectivity of the ionisation is increased, at the cost of increased experimental complexity. Scheme (4) is similar to scheme (3) except that a frequency doubled photon is used to promote the electron from the ground state to the first excited state. Scheme (5) utilises a two-photon resonant transition to populate the excited state. A two-photon transition involves the simultaneous absorption of two photons and can be thought of as involving a virtual electronic state. An advantage of two-photon transitions are that they follow less stringent selection rules than single photon transitions (Birge, 1983). However, the cross-sections for two photon transitions are substantially lower than for those involving one photon and using scheme (5) saturation is not usually obtained. It is also possible to ionise an atom non-resonantly through a two-photon transition, as shown in Fig.1.3. The total cross-section for this method of ionisation is much smaller than for RIS. However, since the photon energy does not need to be tuned it is often possible to harness a higher fraction of the pump laser power for ionisation. The fourth-harmonic wavelength of a Nd:YAG laser, which has a wavelength of 266nm, is often used for non-resonant two-photon ionisation since the power available from most commercial laser systems is considerable, >25mJ. As the ionisation is non-resonant it is also non-selective. This results in all of the elements which have a first ionisation potential lower than the energy of the two-photons being ionised. In the case of the fourth harmonic from a Nd:YAG laser the two-photon energy is 9.32eV, and many elements, including all of the transition metals with the exception of zinc and mercury, can be ionised simultaneously. This allows for the surveying of many elements simultaneously which is not possible using RIS because of the intrinsically selective nature of RIS ionisation.

It is apparent that a major limitation of the RIS technique as described above is that the cross-section for ionisation by a photon (photoionisation)

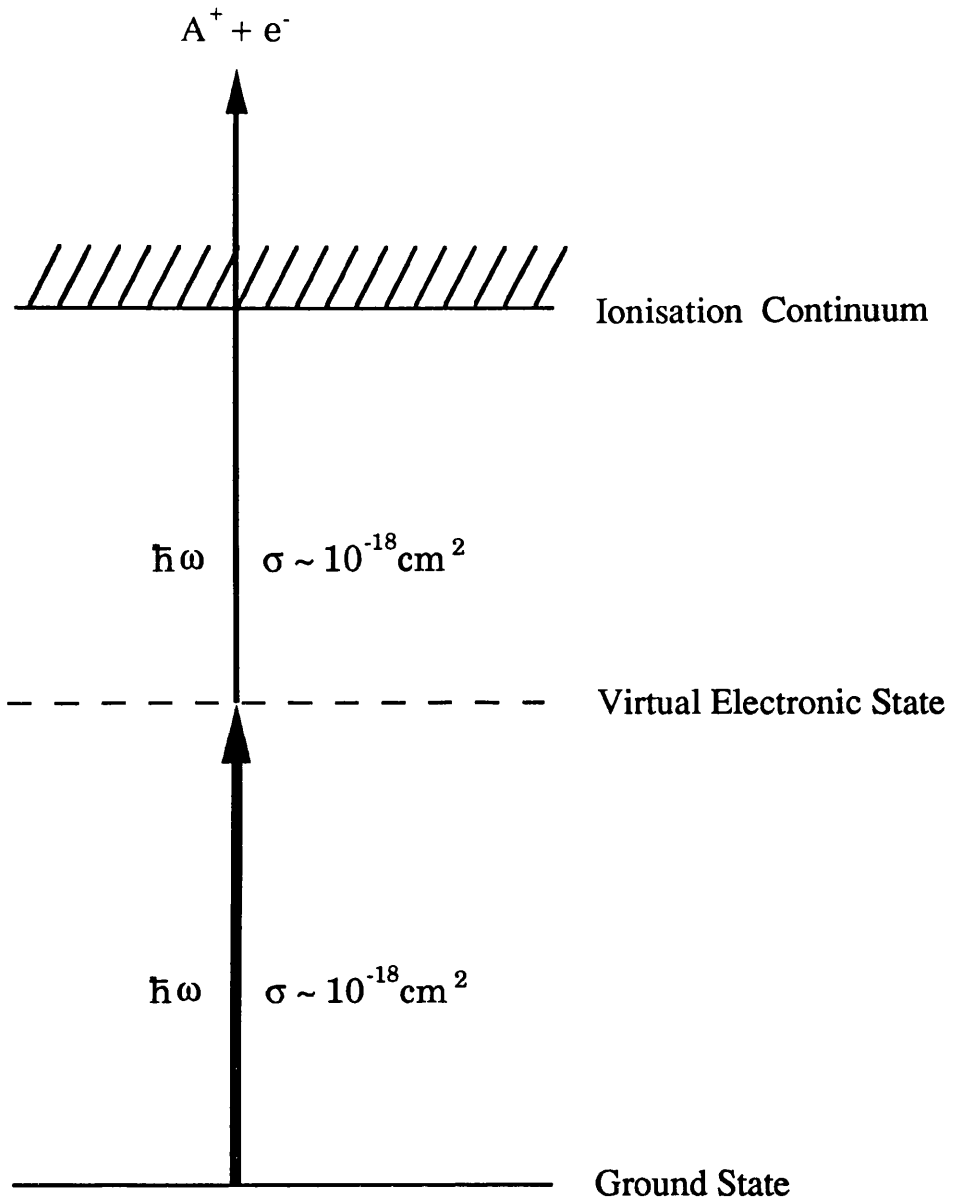


Fig.1.3 The basic concept of non-resonant two-photon ionisation

is many orders of magnitude lower than those for bound-bound transitions. In order to overcome this problem the fundamental wavelength (1064nm) of a Nd:YAG laser can be used for the photoionisation of any state which lies within 1.16eV of the first ionisation potential. This is particularly effective since often a substantial fraction of the Nd:YAG fundamental wavelength is not frequency doubled and is often not used in RIS experiments. Due to its relatively small photon energy, the 1064nm wavelength radiation does not produce two photon ionisation in any elements, so a high power can be employed without producing a multiphoton ionisation background.

There are several other techniques which can be employed to increase the cross-section for ionisation, at the cost of increased experimental complexity. These have been reviewed by Letokhov (1987) and will be briefly detailed. The cross-section for a transition to a high lying Rydberg state of an atom is higher than for a transition directly into the ionisation continuum. The electron can then be excited from the Rydberg level by the application of a large electric field gradient which shifts the energy of the Rydberg state to above the binding energy of the atom. This is termed field ionisation and can cause the ionisation of every atom with an electron in a Rydberg state. Field ionisation usually involves the application of a voltage pulse to generate an electric field gradient of $\sim 10^4 \text{Vcm}^{-1}$, although it can also be achieved with continuous fields (Hergenröder and Niemax, 1991). Autoionisation occurs when two electrons are simultaneously excited into a bound state which lies above the first ionisation potential. The system then decays, resulting in an ion and an electron. Since the transition to the autoionising state is a bound-bound transition it has a cross-section higher than photoionisation, typically 10^{-15}cm^2 . A disadvantage of this technique is that it requires at least two tuneable lasers and a knowledge of the spectra of autoionising states. Excited states can also be ionised through collisions, either with neutral atoms in a buffer gas at a relatively high pressure (~ 1 torr) or with ions and electrons in a flame or discharge. Collisions are not usually a significant ionisation mechanism if RIS is performed in a vacuum. However, in special circumstances, such as those described in Chapter 5, collisions can be the dominant method of ionisation in a system maintained at vacuum.

In order to perform RIS it is necessary to know the atomic structure of the element to be analysed so that the wavelengths required for excitation and ionisation can be calculated. The energies and designations of the states in all neutral elements and many elemental ions have been comprehensively tabulated by Moore (1971) and these values have been used in all the calculations and diagrams in this work. The energies of excited states will be given in the spectroscopic units, cm^{-1} . These values can be used to calculate the wavelength (λ) of a transition using the relationship $\lambda(\text{nm})=10^7/E(\text{cm}^{-1})$, where E is the difference in energy between the two electronic states. When considering energy levels it is often useful to use the conversion factor $8065.541\text{cm}^{-1} = 1\text{eV}$. In order to select the most efficient RIS scheme it is necessary to know the oscillator strengths of the states involved and also the photoionisation cross-sections and the accessibility of any convenient autoionising resonance. In order collate this information for all elements and make it accessible to analytical chemists a RIS data service has been established at the US National Institute for Standards and Technology (Saloman, 1992a). The RIS schemes which have been previously applied to an element are reported, together with the lifetimes of the states involved and the laser powers which have been calculated to saturate the bound-bound transitions and the ionising step. This data service has proved to be very useful, however, data for only some elements has been published thus far. The elements so far covered are As, Au, B, C, Cd, Fe, Ge, Pb, Si and Zn (Saloman, 1990), Mg, Al, Ca, Co, Cr, Cs, Cu, Hg, Ni and Kr (Saloman, 1991) and Na, Bi, P, Sb and Sn (Saloman, 1992b).

§1.5 What is RIMS?

It has been shown that RIS is a highly sensitive and selective ionisation technique for producing ions. Subsequent mass analysis of these ions has several advantages. It allows for the determination of isotope ratios and ensures that ions of any other atom or molecule that has been inadvertently non-resonantly ionised are separated from the analyte ions. This is only the case, of course, if the element of interest and the background species have different masses. The many analytical applications of resonance ionisation mass spectrometry have been reviewed by Fassett and Travis (1988). There is no restriction on the type of mass spectrometer that can be used for RIMS and several designs have

been successfully employed. However, since pulsed dye lasers are normally used for RIS, the ionisation is a pulsed event, ideally suited for time-of-flight mass spectrometry (Price, 1990). This allows a complete mass spectra to be obtained for each laser shot and has the additional advantage of being an instrumentally simple technique. Time-of-flight mass spectrometry has been used exclusively in the work reported in this thesis.

As mentioned in §1.1 the principle concern of the author has been the application of RIMS to the analysis of solids. There are many techniques which have been employed to atomise solid samples so that they can then be analysed by RIMS. Many of the early RIMS experiments used thermal filament sources (Travis *et al*, 1987). Small solid samples can be loaded into small resin beads which are placed onto the filament. Otherwise the sample must be made into solution and then dried or electroplated onto the filament. A more convenient technique for the direct atomisation of solids is the graphite furnace (Bekov *et al*, 1987), in which small solid sample (~1mg) can be directly vaporised. This technique is used intensively at the Institute of Spectroscopy of the Russian Academy of Sciences (Asaro *et al*, 1992) and very high levels of sensitivity has been achieved in many studies. For example ruthenium was detected at the level of 1ppt in solid samples (Bekov *et al*, 1985), although some analyte concentration was employed prior to analysis. The sample atomisation techniques discussed so far require some kind of preprocessing of solid samples. This can increase the total time required for analysis from minutes to several days and also means that the distribution of trace elements throughout the sample cannot be determined. In biological, mineralogical and materials science applications, a knowledge of the variation of the trace element distribution can be more important than knowing the composition integrated through the whole sample. Many of these applications have been described in context of the application of the proton microprobe by Johansson and Campbell (1988). In the remainder of this chapter RIMS will be discussed along with other techniques which have the capacity for trace analysis of small areas of a solid sample. These can be classed as microbeam analysis techniques, although this term is strictly only applied to techniques which interrogate areas of submicron dimensions. Of the

methods described below only static SIMS is usually truly in this category.

§1.6 High energy ion microprobe techniques

High energy ion microprobe techniques employ a high energy (~1-3MeV) beam of protons or other light nuclei to probe the sample. These particles can penetrate tens of microns into the material essentially undeflected without damaging the sample. The probe particles are usually generated from small low energy single-ended Van de Graff accelerators and at least two quadrupole lens are required to bring the beam to a focus. High energy ion microprobe techniques are therefore quite unique in being more instrumentally complex and more expensive than RIMS. The best spot sizes obtained by proton microprobes are of the order of microns, although improvement by a factor of ten is believed to be feasible (McKee and Smith, 1989).

The most versatile high energy ion microprobe technique is particle-induced X-ray emission - PIXE (Johansson and Campbell, 1988). In this technique the high energy ion, usually a proton, causes the excitation of an electron in the inner shell of an atom, the vacancy then de-excites, predominantly by the emission of characteristic X-rays. These X-rays can be detected by a Si(Li) detector to give a survey of the elements present in the sample. PIXE is usually performed in a high vacuum environment, however, it is possible to bring the high energy ion beam through a thin window into the laboratory atmosphere. This allows the analysis of objects which are too large or too fragile to be placed in a vacuum environment. PIXE is very similar to the more prevalent technique of electron-probe microanalysis (EPMA), however the bremsstrahlung emitted by decelerating protons is of negligible intensity in comparison to that of electrons. This results in PIXE having substantially better limits of detection than EPMA. However, because the cross-section for ionisation and the propagation of X-rays is lower for small atomic number materials, PIXE is only applicable to elements heavier than sodium, unless a windowless detector is used, in which case elements down to boron can be monitored. PIXE is particularly suited to the analysis of heavy elements in a light matrix. The limits of detection in optimal conditions can be below 0.1ppm for some elements and are typically around 1ppm for all elements. Although in general PIXE analysis is

reasonable quick and uncomplicated, in many applications a degree of ingenuity is required to obtain satisfactory results. For elements with masses above ~ 50 amu proton beams of 1-3MeV cannot efficiently produce K X-rays. Therefore identification of heavier elements relies upon the identification of their characteristic L X-rays. These are of lower energy than the K X-rays and overlap with K X-rays of lighter elements, causing the overpopulation of the low energy end of the observed energy spectrum. In many cases an absorber can be inserted between the sample and the detector in order to reduce the signal from the major elements in the sample. This is particularly important for archaeological samples where the matrix has a higher atomic number than the trace elements and the absorber has to be designed to preferentially transmit the X-rays of interest.

As discussed above PIXE is difficult to apply to elements lighter than sodium, especially if the matrix has a high atomic number. However, in this situation it is possible to employ the complimentary high energy ion microprobe technique of nuclear reaction analysis (Cookson, 1987). This is based on the principle that a small number of the incident particles can penetrate the Coulomb barrier and undergo reactions with the nucleus. Energy analysis of the emitted particles and a knowledge of the incident particle energy allows the identification of the element involved. The experimental arrangement is similar to that discussed previously, however, the detection limits of this technique are lower than those of PIXE, typically 10-1000ppm.

§1.7 Secondary Ion Mass Spectrometry

Secondary ion mass spectrometry (SIMS) is probably the most widely prevalent of the techniques discussed in this section. The principle of the technique is that a beam of ions, with an energy usually between 0.5keV and 20keV, is focused onto the sample. The energy in the beam is transferred by collisions to the atoms within a few nanometres of the surface. If the energy transferred to the atoms on the surface is higher than the surface binding energy then sputtering of the sample is observed. Usually there is more than one atom ejected for each incident ion. This ratio, which is termed the sputter yield, can be explained by the comprehensive sputtering theory which was developed by Sigmund

(Benninghoven *et al*, 1987). A fraction of the ejected material is ionised and it is these ions, which are termed secondary ions to distinguish them from the primary ions in the incident beam, that are mass analysed. The mechanism of ionisation is not clear (Vickerman, 1990), however, it is accepted that if the primary ions are oxygen the positive secondary ion yield is significantly larger than if noble gas ions are used. Similarly the use of caesium as the primary ion species increases the number of negative secondary ions. Due to the need for mass spectrometry and ion beams, SIMS analysis is carried out under ultra-high vacuum conditions. There are two different types of SIMS and these will be discussed in turn.

§1.7.1 Static SIMS

In static, or imaging, SIMS the distribution of atoms or molecules on the surface layer is of interest. The aim in static SIMS is to obtain an image of the surface in such a way that the collected ions are ejected from a region of surface which has not previously experienced a primary ion impact (Vickerman, 1990). This requires very low current densities in the primary beam, less than 5nAcm^{-2} . Liquid metal ion guns, LMIG, are often used in static SIMS. A LMIG produces a beam of ions with an energy of $\sim 30\text{keV}$ and focused spot sizes down to 20nm , which allows for the acquisition of high resolution images. It is also possible to pulse the primary ion beam and hence facilitate time-of-flight mass spectrometry of the secondary ions. The major applications of static SIMS are for surface science and in the analysis of polymers and large biomolecules. In these applications the charging of the sample due to the incident ions can be alleviated by flooding the sample with low energy electrons between the primary ion beam pulses. Due to the small current densities employed in static SIMS the sensitivity of the technique is not particularly high, being $\sim 10\text{-}100\text{ppm}$, depending on the primary beam parameters (van Vaeck and Gijbels, 1989). RIMS of neutrals produced under the static SIMS conditions described above has been achieved by Winograd and co-workers (1992). This can increase the sensitivity of the technique, since there are between 10^3 to 10^5 more neutrals than ions. The motivation of this work was the imaging of molecules on surfaces for biological applications. Due to the small quantity of material removed per pulse it was concluded that trace analysis could not be performed under imaging conditions.

§1.7.2 Dynamic SIMS

If SIMS analysis is undertaken with a higher primary ion beam current density, so that the surface monolayer is eroded during the analysis, the technique is termed dynamic SIMS. In dynamic SIMS the elemental distributions in the sample can be obtained in two ways (Benninghoven *et al*, 1987). Firstly it is possible to obtain an image, either by scanning a small ion spot over the sample (a microprobe) or by using a large ion beam and a mass spectrometer which maintains the initial spatial distribution of the secondary ions (a microscope). Secondly, the concentration of the elements of interest in the sample can be determined by monitoring the SIMS signals as the sample is eroded. This is known as depth profiling and is one of the major applications of dynamic SIMS. It is possible to determine the concentration of an element in a SIMS depth profile with a maximum resolution approaching one nanometre. However, a difficulty encountered with SIMS is that since both atomisation and ionisation are affected by the primary beam the ion yield is highly dependent on both the matrix and on the element of interest. This gives rise to the matrix effects encountered in SIMS depth profiles where the analyte signal can change by orders of magnitude between two levels of a layered structure when there is no change in the analyte concentration (Sykes, 1990). The limits of detection for dynamic SIMS can be very low but are not the same for all elements. Using typical dynamic SIMS parameters, a primary current of $2\mu\text{A}$ and energy of 12keV , sensitivities of the order of 1ppb were determined for Cr, Mn and Fe, this increased to $\sim 10\text{ppb}$ for Al, Si and Cu, $\sim 100\text{ppb}$ for Sn and Zn, 1ppm for S and was 100ppm for H (Benninghoven *et al*, 1987).

This variation in the observed limits of detection, by five orders of magnitude, can be improved if the neutral atoms liberated by the primary ion beam and not the secondary ions are analysed. This technique is known as secondary neutral mass spectrometry, SNMS. There are several methods which have been used to ionise the secondary neutrals (Wittmaack, 1993). These include focused electron beams, low energy plasma, non-resonant multiphoton excitation and RIS. The use of non-resonant ionisation is known as surface analysis by laser ionisation - SALI (Becker and Gillen, 1985) The application of RIS has been termed SIRIS (Sputter Initiated RIS) and is the most common technique employed

for applying RIMS to solids (Parks, 1990). Using this technique sub-ppb detection limits have been reported by several groups. Workers at Argonne National Laboratory determined a detection limit for ^{56}Fe in a silicon wafer of 240ppt (Pellin *et al*, 1990). Atom Science Inc. have spent several years developing SIRIS technology (Thonnard *et al*, 1989) and have reported a detection limit of 0.3ppb for indium in silicon for an analysis which took less than three minutes. A similar analysis has been performed at Pennsylvania State University and a detection limit of 9ppt was reported (Pappas *et al*, 1989). This analysis took five minutes and consumed approximately one nanogram of the sample. An important aspect of SIRIS analysis is that impurity measurements down to the ppb level in metal matrices can be made quantitative using pure metal samples as calibration standards (Calaway *et al*, 1992). This reduces the effort usually required for quantitative analysis since a single standard can be used for determining concentrations spanning nine orders of magnitude.

§1.8 Laser ablation based techniques

There are several techniques for materials analysis which employ a focused laser beam to vaporise a solid sample. Laser beams used in this way have several advantages over the particle beams employed in the techniques used previously. Since laser beams are electrostatically neutral they can be used to interrogate insulating samples without causing the build up of charge on the sample surface. Laser beams do not need to propagate through a vacuum environment and can pass through magnetic and electric fields unaffected. The optics required to manipulate laser beams are simpler than those needed for particle beams. Unfortunately it is not possible to raster a laser beam over the sample surface to image the elemental composition of the sample. However images can be obtained using laser ablation if the sample is mounted on an automated stage that is scanned while the laser beam position remains unchanged (Arlinghaus *et al*, 1992). The spot size of a focused laser beam depends on the characteristics of the beam and on the focal length of the lens. In the absence of spherical aberration, the size of the focused spot is diffraction limited and for a Gaussian beam is given by $\frac{4\lambda f}{\pi D}$, where D is the diameter of the beam, f is the focal length of the lens and λ is the

wavelength of the laser radiation. It is therefore possible to decrease the spot size by decreasing the focal length of the lens or by increasing the diameter of the beam before the lens. However if $f/D < 10$, aberration becomes significant and the spot size will be greater than expected (Arrowsmith, 1990). The best focused spot sizes obtainable are comparable with the laser wavelength, submicron spots requiring ultraviolet wavelengths. The various techniques which employ laser ablation for sampling will be detailed below.

§1.8.1 Mass spectrometry

When a high power laser is focused onto a solid sample it causes the formation of a dense cloud of partially ionised material. Since the early nineteen-sixties the mass analysis of these ions has been performed in order to characterise the sample. There have been many combinations of different types of lasers and mass spectrometers and the technique has found application in many fields, these have been comprehensively reviewed (Kovalev *et al*, 1978; Conzemius and Capellen, 1980). Several commercial systems have been developed using tightly focused laser beams to perform microprobe analysis (Clark, 1989). This technique can be termed laser microprobe mass spectrometer (LAMMS). The commercial systems each have their own acronyms: LIMA (Kratos, Manchester, UK), LAMMA (Leybold-Heraeus GmbH, Köln, Germany) and LPMS (CEA-CEN, Grenoble, France). All of these systems use the fourth harmonic of Nd:YAG laser focused to micron dimensions and analyse the resulting ions with time-of-flight mass spectrometry. The incorporation of mass spectrometry requires that the sample must be in a vacuum environment. LAMMS is usually performed in a single shot analysis and causes craters in the sample several hundreds of nanometres deep (Mathews *et al*, 1989). The detection limits of LAMMS are of the order of 1ppm (Moenke-Blankenburg, 1989). However, the interaction of laser light with solids is a complex process and the ionisation is due mainly to the plasma processes, detailed in §2.9, and is therefore dependent on the ionisation potential of the analyte. Due to these factors the LAMMS technique is at best semi-quantitative. If the laser power is reduced so that only a single monolayer is ablated the ion yield is not characteristic of the surface composition. This poor correlation was determined to be primarily due to the ion forming step operating too close to its threshold power (Dreyfus, 1989). It

would therefore be beneficial if the neutral atoms liberated by the laser were analysed. It is possible to achieve this using either RIS or non-resonant ionisation, with these ions being analysed by mass spectrometry. However, this technique requires a detailed understanding of the mechanisms and characteristics of laser induced neutral atom liberation. A detailed review of this area has been performed and is reported in Chapter 2, along with an account of the previous studies which have interfaced laser ablation with laser ionisation, either for trace analysis or for studies of laser-material interactions.

§1.8.2 Inductively coupled plasma techniques

The inductively coupled plasma (ICP) is a very important tool in the trace analysis of solutions. It is used to atomise and excite the sample. The analyte can then be detected either by analysing the atomic emission with a spectrometer (ICP-AES) or by mass analysing the ions (ICP-MS). Laser ablation can be used to introduce solid samples to the ICP, thus greatly extending the applicability of the technique. The sample is placed in a small chamber and the laser is focused onto the surface through a microscope objective. The material liberated by the laser is then transferred to the ICP torch through a flexible tube. This material is mainly in the form of relatively large (0.1-10 μ m) particles. These particles are then atomised and excited by the high temperature in the ICP. The mechanism of particle formation depends on the nature of the sample (Thompson *et al*, 1990). Particles obtained from metal samples appear to have been produced from the molten solid, while brittle materials appear simply to be cleaved into sections. The limits of detection of laser ablation coupled with ICP-MS has been determined to be of the order of 1ppm for elements in copper (Arrowsmith, 1987). Similar limits were determined for laser ablation interfaced with ICP-AES (Thompson *et al*, 1981).

§1.8.3 Atomic emission spectroscopy

The direct observation^{of} atomic emission from laser produced plasmas is a relatively simple, yet highly versatile, technique for materials analysis that came to prominence shortly after the development of the laser. Several commercial systems were developed with the capability of performing analysis with spot sizes down to 10 μ m. The capability of the this technique to analyse a large range of samples with detection limits

down to 1ppm has been comprehensively reviewed (Dittrich and Wennrich, 1984; Adrian and Watson, 1984; Moenke-Blankenburg, 1989). This technique can be performed with the sample in the atmosphere, however, the precision and detection limits of the analysis can be improved if the sample chamber contains a low pressure of noble gas. Iida (1990) reported that the amount of material ablated per laser shot is highest under vacuum conditions and decreases as the pressure in the chamber is increased. However, Leis and co-workers (1989) found that the maximum emission signals were observed when a pressure of 140mbar of argon was present in the chamber. The role of the buffer gas is to confine the liberated material and changing the pressure changes the degree of confinement of the laser produced plasma. The pressure of 140mbar appeared to be the optimum pressure for the atomisation of molecules or clusters of atoms liberated by the laser. Under these conditions the amount of material removed was determined to be 30ng/shot and the single shot detection limit was 100ppm. The sensitivity of this technique can be increased by incorporating laser induced fluorescence spectroscopy -LIFS (Niemax and Sdorra, 1990), in which a laser beam is used to excite a resonant transition in the atom of interest. The fluorescence produced by the de-excitation of this state is observed through a spectrometer. The detection limits of this technique are markedly better than those for emission spectroscopy. A detection limit of 45ppb was determined for magnesium in a steel sample. The analysis required ten laser shots, consumed 300ng of sample and the absolute limit of detection was determined to be 5fg.

Chapter 2

Laser Ablation for Sample Atomisation

§2.1 Introduction

A considerable portion of this thesis is concerned with characterising and assessing laser ablation as a technique for atomising samples prior to their analysis by RIMS. Similar work has been undertaken by other researchers and a number of theoretical models have been developed. This chapter will begin by outlining the basic physical principles which result in the laser initiated liberation of material. This will lead to an account of the models developed to describe the velocity distributions of vaporised material, including the Maxwell-Boltzmann distribution and the Knudsen layer model. After considering the onset of plasma formation in the laser generated plume, the chapter will conclude with a review of the work of several researchers, which has been classified by the nature of the sample material and includes metals, semiconductors and insulators. This chapter discusses work which illustrates the current state of understanding of laser induced atomisation processes and also the applications of laser ablation as an atomisation technique for RIMS.

§2.2 Absorption of laser light

If it is to result in any lasting effect, laser radiation must be absorbed by the sample. This can be described classically, in terms of an electromagnetic wave in a homogeneous, non-absorbing medium, interacting with a discontinuity. The incident wave can be represented as:

$$\mathbf{E} = \mathbf{E}_0 e^{-i(\mathbf{k}\mathbf{r} - \omega t)} \quad - \text{Eqn.2.1}$$

Where \mathbf{r} is a vector in the direction of propagation, \mathbf{k} is the wave number, $k = \frac{2\pi}{\lambda} = \frac{\omega}{c/n}$, c is the speed of light, λ is the wavelength and n is the refractive index of the medium (in vacuum $n = 1$).

To describe the propagation of the beam in the sample medium requires the introduction of a complex refractive index $\mathbf{n} = n_1 + in_2$ (von Allmen,

1987). When inserted into Eqn.2.1 this modifies the plane wave propagation by the introduction an attenuation term: $\exp\left[\frac{\omega n_2 r}{c}\right]$. The effect of this term can be expressed as the absorption coefficient:

$$\alpha = \frac{2\pi n_2}{\lambda} \quad \text{- Eqn.2.2}$$

or in terms of the absorption length ($1/\alpha$), which is the depth into which the laser energy is deposited (for metals this is the order of tens of nanometres). Some of the incident laser energy is reflected from the sample, and this too is a material dependent function. For the idealised case of a wave normally incident on the plane boundary of a solid, the reflectance is given by the Fresnel expression:

$$R = \frac{\text{reflected irradiance}}{\text{incident irradiance}} = \left(\frac{n - 1}{n + 1}\right)^2 \quad \text{- Eqn.2.3}$$

The reflectance and absorption coefficient are both highly material dependent and are due to the nature of the interaction of light with the medium. Insulators and semiconductors have only bound electrons and interact only in the vicinity of interband transitions (transitions of valence band electrons to the conduction band). Metals which have free electrons in a Fermi sea interact quite differently. It is possible to illustrate the effect of the nature of the interaction on the reflectivity and absorption coefficient quantitatively (von Allmen, 1987), but only a qualitative description of the effects will be given here. The absorption coefficient of metals is usually relatively constant over the near visible spectrum, while that of semiconductors and insulators can vary by many orders of magnitude over this range. However, the reflectance of these materials is usually quite low while the majority of metals reflect very efficiently. Most metals reflect all of the incident light regardless of wavelength, and are essentially colourless. However, some metals, particularly Au, Cu and Ag, exhibit a marked change in their reflectance at wavelengths in the optical range, this is due to bound-type transitions from d-electrons, and is apparent in the colour of these materials.

The reflectance and absorption coefficients of materials (especially metals)

have been tabulated, although these values are usually for evaporated pure films. For bulk materials the value is usually lower due to surface irregularities and impurities. Laser irradiance can increase the surface temperature, as will be detailed in the next section. This and associated effects, such as surface film removal and melting, are believed to be responsible for the observed drop in the reflectivity of metals with increasing irradiance (Ready, 1971). The reflectivity for Q-switched laser irradiance above 10^8W/cm^2 was observed to decrease and fall to around 10% of the value prior to the illumination. Hence, laser energy can be coupled efficiently to a sample even if the original reflectivity is high.

§2.3 Laser induced heating

The effect of the incident laser radiation is to impart energy to the electrons in the sample. This energy is transferred to the lattice, through electron-phonon collisions, in the electron relaxation time τ_E . This is of the order of 10^{-13} s for metals. Hence, for a laser pulse with a duration, τ , of the order of nanoseconds it is reasonable to assume that thermal equilibrium is established. Therefore the concept of temperature is valid and it is possible to apply equations which model heat flow in a solid. For non-metals τ_E is between 10^{-12} to 10^{-6} s, depending on the material and on the irradiance. In these materials it is not always valid to consider the concept of temperature for nanosecond pulses and the laser-material interaction may be better described in terms of electronic (non-thermal) processes (Kelly *et al*, 1992a), as will be described in section §2.10.

If the concept of temperature is valid, the distribution of the heat inside the sample can be described by solutions of the heat conduction equation (Carslaw and Jaeger, 1959):

$$\nabla \cdot J(r,t) + \rho C \frac{\partial T(r,t)}{\partial t} = A(r,t) \quad \text{- Eqn.2.4}$$

where $J(r,t)$ is the heat flux (thermal energy in unit area per unit time), ρC is the heat capacity per unit volume, $T(r,t)$ is the temperature and $A(r,t)$ is the heat production per unit volume per unit time. To solve the above equation a relationship between heat flux and temperature is required. This relationship, sometimes called Fourier's Law, is given by:

$$J(r,t) = -K \nabla T(r,t) \quad - \text{Eqn.2.5}$$

where K is the thermal conductivity. Substituting Eqn.2.5 into Eqn.2.4 and making the assumption that the thermal properties of the irradiated material are independent of the temperature yields:

$$\nabla^2 T(r,t) - \frac{1}{\kappa} \frac{\partial T(r,t)}{\partial t} = -\frac{A(r,t)}{K} \quad - \text{Eqn.2.6}$$

where $\kappa = \frac{K}{\rho C}$ is the thermal diffusivity of the material.

This is the appropriate form of the heat-conduction equation for the practically important case of a semi-infinite slab, that is where the thermal diffusion length, $2\sqrt{\kappa t}$, is much smaller than the sample thickness. The appropriate boundary conditions for laser heating (Ready 1971) are that there is no heat flux across the sample surface ($z=0$), and the initial condition is $T(r,0) = T_0 = 300\text{K}$. Since the transverse dimension of the beam is considered large compared with the depth to which heat is conducted, the dependence on the x and y coordinates drops out. Therefore, Eqn.2.6 simplifies to:

$$\frac{\partial^2 T(r,t)}{\partial z^2} - \frac{1}{\kappa} \frac{\partial T(z,t)}{\partial t} = -\frac{A(z,t)}{K} \quad - \text{Eqn.2.7}$$

This equation can be solved for a variety of idealised laser conditions (Ready, 1971; Bechtel 1975), however, the results are broadly the same and only the simplest case will be discussed. Assuming that the incident laser has a uniform spatial energy distribution and has a flat temporal energy profile of duration τ , then the source term can be expressed as:

$$A(z,t) = I(1-R)\alpha e^{-\alpha z} \quad - \text{Eqn.2.8}$$

where I is the laser irradiance, R is the reflectance and α is the absorption coefficient, discussed in the preceding section. In that section it was mentioned that the absorption length is of the order of tens of nanometres for metals. As this is much smaller than the depth to which heat is

conducted, it can be assumed that the heat is produced at the surface. This leads to a simplified solution of Eqn.2.7, which, at $z=0$ is

$$T(0,t) = T_o + \frac{2I(1-R)}{K} \left(\frac{\kappa t}{\pi} \right)^{\frac{1}{2}} \quad \text{for } t < \tau$$

and

$$T(0,t) = T_o + \frac{2I(1-R)}{K} \left(\frac{\kappa \tau}{\pi} \right)^{\frac{1}{2}} \left[\sqrt{\frac{t}{\tau}} - \sqrt{\frac{t}{\tau} - 1} \right] \quad \text{for } t \geq \tau$$

- Eqn.2.9

This expression makes no allowance for energy lost in melting or vapourisation and the constants K , κ and R , which have been assumed constant, are in reality all temperature dependent. However, these equations are instructive in illustrating the basic characteristics of the laser induced surface heating. In order to illustrate the general effect of laser heating Fig.2.1 shows the solution of these equations for the irradiation of aluminium with a 10ns laser pulse. The room temperature values for thermal conductivity and thermal diffusivity have been used and a reflectivity of 50% has been assumed. It can be seen that a power of 10^7W/cm^2 , which corresponds to a pulse energy of 100mJ/cm^2 , raises the sample surface by only $\sim 100 \text{K}$. An incident power of 10^8W/cm^2 raises the surface above the melting point (933K), while a power of 10^9W/cm^2 would raise the sample surface to $\sim 10000 \text{K}$, which is above the critical temperature of aluminium ($\sim 6000 \text{K}$). However, as mentioned above, these equations neglect that some energy is expended by overcoming the latent heats of fusion and vapourisation. The volume heating generated by this model has been shown to extend to several microns into the sample (Ready 1971). This is in marked contrast to ion sputtering where the interactions occur within a few nanometres of the surface.

§2.4 Vaporisation

It is important to appreciate that some vaporisation of the sample will occur at all temperatures. The concept of boiling point, which is the temperature at which the vapour pressure exceeds the ambient, is not relevant for evaporation into vacuum. Kelly and Rothenburg (1985a) derived a formula which describes the rate of evaporation, R , from a laser irradiated sample which reaches a maximum surface temperature, \hat{T} :

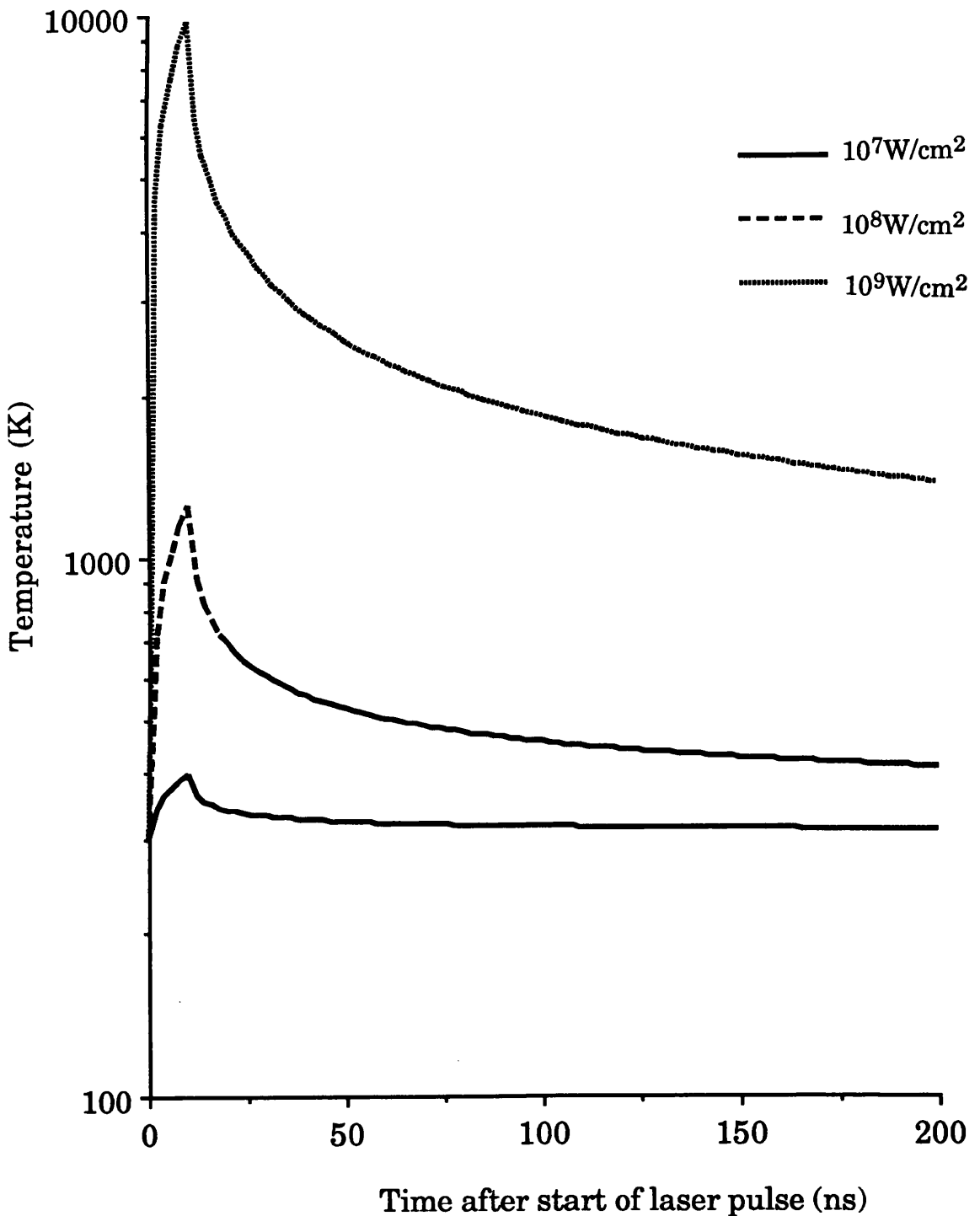


Fig.2.1 Evaluation of the surface source solution of the one dimensional heat flow equation (Eqn.2.9), for laser power densities of 10^7 , 10^8 and 10^9 W/cm². The sample is aluminium and the room temperature values for the thermal properties have been used. A reflectivity of 50% has been assumed.

$$R \approx \left[\frac{\hat{p}_{\text{atm}} \hat{T}^{1/2} \tau}{M^{1/2} \Delta H_v} \right] \times 1.53 \times 10^6 \text{ nm/pulse} \quad - \text{Eqn.2.10}$$

where \hat{p}_{atm} is the vapour pressure at \hat{T} (in units of atm), τ is again the laser pulse length (in nanoseconds), M is the mass of the sample in amu and ΔH_v is the heat of vaporisation (in electron volts). Vapour pressure as a function of temperature have been tabulated for all of the metallic elements (Alcock *et al*, 1984). For the case of aluminium irradiated with a 12ns laser pulse, R has the value of 3.7×10^{-2} nm/pulse at 2000K, which increases to 9nm/pulse at 4500K. Depending on the laser power and the material properties this may not be the main mechanism of material removal. Material may also be expelled in the form of droplets of molten material, which have a radius of several microns (Kelly and Rothenburg, 1985; Thompson *et al*, 1990). However, as the emphasis of this thesis is the application of laser ablation to the atomisation of samples, these mechanisms will not be discussed in detail here.

§2.5 Velocity distribution of the vaporised material

A very common approach to describing the velocity distribution of atoms or molecules liberated from the sample surface is to assume that they can be described by the Maxwell-Boltzmann velocity distribution:

$$\frac{dn}{n} = \left(\frac{m}{2\pi kT} \right)^3 \exp \left[- \frac{m(v_x^2 + v_y^2 + v_z^2)}{2kT} \right] dv_x dv_y dv_z \quad - \text{Eqn.2.11}$$

where $\frac{dn}{n}$ represents the fraction of atoms, or molecules, with velocities between v_x and v_x+dv_x , v_y and v_y+dv_y and v_z and v_z+dv_z . m is the mass of the particle, k is Boltzmann's constant and T is the characteristic temperature. As will become apparent from this chapter, this temperature may or may not represent the temperature of the surface.

The velocity distribution of the ablated atoms, or molecules, is of significance for two reasons. Firstly, as will be illustrated in this chapter, it can give insight into the mechanism which resulted in the atoms being ejected. Secondly, it is important in practical applications where a secondary mechanism is employed to detect the emitted material. Such an

arrangement is shown schematically in Fig.2.2. In the experiments reported in this thesis this secondary mechanism is a pulsed ionising laser, but many other techniques have been used to measure the neutral flux. These include electron ionisation coupled with quadrupole mass spectrometry, laser induced fluorescence spectroscopy (LIFS), atomic absorption spectroscopy (AAS) and laser interferometry.

The familiar form of the Maxwell-Boltzmann (MB) distribution:

$$\frac{1}{n} \frac{dn}{dv} = 4\pi v^2 \left(\frac{m}{2\pi kT} \right)^{\frac{3}{2}} \exp\left(-\frac{mv^2}{2kT} \right) \quad - \text{Eqn.2.12}$$

is derived assuming that the velocity components v_x , v_y and v_z are isotropically distributed. This is not the case for material liberated by a laser where the velocity is directed, in this notation along the z-axis. Assuming that the duration of material emission is much smaller than the time of flight to the secondary technique, the form of the Maxwell-Boltzmann distribution generally applicable to the time-of-flight arrangement shown in Fig.2.2, (sometimes referred to as the half-range Maxwell-Boltzmann distribution) is:

$$\frac{dn}{n} \propto \left(\frac{m}{2\pi kT} \right)^{\frac{3}{2}} \exp\left(-\frac{m}{2kT} \frac{d^2}{t^2} \right) \frac{1}{t^i} \quad - \text{Eqn.2.13}$$

where t is the delay between the ablation laser firing and the secondary technique and d is the distance from the sample to the laser beam or ioniser. The value of i is dependent on the experimental system, and is generally taken as 4 (Kelly and Dreyfus, 1988a). This is arrived at by assuming that the particles are emitted as a flux and that the sampling time is short (Kelly, 1992b). However Lazneva (1991) reports that for an arrangement involving electron impact ionisation and subsequent quadrupole mass spectrometry, a value of $i=2$ is appropriate. Kools *et al* (1992) have discussed the ambiguity arising around the value of i , and from considering the form of the Jacobian to transform from distance to velocity, came to the conclusion that $i=3$ was appropriate. However, as discussed by Kools and co-workers (1992), it is difficult to discriminate experimentally between the differing values of i . This is because the

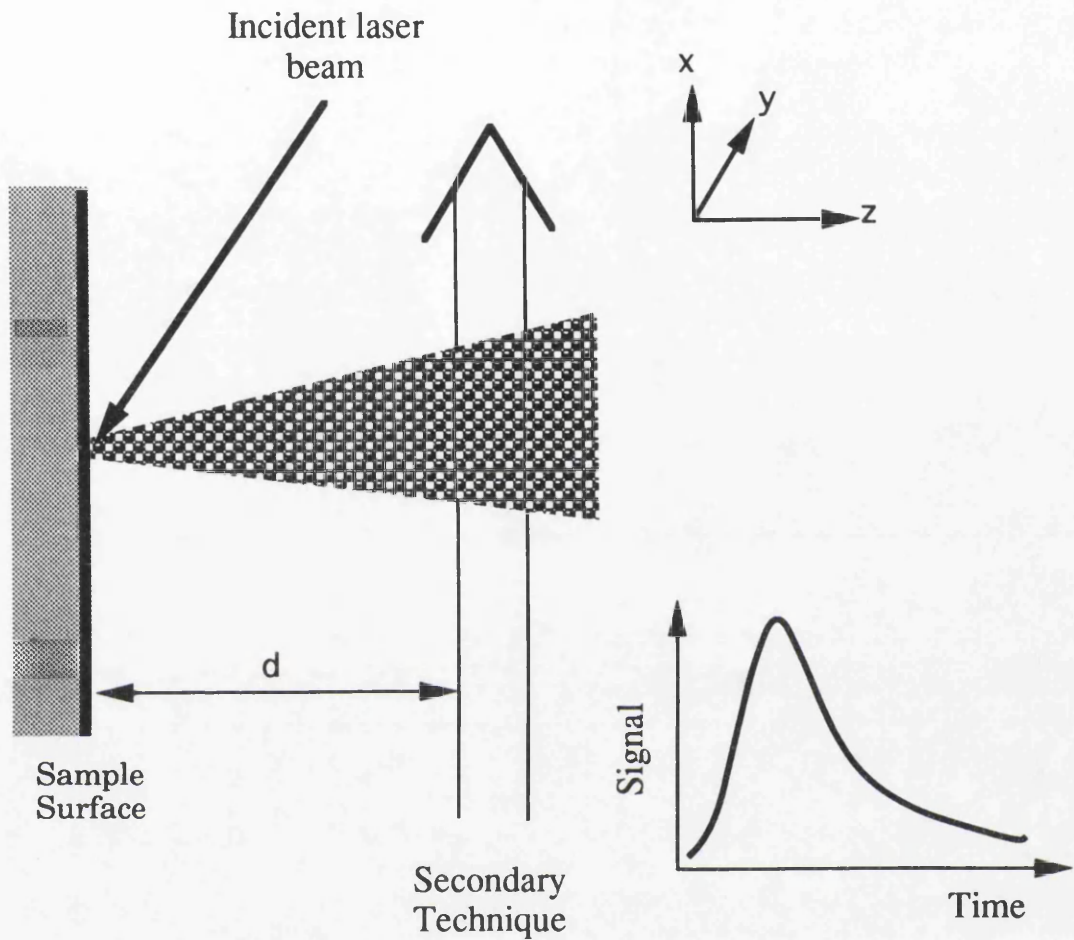


Fig.2.2 Schematic arrangement of an experiment to investigate the laser induced liberation of material. A pulsed laser beam is used to generate a plume which can be sampled by the secondary technique at a distance **d** from the sample surface. The plume is sampled at various times and a velocity distribution of the ablated material is obtained.

distribution is very sensitive to the value of the fitting parameters which occur in the exponential. A change of ~10-15% in these fitting parameters makes it impossible to distinguish between $i=3$ and $i=4$. Fig.2.3 shows the evaluation of Eqn.2.13 with different values of i , for the case of aluminium with a flight distance of 3mm and a characteristic temperature of 1000K. It can be seen that the effect of increasing the value of i is to increase the most probable velocity.

By differentiating Eqn.2.13 with respect to time, it becomes apparent that the characteristic temperature is related to the most probable velocity v_{mp} by:

$$T = \frac{mv_{mp}^2}{ik} \quad - \text{Eqn.2.14}$$

Once the appropriate value for i has been decided it is apparent that for a particular mass the main factor in determining the shape of the distribution is the characteristic temperature. This is illustrated in Fig.2.4 where the vaporised material is again aluminium. It can be seen that the shape of the distribution changes markedly from temperatures corresponding to the melting point (~900K) to the s.t.p. boiling point at 2700K. However, at higher temperatures small increases in temperature result in a less marked change in the distribution. This is because the peak of the distribution is determined by the most probable velocity and hence, from Eqn.2.14, the position of the peak is an inverse quadratic function of T . The characteristic temperature can be related to the energy at the peak of the distribution by:

$$\hat{E} = \frac{ikT}{2} \quad - \text{Eqn.2.15}$$

It is useful to appreciate that an energy of 1eV corresponds to a temperature of 11600K for a conventional Maxwell-Boltzmann distribution.

§2.6 Hydrodynamic velocity

The discussion in the preceding section has assumed that there are no interactions between the particles in the emerging plume. This is not

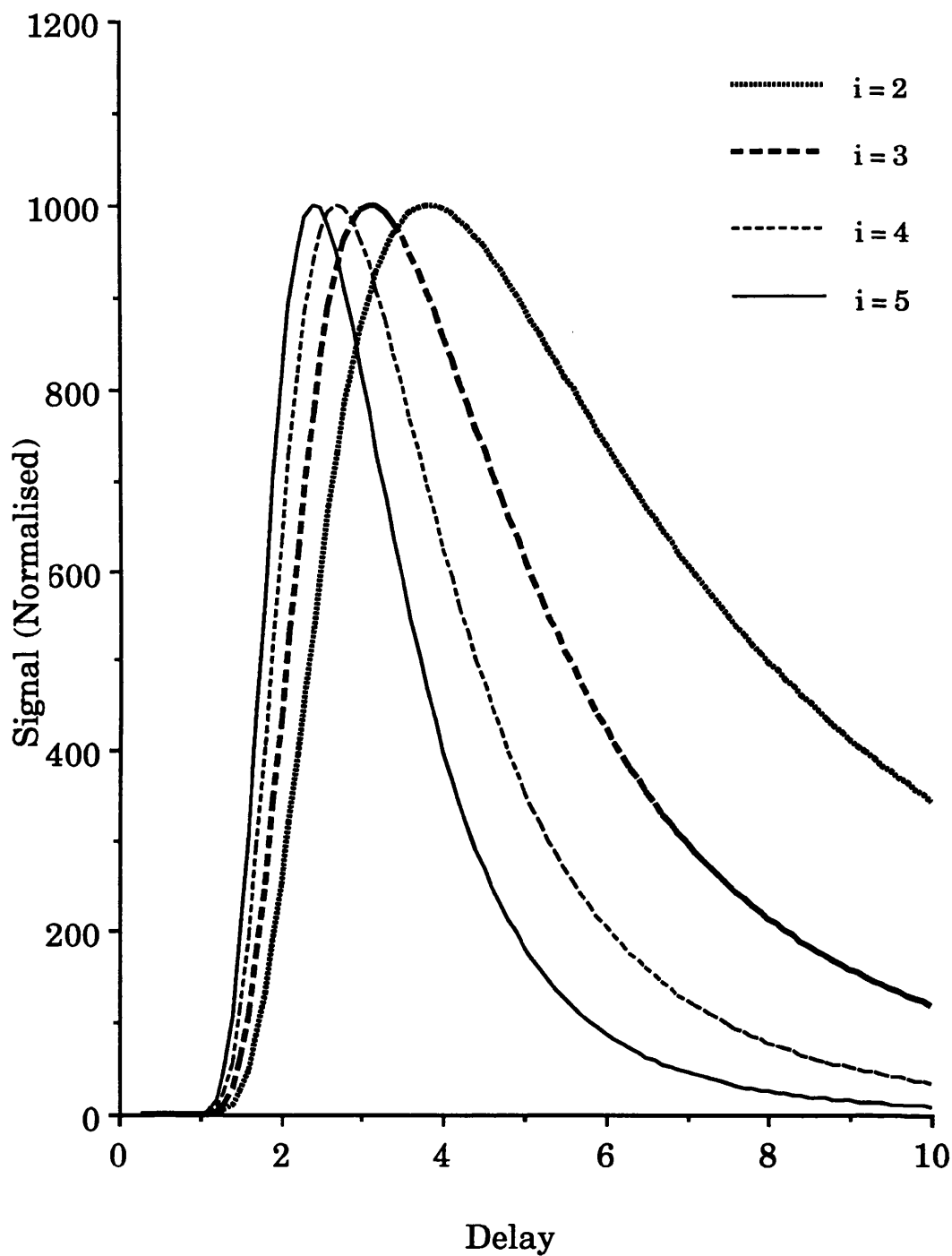


Fig.2.3 Evaluation of Eqn.2.13 for various values of i . The signals have been normalised to the same peak height. Increasing the value of i reduces the arrival time of the peak of the distribution. The sample is aluminium ($m=27\text{amu}$), the flight distance is 3mm and the characteristic temperature is 1000K.

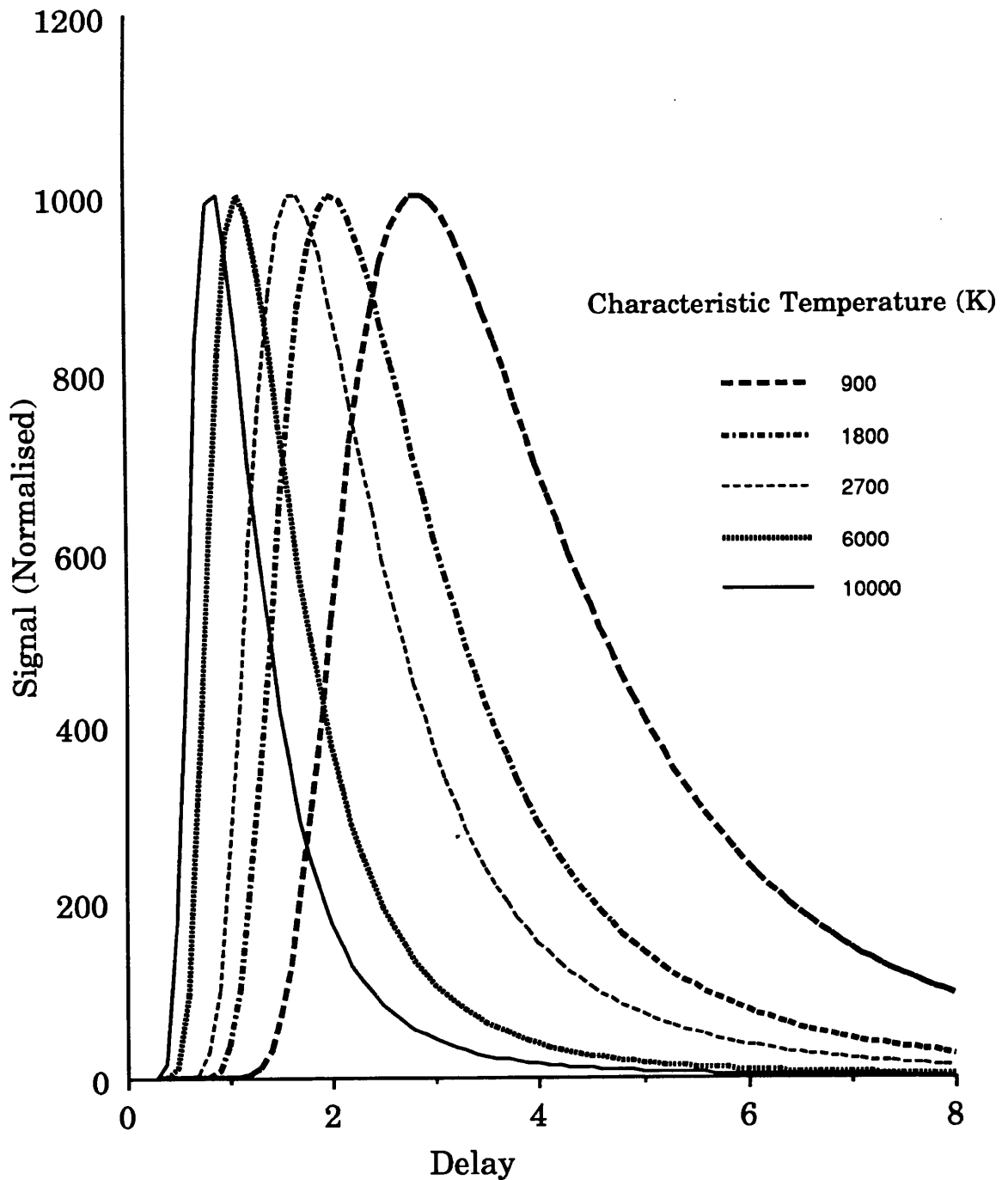


Fig.2.4 Evaluation of Eqn.2.13 for various characteristic temperatures. The signals have been normalised to the same peak height. Increasing the characteristic temperature reduces the arrival time of the peak of the distribution. A value of $i=4$ has been used and again, the sample is aluminium and the flight distance is 3mm.

necessarily the case, for example the vaporisation of a monolayer of silicon by a 60ns pulse results in a local pressure of approximately 3 torr (Bialkowski *et al*, 1990). If during collisions the transfer of energy to internal modes is negligible, the changes in velocity and direction of two colliding atoms or molecules are kinematically restricted, conserving the relative velocity and the centre of mass motion (Cowin *et al*, 1978). For hard sphere like collisions there is a strong tendency for the direction of the velocities of the two particles to lie closer to the centre of mass velocity after the interaction than they were before. For emission from a surface the centre of mass velocity lies along the surface normal. Hence the resulting distribution is that of a Maxwell-Boltzmann velocity distribution, superimposed on the centre of mass velocity. A model was developed to describe the pulsed electron beam sputtering and laser vaporisation of materials (Peugnet, 1977). This involves replacing the exponential term in Eqn.2.13 with:

$$\exp \left[-\frac{m}{2kT}(v-u)^2 \right] \quad \text{- Eqn.2.16}$$

where $v=d/t$ and u is a constant called the hydrodynamic velocity which represents the centre of mass motion. For the electron beam sputtering of aluminium u was determined to be 100m/s, while for laser bombardment u was 1000m/s. The effect of including a hydrodynamic velocity in the Maxwell-Boltzmann velocity distributions is shown in Fig.2.5 for aluminium with a characteristic temperature of 3000K. The effect of a positive hydrodynamic velocity is to increase the temperature, as calculated from the most probable velocity. The effect of the rather unphysical situation of having a negative centre of mass velocity is to reduce the temperature calculated from the peak of the distribution. It is therefore apparent that even if the characteristic temperature is the surface temperature, the temperature determined from the time-of-flight distribution is substantially different if gas phase collisions are taking place.

§2.7 Knudsen layer formation

The account of gas-phase interaction given in the preceding section was qualitative. A more quantitative formalism using gas dynamics, was initiated in the nineteen-sixties (Anisimov, 1968). A summary of how this

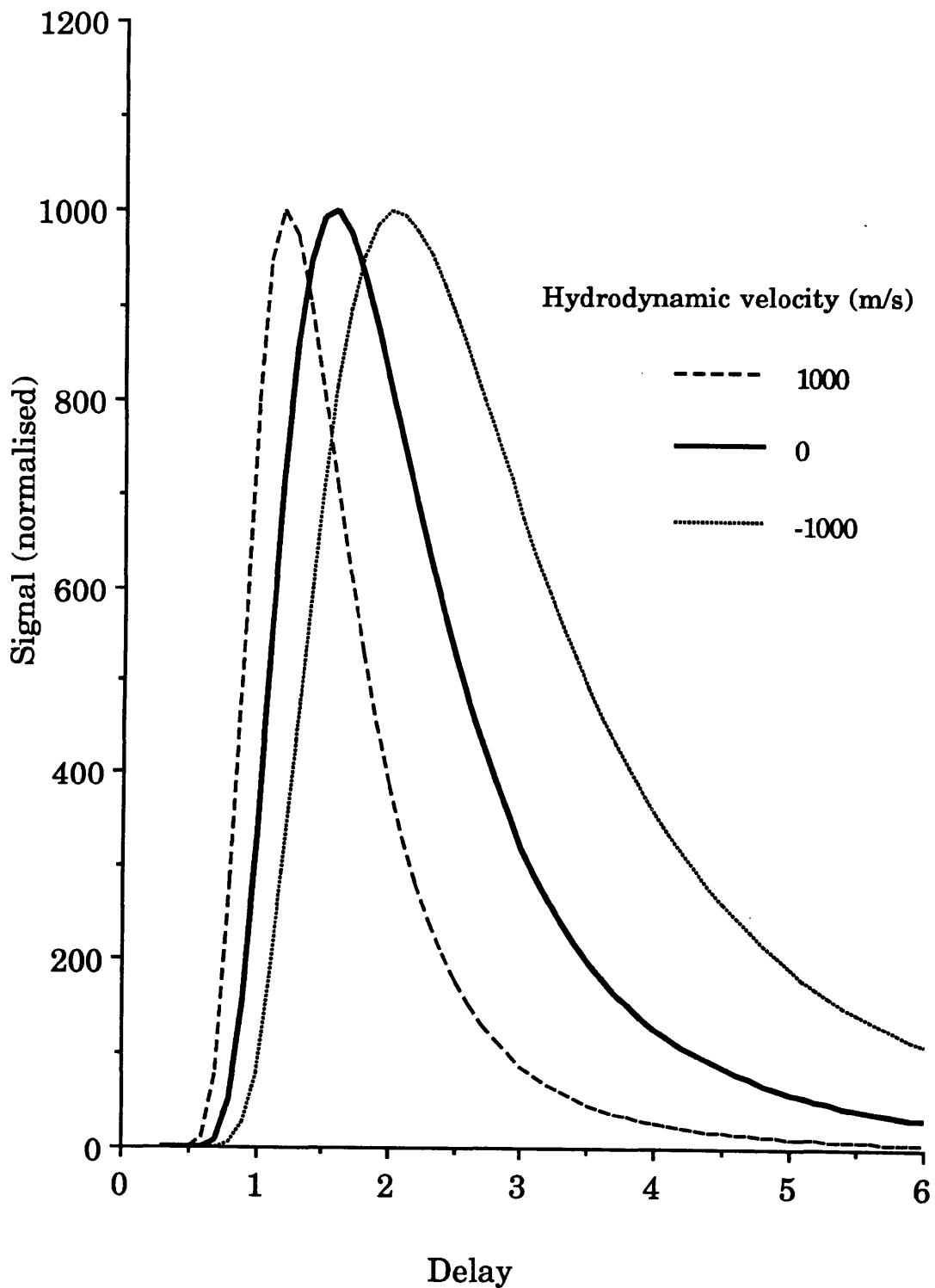


Fig.2.5 The effect of introducing a hydrodynamic velocity on the half-range Maxwell-Boltzmann distribution. The signals have been normalised to the same peak height. The characteristic temperature is 3000K, $i=4$, the sample is aluminium and the flight distance is 3mm.

Chapter 2

work can be applied to the situation detailed here has been recently given by Kelly and Dreyfus (1988a). The region in which the particles undergo collisions to form the centre of mass velocity is termed the Knudsen layer. Beyond the Knudsen layer boundary, no further collisions take place and free flight occurs. This is shown schematically in Fig.2.6. The resulting time-of-flight model is:

$$\frac{dn}{n} \propto \left(\frac{m}{2\pi kT_k}\right)^{\frac{3}{2}} \frac{1}{t^i} \exp\left[-\frac{m}{2kT_k}(v-u_k)^2\right] \quad \text{- Eqn.2.17}$$

where u_k is the centre of mass or flow velocity and T_k is the Knudsen temperature which is lower than the characteristic (or surface) temperature (T_c) by:

$$\left(\frac{T_k}{T_c}\right)^{1/2} = \frac{\left(\frac{\pi\gamma}{2}\right)^{1/2}}{2(j+4)} + \left[1 + \frac{\pi\gamma}{4(j+4)^2}\right]^{\frac{1}{2}} \quad \text{- Eqn.2.18}$$

where j is the number of degrees of freedom accessible to the vaporised particle, ($j=0$ for atoms) and γ is the heat capacity ratio:

$$\gamma = \frac{C_p}{C_v} = \frac{(j+5)}{(j+3)} \quad \text{- Eqn.2.19}$$

The flow velocity is approximately the speed of sound in the vapour, given by:

$$u_k = \sqrt{\frac{\gamma kT_k}{m}} \quad \text{- Eqn.2.20}$$

The effect of Knudsen layer formation is illustrated in Fig.2.7. This example is for aluminium atoms with a characteristic temperature of 3000K and shows the effect of Knudsen layer formation, with $j=0$, compared to the situation where no collisions take place. It can be seen that the effect of collisions is to increase the most probable velocity. The centre of mass velocity calculated from Eqn.2.20 is 1010m/s and the temperature of the distribution T_k is 67% of the characteristic temperature. Also shown in Fig.2.7, for illustration, is the effect of

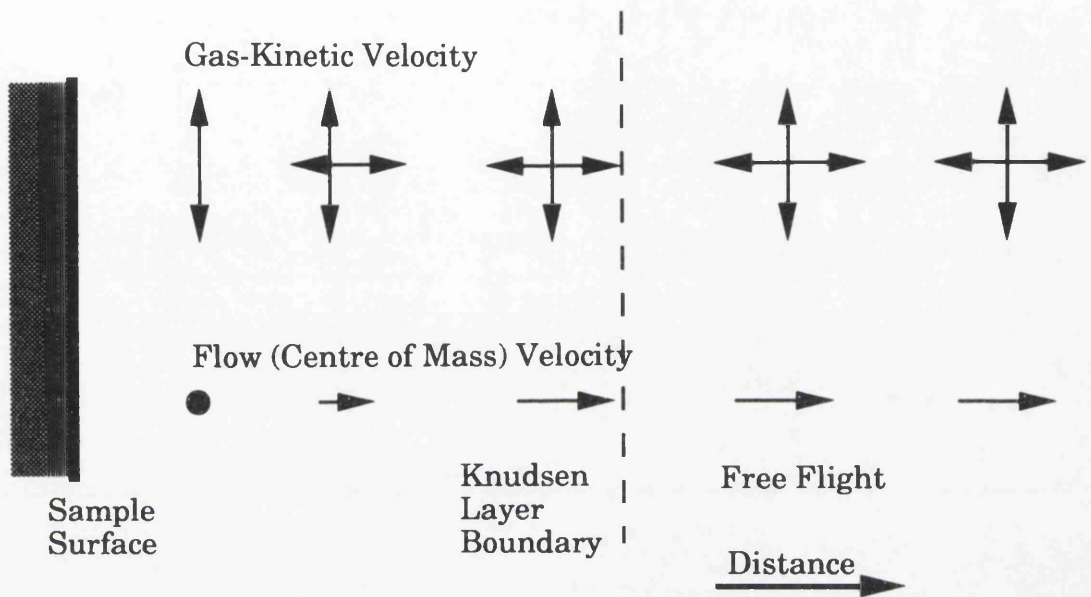


Fig.2.6 Schematic diagram of the Knudsen layer formalism. Collisions occur upto the Knudsen layer boundary, after which the distribution is described by the half-range Maxwell-Boltzmann distribution superimposed on the flow (or centre of mass) velocity.

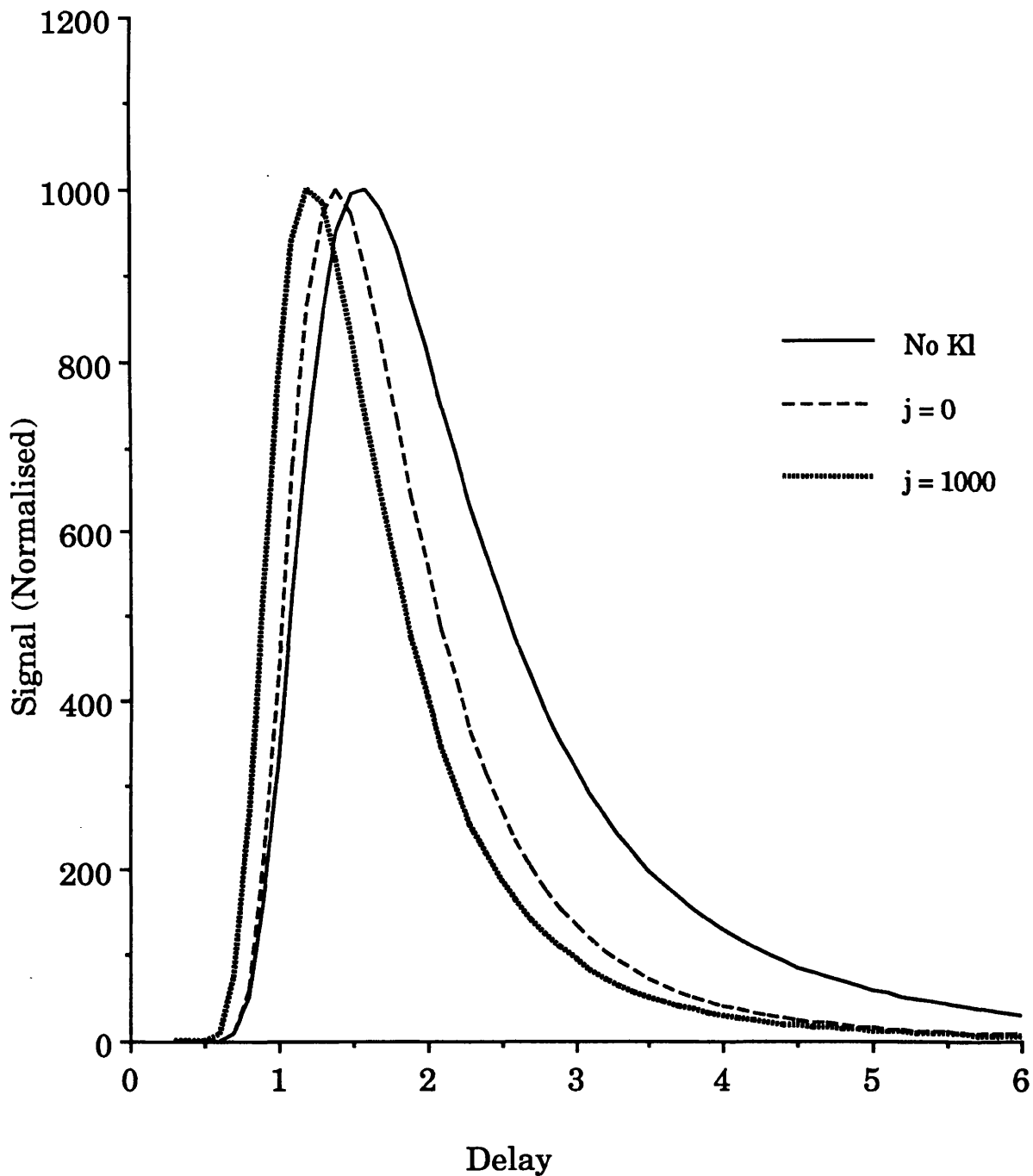


Fig.2.7 The effect of introducing the Knudsen layer formalism. It can be seen that the half-range Maxwell-Boltzmann distribution (no KL) has a lower most probable velocity than the Knudsen layer formalism with $j=0$, which represents a purely atomic beam. Also shown is the case of a Knudsen layer with $j=1000$, which represents an effectively infinite number of internal energy levels in the molecule. The signals have been normalised to the same peak height. The characteristic temperature is 3000K, $i=4$, the sample is aluminium and the flight distance is 3mm.

Knudsen layer formation with $j=1000$, which is effectively an infinite number of internal degrees of freedom. In this case the centre of mass velocity is 958m/s, which is lower than for $j=0$, however the temperature T_k is much higher, being 99.9% of the characteristic temperature.

For practical applications where a temperature is derived from fitting a model to experimental data, the Knudsen layer model will predict a temperature lower than that derived using a half-range Maxwell-Boltzmann distribution. From Eqn.2.15, the characteristic temperature is related to the peak of a half-range Maxwell-Boltzmann distribution, in the case of $i=4$, by:

$$kT_c = \frac{\hat{E}}{2} \quad \text{- Eqn.2.21}$$

In the Knudsen layer formalism this relationship is altered:

$$kT_c = \frac{\hat{E}}{\eta_k} \quad \text{- Eqn.2.22}$$

where the constant η_k depends on j . The relationship is (NoorBatcha *et al*, 1988):

$$\eta_k = \frac{8 \left\{ -\pi^{1/2} S + [4(j+4)^2 + \pi S^2]^{1/2} \right\}^2}{[(\gamma+16)^{1/2} - \gamma^{1/2}]^2 (j+4)^2} \quad \text{- Eqn.2.23}$$

where

$$S = \sqrt{\frac{j+5}{2(j+3)}}$$

Significant values for η_k are 2.52 for atoms ($j=0$), 2.8 for $j=2$, increasing to 3.28 for infinite internal degrees of freedom.

This model of vapour phase collisions has some other important aspects. The angular distribution of the sputtered material is of the form $\cos^p \theta$. For the situation under discussion:

$$P \approx (1+M)^2$$

where M is the Mach number. For the Knudsen layer model, $M=1$. Hence the effect of vapour phase interactions is to give an angular distribution of the form $\cos^4\theta$, that is to increase the forward peaking of the emitted vapour.

A more complex formalism has been developed using a Monte-Carlo simulation procedure (NoorBatcha *et al* 1987, 1988). This is the ellipsoidal Maxwell-Boltzmann distribution and differs from Eqn.2.17 in that it provides a global representation of the translational energy distribution of all the desorbed atoms or molecules. The difference from Eqn.2.17 is that there are two separate temperatures; T_z as before describing the velocity distribution in the direction normal to the surface and T_{xy} which describes the velocity in the plane of the sample surface. The ellipsoidal distribution has the form:

$$\frac{dn}{N} \propto v_{xy} \exp\left[-\frac{m v_{xy}^2}{2kT_{xy}}\right] \cdot \exp\left[-\frac{m (v_z - v_z^*)^2}{2kT_z}\right] dv_{xy} dv_z \quad - \text{Eqn.2.24}$$

where v_z^* is the most probable velocity of the desorbed atoms, or molecules, in the z -direction and *not* the mean velocity or the centre of mass velocity in the z -direction. The three parameters, T_{xy} , T_z and v_z^* are all functions of the number of collisions, and therefore depend on the amount of material removed per shot. It was found, from the Monte-Carlo simulation, that as the number of monolayers removed per pulse increased from 0.1 to 3.0 the number of gas phase collisions increased from 1.9 to 32.6. This corresponded to T_{xy} falling from 294K to 41K, and T_z increasing from 1055K to 2565K. That is, in agreement with the assertion of the Knudsen layer model, that as the amount of material removed per shot increases, the distribution of that material becomes increasingly forward peaked.

The above discussion has been concerned with ablation of a single species. When several species are sputtered from a multi-component system it has been held that collisions would result in all the species attaining the same energy and centre of mass velocity (Kelly and Rothenburg, 1988b). However, this has recently been questioned in experiments concerned

with the ablation of CuCl (Kools *et al*, 1992), where it was found that the data could be described by the ellipsoidal form of the Maxwell-Boltzmann distribution, as discussed above. The two main ablation products, CuCl (98amu) and Cu₃Cl₃ (294 amu), could be described by the same T_{xy} and T_z . However, v_z^* was 1200m/s for CuCl and 775m/s for Cu₃Cl₃, hence it scaled approximately as the inverse of the square root of mass. The fact that there are different values for v_z^* indicates the formation of two gas clouds, one containing mainly CuCl and the other, slower one, consisting mainly of Cu₃Cl₃. It was not ascertained if the two clouds were emitted simultaneously, and if the slower Cu₃Cl₃ cloud was emitted after the CuCl there would be no interactions between the two. Hence the mechanism of velocity convergence proposed by Kelly would not be possible. However, if the two plumes are emitted simultaneously the mechanism proposed by Kelly does not appear appropriate.

§2.8 Adiabatic expansion

As the number of collisions experienced by each particle increases to more than approximately 2-3, a planar unsteady adiabatic expansion begins (Kelly, 1990). This is a complex problem of gas dynamics and will only be dealt with briefly. The pertinent points are illustrated in Fig.2.8. With increasing distance the gas kinetic velocities, which are initially related by the half-range Maxwell-Boltzmann distribution, decrease. At the same time the flow, or centre of mass, velocity increases beyond u_K , the flow velocity for Knudsen layer formation. Thus, adiabatic expansion leads to a continuing decrease in the width of the velocity distribution, but causes little change in the most probable velocity. Hence, for determining temperatures from the most probable velocity in experiments where the particles are detected along the axis of flow, it is only of secondary importance whether adiabatic expansion takes place (Kelly and Dreyfus, 1988a). The Mach number which as discussed in §2.7, is 1 for Knudsen layer formation, can be as high as 8 for an adiabatic expansion. Thus as the number of collisions increases the resulting plume becomes highly directed along the surface normal.

§2.9 Plasma formation

The formation of a plume of vaporised neutrals has been discussed in the preceding section. However, the laser light can couple directly with the

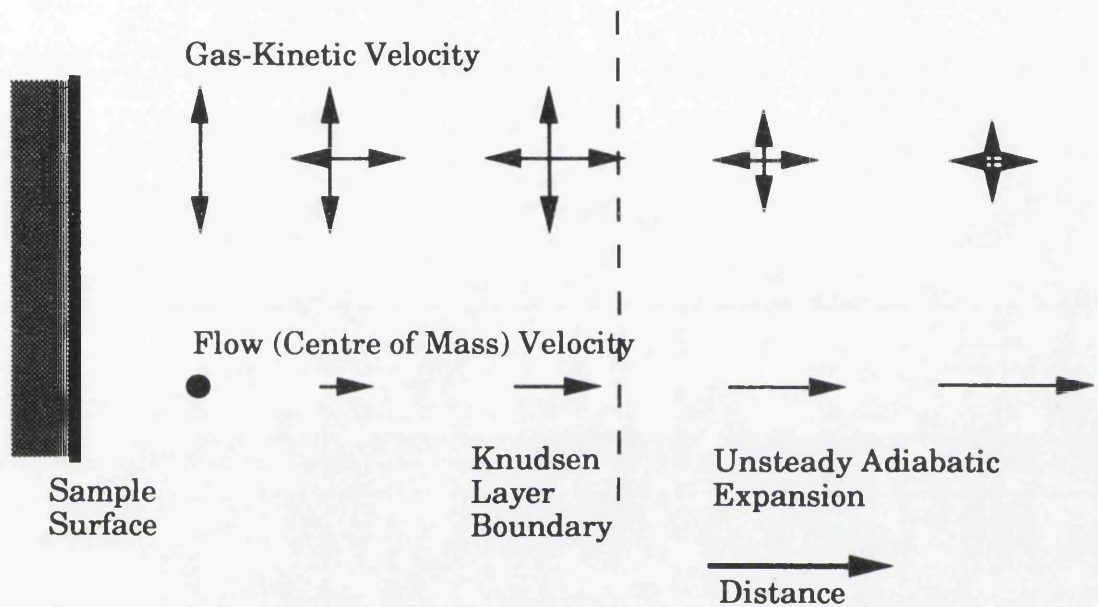


Fig.2.8 Schematic diagram of the effect of adiabatic expansion. In contrast to the Knudsen layer formalism the flow velocity continues to increase after the Knudsen layer boundary and the gas-kinetic velocity continues to decrease. This results in a pronounced forward peaking of the angular distribution.

plume to form a dense gas of ions and electrons, that is a plasma, in front of the target. This is a well known phenomenon which has been the subject of detailed investigation since soon after the invention of the laser. Laser induced plasma formation is of interest, both as an area of fundamental physics and as a practical analytical tool. As mentioned in §1.8, the composition of samples may be determined by mass analysing the ions generated in the plasma (Conzemius and Capellen, 1980; Kovalev *et al.*, 1978), or by optical spectrometry of the emission from the plasma (Adrain and Watson, 1984; Dittrich and Wennrich, 1984). In this section a brief discussion of the processes important in the formation of a plasma will be discussed.

Just as the nature of the laser-material interaction is highly dependent on the nature of both the laser and the sample, this is also true for the laser-plasma interaction. Direct multiphoton ionisation of the plume can be significant when the laser energy is high enough to allow two or three photon ionisation (Dreyfus, 1991). This is usually the case only for ultra-violet photons or if the vaporised material has a particularly low ionisation potential. However, for most situations a more important mechanism is absorption by the plasma, predominantly by inverse bremsstrahlung. This is a process where a free electron, in the Coulomb field of an ion or electron can absorb one or more photons and gain higher kinetic energy. These energetic electrons can then ionise neutral atoms or molecules through collisions. If collisional processes dominate over the other energy transfer processes of radiative decay and recombination, then local thermal equilibrium (LTE), will prevail. This means that the electrons transfer their energy to the ions and neutrals so that they can all be described by the same temperature. Hence the degree of ionisation in the plume can be determined from the Saha-Eggert equation:

$$n_e \frac{N_+}{N_0} = 2 \frac{Z_+}{Z_0} \left(\frac{2\pi m_e kT}{h^2} \right)^{\frac{3}{2}} \exp \left[-\frac{I - \Delta I}{kT} \right] \quad - \text{Eqn.2.25}$$

where n_e , N_+ , N_0 are the numbers of electrons, ions and neutrals respectively. Z_+ and Z_0 are the partition functions of the ions and atoms and h is Plank's constant. I is the ionisation potential and ΔI is the

reduction in the ionisation caused by the high electron density, which can be determined from Debye theory. It is possible to ascertain if a plasma is in LTE from the optical emission intensities of a particular species, and hence to calculate the electron temperature (Adrain and Watson, 1984).

A hydrodynamic model has been developed to describe the expansion of laser generated plasmas assuming LTE (Vertes *et al*, 1988;1989a,b;1990). This model demonstrates the effect of different laser wavelengths and powers on various sample materials. It has predicted the electron density and temperature in the plume and determined experimentally verifiable characteristics, such as crater sizes and relative sensitivity factors (RSF), with reasonable agreement with experiments. Hence, it is possible to gain considerable insight into the processes occurring in a laser generated plasma.

One of the important effects of plasma formation is that it acts to reduce the irradiance reaching the sample surface. This effect is also dependent on the laser wavelength since the absorption coefficient of a plasma has a sharp maxima in the vicinity of the plasma frequency:

$$\omega_p = \sqrt{\frac{n_e e^2}{\epsilon_0 m_e}} \quad \text{- Eqn.2.26}$$

The critical electron density, defined as when the plasma frequency is equal to that of the incident laser (Vertes *et al*, 1989a), determines when the plasma absorption becomes dominant over other processes. The critical electron density is $9.9 \times 10^{18} \text{cm}^{-3}$ for $10.6 \mu\text{m}$ CO₂ laser irradiation and increases to $1.5 \times 10^{22} \text{cm}^{-3}$ for the 266nm fourth harmonic wavelength of a Nd:YAG laser. Hence the coupling of longer wavelength laser beams to the sample surface is less efficient due to plasma absorption.

§2.10 Experimental measurements of laser induced neutral particle emission

Soon after the laser was invented researchers started to investigate material processing applications. Many of these studies involved using lasers to form macroscopically observable craters and investigating the highly ionised plasmas this produced. Most of this work utilised normal (not Q-switched) laser pulses which cause vaporisation distinctly different

to that resulting from irradiation by nanosecond pulses (Ready 1971). As has been previously mentioned, the application of laser ablation as an atomisation technique for RIMS requires an understanding of nanosecond laser pulse ablation in vacuum. Of particular importance are investigations of the velocity distribution of neutral atoms, as this is necessary in forming an understanding of how laser and material parameters affect the characteristics of the liberated material. This section will detail experiments involved with determining the velocity distribution of neutrals emitted from metals, semiconductors and organic and inorganic insulators.

§2.10.1 Metals

As mentioned in §2.5 neutral atoms liberated by the action of a laser beam form a dense cloud which can be detected in several ways. One of the earliest studies (Izawa *et al*, 1968), involved monitoring the light scattered from a ruby laser which was passed through the plasma generated by a Q-switched Nd:Glass laser irradiating a graphite sample. This technique is not particularly sensitive or selective, but it was determined that the density of the plume, measured 5mm from the sample, was reasonably constant from 10 μ s to 300 μ s after the pulse. Friichnicht (1974) used a more selective quadrupole mass spectrometer arrangement, shown in Fig.2.9, to characterise the energy spread of neutral atom beams produced by laser ablation. The quadrupole mass spectrometer was set to transmit the mass of the species of interest, while the electron impact cell ionises all of the neutrals in the plume after they have travelled the same distance. As the quadrupole is a continuous mass filter all of the neutrals of the selected mass produced by a single laser shot and arriving at the ioniser can be recorded. Hence, a complete velocity distribution for a particular species can be acquired in a single laser shot. The motivation for the work of Friichnicht (1974) was to produce atomic or molecular beams for studies of low energy collisions. The samples were thin films deposited on transparent substrates and were irradiated from the rear in order to reduce the effects of plasma formation. Using a comparatively high laser fluence of 36J/cm², beams of neutral atomic aluminium were formed which had average energies of ~5eV. Although this technique produced useful atomic beams, it is not appropriate for the analysis of unprepared

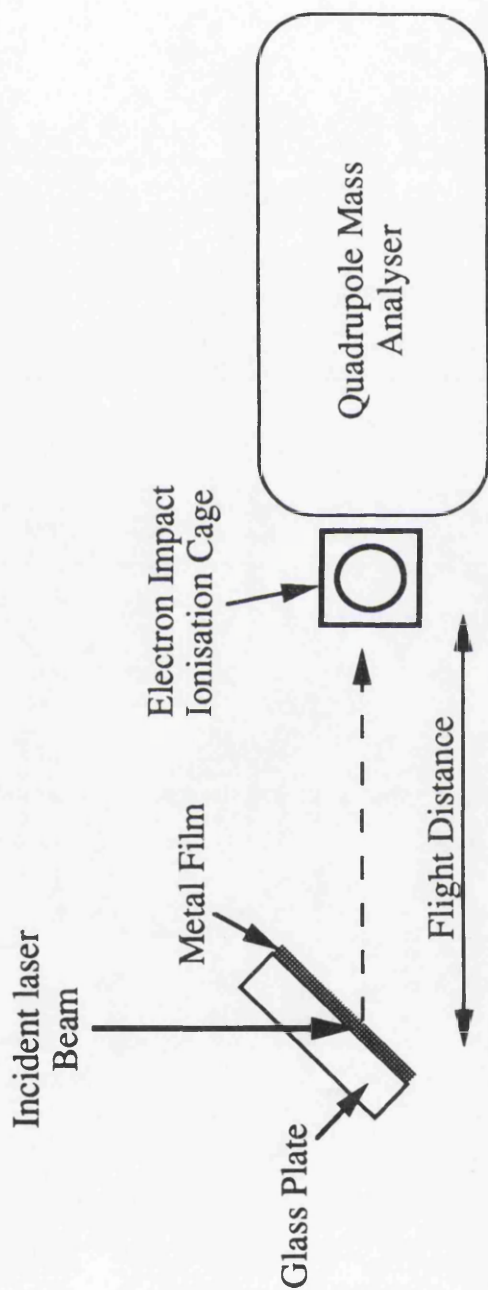


Fig.2.9 Schematic diagram of the arrangement for determining the velocity distribution of laser liberated neutrals utilising a quadrupole mass spectrometer with electron impact ionisation. As the quadrupole allows continuous transmission of one mass, a complete velocity distribution for one species can be determined from a single laser shot.

samples. A similar quadrupole mass spectrometry method was applied to investigations of bulk samples (Olstad and Olander, 1975a,b). No iron neutrals could be detected from an iron sample when the laser was Q-switched, but signals were obtained when normal pulses were employed and when Q-switched pulses were used to irradiate a binary solid (zirconium hydride).

As the technology of both lasers and detection systems has improved neutral particle emission from bulk metal samples has been observed by many researchers. Results of these studies where the velocity distribution of the emitted neutral atoms was investigated are shown in Table 2.1. As discussed in §2.3, the laser heating of metals can be described by thermal mechanisms, and therefore metals should be the most predictable system discussed in this chapter. It would be expected that the characteristic temperature determined from the Maxwell-Boltzmann distribution would be in agreement with the surface temperature, which would be above the melting point and below the critical temperature. Perhaps because it has been considered a deterministic system, relatively few systematic studies of the velocity distributions of atoms liberated from metals have been reported and the motivation of the experimenters has been different. Early work was concerned with investigating the process of laser vapourisation (Prengel *et al*, 1977; Selter and Kunze, 1982). The velocity distributions for Cu, Fe(110) and Cd were obtained during studies of laser induced desorption of gas molecules absorbed on these substrates. Nogar, Beekman and Towrie obtained velocity distributions while determining the optimum experimental arrangement for using laser ablation as an atomisation technique for RIMS. Some of the recent experiments; Dreyfus, Wang and Qu were concerned with characterising parameters for laser deposition of thin films.

Many of the temperatures determined in Table 2.1 are in reasonable agreement with what would be expected if ablation was due solely to thermal processes. The high temperature determined by Harnafi was attributed to the formation of an oxide film on the surface, which would increase the melting point. The extremely high time-of-flight temperature reported by Wang was consistent with that determined from the Doppler velocity distribution. They conjectured that the unexpectedly high

Principle Author	Year	Material	Melting Point (K)	Ablation Laser	Angle between beam & sample surface	Ablation Laser Wavelength	Power (W/cm ²)	Energy Density (J/cm ²)	Amount of material removed (monolayers)	Method of Analysis	Flight Distance (mm)	Velocity from peak of distribution (m/s)	Model	Kinetic Temperature from model (K)	Internal Temp. (K)
Dubreuil	1992	Fe	1808	Nitrogen		337		0.1 0.28	10 ⁻⁴	RIMS	6-11		Maxwellian	1800 3200	900 3300
Harnafi	1991	Li	454	CO ₂	90°	10.6μm	5*10 ⁸	0.8	~1	LIF and AAS	5-12	2445	Maxwellian with Knudsen Layer	8500-10000	
Lazneva	1991	Cd	594	Nd:YAG	45°	1064nm	3*10 ⁸			Electron impact ioniser and QMS			Maxwellian	700	
Qu	1991	U	1405	Nd:YAG	90°	1064nm				LIF			Maxwellian with Knudsen Layer		
Wang, H	1991	Al	933	Excimer	90°	248nm		0.3-6.5		LIF	1-3.5	5000	poor fit to Maxwellian	72000	
Odom	1990	NIST SRM479a Fe & Cr		Nd:YAG	90°	266nm	10 ⁹	5	~100	Non-resonant post-ionisation	0.6	1436	Maxwellian	8700	
Towrie	1990	Ca	1112	Nd:YAG	45°	355nm, 532nm & 1064nm	2.5*10 ⁷	.25		RIMS	2	995	Maxwellian with plume expansion	1758	
Dreyfus	1987	C (graphite)		Excimer	90°	351nm	2.5*10 ⁷	0.5		LIFS of C ₂	5-20	1770	Maxwellian	4600	3650 (Vib.) 4100 (Rot.)
Nogar	1985	Ta at 1200°C	3629	Nd:YAG	90°	1.064μm	10 ⁸	1		RIMS	16	1130	Maxwellian with hydrodynamic vel.		
Beekman	1984	Sm	1345	Nd:YAG	45°	1.064μm	10 ⁹	-9		RIMS	29	690	Maxwellian with hydrodynamic vel.	1100-1400	1600
Hussla	1984	Cu (90K)	1357	Excimer	45°	248nm	5.5*10 ⁸			Electron impact ioniser and QMS	218	3730	Maxwellian (least squares fit)	27000	
Leissmann	1984	Zr	2125	Nitrogen	90°	337nm	5*10 ⁶ - 5*10 ⁷	0.1-1		LIFS	2.25	3515	None		
Selter	1982	Ti	1933	CO ₂	90°	10.6μm	2*10 ⁸	10	< 1	LIFS	5.9	1400	Maxwellian	3300±400	545±75
Wedler	1982	Fe(110)	1808	Nd:Glass	45°	1.06μm	1.5*10 ⁷	0.45		Electron impact ioniser and QMS	220		Maxwellian	6300	
Beekman	1980	K	337	Nd:Glass	45°	1.06μm	10 ⁷	.3		RIMS	25	500	None	1100-1400	
Prengel	1977	Na Ta	371 3269	CO ₂	90°	10.6μm	3.8*10 ⁷	7.6		AAS	8	486 230	Maxwellian	598 917	

Table 2.1 Experiments that have studied the velocity distributions of atom liberated from metals by laser radiation. The abbreviations AAS - atomic absorption spectroscopy and LIF - laser induced fluorescence have been used.

temperature may be caused by explosive material removal due to uneven heating of the surface, or the effect of inverse bremsstrahlung. Most of the other measurements appear to be in approximate agreement with a thermal mechanism. Dubreuil, Dreyfus and Beekman also measured the temperature from the excited state populations, these temperatures were in approximate agreement with those determined from the time-of-flight distribution. However, this was not observed by Selter, who obtained an excitation temperature much lower than that determined from the time-of-flight distribution. To conclude, a compilation of the available velocity distributions shows that a thermal mechanism may describe much of this work, which encompasses various wavelengths and powers. However, there are several cases where a thermal mechanism does not offer a complete explanation for the experimentally observed characteristic temperature.

The application of laser ablation as an atomisation source for the trace analysis of metals by RIMS was first demonstrated for a stainless steel sample (Williams *et al*, 1984). The mass spectrometer was of the linear time-of-flight design and no other technique was used to suppress the ions produced directly by the ablation laser. Hence, a delay of 40 μ s was required between the laser pulses in order to eliminate this interference and this reduced the detection sensitivity of the system. However, ^{54}Cr which represented ~0.3% of the sample was detected in ~5000 laser shots. It was emphasised that the arrangement was far from optimal, and that a detection limit of sub parts-per-million (ppm) should be achievable, although it would require a greater number of laser shots. More recently the analysis of aluminium in a series of standard steels was attempted (Beekman and Thonnard, 1989). The variation of the RIMS signal with the concentration of aluminium in the sample is shown in Fig.2.10. The detection limit was of the order of ppm. It can be seen that there is large scatter and relatively poor linearity, even though this data was obtained after cleaning the sample with several high power laser pulses. However, the averaged signals were consistent, which seemed to suggest a systematic effect. Better linearity was recently obtained at Glasgow for gold in a series of copper samples (McCombes *et al*, 1991a), as will be detailed in Chapter 3.

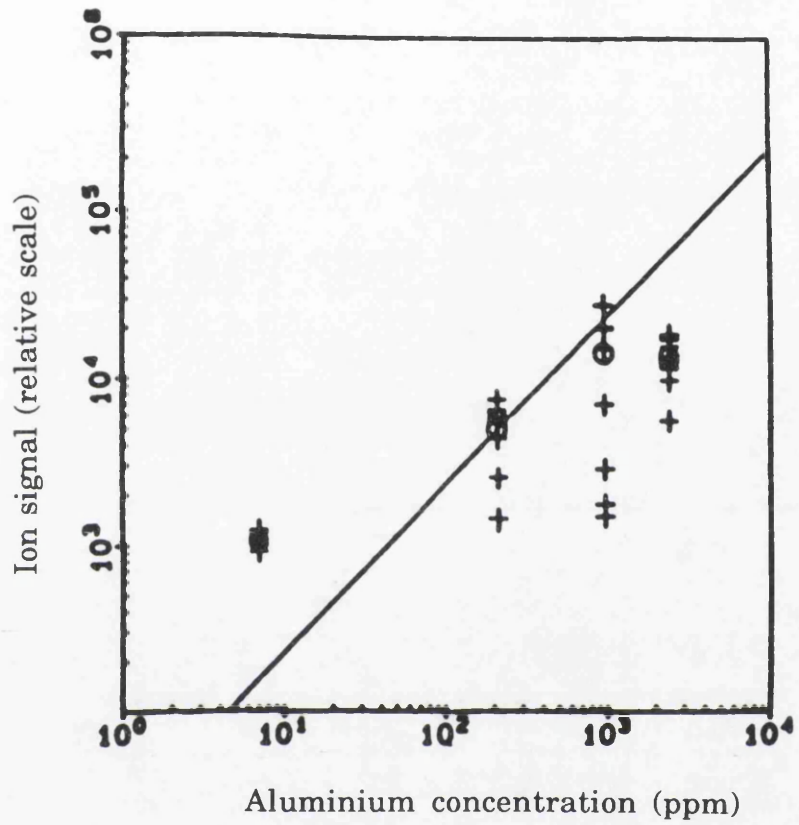


Fig.2.10 RIMS signal of aluminium against certified concentration for a series of steel samples (Beekman and Thonnard, 1989). The ablation laser beam was the second harmonic of a Nd:YAG with a wavelength of 532nm. An ablation laser power of $4 \cdot 10^7 \text{W/cm}^2$ was used for analysis. Prior to analysis the surface was cleaned with a higher laser power ($\sim 3 \cdot 10^8 \text{W/cm}^2$).

§2.10.2 Compound semiconductors

There have been many studies of the effect of laser light on ionic semiconductor crystals. The sputtering process is characterised by a threshold power (P_{th}) below which no emission of atoms is observed. Above this threshold power there is a non-linear dependence of the neutral particle yield on the incident laser power. The nature of the sputtering process depends on whether the energy of the incident photon is above or below the band gap energy (E_{gap}) of the bulk material. Most reported work has involved laser photons above the bandgap energy but the case where the wavelength is below the bandgap (subgap photons) will be considered first.

§2.10.2.1 Photons below the bandgap energy

The bulk optical absorption coefficient of compound semiconductors is several orders of magnitude lower for subgap photons than it is for photons with energy above that of the bandgap. It would be expected therefore, that subgap photons would produce no appreciable heating of the surface. However, particle ejection is still observed above a threshold laser power which does not differ greatly from that for photon energies above the bandgap. Measurements for GaP showed that P_{th} for the emission of Ga neutrals increased as the photon energy was increased above the bandgap (Hattori *et al*, 1990). The detection limit for these studies was estimated to be 10^{-5} monolayers per shot.

The mechanism for the interaction of subgap photons with compound semiconductors presented by Nakai *et al*, (1991), is that the photons excite exciton states, which, because of the weak nature of the electron lattice coupling in these materials are not self trapped and hence the energy is not localised. However, it is contended that localisation of two holes is possible at defect sites on the surface where the interaction could release tremendous lattice energy resulting in the ejection of an atom. This model would account for the observed threshold power required for particle emission since to induce two hole localisation the two holes must overcome the Coulomb repulsion. The probability of this happening increases dramatically as the number of generated electron hole pairs, (sometimes referred to as the e-h plasma) increases. For the typical parameters applicable for these experiments it was calculated that subgap

photons should produce a 5% concentration of e-h pairs on the surface. Photons above the bandgap energy produce more e-h pairs due to interactions in the bulk, which increases the supply of e-h pairs to the surface. However, Auger recombination in the bulk acts to cancel this effect. It is not surprising, therefore, that threshold powers are similar above and below the bandgap.

The number of Ga atoms desorbed per shot from a clean GaP(110) surface was observed to change with repeated irradiation on the same area, and this dependence was a function of the laser fluence, as shown in Fig.2.11 (Nakai *et al*, 1991). This can be explained if the sputtering mechanism involves energy localisation at surface defects. If the defect is an atom in an interstitial site (an adatom), which is sputtered as a result of the interaction, the number of sites available for sputtering is decreased. If the defect is a step (or an island of adatoms) sputtering will produce no change in the number of defect sites, and hence sputter yield will be constant as a function of the number of laser shots. However, if the defect is a vacancy, a second vacancy will be formed as a result of the interaction, and the sputtering yield increases with the number of shots. Progressively higher energy is needed to sputter from adatom sites, steps or vacancies. The effect of increasing the incident laser power would be to go from a regime where the number of desorbed atoms starts high, and then reduces with the number of shots, to one where the number of sputtered atoms starts low and then increases. This is the behaviour shown in Fig.2.11. This dependence of yield on the number of laser shots is therefore a way of differentiating between different sputtering mechanisms. It has been shown using this technique that as the photon energy passes above E_{gap} the sputtering mechanism of Ga from GaP changes (Hattori *et al*, 1990).

Studies of the laser desorption of Cd and Se₂ from CdSe, using electron impact ionisation and a quadrupole mass spectrometer, have reported two components in the temporal distribution (Lazneva 1991). One component is described by a high characteristic temperature, $T=5600\text{K}$, while the second, slower, component corresponds to $T=300\text{-}700\text{K}$. The ruby laser used for ablation had a photon energy just over E_{gap} . The dependence on the laser power of the number of atoms characterised by the high kinetic

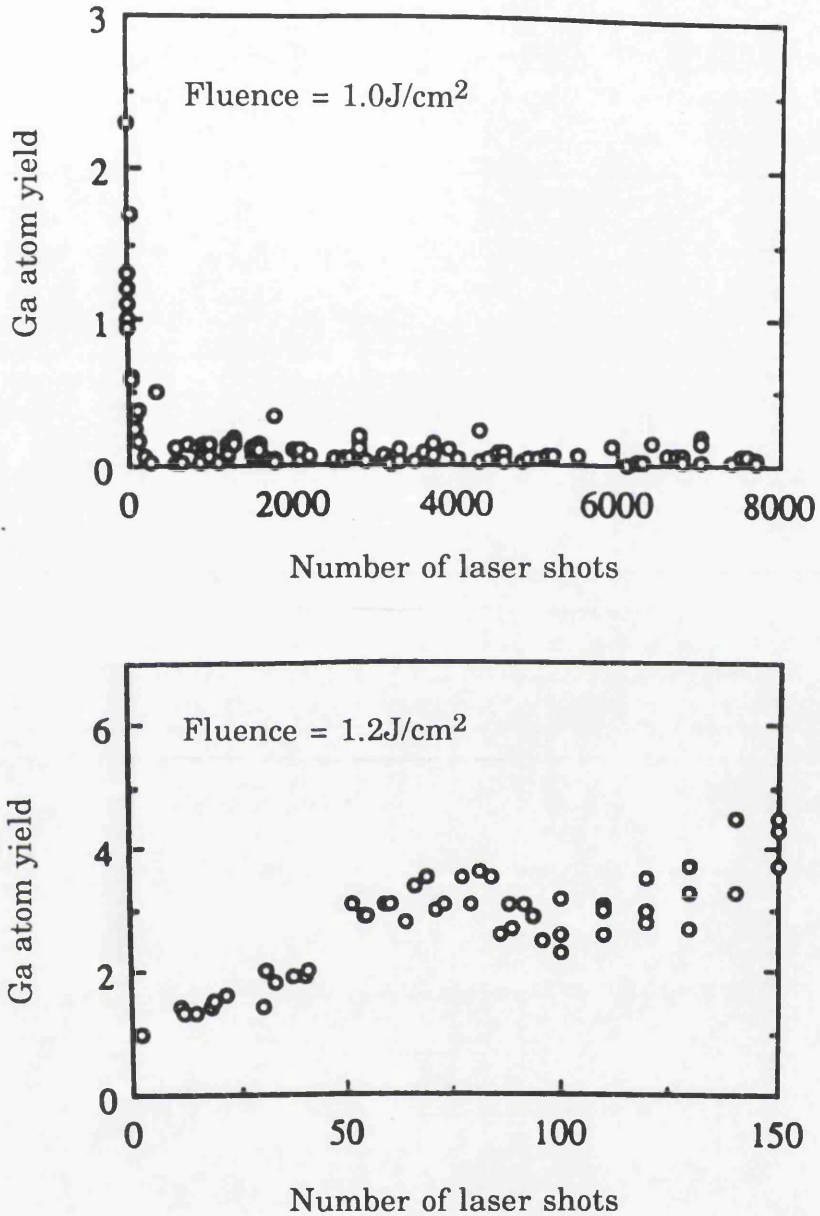


Fig.2.11 Effect of repeated irradiation of a GaP(110) surface by laser radiation with a photon energy below the bandgap energy (Nakai *et al*, 1991). With the lower fluence (upper graph) the Ga atom yield starts high and falls with repeated irradiation. With higher fluence the Ga atom yield increases with repeated irradiation. This difference is believed to be due to the nature of the defect site at which atom ejection takes place. As detailed in the text at the lower power the defect is an adatom, while at the higher power it is a vacancy. The laser wavelength is 600nm.

temperature was linear, while the slow component showed a clear threshold power and a much larger rate of increase. This is shown in Fig.2.12. Although no results were reported for the wavelength dependence of the emission of Cd or Se₂, the kinetic temperature of oxygen desorbed from CdSe was observed to be highly dependent on the incident photon energy, as illustrated in Fig.2.13. With a wavelength of 532nm (above E_{gap}) the fast component, with a kinetic temperature of ~1900K, is dominant. However, for laser irradiation below E_{gap} (1064nm) the slow component, which has a kinetic temperature of ~300K, begins to dominate the distribution. It should be emphasised that the power of the 532nm laser beam was 1.3*10⁸W/cm² while for the 1064nm wavelength it was necessary to increase the power to 21*10⁸W/cm² before any appreciable desorption was observed. The conclusion from these experiments was that when the photon energy is below E_{gap} impurity absorption is dominant leading to the thermal excitation and desorption of molecules in loosely bound surface states. The fast component of the velocity distributions is believed to be related to the concentration of photo-excited carriers that are captured by absorption centres to cause particle ejection. Although this mechanism appears feasible, two component velocity distributions have been reported only occasionally. However, this may be because most of the experiments reported in the ensuing sections use ultra-violet wavelengths, which may act to mask the effects mentioned above.

§2.10.2.2 Photons above the bandgap energy

The sputtering of compound semiconductors by visible and ultra-violet lasers has been studied extensively. The energy of these photons is usually above the band gap energy of these materials, however, as will be discussed in this section, the processes leading to desorption are believed to be of a non-thermal nature. The irradiation of ionic semiconductors normally results in the desorption of atoms of the metallic element and neutral dimers of the non-metallic element in approximately the same amount. The yield of single atoms of the non-metal is much lower. As has already been mentioned the sputtering is characterised by a threshold power. Above the threshold power the yield is characterised by a power law of the form $Y(\theta) \propto I^n$, where Y is the yield and I is the laser intensity (Namiki *et al*, 1985a). For CdS, the yield of Cd and S detected normal to the sample surface has been determined to be described by a value of n=17

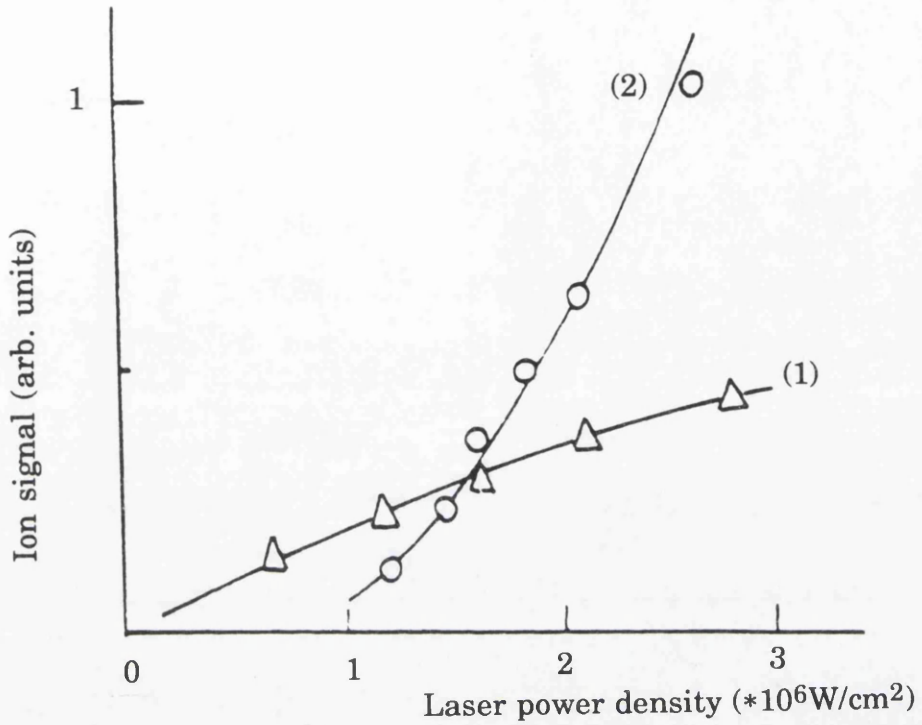


Fig.2.12 Effect of increasing laser power density on the number of Cd atoms desorbed from CdSe described by a fast (1) and slow (2) component of the velocity distribution (Lazneva, 1991). The ablation laser wavelength is 532nm.

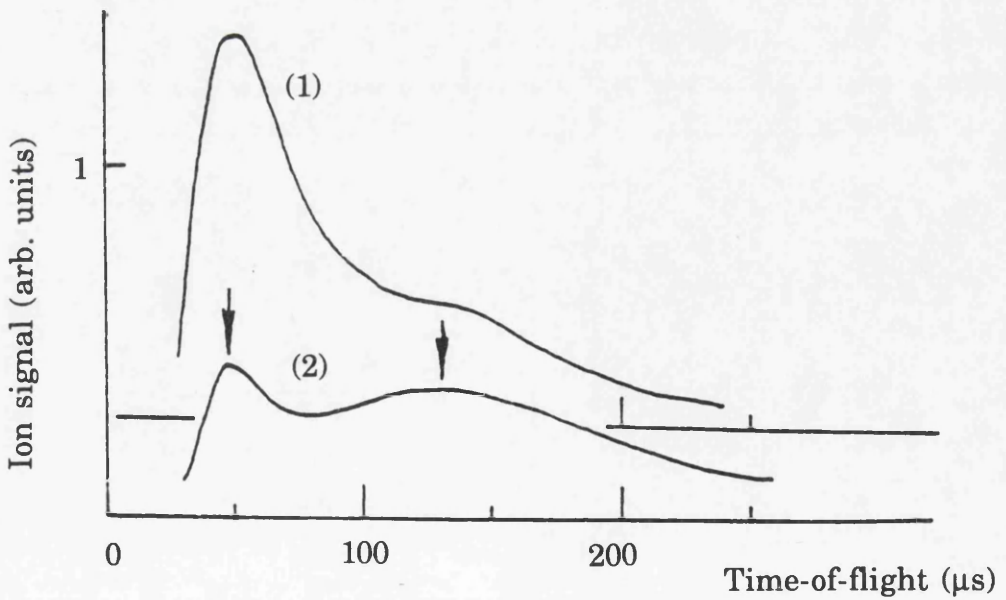


Fig.2.13 Time-of-flight distributions of O₂ desorbed from a CdSe surface (Lazneva, 1991). (1) Laser wavelength of 532nm (above E_{gap}), power density of $1.3 \cdot 10^6$ W/cm². (2) Laser wavelength of 1064nm (below E_{gap}), power density of $21 \cdot 10^6$ W/cm². The fast component is more pronounced at the higher photon energy.

for a substrate temperature of 115K. This falls to $n=8$ for a substrate temperature of 568K. The threshold power also depends on the substrate temperature, being lower at higher temperatures.

These investigations involved repeated irradiation of the same area. The ejection yield has been observed to decrease with an increasing number of shots. For a GaAs sample the rate of decrease of As was much slower than that of Ga (Namiki *et al*, 1985b), and Ga rich precipitates were observed on the surface. The rate of decrease of the As and As₂ signals was not the same. This led to the conclusion that As and As₂ are formed by different mechanisms, and are not due to the fragmentation of the same material by the electron impact ioniser. Preferential sputtering has also been observed in InP, in a study using a nitrogen laser for sputtering and RIMS to detect the emitted material (Dubreuil *et al*, 1992). Again it was the non-metallic element (phosphorous) that was removed initially, leading to the surface becoming indium rich. The surface structure was observed to be modified. However, after ~5000 shots the yield of indium and phosphorous became constant and approximately equal. Similar behaviour was observed in the behaviour of a CdTe(100) surface after irradiation with a KrF excimer laser (Brewer *et al*, 1991). For laser fluences above 40mJ/cm² the surface became rich in Te. However, at lower fluences the surface retained the original stoichiometry. As it was possible to return a Te rich surface to the normal stoichiometry by irradiating it at the lower fluence it was postulated that two processes were competing. At the higher power the formation of Te₂ adsorbed to the surface dominates over the lower energy process of Te₂ desorption. These results illustrate that the composition of the surface after irradiation is another sensitive characteristic of the desorption process.

Studies of the time-of-flight distributions of atoms desorbed at different angles is a powerful technique for elucidating the desorption process. One of the most detailed studies has been undertaken by Namiki and co-workers. These experiments used a nitrogen laser, which generates pulses of 337nm wavelength with a duration of 5ns. The atoms liberated from the surface are analysed by a quadrupole mass spectrometer using an arrangement similar to Fig.2.9, with the laser beam incident on the front surface of the sample. The target is rotatable so that the atoms

emitted at different angles can be analysed (Namiki *et al*, 1985b), although the angle between the incident beam and the sample is also changed. Using this arrangement the laser desorption of CdS, GaAs, GaP and GaN has been investigated. In order that the information can be easily interpreted it is analysed in the following way (Namiki *et al*, 1986). The total yield is defined as:

$$Y(\theta) = \sum_i \frac{d}{t_i} \frac{dn(t_i)}{dt_i} \Delta t_i \quad - \text{Eqn.2.27}$$

where d is the distance from the sample to the ioniser, t_i is the time-of-flight to the ioniser, $\frac{dn(t_i)}{dt_i}$ is the recorded time-of-flight signal for the i th channel and Δt_i is the width of the channel. The term $\frac{d}{t_i}$ is introduced because the ionising efficiency of an electron impact ioniser is velocity dependent. Using this definition it is possible to evaluate both the average velocity and the average squared velocity of the neutrals:

$$\bar{v}(\theta) = \sum_i \frac{1^2}{t_i^2} \frac{dn(t_i)}{dt_i} \frac{\Delta t_i}{Y(\theta)} \quad - \text{Eqn.2.28}$$

$$\overline{v^2}(\theta) = \sum_i \frac{1^3}{t_i^3} \frac{dn(t_i)}{dt_i} \frac{\Delta t_i}{Y(\theta)} \quad - \text{Eqn.2.29}$$

In this work Eqn.2.13 was used with $i=4$. If the sputtered material can be characterised by this velocity distribution the ratio $\frac{\overline{v^2}(\theta)}{\bar{v}^2(\theta)}$ can be evaluated as $\frac{32}{9\pi}$. It is therefore possible to evaluate how well the experimental time-of-flight distribution corresponds to a Maxwell-Boltzmann distribution, by defining the speed ratio:

$$S(\theta) = \left(\frac{32}{9\pi} - 1 \right)^{\frac{1}{2}} \left(\frac{\overline{v^2}(\theta)}{\bar{v}^2(\theta)} - 1 \right)^{\frac{1}{2}} \quad - \text{Eqn.2.30}$$

This will be unity if the experimental distribution corresponds to a Maxwell-Boltzmann distribution. If, however, it is narrower, the average

velocity squared will be greater than the averaged square velocity and $S < 1$. Conversely if the distribution is broader than a Maxwell-Boltzmann, $S > 1$. If all the atoms or molecules have the same energy, $S = 0$. It is also possible to define an angle dependent average energy:

$$\overline{E}(\theta) = \frac{m\overline{v^2}}{2} = 2kT_{\text{Trans}} \quad \text{- Eqn.2.31}$$

It should be pointed out that this definition will result in a marginally different temperature to Eqn.2.15 which relates the temperature to the most probable velocity.

The velocity distribution of the emitted neutrals changes as the angle of the analyser with respect to the surface is varied. This becomes more pronounced as the laser power is increased. For S_2 from CdS the speed ratio was ~ 1 at normal incidence, as shown in Fig.2.14, indicating that the velocity distribution is Maxwell-Boltzmann (Namiki *et al*, 1986). However, at larger angles the speed ratio becomes greater than unity, indicating that the experimental velocity distribution becomes broader than the Maxwell-Boltzmann distribution. The degree of deviation became larger as the laser power was increased. As shown in Fig.2.15, $\overline{E}(\theta)$ was also observed to be dependent on the angle of emission, being far larger at normal incidence. This effect becomes more prominent as the laser power is increased.

Studies of GaP and GaAs samples have shown that the angular dependence of the speed ratio, and the effect of increasing power on the yield and $\overline{E}(\theta)$, is not affected by changing the crystallographic orientation of the surface (Namiki *et al*, 1987). It was concluded that the desorption process was not due to unimolecular dissociation but occurred via events in the bulk. The amount of material sputtered in these studies was determined, using an electro-mechanical stylus, to be a fraction of a monolayer at low powers. This rose to 5-10Å per pulse at the highest power used.

Forward peaking of $\overline{E}(\theta)$ was also observed for As_2 and Ga from GaAs. However, the average energy of Ga from GaN was observed to be much

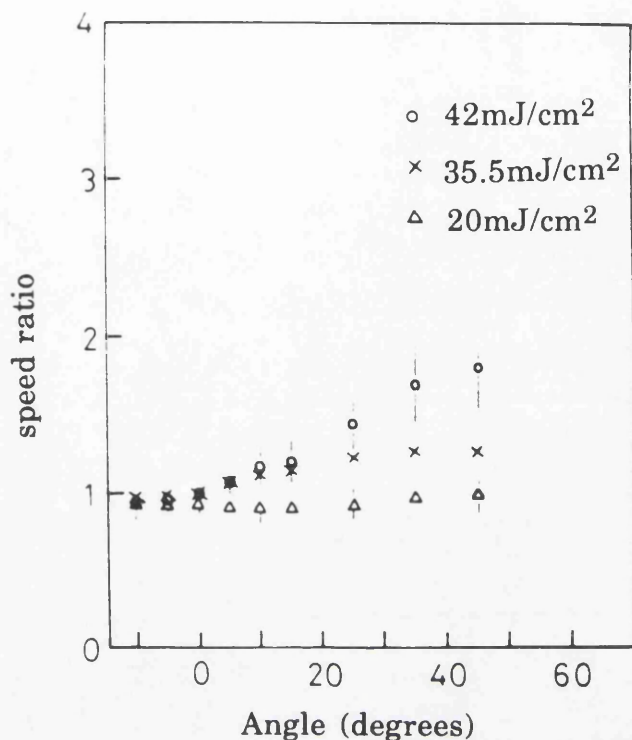


Fig.2.14 Determination of the speed ratio (Eqn.2.30), for desorbed S₂ from CdS at various angles to the surface normal (Namiki *et al*,1986). The laser wavelength is 337nm.

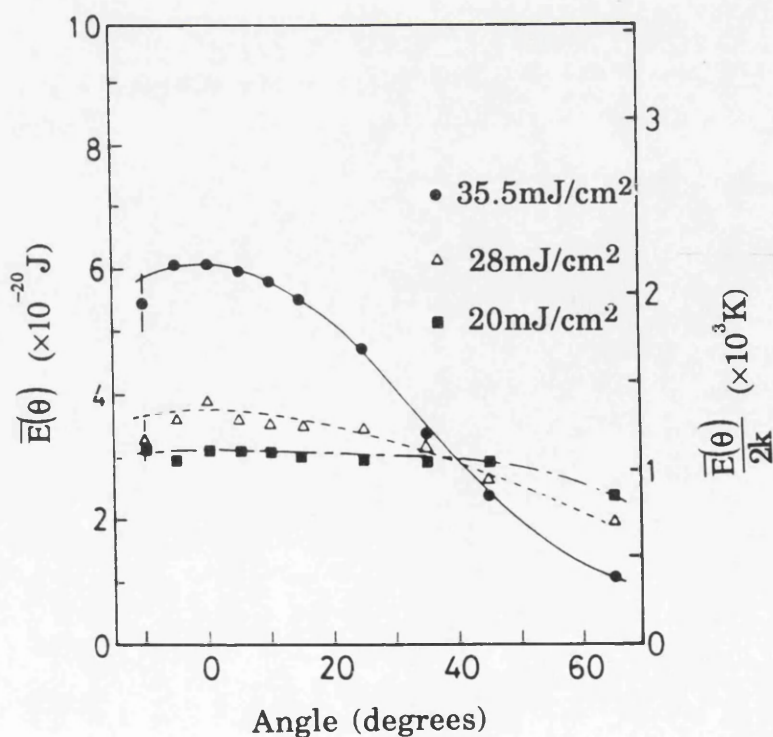


Fig.2.15 Determination of the average energy (Eqn.2.31), for desorbed S₂ from CdS at various angles to the surface normal (Namiki *et al*,1986). The laser wavelength is 337nm.

larger than that of N_2 , especially at higher energies (Namiki *et al*, 1991). Abnormal behaviour was also observed in the angular dependence of the yield which can be approximated by the form $\cos^p \theta$. For Ga and As_2 from GaAs, p has a value of $\sim 5-6$ at low powers and rises to $p \sim 10-13$ at higher powers. At this power $p \sim 1-2$ for N_2 , but is ~ 10 for Ga. Forward peaking of the velocity distribution is expected if Knudsen layers form at the surface, however, as has been discussed in §2.7, the Knudsen layer theory also predicts a velocity distribution narrower than a Maxwell-Boltzmann velocity distribution. In these experiments the speed ratio is always greater than, or equal to, unity. As has been discussed previously, this corresponds to a velocity distribution broader than a Maxwell-Boltzmann distribution. It is therefore difficult to reconcile these results with a thermal mechanism of desorption. Further evidence for a non-thermal mechanism is that the threshold power for desorption of compound semiconductors is observed to be dependent on the stability of the tetrahedral covalent bonds, as defined by the bond ionicity (Namiki *et al*, 1987).

The mechanism proposed (Namiki *et al*, 1991, Ichige *et al*, 1988), is that the laser induced band gap excitation causes the formation of a dense e-h plasma near the surface. This dissipates its excess energy to the lattice phonons. The interaction which is hypothesised to cause desorption is a dimerization interaction between nearest neighbour non-metallic elements. This is an attractive interaction that becomes stronger as the concentration of holes increases, corresponding to an increase in laser power. This attractive interaction reduces the stability of the tetrahedral structure. Once the laser power becomes large enough to generate enough e-h pairs the tetrahedral structure becomes unstable and the crystal stabilizes by taking the ionic rock-salt structure. This phase transition causes some material to be desorbed. This material subsequently collides inelastically to determine the initial velocity distribution. As dimers of the non-metallic element are usually observed in much greater numbers than single atoms it is believed that the dimerization reaction takes place during this phase transition.

This model can be used to explain the unusual behaviour of the material sputtered from GaN, assuming that highly rotationally and vibrationally

excited N_2 is produced due to excess energy generated in the dimerization reaction. These N_2 molecules would be scattered in collisions with the heavier Ga atoms and would transfer translational energy to the Ga atoms. This would produce the forward peaking in the angular dependence of the Ga velocity distribution. However, for the other materials, where the metallic and non-metallic elements are of similar mass, such effects would be expected to be less pronounced, as befits the results discussed above.

Evidence for a phase change during desorption was obtained by making simultaneous HeNe measurements of the reflectivity of the surface (Pospieszczyk *et al*, 1983). These experiments used a 20ns pulse length ruby laser to desorb material from a GaAs sample. The mass spectrometer in these experiments was oriented at 17° to the sample normal. The peak of the experimental time-of-flight distribution was used to determine the translational temperature from Eqn.2.14 (with $i=4$). Ga and As atoms were detected at powers above and below those at which observable reflectivity changes occurred. The translational temperature was not observed to increase dramatically as the reflectivity changed and had values ranging from 500K to 2000K. However, the rate of increase of the yield decreased as laser power became high enough to change the sample reflectivity.

A laser induced change of phase was also required to explain the intermixing of $Al_{0.3}Ga_{0.7}As/GaAs$ superlattices, observed after irradiation with a single pulse of $10^7 W/cm^2$ from an excimer laser (Ralston *et al*, 1987). The laser wavelength was 248nm and the period of the quantum well structure was 10nm. No visible crystal damage was observed, but secondary ionisation mass spectrometry was used to show that the laser had caused the first 11 periods to become intermixed. Raman spectroscopy showed that the laser irradiated material was a uniform crystal of $Al_{0.15}Ga_{0.85}As$. It was proposed that this was formed by melting, with epitaxial regrowth. Therefore, a laser pulse which removes only a few monolayers results in a phase change which penetrates $\sim 200nm$ into the crystal. A solution of the one dimensional heat equation, which was discussed in §2.3, was evaluated, and thermal conduction gave a plausible explanation of the observed effect.

Compound semiconductors have also been investigated using laser ablation in conjunction with laser ionisation of the neutrals and time-of-flight mass spectrometry (Odom and Schueler, 1990). This arrangement used a converted LIMA instrument. The ablation beam was the fourth harmonic of a Q-switched Nd:YAG laser and was incident on the GaAs sample at normal incidence. Non-resonant ionisation of the ablated material was carried out using a fourth-harmonic beam from a second Nd:YAG laser, which was positioned a distance of 0.6mm from the sample surface. As and Ga ions were produced by this second laser, but the detection of As₂ was not reported. A similar experimental arrangement, using the 1.06µm wavelength fundamental beam from a Nd:YAG laser incident on the sample at a glancing angle (Becker and Gillen, 1984), did report a As₂ signal. However, it was much smaller than the As signal. It has been discussed previously that electron ioniser/mass spectrometer studies find an order of magnitude more dimers than neutral As atoms. It is probable that the high power ionising laser causes significant fragmentation of the dimers. This makes the velocity distribution more difficult to interpret. However, the motivation for the non-resonant laser ionisation studies on the LIMA system was material analysis, where the elemental composition of the sample was required, rather than studies of the desorption process.

These studies on a LIMA machine used a much smaller spot size, ~2µm, than the other work reported in this section. Since decreasing the spot size affects the plasma composition (Devyatykh *et al*, 1976), it may also change the sputtering mechanism. At the lowest laser power employed, $E_0 = 5 \cdot 10^8 \text{W/cm}^2$, and $3E_0$ no visibly observed damage was caused to the sample. It was estimated that at $3E_0$, ~100Å was removed per shot. The Ga velocity distribution at the E_0 power was fitted to a Maxwell-Boltzmann distribution with a temperature of 4000K (Odom and Schueler, 1990). However, to fit the As velocity distribution, requires the As signal to originate from either As₂ or GaAs emitted from the sample. When the laser power was increased the Ga distribution could again be fitted assuming that only single atoms were emitted. In order to fit the As signals at the higher powers required the assumption that even larger clusters were emitted from the surface. It would seem probable, therefore,

that the desorption mechanism is similar to that discussed above, causing Ga and As₂ to be emitted.

Another important feature of these experiments is that the ratio of As to Ga varies considerably depending on the delay between the two lasers. The ratio was seen to range from 0.2 to 5. However, if the total signal at all delays is integrated the ratio of As to Ga is found to be ~1, at all the powers used.

These studies also investigated the effect of using 532nm as the ablation laser wavelength (Schueler and Odom, 1987). With a power of $5 \times 10^8 \text{W/cm}^2$ the Ga signal was approximately an order of magnitude larger than that obtained using the same power of the 266nm beam. The peak of the velocity distribution was observed to be delayed using the 532nm wavelength ablation compared to 266nm wavelength. It was suggested that the emitted atoms and dimers had lower energy due to the lower energy of the ablation photons. Ionisation caused by the ablation laser was not observed with the ablation laser wavelength of 532nm. When the same power of 266nm was used the ablation laser alone caused an ion signal, which was however 10^4 times smaller than the ionised neutral signal integrated over all delay times, as would be expected from Eqn.2.25.

Higher powers were available with the second harmonic than could be obtained with the fourth harmonic. At $8.5 \times 10^9 \text{W/cm}^2$ the As and Ga temporal distributions peaked very quickly and fell slowly. Far more material was removed by the higher power, the crater was $0.5 \mu\text{m}$ deep and had a diameter of $4 \mu\text{m}$, twice that of the laser spot. An advantage of this power was that after the initial $0.5 \mu\text{s}$ the ratio of As to Ga was within 30% of that expected, independent of the delay between the lasers.

ZnS is an ionic semiconductor and is used as an optical coating. The laser ablation of ZnS has been investigated by Arlinghaus and co-workers by detecting the fluorescence induced in the ablated material by a 50MHz bandwidth pulsed dye laser (Arlinghaus *et al*, 1989a). The ablation laser was an excimer with a 30ns pulse length and was operated at a wavelength of 308nm, which is above the bandgap energy of ZnS. The narrow bandwidth of the dye laser allowed the Doppler shifted velocity

distribution of the Zn atoms to be determined and compared with the time-of-flight velocity distribution. The agreement between the two techniques was very good, provided the LIFS probe power was kept low. This was so that the probe laser did not cause fragmentation of molecular species, as this would cause the generation of atoms in the probe volume with Doppler velocities lower than those determined by the time-of-flight. Velocity distributions determined by this technique were assigned a kinetic temperature using a half-range Maxwell-Boltzmann distribution. These temperatures ranged from $1880 \pm 60 \text{K}$ at 17mJ/cm^2 to $9250 \pm 200 \text{K}$ at 80mJ/cm^2 . These measurements required several thousand laser shots each and were taken on separate areas of the sample. The amount of material removed per laser shot was determined by comparing the LIFS signals from laser ablated and ion bombarded ZnS (Arlinghaus *et al*, 1989b). The amount of material sputtered by the ion beam was calculated from Sigmund theory. At an ablation laser fluence of 30mJ/cm^2 it was determined that 10^9 atoms were removed per pulse. This corresponded to $1/2500$ of a monolayer. Using this measurement to determine the total yields at fluences from 20 - 60mJ/cm^2 , it was possible to derive a relationship with the surface temperature calculated from the one dimensional heat flow model discussed in §2.3. This indicated that for this range of laser powers a thermal process, such as sublimation, with an activation energy of 2.5eV , was responsible for the material emission. As the power was increased the number of atoms removed per shot rose sharply. This was attributed to the interaction of the laser generated plasma with the surface. At 80mJ/cm^2 , the highest power used, $\sim 10^{12}$ atoms were removed per laser shot, however as the LIFS technique only detects ground state Zn atoms it is possible that the total number of atoms removed is much higher.

This work illustrated that the technique of narrow bandwidth LIFS is probably the most suitable for determining the processes occurring in laser ablation. It allows highly sensitive detection and allows determination of the velocity distribution from both time-of-flight and Doppler profile measurements.

§2.10.3 Elemental semiconductors

The laser processing of elemental semiconductors, particularly silicon,

has been a field of widespread research since the late nineteen-seventies. The vast majority of this work was aimed at developing pulsed laser annealing as an alternative to conventional oven annealing. As has been illustrated in the preceding section, laser induced sputtering can give valuable insight into the mechanism of the laser material interaction and for this reason, laser induced particle emission of both Ge and Si have been investigated. Of the previous applications of laser ablation as a sample atomisation source for RIMS, several have involved silicon samples and these will also be discussed.

Elemental semiconductors, which have a covalent bond type, are appreciably different to ionic semiconductors in their desorption characteristics. Notably, the ablation laser powers required to generate appreciable signals are far higher (Lazneva, 1991), apparently due to the higher sublimation temperature of elemental semiconductors. Using a combination of quadrupole mass spectrometry for time-of-flight measurements, and a HeNe laser to measure the surface reflectivity, it was determined that a power of $0.8\text{J}/\text{cm}^2$ was required to melt the Si surface (Pospieszczyk *et al.*, 1983). This was approximately three times the power required to affect the same change in GaAs. In contrast to GaAs, Si produced no notable neutral emission at powers below those which resulted in surface melting. The temperatures determined from the time-of-flight velocities were at or above the melting temperature, lying between 1700K and 2700K. Similar results were obtained in studies in which RIMS was employed to detect sodium atoms contained in silicon samples (Bakos *et al.*, 1991). The velocity distributions were fitted with a Maxwell-Boltzmann distribution involving a small hydrodynamic velocity. The temperatures determined from this study varied from 1100K to 1800K, and this seems to suggest a thermal mechanism for desorption. The craters resulting from the laser ablation of silicon are usually quite deep, in this experiment they were $\sim 10\text{nm}$ per shot.

As mentioned previously, laser ablation of silicon has been used as an atomisation technique for RIMS by several researchers. The work of Bakos and co-workers discussed above was to investigate the suitability of the technique for determining the surface sodium composition on silicon

exposed to the impurity flux in the scrape off layer of a TOKAMAK plasma. The first application of RIS to the trace analysis of solids also involved detecting sodium in a silicon sample (Mayo *et al*, 1982). A proportional counter was used to detect the RIS ions, accordingly the vaporisation occurred in a 95 torr buffer gas background and there was no mass selection of the ionised material. The limit of detection for sodium was determined to be 10^{11} atoms/cm³. This corresponded to ~40 impurity atoms per pulse, with crater depths of ~1 μ m. Trace analysis of elements in silicon has also been reported recently using RIMS with a reflectron time-of-flight mass spectrometer (Belov *et al* 1992). Iron present at 10ppb and boron present at 1ppb were detected. The limit of detection was estimated to be 0.1ppb. This is similar to the detection limit for a 500 shot analysis reported by Beekman and Thonnard (1989). They used a frequency doubled Nd:YAG laser with a 150 μ m spot to atomise Ga in a silicon sample. After high laser power cleaning to alleviate the alkali interference, good linearity was obtained for a series of samples with Ga concentrations from 50ppm to 0.48ppm.

§2.10.4 High temperature superconductors

The discovery of high temperature superconducting (high T_c) materials in 1986 initiated an intensive research effort in order to produce these materials in forms which allow practical application of their unique properties. One area of intensive interest was the fabrication of thin films, particularly for integration into microelectronic circuits. There are several possible techniques that can be employed (Auciello *et al*, 1990): plasma sputtering, thermal evaporation, electron beam deposition, molecular beam epitaxy (MBE), ion beam sputter deposition and laser ablation deposition. Of these techniques, laser ablation deposition is one of the most successful for producing high T_c films from bulk superconducting targets on a laboratory scale. It has therefore become of interest to study the process occurring during the laser ablation of high T_c materials, in order to determine the composition of the resulting plumes and the transport of the ablated material to the substrate. Many techniques have been utilised to this end (Nogar *et al* 1991), including; mass-spectrometry of the directly produced ions, optical emission spectroscopy, laser induced florescence and RIMS. The application of RIMS and LIFS to this situation will be briefly discussed in this section.

The ablation of a $\text{YBa}_2\text{Cu}_3\text{O}_{7-x}$ sample with the 1064nm fundamental wavelength of a Nd:YAG laser produced a velocity distribution for Cu which could be fitted by the half-range Maxwell-Boltzmann distribution, discussed in §2.5 (Estler and Nogar, 1991). However, changing the wavelength to 355nm, with approximately the same power, resulted in a velocity distribution which was best modelled by a Knudsen-layer analysis (§2.7). This suggested that the influence of collisions was greater, and hence that the ablation caused by the ultra-violet wavelength was not purely thermal and was in part photo-chemical. This work also determined that the temporal distribution of BaO, ablated by $1\text{J}/\text{cm}^2$ of 355nm laser light, could also be described by the Knudsen layer formalism with a characteristic temperature of 6800K. This compared with a value of 9900K determined by LIFS (Okada *et al*, 1992), for the same material with a fluence of $0.2\text{J}/\text{cm}^2$ of 193nm wavelength excimer laser radiation. However, other workers (Singh *et al*, 1990) have determined that a model including adiabatic expansion (§2.8), is appropriate for deposition of these films.

§2.10.5 Insulators

The energy of laser photons is almost invariably below the bandgap energy of insulating samples. Thus, the mechanism of laser sputtering of insulators has similarities with that of semiconductors detailed in §2.10.2.1. In contrast to the situation in semiconductors, however, excitons and holes generated in alkali halides and alkaline earth fluorides, which exhibit a strong electron-lattice coupling, can be localised (Nakai *et al* 1991). This results in self-trapped excitons or holes near the surface. These eventually decompose into a halogen vacancy and an emitted halogen atom. Hence, there is a linear dependence between the number of incident photons, and therefore fluence, and the sputtering yield. This has been observed for RbBr and KI. However, in many insulators the electron excitation energy is not localised and the laser induced particle emission exhibits the threshold power behaviour observed for compound semiconductors. This behaviour has been observed for CuCl, MgO, Al_2O_3 , (Dreyfus *et al* 1986a) and CaF_2 (Estler *et al* 1987). In the remainder of this section the studies into Al_2O_3 and CaF_2 will be detailed because they illustrate how the velocity distribution of the emitted material can

illuminate the mechanism of material ejection.

The laser induced sputtering of Al_2O_3 has been extensively studied, using scanning electron microscopy of the resultant craters (Rothenberg and Kelly, 1984) and by monitoring the sputtered material, using Michelson interferometry (Walkup *et al*, 1986) and LIFS (Dreyfus *et al*, 1986b). The motivation for these experiments was to ascertain if the mechanism of material removal induced by ultra-violet laser light was due to thermal or electronic processes. Electronic sputtering is considered to occur when the laser photons result in weakened or even repulsive bonding. There is also the intermediate situation when the laser photons act to weaken the electronic bonding, which results in vaporisation occurring at well below the temperature expected from the vapour pressure curve. It is possible to make a distinction between thermal and electronic processes by determining if the surface temperature is in agreement with that predicted for thermal vaporisation by Eqn.2.10. For the case of Al_2O_3 temperatures were determined from LIFS measurements of the time-of-flight velocity distribution, as described in §2.5, and from the populations of rotational and vibrational levels. There was not the correspondence between these temperatures that would be expected for a thermal process. The time-of-flight distributions could be fitted with a half-range Maxwell-Boltzmann distribution. The characteristic temperature for Al was 41000K while for AlO it was only 13000K. The internal temperatures determined by the internal energy distribution was much lower, being less than 1000K. Consequently, an electronic sputtering mechanism was proposed, where the laser photons act to raise the energy of each atom by $\sim 2\text{eV}$. This increases the vapour pressure by orders of magnitude, or even renders the lattice unbound (Dreyfus *et al*, 1986a).

As mentioned above, the laser ablation of CaF_2 , a common dielectric used in excimer lasers, has been studied using RIMS of both Ca and CaF (Estler *et al*, 1987). It was found that the Ca velocity distribution resulting from ablation with the 1064nm wavelength fundamental output of a Nd:YAG could be fitted with a half-range Maxwell-Boltzmann distribution. This had a characteristic temperature of 834K which is substantially lower than the CaF_2 melting temperature of $\sim 1500\text{K}$. However, when the same fluence of fourth harmonic, with a wavelength

of 266nm, was used, the results were markedly different, as shown in Fig.2.16. This could not be fitted with the characteristic temperature determined for 1064nm, as there is a considerable component with higher velocities. It was possible to fit this data by using the sum of two Maxwell-Boltzmann distributions. For Ca, the fast component was characterised by a temperature of 4970K and accounted for 33% of the distribution. The remaining 67% was fitted by a temperature of 830K, which is virtually the same as the temperature that was appropriate for the 1064nm ablation wavelength. The CaF component of the plume was also analysed for 266nm ablation, and the results were similar. A fast component with a temperature of 8250K accounted for 44% of the distribution, while the remaining 56% was characterised by a temperature of 1940K. This is similar to the results of Lazneva, discussed in §2.10.2.1. The mechanism presented there was that the slow component was due to thermal vaporisation, while the fast component was due to photon induced electronic processes.

Measurements of the internal temperature of the CaF molecule was also possible. For the 1064nm wavelength these temperatures were of the same order as the kinetic temperature. However, when the ablation wavelength was changed to 266nm the internal temperatures were far lower than the kinetic temperatures determined for both the fast and slow components. This is similar to what was observed in the study of ultra-violet laser ablation of Al₂O₃ discussed above and provides further evidence that the ultra-violet wavelength causes desorption of insulators by electronic processes.

§2.10.6 Polymers

Before concluding this section it is worth mentioning that an active area of research is the ultra-violet laser etching of polymers, particularly polymethylmethacrylate (PMMA). This has been motivated by the desirability of replacing the wet chemical methods currently used in photolithography for the production of microelectronic devices. These materials are organic and the ablation mechanism is very different to that observed with inorganic insulators (Dreyfus *et al*, 1986a). However, the methods of describing the emitted material discussed in this chapter can be employed. For example, the 248nm wavelength ablation of PMMA

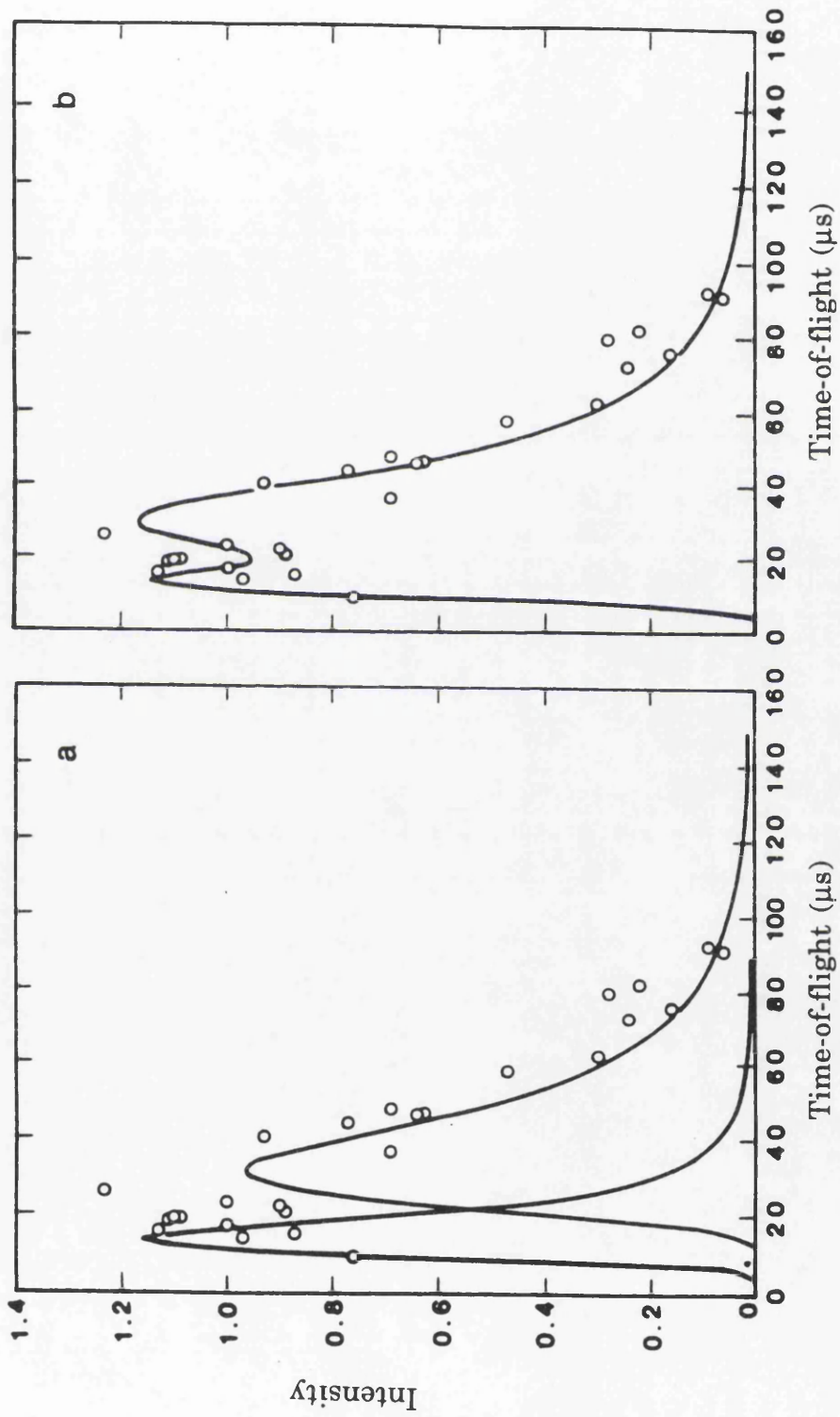


Fig.2.16 Time-of-flight distributions of Ca ablated from CaF₂ by the fourth harmonic of a Nd:YAG laser, with a wavelength of 266nm (Estler *et al*, 1987). This can be modelled by two Maxwell-Boltzmann distributions, shown separately in (a) and superimposed to fit the data in (b).

produced carbon dimers which were monitored by LIFS, these could be fitted by a half-range Maxwell-Boltzmann distribution with a characteristic temperature of 40,000K (Srinivasan *et al*, 1986). A similar study using non-resonant ultra-violet laser ionisation (Hansen, 1990), found that C₃ clusters were produced during the 266nm wavelength ablation of several polymers. The velocity distributions were modelled with temperatures of >10,000K and hydrodynamic velocities in the range of 3-6km/s. The half-range Maxwell-Boltzmann distribution with a lower temperature, ~3000K, has been found appropriate to describe the velocity distribution of products formed by the 193nm wavelength ablation of PMMA (Danielzik *et al*, 1985). However, as the fluence was increased the velocity distribution was observed to become highly directional and non-Maxwell-Boltzmann. Hence, the formalisms presented in this chapter can be useful in the description of the ablation of organic, as well as inorganic material.

Chapter 3

Instrumentation

§3.1 Introduction

A RIMS instrument, combining as it does laser spectroscopy and mass spectrometry, is by necessity a highly complex system. The system can be split into three principle sub-systems for the sake of description:

- (a) Mass spectrometer and vacuum system.

The mass spectrometer is of the time-of-flight type and was designed and assembled in Glasgow (Towrie *et al*, 1990; Land, 1990).

- (b) Lasers.

These are all commercially available Nd:YAG lasers and dye lasers.

- (c) Data acquisition electronics and software.

This is based around a transient recorder and a IBM PC compatible computer. The system was designed and the software was written in Glasgow (McCombes, 1991b)

These sub-systems will be described in detail in this chapter.

§3.2 Mass spectrometer and vacuum system

Mass spectrometry must be performed in a vacuum environment to prevent collisions from neutralising the ions or affecting their trajectory. The system in Glasgow is constructed almost entirely of stainless steel and generally operates at a pressure of $\sim 10^{-9}$ torr. The system consists of a large spherical chamber, in which the sample is atomised and ionised, and a 1.5m time-of-flight mass spectrometer into which these ions are transmitted. The whole system is shown schematically in elevation in Fig.3.1 and in plan in Fig.3.2.

The sample chamber has a diameter of 30cm and has a variety of ports facing towards the centre where the sample is located. Several of these

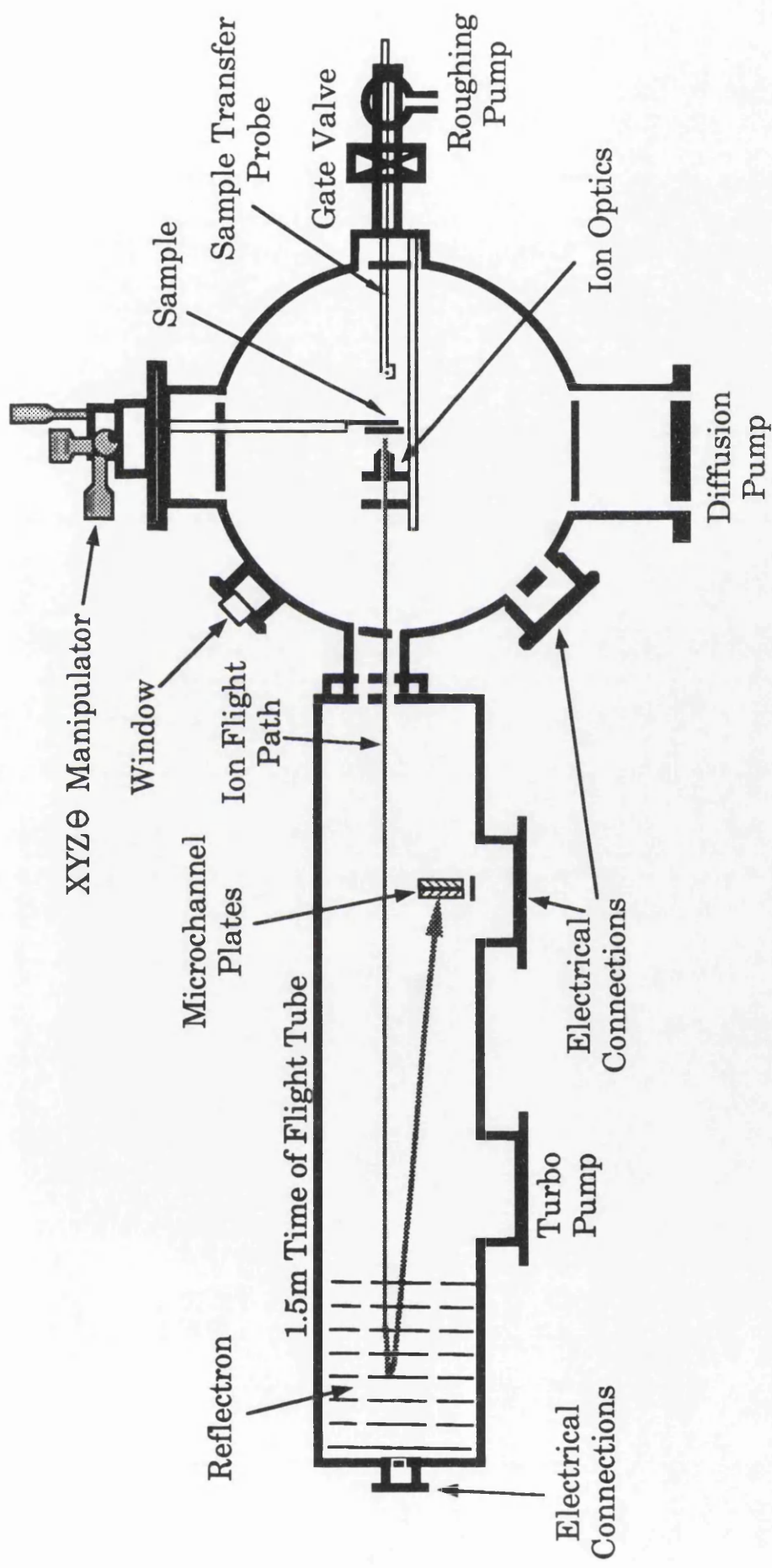


Fig.3.1 Elevation of the analysis chamber and mass spectrometer

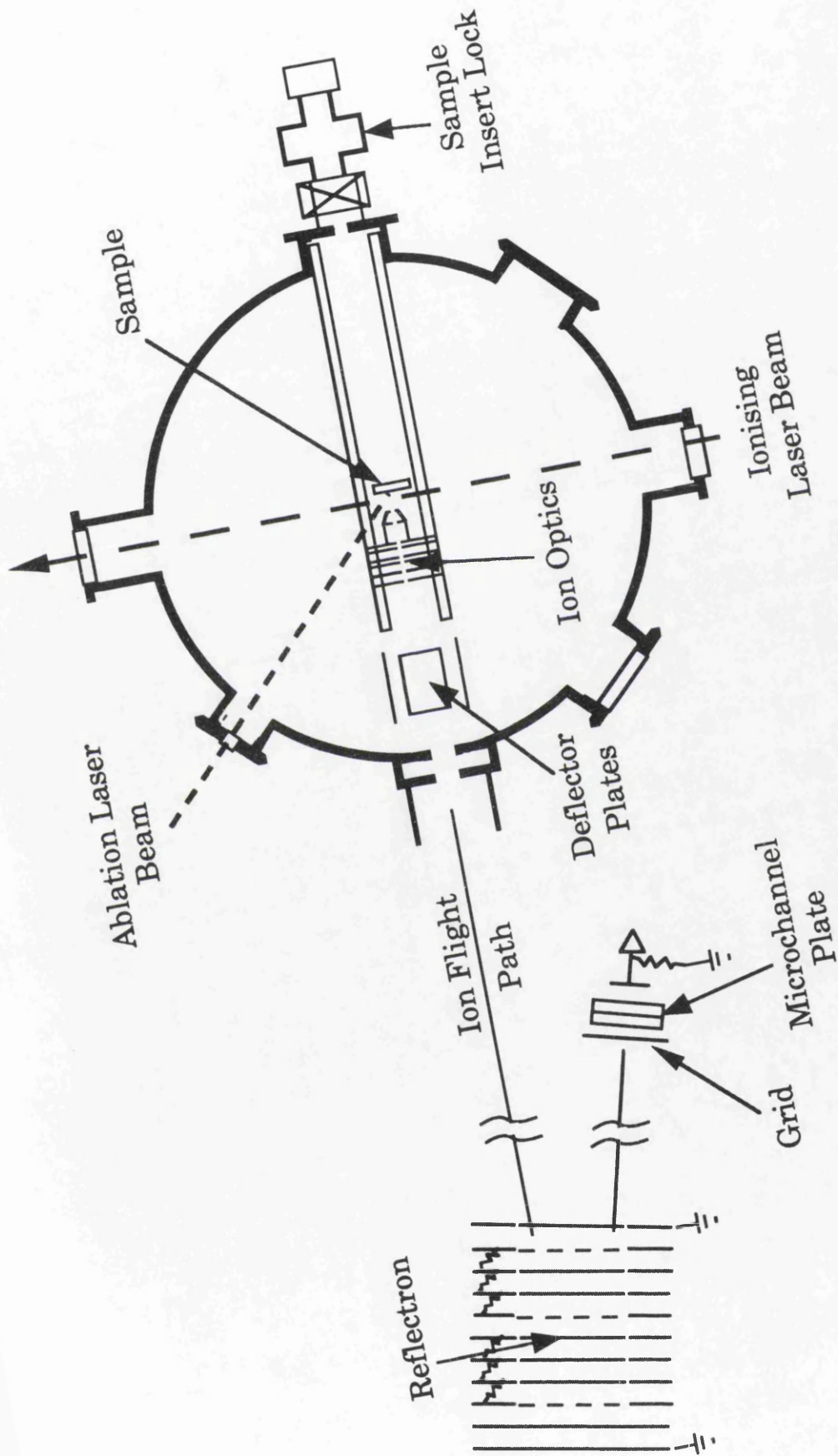


Fig.3.2 Plan view of the analysis chamber and mass spectrometer

ports are used for providing windows for the laser beams and electrical feed-throughs, as can be seen from the schematics. At the base of this chamber is a diffusion pump (Edwards Diffstak Mk2 model 160) which has a pumping speed of 700 litres per second. This pump had a liquid nitrogen cold trap in the neck, but this was not used during the study of atomic samples described in this thesis.

The sample is inserted through a sample insertion port (Kratos WG-707). This arrangement allows a sample to be exchanged and the system returned to the operating pressure in approximately 5 minutes. The sample is introduced on a sample insert probe, which has a tip fitting into a groove at the rear of the sample stub, and is then transferred to the sample manipulator (Kratos WG-194). The sample manipulator allows for precise movement of the sample in three planes and for rotation. This allows the analysed area on the sample to be changed and the distance between the sample surface and the lasers to be set reproducibly.

The sample stub, interaction volume, ion optics and deflector plates are shown in greater detail in Fig.3.3. The sample stubs are constructed from stainless steel and the samples were prepared as detailed in §4.2.1. Ionisation occurs in the interaction volume, between the sample stub and the first ion optic, where the field gradient is $\sim 100\text{V/mm}$. The ions formed have an energy, in electron volts, corresponding to the voltage where they were formed. Only ions formed in a certain area of the ion optics, the acceptance volume, will be transmitted efficiently through to the detector. The acceptance volume has been measured by monitoring the transmission of non-resonantly ionised organic impurities in the chamber as a function of the position of the ionising laser beam (Land, 1990). The acceptance volume determined was small, $\sim 1\text{mm}^3$, and therefore care was taken in all subsequent experiments to ensure that the system was optimised for maximum transmission. Behind the ion optics are a set of deflector plates that can be used in two ways. Firstly, a small voltage, $<50\text{V}$, can be applied to deflect the ions in either the horizontal or vertical plane in order to return them to the path for optimum transmission. Secondly, as discussed in §4.10.1, a high voltage pulse, $>500\text{V}$, can be applied in order to deflect any unwanted ions from the transmission axis. This allows for the removal of ions created by the ablation laser.

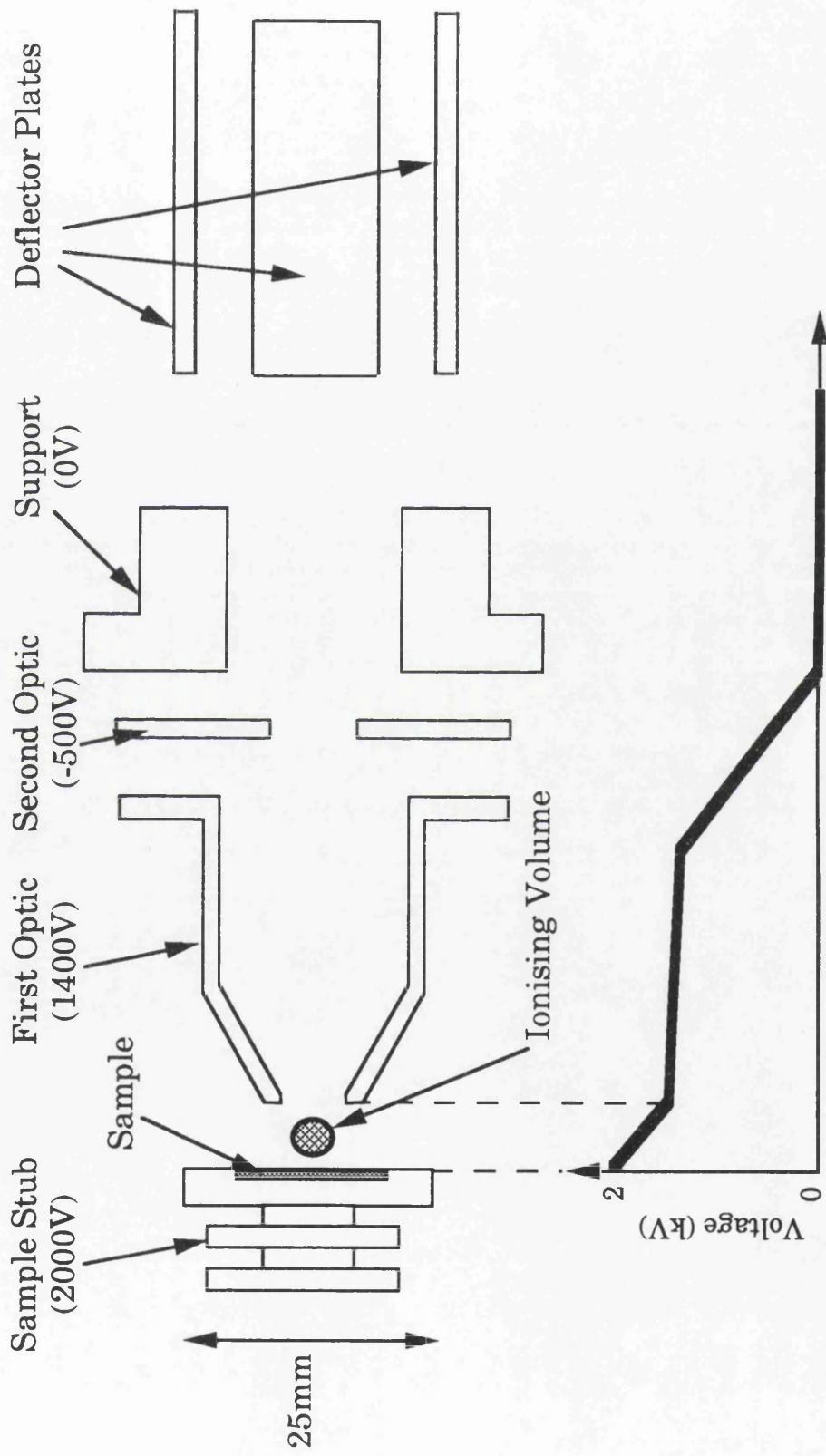


Fig.3.3 A section through the conical ion optics, showing the typically operating voltages. The variation of the potential at the centre of the optics along the ion flight path is shown schematically.

Chapter 3

Ions transmitted through the ion optics are then analysed in the mass spectrometer. This consists of a stainless steel tube 1.5m long which is pumped by a turbo-molecular pump (Edwards ETP6) with a pumping speed of 200 litres per second. The basic principle of operation of the mass spectrometer is very straight-forward. Since all of the ions transmitted through the ion optics have approximately the same kinetic energy, the arrival time at the end of a field free region depends only on the charge to mass ratio. As ionisation in RIMS is precisely governed, there are generally only singly charged ions. Hence, the time-of-flight spectra can be simply converted to a mass spectra using the relationship:

$$m = \frac{2E_k}{l^2} t^2 \quad \text{- Eqn.3.1}$$

where m is the mass, E_k is the initial kinetic energy of the ions upon entering the time-of-flight tube, l is the total length of the flight path and t is the time-of-flight. However, applying this relationship requires a knowledge of several system parameters that are usually not well known. It is normal practice, therefore, to use the simpler relationship:

$$m = k t^2 \quad \text{- Eqn.3.2}$$

where k is a constant which is determined from a peak whose mass can be assigned unambiguously. An important parameter in defining the performance of any mass spectrometer is the mass resolution, $m/\Delta m$, where Δm is the width of a recorded peak at some fraction of its height, usually the full-width at half maximum. The mass resolution for a time-of-flight mass spectrometer can be related to the temporal resolution, $t/\Delta t$, by differentiating Eqn.3.2, hence:

$$\frac{m}{\Delta m} = \frac{1}{2} \frac{t}{\Delta t} \quad \text{- Eqn.3.3}$$

This discussion has assumed an ideal case, however, in a practical instrument all the ions do not have exactly the same energy. The main reason for this is that although ions produced by RIMS are formed virtually instantaneously, within ~10ns, they are created in different

regions of the acceptance volume and are therefore subjected to different extraction voltages. This results in the transmitted ions having a range of different kinetic energies. For example, if the field gradient in the acceptance region is $\sim 100\text{V/mm}$ then ions created at opposite sides of an ionising beam 1mm in diameter would have a difference in energies of $\sim 100\text{eV}$, or 5% assuming that the sample voltage is 2kV. To help to compensate for this spread in the kinetic energies the mass spectrometer employs a reflectron electrostatic mirror, based on the design of Mamyrin *et al* (1973). The reflectron consists of a series of 20 plates which are connected by precision resistors to generate a smoothly varying static electric field. Two voltages are applied to the reflectron, V_{reflect} which is approximately the voltage at the ionisation volume and V_{retard} which is approximately half this voltage. The front of the reflectron is earthed, as shown in Fig.3.4. The basic principle of operation is that ions of the same mass which arrive at the reflectron with different kinetic energies will become more focused temporally since the higher energy ions will penetrate deeper into the reflecting fields, and therefore travel further, than the ions which initially have a lower kinetic energy. By adjusting the field gradients in the reflectron it is possible to arrange that the spread in arrival times of the ions at the detector can be reduced. This increases the mass resolution of the spectrometer to ~ 1000 . A linear time-of-flight mass spectrometer of 1.5m length typically has a mass resolution 200.

Besides energy compensation the reflectron also acts to filter any ions which have been accelerated through a voltage greater than V_{reflect} , since these ions pass straight through the reflectron onto the earthed plate at the back of the system. This provides a high degree of suppression for ions generated at the sample stub by the atomisation process and unlike the technique of pulsing the deflector plates mentioned above, this does not require the addition of any extra voltages to the system.

The transmission efficiency of the mass spectrometer was increased by applying a small negative voltage, $<30\text{V}$, to a fine wire strung along the flight path. This is known as an 'electrostatic particle guide' (Oakey and MacFarlane, 1966) and provides a degree of correction for the radial dispersion of the ion packet.

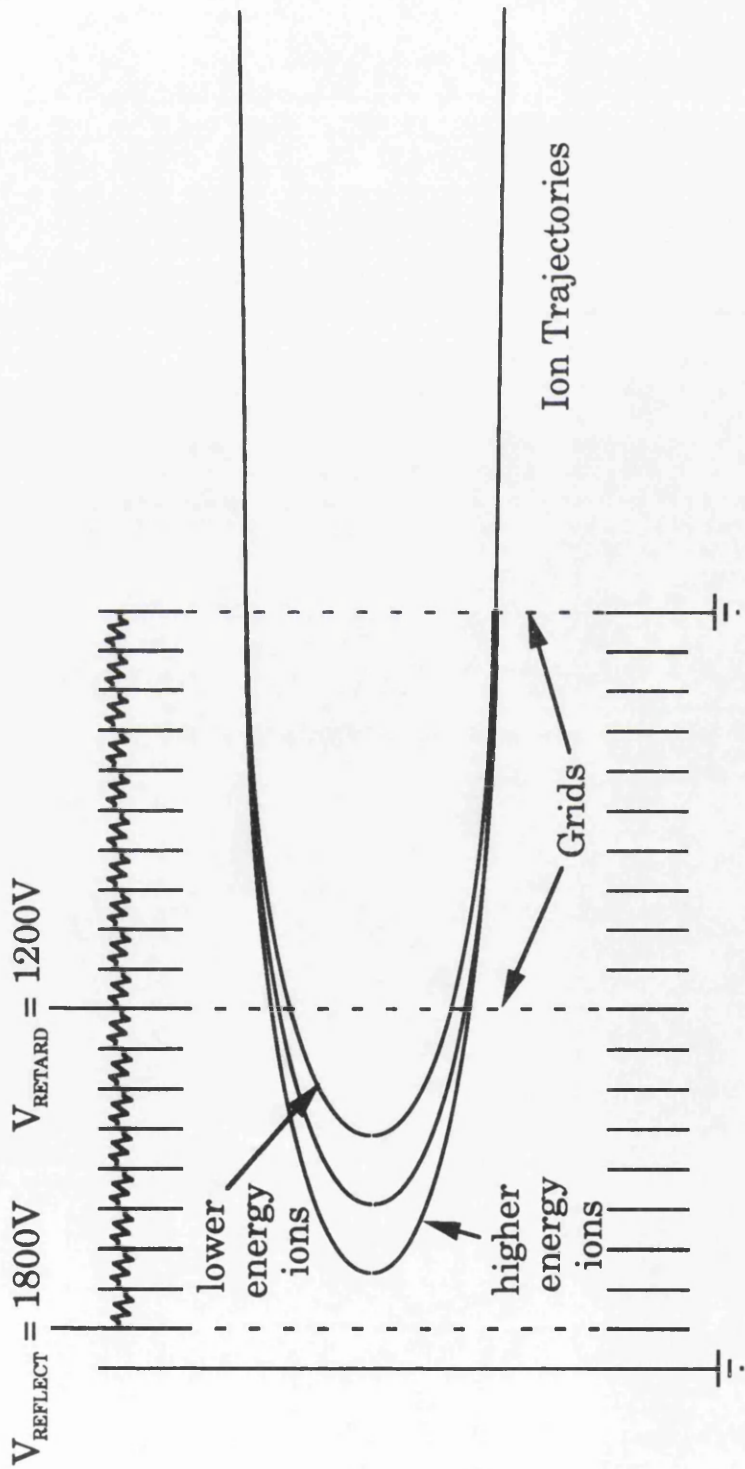


Fig.3.4 Diagram showing the construction of the 'reflectron' electrostatic mirror. Higher energy ions penetrate deeper into the field than lower energy ions, resulting in a reduction in the spread of arrival times at the detector.

The ion detector is a Galileo 3025-10V dual microchannel plate (Wiza, 1979) which is biased as shown in Fig.3.5. The anode is not impedance matched to the rest of the detection system so a degree of ringing and signal overshoot was observed for large ion pulses. This detector was initially installed in the system in 1988 and when the experiments reported in this thesis were undertaken its gain had reduced so that single ions were not readily detected above the noise level of $\sim 1\text{mV}$. However, as the experiments it was used for were concerned mainly with studies of major elements this was not problematic. In order to prevent the output from the detector from exceeding 10V it was sometimes necessary to decrease the applied voltage. The dependence of the detector signal on the applied voltage was determined so that the signals obtained with the reduced detector voltage could be related to the signal obtained under the normal operating conditions. Directly in front of the detector is a grid which is held at a potential just below that of the signal ions. This acts to prevent any secondary ions, formed by the scattering of signal ions on the plates and grids of the reflectron, from being transmitted to the detector.

§3.3 Laser system and optics

Lasers were used in this work for two different purposes: atomisation of the sample and ionisation of the resulting atoms in the gas phase. These applications require different characteristics from the laser system. The ablation laser, which produces atomisation, should have a stable pulse energy and a reproducible, preferably purely Gaussian or flat, spatial profile. The wavelength of the ablation beam does not need to be variable but in order to study the characteristics of the ablation process a range of wavelengths from the infra-red to the ultra-violet were needed. Ionisation of the gas phase atoms requires a beam that is tunable, so that the resonance in the atom of interest can be selected. In this system, as in most other RIMS systems, a pulsed dye laser is used for this purpose. Such a system is limited to producing wavelengths principally in the visible range. However, many RIMS schemes require wavelengths in the ultra-violet and frequency doubling, using non-linear effects in crystals which exhibit a second order susceptibility, is often employed. It is possible to utilise continuous wave (CW) lasers for RIMS, although due to their lower instantaneous power it is more difficult to frequency double these

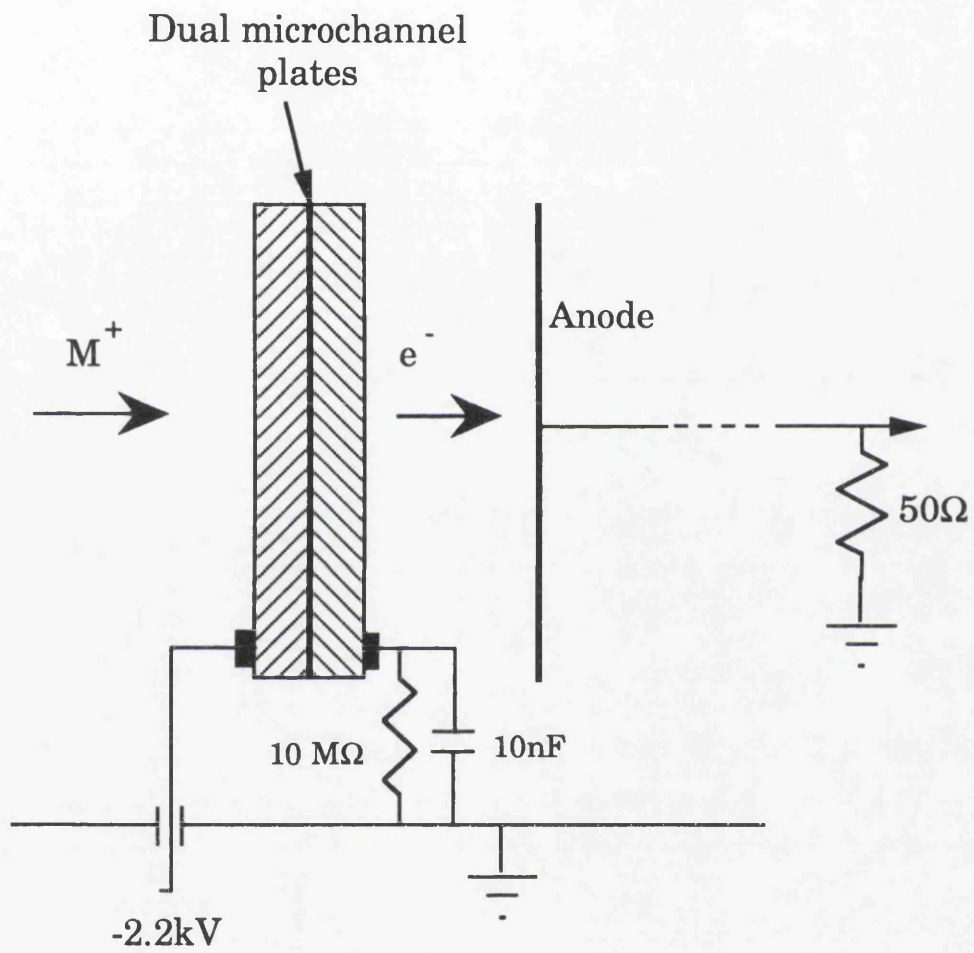


Fig.3.5 Biasing of the detector

beams. Therefore, the utilisation of CW lasers have been limited to applications where visible wavelengths can be employed, such as in thorium (Fearey *et al*, 1992) or barium (Cannon *et al*, 1985) where the narrow bandwidth of CW lasers allows the selective ionisation of a chosen isotope. CW lasers have also been used to selectively ionise metastable rare gas atoms (Hotop *et al*, 1992). Perhaps the most significant application of CW RIMS is where a relatively inexpensive diode laser was used to populate excited states in rubidium (Shaw *et al*, 1992) and lanthanum (Shaw *et al*, 1989), which were subsequently ionised by a pulsed dye laser. This work shows the potential for a less expensive laser system, which would greatly reduce the cost of a RIMS system, and almost certainly increase its applicability. However, the range of wavelengths obtainable from diode lasers is limited, mainly to the near infra-red, and it can be difficult to tune the laser wavelength to that of the resonant transition. It is therefore not envisaged that these lasers will be used routinely in RIMS analysis until these problems can be overcome.

The laser systems will now be discussed in detail.

§3.3.1 Ionising lasers

This system consists of two Spectralase 4000 dye lasers (Spectron Laser Systems, Rugby, UK) pumped by a Spectron SL2Q & SL3A Q-Switched Nd:YAG laser. The Nd:YAG laser, shown schematically in Fig.3.6 consists of a flashlamp pumped oscillator rod and an amplifier rod pumped by two flashlamps. The laser operates with multiple spatial and temporal modes and has a specified fundamental (1064nm) output power of ~800mJ at the normal system operating frequency of 10Hz. The laser also incorporates potassium di-deuterium phosphate (KD*P) crystals which can generate frequency doubled (532nm), tripled (355nm) and quadrupled (266nm) beams. These crystals are maintained at 55°C which results in a very good power stability, specified at ±5% for the second and third harmonics. The fundamental and second harmonic and either the third or fourth harmonic are available at any one time.

The two dye lasers are transversely pumped and are virtually identical. The layout of the dye lasers is shown in Fig.3.7. The laser used in the studies reported in this thesis had two amplifier cells and was pumped by

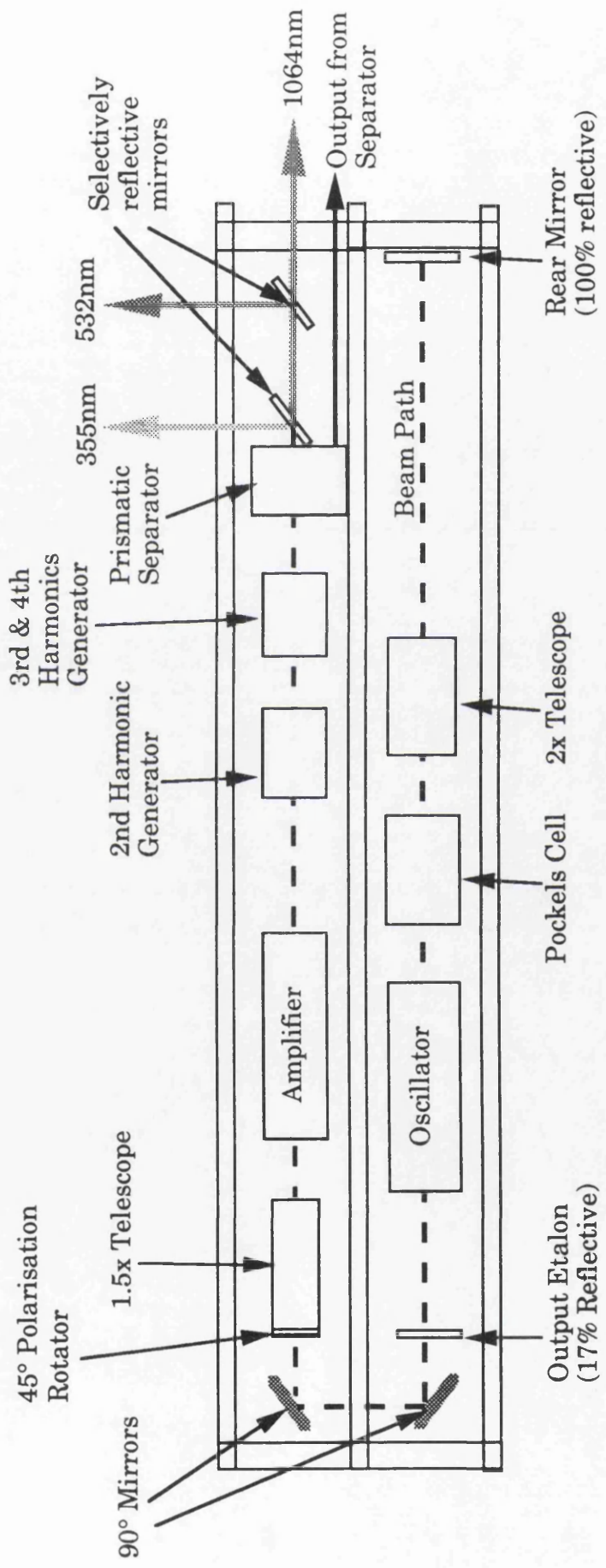


Fig.3.6 Diagram of the layout of the Spectron Nd:YAG laser

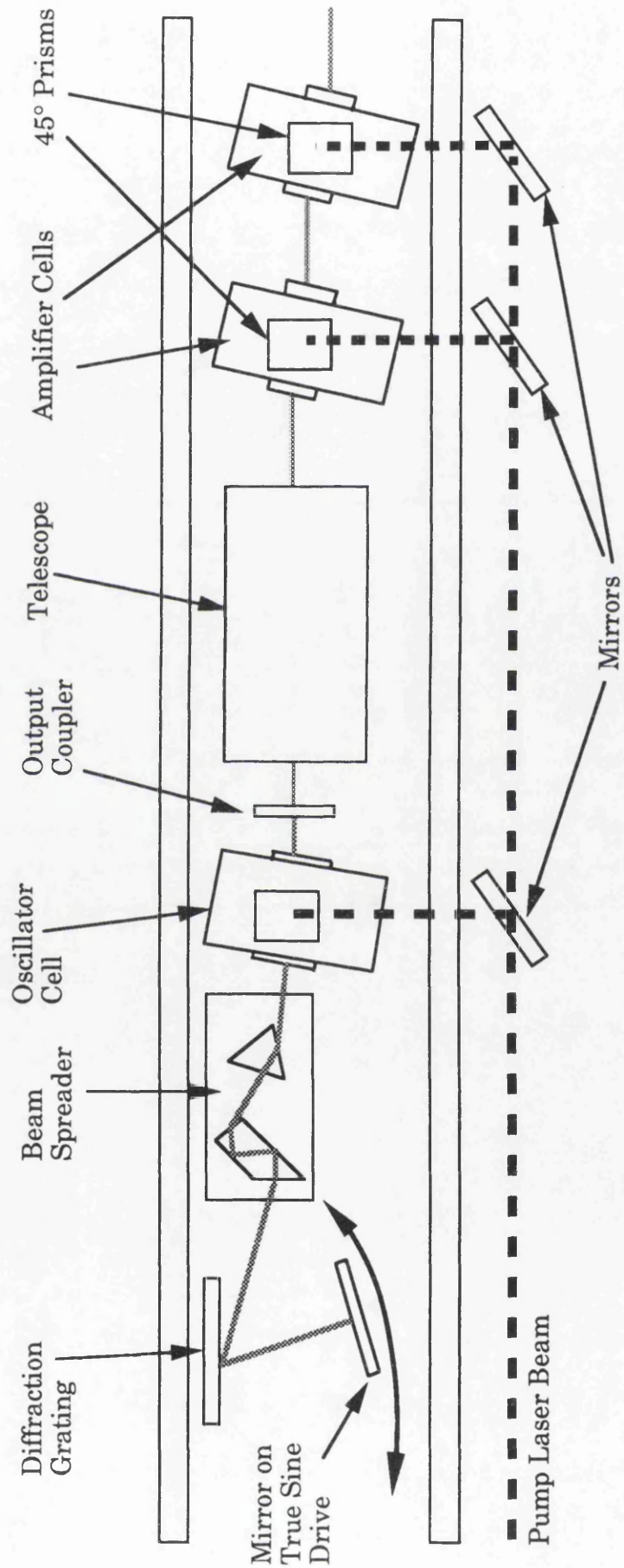


Fig.3.7 Diagram of the layout of the Spectron dye lasers

the second harmonic of the Nd:YAG laser. This laser could cover the wavelength range from 540-750nm, but several different dyes would be required. The other laser had only one amplifier and was pumped by the third harmonic wavelength of the Nd:YAG laser. This laser can pump dyes from 400-750nm, however, because the power of the third harmonic wavelength is lower than that of the second, this laser was used only for pumping dye below 540nm. The wavelength is selected by rotating the mirror which is on a sine drive. This is controlled by a dedicated unit that allows a desired wavelength and a scan speed to be specified, however, this unit is not computer controlled and must be manually programmed.

As mentioned above, many RIMS experiments demand wavelengths from 200nm-400nm which requires frequency doubling of the output of the dye laser. When the wavelength needed to be scanned an Inrad J-12 Autotracker unit (Interactive Radiation Inc., NJ, USA) was used. This system continually monitors the ultra-violet power and makes adjustments to ensure that the crystal is constantly at the optimal angle for second harmonic generation as the incident wavelength varies. When scanning of the wavelength was not required the crystal was placed in a mount which was rotated manually until the maximum frequency doubled power was obtained.

The ionising laser beams are directed from the lasers into the analysis chamber through a series of 45° quartz prisms. In experiments where two different wavelength beams were combined a broadband dichroic mirror was used. A Newport 935-5 precision attenuator could be used to vary the power of the beams before they entered the chamber. The laser beams were focused into the system through a 30cm quartz lens which was mounted to allow adjustment of the beam position in both the horizontal and vertical planes.

Accurate determination of the laser wavelength is required if it is to be tuned to an atomic resonance. The dye lasers had a specified resetability of 0.001nm and an accuracy of 0.005nm, however, in practice it proved necessary to calibrate them for wavelength from some external source each time the laser dye was changed. Wavelength calibration could be achieved by employing the optogalvanic effect in a hollow cathode

discharge lamp (Duncan and Devonshire, 1991). The basic principle of this technique is that when the laser wavelength is in resonance with an allowed transition of the atoms in the discharge then the equilibrium in the discharge is disturbed and there is a variation in the discharge current. If the current is monitored as a function of wavelength a series of peaks are observed, each of which corresponds to a transition of one of the species in the discharge. It was found that the great majority of the observed transitions occur in the buffer gas of the lamp, which is usually argon or neon. Many of the observed transitions can be assigned by comparison with known emission lines in these gases. This can be a rather time consuming procedure. It is possible to computerise the assignment of the lines, however, this has not been implemented in Glasgow. In practice, if it was believed that the laser wavelength was close to that required for RIMS then it was easier to simply scan the laser wavelength until a RIMS or RLA (see Chapter 5) signal was obtained. Whichever method was employed it usually took a significant time to tune the lasers to the required resonance. If RIMS is to be employed in routine analysis this problem must be alleviated, this would probably require an interferometry based wavemeter. These instruments can determine the wavelength of a pulsed laser with an accuracy of $\sim 0.001\text{nm}$. However, these systems are expensive and would constitute a substantial element in the cost of a commercial RIMS system.

§3.3.2 Ablation lasers

The requirements for an ablation laser detailed in §3.3 can be obtained from a Q-switched Nd:YAG laser with harmonic generation facilities. Two such lasers were used during the course of the work reported in this thesis. Initially, a Quantel YG 585 'Compact' (Quantel, Cedex, France) was used. This system had an oscillator rod pumped by two flashlamps. The crystals for harmonic generation were not in a temperature stabilised environment and as a consequence the stability of the outputs was not good (McCombes, 1991b). Therefore, for the work detailed in Chapter 4, a JK HyperYAG 750 (Lumonics, Rugby, UK) was obtained from the Rutherford Appleton Laboratory Laser Loan Pool. This system is very similar to the Spectron Nd:YAG illustrated in Fig.3.6, with two significant differences. Firstly, since only one wavelength was required at one time, selectively reflective mirrors were not necessary and the required wavelength was

selected with a prismatic separator. Secondly, in order to provide an output with a single spatial mode, a ceramic aperture was inserted into the oscillator cavity. This reduces the power of the fundamental output by approximately a factor of three, but since pulse energies of $\sim 1\text{mJ}$ were required for ablation experiments, this was not problematic. A detailed discussion of the arrangement used to apply this laser for ablation studies is given in §4.2.1.

§3.4 Data acquisition electronics and software

This system has to synchronise the firing of both laser systems and to record the resulting detector signals along with other significant experimental parameters, such as the laser power, on a pulse to pulse basis. The whole process is controlled by an Compaq Deskpro 386/25 IBM PC compatible computer and the complete data acquisition system is shown in Fig.3.8. A detailed discussion of the design and development of this system has been given previously (McCombes, 1991b). A brief account of each element will be given below, followed by a description of the operation of the system.

The signal from the detector is digitised by a LeCroy 2261B image chamber analyser (LeCroy, Spring Valley, NY, USA), which operates as a transient recorder. This is configured to digitise a negative signal from 0.1-1.9V with a resolution of 1mV at a speed of up to 100MHz. The signal is divided into 640 temporal bins, which are each of 10ns duration when the system is operated at 100MHz. This gives a $6.4\mu\text{s}$ window on the detector output. The 2261 acts to integrate the total charge in each of the 10ns windows during the $6.4\mu\text{s}$ immediately prior to the application of an external 'stop' pulse. The clock frequency of the device can be reduced to 40MHz, 20MHz or 10MHz, using a custom built frequency generator, allowing the temporal window to be increased to $16\mu\text{s}$, $32\mu\text{s}$ or $64\mu\text{s}$. However, as the number of bins is fixed at 640, the temporal size of each bin is also increased, resulting in poorer time resolution.

It was found that the base level of the charge coupled device in the 2261 was prone to temporal drift. To overcome this problem the 2261 was run at 20Hz so that the baseline of the 2261 could be determined after every laser shot. The software then corrects the data for the background by

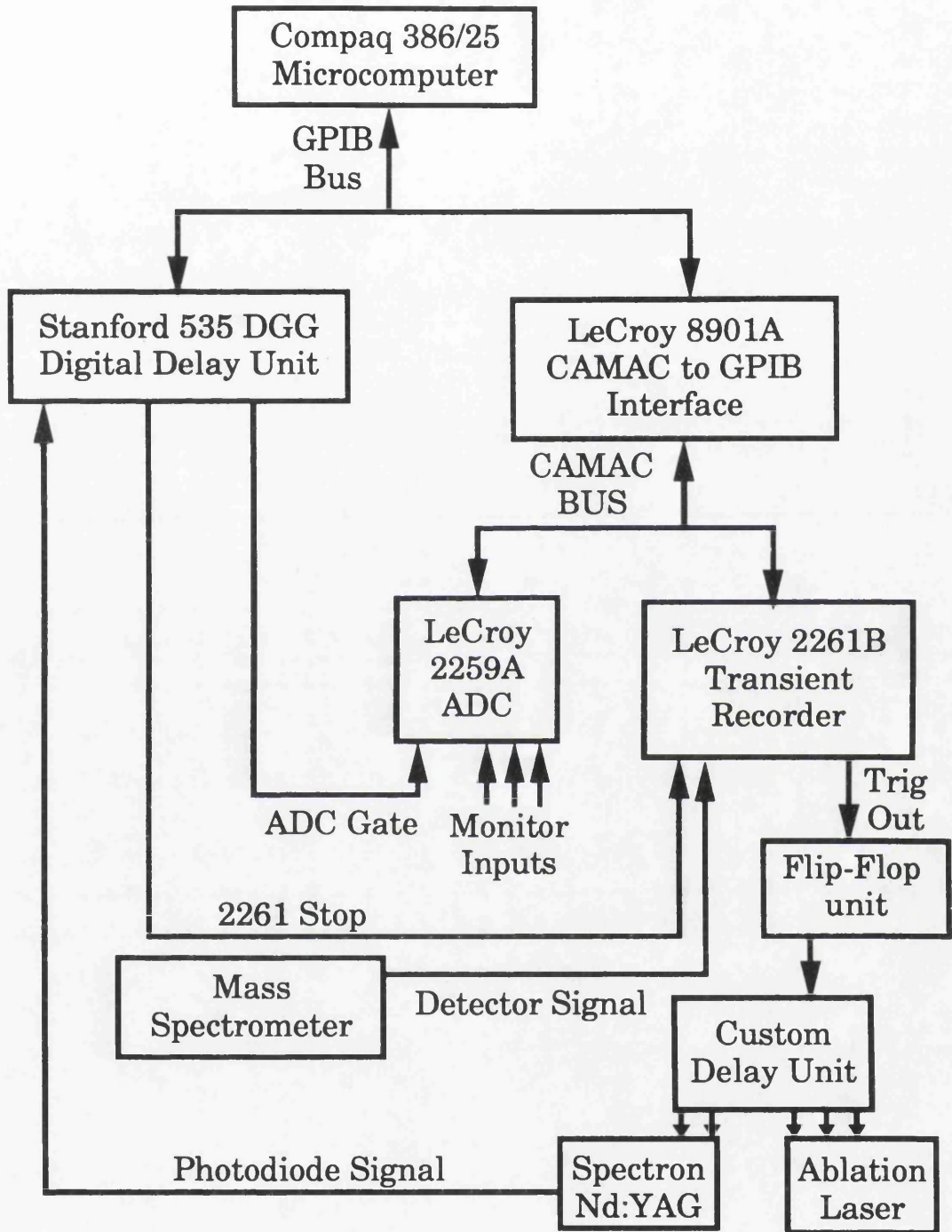


Fig.3.8 Schematic of the data acquisition system

subtraction and the remaining signal is recorded. This was known as the flip-flop mode of operation, since a unit based around a digital flip-flop was used to ensure that the lasers were only fired on every second trigger from the computer. The dynamic range of the instrument operating in this fashion was determined to be >60dB. It is also possible to operate the 2261 in a pulse counting mode, using a software set discriminator threshold. However, this requires single ion signals to be larger than was the case during the experiments detailed in this thesis. The 2261 is interfaced to the computer by a GPIB bus via a CAMAC to GPIB interface (LeCroy 8901A). A third CAMAC unit, a LeCroy 2259B 12 channel, 11 bit, peak sensing analog to digital converter (ADC) is also housed in the CAMAC crate. This allows for experimental parameters, such as the laser power or the hollow cathode lamp signal to be recorded during data acquisition. This unit also produces an essential LAM interrupt, which cannot be generated by the 2261. Hence the ADC must always receive a gate signal even if there is no requirement to record any other signals.

A Stanford DG535 digital gate and delay generator (SRS, Sunnyvale, CA, USA) was used to provide the gate signal for the ADC and the 'stop' signal for the 2261. This unit was also interfaced to the computer through the GPIB bus. The trigger for this unit was provided from a fast photodiode responding to the output of the ionising laser. A custom delay unit is used to trigger both the ablation and ionising lasers. This unit has to fire the flashlamps of both lasers and then fire the Q-switches of the ablation and ionising lasers with a precise and variable delay between them. The timing sequence used with the Quantel Nd:YAG is shown in Fig.3.9(a). However, these delays were not appropriate for the JK HyperYAG and a new delay unit was designed and built so that this laser could be incorporated into the system. The timing sequence of this unit is shown in Fig.3.9(b). The delay between the firing of the ablation laser and the ionising laser is variable, as is the delay between the firing of the flashlamps and the Q-switch of the JK HyperYAG. This facility allows the output power of the laser to be varied without any effect on the beam position, which was very useful in experiments where the power of the ablating beam had to be varied.

As mentioned above, computer software was developed to control the data

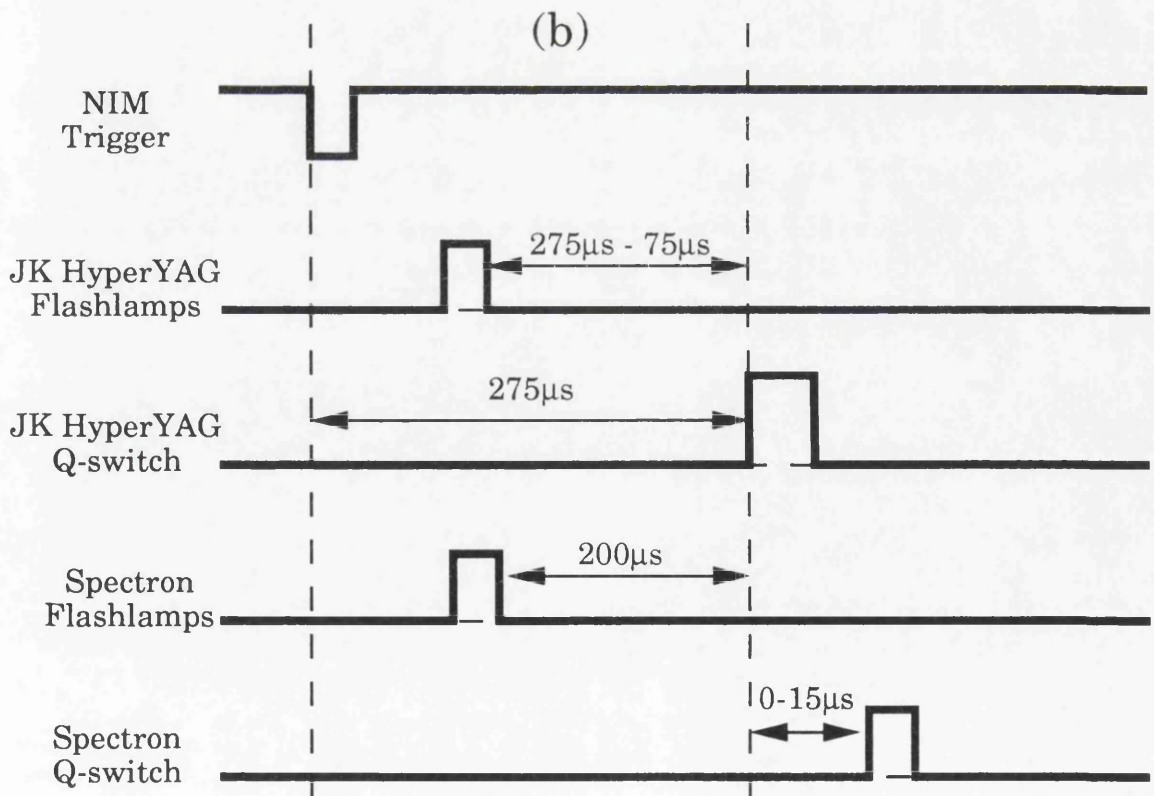
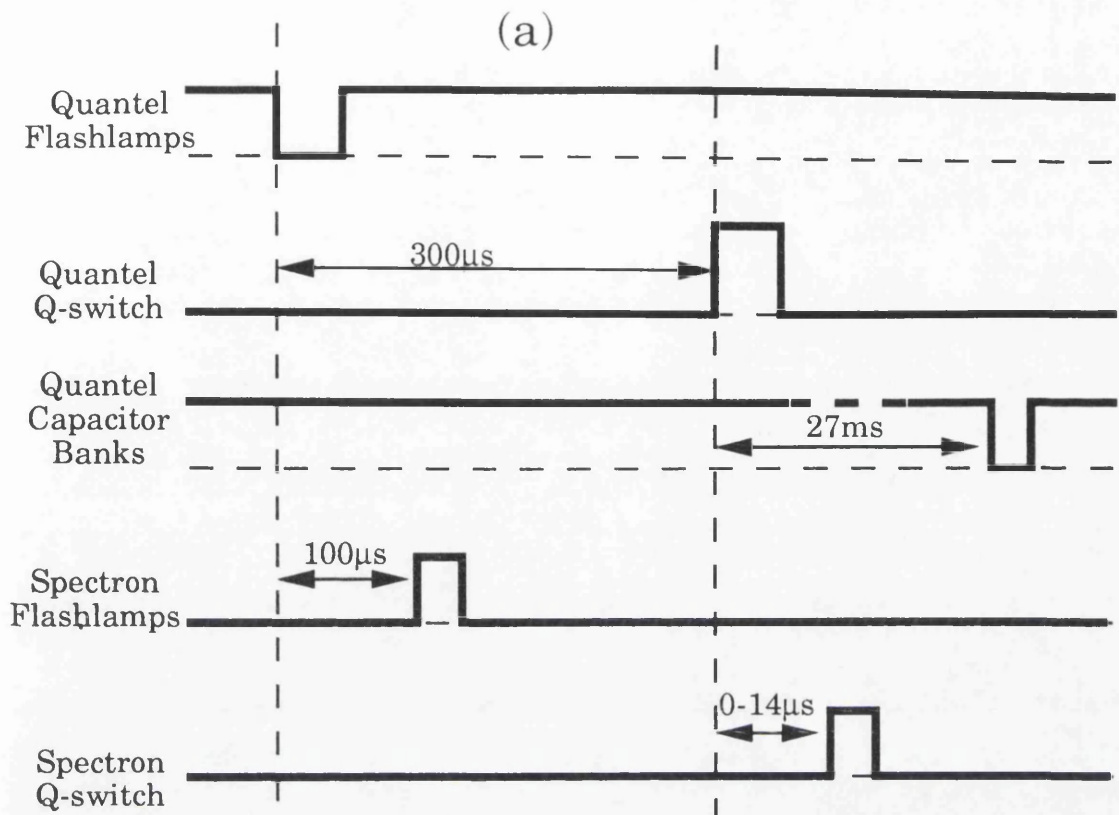


Fig.3.9 Timing sequence of custom pulse generators for (a) Quantel Nd:YAG and (b) JK Hyper YAG ablation lasers.

acquisition cycle, record the data and allow the subsequent analysis of this data graphically. This was all achieved with one FORTRAN program, called PLOT5, which was written and developed by Dr P T McCombes. There are two different modes of data taking. A subprogram called READ2261 allows the system to perform essentially as a digital storage oscilloscope in summation mode. After each laser shot the section of the time-of-flight spectrum recorded in the 640 time bins is added to the data previously recorded. It is possible to record a summed spectrum with a user specified number of shots. However, more useful is the facility where a number of such summed spectra are acquired consecutively. This is known as a 'many spectra run' and between the acquisition of each spectrum the stop time can be incremented by the software, allowing the compilation of a mass spectrum. Alternatively, some other experimental parameter can be altered in the interval between the acquisition of spectra. In many of the experiments reported in this thesis the delay between the ablation laser and the ionising laser was varied in this interval. The second mode of data collection was used for recording the dependence of a specific ion peak on a time varying parameter, usually the dye laser wavelength. This subprogram is called SPEC. The time-of-flight and width of the peak of interest are entered and the ion signal recorded in this interval at each laser shot is recorded. It is also possible to record two ADC channels, which allows the optogalvanic signal and the laser power to be monitored.

The program also allows for the analysis of the recorded data after acquisition. In particular it is possible to convert time-of-flight spectra to mass spectra, using the relationship in Eqn.3.2. It is also possible to integrate ion peaks and to obtain a hard copy via a colour plotter.

The acquisition of the data produced by a single laser shot involves the following sequence, shown schematically in Fig.3.10. A start pulse is transmitted from the computer across the GPIB bus through the LeCroy 8901A to the 'CAMAC Trig out' terminal of the 2261. This signal is then transmitted to the flip-flop unit. If data is to be acquired that shot the custom delay generator is triggered, which results in the firing of the lasers. As mentioned above this results in a photodiode signal which triggers the Stanford 535. If a background spectra is to be acquired then

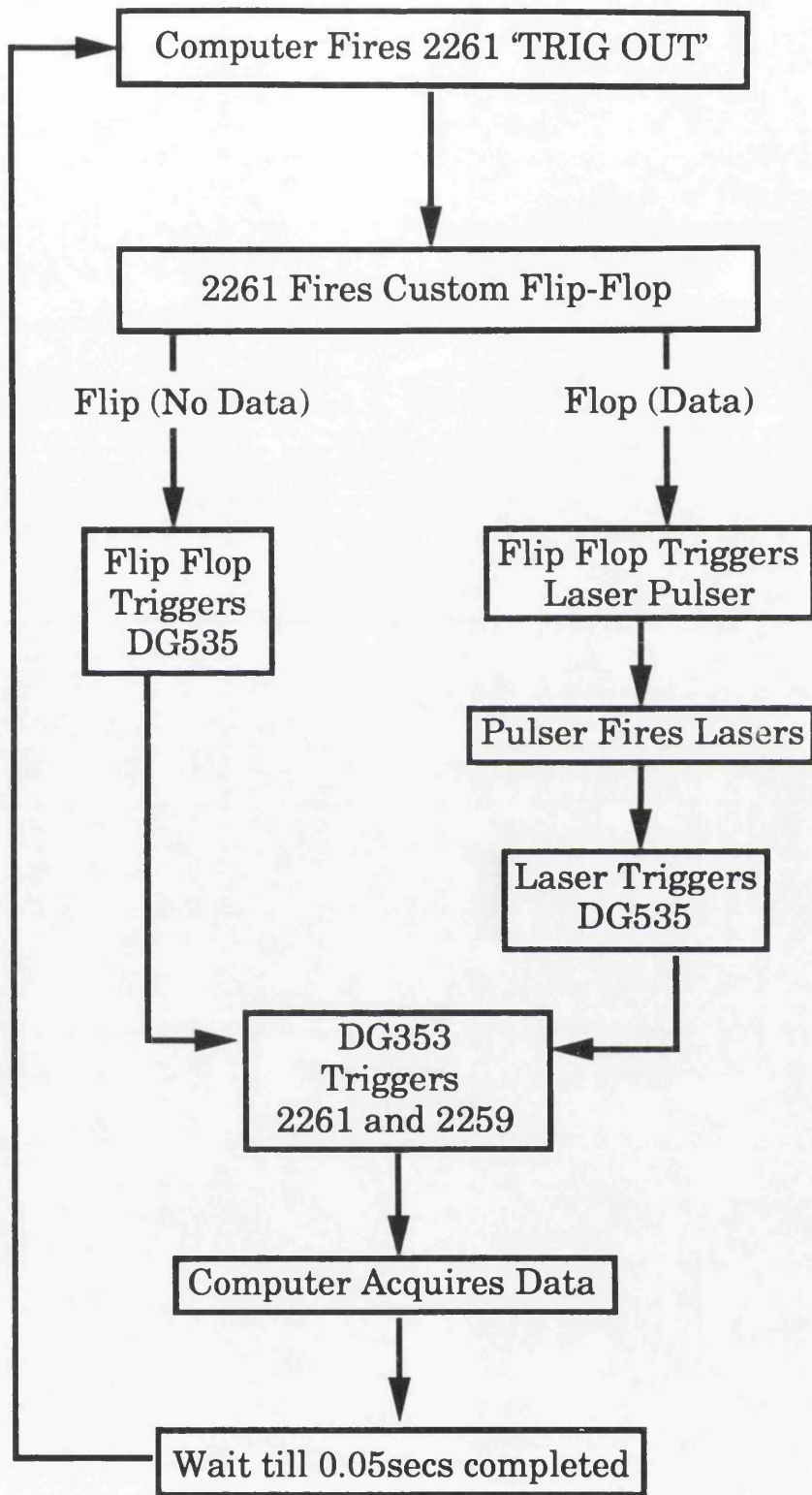


Fig.3.10 Timing of the data acquisition system

the flip-flop unit triggers the Stanford 535 directly. A fail-safe facility is incorporated in the flip-flop unit. This ensured that if the laser was triggered and for some reason the photodiode did not register, the Stanford 535 was triggered after 20ms. This prevented that the data run from stalling if the laser fail to fire when triggered, which it did occasionally. The Stanford 535 generates two pulses, a stop pulse for the 2261 and a gate signal for the ADC. These delays can be set manually directly into the Stanford, or the stop time can be set from the computer across the GPIB bus. The signal from the detector and any other experimental signals are amplified or attenuated to ensure that they fall within the range of -100mV to -1.9V and are fed into the data acquisition equipment. The signals are then digitised and the data is transferred to the computer, again across the GPIB bus.

§3.5 Previous studies with the RIMS system

After the construction of the system in 1988 a series of experiments were undertaken to utilise its capability for both trace analysis and atomic spectroscopy. Some of these experiments will be discussed briefly in this section, with particular significance being given to those results which have relevance to the work of the author reported in this thesis. The first trace analysis performed involved the detection of rubidium present at a trace level in a coal standard (Towrie *et al*, 1990). The sample was US National Institute of Standards and Technology (NIST) standard 1632a, with a certified concentration of rubidium of 15 parts per million (ppm), mixed with a equal mass of graphite. A rubidium signal was readily observed when the laser wavelength was tuned to an atomic resonance in rubidium, illustrating the trace analysis capability of the system. However, as can be seen from the portion of the mass spectrum shown in Fig.3.11, carbon clusters formed by the ablation laser are also detected. These clusters were detected when the ionising laser was switched off and therefore constituted an unwanted background to the RIMS signal. A discussion of the methods investigated to prevent this interference is given in §4.10. In order to further investigate these carbon clusters experiments were performed with a pure graphite sample, with ionisation achieved only by the ablation laser (Singhal *et al*, 1991). Similar studies had been performed previously (O'Keefe *et al*, 1986) and the prominent features reported by these researchers were observed. Specifically clusters, C_n ,

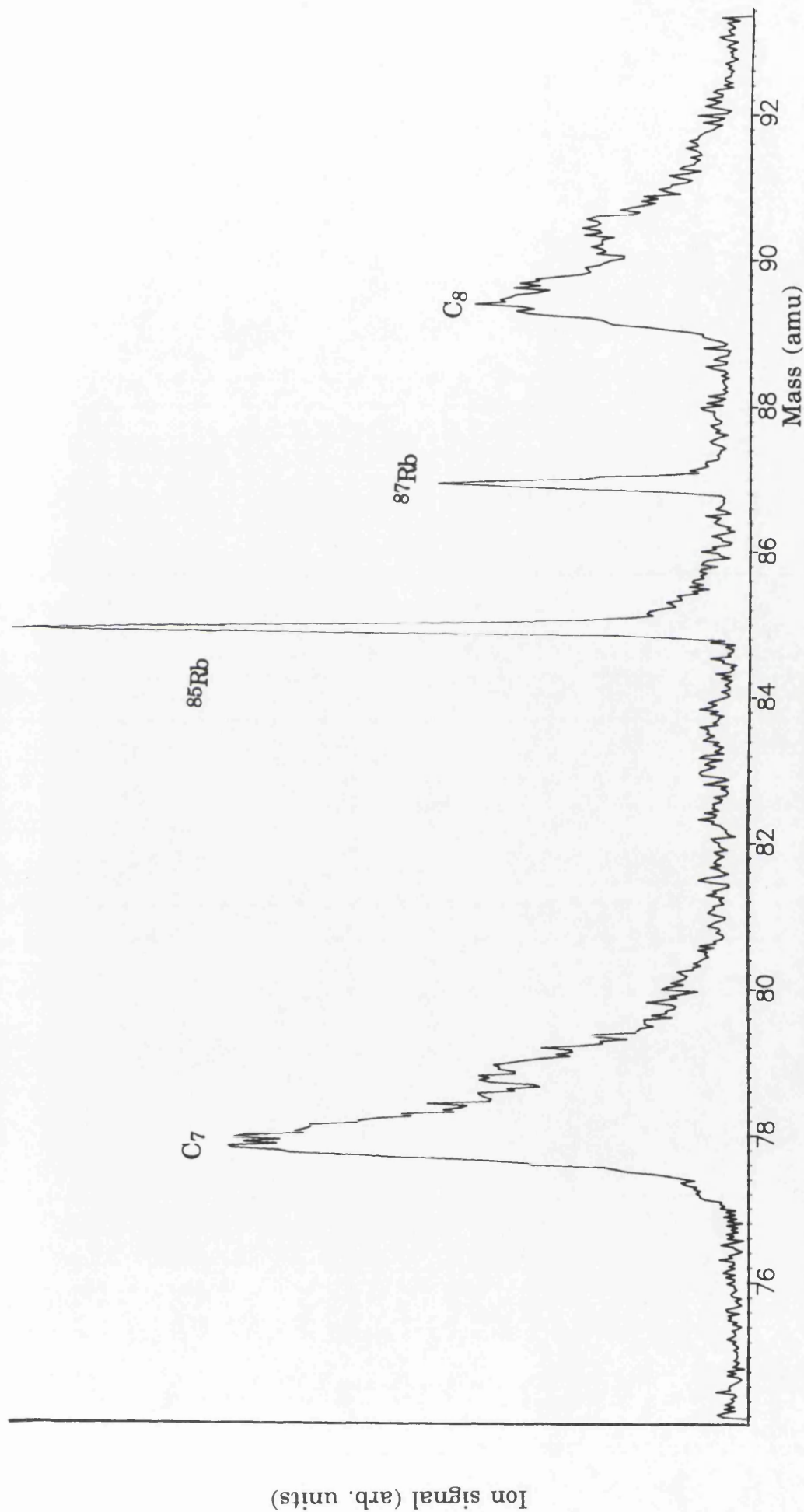


Fig.3.11 Section of a mass spectra from the analysis of a NBS 1632a coal standard that contains rubidium at 15ppm. The ionising laser is tuned to 420.7nm which is resonant with a transition in Rb. The C_7^+ and C_8^+ peaks are formed from graphite in the sample by the ablation laser.

were observed for all $n < 31$, whereas the higher mass clusters only have even n . The formation and structure of carbon clusters, especially the C_{60} cluster or 'Buckyball' has been the subject of much research in recent years (Duncan and Rouvray, 1989; Krätschmer *et al.*, 1990). A significant property of carbon clusters is that their mass can be accurately assigned. Therefore, the mass spectrometer can be calibrated for masses up to 2568amu ($n=214$). Fig.3.12 shows that the dependence between the time-of-flight and the square root of the cluster index (and therefore mass) is described by a straight line. This illustrates that the system shows good linearity over a large mass range.

The application of the system to laser spectroscopy was demonstrated for atomic calcium (Land, 1990; Land *et al.*, 1992). The calcium vapour was formed by laser ablation of a calcium metal sample. During these investigations a study of the characteristic laser ablation of calcium metal was undertaken (Towrie *et al.*, 1990). These studies involved monitoring the RIMS signal as a function of the delay between the ablation and ionising lasers. As was discussed in Chapter 2 this temporal distribution can be simply converted to a velocity distribution of the ablated atoms if the distance from the sample to the ionising beam is accurately known. Using the Quantel Nd:YAG laser for ablation three different ablation laser wavelengths were investigated; 1064nm, 532nm and 355nm. The fourth harmonic proved to be too unstable to obtain reasonable data. The distributions obtained are shown in Fig.3.13. This data was fitted by the half-range Maxwell-Boltzmann distribution, Eqn.2.13, using the s.t.p. boiling point of calcium as the characteristic temperature. However, this was not a good fit to the experimental data. To obtain a better fit it was assumed that the ablated material was emitted with a significant velocity in the plane of the sample. This was assumed to be a fraction, $\alpha=15\%$, of the most probable velocity normal to the sample. Hence the material can be thought of as forming a cone and since, as mentioned above, the ionising volume of the system is limited, not all of the material in the cone is ionised. This effect is more pronounced for material with a lower initial velocity, which is detected at the longer delay times. As shown in Fig.3.13, this addition to the model resulted in an improved fit to the data. The difficulty with this approach is that the value of α is difficult to determine

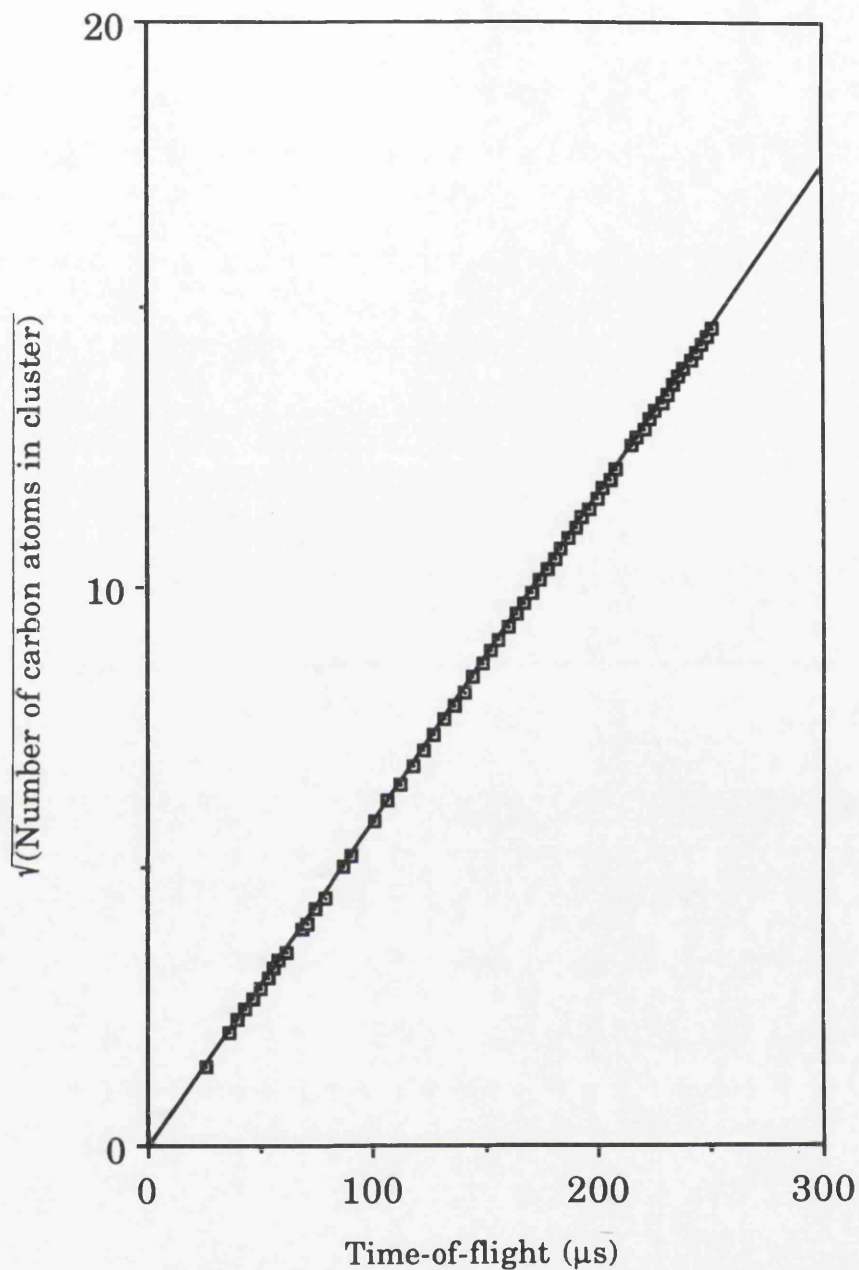


Fig.3.12 The time-of-flight of C_n ions formed by the laser ablation of graphite against the square root of the number of atoms in the cluster (which is directly related to the mass). This graph illustrates that the mass spectrometer displays good linearity up to $\sim 2500\text{amu}$.

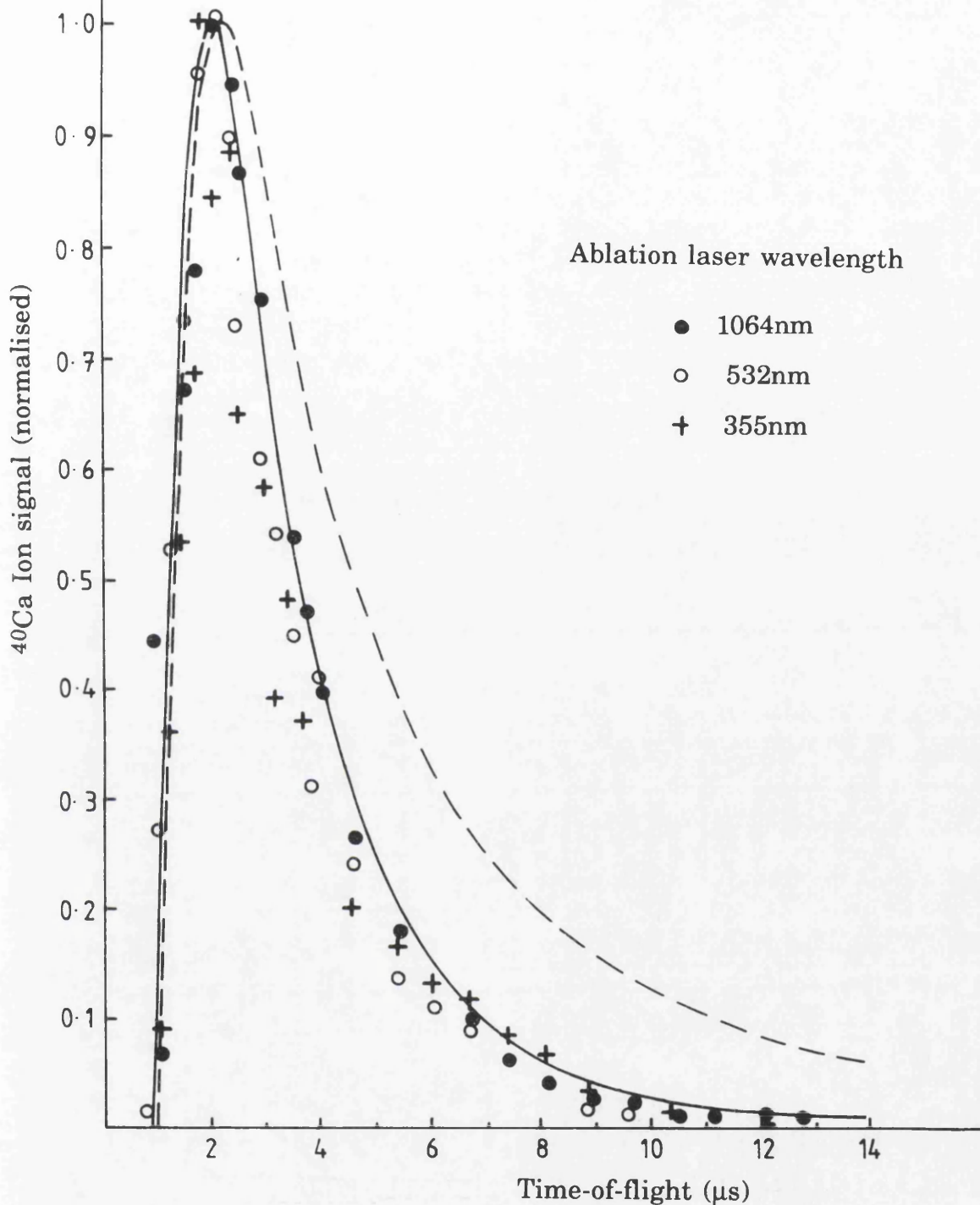


Fig.3.13 The variation of the calcium RIMS signal with the delay between the ablating and ionising lasers. Three different wavelengths were used for ablation: 1064nm, 532nm and 355nm. The data is modelled by a full-range Maxwell-Boltzmann distribution (Eqn.2.13), using the boiling point of calcium as the characteristic temperature (broken line). An improved fit was obtained when this model was modified by assuming that the ablated atoms had a component of velocity in the direction parallel to the sample surface (solid line).

unless the characteristic temperature is assumed. For this reason this approach was not employed by the author. Instead, in §4 the only variable parameter was the characteristic temperature.

The application of laser ablation with RIMS for trace analysis has also been investigated (McCombes *et al*, 1991a; McCombes, 1991b). In this work a series of five copper samples containing various well characterised trace quantities of gold were analysed. The 532nm harmonic of the Quantel Nd:YAG was focused onto the sample to cause atomisation. The gold atoms were resonantly ionised using 267.6nm photons for both excitation and photoionisation. The laser power available was low, $\sim 100\mu\text{J}$. This power was sufficient to saturate the bound-bound transition, but the ionisation step was not saturated. It was estimated that 10% of the atoms in the ionisation volume were ionised. For each of the five samples, the gold ion signal was summed for 1000 shots and this procedure was repeated twenty times utilising the many spectra run feature discussed in §3.4. A plot of RIMS signal against the sample concentration is shown in Fig.3.14. It can be seen that the average RIMS signal for each sample lies close to the line of unity gradient. It was assumed that the 10ppm lay below the line of unity gradient because the ionising laser power was observed to decrease during the acquisition of this data. The detection limit for this arrangement was determined to be ~ 200 parts per billion (ppb) for a one thousand shot analysis. Increasing the laser power so that the ionisation step would be saturated would be expected to improve the detection limit. It should be emphasised that these samples were ideal for analysis. The mass of gold is much higher than that of the copper matrix and so there is no interference from any matrix ions formed by the ablation laser. The homogeneity of these samples was believed to be excellent and the thermal properties of both matrix and analyte are very similar. It may be a combination of these factors which result in the good linearity shown in Fig.3.14 compared to the poor linearity obtained in similar work by Beekman and Thonnard, which was discussed in §2.10.1.

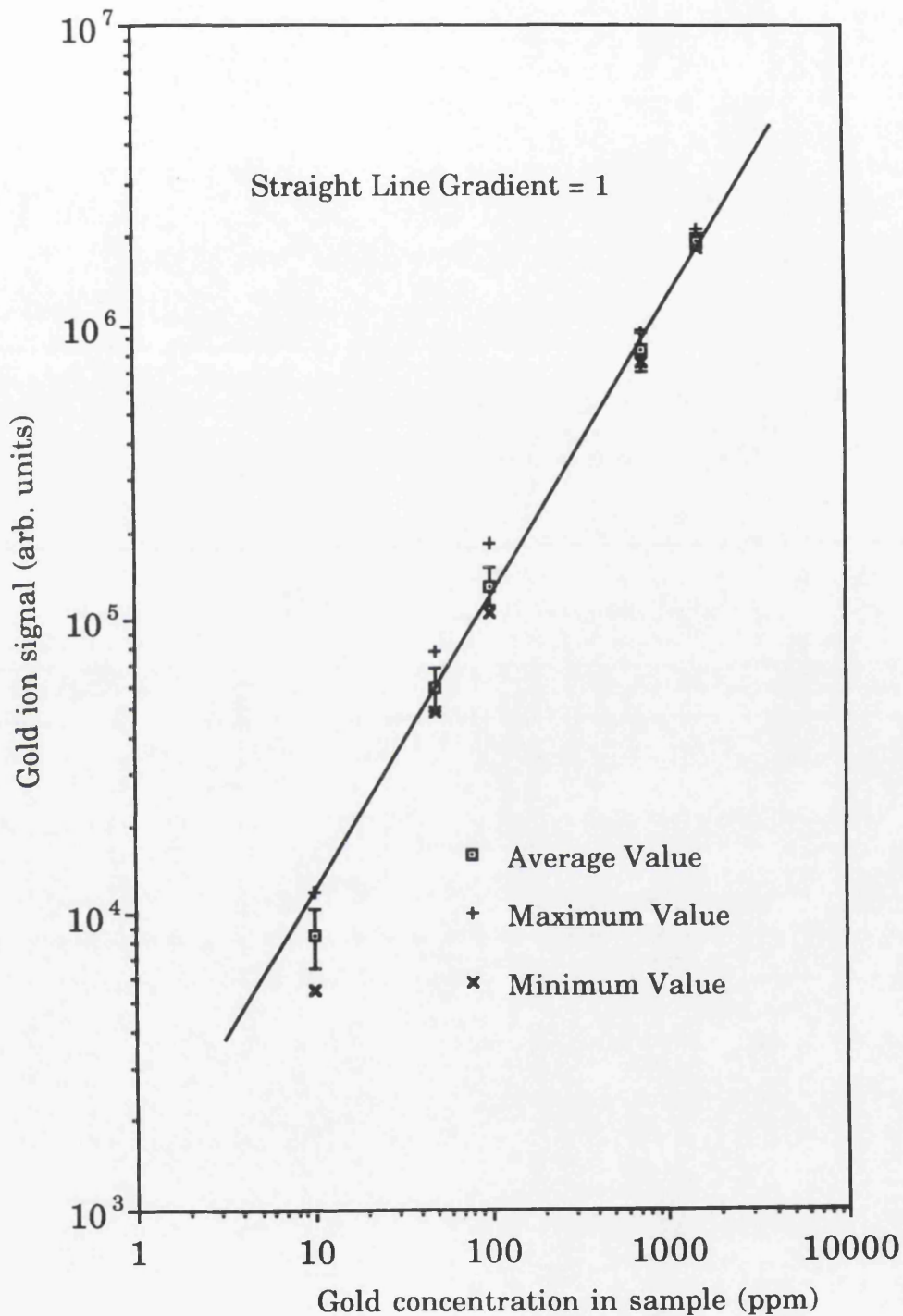


Fig.3.14 The recorded gold RIMS signal against the certified concentration of gold in a copper sample (in ppm). This graph illustrates that laser ablation initiated RIMS displays good linearity for trace analysis for these samples. The error bars show the standard deviation of the 20 recorded peaks. Each peak was accumulated over 1000 shots.

Chapter 4

Experimental Investigation of Laser Induced Atomisation

§4.1 Introduction

This chapter discusses experiments concerned with characterising and assessing laser ablation as a technique for atomising samples prior to their analysis by RIMS. This chapter will initially discuss the detailed application of this technique to aluminium, using both resonant and non-resonant laser ionisation techniques. A range of ablation laser powers and wavelengths were investigated. The applicability of the models discussed in Chapter 2 is discussed. Studies of other materials, including gold, lead and steel, will also be detailed. During the course of this work several procedures intended to increase the quantification or applicability of the technique were investigated, and these will be discussed.

§4.2 Aluminium

Aluminium was chosen as a suitable material for initial studies on the effects of changing the ablation laser parameters for several reasons. It is a highly abundant metal with only one isotope, which makes mass spectrometry very straightforward. It is considered to be the simplest nearly-free electron metal and its optical response and absorption have been studied extensively (Combis *et al*, 1991). The reflectance of aluminium is more constant over the visible wavelength range than is the case for most other metals. Over the range 200nm-1µm the reflectivity of aluminium varies by less than 10% (AIP Handbook, 1972; Combis *et al*, 1991). Furthermore, aluminium is available in many forms, both single crystal and polycrystalline, and can be easily deposited as a film or coating. It can also be obtained with certified concentrations of trace elements, as will be discussed in Chapter 6.

The spectroscopic properties of aluminium also make it an appropriate sample for routine investigations by RIMS. Aluminium has been studied previously by RIMS, both in Glasgow (McLean, 1990a), and by other researchers. This work has been reviewed recently by Saloman (1991). A

particularly efficient photo-ionisation scheme for aluminium is shown in Fig.4.1. This scheme has been the subject of detailed experimental and theoretical study (Saloman, 1991). The power density required to saturate the transition from the ground state to the excited state was calculated to be $<10\mu\text{J}/\text{cm}^2$. Due to the photon energy of the fundamental (undoubled) beam being only $\sim 350\text{cm}^{-1}$ greater than that of the transition from the excited state to the ionisation continuum, the cross-section for photo-ionisation is particularly high. It was calculated that a fundamental beam energy density of $\sim 1\text{mJ}/\text{cm}^2$ was required to saturate the photoionisation transition. This makes aluminium a particularly straight-forward element for analysis by RIMS, as these powers are easily obtainable with the laser system used for this work. The ionisation potential of aluminium (5.99eV) is below that of two photons of wavelength 266nm (an energy of $\sim 9.32\text{eV}$). Hence it is possible to ionise aluminium non-resonantly utilising the fourth harmonic output of the Nd:YAG laser.

§4.2.1 RIMS studies of 532nm wavelength laser ablation of aluminium

Initial studies used 99.0% pure aluminium metal samples, 1.02mm thick, from Goodfellow Metals (Cambridge, UK), which were cut into square sections of area $\sim 1\text{cm}^2$. These samples had a reflective front surface. To reduce the effect of this on systematic studies carried out on several samples, the front surface was roughened with 800 grit silicon carbide paper. The samples were then washed successively in high purity methanol and acetone in an ultra-sonic bath. In common with the other materials studied in this chapter the aluminium samples were attached to the sample stub using silver loaded conductive paint (RS Components, Northants, UK.). This arrangement was designed to allow a free flow of both heat and charge from the sample surface.

As mentioned in §4.1 the purpose of these studies was to gain insight into the optimum operating conditions for using laser ablation as an atomisation technique for RIMS. In the initial work the ablation laser wavelength was kept constant at 532nm, which was generated by frequency doubling the output of the JK HyperYag-750 laser described in Chapter 3. This laser was fitted with an inter-cavity aperture to generate essentially TEM_{00} output. The beam was passed through a Newport 935-5 precision attenuator and focused onto the sample with a $\sim 30\text{cm}$ focal

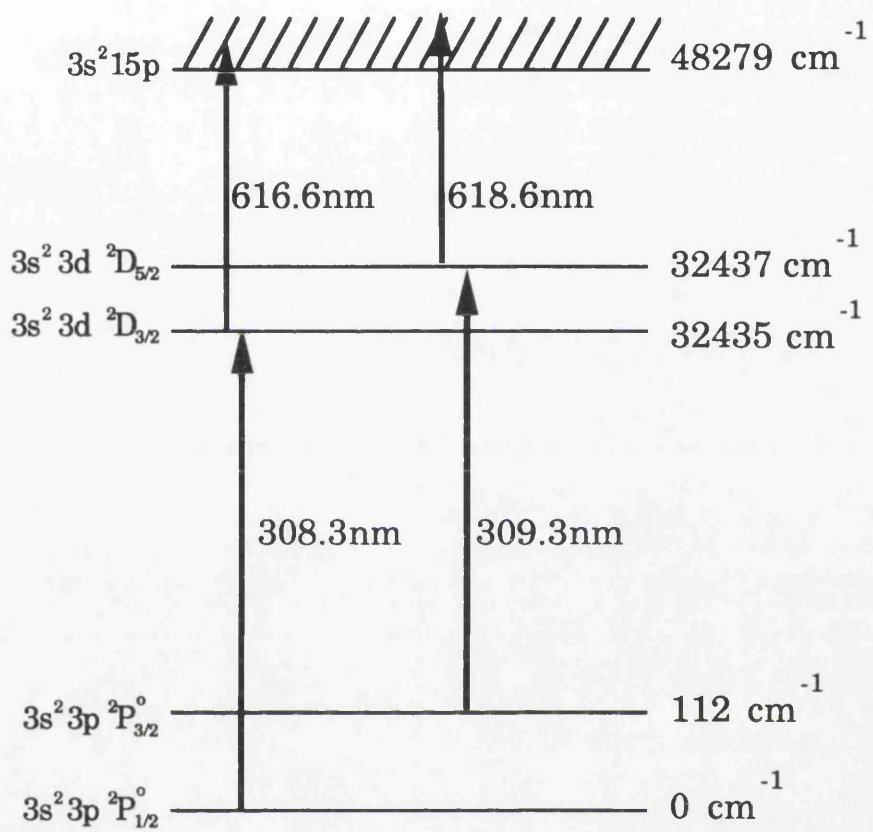


Fig.4.1 RIS scheme for aluminium

length fused silica lens, which was manoeuvrable in three directions. The arrangement is shown schematically in Fig.4.2. The stability of the power of the ablation laser beam was monitored by diverting a fraction of the pulse into a Molectron J3-09 joulemeter, the output of which was amplified and recorded by a multichannel analyser. The average power of the ablation laser beam was measured using an Ophir 2A-P thermopile meter and these values will be given in this chapter. As the laser systems were operated at 10Hz the average power in milli-Watts can be converted into the pulse energy in milli-Joules simply by dividing by ten. The ablation laser spot was positioned on the central axis of the ion optics. The laser causing the post ablation ionisation (PAI) was focused to a spot size of $\sim 400\mu\text{m}$, using a 20cm fused silica lens. The PAI laser spot was kept as small as practical for two main reasons. Firstly, this ensures that the distance from the sample to the ionising beam is well defined, which allows the velocity distribution of the neutral atoms ablated from the sample to be determined accurately. Secondly, keeping the ionisation volume as small as possible would allow the greatest density of ablated material to be analysed before instrumental saturation affected the reliability of the data. Two possible saturation mechanisms were identified; 'space charge effects' and detector saturation. Space charge effects involve Coulomb repulsion between the ions in a dense plume, and would act to broaden the energy spread of the ion packet. This can limit the density of the ion packet that can be transmitted through the ion optics (Hutt *et al*, 1989). The second area where saturation could occur is in the ion detector. This is of the dual multichannel plate (MCP) type, as discussed in Chapter 3, and is effectively an array of electron multipliers. The MCP used in this work had an active area of 4.9cm^2 and contained $\sim 4 \times 10^6$ separate channels. Non-linearity can occur when the interval between successive ions arriving at the same channel is less than the single channel dead time, which is the time required for the walls of the pore to become completely replenished with charge. The single channel dead time can be calculated by a variety of methods and is of the order of milliseconds (Anacker and Erskine, 1991). This is much larger than the delay in arrival times between individual ions of the same mass, $< 100\text{ns}$, and between different mass ions generated by the same laser pulse, typically $< 100\mu\text{s}$. The dead time is, however, much smaller than the time between successive laser shots, which at 10Hz is 100ms. Hence, for the

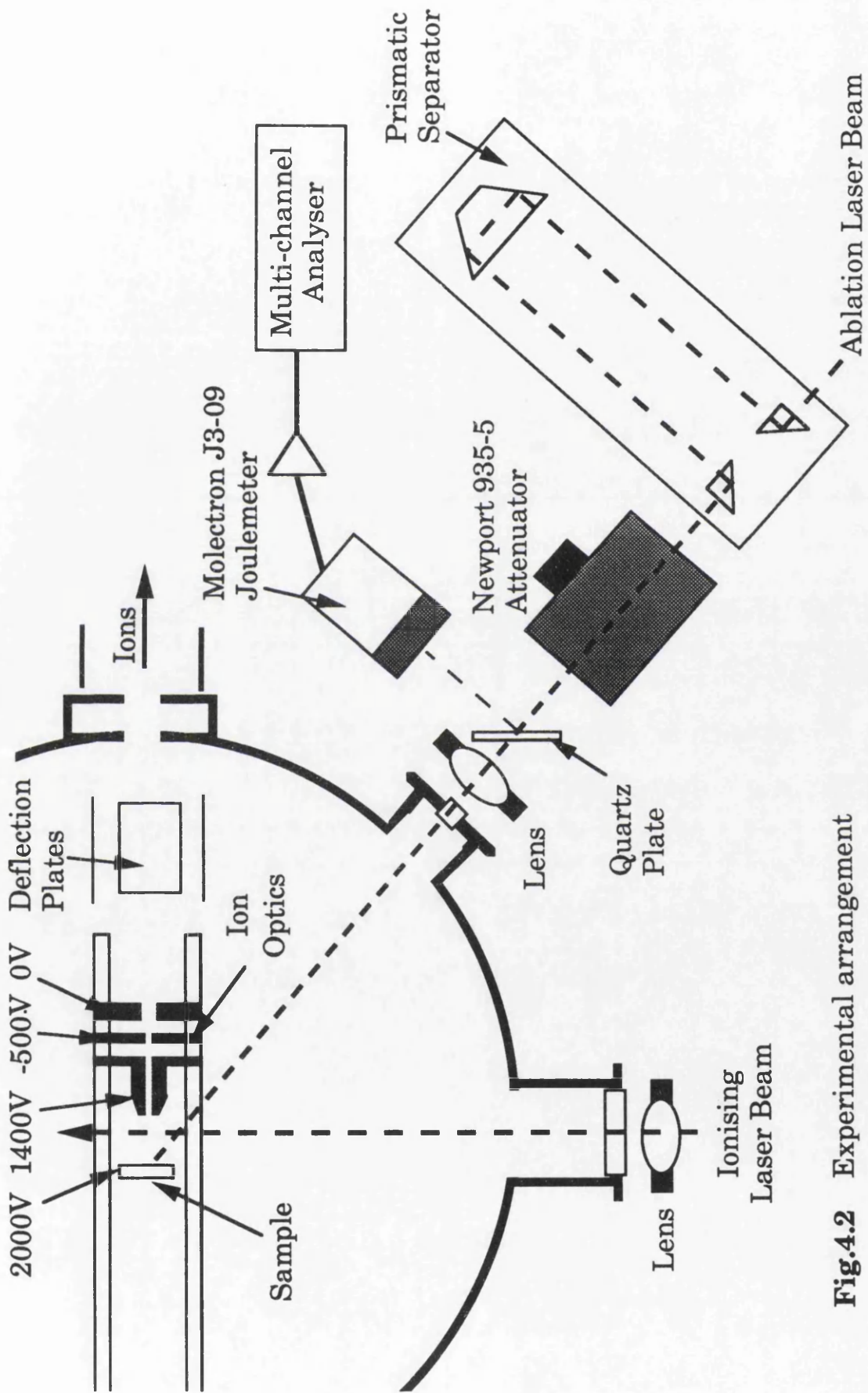


Fig.4.2 Experimental arrangement

MCP used in this work, the largest number of ions generated in a single laser pulse that could be expected to be detected linearly is $\sim 4 \times 10^6$. However, this may be an overestimate, as this would require that the ions were spread uniformly over the whole active area of the MCP, which has a diameter of 2.5cm. This may not be the case, and hence the limit for detector linearity may be lower. These arguments illustrate why it was perceived as expedient to keep the PAI laser volume as small as possible in these experiments.

The resonant ionisation scheme described above was used, with a fundamental laser pulse energy of 3mJ and a frequency doubled energy of 5 μ J. This would result in a laser power well above that required to saturate the ionisation process as described above. Indeed, it was found that increasing the fundamental laser power by 300% and increasing the power of the ultra-violet beam by over ten times, only increased the ion signal by 10%. This was attributed to the higher laser power increasing the ionising volume slightly. Therefore, the lower powers detailed above were used, as the probability of these laser powers fragmenting molecular species would be lower.

Using the arrangement described above with a sample to laser distance of 3mm, the temporal distribution of aluminium atoms ablated with the 532nm laser beam was investigated. These distributions are shown in Fig.4.3 for a range of laser powers. This data was obtained using the PLOT5 software discussed in Chapter 3. This allows a chosen number of spectra to be taken, each with a number of laser shots selected by the operator. Each spectrum consists of the contents of the 640 temporal bins of the transient recorder and gives a section of the mass spectrum. The size of this window depends on the clock rate of the data acquisition system and the masses of interest. For this work, where the transient recorder was operated at 100MHz, the window was approximately from 23-32amu and only the aluminium ion signal was of interest. However, this method of data acquisition allows several species in a multicomponent plume to be monitored simultaneously, as will be discussed in §4.5. In order to obtain temporal distributions, the delay between the two lasers was altered manually between the acquisition of spectra, using the laser delay generator that was described in Chapter 3. To achieve a reasonable

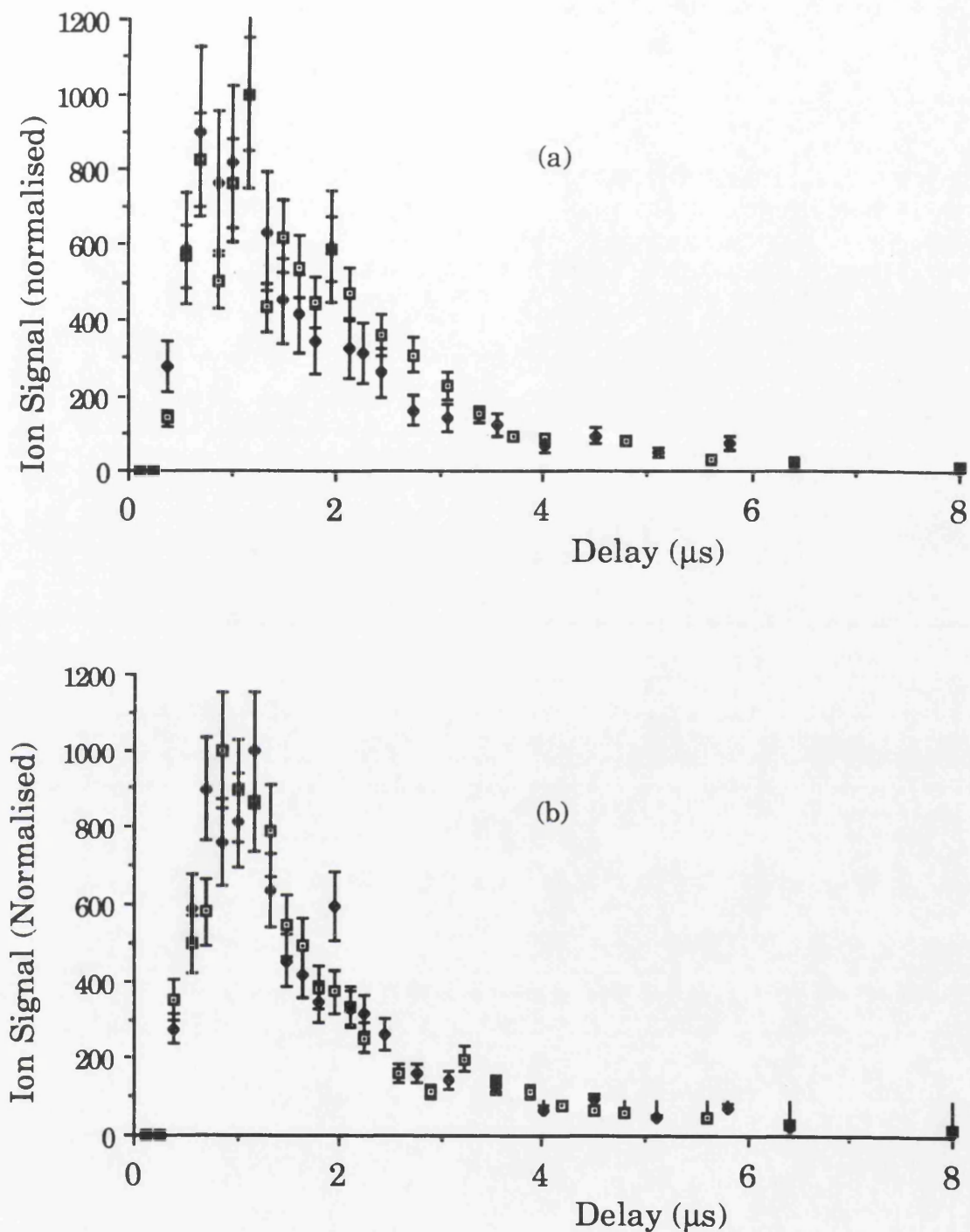
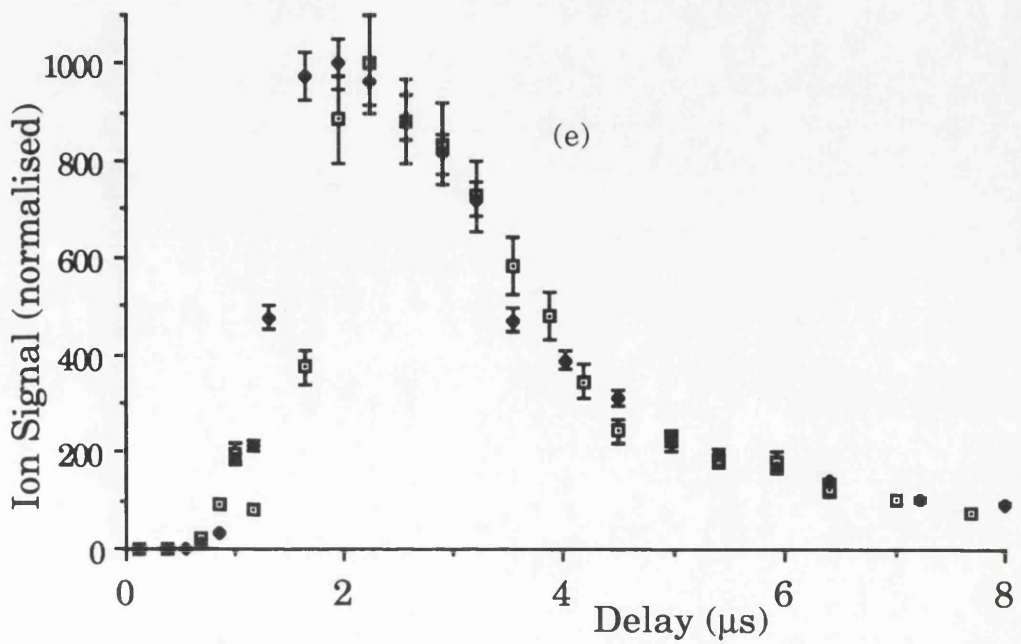
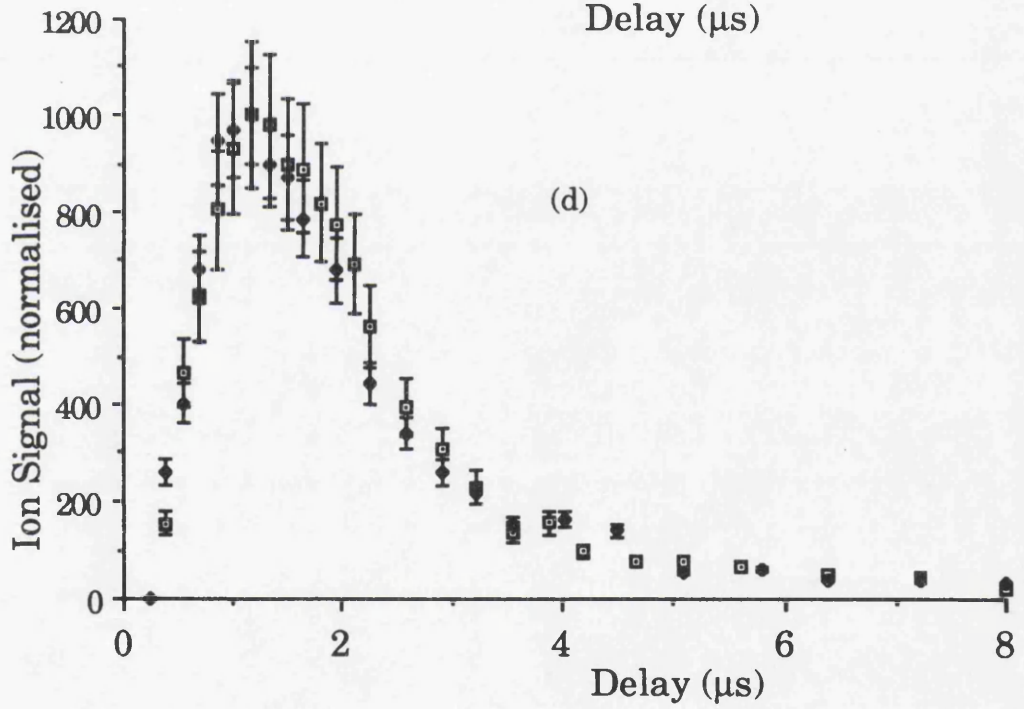
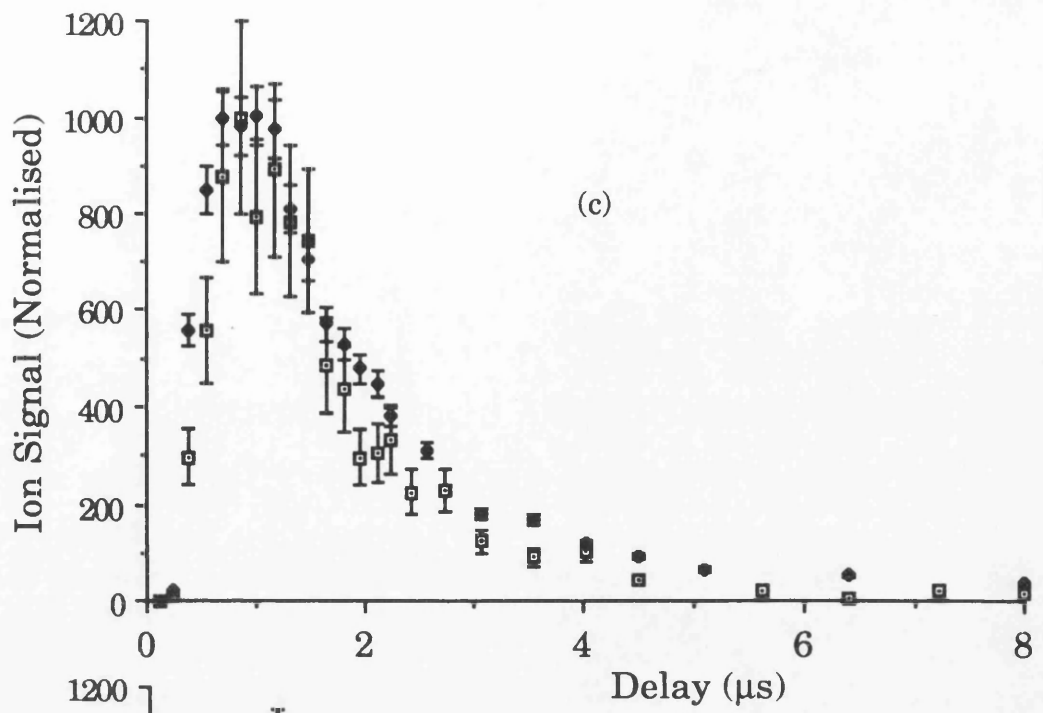


Fig.4.3 Normalised plots of the variation of the RIMS signal with increasing delay between the ablation and PAI laser. The sample was aluminium and the ablation laser powers are (a) 1.2mW, (b) 1.9mW, (c) 2.75mW, (d) 3.5mW and (e) 4.1mW. These powers correspond to values of R_{stb} (defined in the text) of 109%, 87%, 78%, 86% and 75% respectively. In each graph the open symbol signifies sampling of the $j=1/2$ level of the split ground state, while the filled symbol signifies sampling of the higher energy $j=3/2$ level. The ablation laser wavelength was 532nm.



compromise between a large enough data set for good statistics, and a sensible time for the acquisition of each distribution, 300 shots were acquired in each spectra. Each distribution required >30 spectra and between each spectra an interval of ten seconds allowed time to manually change the delay between the lasers. Hence, the acquisition of each of the distributions illustrated in Fig.4.3 required >12000 laser shots on the sample. Prior to each run the sample was moved so that the ablation laser was incident on a fresh area of the sample. It was found that during the initial several hundred shots a large ablation laser induced signal was generated. This then decayed allowing the RIMS signal to be detected. It is possible to distinguish between these two signals because of their differing shapes and times-of-flight, as will be illustrated in §4.2.2. This initial instability was always observed and has been encountered by other researchers with a similar experimental arrangement (Dubreuil *et al*, 1992). It was found that after irradiating the surface for ~2000 shots, a time-of-flight distribution could be acquired from repeated irradiation of the same area. To assess the stability and the statistics of each distribution the following procedure was undertaken. At a delay time corresponding approximately to the peak of the distribution, four spectra were taken with the same delay. This procedure was repeated at the end of the distribution with the same delay as before. Thus a qualitative assessment of both the signal stability and the effect of repeated irradiation could be gauged.

The temporal distributions shown in Fig.4.3 have all been normalised to the same peak height. For each power two distributions were obtained, at different times, by monitoring the populations of both of the levels of the split ground state. These levels are separated by 112cm^{-1} , which corresponds to a temperature of 161K from $E=kT$. Hence, these states should be in thermal equilibrium at room temperature. The measurements of the populations of the two levels were performed on separated days and therefore give an indication of the repeatability of the system. As mentioned above, an estimate of the signal stability was obtained at the start and the end of each run. To illustrate this graphically the average of the two adjusted r.m.s. standard deviations was used as the percentage error for all the data points. It should be emphasised that this is only an estimate of the stability, especially for larger delay times at low powers, where the signals are small, the uncertainty in the integrated

peak area may be larger than the stability estimate. Therefore, at long delay times the illustrated errors may be an underestimate. The size of the signal at the end of the run is expressed as a percentage of the measurement made near the start, this will be referred to as R_{stb} . Values of R_{stb} are given for each of the distributions in Fig.4.3, and are generally below 100% with the largest variance being observed at the lowest ablation laser powers. It is perhaps surprising that many thousand laser shots on the same area only changes the yield by ~20%.

There are also, of course, errors in the delay, which was set with the laser delay generator. The stability of the output of this device was good and the calibration was checked before and after the experiments described in this chapter. It was estimated that the error in the delay values was ~100ns, determined by the accuracy with which the vernier dial could be set. This is much smaller than the error in the ordinate and is not shown graphically.

It can be seen from Fig.4.3 that the form of the distribution appears to be independent of which level of the ground state was monitored. The stability of the data, and hence of the number of ground state neutral aluminium atoms in the plume, improves as the ablation laser power is increased. The effect on the yield of changing the ablation laser power is illustrated in Fig.4.4. This is a logarithmic plot and errors are not shown. Increasing the ablation laser power by a factor of three results in a change in the neutral yield of over two orders of magnitude. It should be noted that a RIMS signal could be obtained at laser powers lower than the lowest shown in Fig.4.4, but this did not produce distributions with acceptable statistics. As discussed in Chapter 2, the velocity distribution of laser liberated material can be described by a half-range Maxwell-Boltzmann distribution. Fig.4.5 shows the evaluation of Eqn.2.13 with a characteristic temperature of 12000K with some of the experimental data from Fig.4.3. A value of $i=3$ was used in this fit because this value had been used in the modelling of the experiments previously performed in Glasgow and discussed in Chapter 3. The characteristic temperature of 12000K is approximately twice the critical temperature of aluminium. The effect of reducing the temperature in this model is illustrated in Fig.4.6. It is apparent that lowering the temperature to one which could be conceived to

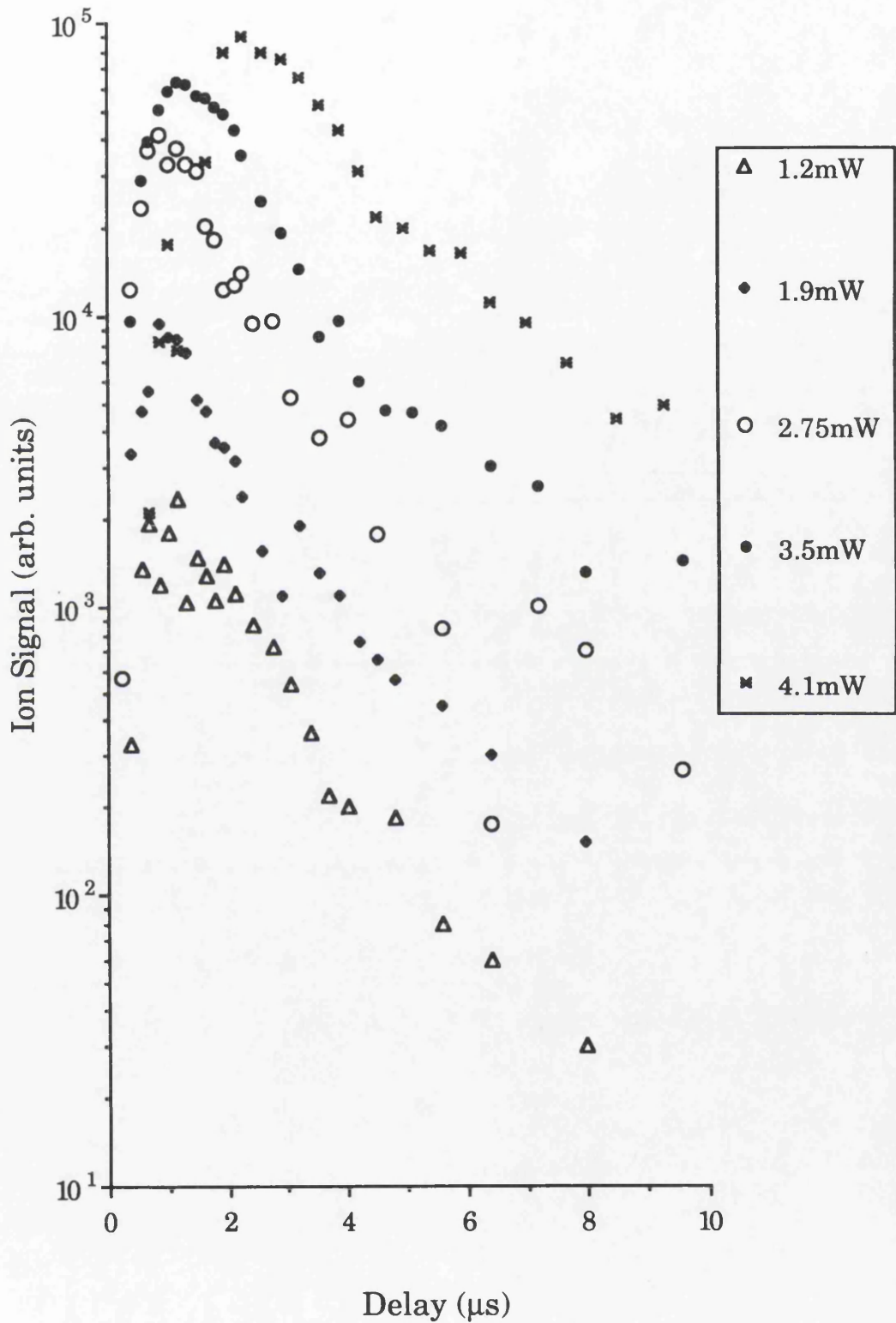


Fig.4.4 Variation of the RIMS signal with increasing delay between the ablation and PAI laser, for the laser powers in Fig.4.3. The ablation laser wavelength was 532nm.

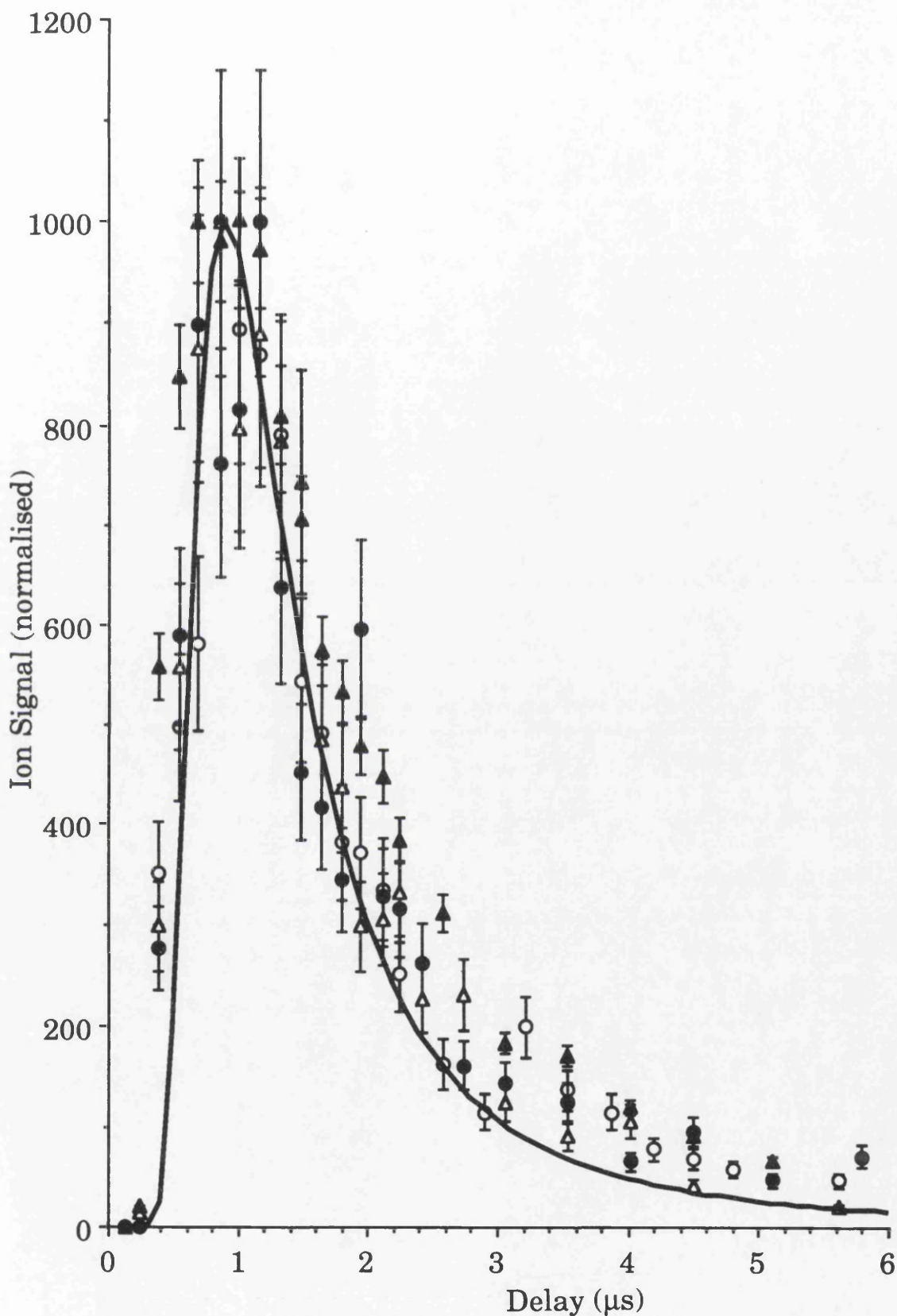


Fig.4.5 Temporal development of the RIMS signal from an aluminium sample fitted with a half-range Maxwell-Boltzmann distribution with a characteristic temperature of 12000K. The ablation laser powers were 1.9mW (circle) and 2.75mW (triangle). An open symbol signifies sampling of the $j=1/2$ level of the split ground state, while the filled symbol signifies sampling of the higher energy $j=3/2$ level. The ablation laser wavelength was 532nm.

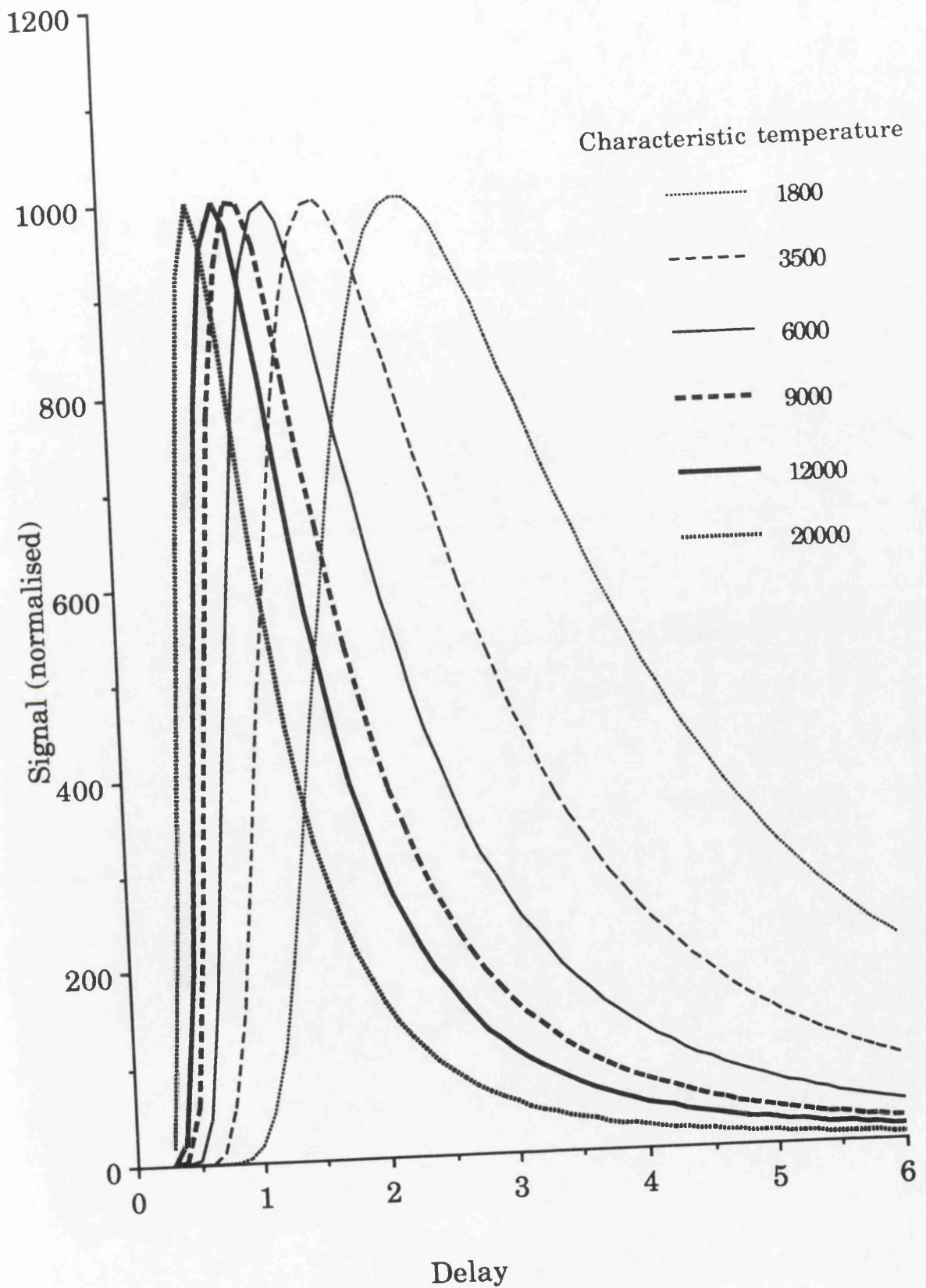


Fig.4.6 Temporal development of the half-range Maxwell-Boltzmann distribution of aluminium for various characteristic temperatures. A value of $i=3$ was used.

be consistent with thermal vaporisation, $\sim 6000\text{K}$, does not fit the data appropriately. To assess if a model could be found that was consistent with a lower characteristic temperature the Knudsen layer formalism was employed. As explained in §2.5, increasing the value of the power term, i , acts to increase the most probable velocity for a certain characteristic temperature. Hence when modelling the Knudsen layer formalism through the equations in §2.7 a value of $i=4$ was used; this is, as mentioned in §2.5, the value used by most researchers. Fig.4.7 shows the evaluation of these equations for a surface temperature of 3000K . This temperature was chosen as it was above the s.t.p. boiling point, and hence corresponds to a vapour pressure of aluminium greater than one atmosphere. The half-range Maxwell-Boltzmann distribution with a characteristic temperature of 12000K , which provided an approximate fit to the experimental data in Fig.4.5, is shown in Fig.4.7 for comparison. It is apparent that to achieve a similar most probable velocity for the Knudsen layer model the laser-sample distance should be reduced to 2mm . As mentioned previously, the laser to sample distance in this work was 3mm . The procedure for aligning the laser involved moving the sample surface forward 3mm using the manipulator. The PAI laser beam, which was carefully aligned to be parallel to the sample surface, was then positioned with the lens so that it was just stopped from exiting the chamber by the sample. The sample was then returned to its original position. The accuracy of the manipulator scale was subsequently verified to be within 10% . From the relationship between temperature and the laser-sample distance in Eqn.2.13, this would result in an error of $\sim 20\%$ in the characteristic temperature. It would appear, therefore, that a temperature somewhat higher than 3000K is required if the Knudsen layer formalism is to be used to fit the data. Hence, it would appear that a temperature appropriate to a thermal mechanism cannot be fitted sensibly to the data. The model illustrated in Fig.4.5 does, however, appear to give a reasonable fit to the experimental data.

Fig.4.4 shows that the velocity distribution at the highest powers becomes markedly broader. As shown in Fig.4.8 the model detailed above gives a reasonable fit with a lower temperature of 2500K . This is, as mentioned above, in the range of temperatures believed to be appropriate for a thermal mechanism. A possible explanation for the deviation from a

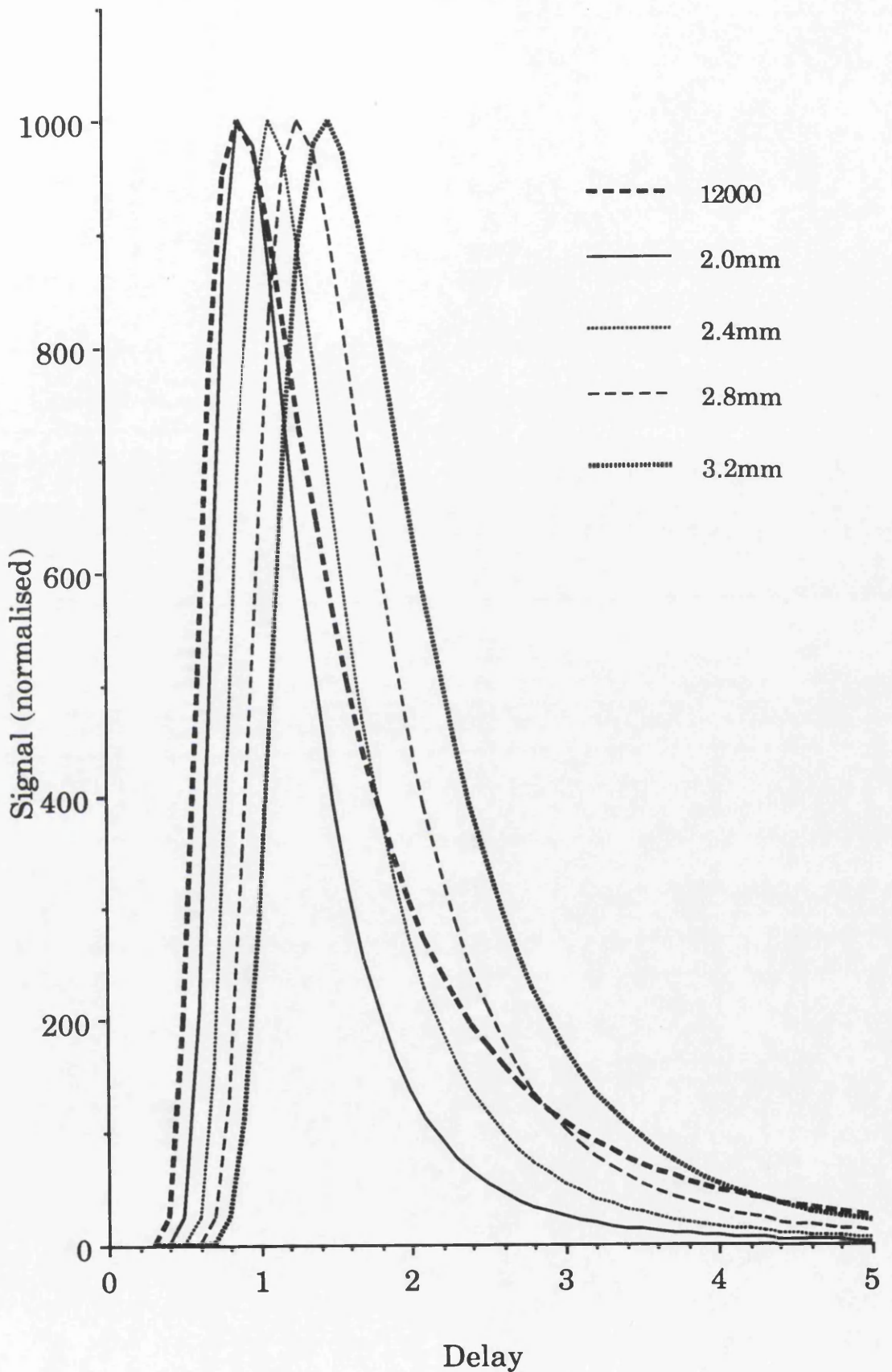


Fig.4.7 Temporal development predicted by the Knudsen layer model for aluminium with various laser to sample distances. The characteristic temperature was 3000K and $i=4$. Also shown for comparison is the half-range Maxwell-Boltzmann distribution with a characteristic temperature of 12000K where a value of $i=3$ was used.

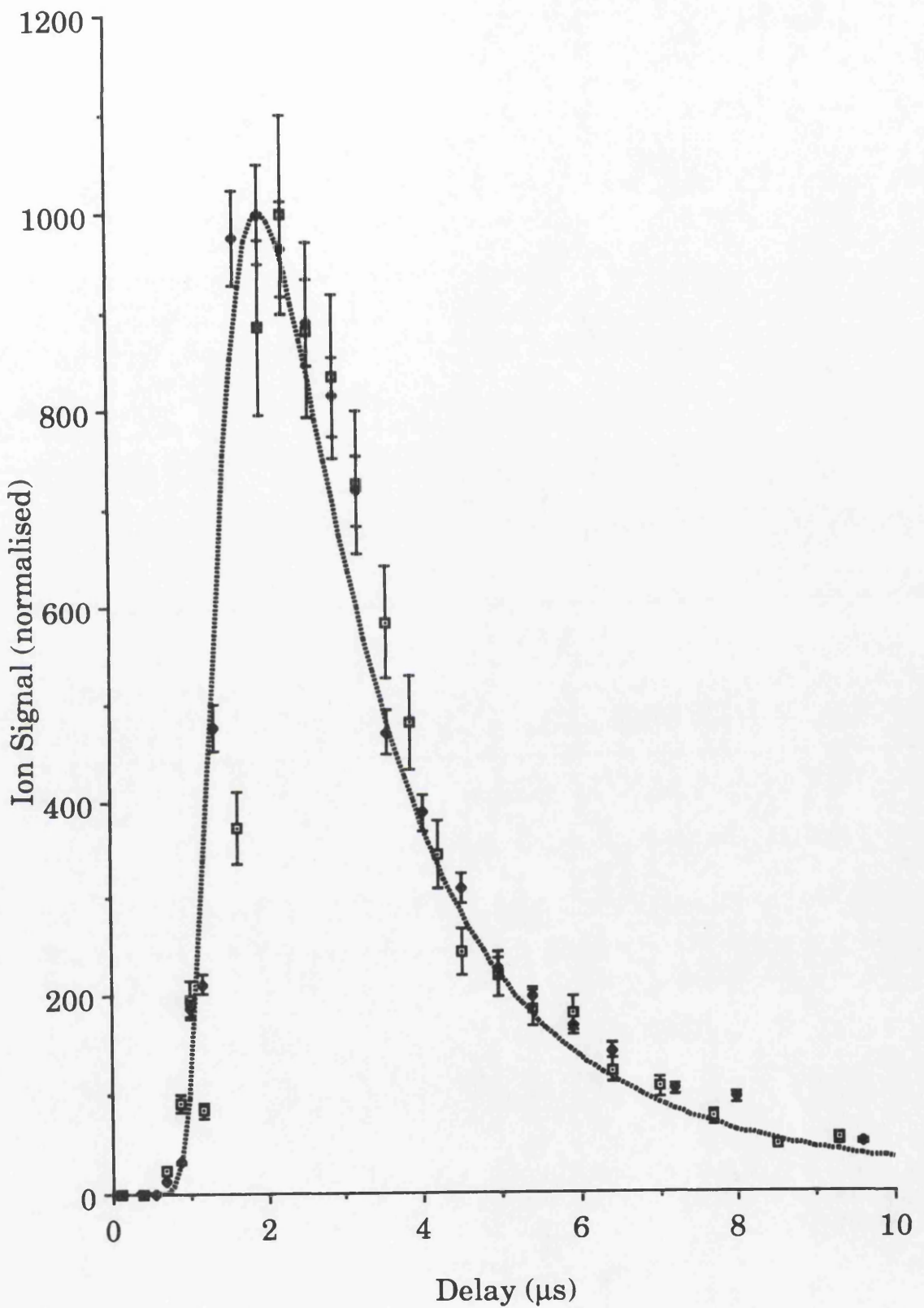


Fig.4.8 Temporal development of the RIMS signal from an aluminium sample fitted with a half-range Maxwell-Boltzmann distribution with a characteristic temperature of 2500K. The ablation laser powers was 4.1mW and the wavelength was 532nm. An open symbol signifies sampling of the $j=1/2$ level of the split ground state, while the filled symbol signifies sampling of the higher energy $j=3/2$ level.

thermal mechanism at lower powers will be discussed in §4.11.

§4.2.2 Effect of increasing laser power

The effect of increasing the ablation laser power is illustrated in Fig.4.9. The experimental conditions are the same as for the work discussed above, except that ionisation was effected non-resonantly using the fourth harmonic of the Spectron Nd:YAG laser. The PAI laser energy was kept low, ~2mJ, which would result in a power density of $\sim 2 \times 10^8 \text{W/cm}^2$. This was monitored using the thermopile meter and was stable to ~10%, both shot to shot and over the duration of a run. This power is lower than is typically used in non-resonant laser ionisation (10^9 - 10^{11}W/cm^2), as it was hoped that this would prevent excessive fragmentation of molecular species. It was not determined if the ionisation process was saturated, however, changing from resonant to non-resonant ionisation did not alter the signal stability to any degree and gave a simpler and more versatile experimental arrangement.

There are three sets of data plotted in Fig.4.9, which correspond to:

- (a) Ions created by the ablation laser alone. These are detected with the reflectron voltages set to transmit ions created at the sample surface with maximum efficiency. This arrangement is essentially that of the laser microprobe mass spectrometer (LAMMS), as discussed in §1.8.1, and a signal recorded in this mode of operation will be referred to hereafter as a LAMMS signal.
- (b) Ions created by laser ionisation of the ablated material. The reflectron voltages are set to transmit ions created 3mm from the sample surface. This is the PAI signal which has been discussed above.
- (c) Ions generated by the action of the ablation laser, but detected with the reflectron voltages set as in (b). This signal could be easily distinguished from (b) as it was observed when the PAI laser did not enter the chamber.

It can be seen that at low ablation laser energies the leakage signal is very

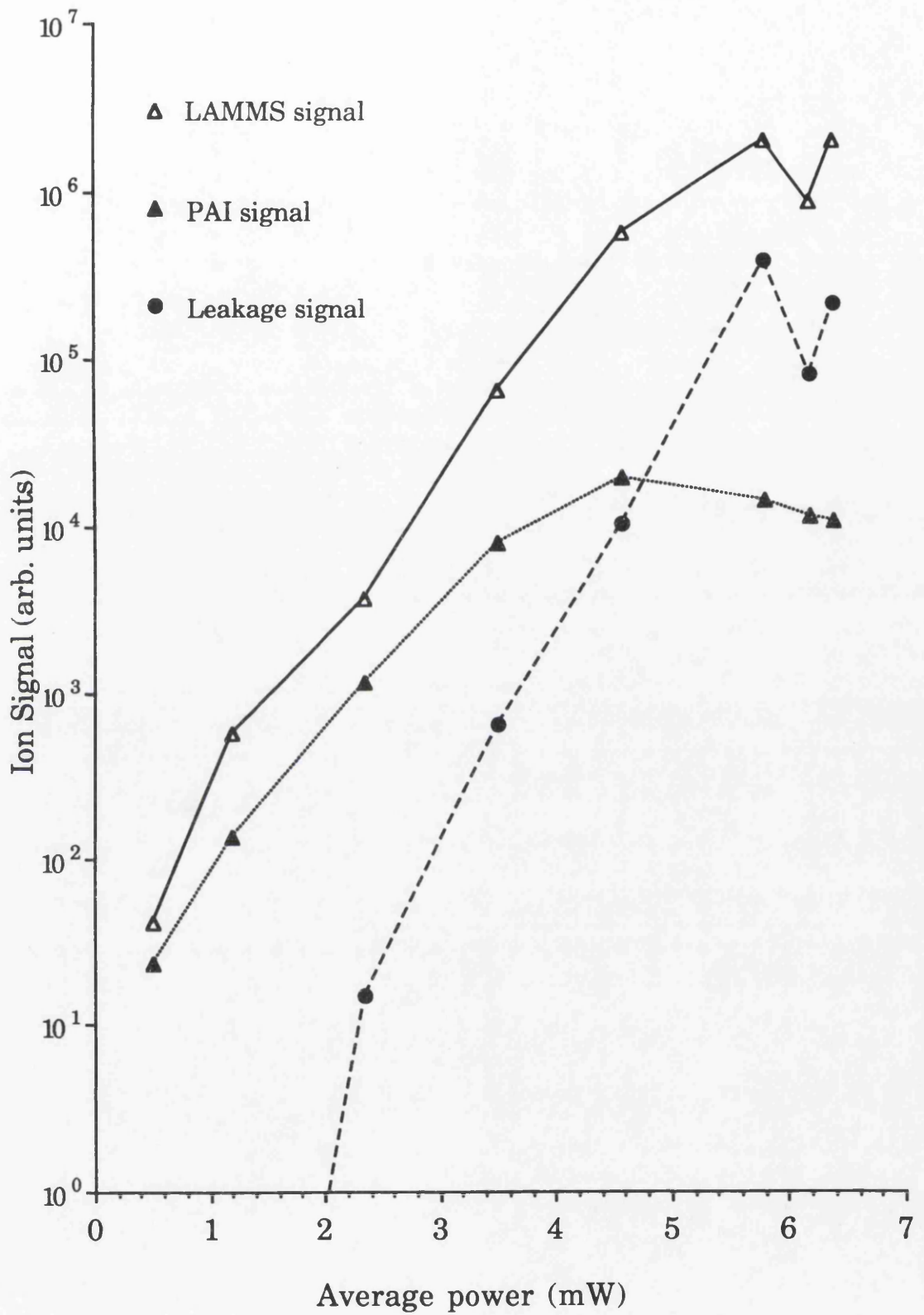


Fig.4.9 Ablation laser power dependence of ion signals obtained from an aluminium sample. The definitions of the LAMMS, PAI and leakage signal are given in the text. The ablation laser wavelength was 532nm.

low and the PAI and LAMMS signals are of similar size. Although the PAI signal is consistently lower than the LAMMS signal this does not mean that equal numbers of neutrals and ions were produced. The PAI signal was always taken with the delay between the lasers adjusted so that the largest possible signal was produced, but the overlap between the plume and the PAI laser would not be high since the volume of the ionising laser beam is small. Also, as discussed above, the ionising efficiency of the PAI laser is probably not 100%.

As the power is increased the PAI signal reaches a plateau before the LAMMS signal and the leakage signal increases with a higher power dependence. This plateau may be due to the high ion density affecting the detector, since the recorded ion signal per unit time at the plateau region is within a factor of three for all three signals. However, saturation of the neutral yield has been observed by other workers. Notably this was observed for the yield of ground state copper neutrals ablated from a copper metal surface, measured by LIFS, while the Cu^+ signal continued to increase (Dreyfus, 1991). This was attributed to the onset of laser induced breakdown in the vapour. LIFS was preferable to mass spectroscopy in this experiment since LIFS will not detect the ionic signal while monitoring the neutral yield, therefore, these measurements are not susceptible to distortion from the plasma ions. Each point in Fig.4.9 was taken as a single spectrum, accumulated over 500 shots. The laser spot remained on the same area throughout this work to reduce the effects, discussed previously, that occurred upon the irradiation of a fresh area.

Fig.4.10 shows the LAMMS and PAI spectra at the relatively low average ablation laser power of 2.3mW. The two peaks are of similar shape, although the mass resolution of the LAMMS peak is lower than that of the PAI signal. When the laser power is increased the LAMMS signal becomes considerably broader, as illustrated in Fig.4.11(a). The width of the time-of-flight corresponds to a spread in ion energies of $>200\text{eV}$. Such behaviour has been observed previously (Housden *et al*, 1989) and has been attributed to processes in the extraction region. Fig.4.11(b) shows that when the reflectron voltage is lowered to allow the PAI signal to be

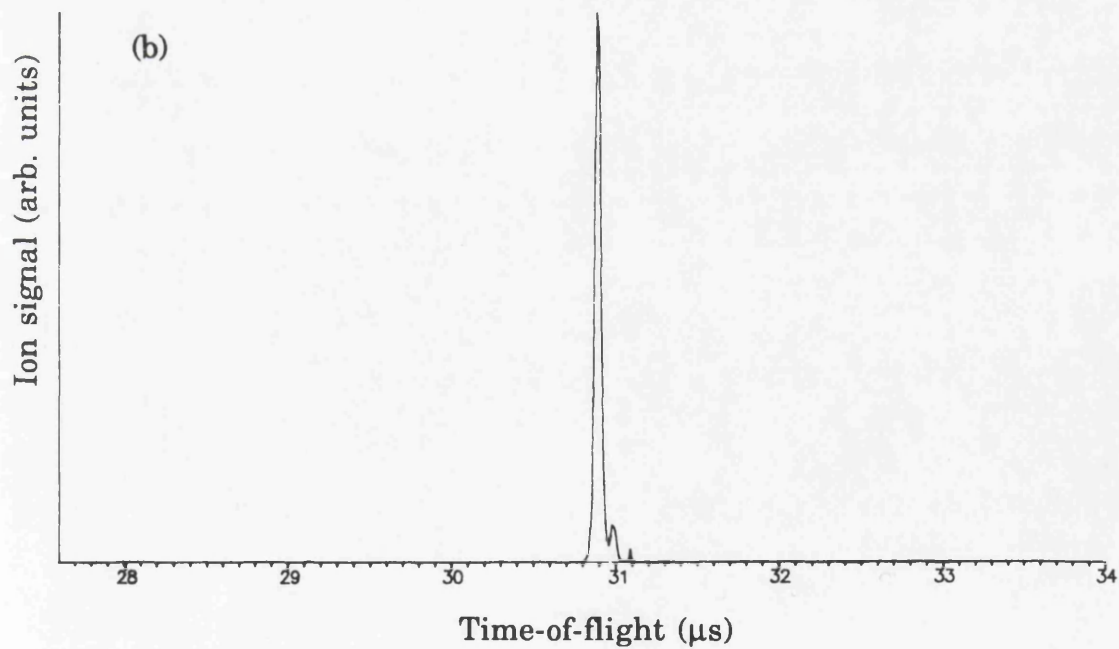
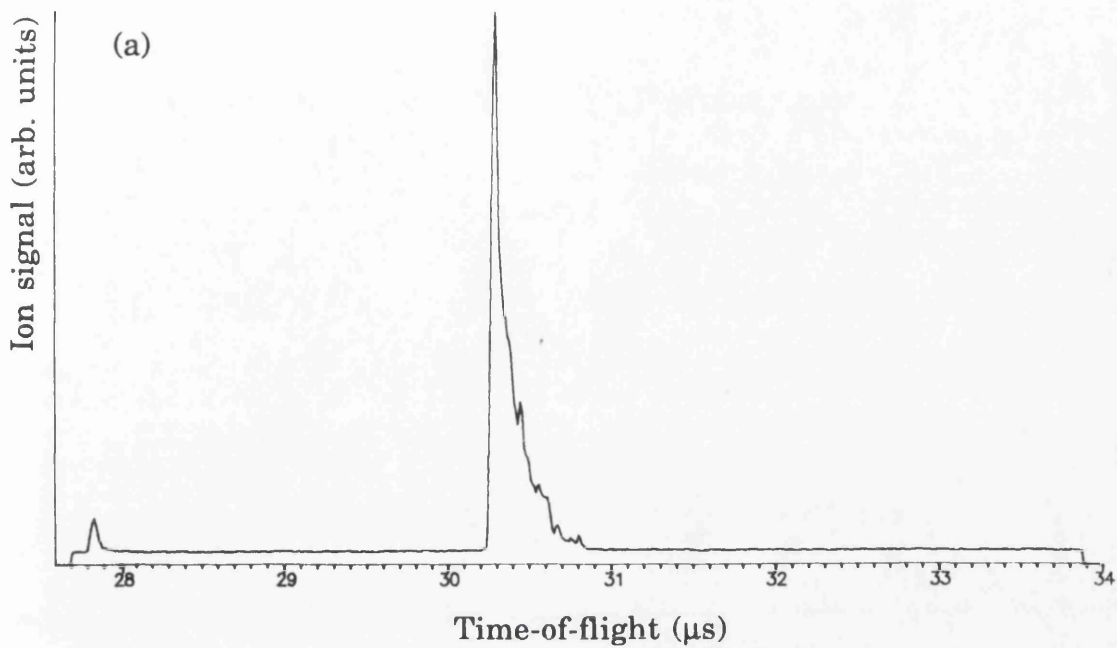


Fig.4.10 Time-of-flight spectra of (a) LAMMS signal and (b) PAI signal for an ablation laser power of 2.3mW. The ablation laser wavelength was 532nm.

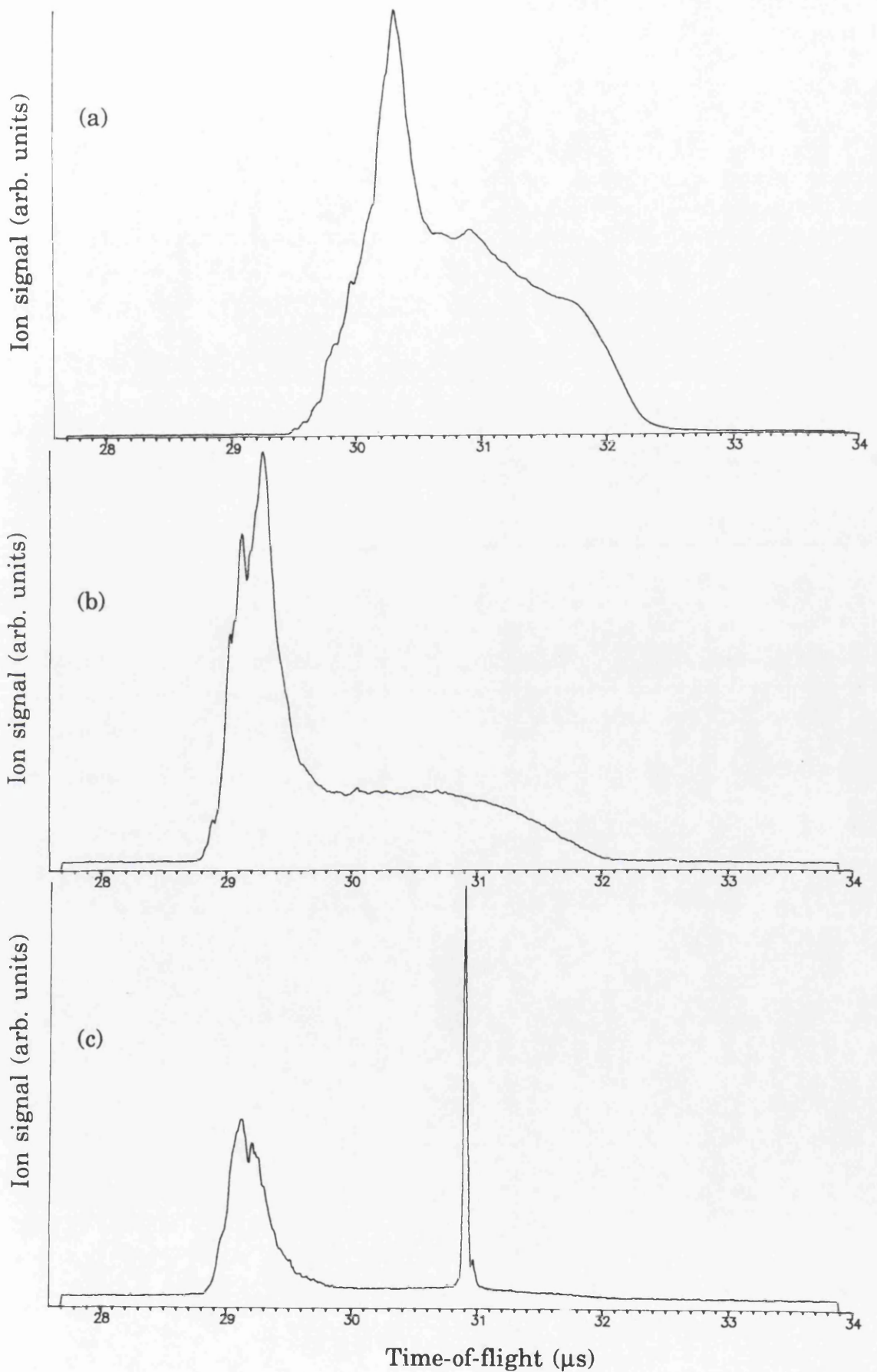


Fig.4.11 Time-of-flight spectra of (a) LAMMS signal, (b) Leakage signal and (c) PAI signal superimposed on the leakage background, for an ablation laser power of 5.8mW. The ablation laser wavelength was 532nm.

monitored the lower energy ions created by the ablation laser are also transmitted. This creates the leakage signal, which is a background to the PAI signal as can be seen in Fig.4.11(c). Methods for alleviating this problem will be discussed in §4.10.

Temporal distributions were obtained for each of the powers shown in Fig.4.9. These are shown on a logarithmic scale in Fig.4.12. The experimental conditions are the same as for Fig.4.4 except that the PAI laser is non-resonant. The two graphs are similar, except that the signal size at the highest level, where the signal appears to be saturated, is approximately a factor of five lower when the PAI laser is non-resonant. The experiments with resonant and non-resonant PAI were carried out several months apart, and the lens, sample and incident beam position had been moved in the interval. It is an illustration of the repeatability of the arrangement that the laser powers in the two graphs are of similar order.

This data can be fitted with the same model as the distributions obtained with resonant PAI. Fig.4.13 shows the distribution obtained at the highest ablation laser power which can again be fitted with a characteristic temperature of 2500K. The lower powers require a higher characteristic temperature, and as for the RIMS data a fit was obtained with a temperature of ~12000K, as shown in Fig.4.14. The deviation from the fit at longer delay times is larger for the lower average ablation laser power. This may be due to a component of the distribution being due to PAI laser induced fragmentation and ionisation of molecules in the plume. A major disadvantage of employing non-selective PAI is that it is not possible to distinguish between signals which are due to the direct ionisation of atoms from signals arising from the fragmentation of molecules. This makes the unambiguous interpretation of mass spectra, and hence velocity distributions, impossible in some cases, as will be illustrated in this chapter. The effect of introducing a component corresponding to a molecular species, with the same characteristic temperature as the atomic aluminium, into the model was investigated. A molecular component with a mass of 108amu, which could be clusters of four aluminium atoms or Al_2O_3 , was found to improve the fit to the data at longer delays, as shown in Fig.4.14. Hence, ~30% of the plume could be

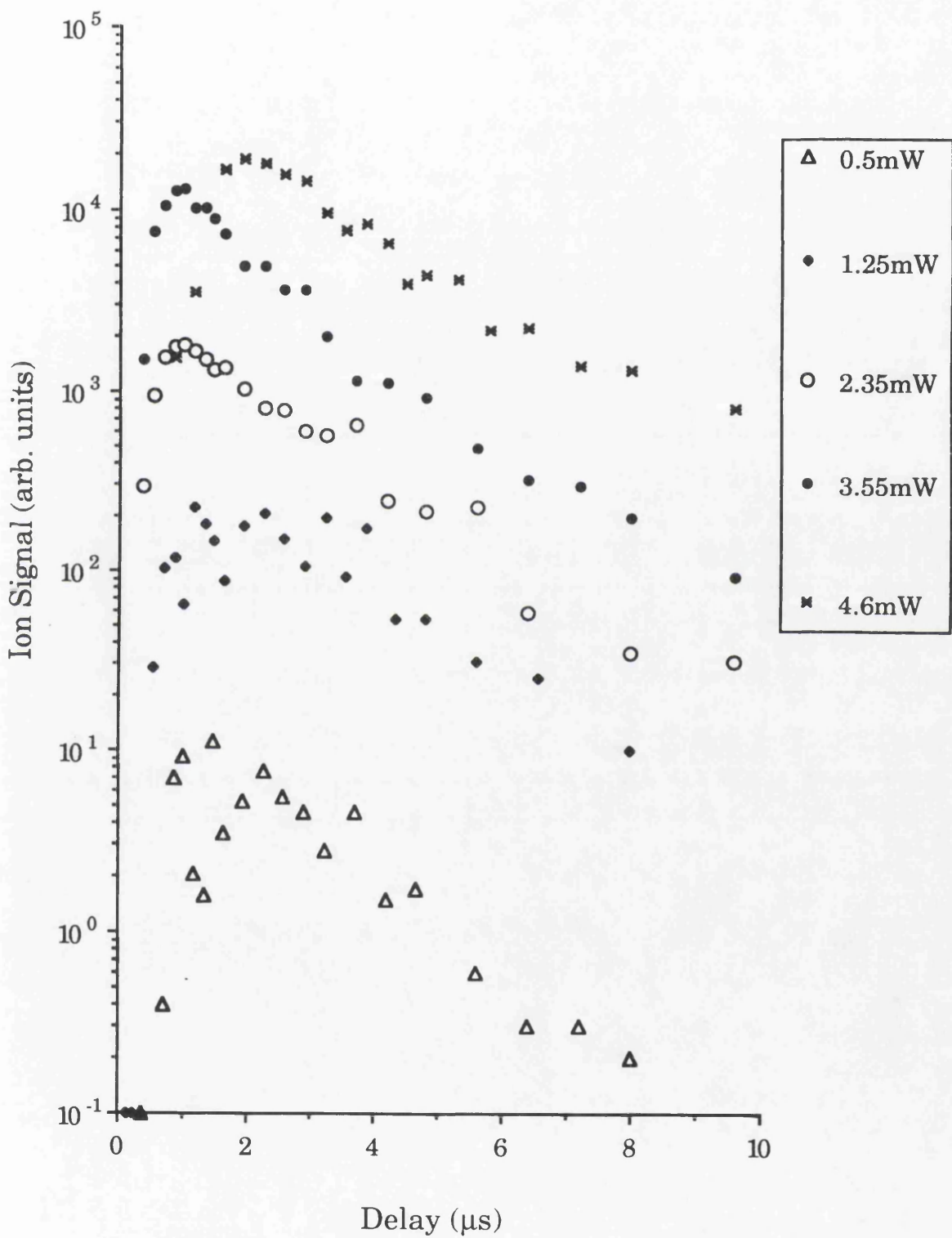


Fig.4.12 Temporal distributions obtained the powers shown in Fig.4.9. The ablation laser wavelength was 532nm and sample is aluminium.

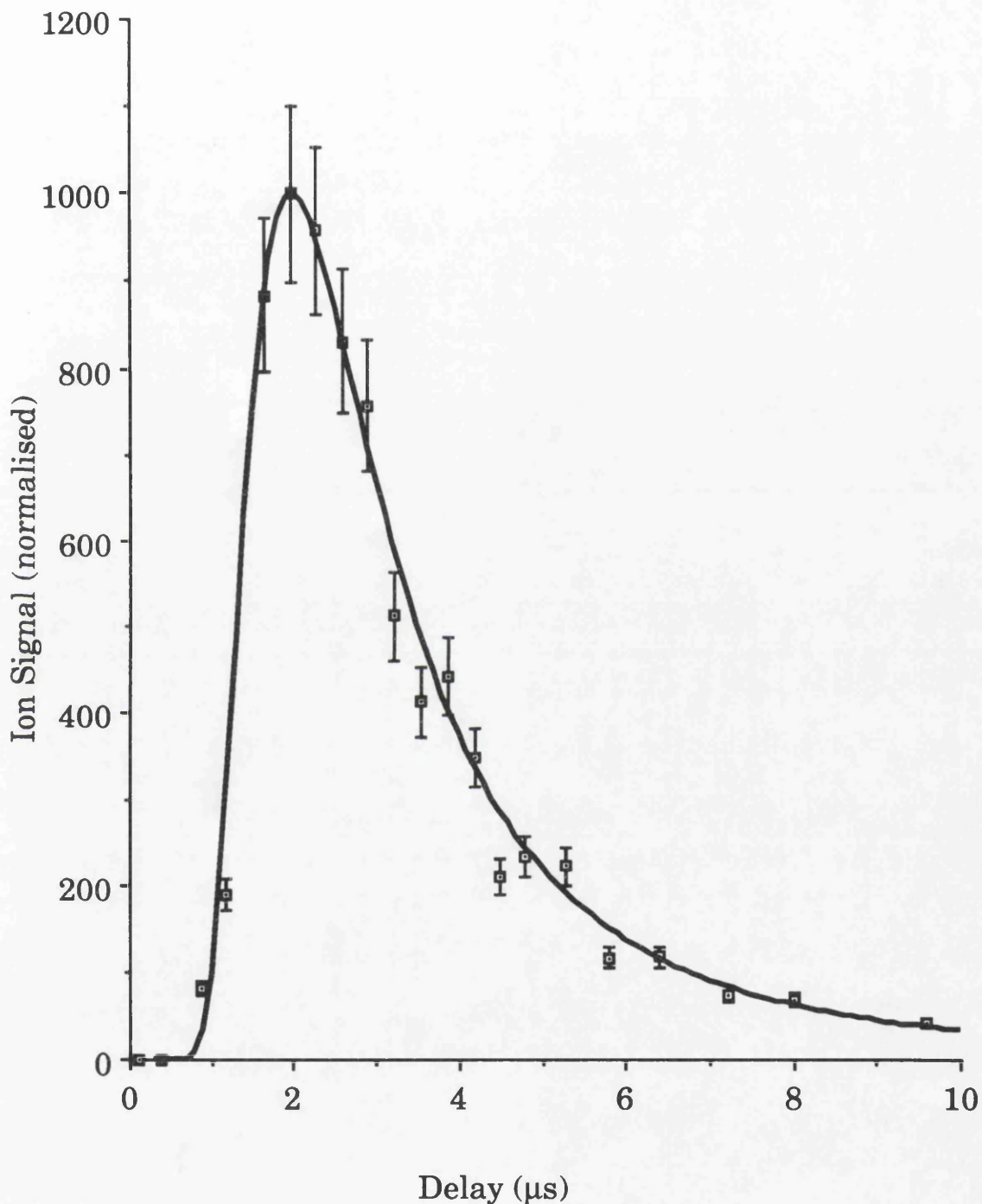


Fig.4.13 Temporal development of the non-resonant PAI signal from an aluminium sample, fitted with a half-range Maxwell-Boltzmann distribution with a characteristic temperature of 2500K. The ablation laser wavelength was 532nm and the power was 4.6mW.

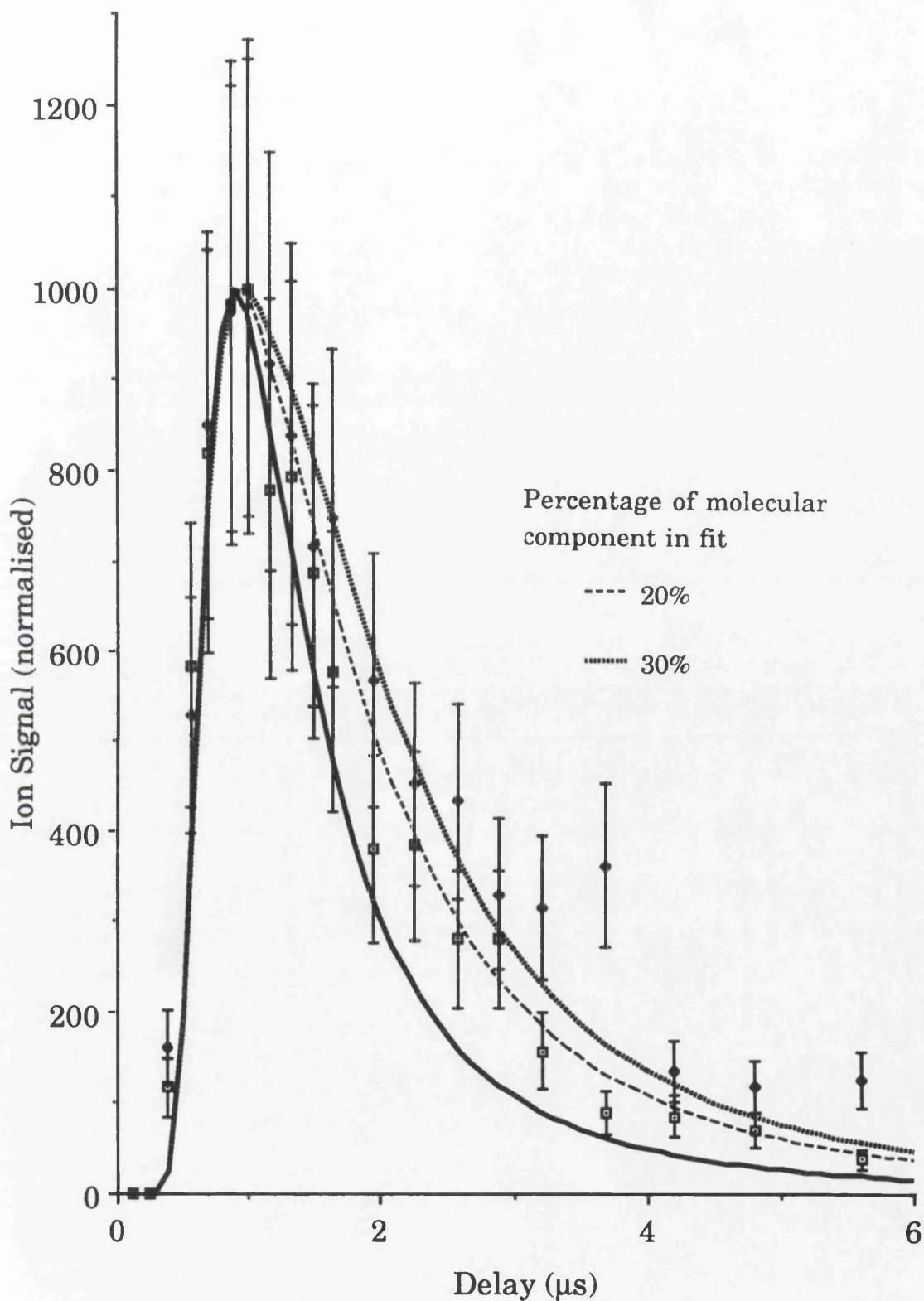


Fig4.14 Temporal development of the non-resonant PAI signal from an aluminium sample for ablation laser powers of 2.35mW (filled symbol) and 3.5 mW (open symbol). The ablation laser wavelength is 532nm. The data is fitted with a half-range Maxwell-Boltzmann distribution with a characteristic temperature of 12000K (solid line). Also shown is the effect of incorporating a specified percentage of mass 108 amu, which represents a molecular cluster, into the fit.

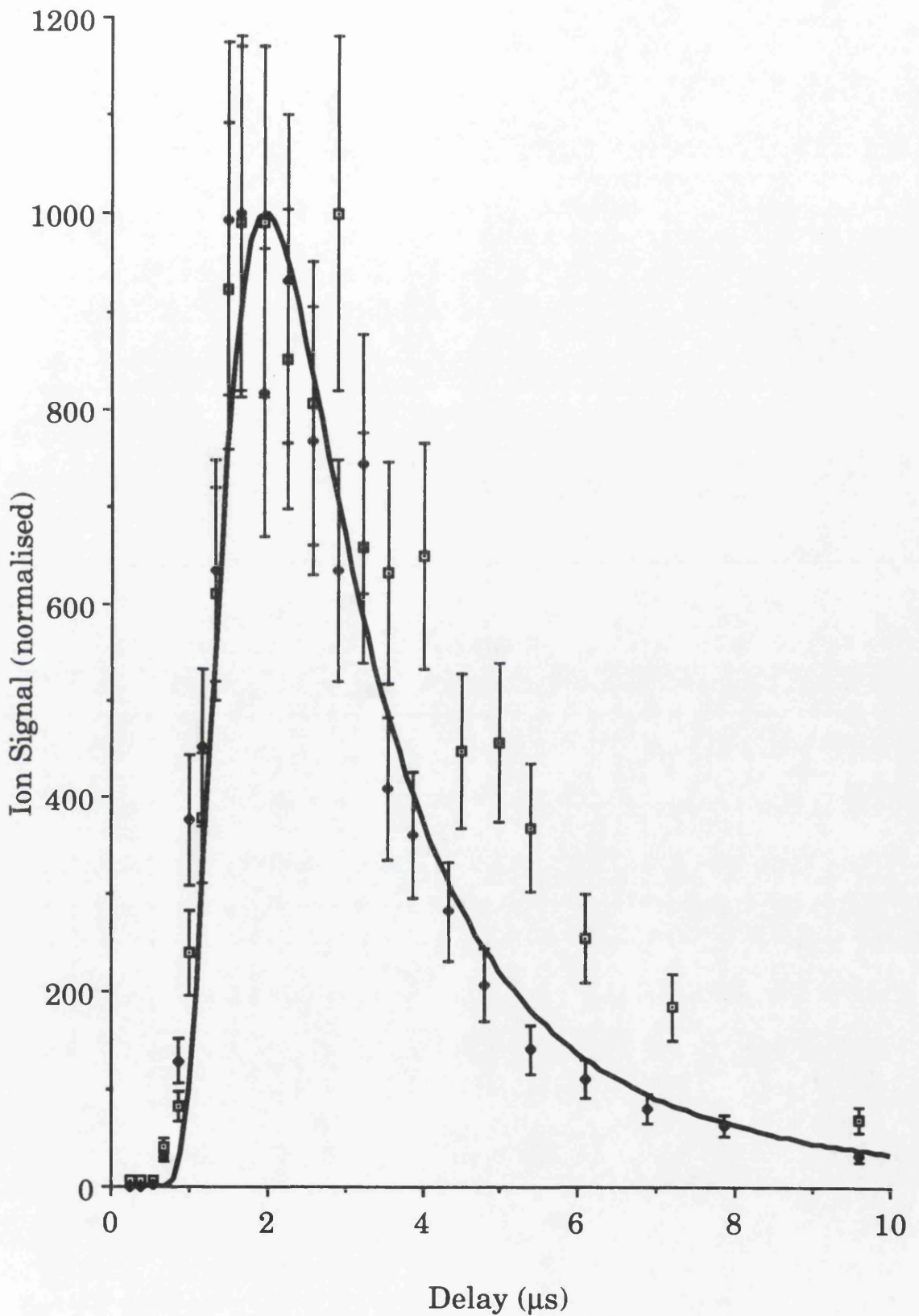


Fig.4.15 Temporal development of the non-resonant PAI signal from an aluminium sample for ablation laser powers of 4mW (open symbol) and 7mW (filled symbol). The ablation laser wavelength is 1064nm. The data is fitted with a half-range Maxwell-Boltzmann distribution with a characteristic temperature of 2500K.

composed of molecular species. This would account for the same mass in the plume as the atomic aluminium.

§4.2.3 Effect of changing the ablation laser wavelength

Changing the wavelength of the ablation laser was also investigated. Using the fundamental output of the Nd:YAG, which has a wavelength of 1064nm, resulted in a series of temporal distributions which were similar to those obtained with the 532nm ablation laser wavelength, shown in Fig.4.12. A plateau level of $\sim 2 \times 10^4$ was observed with the highest power of the fundamental beam. Fig.4.15 shows the distributions obtained with the lowest powers investigated, 4mW and 7mW. These powers are higher than were required in the earlier work with the ablation laser wavelength of 532nm. This would be expected since the lens to sample distance was kept the same for all of the ablation laser wavelengths investigated. Hence, the size of the spot on the surface would be larger at the longer wavelength and a higher laser power would be required to produce the same power density. The data in Fig.4.15 can be fitted by a Maxwell-Boltzmann distribution with a relatively low characteristic temperature ($\sim 2500\text{K}$) assuming that the plume consists entirely of atomic aluminium. However if the plume is composed of Al_2O_3 or clusters of four aluminium atoms, the same curve would correspond to a characteristic temperature of $\sim 10,000\text{K}$. Increasing the ablation laser power resulted in a distribution that could reasonably be described by a characteristic temperature for atomic aluminium of 12000K, as shown in Fig.4.16. This is the same characteristic temperature that was found appropriate for the ablation laser wavelength of 532nm at low powers.

When the ablation laser wavelength was changed to 355nm the effects were broadly similar to those discussed above. Fig.4.17 shows the distributions obtained at various ablation laser powers on a logarithmic plot. At the low power the distribution can be fitted with a characteristic temperature of 3000K, as shown in Fig.4.18. The fit to the data is not as good as for the longer wavelengths. This is more apparent in Fig.4.19 which shows the distributions at higher powers, compared with the half-range Maxwell-Boltzmann curve for 12000K that was an appropriate fit for the longer wavelengths. The leading edge of the experimental distribution obtained with the 355nm ablation laser wavelength can be described by this

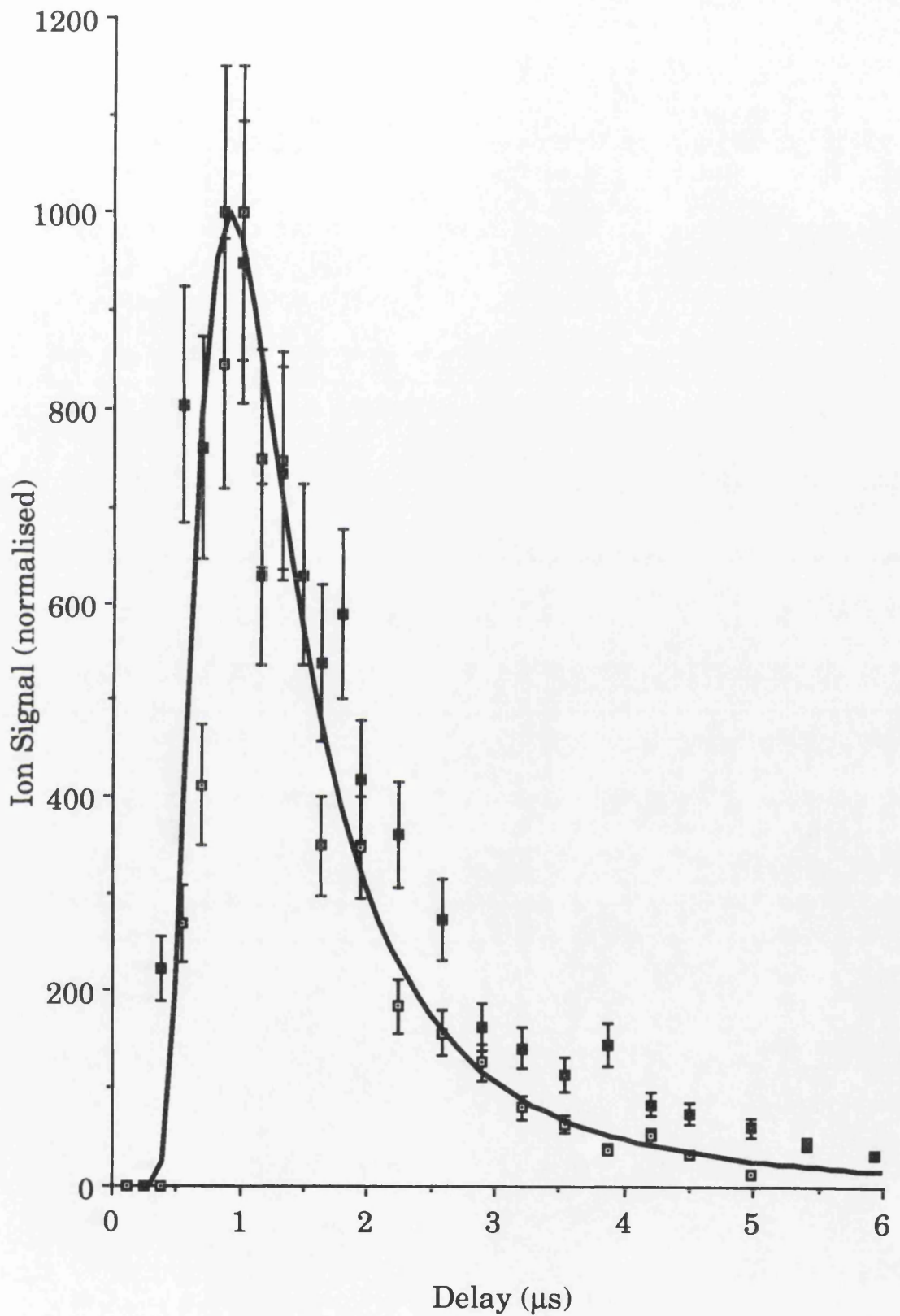


Fig.4.16 Temporal development of the non-resonant PAI signal from an aluminium sample for ablation laser powers of 10mW (filled symbol) and 13.5mW (open symbol). The ablation laser wavelength is 1064nm. The data is fitted with a half-range Maxwell-Boltzmann distribution with a characteristic temperature of 12000K.

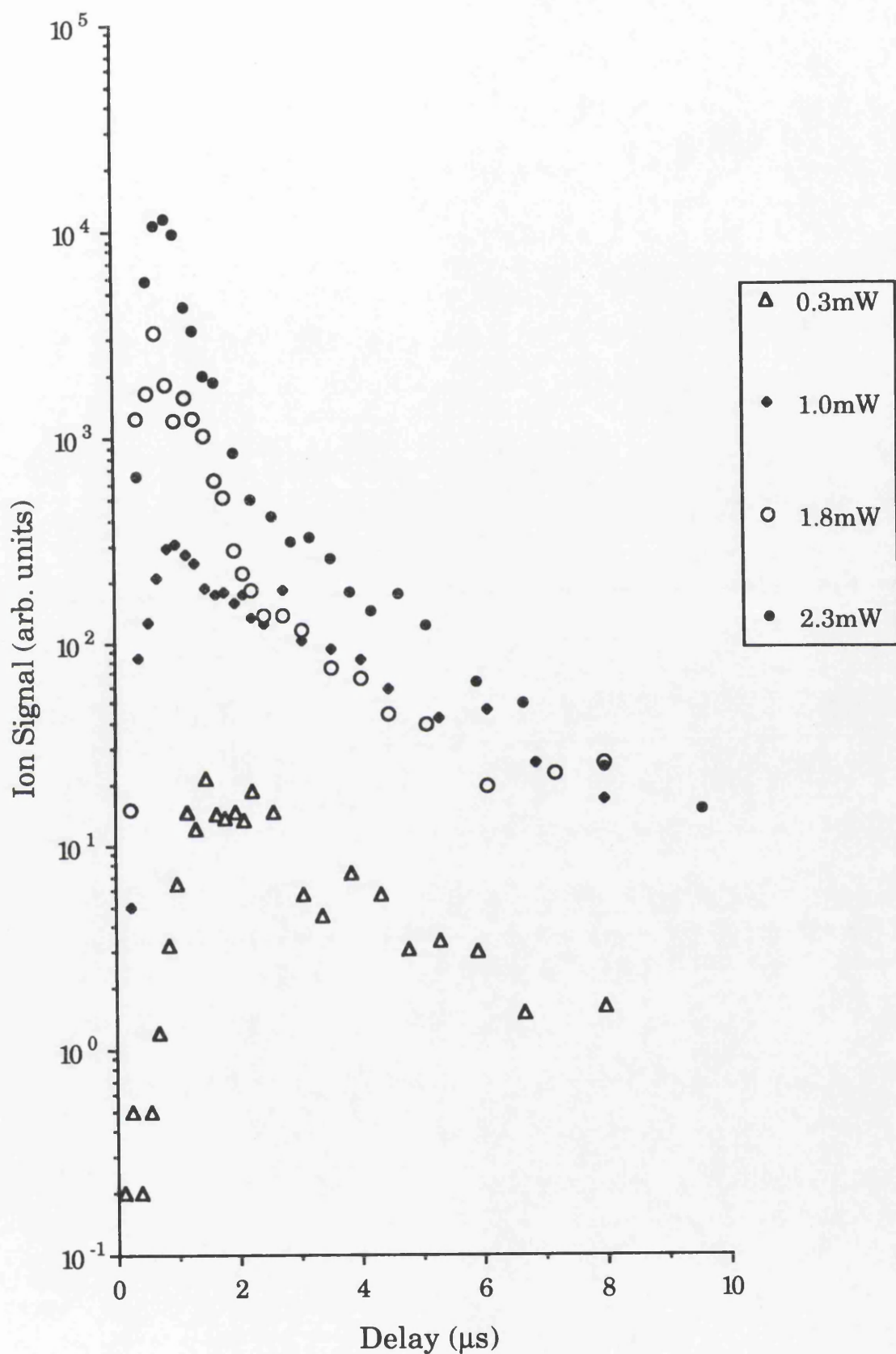


Fig.4.17 Variation of the PAI signal with increasing delay between the ablation and PAI laser, for various ablation laser powers. The ablation laser wavelength was 355nm and the sample was aluminium.

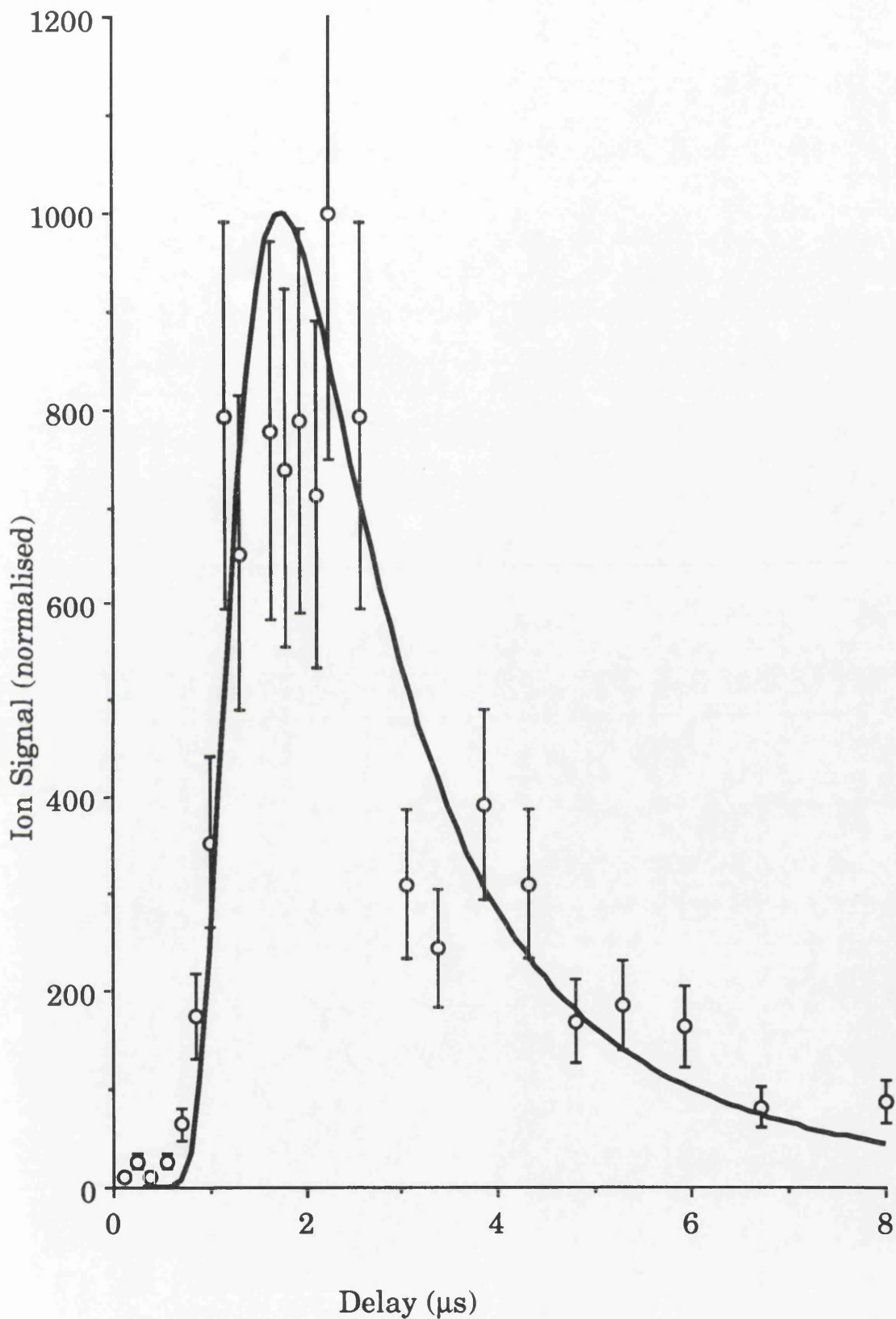


Fig.4.18 Temporal development of the non-resonant PAI signal from an aluminium sample for an ablation laser power of 0.3mW. The ablation laser wavelength was 355nm. The data is fitted with a half-range Maxwell-Boltzmann distribution with a characteristic temperature of 3000K.

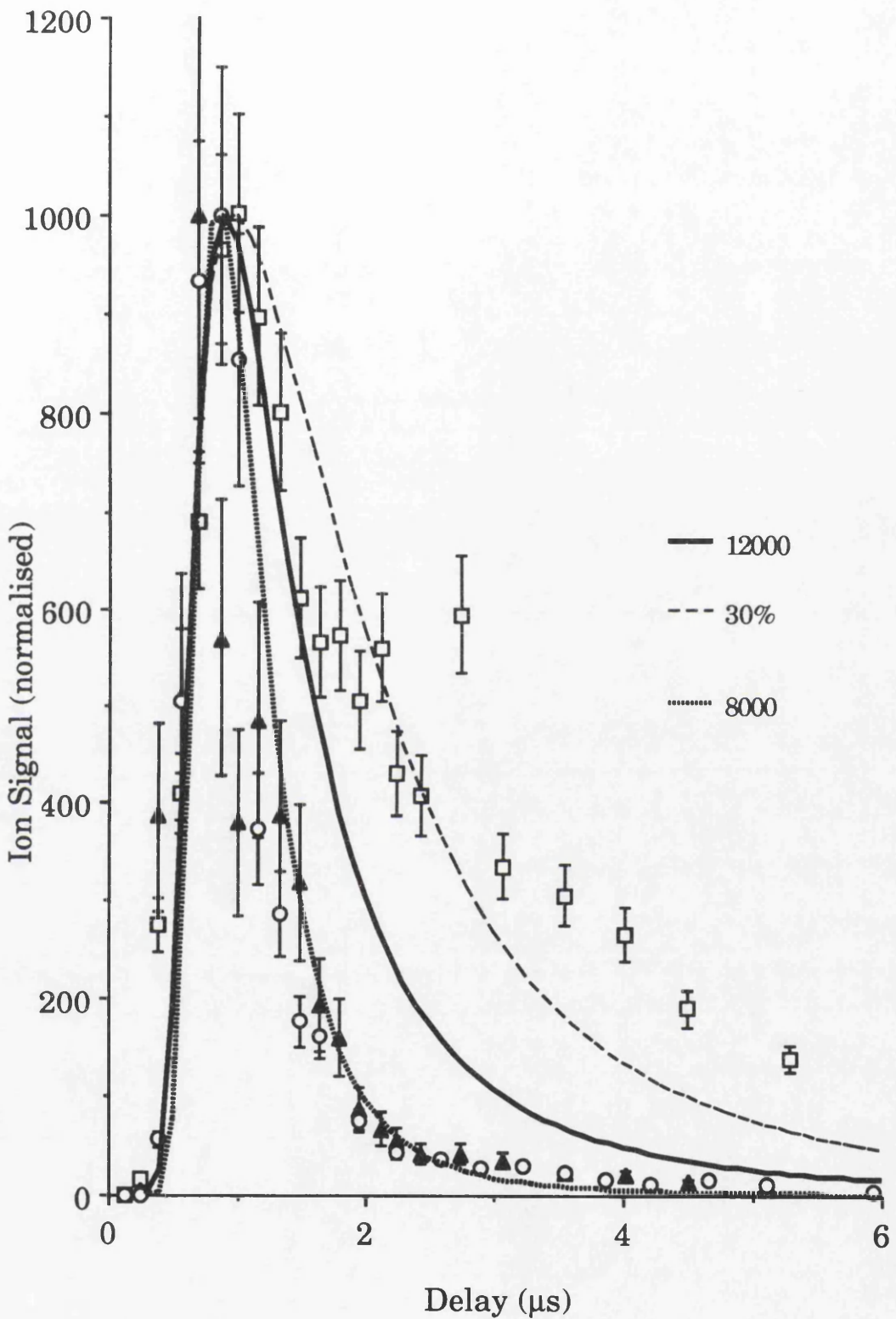


Fig.4.19 Temporal development of the non-resonant PAI signal from an aluminium sample for ablation laser powers of 1mW (squares), 1.8mW (triangle) and 2.3mW (circles). Values of R_{stb} are 69%, 40% and 86% respectively. The ablation laser wavelength was 355nm. The data is fitted with a half-range Maxwell-Boltzmann distribution with a characteristic temperature of 12000K (solid line). Also shown is the effect of adding 30% of a molecular component of mass 108 amu (broken line) and the Knudsen layer formalism with a characteristic temperature of 8000K (dotted line).

model, although the fit is poor for the tail. A cluster component and the Knudsen layer formalism can be employed to improve the fits. However, as R_{stb} for this data was poor it is not obvious that these more complex models illuminate any underlying physical processes.

The stability of the data obtained with the 355nm ablation laser wavelength was not as good as for the longer wavelengths. This was believed to be a consequence of the lower shot to shot stability of the ultra-violet wavelengths. The stability is poorer because to generate the third and fourth harmonics requires the use of two non-linear crystals. This is especially problematic for fourth harmonic generation where the ultra-violet photons can be absorbed by the crystal, which results in heating. The efficiency of frequency doubling depends on both the angle of the crystal, with respect to the incident beam, and the crystal temperature. Hence, the photon induced heating acts to increase the instability of the fourth harmonic. To utilise the 266nm beam the data was taken using the PLOT5 software to monitor the pulse energy measured by the Molectron energy meter. Every laser shot was incident on the sample and produced a mass spectrum, but only if the laser power was within $\pm 5\%$ of that desired was the data added to the recorded spectrum. This increased the number of shots required to produce a distribution, usually by at least a factor of two, and would result in larger signal fall-off over the run, typically values for R_{stb} being $\sim 60\%$.

The distributions obtained at various powers, with the 266nm wavelength, are shown on a logarithmic plot in Fig.4.20. The most obvious point is that the signals do not reach the plateau level that was obtained with the longer wavelengths. As will be discussed in §4.2.4 the spot size on the surface did not differ greatly for the different wavelengths. Hence, it can be concluded that the number of neutrals in the PAI laser volume was not as high as it was for the lower ablation laser photon energies. This may be due to the relatively high photon energy causing two photon ionisation of the liberated material. This would enhance the degree of ionisation in the plasma, for the same power density, relative to the other wavelengths. This would, of course, decrease the number of neutrals in the plume. As discussed in §2.9 the formation of a plasma could also limit the neutral yield by reducing the fluence transmitted to the sample surface. As shown

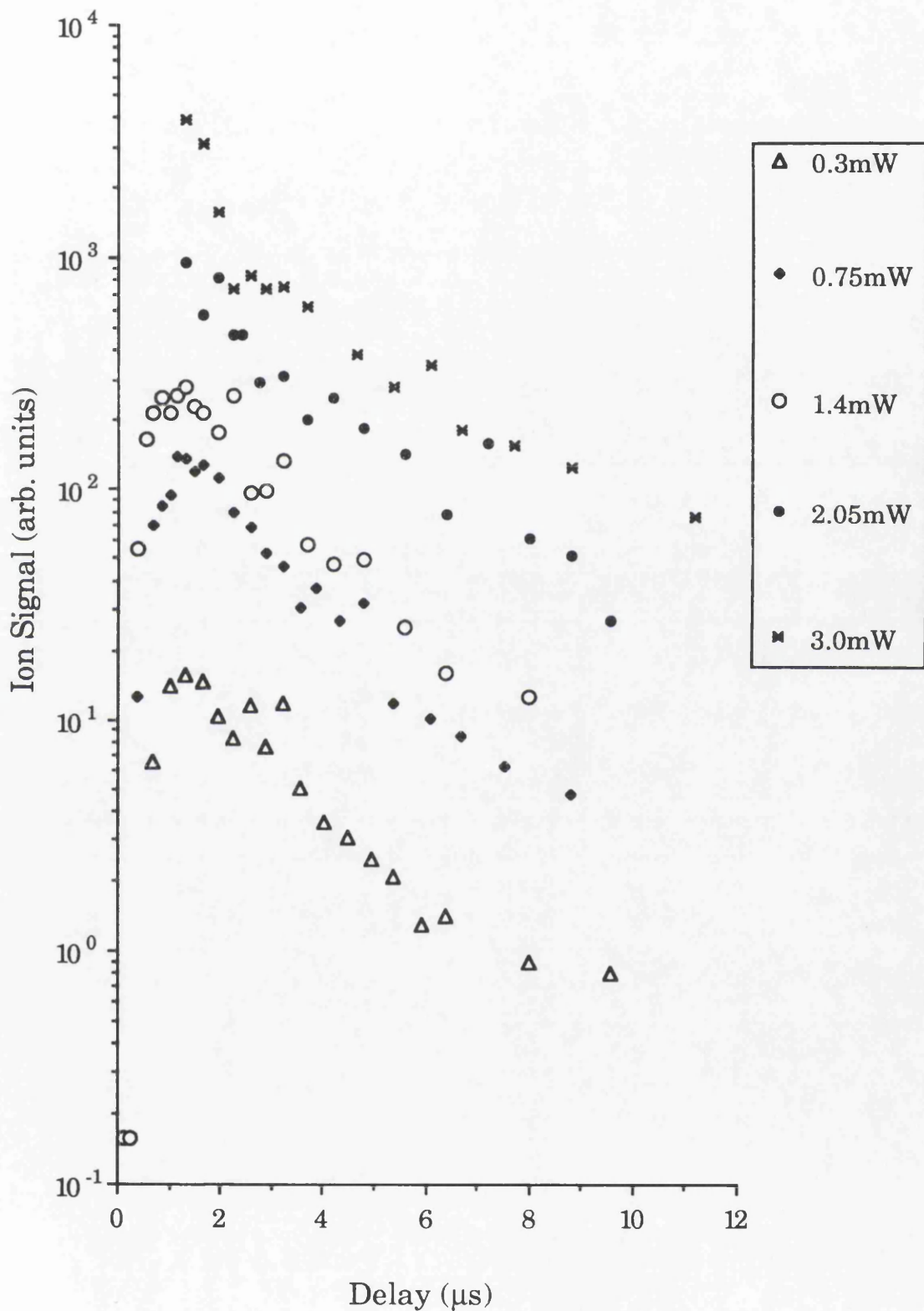


Fig.4.20 Variation of the PAI signal with increasing delay between the ablation and PAI laser, for various laser powers. The ablation laser wavelength was 266nm and the sample was aluminium.

in Fig.4.21(a), a lower characteristic temperature, ~6000K, is required to fit the data obtained with the 266nm ablation laser wavelength, using the model utilised previously for atomic aluminium. A reasonable fit can be achieved with a characteristic temperature of 12000K, if a contribution of 50% from the molecular species discussed above is assumed. The work on the sputtering of Al_2O_3 with ultra-violet wavelengths discussed in §2.10.5, determined that the plume contained Al and AlO in approximately equal parts. The detection of Al_2O_3 was not reported. Thus, it would seem unlikely, even if the sample was covered with an oxide film, that the plume would contain 50% Al_2O_3 . This illustrates the difficulty in accurately fitting the observed distribution when the monitoring technique cannot distinguish between the signal from atoms liberated from the surface and that generated by molecular fragmentation.

§4.2.4 Surface modification resulting from the laser ablation of aluminium

In these studies the laser was tightly focused, both to stimulate a microprobe application and to reduce the amount of material emitted. It was, therefore, difficult to evaluate accurately the irradiated area. To evaluate the size of the laser affected area and to gain insight into the material removal mechanism, scanning electron microscopy (SEM) was employed. The microscope was a Hitachi S-800 and was operated at 20-30keV. To obtain samples for SEM, where the laser power and the number of shots that produced each crater were known, samples were irradiated specifically for this purpose. The sample surface was not roughened so that the best contrast could be obtained for electron and optical microscopy. It was supposed that after some initial number of shots the surface conditions would be the same as those for the studies reported previously.

Fig.4.22 shows the surface modification caused by three different powers of the 532nm wavelength ablation laser. The laser powers were 2mW, 3.5mW and 5mW, which, it can be seen from Fig.4.9 would correspond to a relatively low neutral yield, the highest yield that could be described by a 12000K distribution and apparent saturation of the PAI signal, respectively. It can be seen that the surfaces irradiated at the two lower powers appear distinctly different to the one irradiated at the highest power. Concentrating initially on the effects of the two lowest powers,

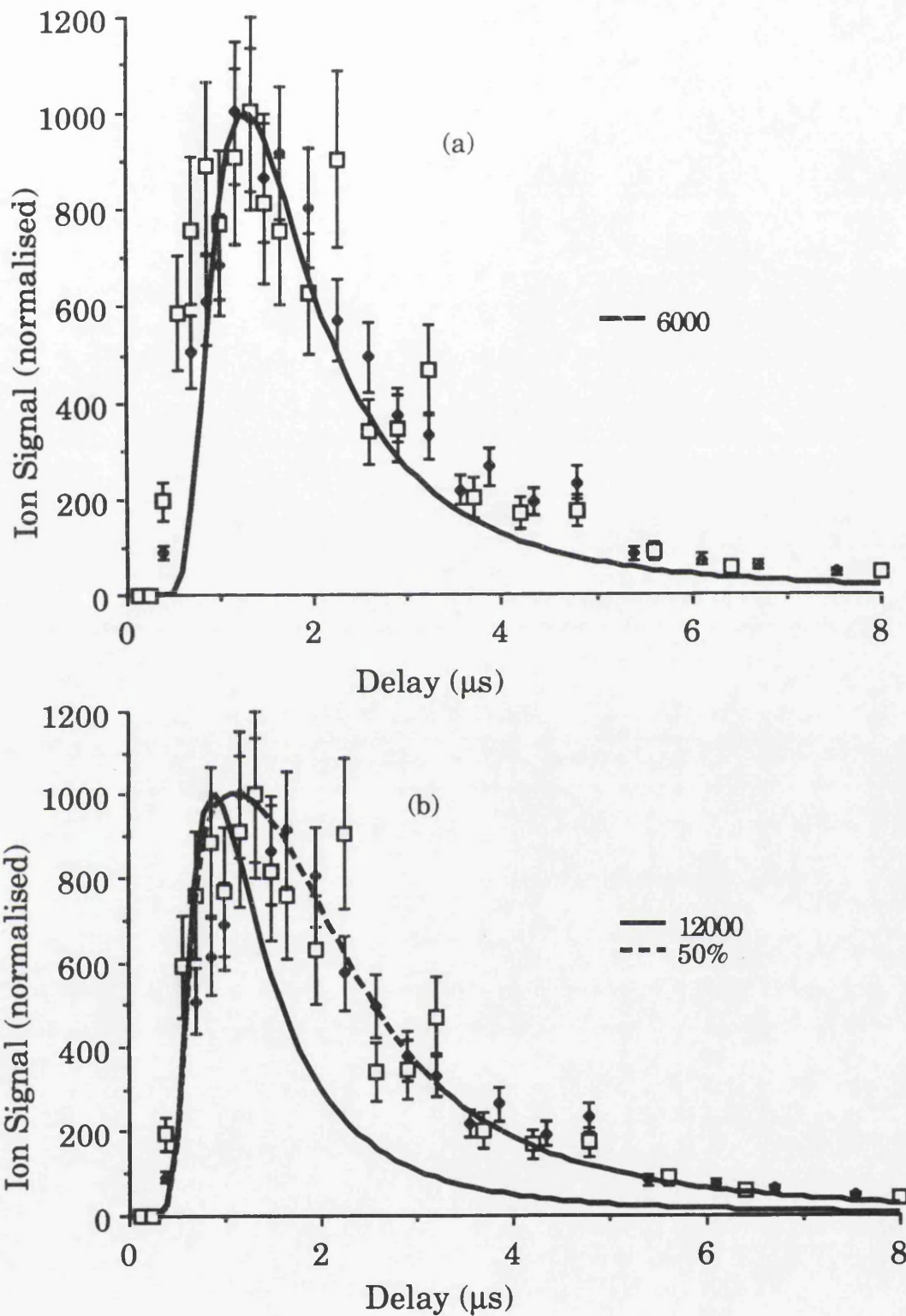
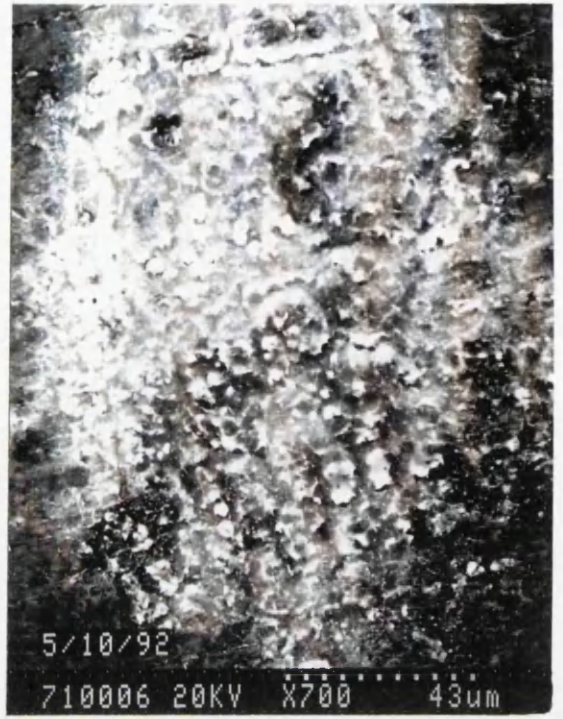


Fig.4.21 Temporal development of the non-resonant PAI signal from an aluminium sample for ablation laser powers of 0.75mW (diamonds) and 1.4mW (squares). Values of R_{stb} are 61% and 62% respectively. The ablation laser wavelength was 266nm. (a) The data is fitted with a half-range Maxwell-Boltzmann distribution with a characteristic temperature of 6000K. (b) The effect of adding 30% of a molecular component of mass 108 amu (broken line) to the half-range Maxwell-Boltzmann distribution with a characteristic temperature of 12000K (solid line).



(a)



(b)



(c)

Fig.4.22

SEM micrographs of an aluminium surface irradiated with a laser wavelength of 532nm. The laser powers are (a) 2mW, (b) 3.5mW and (c) 5mW. (a) and (b) correspond to ten thousand laser shots and (c) to one thousand.

where the surfaces was exposed to ten thousand shots, it would appear that although extensive surface modification appears to have taken place, no discernible crater is observed. The surfaces appears to have experienced melting and re-solidification. Fig.4.23(a) is a higher magnification micrograph of a surface irradiated by one thousand laser shots with an average ablation laser power of 3.5mW. It can be seen that the surface is covered with unevenly spaced irregularities, which could indicate uneven heating of the surface. In contrast, the effect of the highest laser power is to produce a crater that could be examined in three dimensions with the SEM, as shown in Fig.4.22(c). The material in the centre of the micrograph, shown at higher magnification in Fig.4.23(b), is markedly different to that observed at the lower laser powers. Spherical structures, with a diameter of $\sim 3\mu\text{m}$, are apparent. Such structures have been observed previously (Kelly and Rothenberg, 1985) and the liberation of such droplets has been determined to be the major mechanism for material removal in the laser etching of aluminium, with a laser wavelength of 248nm. This mechanism is termed hydrodynamical sputtering, however, this is not in any way related to the hydrodynamic velocity discussed in §2.6. Hydrodynamical sputtering involves the liberation of droplets formed on the sample surface as a result of the volume changes during melting and thermal expansion. This mechanism requires the cumulative effect of many laser shots. Fig.4.23(c) shows the surface modification resulting from a single laser shot of 5mW power. Although some structure is evident, droplets cannot be observed. At the appropriate laser power densities, hydrodynamical sputtering will occur simultaneously with vaporisation and will account for the majority of the material removed.

As mentioned previously, it is of interest to determine the power density of the laser beam at the sample surface. It is well known that the dimensions of laser produced craters do not always correspond to the laser spot size on the sample (Duckworth *et al*, 1992). However, in the absence of a mechanism for direct observation of the spot on the surface, the crater size is a very useful indication of the spot size. The affected area in Fig.4.22(b) was calculated to be $\sim 1.5 \times 10^{-4} \text{cm}^2$. This is a factor of two larger than that determined from Fig.4.22(c), which is in turn a factor of three higher than the area of the distortion caused by a single shot, shown in



(a)



(b)



(c)

Fig.4.23

SEM micrographs of an aluminium surface irradiated with a laser wavelength of 532nm. (a) 1,000 shots of 3.5mW power, (b) 1,000 shots of 5mW power, (c) 1 shot of 5mW power.

Fig.4.23(c). Assuming a laser pulse length of 10ns and a spot size of 10^{-4}cm^2 , an average power of 10mW (a pulse energy of 1mJ) would correspond to a power density of $10^9\text{W}/\text{cm}^2$. Thus the average powers used in this work, 2mW, 3.5mW and 5mW would correspond to power densities of $2 \cdot 10^8$, $3.5 \cdot 10^8$ and $5 \cdot 10^8\text{W}/\text{cm}^2$ respectively. Spot sizes were also assessed by irradiating exposed Polaroid film and measuring the size of spots. It was found that the size of the spots was highly dependent on the laser power. The irradiated areas ascertained by this method were larger than those measured from the SEM micrographs. This resulted in power densities approximately five times lower than those determined by SEM.

The effect of changing the ablation laser wavelength was also investigated, as shown in Fig.4.24. The modified areas varied from $0.8 \cdot 10^{-4}\text{cm}^2$ to $1.6 \cdot 10^{-4}\text{cm}^2$, which is the same range as the measurements detailed above. The features observed differed markedly depending on the wavelength, but this was believed to be due to the different powers employed. The power of the 1064nm beam was 15mW, which corresponds to the highest power at which a velocity distribution of the neutrals could be obtained. The crater has definite depth, similar to Fig.4.22(c), and droplets of molten material can be seen. Attempts to determine the depth of similar laser produced craters using both diamond tipped profilers and microbalances had previously proved to be very difficult. This was due to the small dimensions of the craters and the nonuniformity of both the crater and sample surfaces. However, the amount of material removed can be gauged by ion sputtering (§6.4) or by monitoring the stage current (§.4.9). Fig.4.24(b) shows the effect of ten thousand shots of the 355nm wavelength beam which had a power of 1.5mW. This is broadly similar to what was observed with low powers of the 532nm wavelength. The effect of increasing the average laser power to $\sim 2.3\text{mW}$ was to produce droplets similar to those in Fig.4.23(b). The fourth harmonic beam was not a pure Gaussian, as is apparent from Fig.4.24(b) there are two spots of the same area separated by $\sim 20\mu\text{m}$. This was observed in all the irradiated areas and was attributed to the beam being TEM_{01} . As the two spots are large compared to their separation the effect on the characteristics of the emitted vapour was considered to be negligible. The structure of the craters is again similar to that observed for low powers with the 532nm wavelength.



(a)



(b)



(c)

Fig.4.24

SEM micrographs of an aluminium surface irradiated with various laser wavelengths (a) 10,000 shots of 1064nm wavelength with a power of 15mW, (b) 1,000 shots of 355nm wavelength with a power of 1.5mW, (c) 10,000 shots of 266nm wavelength with a power of 2mW.

It can be concluded that the neutral emission described above corresponds closely to the threshold where hydrodynamical sputtering becomes energetically possible. The surface morphology of all the samples suggest that melting has occurred which would be expected from the one dimensional heat flow equation with the determined laser power density, as shown in Fig.2.1.

§4.3 Gold

Gold was studied because it had only one stable isotope with a high atomic weight and had been the subject of earlier work at Glasgow (McCombes *et al*, 1991a). The ionisation potential of gold is 9.22eV which allows two photon non-resonant ionisation by the fourth harmonic of the Nd:YAG laser. The sample was a foil, 1mm thick, which had a reflective, unroughened surface. Logarithmic plots of PAI signal versus delay time for a range of ablation laser powers are shown in Fig.4.25 for all the ablation laser wavelengths investigated previously. The distributions for the second, third and fourth harmonic wavelengths appear broadly similar. The powers required were of the same order as those used in the studies of aluminium. However, the PAI signals obtained using the fundamental wavelength for ablation are two orders of magnitude smaller, although the average powers are broadly similar to those used with aluminium. As mentioned in §2.2 the colour of gold results from a marked change in the reflectivity in the visible wavelength range. The reflectivity of gold for a wavelength of one micron is very high (>98%, AIP Handbook, 1972) and therefore, much of the incident laser energy is not absorbed. This probably accounts for the signals obtained with 1064nm wavelength ablation being smaller than those resulting from the shorter ablation laser wavelengths. It is perhaps surprising, however, that the temporal distributions obtained with the 532nm wavelength are similar to those for the ultraviolet wavelengths, since the reported values for the reflectivity of gold at the wavelength of 532nm are appreciable (>70%, AIP Handbook, 1972).

The temporal distributions were again fitted with a half-range Maxwell-Boltzmann distribution. A characteristic temperature of 6000K was found

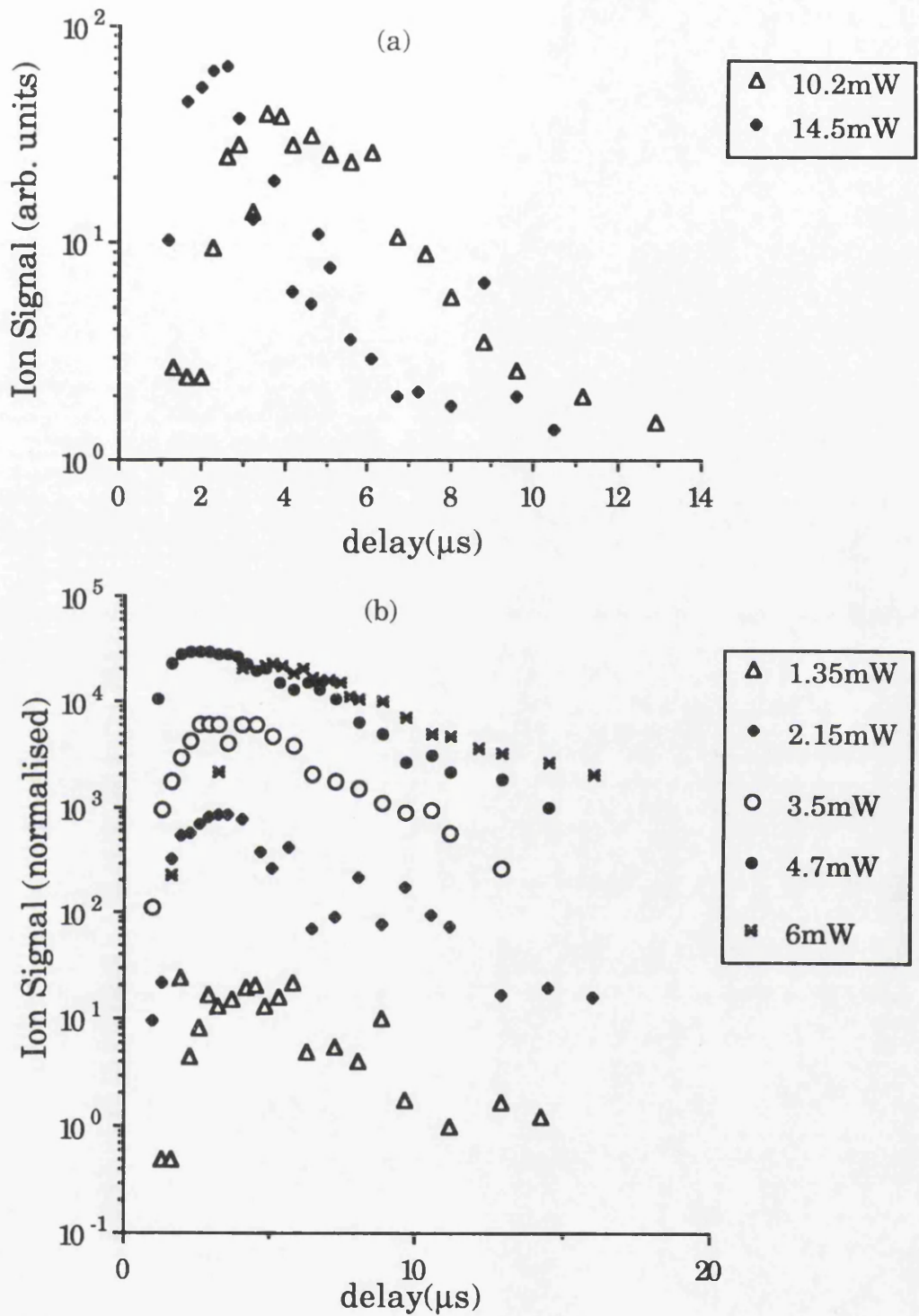
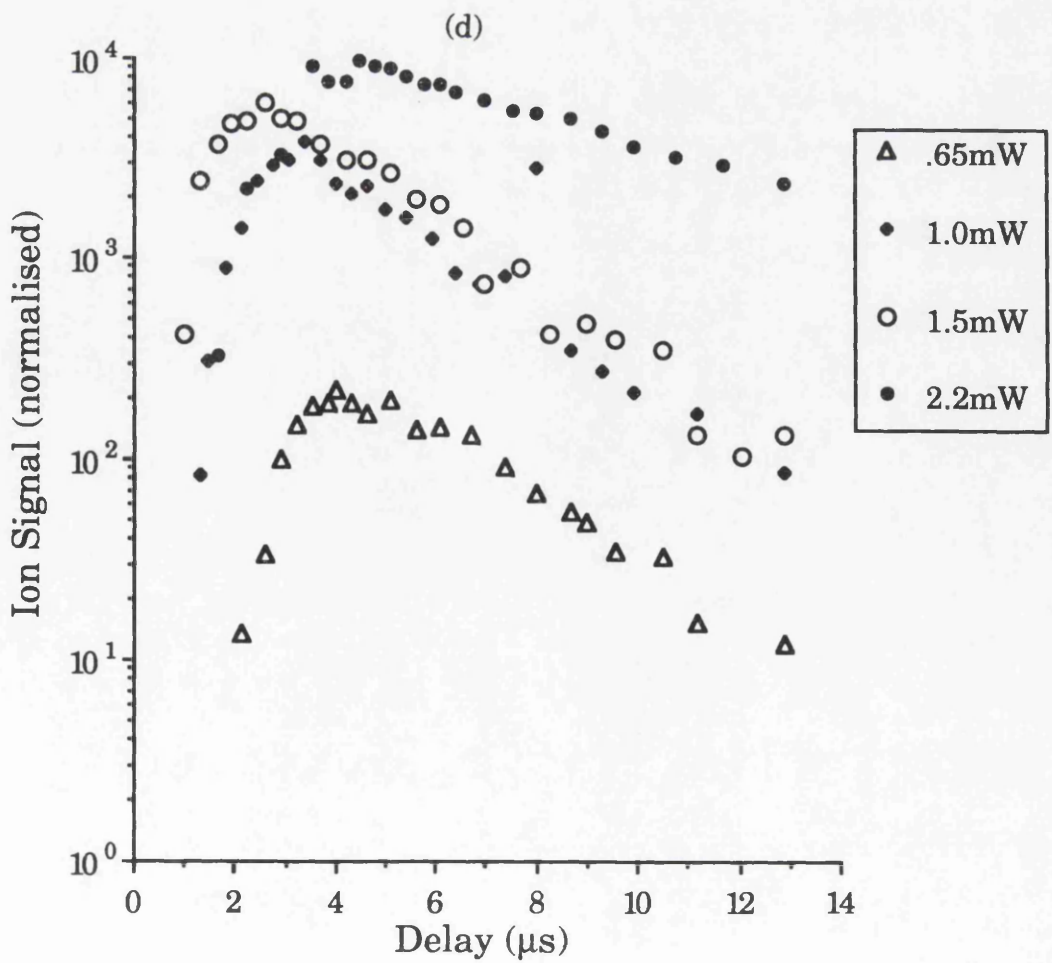
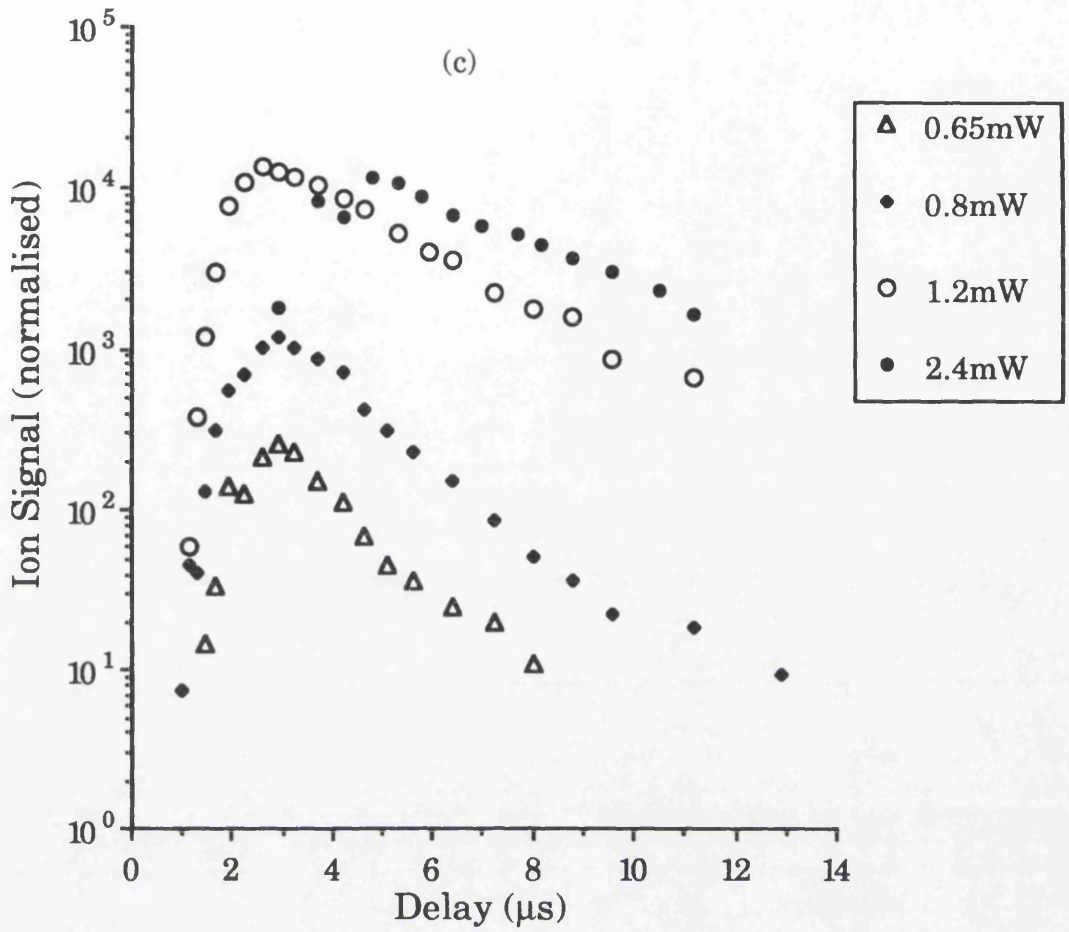


Fig.4.25 Variation of the PAI signal with increasing delay between the ablation and PAI laser, for various ablation laser wavelengths: (a) 1064nm, (b) 532nm (c) 355nm and (d) 266nm. The sample was gold.



to give a distribution in reasonable agreement with the experimental data obtained at the higher powers for the first, second and third harmonics, as shown in Fig.4.26. As was the case for aluminium, this characteristic temperature is much higher than the melting point (1065K for gold). The distribution obtained by the fourth harmonic cannot be reasonably described by this temperature. As shown in Fig.4.27, a better fit is achieved if the temperature is increase to $\sim 10,000\text{K}$, or if the Knudsen layer model is used. As discussed in §4.2.3, the distribution obtained from the 266nm wavelength laser ablation of aluminium was also different to that obtained at the longer wavelengths. However, in that case a substantially lower temperature had to be employed to fit the data. This would appear to eliminate the possibility that different temperatures are obtained for the fourth harmonic due to a systematic error in the laser to sample distance, as this would result in the distributions being higher (or lower) than expected for both materials.

During these studies it was apparent that, as well as Au^+ , an ion of $m/z=394$ was also produced by the PAI laser. This was observed at all powers and wavelengths and was attributed to the formation of gold dimers, Au_2^+ . Fig.4.28 shows the temporal distributions of the $m/z=394$ signal obtained at two different powers of both the second and third harmonics. Also shown is the half-range Maxwell-Boltzmann distribution, with $m=197\text{amu}$ and $T=6000\text{K}$, which was found to describe the atomic distributions. The ratio of the atomic signal to dimer signal, $\text{Au}^+/\text{Au}_2^+$, is shown as a function of the delay between the lasers in Fig.4.29. The two signals were not monitored simultaneously, but the distributions were taken consecutively. The ratio does not appear to be highly dependent on the laser wavelength. The temporal dependence of the atomic signal and the dimer signal can be modelled using the Maxwell-Boltzmann distribution if it is assumed that the atoms and dimers which are laser-ionised are formed by vaporisation from the surface. Fig.4.30 shows the distributions for the two masses assuming a characteristic temperature of 6000K for both cases. The dependence of the ratio on the delay between the lasers can be obtained from these Maxwell-Boltzmann distributions and is shown in Fig.4.31. It has been assumed that the maximum atomic signal is 100 times larger than the maximum dimer signal. Only one set of the experimental data, 1.5mW at 355nm,

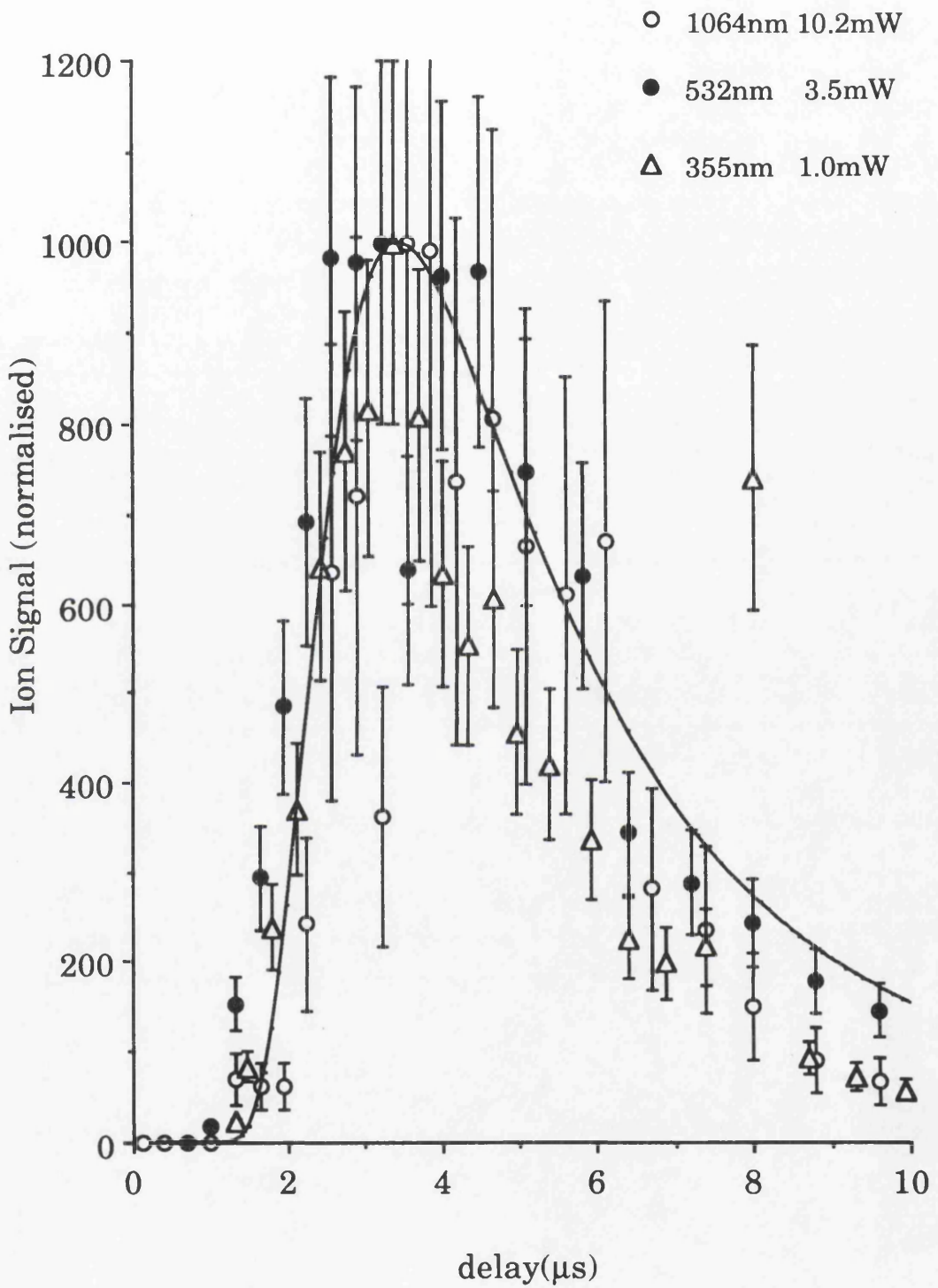


Fig.4.26 Temporal development of the non-resonant PAI signal from a gold sample for various ablation laser wavelengths and powers. The data is fitted with a half-range Maxwell-Boltzmann distribution with a characteristic temperature of 6000K.

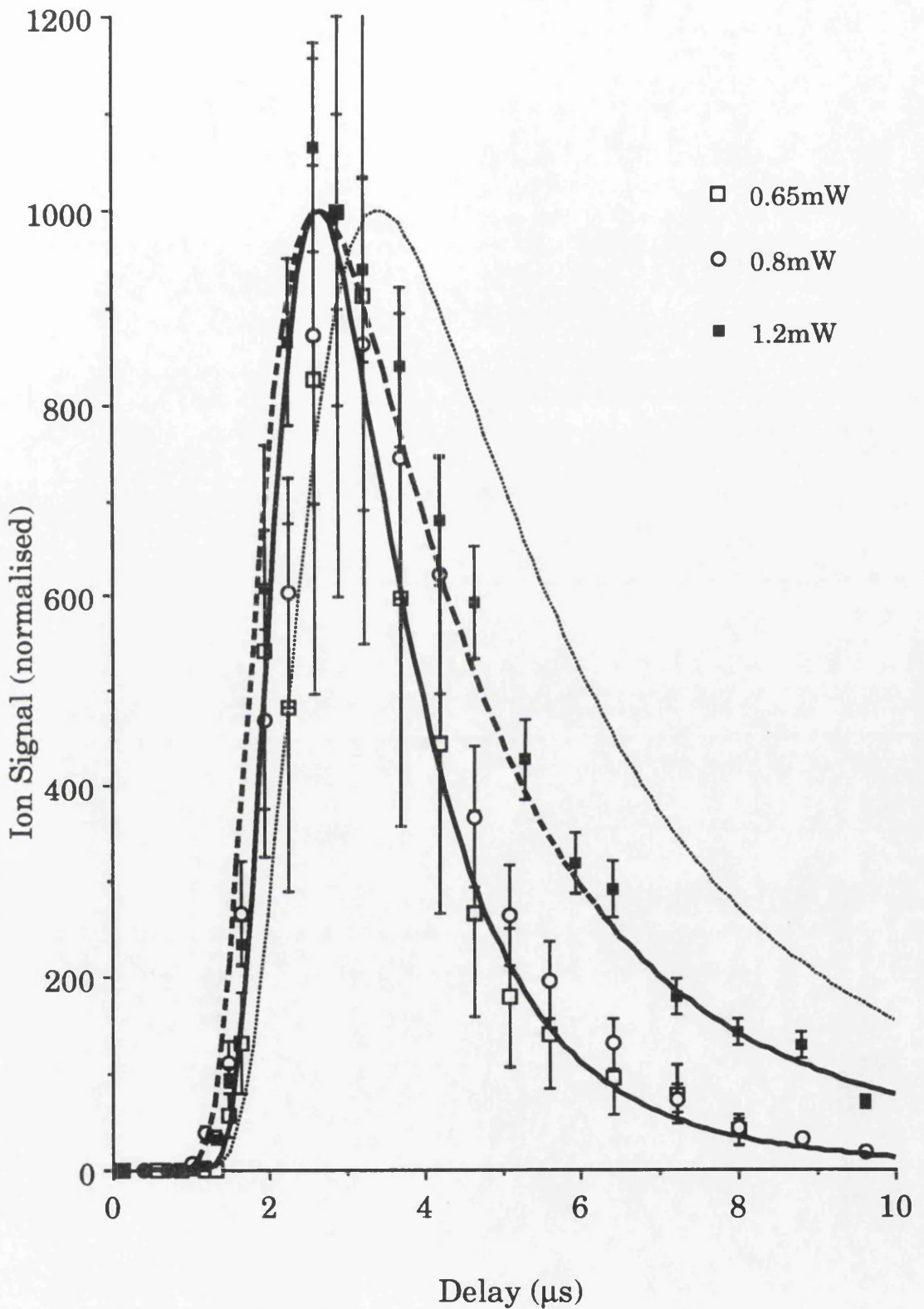


Fig.4.27 Temporal development of the non-resonant PAI signal from a gold sample for various ablation laser powers. The ablation laser wavelength was 266nm. The data is fitted with a half-range Maxwell-Boltzmann distribution with characteristic temperatures of 6000K (dotted line) and 10,000K (broken line). The prediction of the Knudsen later formalism with a characteristic temperature of 6000K is also shown (solid line).

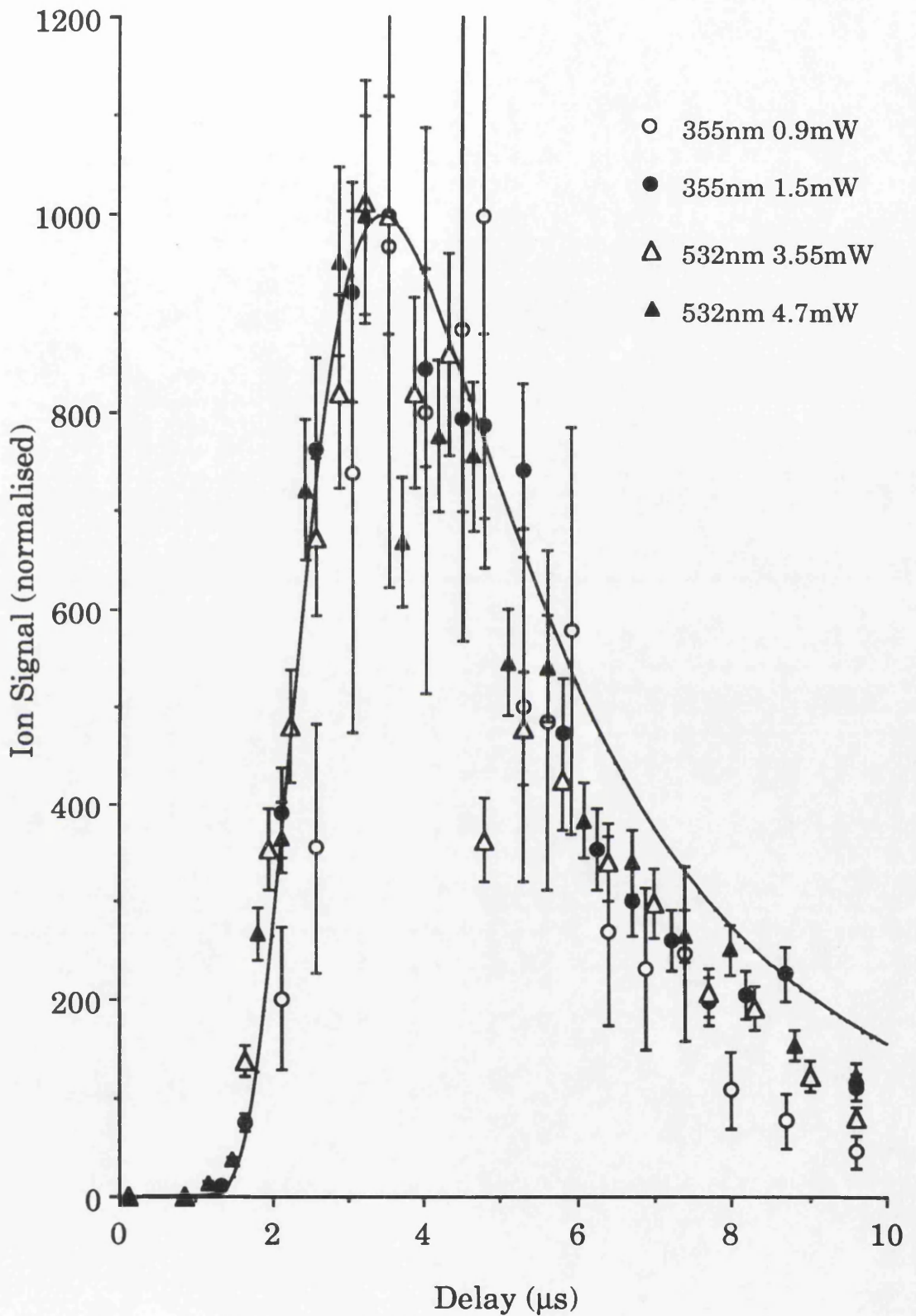


Fig.4.28 Temporal development of the gold dimer signal for various ablation laser powers and wavelengths. The data is fitted with a half-range Maxwell-Boltzmann distribution with a mass of 197amu and a characteristic temperature of 6000K.

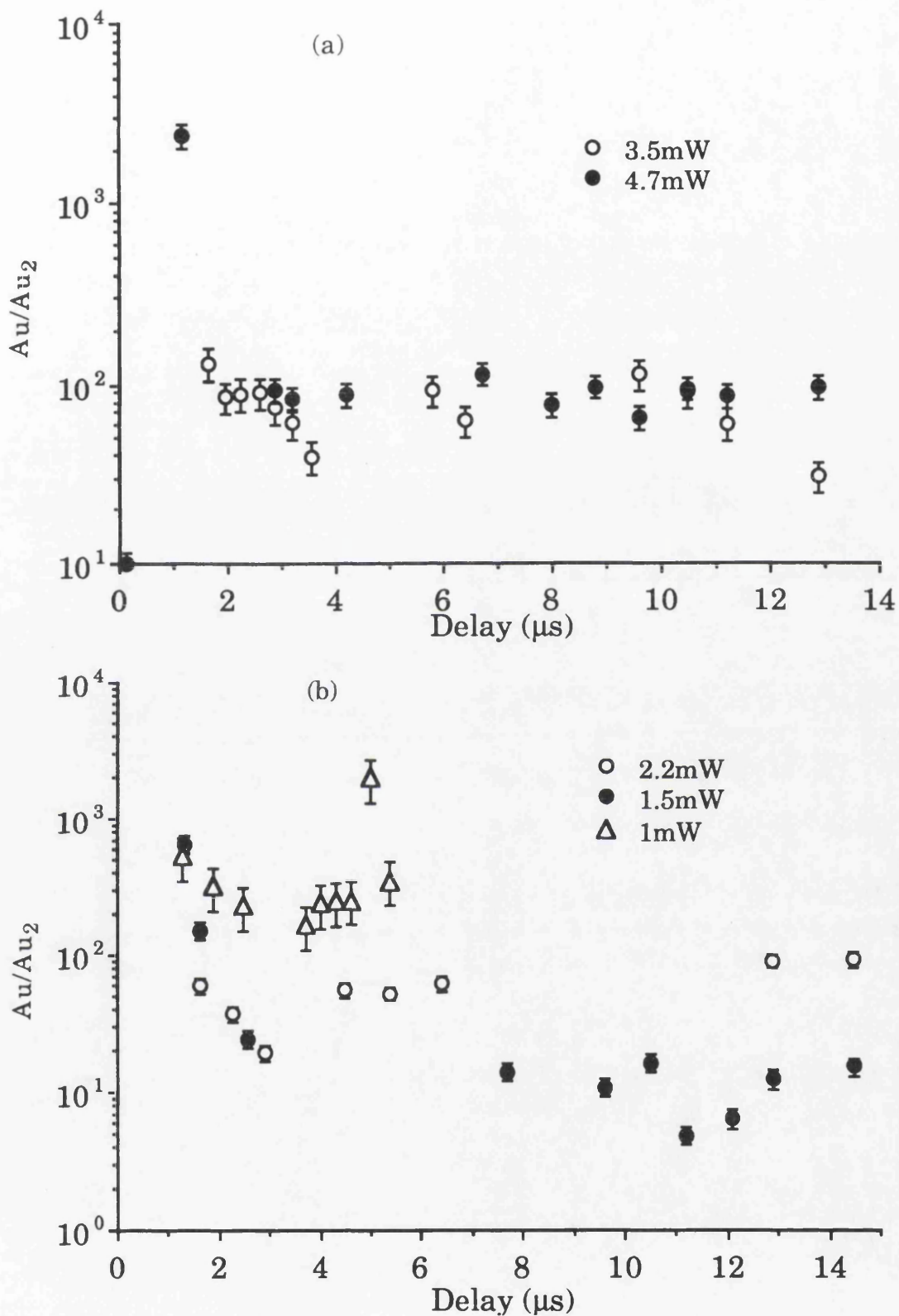


Fig.4.29 Temporal development of the ratio of gold atom to dimer signal for various ablation laser powers. The ablation laser wavelength was (a) 532nm, (b) 355nm.

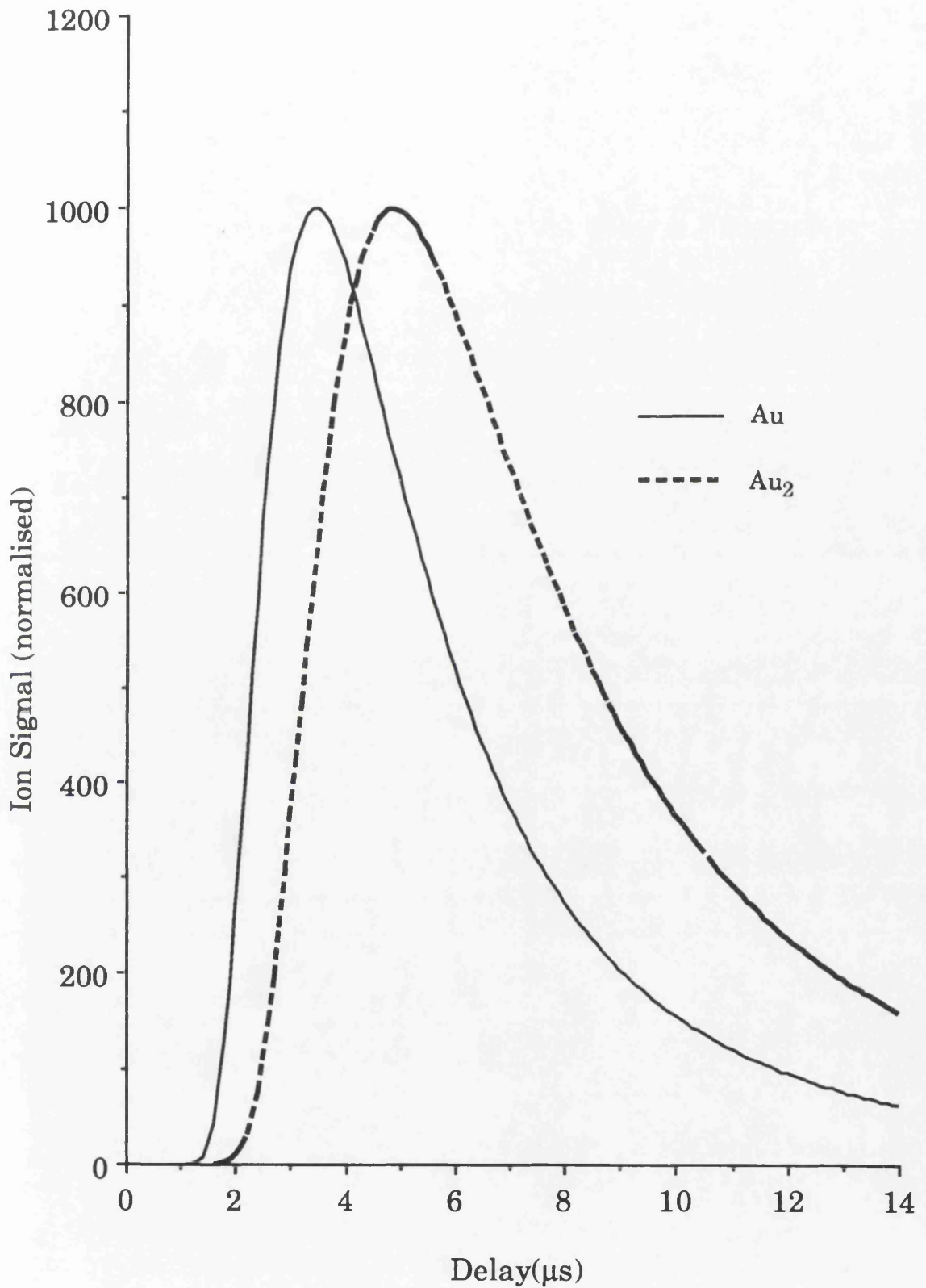


Fig.4.30 Temporal development of the half-range Maxwell-Boltzmann distribution for gold (197amu) and the gold dimer (394amu). A characteristic temperature of 6000K was used for both distributions and a value of $i=3$ was used.

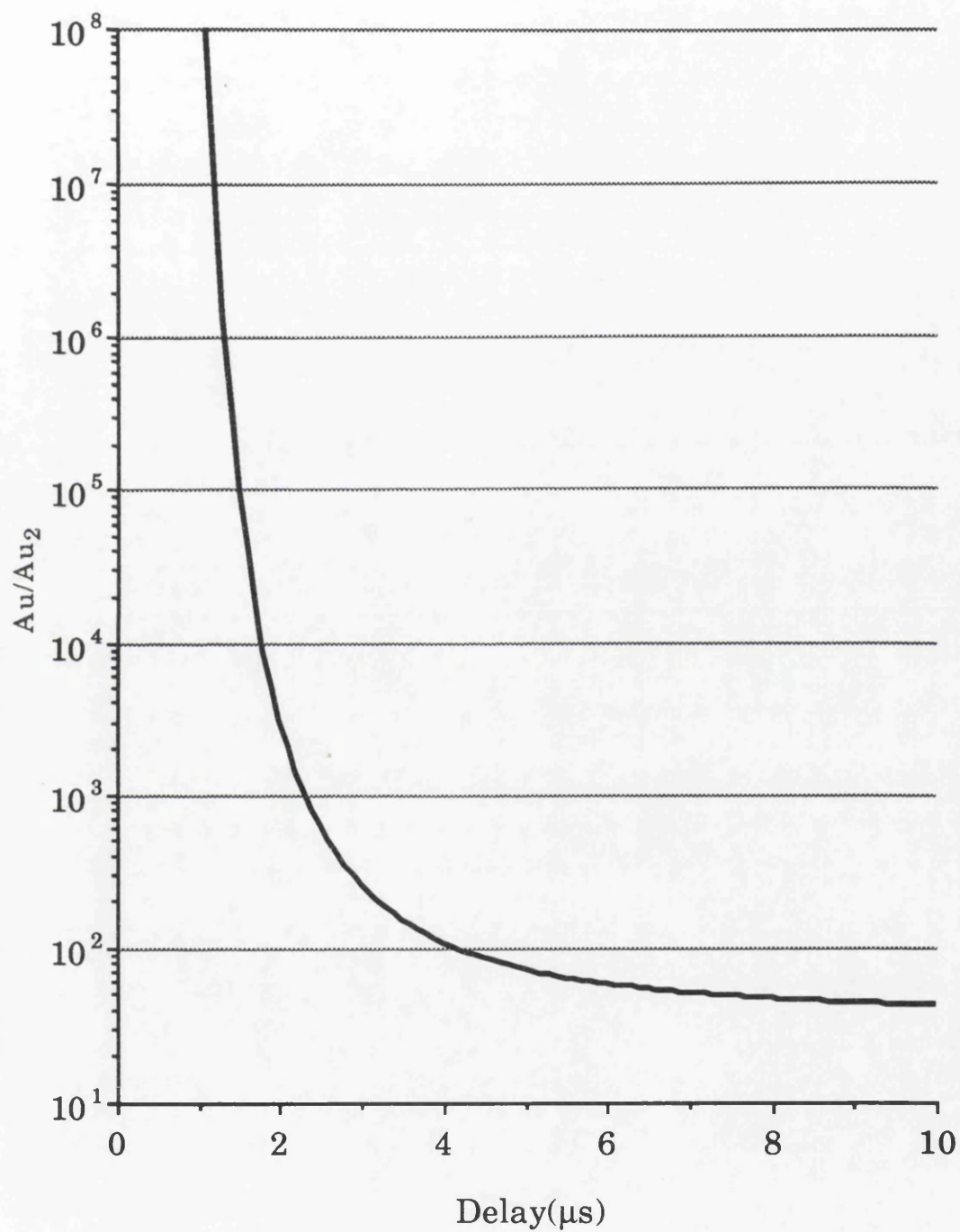


Fig.4.31 Modelled temporal development of the ratio of gold atom to dimer signal. This is obtained assuming both species can be described by a half-range Maxwell-Boltzmann distribution with a characteristic temperature of 6000K.

bears any resemblance to the theoretical ratio and this varies by a maximum of a factor of a hundred from the shortest to the longest delay. It would appear to be more probable that the dimers are produced in the gas phase. The conservation of momentum would result in the velocity distribution of the dimers being the same as that of the atoms, as is observed in Fig.4.26 and Fig.4.28. It would appear probable, therefore, that gas phase reactions occur, even though a collision free model can be used to describe the data.

§4.4 Lead

To investigate more quantitatively the evolution of multicomponent plumes, lead was studied. This choice was made because lead has three isotopes of similar abundance and could be ionised by two photons of 266nm wavelength. The natural isotopic distribution of lead is ^{204}Pb 1.4%, ^{206}Pb 24.1%, ^{207}Pb 22.1% and ^{208}Pb 52.4%. It would be expected that the ablated material would maintain this composition. Fig.4.32 shows the temporal distributions of the ^{208}Pb PAI signal obtained at various laser powers, with an ablation laser wavelength of 532nm. These are shown on a normalised scale in Fig.4.33, together with a Maxwell-Boltzmann distribution with a characteristic temperature of 6000K.

A section of the time-of-flight spectrum for an ablation laser power of 1.5mW is shown in Fig.4.34. There is no appreciable leakage signal. This section of the mass spectra can be recorded as a function of the delay between the lasers, which enables the temporal distributions for all the isotopes to be obtained simultaneously, as shown in Fig.4.35. It would appear that there is no discernible difference between the isotopes. Hence, it should be possible to describe all the isotopes of an element by the same characteristic temperature. The isotope ratios of ^{208}Pb and ^{206}Pb as a function of the delay between the lasers is shown in Fig.4.36. At small delay times the isotope ratio of the ionised material is furthest from the expected ratio, due to the lighter isotopes, which have the higher velocities, arriving at the PAI laser prior to the other, heavier, isotopes. As the delay between the two lasers is increased, the sampled plume becomes more characteristic of the sample composition. Hence, when this technique is used to measure isotope ratios attention must be paid to ensure that there is sufficient delay between the lasers. The difference in

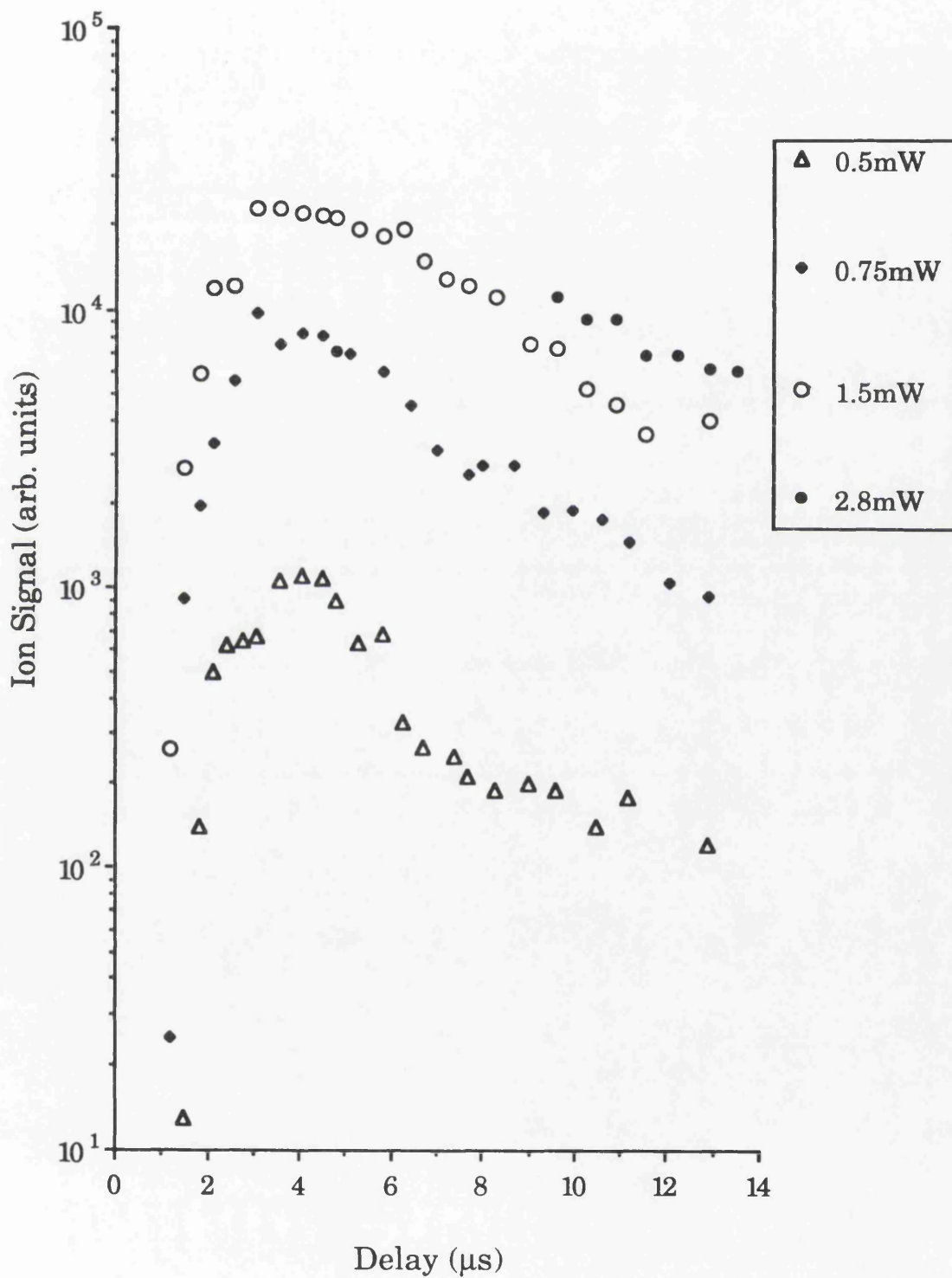


Fig.4.32 Temporal development of the ^{208}Pb PAI signal for various ablation laser powers. The ablation laser wavelength is 532nm.

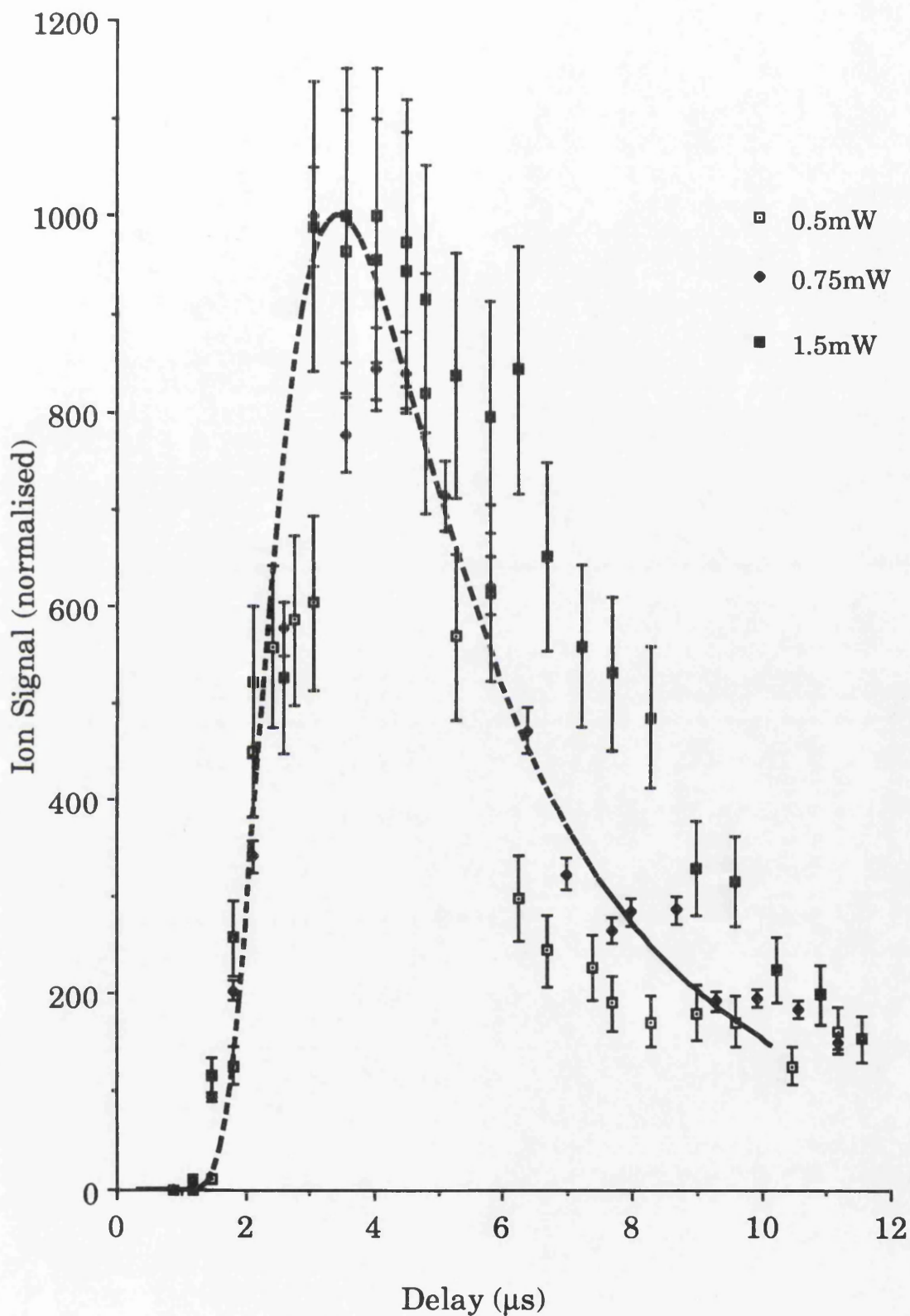


Fig.4.33 Temporal development of the ^{208}Pb PAI signal for various ablation laser powers. The ablation laser wavelength is 532nm. The broken line represents a half-range Maxwell-Boltzmann distribution with a temperature of 6000K.

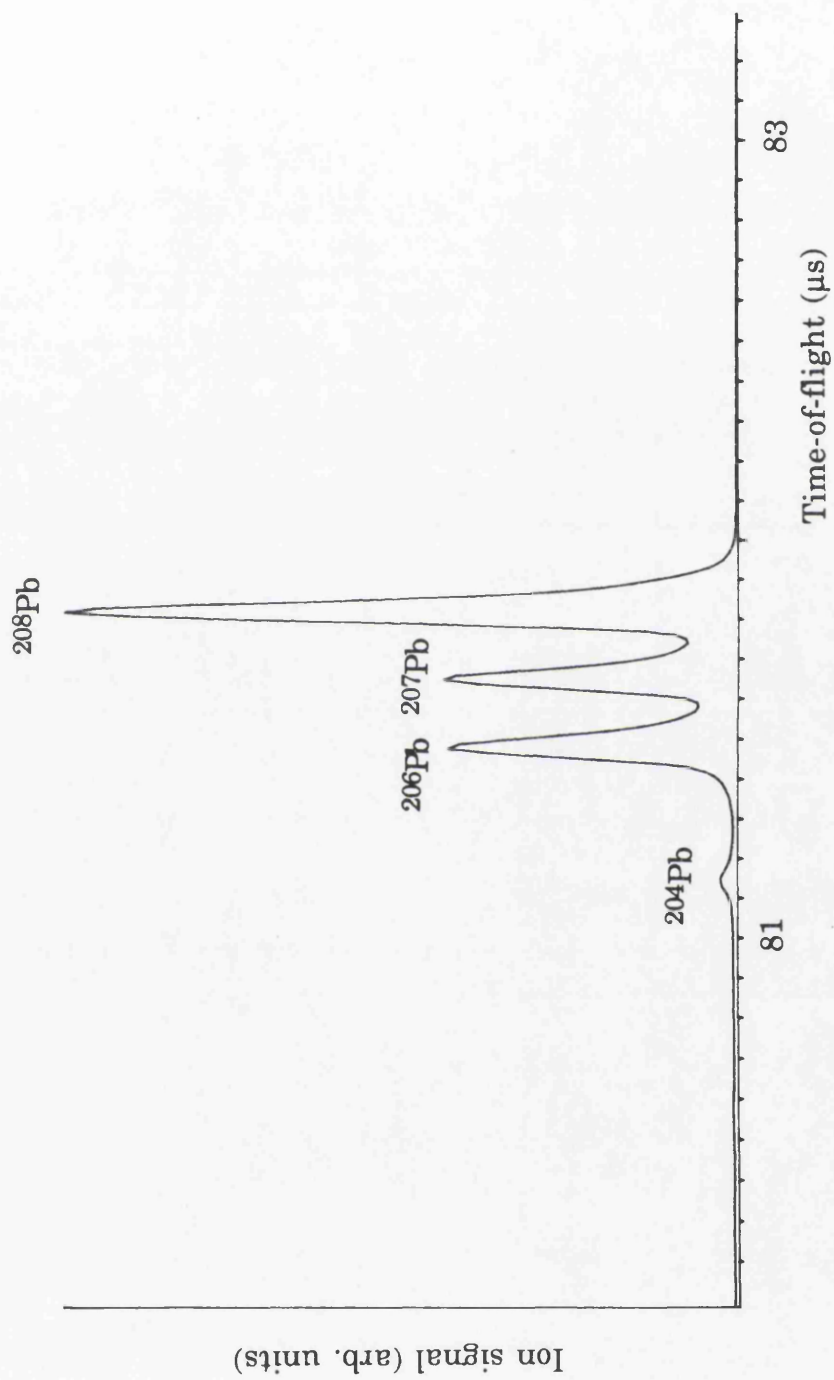


Fig.4.34 Section of the PAI time-of-flight spectrum produced by laser ablation of a lead target with an ablation laser power of 1.5mW. The four isotopes are well resolved. The delay between the ablation laser and the PAI laser firing was 5μs.

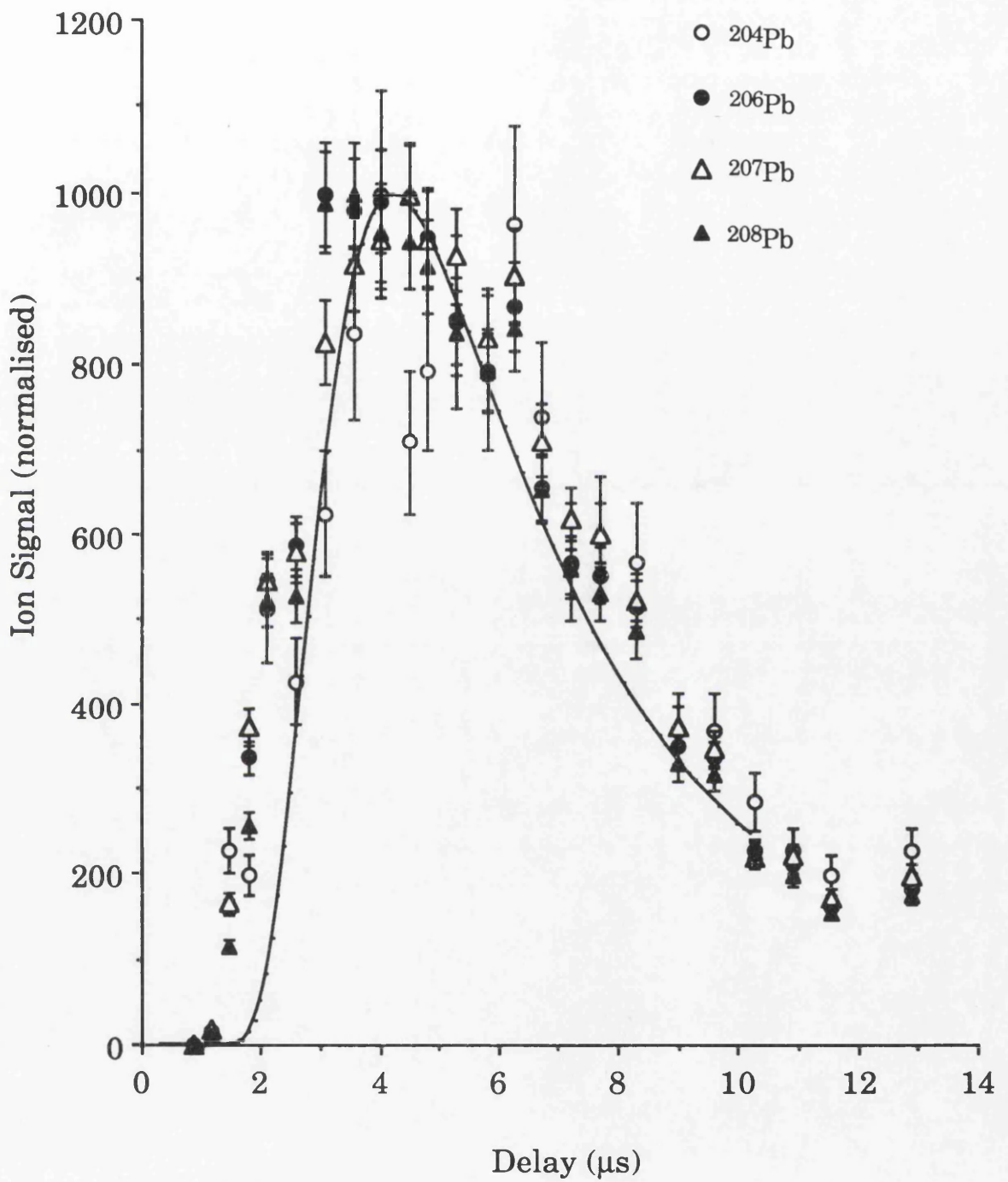


Fig.4.35 Temporal development of the PAI signals of the different lead isotopes for an ablation laser power of 1.5mW. The ablation laser wavelength is 532nm. The line represents a half-range Maxwell-Boltzmann distribution with a temperature of 4000K.

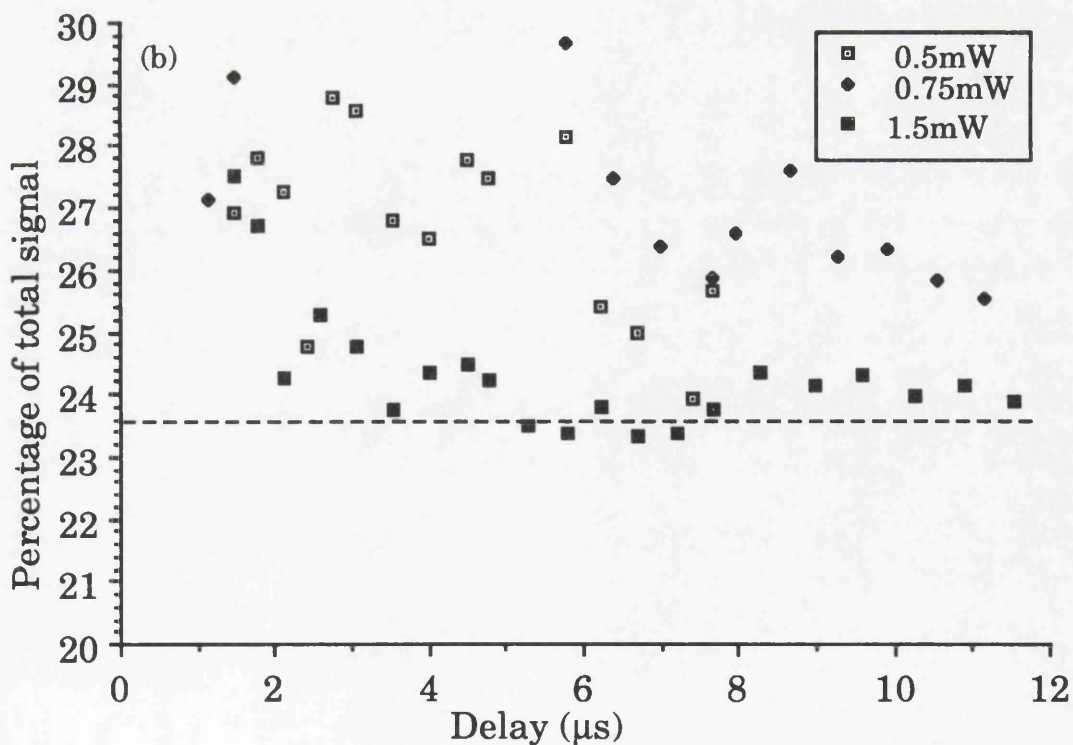
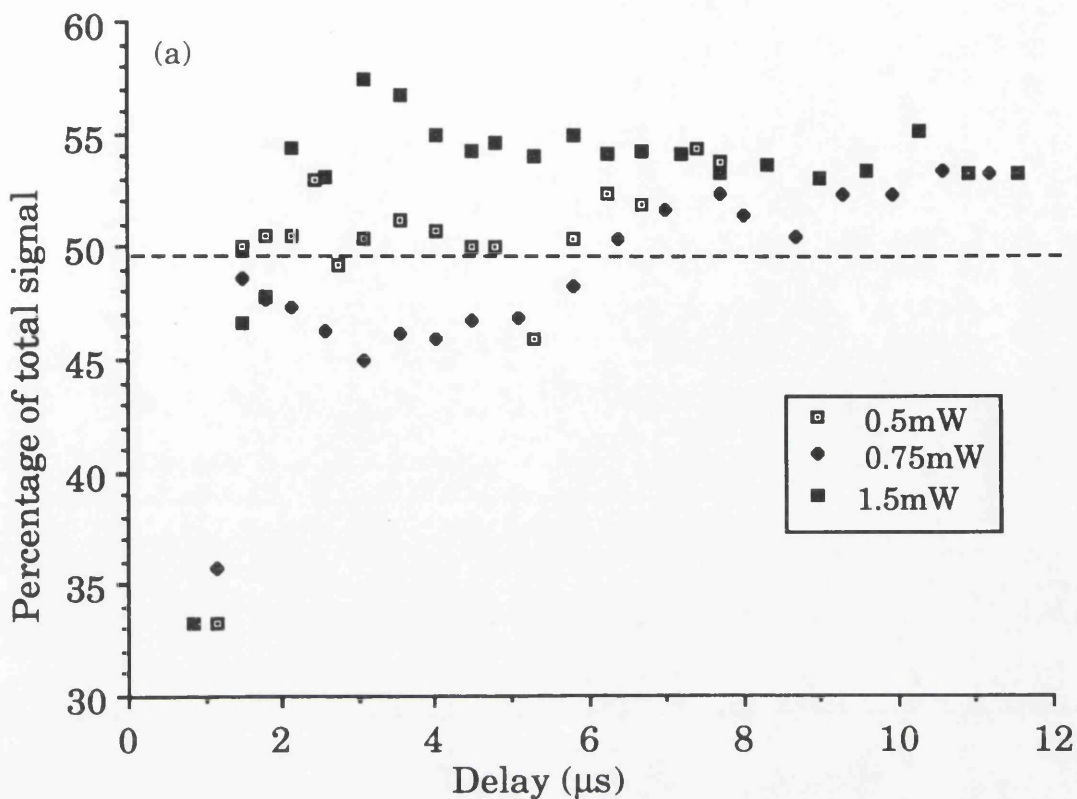


Fig.4.36 Temporal development of the isotope ratios calculated from the PAI signals for different ablation laser powers, for (a) ^{208}Pb and (b) ^{206}Pb . The ablation laser wavelength is 532nm. The broken line represents the natural isotopic abundance.

mass between the heaviest and lightest isotopes of lead is less than 2%, this isotope biasing effect will be more pronounced for lighter elements where the difference between the heaviest and lightest isotopes can be larger, ~20% for Ca (McCombes, 1991b) and 8% for Fe and Ti.

§4.5 Low alloy steel

To assess the applicability of laser atomisation with PAI to the analysis of trace elements, a Cr-V modified low alloy steel sample, with certified concentrations of trace and minor elements was analysed. The sample was a standard reference material (SRM) 1263a, purchased from the US National Institute of Standards and Technology (NIST). The SRMs are prepared to ensure high homogeneity, this has been verified for silicon in this SRM by LIFS using laser atomisation (Sdorra *et al*, 1989). The ablation laser spot size in the LIFS study was ~100µm, which is similar to that used in this work. The composition of this sample for elements of interest is shown in Table 4.1. The ionisation potentials of all of these elements are below 9.32eV, so they can all be ionised non-resonantly by two photons of the fourth harmonic of the Nd:YAG laser.

A mass spectrum obtained with this arrangement, using 532nm wavelength ablation, is shown in Fig.4.37. The peak of the major iron isotope, ⁵⁶Fe, is much larger than the other ion peaks and so to maximise the dynamic range of the analysis, the less abundant isotope ⁵⁴Fe was used as the reference element. The atomic concentrations in the sample of the isotopes apparent in Fig.4.37, (I_{det}) relative to ⁵⁴Fe are given in Table 4.1.

It was found that the composition of the mass spectrum changed with repeated irradiation as shown in Fig.4.38, the ablation laser wavelength was 532nm and the power 3.6mW. The sample had been prepared as described for aluminium in §4.2.1 and a virgin area of the surface was selected. The development of the ratio of the Mn and Ti signals to the ⁵⁴Fe signal is shown in Fig.4.39. Each point is obtained from the spectrum accumulated over the previous 500 laser shots. Approximately ten thousand laser shots are required before the ratios become apparently independent of the number of laser shots. This is obviously far from satisfactory if qualitative analysis is required. It was postulated that the

Element	Certified Concentration (Wt %)	Melting Point (Kelvin)	Boiling Point (Kelvin)	Ionisation Potential (eV)	ΔE (cm^{-1})	Detected Isotope (I_{det})	Atomic Composition $I_{\text{det}}/^{54}\text{Fe}$
Al	0.24	933	2740	5.99	3893	27	0.09
Ti	0.050	1933	3560	6.82	39	48	0.00784
V	0.31	2163	3653	6.74	35	51	0.06
Cr	1.31	2130	2945	6.77	3404	52	0.216
Fe	94.4	1808	3023	7.87	828	54	1
Mn	1.50	1517	2235	7.43	1824	55	0.279

Table 4.1 Composition of NIST low alloy steel SRM 1263a.

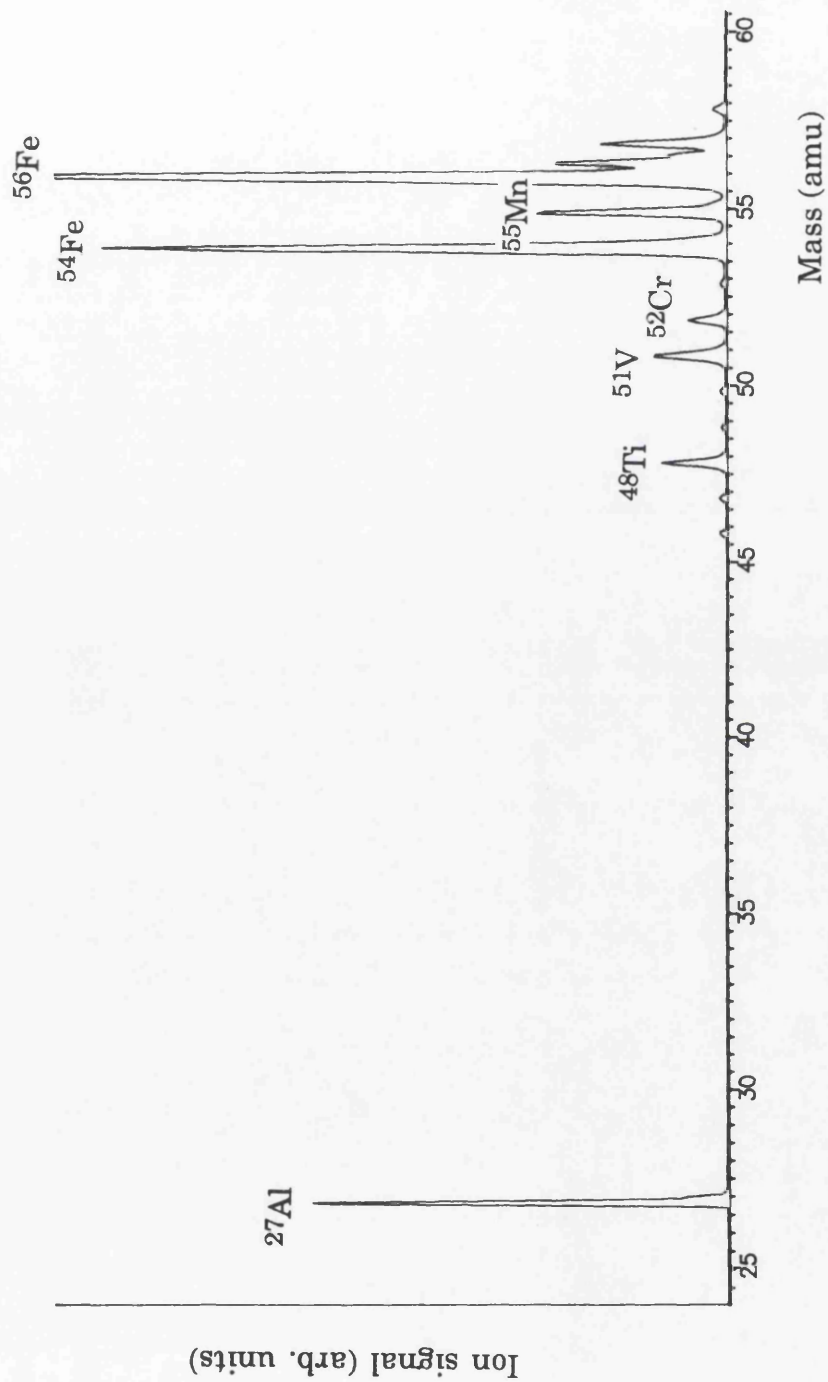


Fig.4.37 Section of the PAI mass spectrum produced by laser ablation of NIST SRM 1263a, with an ablation laser wavelength of 532nm.

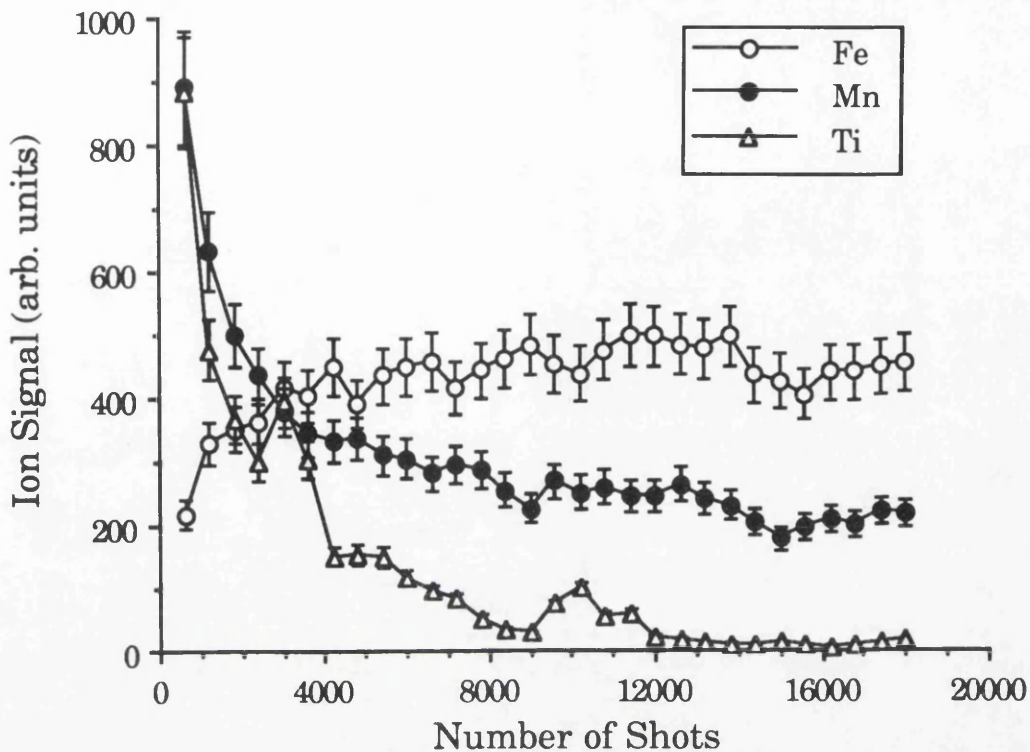


Fig.4.38 Temporal development of the ^{54}Fe , ^{55}Mn and ^{48}Ti PAI signals, obtained with an ablation laser power of 3.6mW and a wavelength of 532nm. The sample is NIST SRM 1263a.

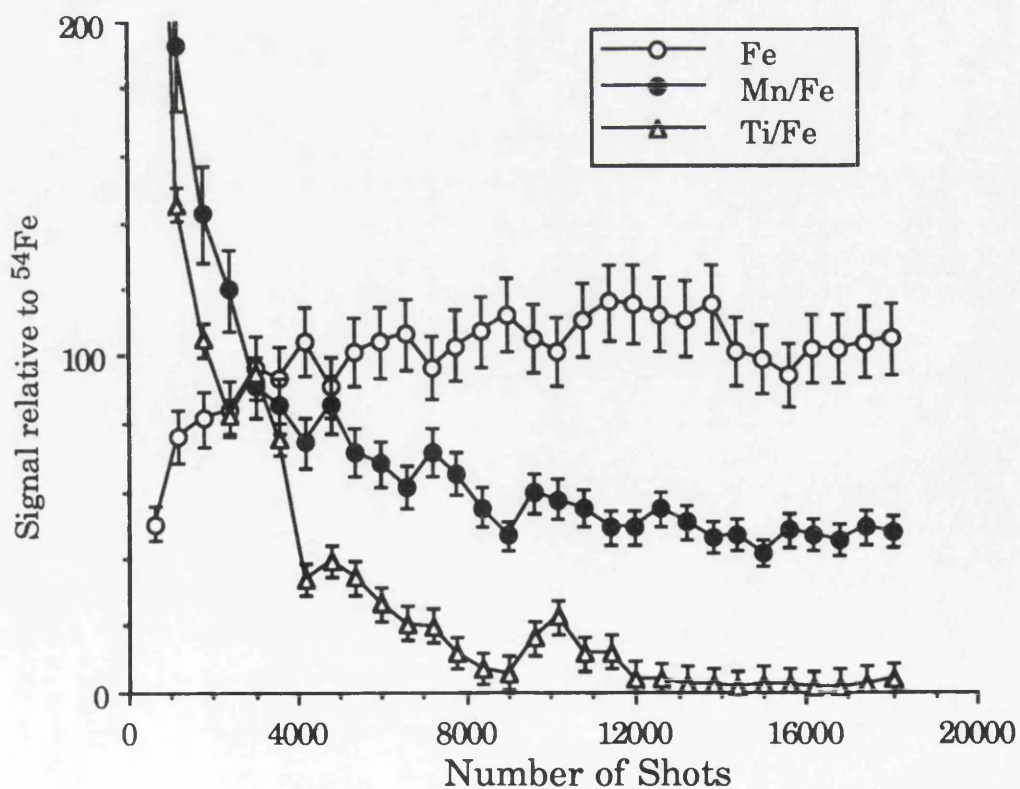


Fig.4.39 Temporal development of the ratio of $^{55}\text{Mn}/^{54}\text{Fe}$ and $^{48}\text{Ti}/^{54}\text{Fe}$ PAI signals, obtained with an ablation laser power of 3.6mW and a wavelength of 532nm. The sample is NIST SRM 1263a.

sample preparation may have resulted in a surface composition distinctly different from that of the bulk. To investigate this possibility the sample was irradiated with a higher laser power, ~25mW, prior to the measurements. This power was well above that where plasma formation prevents the acquisition of PAI signals and from the surface modification observed for aluminium, significant cratering and material removal would be expected. The ratios obtained using 30 and 300 cleaning shots are shown in Fig.4.40(a) and (b) respectively. The surface cleaning does not alleviate the problem, but does reduce the number of shots required before the ratios are apparently constant, by approximately a factor of two. It would appear, therefore, that this behaviour is largely due to the atomisation process. It has long been established that material removed by laser induced vaporisation does not reflect the composition of the solid. Baldwin (1970) employed X-ray fluorescence to analyse the vapour collected after the Q-switched irradiation of a series of brass standards. It was seen that the vapour composition, which was independent of the energy of the laser beam, was in good agreement with the predicted composition of the equilibrium liquid phase. That is, the vapour and the molten phase both contained a higher proportion of zinc than the solid. The bottom of the crater was observed to be significantly enriched in copper. Deviation in the plume from the stoichiometry of the solid has also been discussed by von Allmen (1987). It was contended that the composition of a vapour is different from that of a liquid in equilibrium with it, in accordance with the vapour-liquid phase diagram. As the most volatile element, that is the one with the highest vapour pressure at the surface temperature, is evaporated the melt becomes enriched in the less volatile component. This will continue until either the most volatile component is lost or a congruently evaporating, or azeotropic, molten phase is achieved. The results shown in Figs.4.38-40 could be attributed to the more volatile Mn being vaporised preferentially until an azeotropic composition is achieved. To reduce the significance of this effect in the subsequent analysis the sample surface was irradiated for five thousand laser shots before any experimental measurements were taken.

The effect of increasing the ablation laser power on the temporal distribution of ^{54}Fe is shown in Fig.4.41. The ablation laser wavelength was 532nm and each distribution was taken on a fresh sample area. The

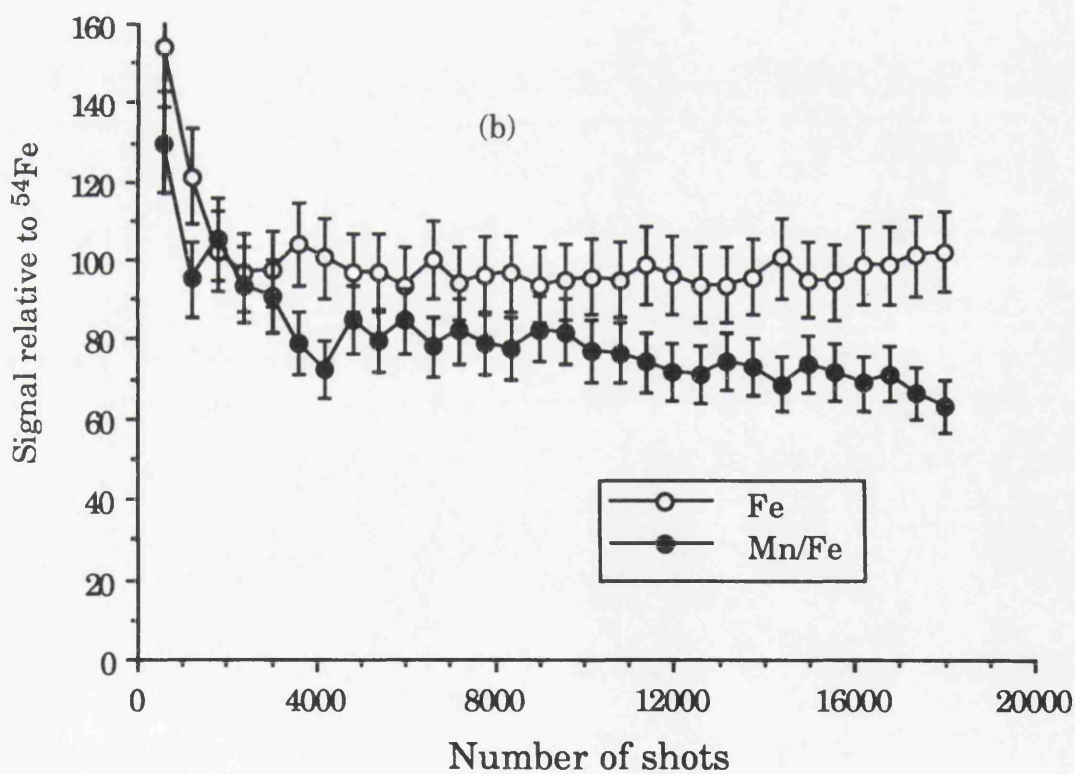
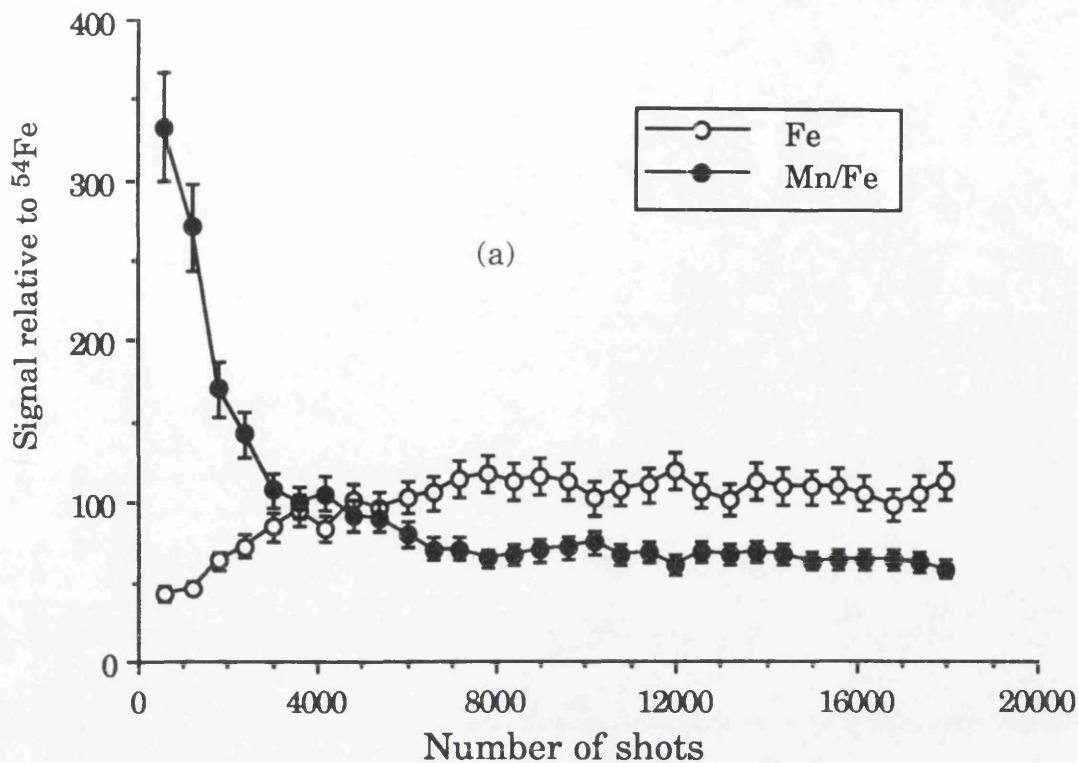


Fig.4.40 Temporal development of the ratio of $^{55}\text{Mn}/^{54}\text{Fe}$ PAI signals, obtained after sample cleaning with (a) 30 and (b) 300 laser shots of 22mW power. The analysis was carried out with an ablation laser power of 3.6mW and a wavelength of 532nm. The sample is NIST SRM 1263a.

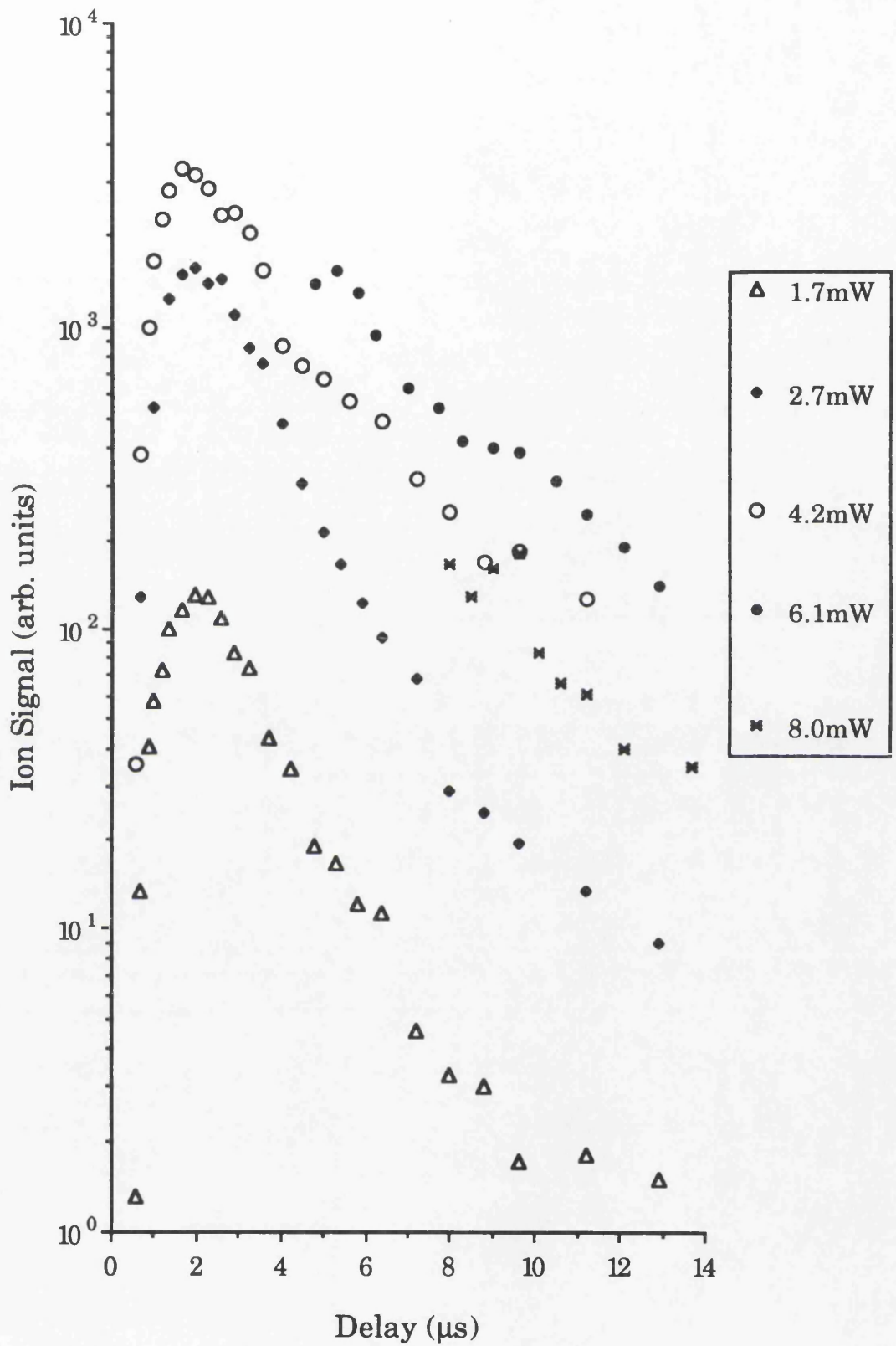


Fig.4.41 Temporal development of the PAI signal of ^{54}Fe for different ablation laser powers, from the NIST SRM 1263a sample. The ablation laser wavelength is 532nm.

distributions are broadly the same as those which have been shown previously, except that the plateau level is approximately a factor of ten lower. This does not correspond to less material in the plume, but reflects the fact that the ^{54}Fe isotope accounts for only 5.6% of the sample. Similar behaviour was observed for the aluminium component, as shown in Fig.4.42. As the mass of aluminium is significantly less than that of iron, the PAI produced aluminium ions arrive at the detector prior to the large packet of iron leakage ions. It would appear, therefore, that detector saturation can be ruled out as the cause of the plateau in the distribution, which could be attributed to space charge effects in the source region or plasma shielding of the sample surface.

The temporal distributions of all of the elements detailed in Table 4.1, for a laser power of 4.2mW, is shown in Fig.4.43. Except for aluminium, all of the elements were monitored simultaneously, using the procedure described for lead. It can be seen, as would be expected, that the distributions for the elements with approximately the same mass are similar. However, the aluminium PAI signal starts the same size as the ^{54}Fe signal, but decreases to be an order of magnitude lower than the ^{54}Fe signal at the longest delay. This illustrates the difficulty of determining the sample composition by this technique, since the measured sample composition would be a strong function of the delay between the lasers. A system to eliminate this problem was developed utilizing a pulsed jet of helium to transport the ablated material from the sample to the PAI laser (Nicholas *et al*, 1989). This technique markedly reduced the effect of the delay between the lasers on the relative signal sizes. However, pulsed jet introduction, which is widely used in molecular spectroscopy, has a very poor transport efficiency, $\sim 10^{-4}$ (Tembreull and Lubman, 1986).

Temporal distributions for all of the elements shown in Fig.4.43 were obtained for the powers detailed in Fig.4.41. As mentioned above, the distributions were monitored simultaneously for all the elements except aluminium. This arrangement allows the effect of changing the ablation laser power to be characterised for the various elements, while the surface conditions were identical. Fig.4.44 shows the distributions obtained for aluminium at various ablation laser powers, which have been fitted using

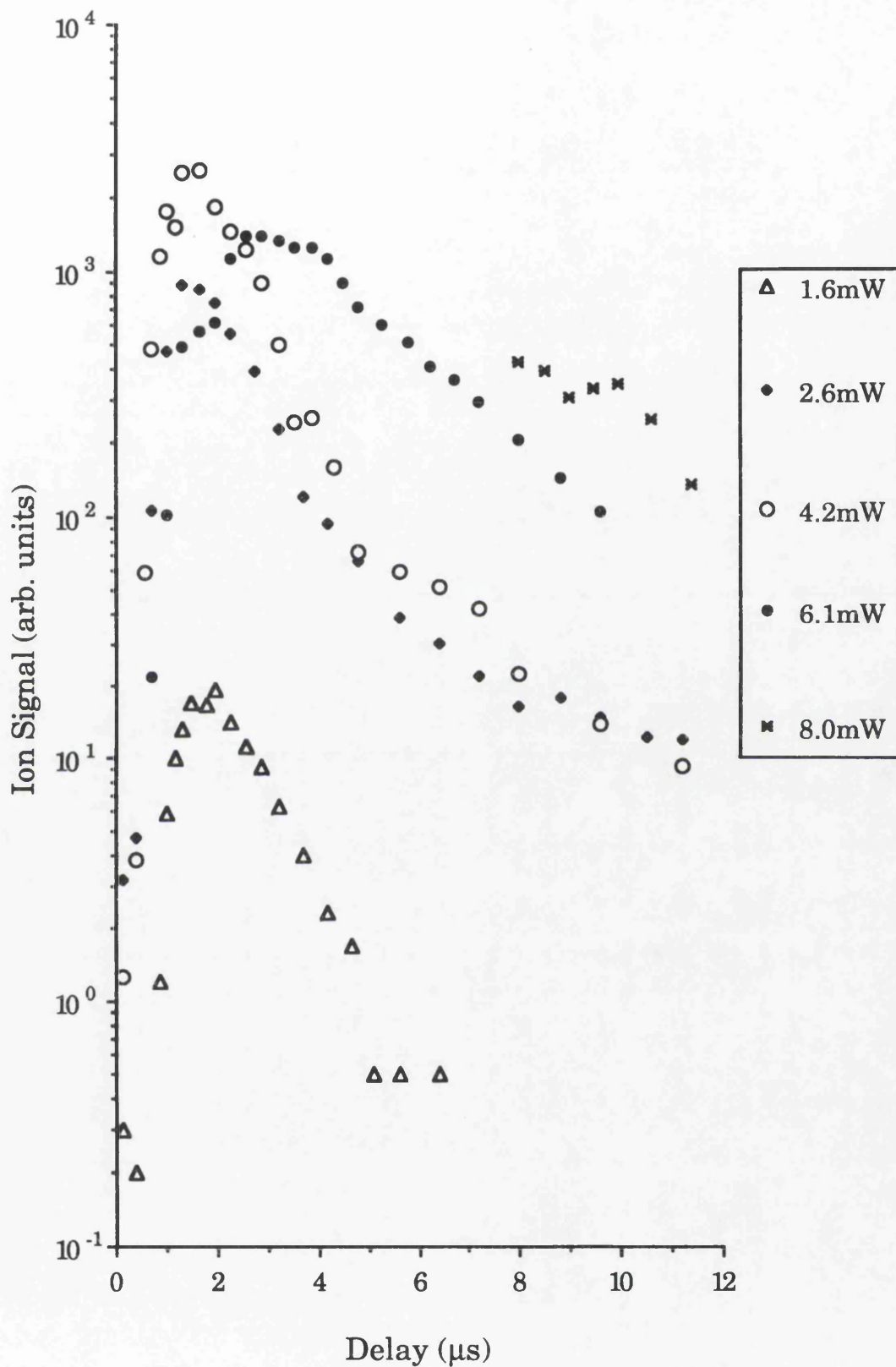


Fig.4.42 Temporal development of the PAI signal of ^{27}Al from the NIST SRM 1263a sample for different ablation laser powers. The ablation laser wavelength is 532nm.

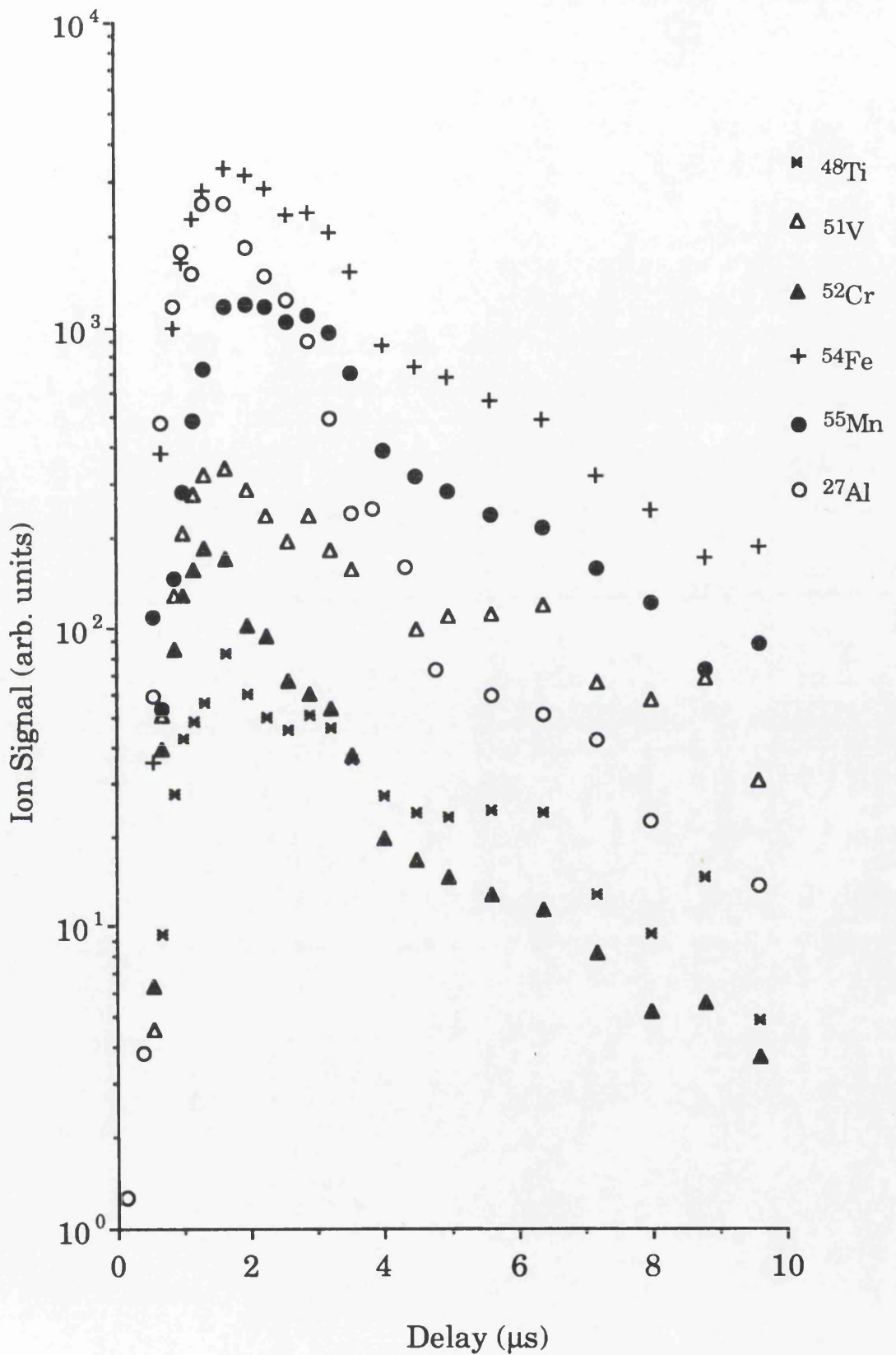


Fig.4.43 Temporal development of the PAI signal of several elements ablated from the NIST SRM 1263a sample. The ablation laser power is 4.2mW and the wavelength is 532nm.

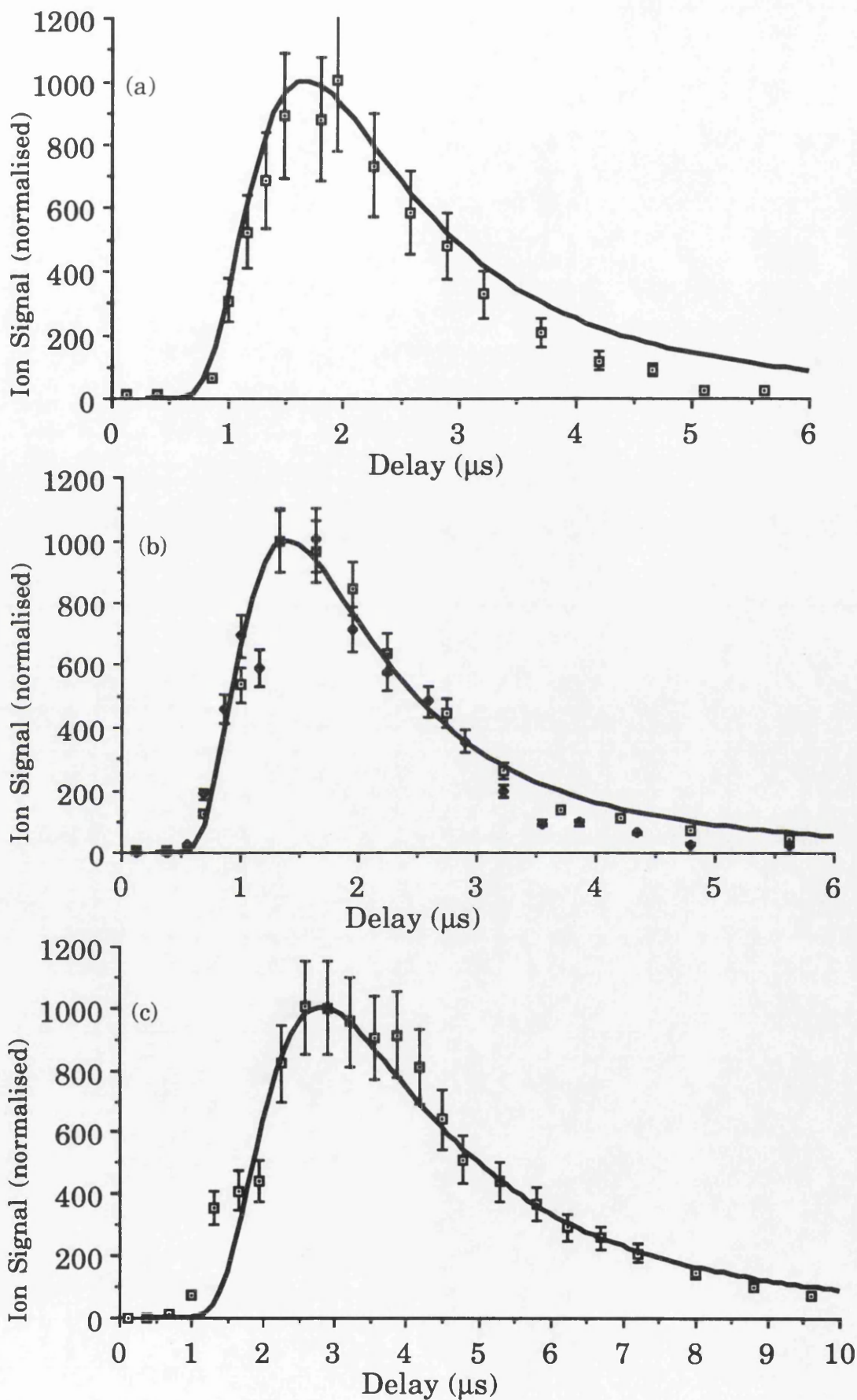


Fig.4.44 Temporal development of the PAI signal of ^{27}Al ablated from the NIST SRM 1263a sample, for several laser powers: (a) 1.7mW, (b) 2.6mW (open symbol) & 4.2mW (filled symbol) and (c) 6.1mW. The solid line represents a half-range Maxwell-Boltzmann distribution with a characteristic temperature of (a) 3500K, (b) 5000K and (c) 1250K. The ablation laser wavelength is 532nm.

the half-range Maxwell-Boltzmann distribution, as detailed above. The characteristic temperatures of these fits, 1250-5000K, are substantially lower than those obtained for pure aluminium samples, ~12,000K. (A comparison of the distributions obtained for various characteristic temperatures has been shown in Fig.4.6.).

It was found that higher characteristic temperatures were required to account for the distributions obtained for the other elements. Fig.4.45 shows the temporal dependence of the manganese signal and half-range Maxwell-Boltzmann distributions of 4500K and 6000K. It would appear, therefore, that the characteristic temperature appropriate for this data is lower than that obtained for ^{54}Fe , 6000K, as shown in Fig.4.46. A characteristic temperature of 6000K was found to be appropriate to fit the leading edge of the Ti distribution, as shown in Fig.4.47. A higher characteristic temperature, 9000K, was required to model the Cr and V distributions, as shown in Fig.4.48 and Fig.4.49 respectively. It is interesting to note that the increasing characteristic temperatures for the different elements can be correlated with the melting points of the elements. That is the element with the lowest melting point, aluminium, has a velocity distribution described by the lowest characteristic temperature, while those with the highest melting points, Cr and V, have the highest characteristic temperatures.

It is apparent that while the distributions for Al, Fe, Mn and Cr are fitted well at longer delay times by the half-range Maxwell-Boltzmann distribution, significant deviation is observed for Ti and V. This was believed to be due to a significant fraction of the vaporised material for these elements being in the form of atomic clusters. The prevalence of clusters may be related to the comparatively low vapour pressures of Ti and V, which is reflected in their high boiling points. Other mechanisms that could explain the deviation from the fit in the tail were believed to be less feasible. One possible mechanism would involve a second, lower temperature atomic component in the plume. However, such a mechanism has not been observed previously for any metal, in this work or by other researchers. Delayed emission of atoms of Ti and V was also deemed highly unlikely since these elements have lower vapour pressures than all the other elements monitored in the sample.

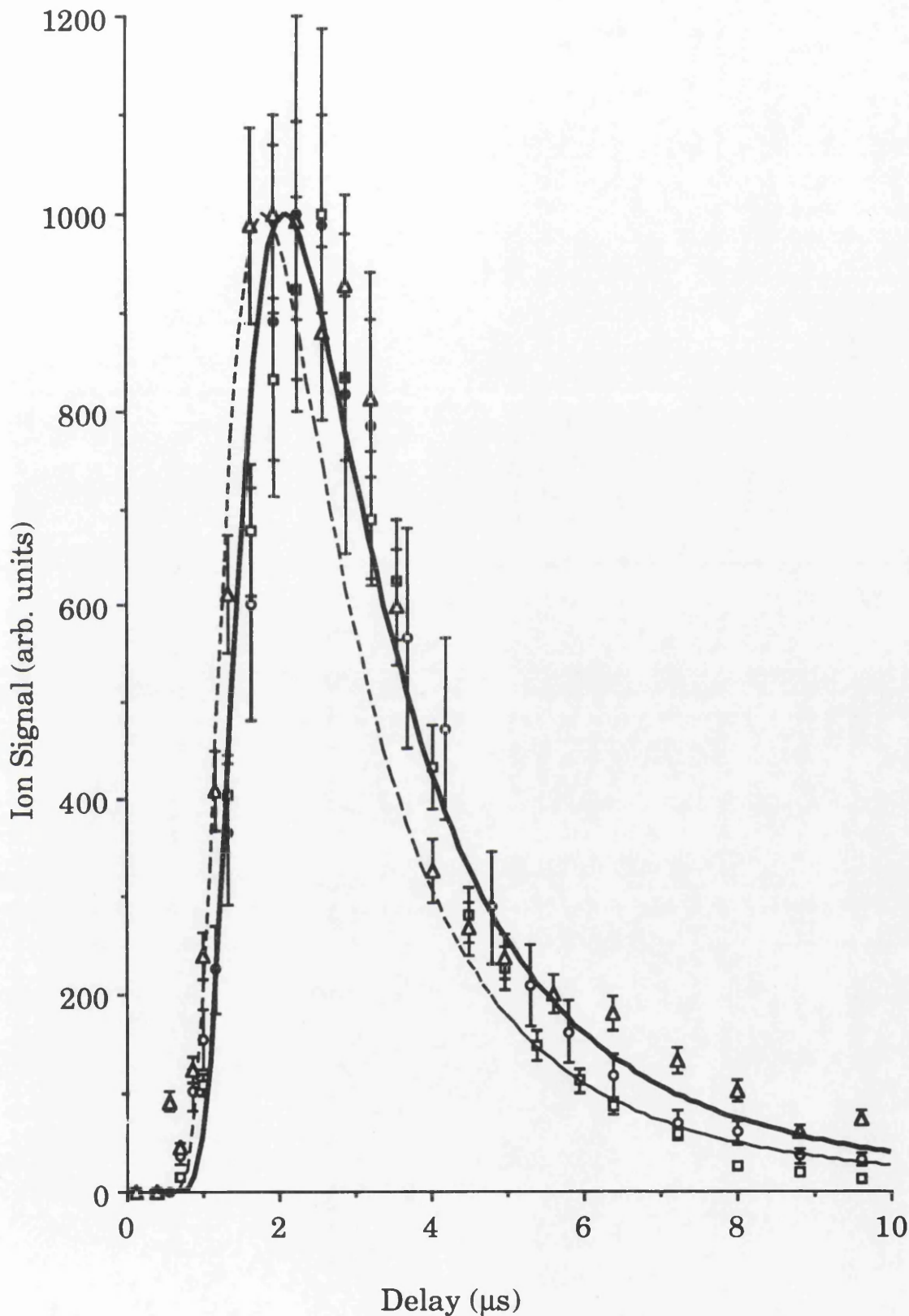


Fig.4.45 Temporal development of the PAI signal of ^{55}Mn ablated from the NIST SRM 1263a sample, for several ablation laser powers: 1.7mW, 2.7mW and 4.2mW. The data is fitted with a half-range Maxwell-Boltzmann distribution with a characteristic temperature of 4500K (solid line) and 6000K (broken line). The ablation laser wavelength is 532nm.

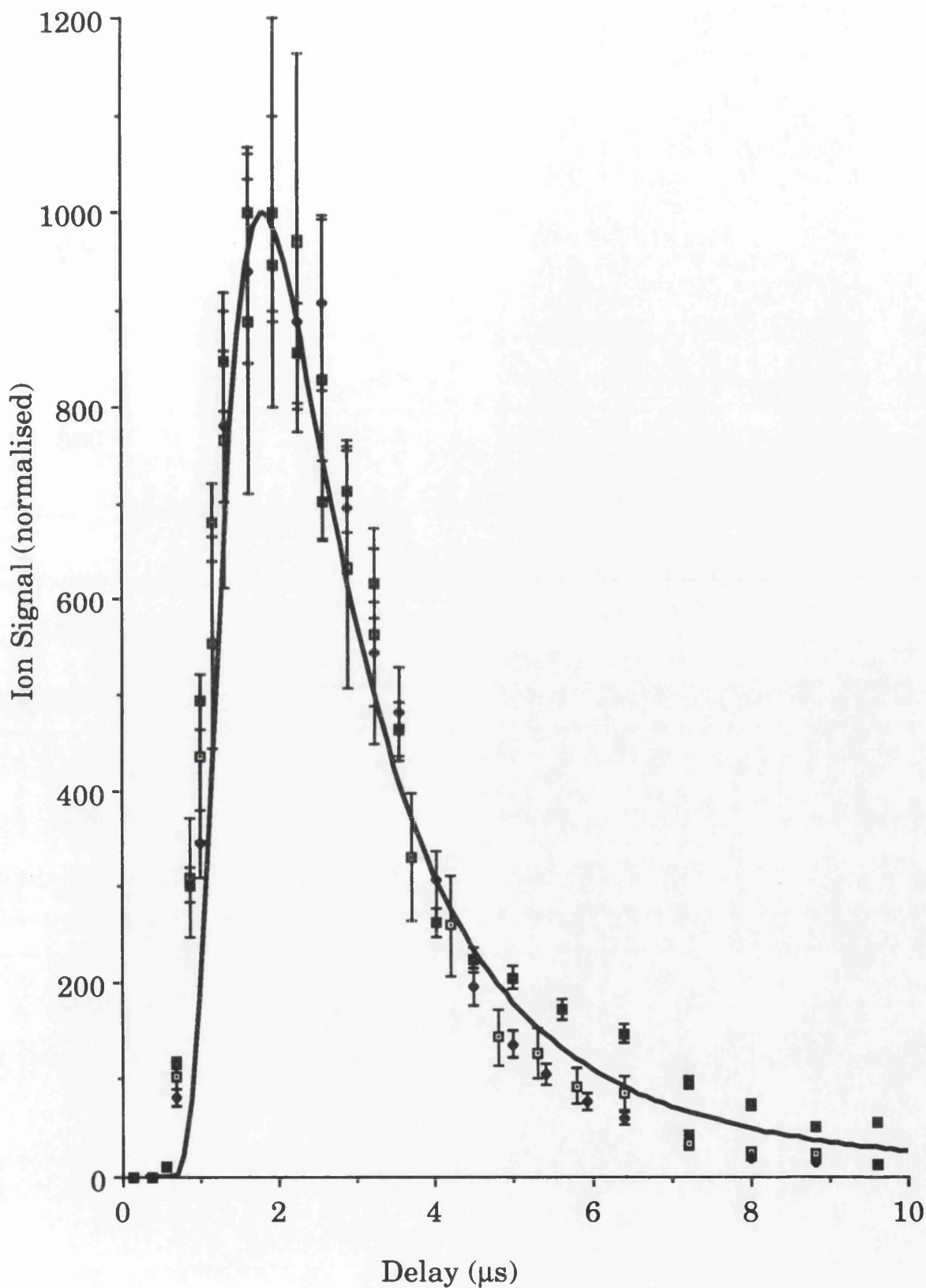


Fig.4.46 Temporal development of the PAI signal of ^{54}Fe ablated from the NIST SRM 1263a sample, for several laser powers: 1.7mW, 2.7mW and 4.2mW. The data is fitted with a half-range Maxwell-Boltzmann distribution with a characteristic temperature of 6000K. The ablation laser wavelength is 532nm.

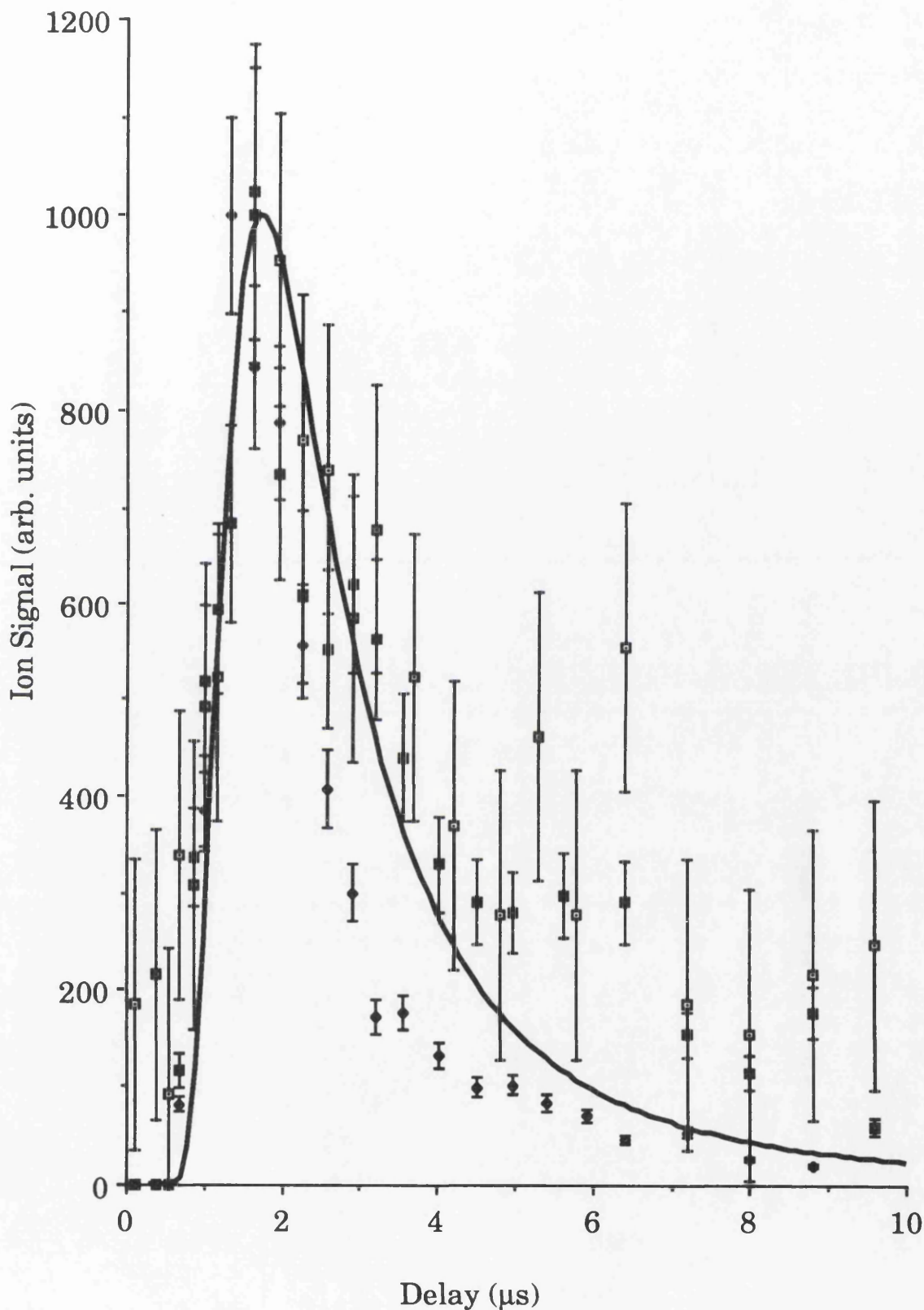


Fig.4.47 Temporal development of the PAI signal of ^{48}Ti ablated from the NIST SRM 1263a sample, for several laser powers: 1.7mW, 2.7mW and 4.2mW. The data is fitted with a half-range Maxwell-Boltzmann distribution with a characteristic temperature of 6000K. The ablation laser wavelength is 532nm.

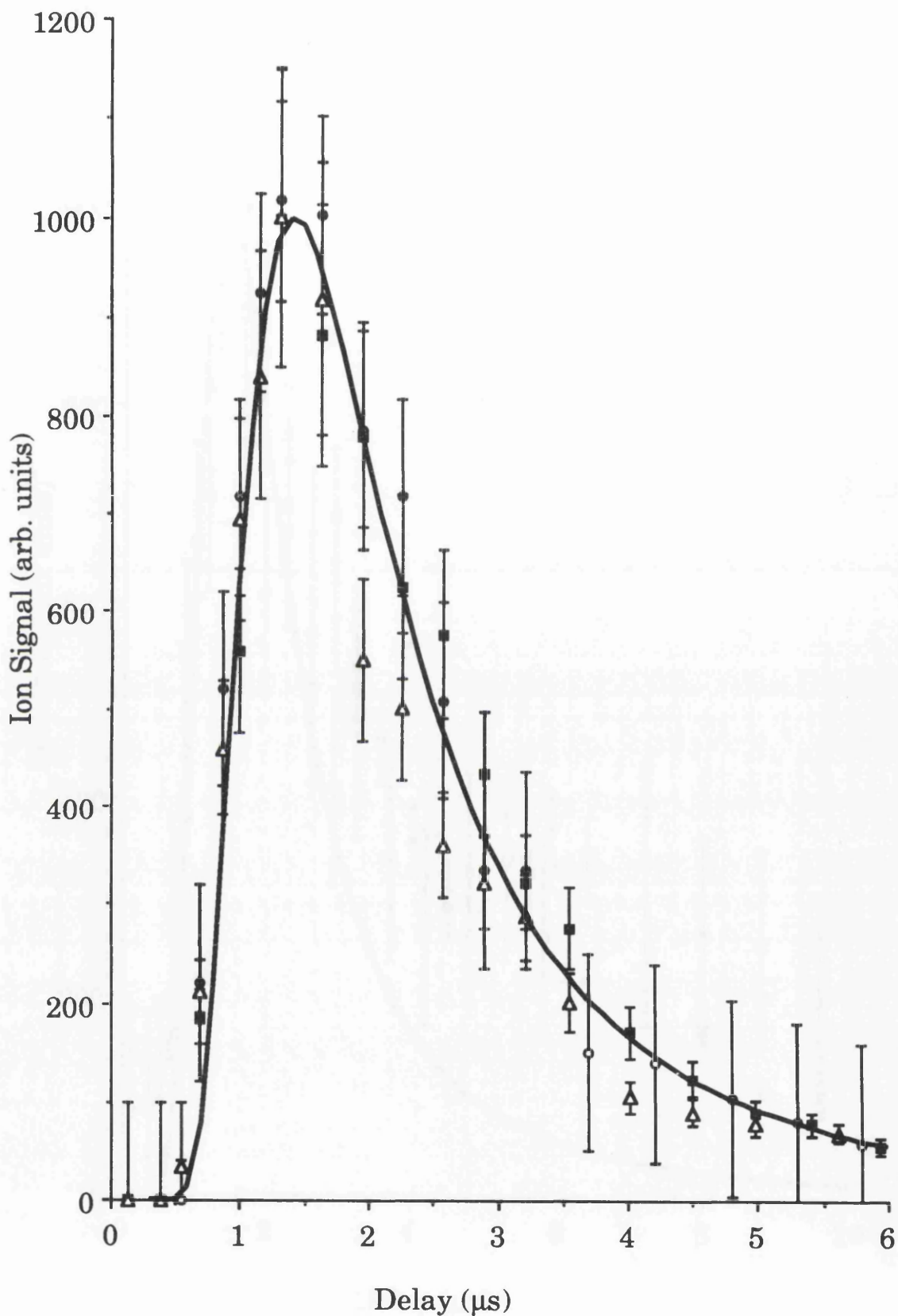


Fig.4.48 Temporal development of the PAI signal of ^{52}Cr ablated from the NIST SRM 1263a sample, for several laser powers: 1.7mW, 2.7mW and 4.2mW. The data is fitted with a half-range Maxwell-Boltzmann distribution with a characteristic temperature of 9000K. The ablation laser wavelength is 532nm.

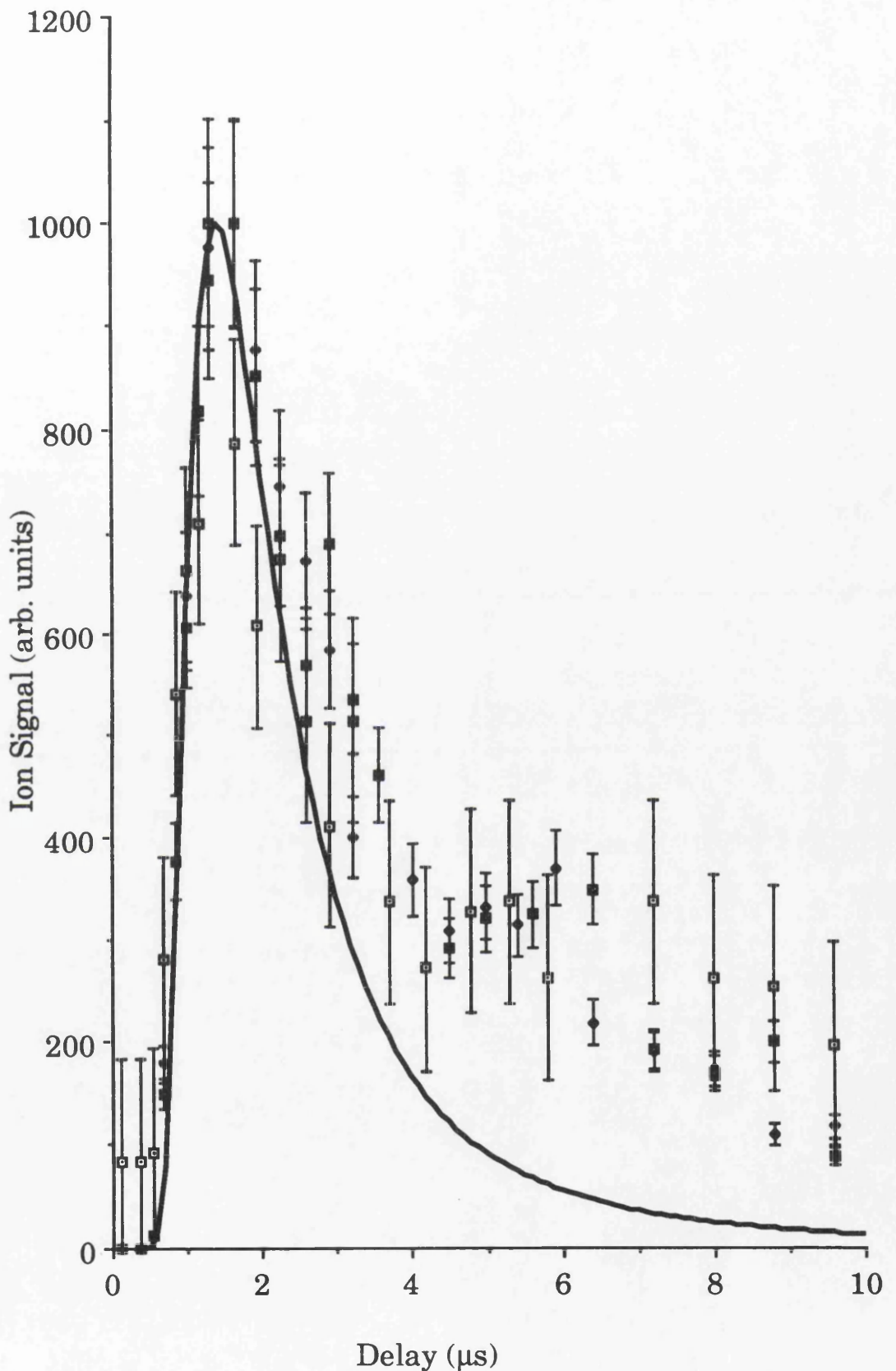


Fig.4.49 Temporal development of the PAI signal of ^{51}V ablated from the NIST SRM 1263a sample, for several laser powers: 1.7mW, 2.7mW and 4.2mW. The data is fitted with a half-range Maxwell-Boltzmann distribution with a characteristic temperature of 9000K. The ablation laser wavelength is 532nm.

To assess the quantitative capability of this analysis the relative sensitivity factors (RSFs) for the various elements were calculated. RSFs are widely used in laser microprobe mass spectrometry, where a single laser causes both ablation and ionisation (Conzemius and Capellen, 1980). The RSF for this type of analysis is defined (Odom and Schueler, 1987) as:

$$\text{RSF}\left(\frac{X}{Y}\right) = \frac{I_x/[X]}{I_y/[Y]} \quad - \text{Eqn.4.1}$$

where I_x and I_y are the measured intensities of species X and Y, and [X] and [Y] are their respective concentrations. If I_x and I_y are the intensities of specific isotopes of an element, then their respective isotopic abundances must be included in the calculation. Ideally the RSF values for different elements would be unity, and these RSF values would be independent of the sample composition. For these studies, as discussed above, the ^{54}Fe signal has been used as the reference. The RSF can then be expressed as:

$$\text{RSF}\left(\frac{X}{^{54}\text{Fe}}\right) = \frac{I_x}{I_{^{54}\text{Fe}}} \cdot \frac{1}{\text{Atomic Composition}} \quad - \text{Eqn.4.2}$$

where the atomic composition for the elements studied has been given in Table 4.1. As discussed previously, the ratio of the elements in the plume is a function of the delay between the lasers, therefore, the RSF changes as the delay between the lasers is changed, as shown in Fig.4.50. The temporal dependence of the RSF is different for the various elements; while for Mn the RSF increases with increasing delay, the RSF for Cr decreases as the delay is increased. This is a consequence of the different elements having different temporal distributions. The characteristic temperature of Cr is higher than that of ^{54}Fe and so the peak of the Cr distribution occurs prior to that of ^{54}Fe . Therefore, the RSF obtained for Cr starts comparatively high. However, for Mn, where the characteristic temperature is lower than that of ^{54}Fe , the opposite behaviour is observed. If two elements are described by identical characteristic temperatures then the RSF would still have a temporal dependence, due to the different masses of the elements. This was illustrated by the temporal dependence

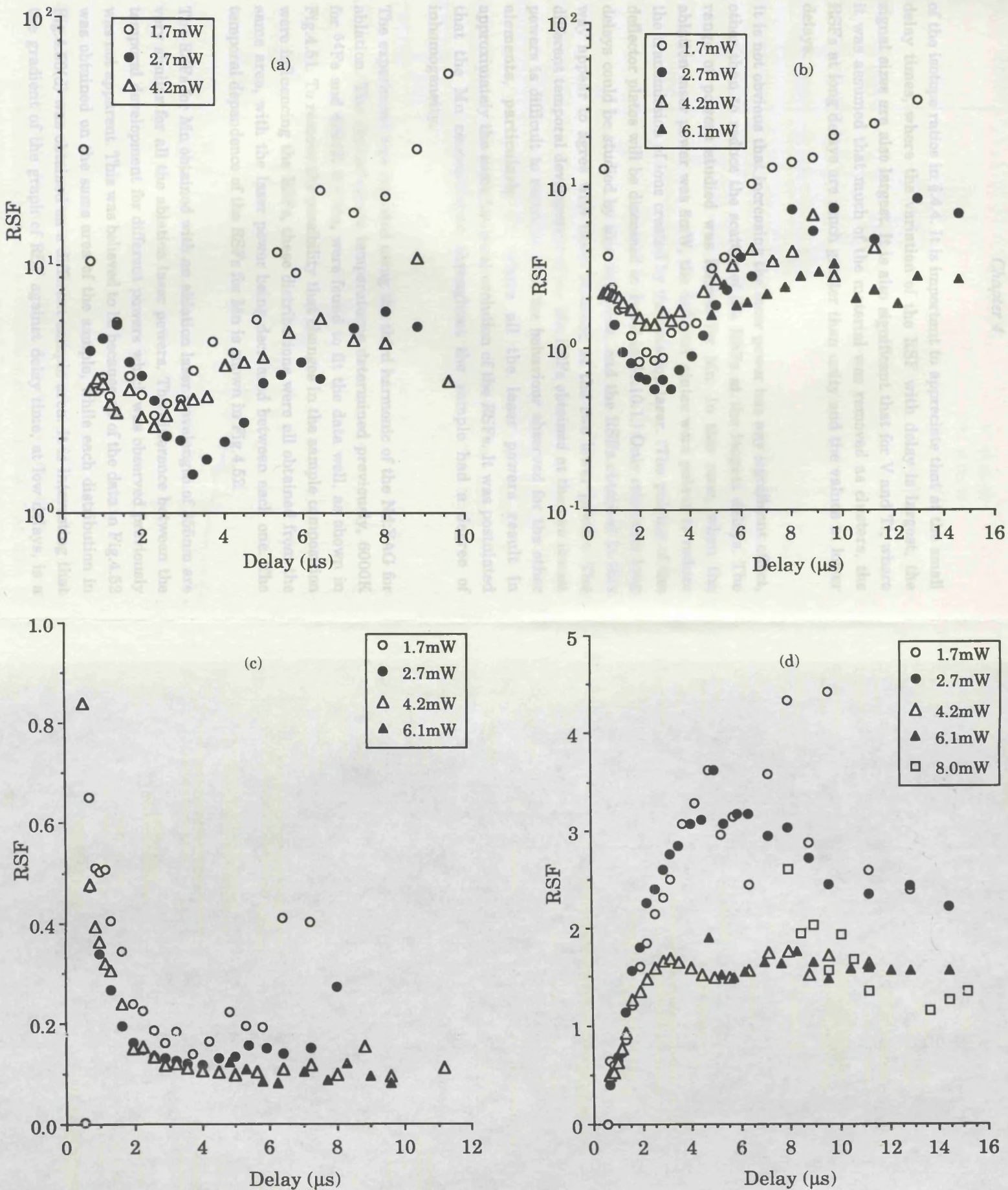


Fig.4.50 Temporal development of the relative sensitivity factors, RSFs, for several laser powers for (a) Ti, (b) V, (c) Cr and (d) Mn. The sample is NIST SRM 1263 and the ablation laser wavelength is 532nm.

of the isotope ratios in §.4.4. It is important to appreciate that at the small delay times, where the variation of the RSF with delay is largest, the signal sizes are also largest. It is also significant that for V and Ti, where it was assumed that much of the material was removed as clusters, the RSFs at long delays are much greater than unity and the values at lower delays.

It is not obvious that increasing the laser power has any significant effect, other than to reduce the scatter of the RSFs at the longest delays. The range of powers studied was largest for Mn. In this case, when the ablation laser power was 8mW, the deflector plates were pulsed to reduce the transmission of ions created by the ablation laser. (The pulsing of the deflector plates will be discussed in detail in §4.10.1.) Only relatively long delays could be studied by this technique, and the RSFs obtained in this way appear to agree with those obtained at the two lower powers. The different temporal development of the Mn RSFs obtained at the two lowest powers is difficult to reconcile with the behaviour observed for the other elements, particularly Cr, where all the laser powers result in approximately the same temporal evolution of the RSFs. It was postulated that the Mn concentration throughout the sample had a degree of inhomogeneity.

The experiment was repeated using the third harmonic of the Nd:YAG for ablation. The characteristic temperatures determined previously, 6000K for ^{54}Fe and 4000K for Mn, were found to fit the data well, as shown in Fig.4.51. To remove the possibility that changes in the sample composition were influencing the RSFs, these distributions were all obtained from the same area, with the laser power being decreased between each one. The temporal dependence of the RSFs for Mn is shown in Fig.4.52.

The RSFs for Mn obtained with an ablation laser wavelength of 355nm are very similar for all the ablation laser powers. The difference between the temporal development for different powers which was observed previously was not apparent. This was believed to be because all of the data in Fig.4.52 was obtained on the same area of the sample, while each distribution in Fig.4.50(d) was obtained on a different sample area. It is interesting that the gradient of the graph of RSF against delay time, at low delays, is a

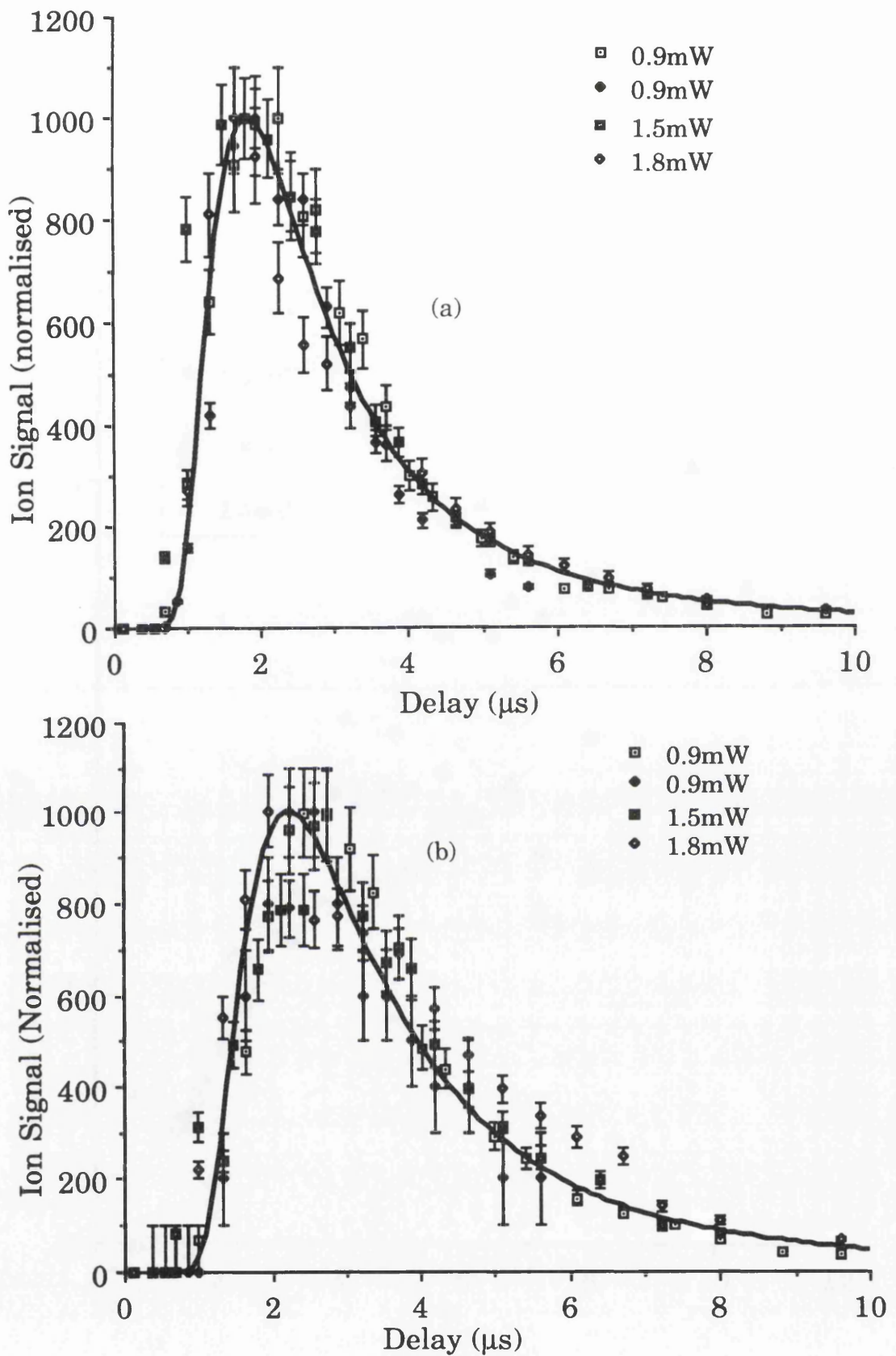


Fig.4.51 Temporal development of the PAI signal of (a) ^{54}Fe and (b) ^{55}Mn ablated from the NIST SRM 1263a sample, for several laser powers. The ablation laser wavelength is 355nm. The data is fitted with a half-range Maxwell-Boltzmann distribution with a characteristic temperature of (a) 6000K and (b) 4000K.

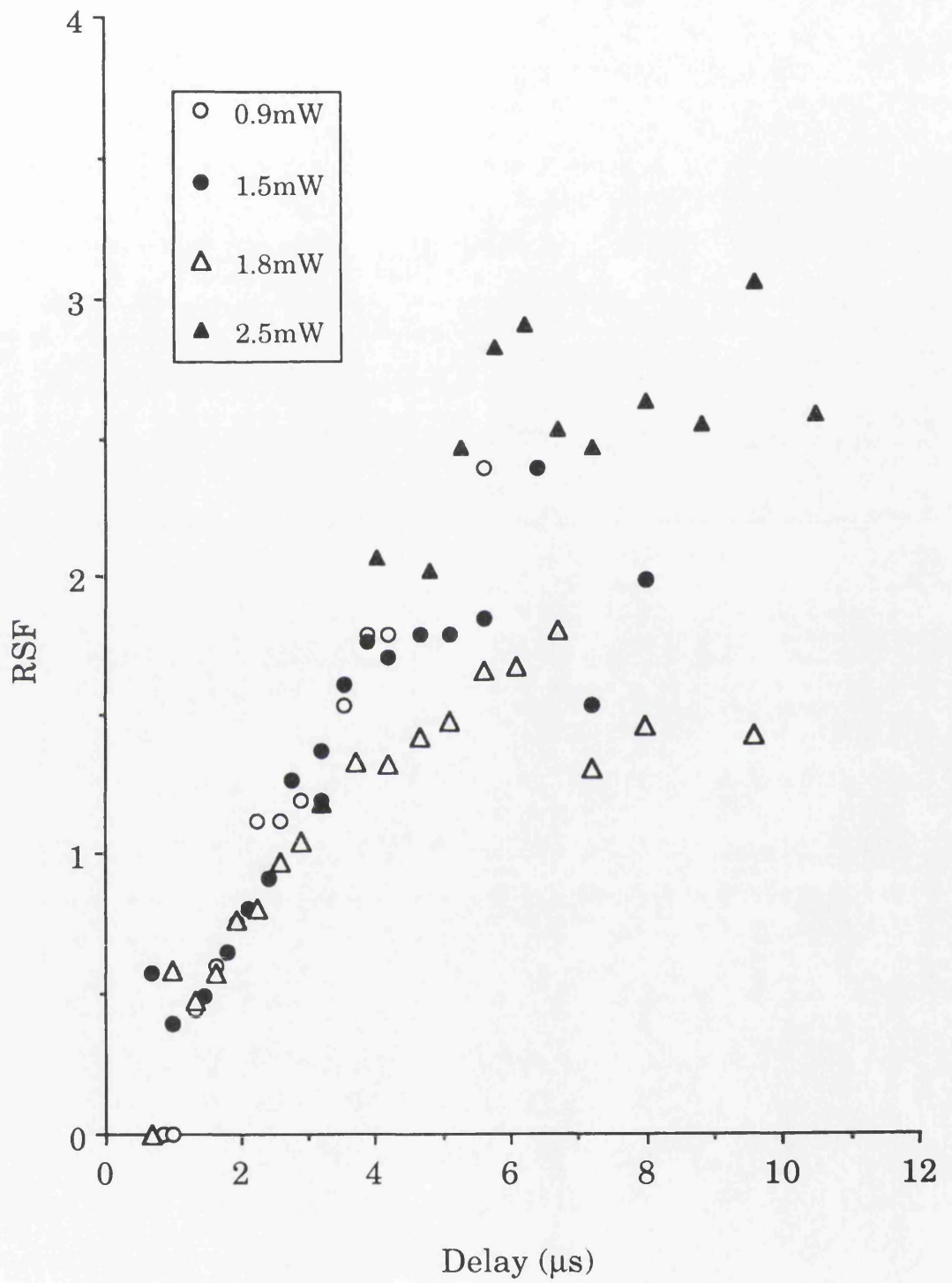


Fig.4.52 Temporal development of the relative sensitivity factor, RSF, for Mn from the NIST SRM 1263a sample, with an ablation laser wavelength of 355nm.

factor of two higher for the 532nm ablation laser wavelength than for the shorter wavelength. This arises from the slightly lower characteristic temperature of the Mn distribution acquired at the 355nm wavelength compared to the distribution obtained with the 532nm ablation laser wavelength. There is no physical mechanism apparent which would explain this behaviour.

To remove the dependence of the RSFs on the delay between the lasers, they were recalculated by integrating the temporal distributions. These RSFs are shown in Table.4.2. The results obtained with the 355nm ablation wavelength show less variation between the various laser powers. This was attributed to the same sample area being used for all of these measurements. These values are also closer to unity than those obtained with 532nm wavelength ablation, for which there is no obvious explanation. For both wavelengths, the RSFs for Mn, Ti and V are close to unity, whereas those for Cr appear to be consistently lower. As mentioned in §4.2.2, the power of the PAI laser was not as high as that normally used in non-resonant ionisation experiments and the ionisation cross-section may not be the same for all the elements. The proximity of an allowed transition to the 266nm photon energy, ΔE , is shown in Table 4.1. It is apparent that the possibility for enhancement of the two photon transition probability, from a proximate real state, would be lower for Cr than for the other elements in the sample. It is possible, therefore, that the small RSFs for Cr are due to biases in the ionisation process, rather than an effect at the atomisation stage. It would appear from Table 4.2 that the RSFs are not greatly dependent on the ablation laser power. Indeed at the highest powers the RSFs are further from unity than those obtained at lower powers. However, due to the high density of the laser produced plasma at the high powers it was only possible to detect PAI signals at long delay times, as is evident from Fig.4.41. Therefore, it was not possible to integrate over the full temporal distribution. This may be why the RSFs appear to be less close to unity than those obtained at lower powers, where integration over the full range of delay times is possible. As mentioned above, it can be seen from Fig.4.50 and Fig.4.52 that the RSFs at the highest powers are not essentially different to those obtained at lower powers. It would appear, therefore, that changing the ablation laser power does not significantly alter the plume composition, which agrees

Ablation Laser Wavelength	Power (mW)	RSF (Ti/ ⁵⁴ Fe)	RSF (V/ ⁵⁴ Fe)	RSF (Cr/ ⁵⁴ Fe)	RSF (Mn/ ⁵⁴ Fe)
532nm	1.7	6.38	1.93	0.25	2.03
	2.7	3.19	1.08	0.16	2.24
	4.2	3.44	2.08	0.17	1.42
	6.1		2.22	0.08	1.62
	8.0				1.74
355nm	0.9				1.11
	1.5		0.92	0.19	1.08
	1.8		0.93	0.20	1.01
	2.5				1.86

Table 4.2 Relative sensitivity factors determined for various elements during the analysis of NIST SRM 1263a.

with the results of Baldwin (1970), discussed earlier. However, increasing the laser power increases the amount of material in the plume, allowing detection of the less abundant elements with a better signal to noise ratio.

A similar study to the one described here was undertaken on an adapted LIMA system (Odom and Schueler, 1987). The sample was also a NIST low alloy steel standard; SRM 661. This standard was specially prepared with homogeneity to better than one micron for the calibration of techniques such as electron probe microanalysis. The ionising and ablation laser wavelengths were both 266nm. The power of the PAI laser was $5 \times 10^{10} \text{W/cm}^2$. The RSFs of several elements were obtained by integrating the temporal distribution in the same way as described above. These values are shown in Table 4.3. Only one ablation laser power was investigated. It is apparent that the RSFs reported by Odom and Schueler are further from unity than those obtained in this work. This is especially apparent for Ti, where this work determined an RSF an order of magnitude closer to unity than that found by Odom and Schueler. The Cr RSF obtained on the converted LIMA instrument was higher than unity, which may be due to the higher ionising laser power. The sample was also analysed in the normal LIMA mode of operation (using only the ablation laser), and the RSFs obtained by PAI are inferior to those determined by LIMA analysis for Si, Ti and Mn. However, the PAI enhanced the detection sensitivity for C, P and Ti.

§4.6 AlGaAs

To investigate the application of this technique to non-metals a semiconductor sample was studied. $\text{Al}_{0.3}\text{Ga}_{0.7}\text{As}$ was chosen for this work because the ablation of aluminium has been extensively studied. The sample was grown by molecular beam epitaxy (MBE) and had the form of a $1.3\mu\text{m}$ thick layer on top of a $500\mu\text{m}$ thick GaAs substrate. A typical mass spectrum, obtained with non-resonant ionisation, is shown in Fig.4.53. Peaks attributed to atomic aluminium and gallium are apparent in a ratio of 0.35/0.65, which is approximately the same as the composition of the sample. Atomic As and As_2 peaks are also apparent. Only the aluminium peak was apparent in the spectra obtained when the resonant ionisation scheme for aluminium was used with a similar ablation laser power, as shown in Fig.4.54. This illustrates the highly selective nature of

Element	PAI RSF ($X/^{56}\text{Fe}$)	LIMA RSF ($X/^{56}\text{Fe}$)
C	1782.0	
Al	44.2	151.0
Si	63.6	4.5
P	4.1	
Ti	61.9	7.2
Cr	3.4	4.3
Mn	5.2	4.0
Ni	0.96	0.6
Cu	20.1	30.7

Table 4.3 Relative sensitivity factors determined by Odom and Schueler (1987) for various elements during the analysis of a steel sample by both PAI and LIMA.

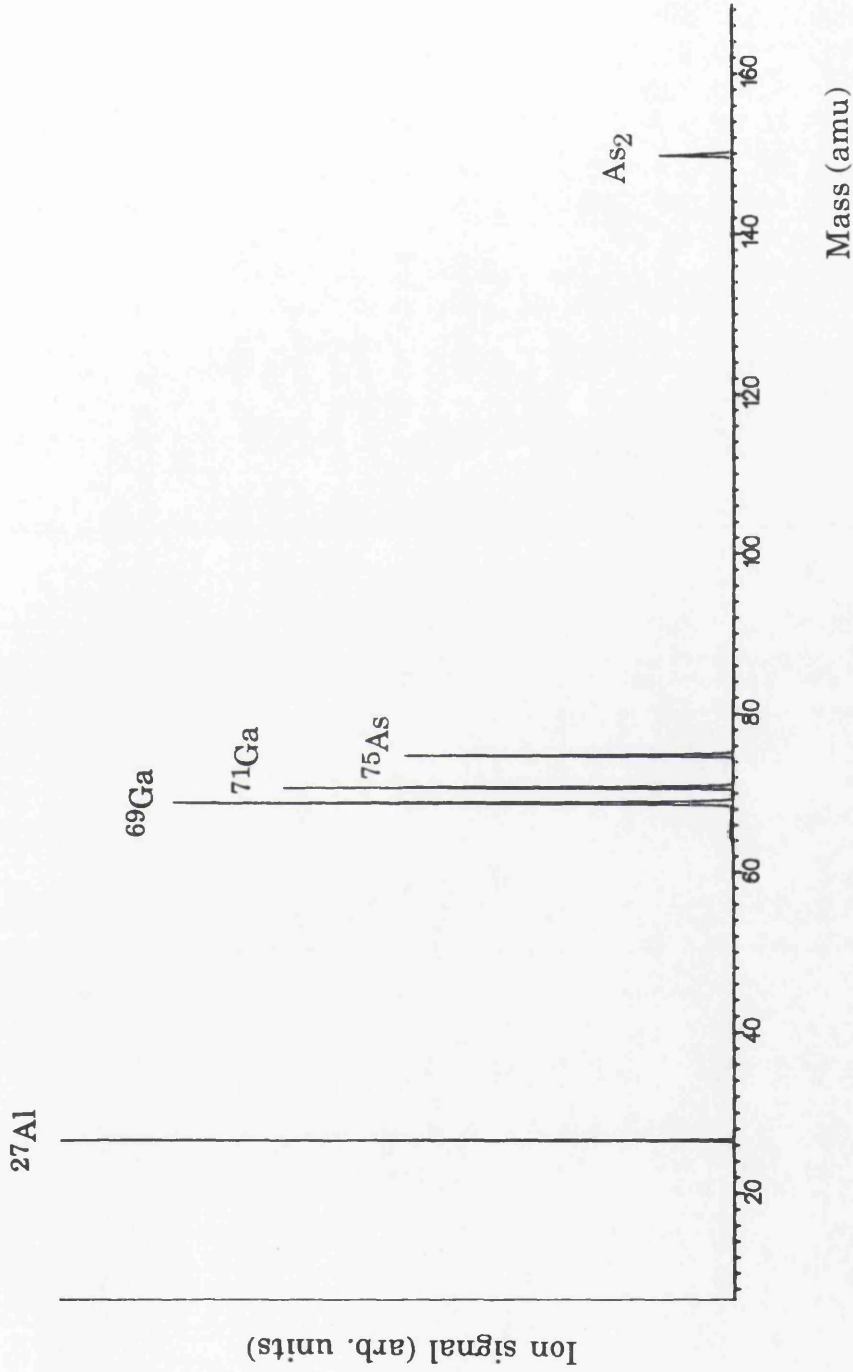


Fig.4.53 Section of the PAI mass spectrum produced by laser ablation of $\text{Al}_{0.3}\text{Ga}_{0.7}\text{As}$, with an ablation laser wavelength of 532nm. The PAI was non-resonant two-photon ionisation and the ablation laser power was ~1mW.

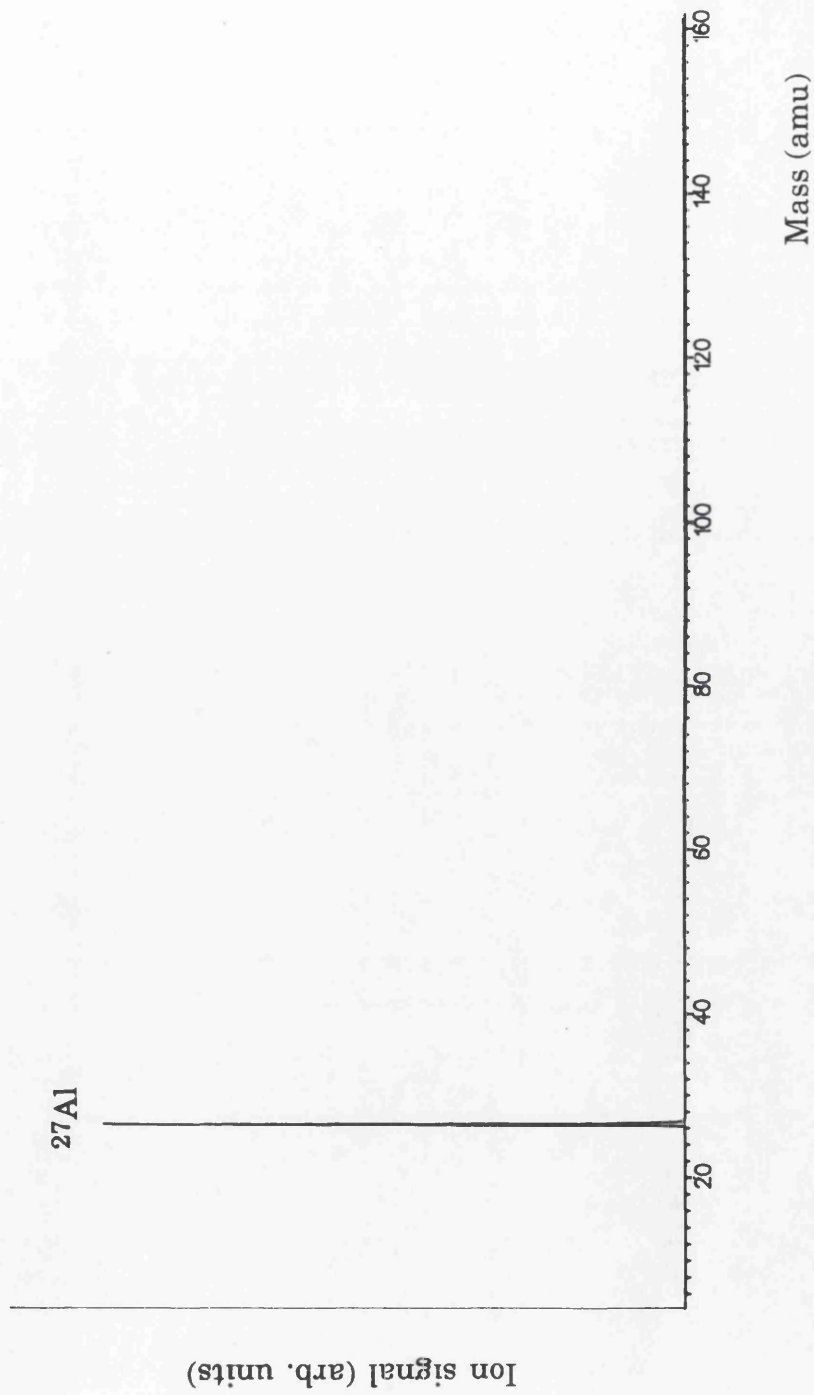


Fig.4.54 Section of the RIMS mass spectrum produced by laser ablation of $\text{Al}_{0.3}\text{Ga}_{0.7}\text{As}$, with an ablation laser wavelength of 532nm. The RIMS scheme shown in Fig.4.1 was used and the ablation laser power was ~1mW.

RIMS.

The temporal distributions obtained at various powers for the four different ablation laser wavelengths are shown in Fig.4.55. When the ablation laser wavelength was 532nm the PAI laser was resonant, while for the other ablation laser wavelengths non-resonant ionisation, using the fourth harmonic wavelength of the Nd:YAG laser, was employed. The bandgap of $\text{Al}_{0.3}\text{Ga}_{0.7}\text{As}$ is 693nm and that of GaAs is 873nm (Sze, 1985). The photon energy of the fundamental wavelength beam is therefore below the bandgap of both materials. However, it proved possible to obtain a temporal distribution with this ablation beam wavelength, this was believed to be due to absorption by exciton or impurity states, as detailed in §2.10.2.1. The distributions obtained with the ablation laser wavelength of 532nm are similar to those obtained for a pure aluminium sample, shown in Fig.4.4. However, the ablation laser powers required to obtain similar signal sizes are a factor of two lower. As the ablation laser wavelength is decreased the maximum magnitude of the PAI signal detected becomes lower. This was attributed to multiphoton ionisation by the ultraviolet photons causing the plasma density to increase more rapidly than would result from lower energy photons. A similar observation was made for the 266nm wavelength ablation of aluminium, as discussed in §4.2.3. This mechanism would appear feasible for $\text{Al}_{0.3}\text{Ga}_{0.7}\text{As}$ since the ionisation potential of Ga is the same as that of Al.

The temporal distributions obtained for the $\text{Al}_{0.3}\text{Ga}_{0.7}\text{As}$ sample are shown on a normalised scale in Fig.4.56. The Maxwell-Boltzmann model, detailed previously, gives a fit to the data with a characteristic temperature of 3000K. The fit appears least good for the 1064nm wavelength data, however, the stability of this data was poor, $R_{\text{stb}} \sim 40\%$. It would be expected that the tail would fit the experimental distribution better if the stability of the data was improved.

Since an aluminium atom in $\text{Al}_{0.3}\text{Ga}_{0.7}\text{As}$ is present as a substitutional replacement for a Ga atom, the sputtering mechanism is believed to be the same as that described for other ionic semiconductors in §2.10.2.2. Evidence for this is that the mass spectra shows evidence of dimers of As,

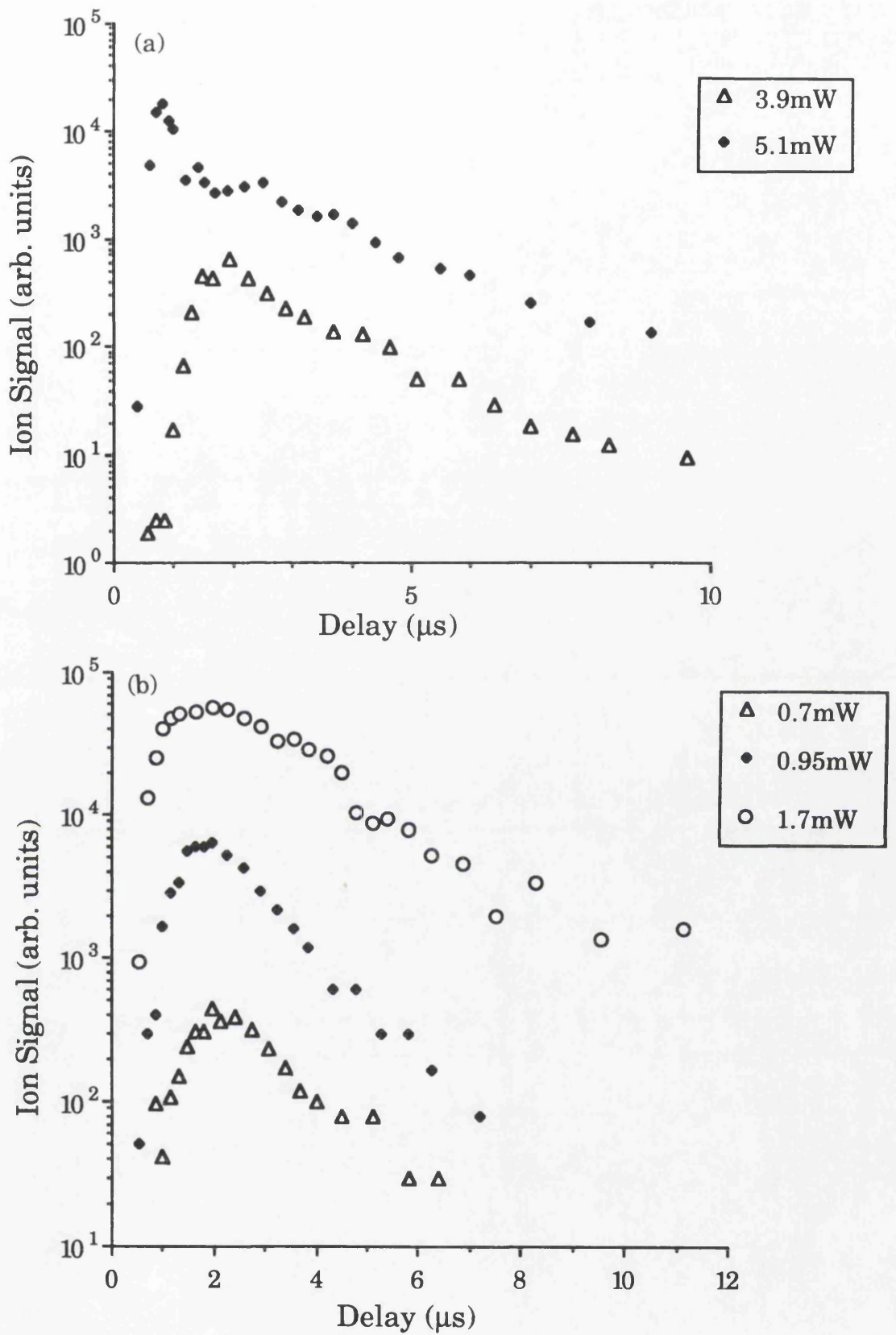
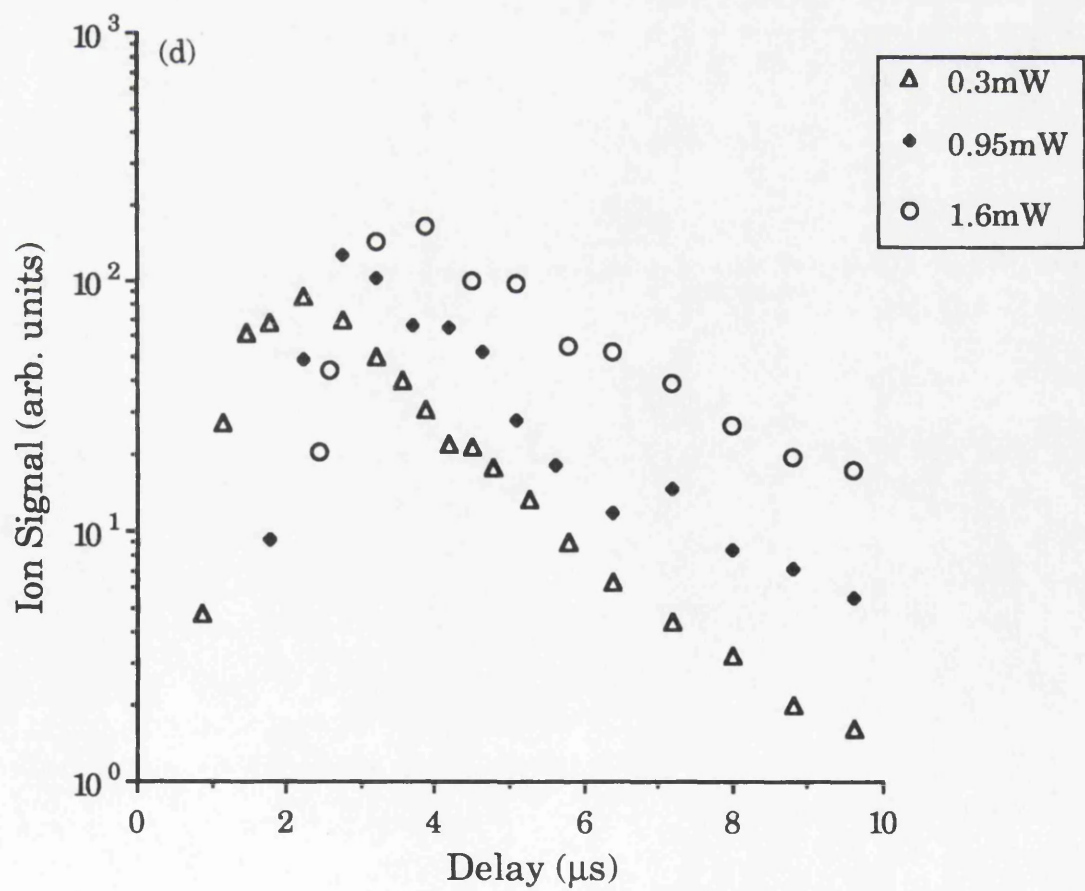
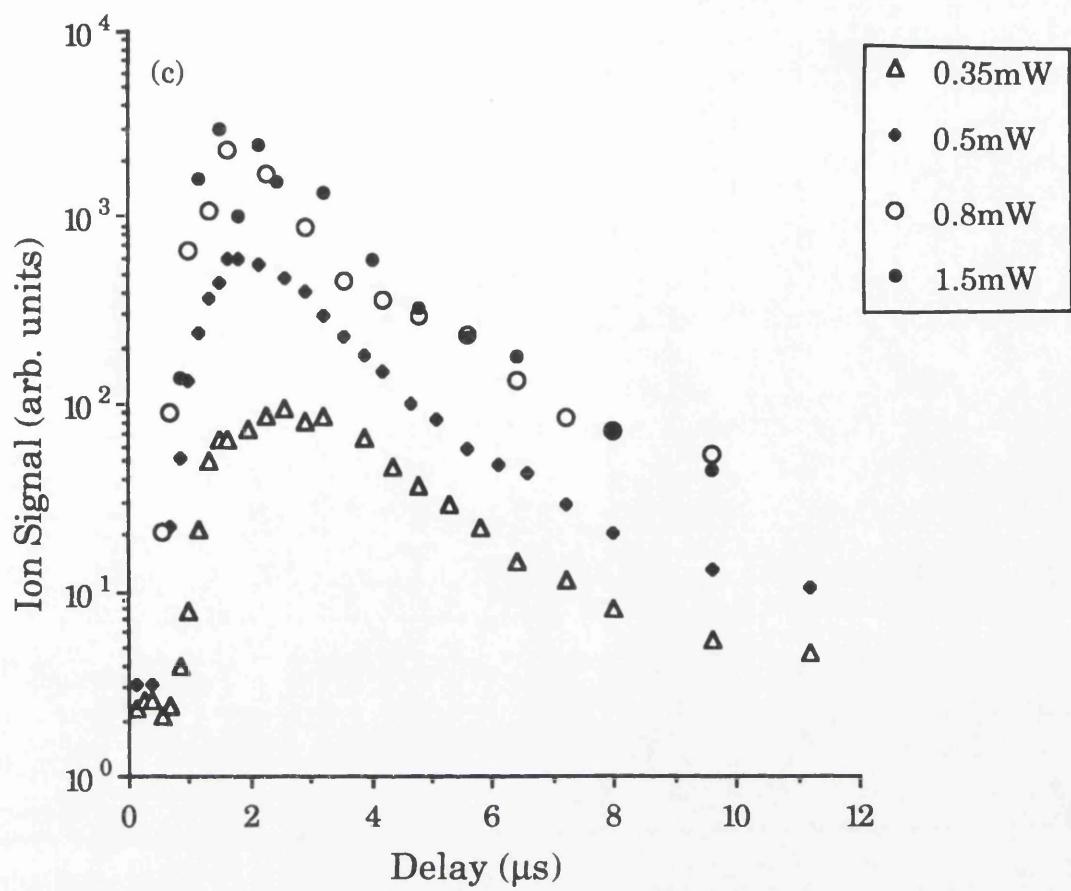


Fig.4.55 Variation of the PAI signal with increasing delay between the ablation and PAI laser, for various ablation laser wavelengths: (a) 1064nm, (b) 532nm (c) 355nm and (d) 266nm. The sample was $\text{Al}_{0.3}\text{Ga}_{0.7}\text{As}$.



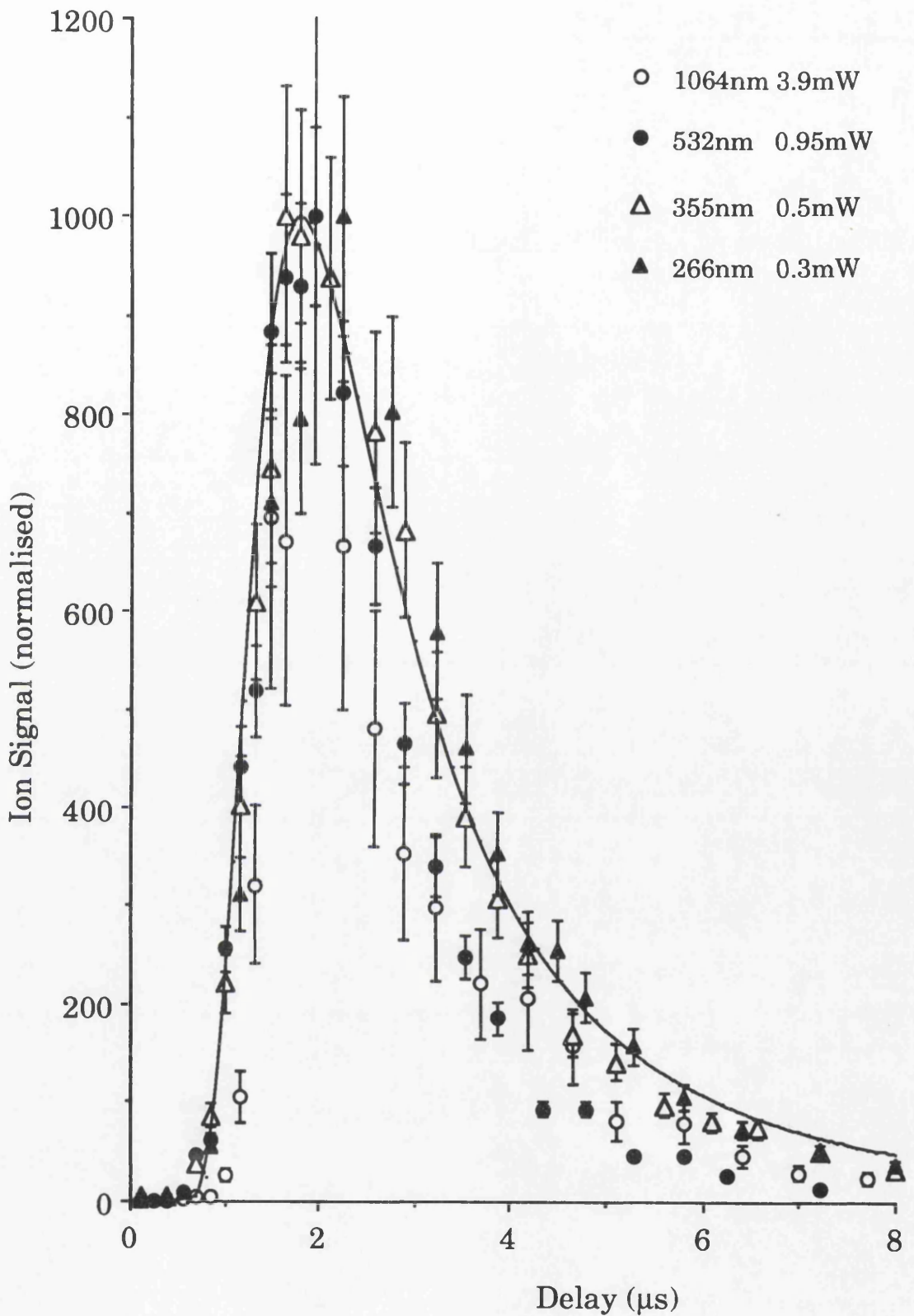


Fig.4.56 Temporal development of the PAI signal of Al ablated from a $\text{Al}_{0.3}\text{Ga}_{0.7}\text{As}$ sample, for several ablation laser wavelengths and powers. The data is fitted with a half-range Maxwell-Boltzmann distribution with a characteristic temperature of 3000K.

but not of Al or Ga, and the characteristic temperature obtained in this work is the same as that obtained for the sputtering of Ga from GaAs by medium power nitrogen laser pulses (Namiki *et al*, 1991). It is also significant that the distribution obtained using the 1064nm wavelength was not significantly different from that obtained at the other wavelengths. There is no evidence of the very low temperature component in the temporal distribution, which was described in §2.10.2.1.

§4.7 Sapphire

As discussed previously, the characteristic temperatures obtained from the application of the half-range Maxwell-Boltzmann model to the temporal distributions of laser ablated aluminium metal were higher than that obtained for other pure metals. These characteristic temperatures were also higher than those obtained for aluminium from $\text{Al}_{0.3}\text{Ga}_{0.7}\text{As}$ and low-alloy steel. It was also found that the existence of a considerable cluster contribution in the plume could be implied from the temporal distribution for aluminium metal. It was decided that an investigation of the laser ablation of Al_2O_3 would be profitable. The sample was a 0.5mm thick sapphire single crystal (Al_2O_3 99.9%) purchased from Goodfellow Metals (Cambridge, UK). Since this material is an insulator a coarse copper grid was mounted in front of the sample to maintain the electric fields in the extraction region. In all other respects the experimental arrangement was the same as in §4.2.2. It has been shown (Rothenberg and Kelly, 1984) that the 532nm wavelength sputtering of Al_2O_3 occurs mainly due to the detachment of macroscopic flakes of material. Ultra-violet wavelengths cause sputtering by electronic processes and result in detectable quantities of atoms and molecules, as detailed in §2.10.5. Therefore, the third harmonic of the Nd:YAG laser, 355nm wavelength, was used for ablation.

It proved to be very difficult to obtain stable and reproducible signals from the sapphire sample and the ablation laser powers required were considerable higher than those required for other materials. Three major species were detected: Al, AlO and AlO_2 . The temporal dependence of the aluminium signal is shown in Fig.4.57. Although the statistics of this data are poor, it would appear that a Maxwell-Boltzmann distribution with a characteristic temperature of 12000K fits the data reasonably.

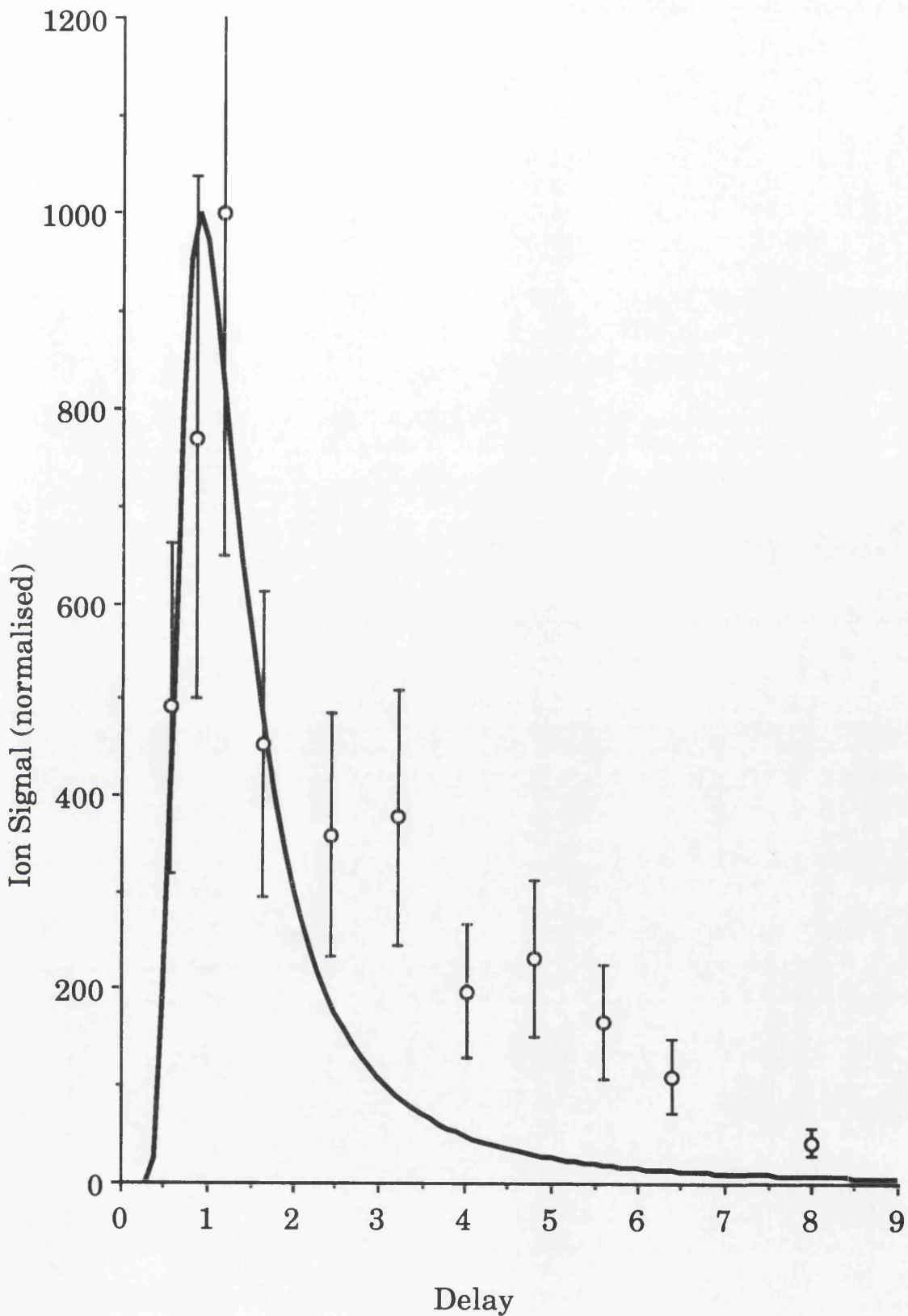


Fig.4.57 Temporal development of the PAI signal of Al ablated from a Al_2O_3 sample, for an ablation laser wavelengths of 355nm and a power of 3.2mW. The stability of the data is poor; $R_{\text{stb}} = 60\%$. The data is fitted with a half-range Maxwell-Boltzmann distribution with a characteristic temperature of 12000K.

Deviation from the model at longer delays can be attributed to the fragmentation of the large molecular species that would be expected to be present in the plume. The variation of the plume composition as the delay between the laser was varied is shown in Fig.4.58. The AlO₂ component accounts for 10% of the recorded species and shows less temporal variation than the AlO. However, the composition of the mass spectra would not be expected to represent the composition of the plume due to fragmentation induced by the PAI laser. Using LIFS Dreyfus and co-workers (1986a) showed that ablation by a laser of 248nm wavelength produced a plume with a ratio of AlO to Al of approximately unity. It could be tentatively proposed, therefore, that the PAI laser induced fragmentation is more significant for AlO than for AlO₂. The rather limited study reported in this section would suggest that the 355nm wavelength ablation of sapphire results in the emission of aluminium with a high kinetic energy, and several higher mass species.

§4.8 Stability of the PAI signal

During the course of this work it was suspected that the shot to shot stability of the PAI signal did not reflect the shot to shot stability of the ablation laser power. Therefore, an experiment was devised to assess how the stability of the PAI signal was related to that of the ablation laser. The manganese component of a stainless steel sample stub was analysed using resonant ionisation, with an ablation laser wavelength of 532nm. This is not a certified standard, and the homogeneity of the Mn concentration in the sample has not been verified. The ionisation scheme was resonant and will be detailed in §6.5. The process was saturated and therefore it would be expected that any instability in the PAI signal would be due to variation of the neutral yield. The stability of five hundred ablation laser shots was assessed by digitising the Molectron Joulemeter signal and using the PLOT5 software to record a histogram of this signal. This is shown in Fig.4.59 and reflects a peak power of 3mW with a standard deviation of 5.3%. A software gate was then used so that the PAI signal was only recorded when the Molectron signal was within a specified window. For example, a window of 2 would ensure that the laser power resulting in the recorded PAI signal was constant to within 0.25%. This is higher than the shot to shot stability of most commercial laser systems. Using this arrangement to stabilise the laser power 25 single

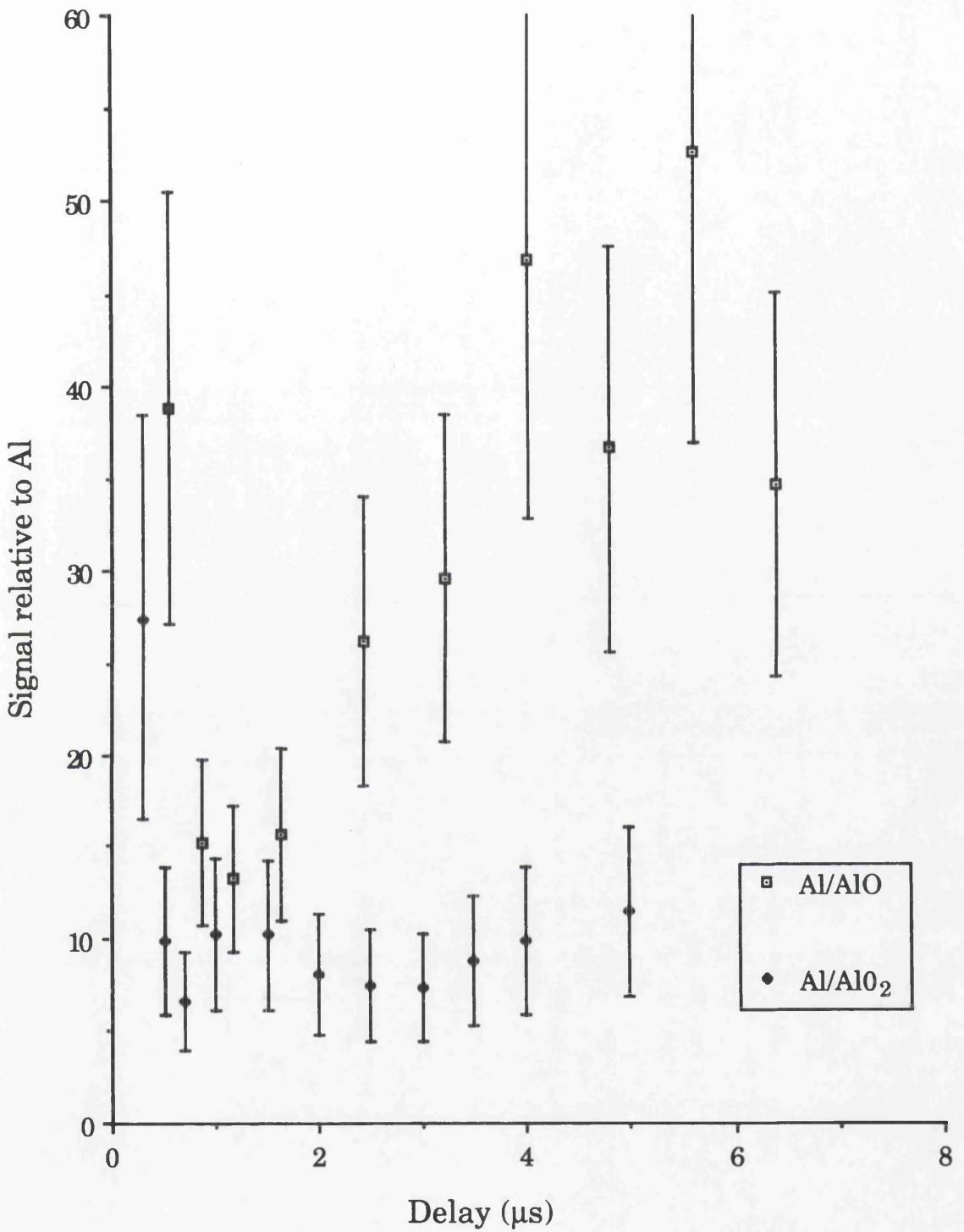


Fig.4.58 Temporal development of the PAI signals for AlO and AlO₂ relative to Al. The sample is Al₂O₃ and the ablation laser wavelength is 355nm. The power is 3.2mW.

shot PAI spectra were acquired consecutively. This involved repeated irradiation of the sample surface. For the 0.25% window discussed above, acquiring these 25 spectra involved irradiating the surface with ~5000 laser pulses. The standard deviation of the 25 PAI signals corresponding to various gates on the ablation laser power is shown in Fig.4.60. The standard deviation does not appear to be a function of the stability of the ablation laser power. This can be interpreted in two ways. It could be that the vapourisation rate of Mn from the stainless steel stub is less reproducible than the laser pulse power and hence the sample surface temperature. This could be due to variation of the composition of the molten surface layer. Conversely the localised heating of the sample may not reflect the stability of the incident laser beam. This could be due to changes in the distribution of the energy in the beam, due to processes such as thermal lensing in the laser rods. Therefore, it would appear that the statistics of PAI signals from laser ablated neutrals cannot be attributed simply to the stability of the incident laser beam. This is a factor which may limit the applicability of this technique compared to more stable techniques, such as ion sputtering.

§4.9 Stage current

In this work it was not possible to quantify the number of atoms removed from the sample by integrating the recorded ion signal because the gain of the detector and the transmission of the system were not accurately known. A method for overcoming this problem has been developed for LAMMS analysis (Hutt *et al*, 1989). This involves measuring the current flowing through the sample stage during and after the laser pulse. This signal is called the stage current, and can be interpreted as the number of singly charged positive LAMMS ions leaving the sample. If the detector is well characterised it is possible to calibrate the transmission of the system since the number of ions produced at the sample is known.

The circuit developed for measuring the stage current is shown in Fig.4.61. A LeCroy 9410 digital oscilloscope was used to sum and integrate the current developed across the 200 Ω resistor. The 4.7M Ω resistor ensures that the stage current pulse is not transmitted through to the high voltage supply. The supply is isolated from the oscilloscope by the capacitor. A typical oscilloscope trace of the averaged stage current

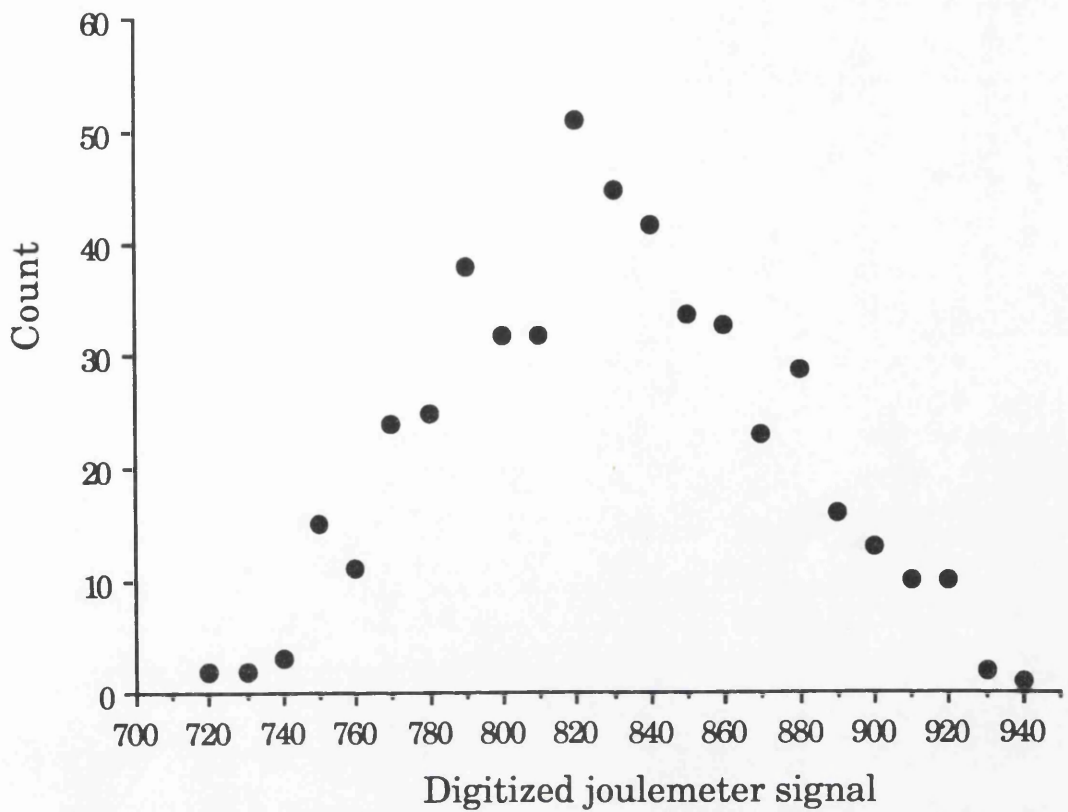


Fig.4.59 Histogram of the digitised laser energy measured each shot by the Molectron joulemeter. The power recorded by the thermopile meter was 3mW, and the laser wavelength was 532nm.

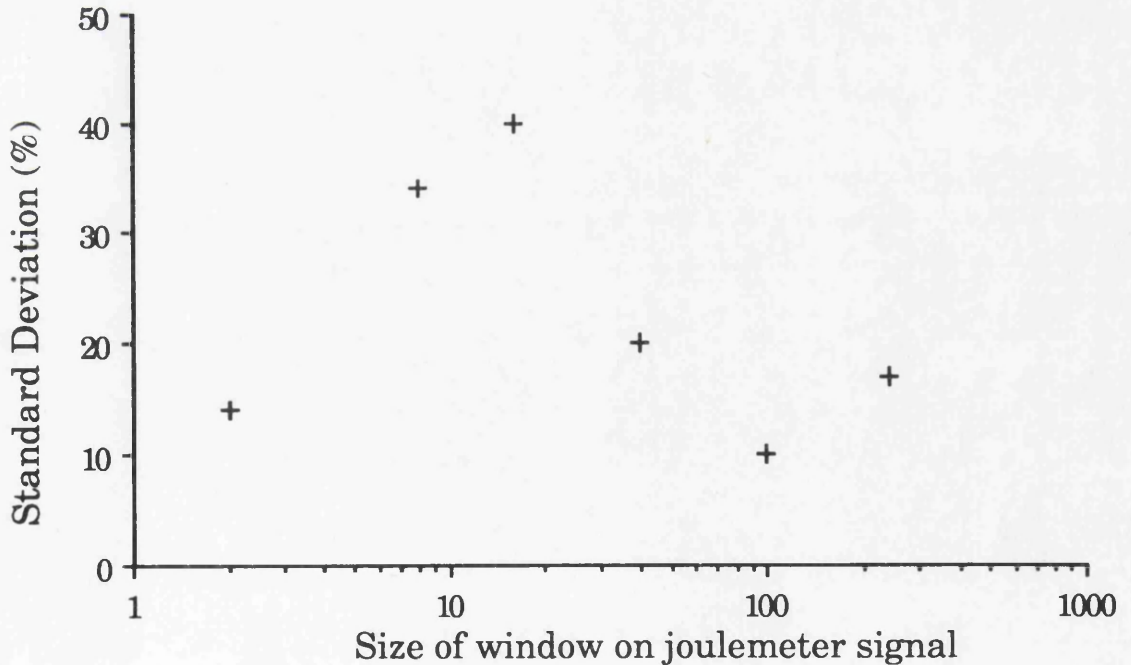


Fig.4.60 Standard deviation of 25 single shot RIMS peaks for Mn, against the size of the acceptance window on the ablation laser energy (in the units of digitised signal in Fig.4.59).

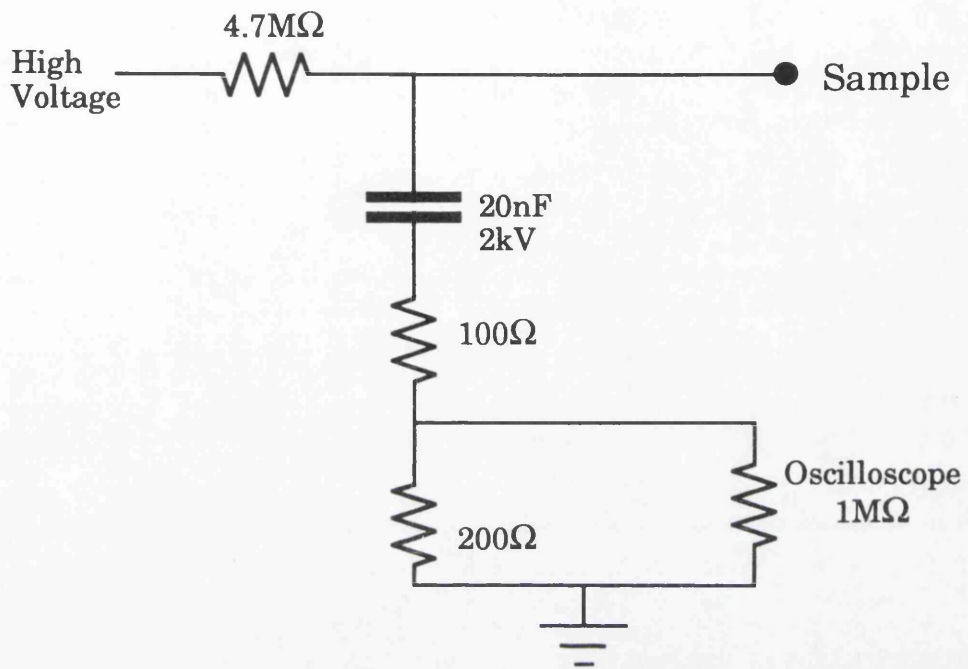


Fig.4.61 Circuit developed for measuring the stage current due to the ions created by the ablation laser

obtained during the RIMS analysis of aluminium is shown in Fig.4.62. The ablation laser power was 3.4mW and the arrangement was the same as that which resulted in the temporal distribution shown in Fig.4.3(d). Two peaks are observed in the stage current signal, the first was induced by the ablation laser produced ions and the second was the result of the ions produced by the PAI laser. The stage current can be related to the number of laser produced ions, N_{stg} , by:

$$N_{stg} = \frac{1}{eR} \int_0^{\infty} V dt \quad - \text{Eqn.4.3}$$

where R is the resistance over which the voltage, V, is developed. The number of ions produced by the ablation laser was determined to be $(8.5 \pm 1.4) \times 10^7$ per shot. The fraction of ions in a laser produced plume has been experimentally evaluated as 10^{-5} to 10^{-3} (Fürstenau, 1981). This would result in the number of atoms removed per pulse being $\sim 10^{11}$ to 10^{13} , which would correspond to ~ 0.5 -50 monolayers per shot, assuming the crater size shown in Fig.4.22(b). This is somewhat higher than the sub-monolayer removal rate predicted by ionising the atoms liberated from the surface by ion sputtering (§6.4). However, this was deemed acceptable since the development of stage current analysis on this system is of a preliminary nature and the actual degree of ionisation in the plume is not known.

The stage current signal attributed to the PAI signal was an order of magnitude smaller than that caused by the ablation laser. Also the temporal distribution of the stage current signal resulting from the PAI ions was markedly different to that obtained by monitoring the mass analysed ions. It was therefore concluded that the stage current signal induced by the PAI laser was not an accurate representation of the number of PAI ions. This was not unexpected since the PAI ions are formed in the middle of the extraction volume and so the electrons liberated by the laser ionisation would contribute significantly to the induced current. This electron current may have a subnanosecond duration (Hutt *et al*, 1989). Also, the PAI ion packet would be expected to have a faster rise-time than the ablation laser produced ions. It is highly conceivable that the detection circuit cannot respond to the fast transient the PAI ion induced stage current would represent. This problem not

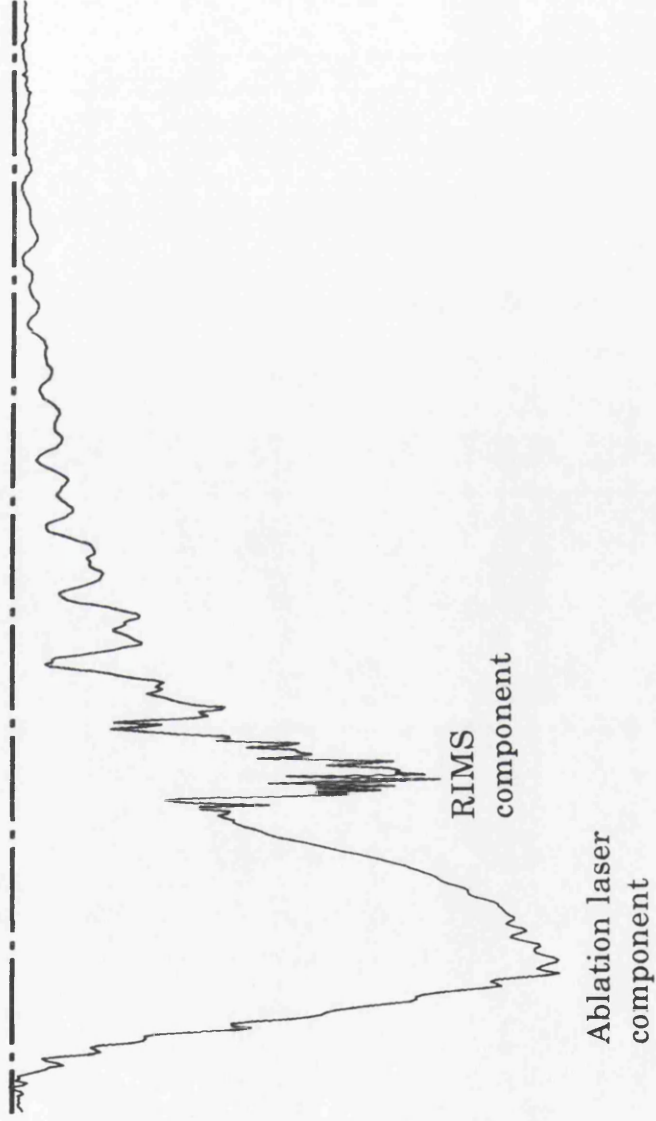


Fig.4.62 Signal induced by the laser produced ions, monitored by the circuit shown in Fig.4.61, and averaged on a LeCroy 9410 oscilloscope. The peak signal is 100mV and the total length of the trace is 5 μ s. The sample was aluminium, the ablation laser power was 3.4mW and the wavelength was 532nm.

withstanding, this work indicated that the stage current technique is a relatively simple method for quantitative monitoring of the ablation process.

§4.10 Methods for eliminating interference from ions created by the ablation laser

The ablation laser causes the formation of both neutral atoms and ions, as has been discussed in §4.2.2. In this work the reflectron energy filter suppressed the transmission of these ions very efficiently at low ablation laser powers. However, as the laser power is increased a significant fraction of these ions are transmitted through the reflectron and form an unwanted interference to the RIMS signal. Several techniques for reducing this interference have been investigated and are discussed in this section.

§4.10.1 Pulsing the deflector plates

The basic principle of this technique is very straightforward (Krönert et al, 1987). A voltage is applied to the plates behind the ion optics, which deflects the ions produced by the ablation laser from the transmission axis of the spectrometer. This voltage is then removed to allow the PAI ions to be transmitted. The technique works because the two ion packets are produced at separate times, which depends on the delay between the lasers. The flight time of ions through ion optics to the deflector plates were calculated using the ion trajectory simulation program SIMION3, (Dahl and Delmore, 1987), and are shown in Fig.4.63. The flight time of the PAI ions, assumed to be generated 1 μ s later, is also shown. To transmit only the PAI signal requires that the voltage is removed from the plates between the two ion packets arriving at the deflector plates. If the sample is a single element this time is essentially the delay between the lasers. Therefore, the voltage must be removed from the plates in microseconds. Accordingly a high voltage pulse generator was required. Using a D.C high voltage supply it was found that a voltage of 500V across the deflector plates was sufficient to inhibit the ablation laser produced ion signal. The specification for a high voltage pulse generator was a >500V stable peak height, a \sim 5 μ s duration and a sharp falling edge. A device with these characteristics was designed and built in the Department of Physics and Astronomy, and the output is shown in Fig.4.64.

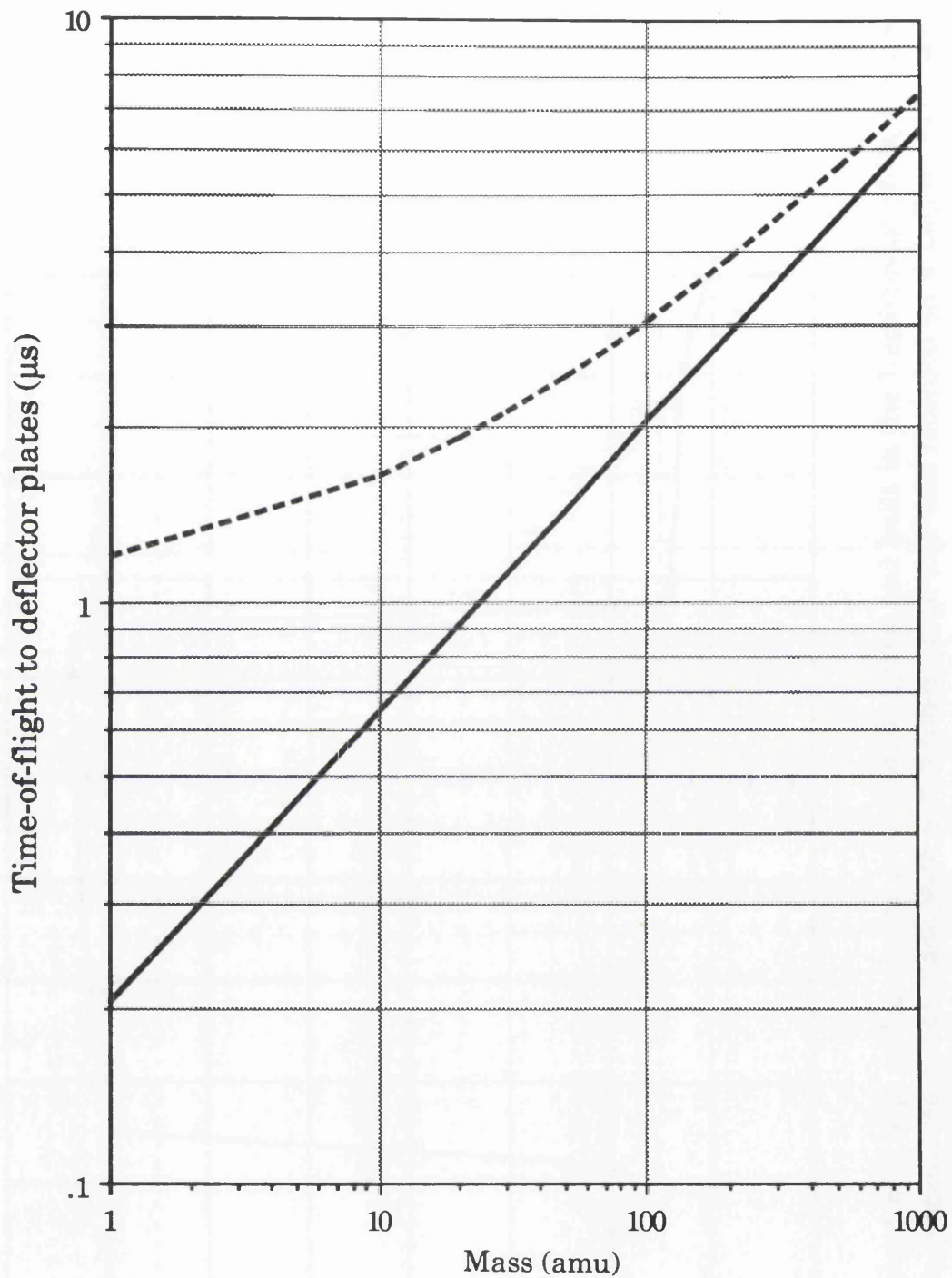


Fig.4.63 Time-of-flight, for ions of various masses, from the sample surface to the deflector plates, calculated using the ion trajectory simulation program SIMION3. The sample voltage is 2kV. The solid line represents LAMMS ions and the broken line PAI ions, assumed to be generated 1 μ s later.

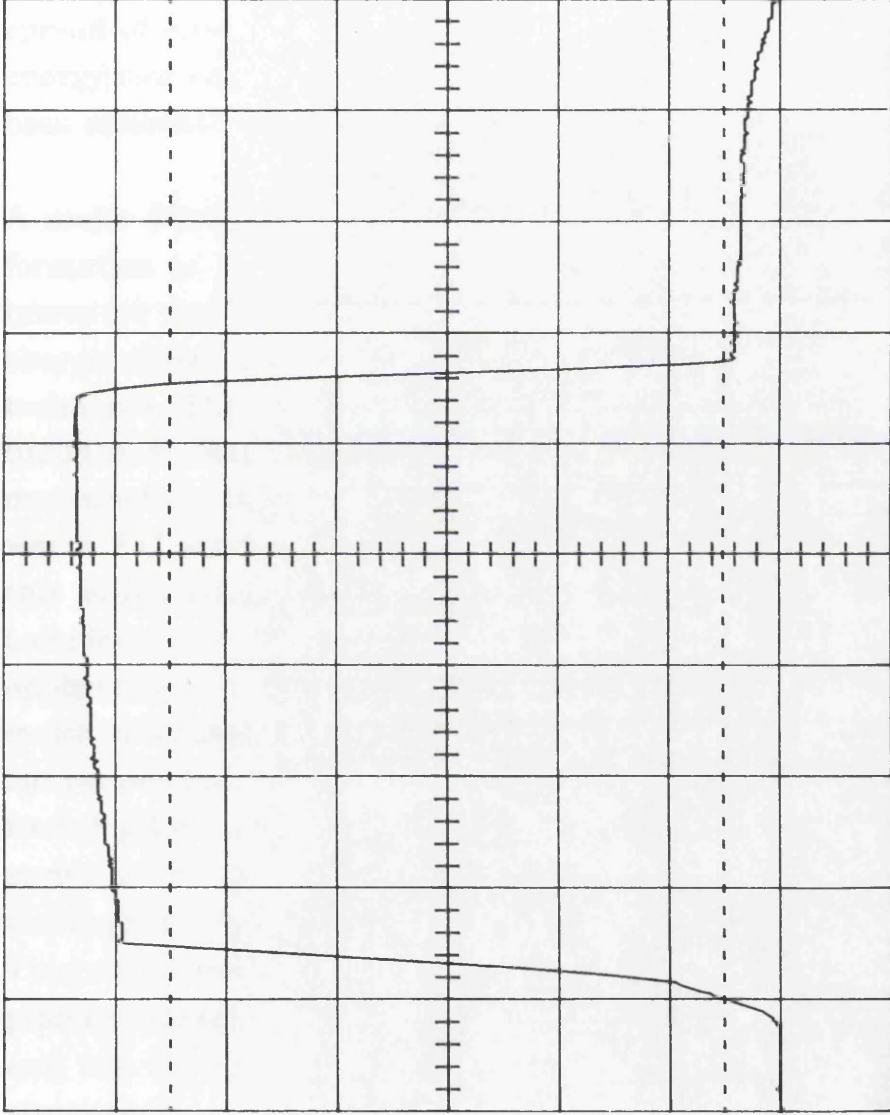


Fig.4.64 Output of a high voltage pulse generator, designed and built in the Department of Physics and Astronomy. The measurement was made with a 100 times probe and was recorded on a LeCroy 9410 oscilloscope. The peak height is 600V and the pulse duration is 5 μ s.

The application of this technique to eliminate the leakage signal interference from the spectrum obtained with a pure aluminium sample is shown in Fig.4.65. The leakage signal is completely removed, however, this required that the delay between the lasers was set to $\sim 3\mu\text{s}$. As can be seen from Fig.4.3 this does not correspond to the maxima of the temporal distribution. This technique does not stop all the ablation laser induced signal from being transmitted to the detector, as can be seen in Fig.4.65(c). This tail occurs because the ions created by the ablation laser have a large spread of energies, due to space charge effects, and some of the lower energy ions arrive at the deflector plates after the high voltage pulse has been removed.

A major limitation of this technique is that it does not prevent the formation of a plasma in front of the sample. If the laser power is increased much beyond the powers used previously in this work space charge effects in the plasma prevent the successful application of this technique. This is illustrated in Fig.4.66, where the ion signal as a function of the time of removal of the voltage on the plates has been measured for three laser powers. The lower power corresponds to that where PAI signals can be detected above the leakage signal background, this is not possible at the higher powers. A second limitation of this technique, even at relatively low ablation laser powers, is the difficulty of application to samples where the element of interest is lighter than the major constituent of the sample. This is because the delay between the two ion packets arriving at the deflector plates can be negligible. For example, from Fig.4.63, ablation laser produced ions with a mass of 100amu would arrive at the plates after the PAI ions of 10amu. In order to use this technique the delay between the lasers would have to be increased, to $\sim 2\mu\text{s}$. This would have the detrimental effect of reducing the fraction of the plume analysed. However, this technique is still relatively straightforward and can be very successfully applied to a somewhat limited range of situations.

§4.10.2 Pulsed extraction voltages.

In an effort to develop a technique that would allow data to be taken at powers higher than those studied previously the feasibility of pulsing the

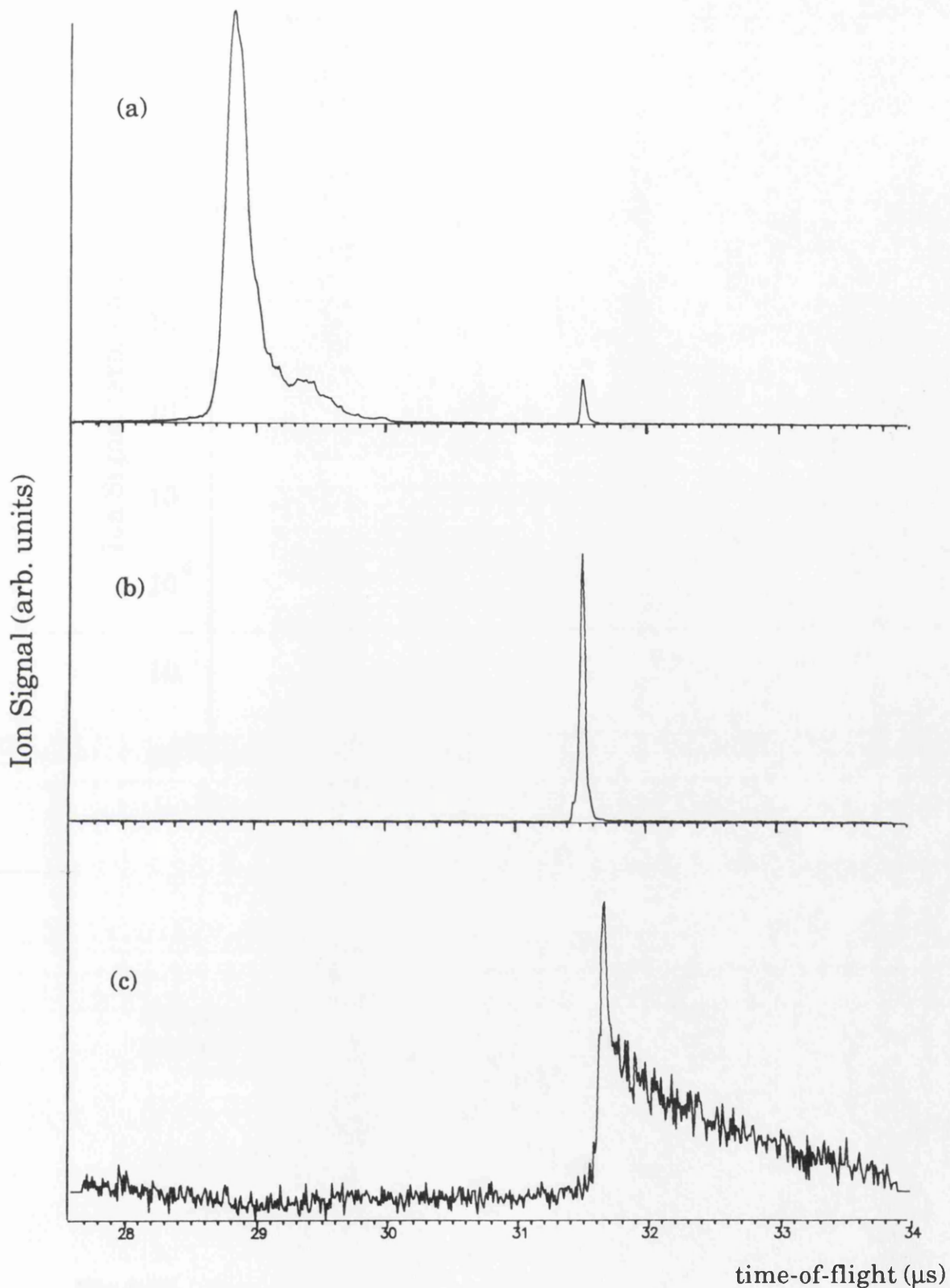


Fig.4.65 Demonstration of background removal achieved by pulsing the deflector plates: (a) no pulse; leakage signal and PAI signal apparent, (b) pulse applied to plates; only PAI signal obvious, (c) leakage signal transmitted with the pulse applied (magnification 64x greater than for the other spectra). The sample was aluminium and the ablation laser wavelength was 532nm.

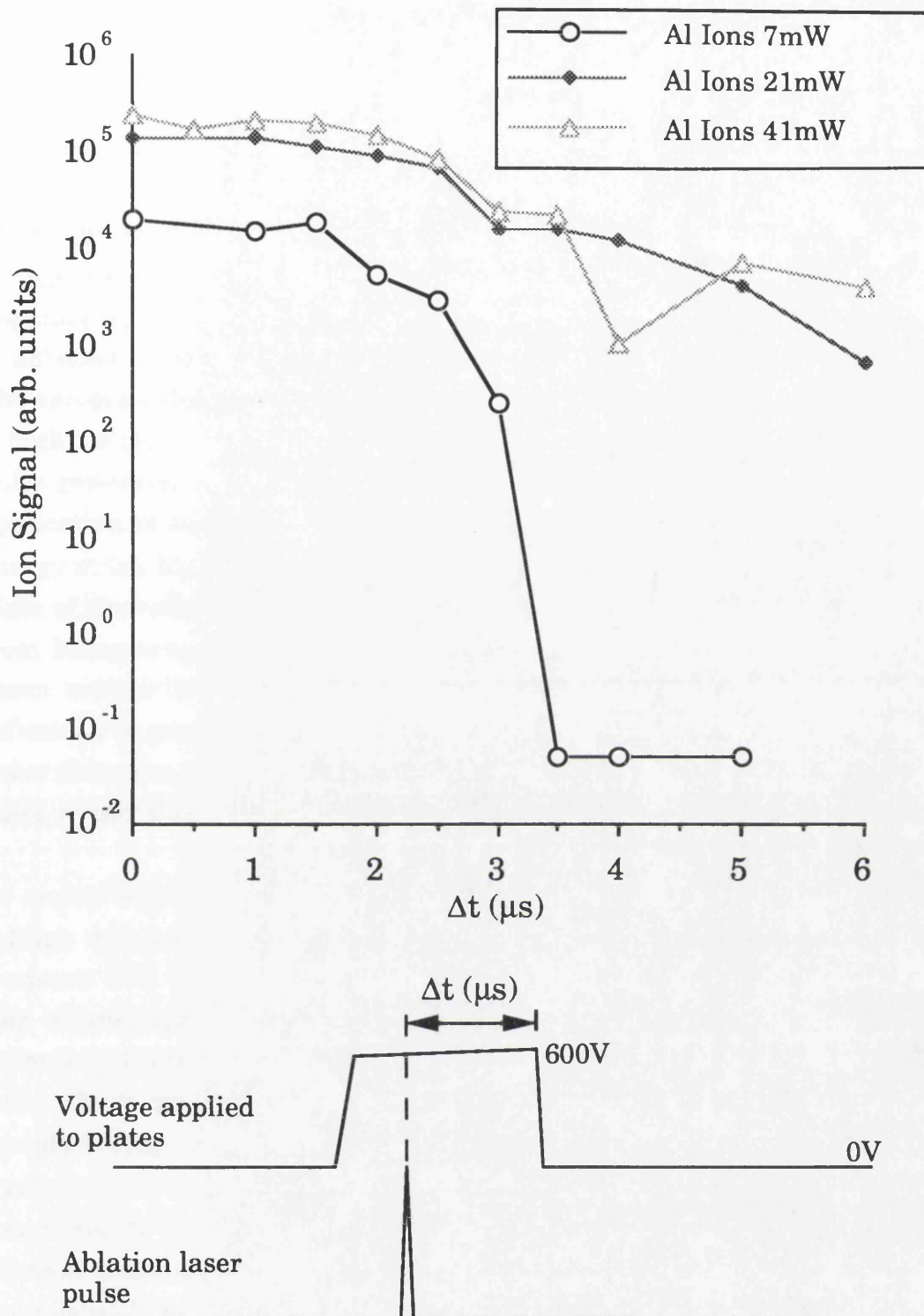


Fig.4.66 Demonstration of the effect of changing the delay, Δt , between the ablation laser pulse and the removal of the high voltage from the deflector plates, for various laser powers. A PAI signal could be detected at 7mW, but not at the higher powers. The sample was aluminium and the ablation laser wavelength was 532nm.

extraction field was studied. Two possible methods were considered. The simplest involved using the high voltage pulse generator, developed for the pulsing of the deflector plates described above, to pulse only the sample stub. This could be achieved by holding the sample stub either below or above the normal voltage during the ablation laser pulse. If the stub voltage was reduced, the stub and the first optic would be at approximately the same voltage. This would be expected to reduce drastically the fraction of ablation laser produced ions being transmitted from the source region. The sample voltage could then be returned to normal by the application of a high voltage pulse, to allow the transmission of the PAI signal. The pulse generator could also be used to increase the stub voltage during the application of the ablation laser pulse. The ions produced would have an energy much higher than normal and would be transmitted to the earthed plate of the reflectron. This would not prevent ablation laser produced ions from being transmitted from the source region, but by increasing their mean energy it would ensure that any ions transmitted through the reflectron to generate a leakage signal would have to have energies $\sim 1\text{keV}$ lower than the mean. The removal of this voltage prior to the second laser pulse would allow the PAI ions to be transmitted unaffected.

To assess which of these arrangements was most applicable, the sample voltage was varied from 0 to 2400V, while the system was optimised to transmit PAI ions created with a sample voltage of 2000V. The sample was aluminium and the result of changing the stub voltage for two different ablation laser powers is shown in Fig.4.67. At the lower laser power the large increase in the signal at $\sim 1800\text{V}$ is expected, as this is the sample voltage for which the transmission through the reflectron of ions created at the sample surface is optimised. As the voltage is increased the mean energy of the ablation laser created ion packet becomes too high for efficient transmission through the reflectron to the detector and the signal decreases. It is more surprising to find that when the sample voltage is reduced to zero a significant signal is recorded. This is not a well defined single peak, but is a broad signal with a duration of several microseconds. For positive ions to be transmitted they would have to overcome a potential of $\sim 200\text{V/mm}$ in the extraction region. It is also possible that this signal could be the result of negative ions, or electrons, which would be accelerated causing the sputtering of atoms from the first ion optic. It

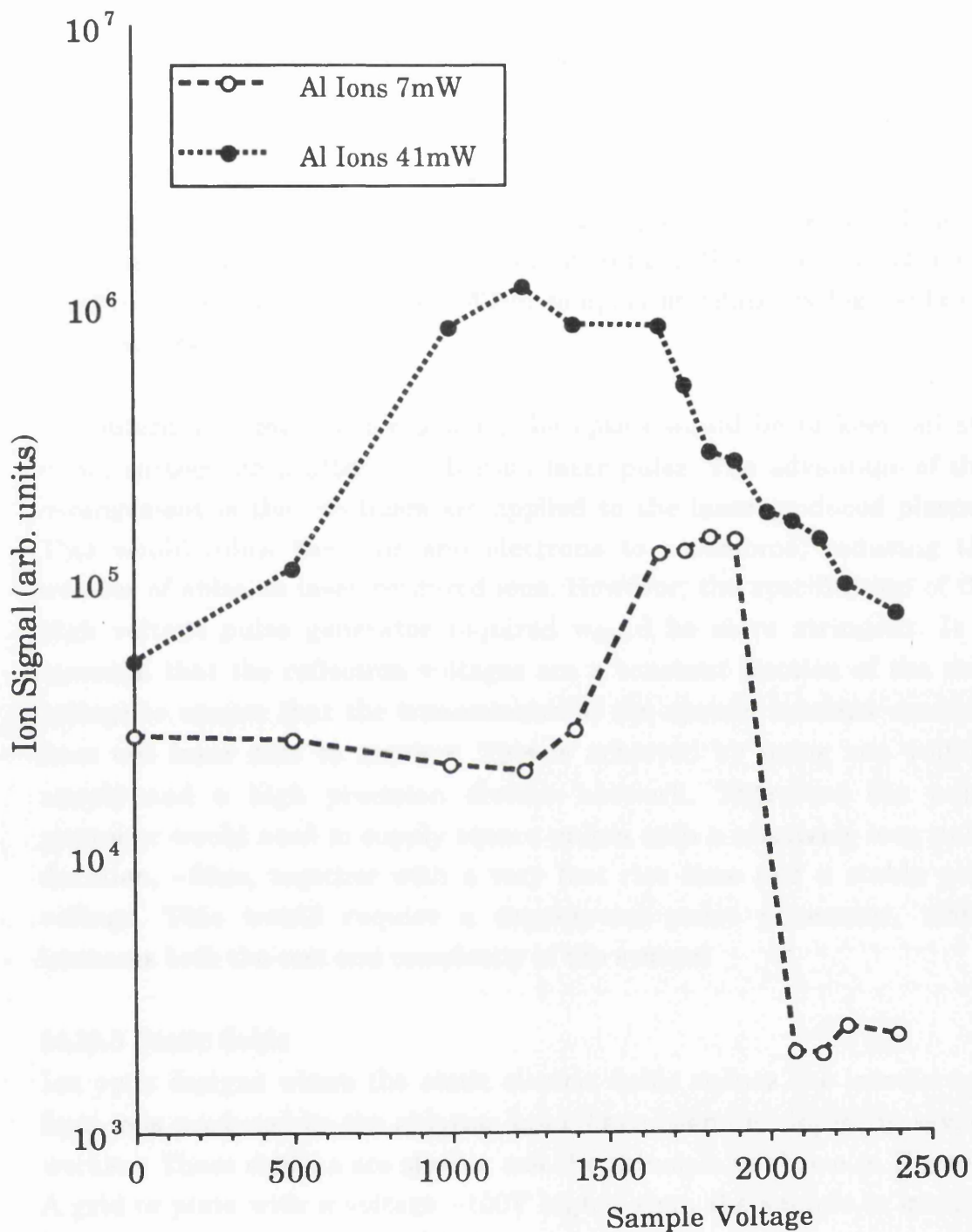


Fig.4.67 Demonstration of the effect of changing the voltages on the sample stub from on the detected ion signal. The system was set-up to transmit ions produced 3mm from the stub when the sample voltage was 2000V. A PAI signal could be detected at 7mW, but not at the higher power. The sample was aluminium and the ablation laser wavelength was 532nm.

would appear, therefore, that the best arrangement would be to pulse the stub to $\sim 2600\text{V}$ for the duration of the ablation laser pulse, and then fire the PAI lasers after the voltage pulse has decayed.

At the higher ablation laser power the average energy of the ions appears to be lower. The signal does not decrease as rapidly as the stub voltage is increased above 2000V . Hence, it would appear that the arrangement described above would be more difficult to apply at relatively high ablation laser powers.

The alternative method for pulsing the optics would be to keep all the optics earthed until after the ablation laser pulse. The advantage of this arrangement is that no fields are applied to the laser produced plasma. This would allow the ions and electrons to recombine, reducing the number of ablation laser produced ions. However, the specification of the high voltage pulse generator required would be more stringent. It is essential that the reflectron voltages are a constant fraction of the stub voltage to ensure that the transmission of the system remains constant from one laser shot to another. This is achieved by using one voltage supply and a high precision divider network. Therefore the pulse generator would need to supply square pulses with a relatively long pulse duration, $\sim 50\mu\text{s}$, together with a very fast rise time and a stable peak voltage. This would require a commercial pulse generator, which increases both the cost and complexity of the system.

§4.10.3 Static fields

Ion optic designs where the static electric fields reduce the interference from ions produced by the ablation laser have been developed by several workers. These designs are similar and the principle is shown in Fig.4.68. A grid or plate with a voltage $\sim 100\text{V}$ higher than the sample is inserted between the sample and the PAI laser region. In the simplest case, where the density of the laser produced plasma is not high enough for space charge shielding to be considered, ions formed at the sample surface will not be transmitted because of the potential gradient. This technique has been used in RIMS studies of exotic heavy isotopes, to eliminate interference from the graphite substrate (Crawford, 1992). The field

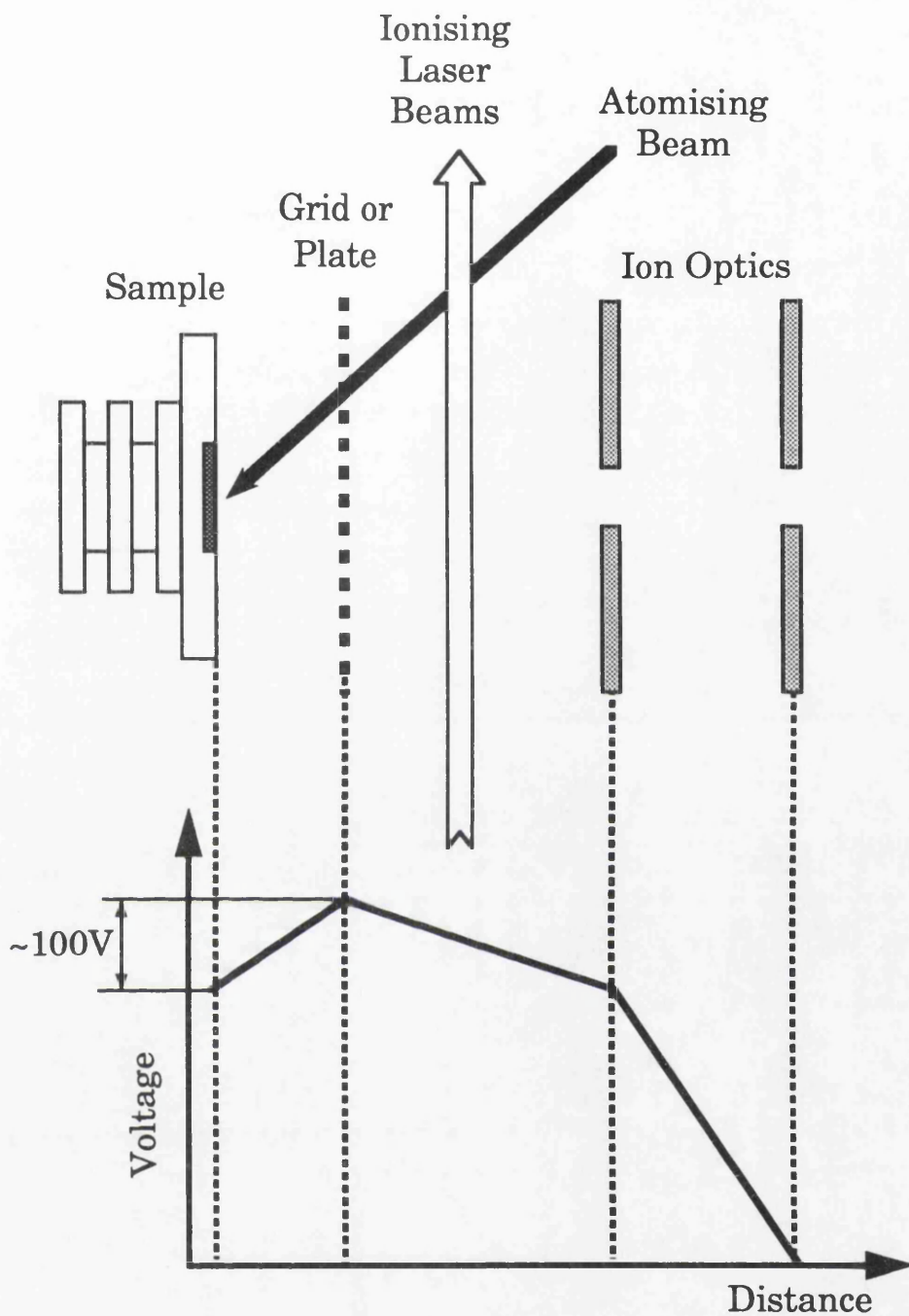


Fig.4.68 Schematic diagram of the static field arrangement used by some researchers to alleviate background resulting from ions created by the ablation laser.

gradient is 100V/cm and is applied between the sample and an apertured electrode. A similar technique, using a grid to introduce the potential gradient was used in RIMS studies of $\text{YBa}_2\text{Cu}_3\text{O}_{7-x}$ (Estler and Nogar, 1991). However, the mass spectrometers used in these both of these studies are of the linear time-of-flight design and so if this technique was not employed the PAI and LAMMS signals would not be separated. This technique was not employed in the studies reported in this chapter because, as shown in Fig.4.67, a voltage gradient of $>2\text{kV/cm}$ did not eliminate the ablation laser produced ion signal. Indeed, this static field arrangement has been incorporated in the ion optics of a recently developed system for performing LAMMS analysis (Duckworth *et al*, 1992). In this work a repulsive field gradient of $\sim 300\text{V/cm}$ was provided by a movable grid in front of the sample. When the grid was not used it was found that the maximum laser power density at the sample surface was restricted by the occurrence of flashovers to the flight tube. This was attributed to the high charge density between the flight tube and the sample. The Debye length of the plasma was calculated and it was asserted that the ions were probably shielded from the grid voltage.

It would appear that this technique is not appropriate for the removal of ions generated by dense laser produced plasmas. A further problem with this technique is that it would involve incorporating a grid or plate close to the sample surface. This would raise the possibility that some of the material liberated would be deposited on the plate or grid. This material could be resputtered by the plasma created by subsequent pulses and this would represent an unacceptable interference for quantitative trace analysis.

§4.11 Conclusions

The application of laser ablation to the atomisation of a number of materials has been detailed. These have included pure metals (aluminium, gold and lead), low alloy steel, semiconductors and an insulator. The half-range Maxwell-Boltzmann velocity distribution has been shown to describe the temporal variation of the ablated atoms for all these substances. For all of the materials, except aluminium, the characteristic temperature determined from the Maxwell-Boltzmann distribution was within 2-3 times the s.t.p. boiling point, which can be

regarded as an approximate value of the critical temperature. Thus it would appear that for these metals a thermal mechanism for atomisation could be reconciled with the observed velocity distributions. The case of aluminium is more problematic, the characteristic temperature obtained in some instances appears reconcilable with a thermal mechanism, however, for a range of ablation laser powers and wavelengths a much higher characteristic temperature $\sim 12000\text{K}$ was obtained. This was the case for both resonant ionisation and non-resonant two-photon ionisation. It has been mentioned previously that 12000K is approximately twice the critical temperature of aluminium: $\sim 5726\text{K}$ (Gathers, 1986). This would suggest that in this case the material interrogated by the PAI laser has not been liberated by a thermal mechanism. It is well known, however, that when freshly abraded aluminium is exposed to the atmosphere a thin layer of oxide is immediately formed. This layer of Al_2O_3 has a defect rock-salt structure, which is different to the structure of the two crystalline forms of Al_2O_3 (Cotton and Wilkinson, 1972). The thickness of the oxide layer is generally 5-15nm, but depends on the surface condition and the duration of the exposure to the atmosphere (Wernick and Pinner, 1972). It could therefore be postulated that the characteristic temperature of 12000K was obtained when the sample preparation had resulted in the formation of an appreciable oxide layer. This would seem plausible since it was demonstrated that, even when the 12000K characteristic temperature was obtained, at the highest ablation laser powers studied the observed characteristic temperature was markedly lower, $\sim 2500\text{K}$. This is in agreement (within 15%) of the characteristic temperatures obtained for aluminium metal by other workers using a similar experimental arrangement (Bickel, 1992). The energy of the aluminium atoms described by the 12000K characteristic temperature is $\sim 70\%$ of that determined as the threshold energy of aluminium sputtered from sapphire (Dreyfus *et al* , 1986). However, there are some notable differences between the ablation of these high energy aluminium atoms from the aluminium metal and the sputtering of crystalline alumina. Dreyfus and co-workers observed that the kinetic energy of the aluminium atoms increased sharply as the ablation laser fluence was increased, up to $>10\text{eV}$. This was not observed for the aluminium metal samples. This is conceivably due to the higher ablation laser power causing removal of the film, which then exposes the pure metal underneath. It is also curious that the high characteristic

temperature is observed at a visible wavelengths, whereas the mechanism proposed by Dreyfus *et al* involves electronic sputtering, and would be expected to be applicable only at ultraviolet wavelengths. If the thickness of the oxide film is as mentioned above, it would suggest that the typical removal rate at low and medium ablation laser powers is a fraction of a monolayer. This is consistent with the applicability of a model which does not involve gas phase collisions, as the models which involve collisions are appropriate for material removal rates of the order of a monolayer per pulse (§2.7).

A detailed understanding of the mechanism of material removal mechanism is necessary if laser ablation is to be used in quantitative analysis. The study of the laser ablation of a steel standard proved particularly illuminating. This work illustrated that for the powers that could be utilised without the onset of a dense laser produced plasma, the characteristics of the emitted material appeared to depend on the thermal characteristics of the element monitored, and not on the properties of the matrix. It was apparent that the sputtered material appeared to be composed of the more volatile elements until the sample had been irradiated with a high number of shots. This was attributed to the formation of an azeotropic molten phase, which may not have the same composition as the solid. It was also illustrated that there did not appear to be simple technique which would allow the utilisation of higher laser powers, which could be expected to effect atomisation without an intermediate molten phase. The only arrangement which was considered feasible was to allow the dense plasma to recombine before voltages were applied to the source region. However, this could be expected to take a considerable time. The optical emission from ionised species in laser plumes, formed in the presence of a buffer gas, have been seen to last for many microseconds (Leis *et al*, 1989). The depth of craters produced by high laser power densities is of the order of several microns per pulse. This is much higher than the sub-monolayer removal rate achieved by the laser power densities discussed in this chapter. Therefore, analysis carried out using pulsed extraction voltages and high laser power densities would be expected to be of a bulk rather than a surface nature.

It is one of the major limitation of RIMS that almost invariably only one

element can be analysed at a time. However, RIMS is usually only applied where the ultra-trace analysis capability of the technique is required. Often only a quantitative assessment of the concentration of one element is required. For such applications laser ablation could be profitably employed for surface analysis, if the linearity of the ablation process with analyte concentration can be assessed. This question will be addressed in Chapter 6.

Chapter 5

Resonant Laser Ablation

§5.1 Introduction

The use of laser ablation as a sample atomisation technique for RIMS has been discussed in much detail previously in this thesis. This work used a fixed wavelength laser pulse, of nanosecond duration, for ablation and then a second pulsed dye laser to ionise the liberated neutral atoms. The experimental arrangement is complicated and the number of neutral atoms interrogated is dependent on the delay between the two lasers. The experimental arrangement can be simplified and the dependence on the delay between the lasers removed, if both the atomisation and ionisation are achieved by a single laser pulse. This is the principle of LAMMS analysis, where the fourth harmonic of a Nd:YAG laser is usually employed. Ionisation in LAMMS is principally due to the plasma processes described in §2.9. It is possible to effect ionisation more efficiently if the laser causing atomisation is tuned to be resonant with an atomic transition in the element of interest. This has been termed resonant laser ablation (RLA). This is a technique which has been the subject of surprisingly little research, compared to conventional LAMMS. In this chapter the RLA studies of other researchers will be reviewed and an account of the work undertaken in Glasgow will be given.

It should be emphasised that in RLA the laser wavelength is tuned to be in resonance with an electronic transition in the species of interest, which is usually an element. This is quite different to the technique, usually called matrix assisted laser desorption and ionisation (MALDI), where the molecule of interest is diluted in a matrix which is known to absorb strongly in the wavelength range of the ultra-violet laser beam (Karas *et al*, 1985, 1991; Tang *et al*, 1992). Ions of the molecule of interest are readily formed upon irradiation by a mechanism which is not fully understood. Therefore, MALDI is very useful for molecular weight determination and can be used, for example, to identify compounds in biochemical applications. However, MALDI is obviously different to RLA

which can be applied to unprepared solid samples.

§5.2 RLA experiments performed by other researchers

The first application, known to the author, of tuning the ablation laser to be in resonance with known transitions in the species of interest was performed by Muller *et al* (1985). The experiments were performed on a LAMMA 500 system which was modified by the addition of a dye laser to generate a wavelength tuneable beam. The LAMMA 500 system operates in a transmission arrangement. This involves the laser beam being incident on the rear of a thin sample, while the ions are extracted through to the mass spectrometer at 180° to the incident beam. The initial work of Muller and co-workers was concerned with molecular films and the laser beam was focused on the edge of the sample. It was observed that the threshold fluence required for the detection of molecular ions decreased as the laser wavelength was changed from 286.5nm to 225.7nm. However, the observed enhancement depended on the molecule analysed. For dibenzothiophene the threshold power was ~140 times higher for the longer wavelength, whereas for anthracene the threshold power was only ~17 times higher. Most notably, for pyrene the threshold power at the higher wavelength was only twice that obtained at the lower wavelength.

This work was extended to the analysis of trace elements in different matrices (Verdun *et al*, 1987), using the same experimental arrangement. Initial work involved araldite polymer homogeneously doped with precise quantities of cadmium acetylacetonate complex (Cd(acc₂)). The samples were sliced on a microtome into sections 0.2µm thick. The Cd ion signal was observed to increase by a factor of ~100 when the laser wavelength was changed from ~290nm to be resonant with an atomic transition at 228.8nm. The width of the observed enhancement was much larger than the known width of the atomic transition. The full width at half maximum (FWHM) of the peak, above background, was 3.5Å. The signal on resonance was only ~5 times greater than that at 226.7nm. This experiment was repeated on a variety of matrices doped with copper acetylacetonate. The laser was scanned over the allowed atomic transitions at 327.4nm and 324.8nm. It is important to note that the energy of these photons is not sufficient to affect photoionisation from the excited states. As can be seen from the partial Grotrian diagram of copper

in Fig.5.1, the energy of two 327.4nm is 0.15eV lower than the ionisation potential, while two 324.8nm photons have 0.09eV less energy than that required for ionisation. However, enhancement of the ion yield was observed when the dye laser wavelength was scanned over these transitions. This was attributed to the electrons being excited from Rydberg levels due to collisions between atoms in the plume. It was also hypothesised that autoionisation could account for the observed ionisation. However, this seems less plausible since the transition from the excited state to the closest known autoionisation state requires a laser wavelength of less than 311nm (Saloman, 1991). The FWHM of the observed enhancement in the copper ion signal was $\sim 6\text{\AA}$. This is larger than was observed for Cd and this may be due to the need for energy additional to that provided by the photons in order to effect ionisation. The enhancement in the ionisation yield observed upon tuning to an atomic resonance was found to be dependent on the matrix. For copper in epoxy resin the ion signal was found to increase by a factor of ~ 50 when the laser wavelength was changed from 324.8nm to 330nm. However, the enhancement was only ~ 5 times when the matrix was an albumin film. The detection limit was also dependent on the matrix, being 0.04ppm for the epoxy resin and 3ppm for the albumin film. These detection limits are markedly better than those obtained by employing the normal LAMMA technique, that is using a beam of 266nm wavelength, which was ~ 20 ppm for copper in epoxy resin.

This work was also extended to the study of a steel standard where an enhancement of a factor of five was observed for Mo, which was present in the sample at 0.538%. Again the width of the observed enhancement was large, FWHM $\sim 4\text{\AA}$. This was attributed, rather tentatively to collisional broadening of the transition due to the dense plasma.

Similar work has been performed without mass spectrometry, detecting the ions between a pair of charged plates (Pang and Yeung, 1989). The ablation laser was an excimer pumped dye laser and higher frequency generation was not employed. This limited the photon energy of the laser beam and so two photon ionisation was not energetically possible for any of the elements studied. Therefore ionisation would require the assistance of collisions, as described above. Enhancement of the ion signal generated by

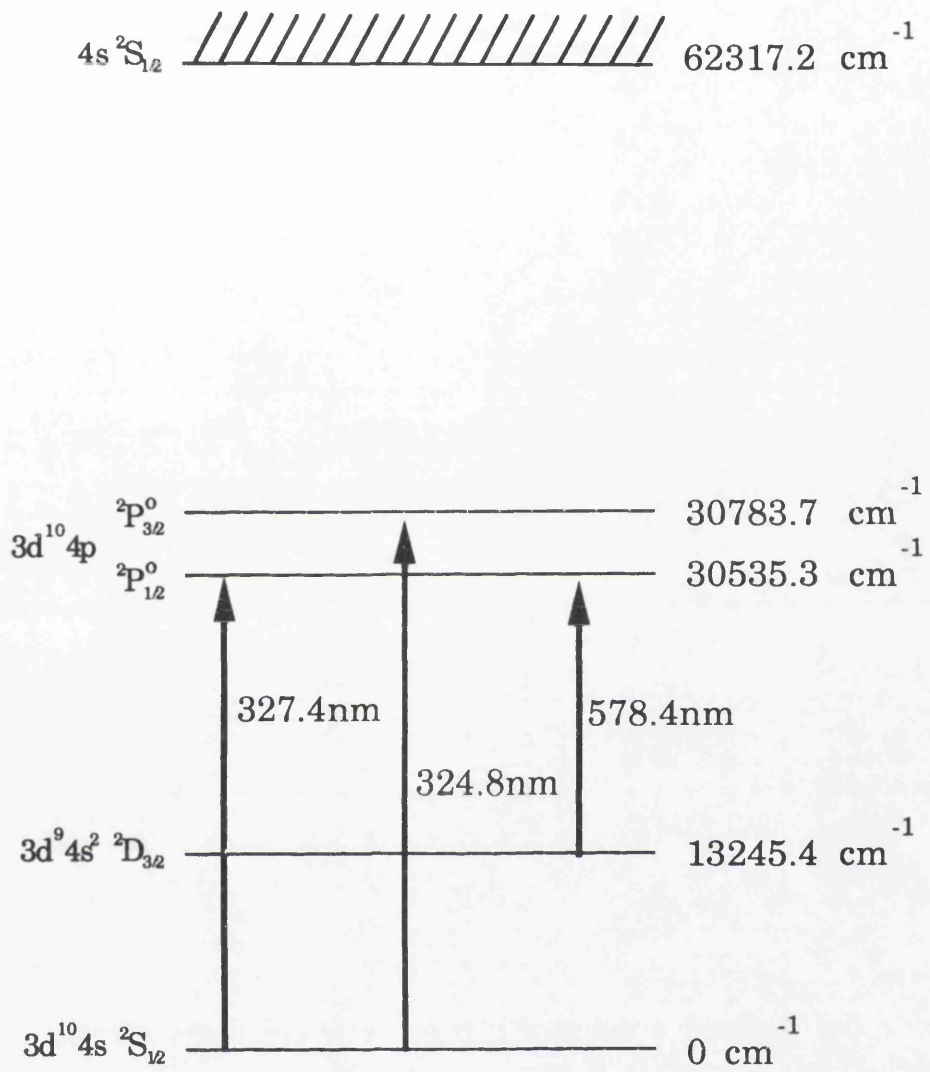


Fig.5.1 Grotrian diagram of copper showing transitions of relevance to RLA experiments

ablation of $\text{Na}_{0.7}\text{WO}_3$, was observed when the laser wavelength was scanned over the allowed sodium transition at 589nm. The width of the observed enhancement, FWHM = 2.2nm, was much larger than would be expected for a radiative transition. This was attributed to collisional broadening due to the high density of the laser produced plasma. This hypothesis was supported when the experiment was repeated in one atmosphere of helium and a line width of ~6nm was observed. Similar results were obtained for a copper foil, where enhancement of the ion signal was observed in the vicinity of an allowed transition at 578.4nm. As is apparent from Fig.5.1, this is not a transition from the ground state but is from an excited state which lies ~1.6eV above the ground state. This indicates that there is a considerable proportion of atoms in excited states in the plume. Another significant point is that three photons are required to promote an electron from this state to the ionisation continuum, however, the ion signal had a linear dependence on laser power. Since it was found that the amount of material produced per shot was linearly dependent on the laser power it was concluded that there is a zeroth-order dependence on the laser energy for the ionisation process. Therefore, multiphoton excitation was not regarded as the main mechanism responsible for ionisation. This was accepted as further evidence that atomic collisions were the predominant ionising mechanism. The FWHM of the enhancement was also large, 1.4nm under vacuum conditions.

A significant aspect of these studies was that the amount of material removed per shot could be gauged by monitoring the acoustic wave generated by the laser produced plasma. To make these measurements the cell was filled with 50 torr of helium gas. As mentioned above, enhancements were still observed when a gas atmosphere was present in the chamber. From these acoustic wave signals it was concluded that the same amount of material was removed when the laser was not tuned to an atomic resonance as when it was. Therefore, the observed signal enhancement was due solely to the higher efficiency of ionisation in the gas phase.

§5.3 Broadening mechanisms

It is apparent from the preceding discussion that the wavelength dependent enhancements of the ion signal observed by other researchers

have relatively large linewidths. Before discussing the RLA experiments performed in Glasgow a brief account of the mechanisms which can cause broadening of optical transitions will be given

§5.3.1 Natural radiative linewidth

Even in the absence of all of the broadening mechanisms detailed in this chapter, the wavelength of a transition between two states in an atom has a finite width. This is because, as a consequence of Heisenberg's uncertainty principle, the lifetime of an energy level, τ is related to the width of that state, δE , by:

$$\delta E \tau = \hbar \quad \text{- Eqn.5.1}$$

The width, ΔE , of a transition from Eigenstates E_a to E_b is, therefore, given by:

$$\Delta E = \hbar \left(\frac{1}{\tau_1} + \frac{1}{\tau_2} \right) \quad \text{- Eqn.5.2}$$

When the lower level is the ground state, $\tau_1 \approx \infty$, and hence:

$$\Delta E = \frac{\hbar}{\tau_2} \quad \text{- Eqn.5.3}$$

As an example, the $3s^2 3d$ level in aluminium, shown in Fig.4.1, has a lifetime of 14ns (Saloman, 1991). The transition from the ground state to this level would have a natural linewidth of 11MHz, or $\sim 4 \times 10^{-4} \text{cm}^{-1}$. This is much narrower than the bandwidth of the laser used in this work, which was greater than 10GHz (McCombes, 1991b). Therefore, the resonant enhancement measured by RIMS would reflect the laser bandwidth and not the natural linewidth.

§5.3.2 Doppler broadening

If the atoms, or molecules, in a gas have a range of velocities this leads to a distribution in the frequency of absorbed or emitted radiation due to the Doppler effect. It is possible to show that for a gas in thermal equilibrium, the FWHM of a Doppler broadened line is (Demtröder, 1982; O'Shea *et al*,

1978):

$$\Delta\nu_D = \frac{2\nu}{c} \sqrt{\frac{2kT \ln 2}{m}} \quad - \text{Eqn.5.4}$$

where ν is the natural frequency of the transition, k is Boltzmann's constant, c is the speed of light, m is the mass of the atom or molecule under consideration and T is the temperature of the gas. As an example, the transition from the ground state to the $3s^2 3d$ level of aluminium will again be considered. If the temperature is 300K the Doppler broadened width is 2.3GHz. This is two orders of magnitude larger than the natural linewidth, but is smaller than the bandwidth of the dye laser. The square root dependence of the broadening on temperature means that if the temperature increases to 3000K the Doppler width would increase to ~7.3GHz. This may still not be the dominate broadening mechanism for the arrangement detailed in this thesis.

§5.3.3 Power broadening

The discussion so far has taken no account of the fact that the populations of the states can be effected by the interaction with the laser field. This effect can be simply illustrated if it is considered that the electrons promoted to the excited state may be de-excited by stimulated emission. These electrons would be in the excited state for less than the natural lifetime. Hence, from Eqn.5.3, the observed transition width would be broadened. This situation can be modelled for a two level system by time dependent perturbation theory, assuming that the populations of the states has a temporal variation (Demtröder, 1982). The Rabi frequency, Ω , is an important parameter in this model. For a two level system the Rabi frequency can be expressed as (Clark *et al*, 1992):

$$\Omega = 4.90 \sqrt{\frac{\lambda^3 (\text{nm})^3 g I (\text{W/cm}^2)}{\tau (\text{ns})}} \quad - \text{Eqn.5.5}$$

where τ is the lifetime of the upper state, which has degeneracy $g = 2j+1$. I is the power density of the laser and the transition wavelength is λ . For a transition for which the Rabi frequency is very much larger than the natural linewidth, the FWHM of the observed transition is simply 2Ω . Taking the example of the transition shown in Fig.4.1, and assuming an

ultra-violet pulse energy of $20\mu\text{J}$, focused to a diameter of 0.5mm , hence $I \sim 10^6\text{W/cm}^2$, the Rabi frequency is:

$$\Omega = 4.90 \sqrt{\frac{(308.2)^3 \cdot 4 \cdot 10^6}{14 \cdot 10^{-9}}} = 4.5 \cdot 10^{11} \text{Hz}$$

Therefore, the transition is broadened to $\sim 10^{12}\text{Hz}$, ($\sim 0.3\text{nm}$), which is much greater than the broadening produced by the mechanisms discussed previously. However, this assumes that the laser is totally monochromatic and, as discussed above, this is not the case for the pulsed lasers used in this work. If it is assumed that the fraction of the pulse energy which causes the broadening is the ratio of the laser bandwidth to the transition linewidth, $\sim 10^3$, then the effective laser intensity becomes $I = 10^3\text{W/cm}^2$. This would result in an observed broadening of $\sim 30\text{GHz}$. Hence, power broadening results in an observed linewidth larger than that produced by the other mechanisms described above and comparable to the laser bandwidth.

§5.3.4 Collisional broadening

In the preceding sections it has been assumed that the atoms are isolated from each other and only interact with the incident radiation. It has been mentioned in §5.2 that this may not be a valid assumption when considering laser generated plumes where the pressure in the interaction volume may be considerable. For example, the pressure in the plume formed immediately after the vaporisation of a monolayer of aluminium by a 10ns pulse can be calculated to be ~ 10 torr, assuming that the atoms have a velocity of 1000m/s and a temperature of 2500K . A thorough treatment of the collisional broadening of emission lines is dependent on the system and is rather complicated (Hindmarsh, 1967). In this section only sufficient detail will be given to illustrate the nature of the collisional broadening mechanism.

There are two types of atomic collisions: elastic and inelastic. Inelastic scattering causes de-excitation of the atom, which results in the electron occupying the excited state for less than the natural lifetime. This reduction of the excited state lifetime causes broadening of the observed

linewidth. This broadening is usually very much smaller than that caused by elastic collisions (Eastham, 1986), although this is dependent on the states involved and on the pressure and the temperature. Elastic collisions, where the electron remains in an excited state, interrupt the phase between the atom and the emitted wave-train. If the duration of the collision is sufficiently brief, the emission is broadened because the wave is chopped into finite sections, whose Fourier decomposition includes frequencies other than the pure harmonic. The linewidth of a collision broadened line is twice the mean rate at which collisions occur (Loudon, 1973). The mean time-of-flight between any kind of collision, τ_0 , can be expressed from kinetic theory as:

$$\frac{1}{\tau_0} = \frac{4d^2N}{V} \sqrt{\frac{\pi kT}{m}} \quad \text{- Eqn.5.6}$$

where d is the distance between the centres of the atoms during a collision, N is the number of atoms in the volume V , and the other symbols have the same meaning as in Eqn.5.4. This only gives an approximate relationship between the atomic density and the resulting broadening since τ_0 is the time between any collisions and not only those which effect the states involved. The collision diameter, d , is very difficult to evaluate but can be assumed to be between 4\AA and 10\AA (Hindmarsh, 1967).

Assuming a collision diameter of 5\AA , Eqn.5.6 can be evaluated for aluminium. For instance, the liberation of a monolayer by a ten nanosecond pulse, which would result in an atomic density of 10^{18}cm^{-3} and a temperature of $\sim 2500\text{K}$, would result in a mean rate of collisions of 10^9s^{-1} . Therefore, any broadening caused by thermal collisions would be $< \text{GHz}$. This is less significant than the power broadening mechanism discussed earlier.

The preceding discussion has not taken into account the presence of the high intensity of laser photons present in RLA experiments. The modification of atomic collisions in the presence of intense laser fields has been the subject of extensive study (Rahman and Guidott, 1982; Sizer and Raymer, 1987). Under these conditions it is possible for a system to undergo transitions which are not possible in the absence of either atomic

collisions or the applied radiation field. These interactions can be classified into two categories. The first involves transitions which result in the excitation of one atom, while the second atom remains in its initial state. Hence:

$$A_i + B_i + h\nu = A_f + B_i \quad - \text{Eqn.5.7}$$

where *i* represents the initial state and *f* the final state. This has been termed an optical collision or collisionally aided radiative excitation (CARE). In the second class of interaction both atoms emerge in a different final state:

$$A_i + B_i + h\nu = A_f + B_f \quad - \text{Eqn.5.8}$$

This type of interaction has been called both laser induced (or assisted) collisional excitation transfer and radiatively aided inelastic collisions. Both categories of interactions can occur for the laser intensities and atom densities which occur in the experiments reported in this chapter. It is optical collisions which are believed to cause the broadening of the transition linewidths observed in RLA experiments. The mechanism can be described quantitatively (Berman and Robinson, 1982), but can be illustrated quite simply. A photon which has an energy that is not resonant with an atomic transition when an atom is isolated, can excite an electron when two atoms collide since their proximity causes a time-dependent shifting of their combined energy levels. As shown in Fig.5.2(a) the effect of the laser photon is to create a dressed state which is a copy of the ground state raised by the photon energy. When the system is at a particular interatomic spacing, R_c , these states intercept and excitation may be achieved. As illustrated in Fig.5.2(b), the collision induced shift in the levels moves the resonance towards lower energies and hence longer wavelengths, resulting in an asymmetric broadening of the observed linewidth.

§5.4 Initial RLA experiments performed in Glasgow

Wavelength dependent enhancements in the ion yield similar to those described in §5.2 have been observed using a RIMS system, by simply directing the dye laser beam onto the sample surface, which was rotated

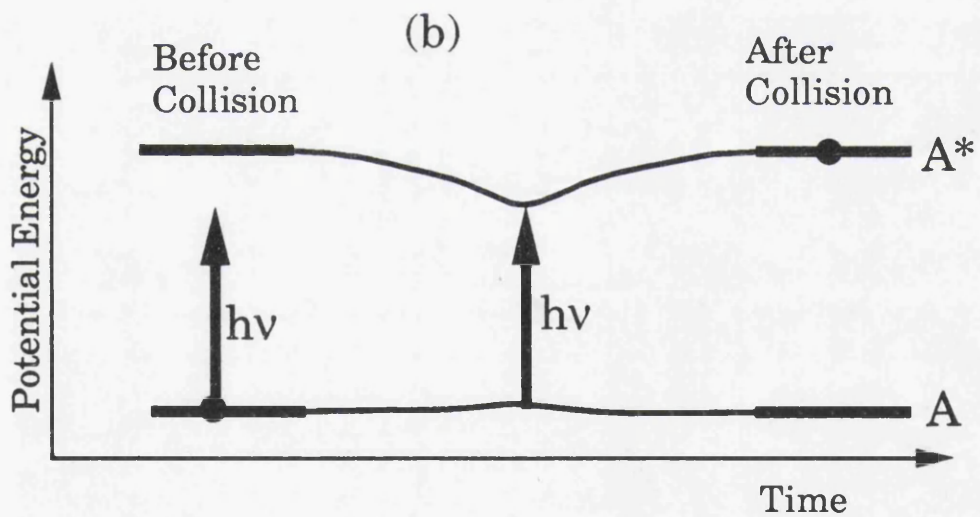
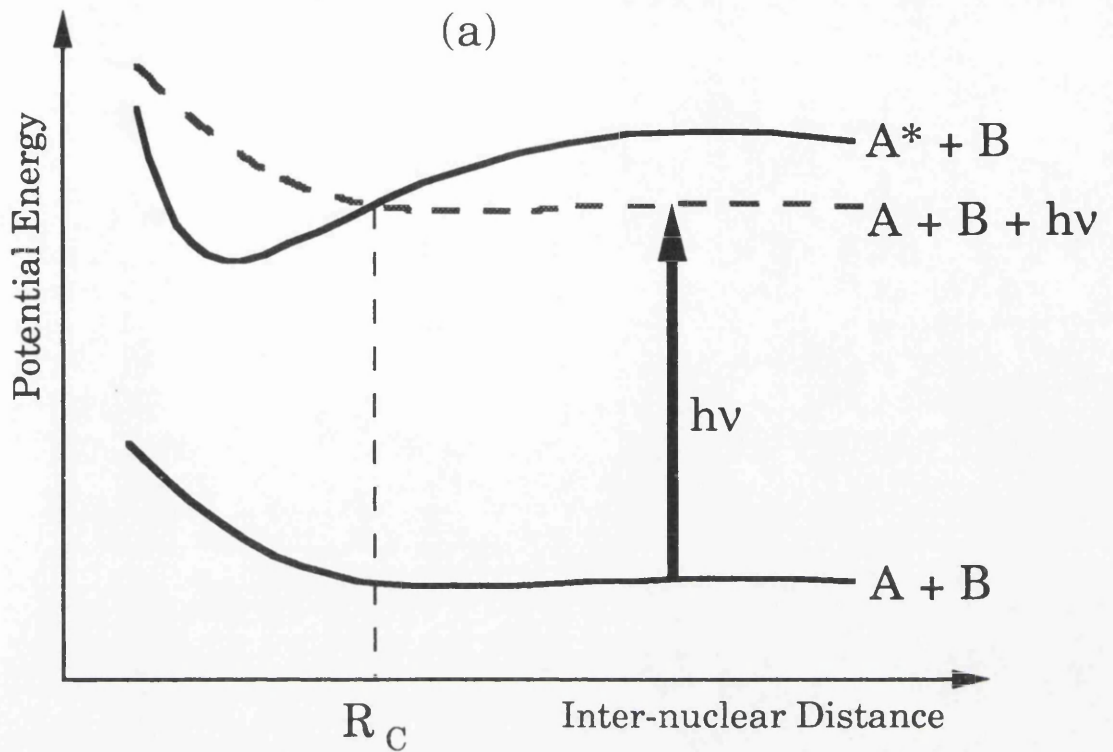


Fig.5.2 The basic principle of laser assisted collisions. (a) As two atoms come closer the energy levels are modified so that a photon which normally has insufficient energy to promote a transition can do so. (b) The temporal dependence of the modification of the energy levels is shown schematically.

slightly (McLean *et al.*, 1990b). This grazing incident arrangement is illustrated in Fig.5.3. Initial experiments were performed on an instrument substantially similar to that described in Chapter 3, except that the mass spectrometer was of the linear time-of-flight design (McLean, 1990a). The ion signal was detected by an electron multiplier and recorded using a 12 bit analogue to digital converter. The sample was a 1.3 μm thick $\text{Al}_{0.3}\text{Ga}_{0.7}\text{As}$ layer on a GaAs substrate. This sample has also been studied by laser ablation with PAI, as described in §4.6. The laser system was a Lumonics EPD330 dye laser pumped by a Lumonics TE 860-3 excimer laser. The output of the dye laser was frequency doubled using the Inrad Autotracker described in §3.3.1. The pulse energies on the sample were $\sim 1\text{mJ}$ for the fundamental beam and $\sim 100\mu\text{J}$ for the frequency doubled beam. The beam was focused to a spot of area $\sim 2\text{mm}^2$. This resulted in a laser power density on the surface of $\sim 10^7\text{W}/\text{cm}^2$, with the fluence of the ultra-violet beam being an order of magnitude lower. With this apparatus substantial enhancement was observed in both the Al and Ga ion signals as the laser wavelength was tuned across known atomic resonances. Fig.5.4 shows the two order of magnitude enhancement in the aluminium ion signal as the laser wavelength was tuned over the resonances shown in Fig.4.1. The width of the enhancements, $<0.05\text{nm}$ FWHM, is substantially smaller than the linewidths reported in the experiments in §5.2. A narrow resonance enhancement was also observed in the Ga ion signal when the laser wavelength was tuned over the two photon resonance shown in Fig.5.5. The wavelength spectra obtained for both of the gallium isotopes are shown in Fig.5.6. Both isotopes showed identical behaviour and the signal strengths on resonance showed the correct isotopic ratio. Sodium, which was believed to be present as a surface impurity, was also detected as an ionic species. Over the range of wavelengths studied no atomic transitions in sodium were encountered and the ion signal was observed to be independent of the laser wavelength. It was believed that the sodium ion signal was due to the laser induced fragmentation of ionic salts present on the sample surface.

A similar resonant enhancement was observed when the same procedure was applied to a Ca metal sample, using the system described in Chapter 3. Using this apparatus it was possible to compare the wavelength

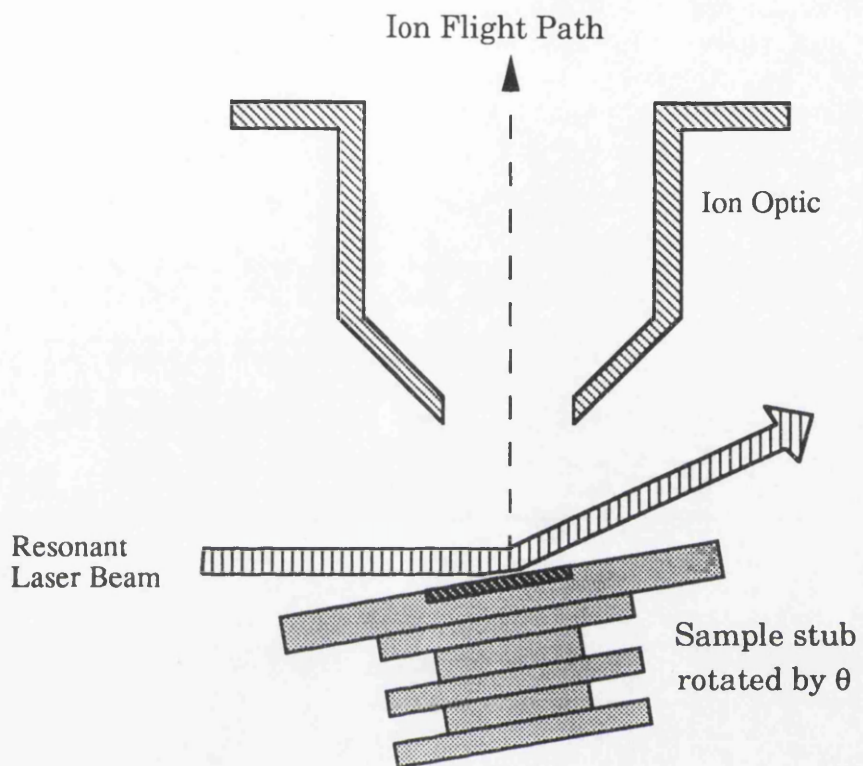


Fig.5.3 Experimental arrangement for grazing incidence resonant laser ablation

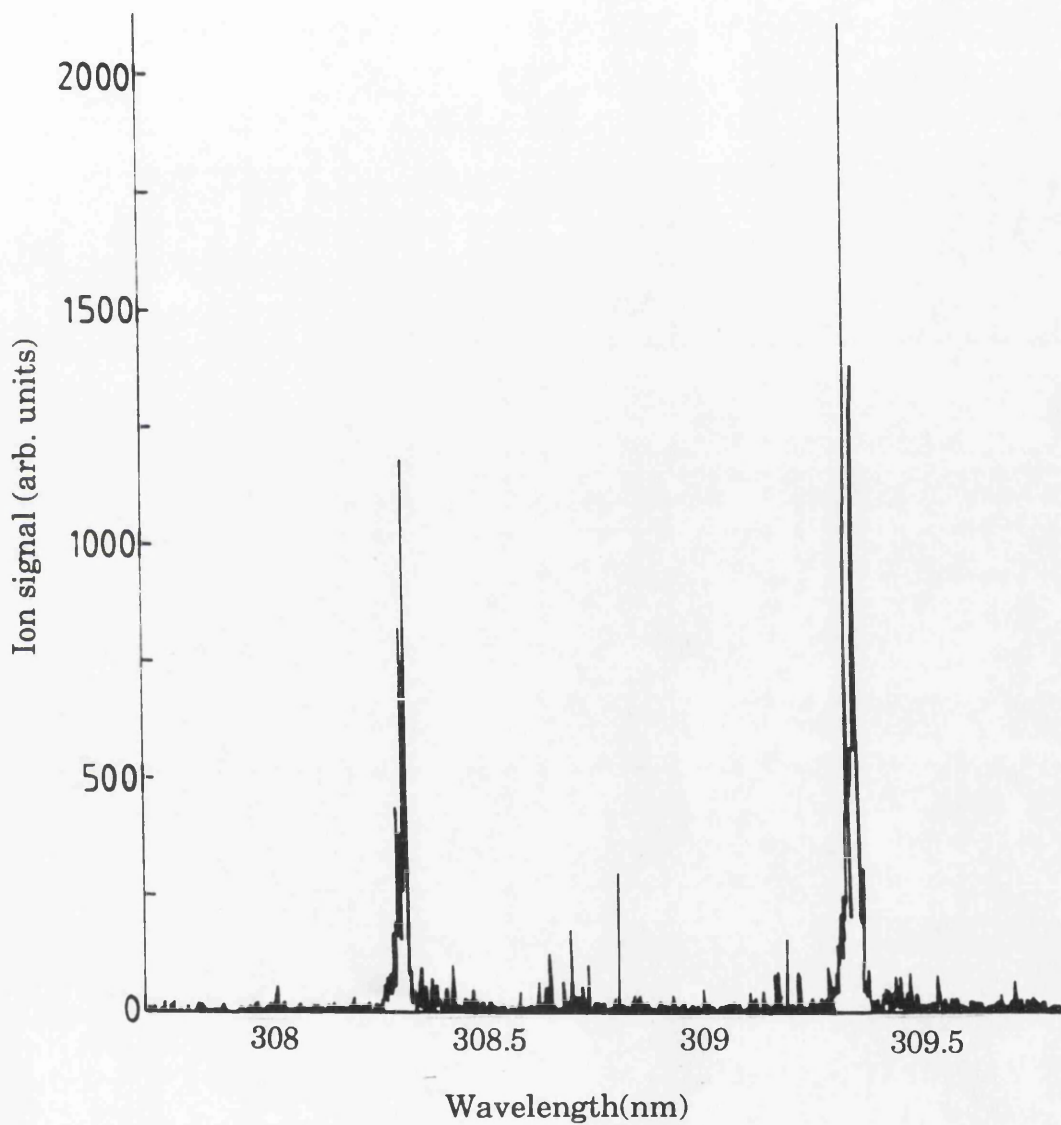


Fig.5.4 Aluminium ion signal from a $\text{Al}_{0.3}\text{Ga}_{0.7}\text{As}$ sample as a function of the ablation laser wavelength. The enhancements occur at wavelengths corresponding to transition in aluminium shown in Fig.4.1.

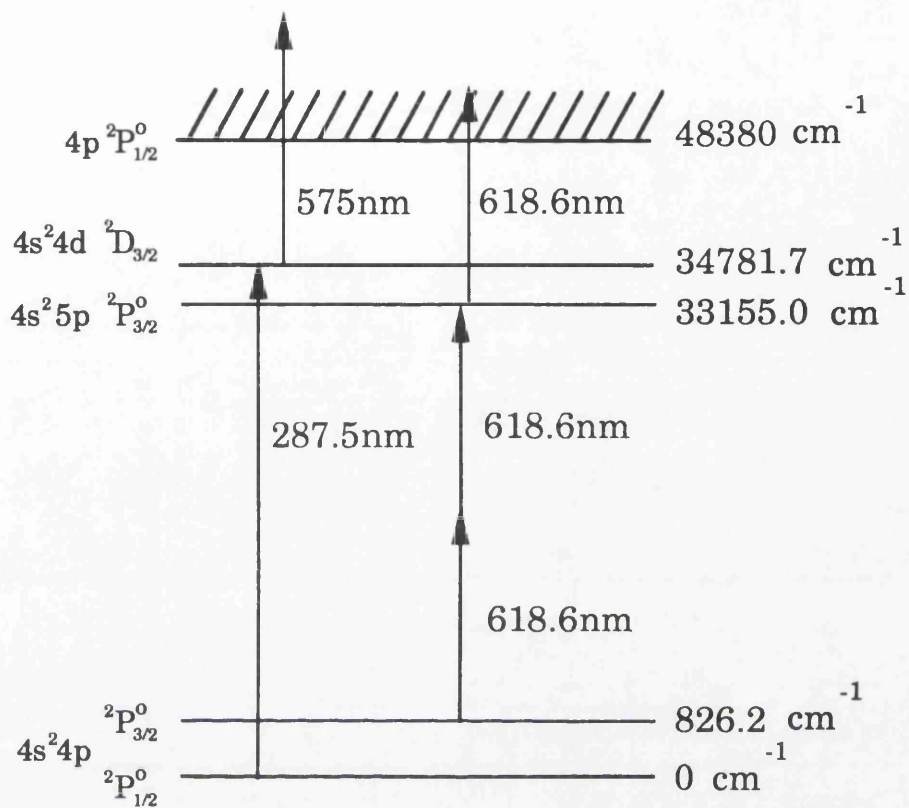


Fig.5.5 Grotrian diagram of gallium showing transitions used in RLA experiments

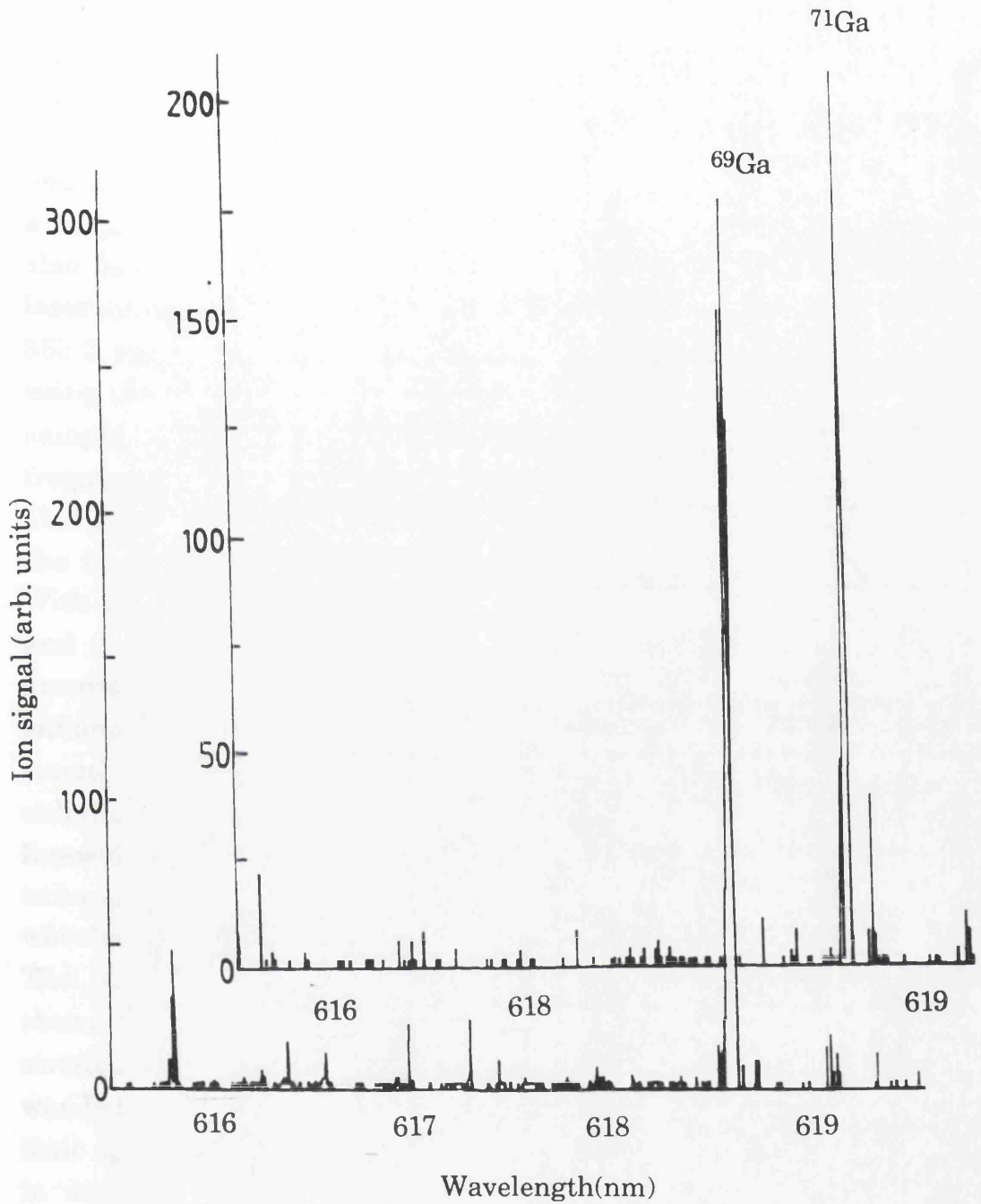


Fig.5.6 Ion signals recorded for the two gallium isotopes as a function of the ablation laser wavelength. The enhancement occurs at a wavelength corresponding to the two photon transition shown in Fig.5.5. The sample was $\text{Al}_{0.3}\text{Ga}_{0.7}\text{As}$.

slightly (McLean *et al.*, 1990b). This grazing incident arrangement is illustrated in Fig.5.3. Initial experiments were performed on an instrument substantially similar to that described in Chapter 3, except that the mass spectrometer was of the linear time-of-flight design (McLean, 1990a). The ion signal was detected by an electron multiplier and recorded using a 12 bit analogue to digital converter. The sample was a 1.3 μm thick $\text{Al}_{0.3}\text{Ga}_{0.7}\text{As}$ layer on a GaAs substrate. This sample has also been studied by laser ablation with PAI, as described in §4.6. The laser system was a Lumonics EPD330 dye laser pumped by a Lumonics TE 860-3 excimer laser. The output of the dye laser was frequency doubled using the Inrad Autotracker described in §3.3.1. The pulse energies on the sample were $\sim 1\text{mJ}$ for the fundamental beam and $\sim 100\mu\text{J}$ for the frequency doubled beam. The beam was focused to a spot of area $\sim 2\text{mm}^2$. This resulted in a laser power density on the surface of $\sim 10^7\text{W}/\text{cm}^2$, with the fluence of the ultra-violet beam being an order of magnitude lower. With this apparatus substantial enhancement was observed in both the Al and Ga ion signals as the laser wavelength was tuned across known atomic resonances. Fig.5.4 shows the two order of magnitude enhancement in the aluminium ion signal as the laser wavelength was tuned over the resonances shown in Fig.4.1. The width of the enhancements, $<0.05\text{nm}$ FWHM, is substantially smaller than the linewidths reported in the experiments in §5.2. A narrow resonance enhancement was also observed in the Ga ion signal when the laser wavelength was tuned over the two photon resonance shown in Fig.5.5. The wavelength spectra obtained for both of the gallium isotopes are shown in Fig.5.6. Both isotopes showed identical behaviour and the signal strengths on resonance showed the correct isotopic ratio. Sodium, which was believed to be present as a surface impurity, was also detected as an ionic species. Over the range of wavelengths studied no atomic transitions in sodium were encountered and the ion signal was observed to be independent of the laser wavelength. It was believed that the sodium ion signal was due to the laser induced fragmentation of ionic salts present on the sample surface.

A similar resonant enhancement was observed when the same procedure was applied to a Ca metal sample, using the system described in Chapter 3. Using this apparatus it was possible to compare the wavelength

dependent ion signals resulting from RLA to those obtained using laser ablation with subsequent RIMS. It was found that the wavelength causing the enhancement was the same for both techniques and the observed widths obtained by the two techniques were also similar, $\sim 0.02\text{nm}$ FWHM. It was therefore concluded that the RLA signal was the result of excitation and ionisation of gas phase Ca atoms.

§5.5 Collisional mechanisms in RLA

The work discussed in §5.4 illustrated that resonant enhancements in the ion signal could be obtained with a relatively simple arrangement. In order to investigate the processes resulting in this enhancements a detailed study of the RLA of GaAs was undertaken (Wang *et al.*, 1991b, 1992). An enhancement in the Ga ion signal was obtained when the laser wavelength was tuned over the 287.5nm single photon resonance shown in Fig.5.5. The profile of this enhancement was found to highly dependent on the total laser pulse energy, as illustrated in Fig.5.7. The sample stub was inclined at $\theta=5^\circ$, hence the angle of grazing incidence was 5° . The laser power was varied using a Newport 935-5 precision attenuator which attenuates the power of both the fundamental and frequency doubled beams by approximately the same amount. It is apparent that as the laser power is increased the width of the resonant enhancement increases asymmetrically towards the longer wavelengths. At the lower powers the ion signal has a symmetric variation with wavelength and has a FWHM of 0.6\AA . This is larger than the bandwidth of the laser used in this work, $\sim 0.1\text{\AA}$ and the observed broadening was attributed to power broadening, which has been discussed in §5.3.3. The asymmetric broadening observed as the laser power was increased was attributed to optical collisions (Eqn.5.7). As these mechanisms occur in the gas phase it was asserted that the sample was atomised by the mechanisms discussed in §2.10.2.2, with excitation and ionisation occurring subsequently in the high density plume. The density of this plume was estimated assuming, from the measurements of Arlinghaus detailed in §2.10.2.2, that $\sim 10^{10}$ atoms were liberated during each laser pulse. If these atoms are emitted at a constant rate throughout the duration of the pulse, $\sim 10\text{ns}$, with a most probable velocity of $\sim 1000\text{m/s}$ (Schueler and Odom, 1987), then the density of atoms in the laser volume is $\sim 10^{14}$ atom/cm³. This is a sufficient atomic density for laser assisted collisions to occur (Spiess *et al.*, 1982).

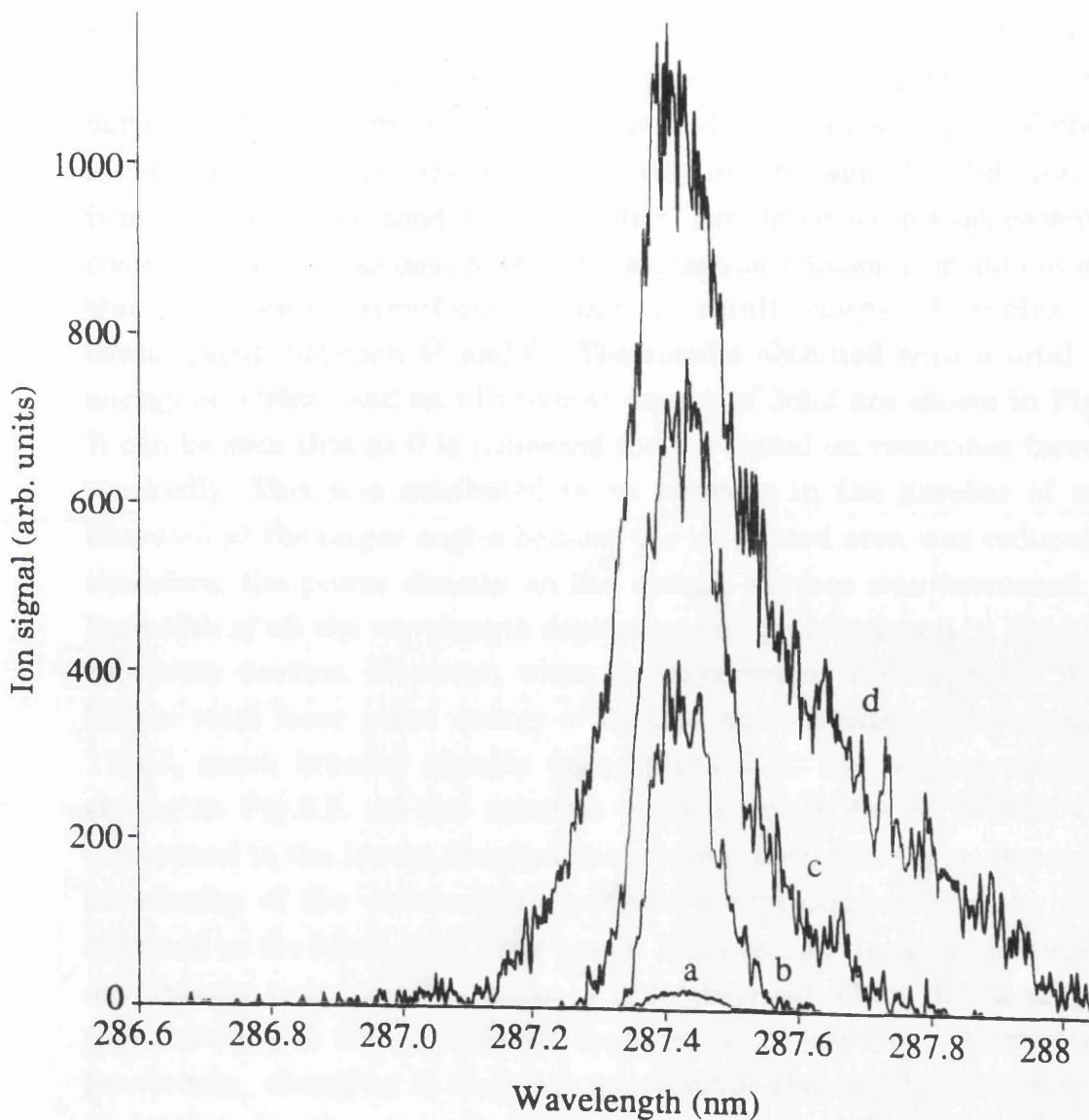


Fig.5.7 Gallium ion signal from a GaAs sample as a function of the frequency doubled laser wavelength for various total laser pulse energies: (a) 0.39mJ, (b) 0.66mJ, (c) 0.79mJ and (d) 0.98mJ. The angle of incidence of the laser beam on the sample is 5° . The enhancement occurs at a wavelength corresponding to the one photon transition shown in Fig.5.5.

The enhancements discussed in the preceding section were obtained by varying the power of the incident beam and, therefore, both the number of incident photons and the photon density on the sample surface varied simultaneously. In order to gain further insight into atomisation mechanism the pulse energy was kept constant while the wavelength dependence of the ion signal was recorded at various angles of grazing incidence, θ . Hence, the power density on the sample stub could be increased while the conditions for optical excitation were kept essentially constant. In order to ensure that the extraction efficiency of the ion optics was not varied significantly only a small range of angles were investigated, between 5° and 8° . The results obtained with a total laser energy of 0.26mJ and an ultra-violet energy of $56\mu\text{J}$ are shown in Fig.5.8. It can be seen that as θ is increased the ion signal on resonance increases markedly. This was attributed to an increase in the number of atoms liberated at the larger angles because the irradiated area was reduced and therefore, the power density on the sample surface was increased. The linewidth of all the wavelength dependent ion signals shown in Fig.5.8 are relatively narrow. However, when the experiment was repeated with a higher total laser pulse energy of 0.61mJ and an ultra-violet energy of $110\mu\text{J}$, much broader signals were obtained at the largest angles, as shown in Fig.5.9. At the smallest angle studied, $\theta = 5^\circ$, which would correspond to the lowest density of liberated atoms, there is no appreciable broadening of the wavelength dependent signal compared to the results obtained at the lower total laser power. However, as the angle is increased asymmetric broadening, similar to that observed when the laser power was varied with a fixed incident angle, becomes apparent. As mentioned previously, changing θ does not appreciable change the conditions for excitation in the gas phase. It would appear therefore, that the asymmetric broadening is related to the increasing number of neutrals. Hence, this result supports the hypothesis that optical collisions are responsible for the observed broadening.

It is apparent that the asymmetric broadening of the resonant enhancement obtained with single photon excitation and a GaAs sample, illustrated in Fig.5.7 and Fig.5.9, was not observed in the spectra obtained for gallium from the $\text{Al}_{0.3}\text{Ga}_{0.7}\text{As}$ sample, shown in Fig.5.6. This

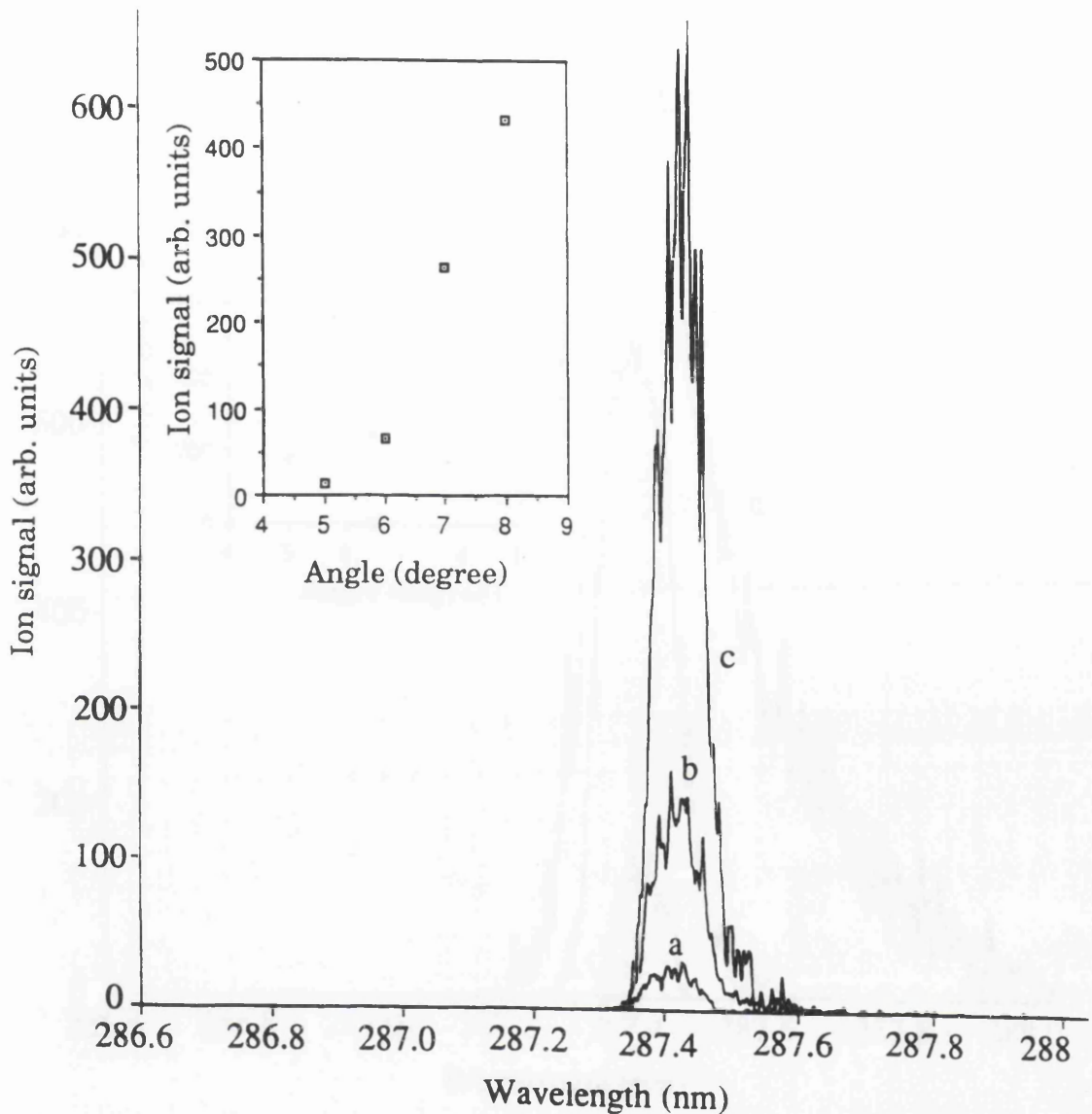


Fig.5.8 Gallium ion signal from a GaAs sample as a function of the frequency doubled laser wavelength, for various angles of incidence of the laser beam on the sample: (a) 5°, (b) 6° and (c) 7°. The total laser pulse energy is 0.26mJ with an ultra-violet pulse energy of 56 μ J. The insert shows the dependence of the peak pulse height on the angle of incidence. The enhancement occurs at a wavelength corresponding to the one photon transition shown in Fig.5.5.

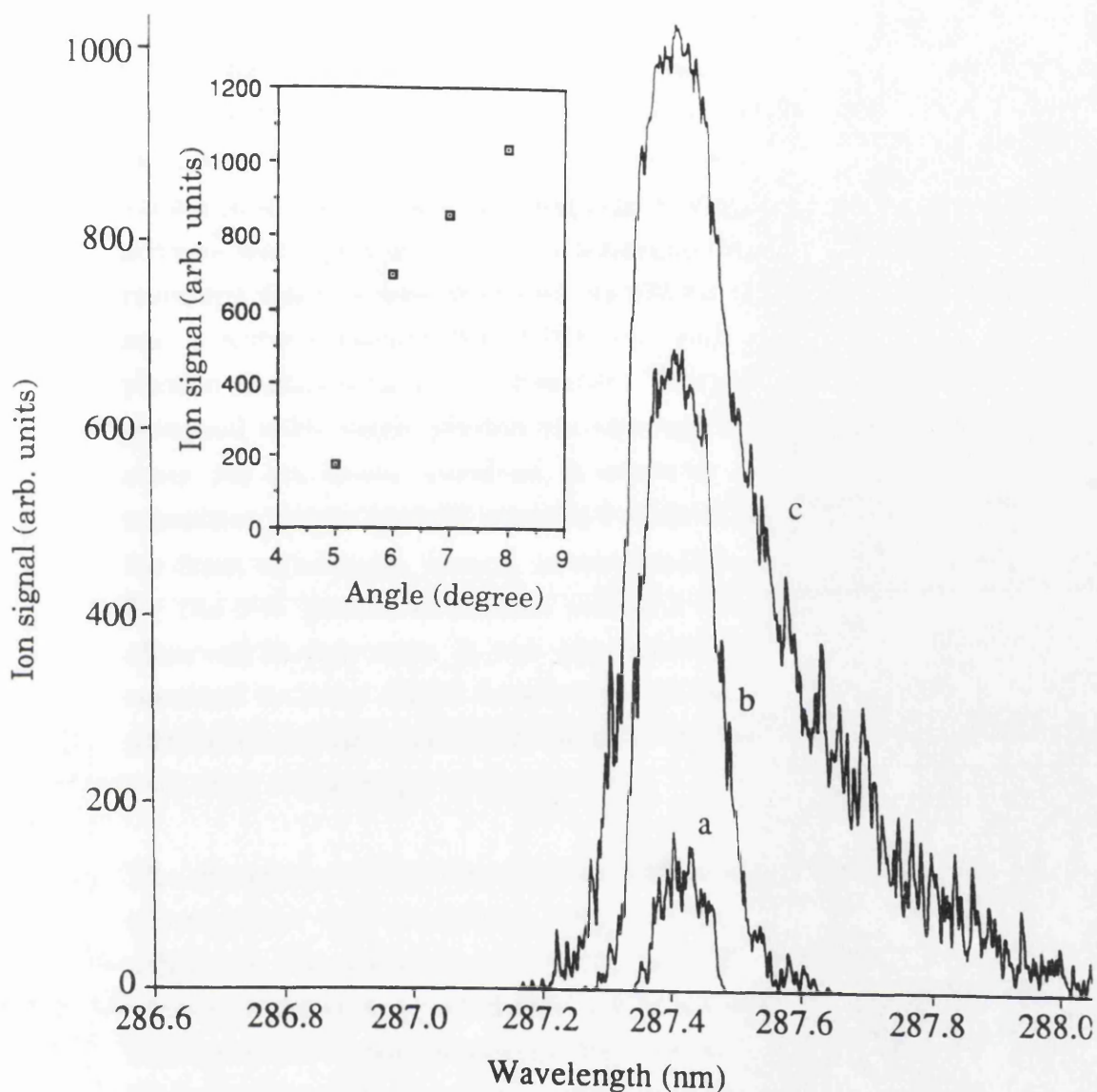


Fig.5.9 Gallium ion signal from a GaAs sample as a function of the frequency doubled laser wavelength, for various angles of incidence of the laser beam on the sample: (a) 5°, (b) 6° and (c) 8°. The total laser pulse energy is 0.61mJ with an ultra-violet pulse energy of 110 μ J. The insert shows the dependence of the peak pulse height on the angle of incidence. The enhancement occurs at a wavelength corresponding to the one photon transition shown in Fig.5.5.

difference was not attributed to the small difference in the physical properties between the two materials but was believed to be due to the differences in the excitation schemes used. The significant broadening was observed when single photon excitation was employed, using a wavelength of 287.5nm, while in the experiments on $\text{Al}_{0.3}\text{Ga}_{0.7}\text{As}$ excitation was achieved by two 618.6nm photons. The two transitions are shown in a partial Grotrian diagram in Fig.5.5. The two photon excitation scheme was applied to the GaAs sample (Wang *et al.*, 1992) and a narrow resonant feature was observed, as shown in Fig.5.10. This enhancement had a narrow bandwidth of 0.015nm and a symmetric profile. The two photon enhancement is therefore markedly different to the spectra obtained with single photon excitation. However, this is not unexpected, since, for the powers involved, it would be expected that the single photon transition would be well saturated while the two photon process would be far from saturation. Hence, power broadening would not be considerable for the two photon excitation and this results in the narrow bandwidth observed in this case. It was also found that increasing the laser power resulted in only slight broadening of the enhancement. This was also attributed to the small probability of the two photon excitation compared with that of the single photon process.

The discussion so far has detailed the mechanisms believed to be causing atomisation and excitation, but has not described how ionisation is achieved. As mentioned in §5.2, both of the previous studies of this technique have suggested that collisions may play an important role in this process. It was apparent from investigating the dependence of the RLA signal on the incident laser power that this may also be the case in this work. Fig.5.11 shows the power dependence obtained using the single photon excitation, with the wavelength tuned to the centre of the resonant enhancement. Fig.5.12 shows the result of the same experiment using the two photon excitation process mentioned above. Both graphs can be described by a relationship of the form:

$$\text{RLA Ion Signal} \propto I^P \quad \text{- Eqn.5.9}$$

where I is the incident laser power and P is the power index. However, the power index is not the same for the two excitation methods, for single

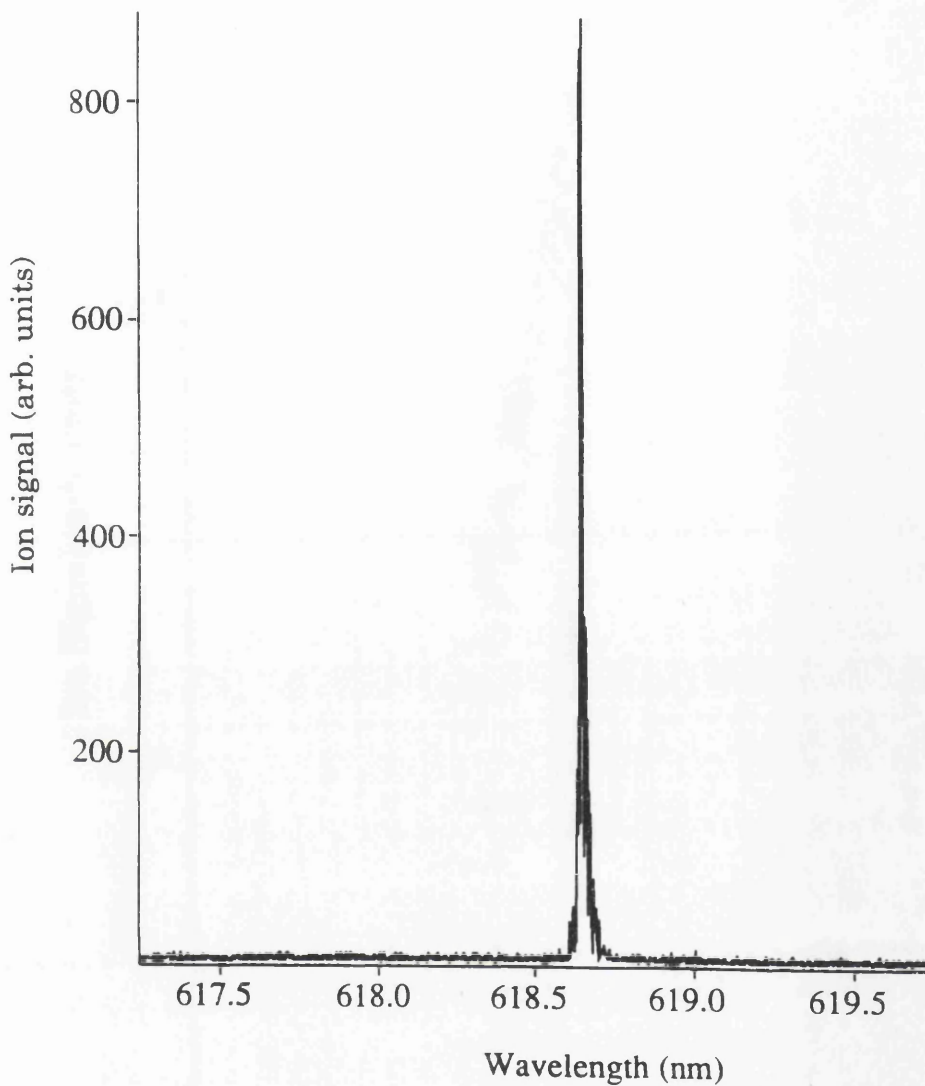


Fig.5.10 Gallium ion signal recorded as a function of the ablation laser wavelength. The laser energy was $97\mu\text{J}$. The enhancement occurred at a wavelength corresponding to the two photon transition shown in Fig.5.5. The sample was GaAs.

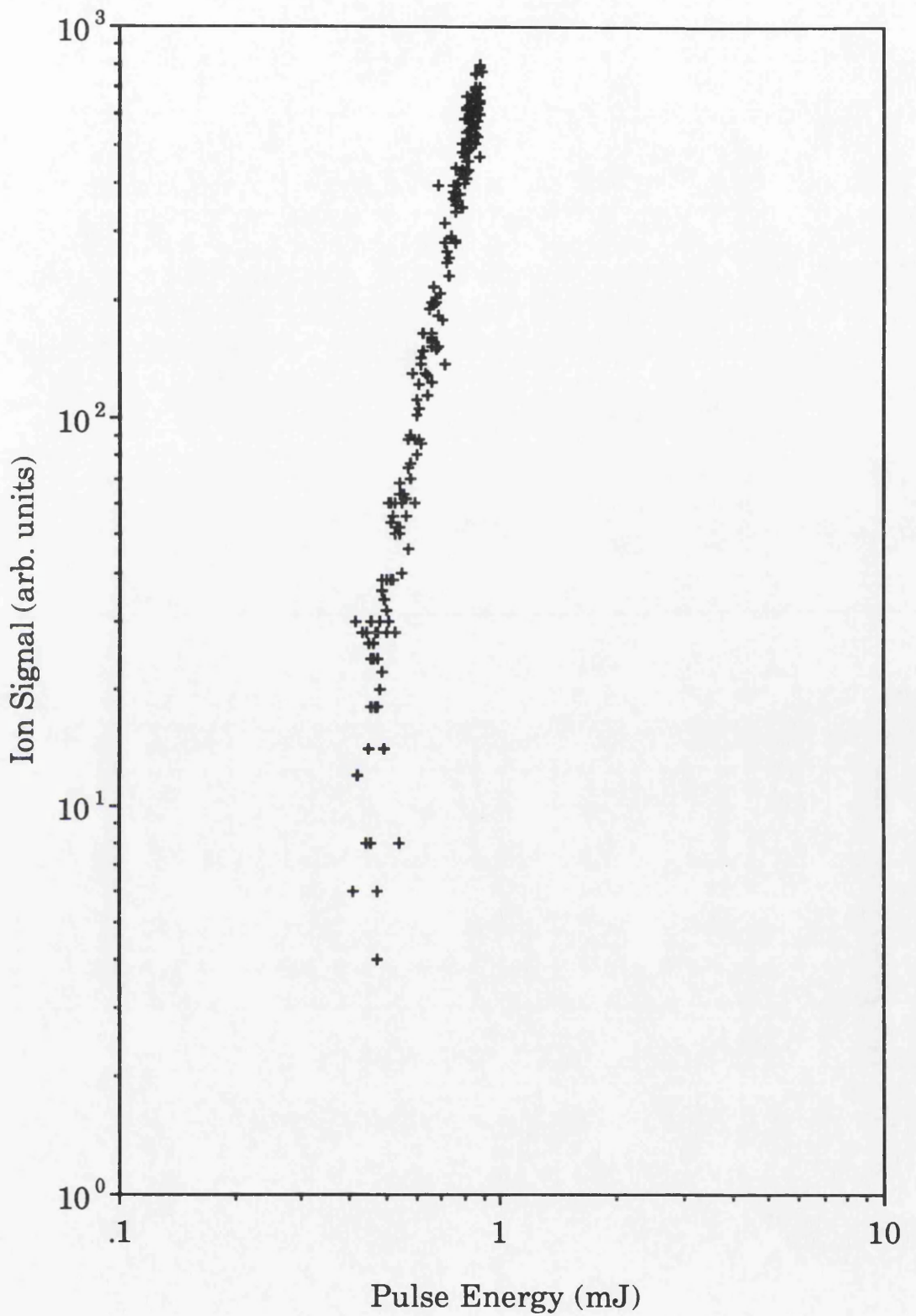


Fig.5.11 Dependence on the total laser pulse energy of the gallium ion signal. The wavelength of the frequency doubled beam was tuned to 287.5nm, which corresponds to a one photon transition in atomic gallium. The sample was GaAs.

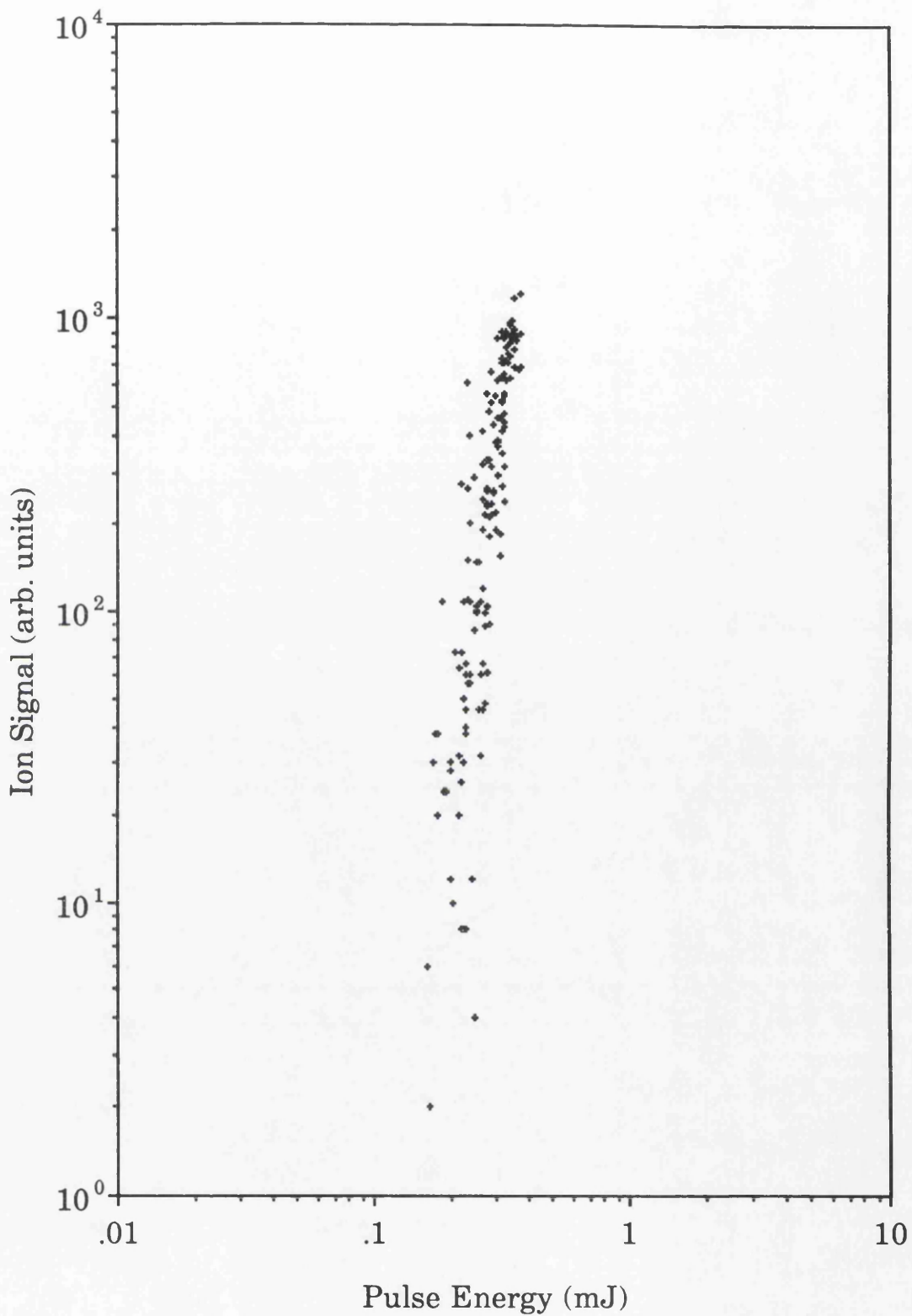


Fig.5.12 Dependence on the total laser pulse energy of the gallium ion signal. The wavelength was tuned to 618.6nm, which corresponds to a two photon transition in atomic gallium. The sample was GaAs.

photon excitation $P = 4 \pm 0.5$, while for the two photon scheme $P = 9 \pm 1$. This can be explained if the RLA signal is believed to result from three discrete processes: atomisation, excitation and ionisation. The power dependence of each stage can then be considered individually.

(1) Atomisation

As discussed in §2.10.2.2 the atomisation yield of ionic semiconductors is related to the incident power by a relationship of the form $Y(\theta) \sim I^n$, where n is dependent on the substrate and the surface temperature. It would not be expected that the value of n would differ for the two different excitation schemes as the wavelengths involved are not substantially different and there is no specific absorption structure in GaAs in this wavelength range (Palik, 1985). The pulse energy of the ultra-violet component of the beam in the single photon excitation experiment was several times smaller than that of the fundamental wavelength and it was not considered that this would affect the power dependence of the neutral yield appreciably. Therefore, the difference in the power index observed for the two excitation schemes was believed to result from the excitation and ionisation stages.

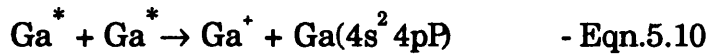
(2) Excitation

The power density of the ultra-violet beam was 10^5 - 10^6 W/cm² which, as mentioned above, would result in the one photon transition being saturated. Hence, increasing the laser power would not increase the fraction of excited atoms, that is the number of excited atoms is proportional to I^0 . The two photon transition, however, would be far from saturation and the process would exhibit a I^2 dependence on the laser fluence. Therefore, the observed difference in the value of P between the two excitation schemes, which was 5 ± 1.5 (assuming maximum uncertainties), was not due solely to the differences in the cross-section for the excitation process.

(3) Ionisation

It would appear, therefore, that the ionisation process must result in the different power dependences observed for the two schemes. Photoionisation would not cause this effect, and was not considered to be the major mechanism responsible for ionisation in these RLA

experiments. Energy pooling collisions are interactions of the type expressed in Eqn.5.8 and have been studied extensively in alkali-metal atomic vapours (Gabbanini *et al*, 1989) These processes have been shown to be highly efficient, having cross sections of 10^{-14} - 10^{-16}cm^2 (Allegrini *et al*, 1985). This is significantly higher than the typical photoionisation cross section, $\sim 10^{-17}$ - 10^{-19}cm^2 . Recently, Bicchi *et al* (1990) have observed energy pooling collisions populating an autoionising state of indium. It was also postulated that direct ionisation was caused by energy pooling collisions, although this was not directly observed. It was therefore hypothesised that energy pooling collisions play a significant role in the ionisation stage in RLA experiments. Such an interaction, known as energy pooling ionisation, EPI, involves an inelastic collision between two excited atoms and results in one ionised atom with the other atom returned to the ground state. This can be expressed as:



where Ga^* is the appropriate excited state shown in Fig.5.5. For this case, where both of the colliding atoms are in the same initial state the energy pooling ionisation rate per unit volume, R , can be expressed as (Kelly *et al*, 1988c):

$$R(\text{cm}^{-3}\text{s}^{-1}) = \frac{1}{2} k(\text{cm}^3\text{s}^{-1}) N_e^2 \quad \text{Eqn.5.11}$$

where k is the ionisation rate coefficient, N_e is the density of excited atoms and the factor of $1/2$ is included to avoid each colliding pair being counted twice. As has been discussed previously, the atomisation yield has a power dependence I^n and the excitation term has a power dependence I^0 for the single photon excitation and I^2 for the two photon case. Hence the ionisation rate for the two cases is:

$$R_w \propto I^{2n} \quad - \text{Eqn.5.12}$$

$$R_{2\omega} \propto (I^n I^2)^2 \propto I^{2n+4} \quad - \text{Eqn.5.13}$$

Therefore, if EPI plays a significant role in RLA experiments, the

difference in gradients between Fig.5.11 and Fig.5.12 would be 4. This was within the range of error of the experimental observations, and it was therefore concluded that energy pooling collisions were the principle ionisation mechanism in this case. This has some significant implications for the applicability of the technique for trace analysis. EPI in this situation is more efficient than photoionisation and as mentioned previously, a higher fraction of the atomised material would be interrogated than in the conventional RIMS analysis where separate beams are used to effect atomisation and ionisation. Therefore, it would appear that RLA could be a more sensitive technique than conventional RIMS for determining the presence of a particular element on a surface. However, since the collisional ionisation rate is dependent on the number density of excited atoms the ionising efficiency would fall if the concentration of the analyte in the sample was reduced. This could be a major problem if RLA is to be applied to quantitative trace analysis as the linearity between ion signal and trace concentration, which is observed in conventional RIMS, would not be achieved.

§5.6 The application of RLA to trace analysis

In order to assess the application of RLA to trace analysis a series of experiments were performed by the author (Borthwick *et al*, 1992) using the system described in Chapter 3. Initial studies concentrated on a pure aluminium sample, prepared as described in §4.2.1. The laser beam was focused upon the sample to a spot of approximate dimensions 3mm×0.5mm at an angle, θ , of $\sim 5^\circ$. The ionisation scheme shown in Fig.4.1 was employed, this involves excitation by an ultra-violet photon followed by photoionisation by a photon of the fundamental wavelength. As mentioned in §4.2 this scheme was found to be highly efficient since the energy of the red photons is similar to that of the transition from the excited state to the ionisation continuum. Enhancements similar to those discussed previously were observed when the laser wavelength was scanned over the transition in atomic aluminium. The linewidth of the enhancement was $\sim 0.5\text{\AA}$ when the total laser power was 0.5mJ and the ultra-violet power was $\sim 5\mu\text{J}$. The significant asymmetric broadening observed in the experiments on GaAs was not observed in this study. Increasing the power of the ultra-violet beam by a factor of ten, or the pulse energy of the fundamental beam to 1.9mJ only increased the

observed linewidth marginally, to a maximum of 0.8Å. It was assumed that asymmetric broadening was not observed because the power of the ultra-violet beam used in these experiments was lower than that in the studies of GaAs. This was due to the comparatively low output power of the dye laser during the course of this work.

The effect of increasing the laser power on the recorded signals of the major species observed; Al, Na and K, is shown in Fig.5.13. This experiment was performed with the laser wavelength tuned to the atomic resonance at 308.3nm and repeated off resonance with the wavelength shifted to 307.5nm. The off resonance wavelength was chosen to be lower than the resonant wavelength because the broadening observed previously had been asymmetric towards longer wavelengths. The signals were integrated from a mass spectrum accumulated over 500 laser shots and the pulse energy of the ultra-violet beam was kept constant throughout the experiment at $10 \pm 3 \mu\text{J}$. It can be seen that the Na and K signals increase by approximately two orders of magnitude as the laser power is increased. The on resonance and off resonance signals were recorded on different areas of the same sample and since the alkali metals are believed to be present on the surface as impurities, no significance was given to the small deviation between the relationships on and off resonance. However, there is a significant difference between the aluminium ion signals recorded on and off resonance, as large as three orders of magnitude at the lower powers. The apparent saturation of the on resonance signal at higher powers was believed to be due, in part, to an instrumental effect since the voltage of the detector was not reduced, as described in §3.2, when large ion signals were recorded.

As mentioned previously the proportion of ions to neutrals in a plasma, $\left(\frac{n^+}{n^o}\right)$, can be described by the Saha-Eggert equation (Eqn.2.25), if the ions, neutrals and electrons are in local thermal equilibrium. This is often assumed to be the case for plumes created by laser ablation. The ion to neutral yield has often been determined in conventional LAMMS studies by relating the volume of the resulting crater to the ion signal, and has been typically found to range from 10^{-2} - 10^{-5} (Conzemius and Capellen, 1980). However, at the laser fluences used in this work significant

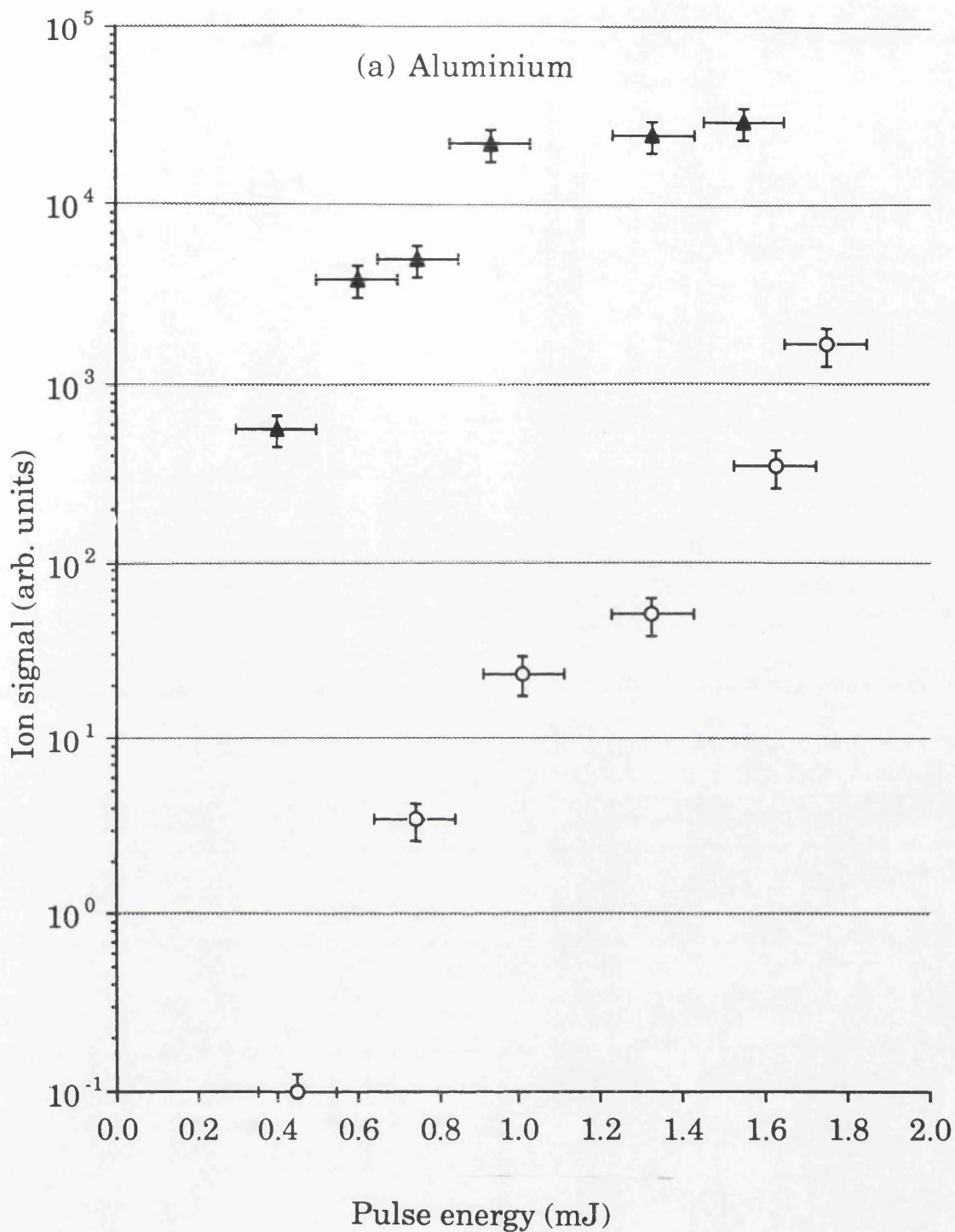
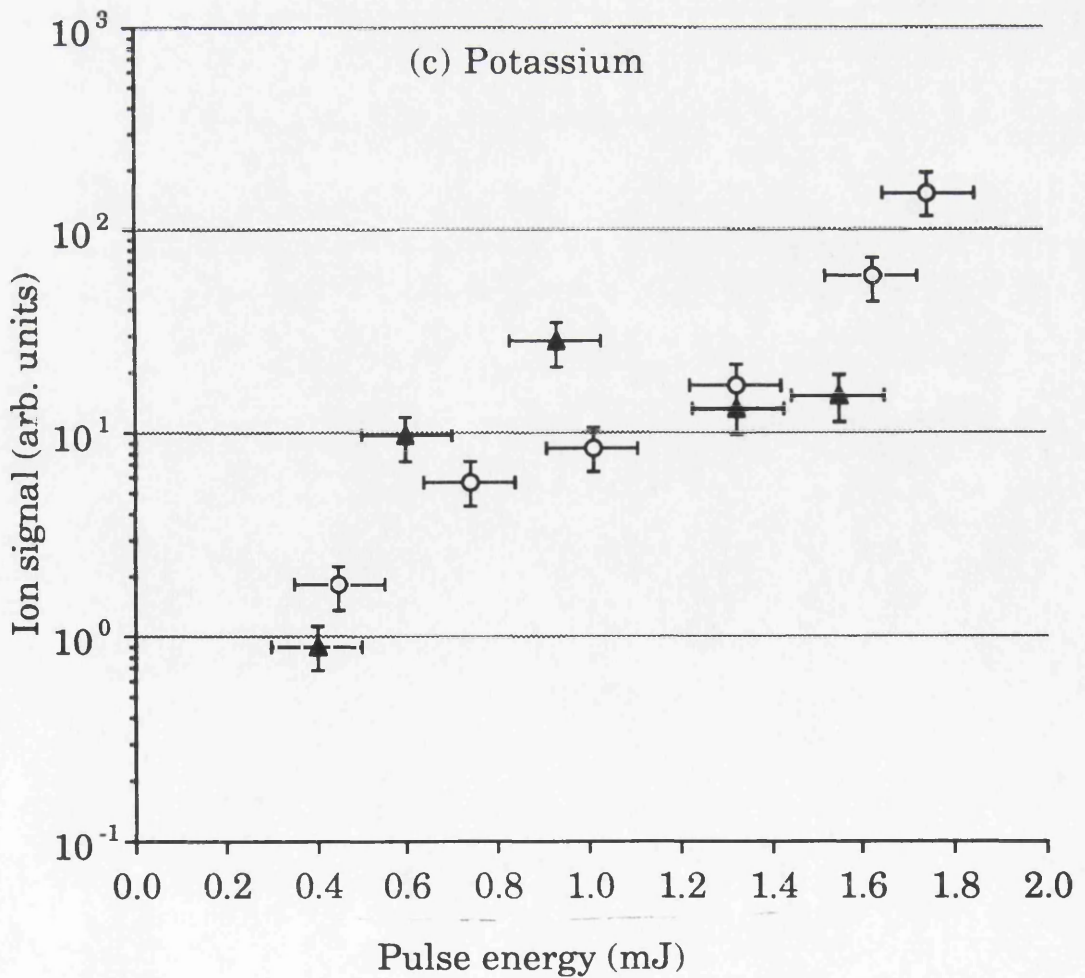
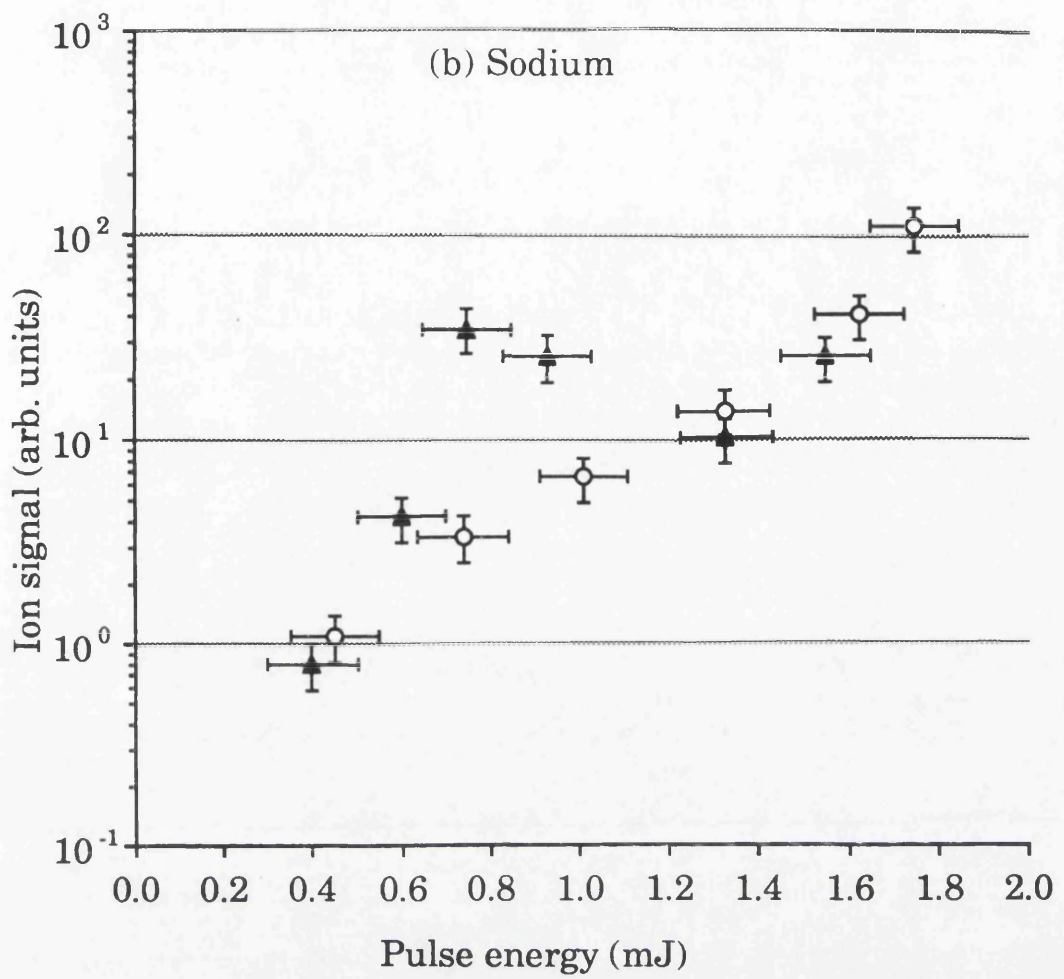


Fig.5.13 Dependence on the dye laser pulse energy of several ion signals (a) Aluminium, (b) Sodium and (c) Potassium. The sample was aluminium metal. In each case a filled symbol signifies that the frequency-doubled wavelength was 308.3nm, which corresponds to a one photon transition in atomic aluminium. An open symbol signifies that the wavelength was detuned to 307.5nm. The pulse energy of the ultra-violet beam was kept constant at $10 \pm 3 \mu\text{J}$.



cratering was not observed and therefore $\left(\frac{n^+}{n^o}\right)$ is difficult to determine. Since in RLA the ablated atoms are ionised within $\sim 10\mu\text{m}$ of the sample surface it can be assumed that there is a good geometric overlap between the laser beam volume and the neutral atoms. The efficiency of the ionisation would also be expected to be high, as has been discussed in §4.2. Hence, it would be expected that on resonance a high proportion of the atomised material would be ionised. Off resonance the ions are believed to be in thermal equilibrium with the atoms and electrons. Therefore, RLA would appear to be a useful technique for determining an upper limit on $\left(\frac{n^+}{n^o}\right)$ for low density plasmas.

In an attempt to apply RLA to the detection of trace elements, the low alloy steel NIST SRM 1263a sample was studied. This sample has also been studied by laser ablation with subsequent PAI, as described in §4.5. Aluminium is present in this sample at a certified concentration of 0.24% by weight. As shown in Fig.5.14, enhancement in the aluminium ion signal was observed as the laser wavelength was scanned over the resonant transitions. The linewidth of the observed enhancements are similar to those obtained when the sample was pure aluminium, $\sim 0.5\text{\AA}$. The effect of increasing the laser power on the ion signals of the major elements detected is shown in Fig.5.15. The pulse energy of the ultra-violet beam was $7\pm 3\mu\text{J}$. The relationship between incident laser power and ion signal does not appear to be highly wavelength dependent for the alkali metals and iron. However, the Al ion signal is seen to increase by approximately three orders of magnitude when the laser wavelength is tuned to the atomic resonance. Mass spectra obtained using this arrangement were subsequently obtained for the SRM 1263a and another low alloy steel standard SRM 1261a. This standard contains aluminium at the lower concentration of 0.021%, by weight. The mass spectra obtained on resonance for SRM 1261a is shown in Fig.5.16. An aluminium signal was clearly apparent, which was approximately an order of magnitude larger than that obtained off resonance. The detection limit for Al in steel was determined to be $\sim 5\text{ppm}$ for a five hundred shot analysis. Due to the difficulty of precisely reproducing the sample rotation, and hence laser power density on the surface, when the sample was exchanged it was not possible to compare the absolute ion signals obtained for the two

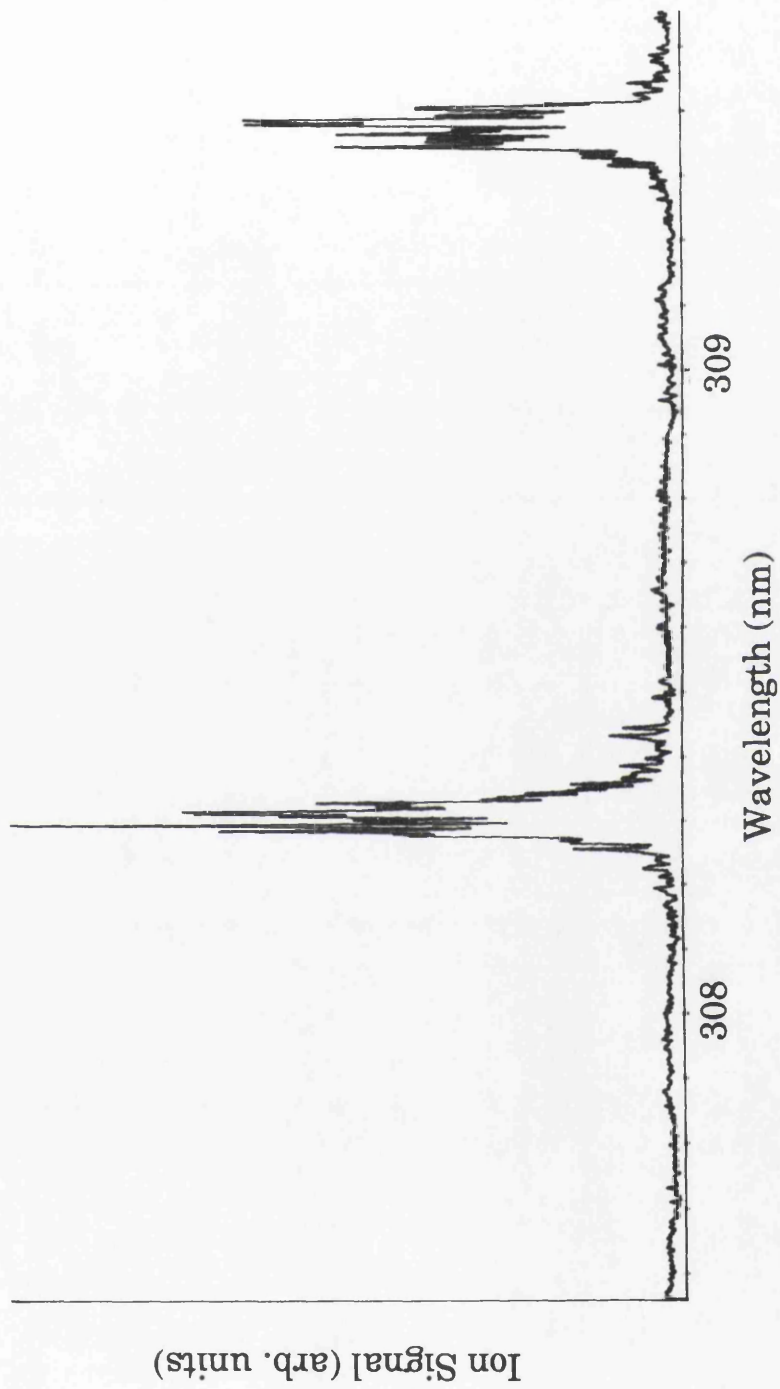


Fig.5.14 Aluminum ion signal from a low alloy steel NIST SRM 1263a sample as a function of the ablation laser wavelength. The enhancements occur at wavelengths corresponding to the transitions in atomic aluminium shown in Fig.4.1.

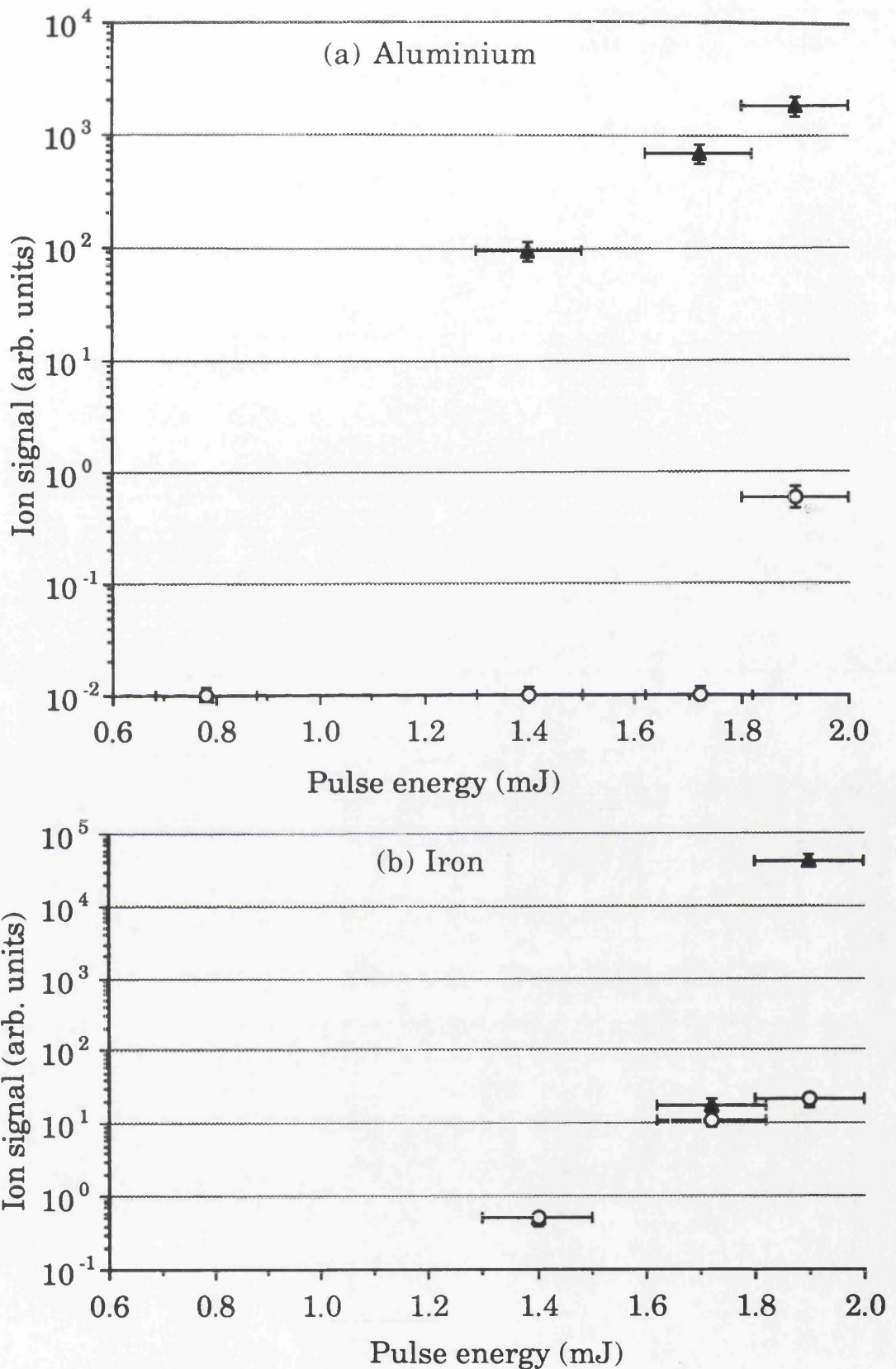
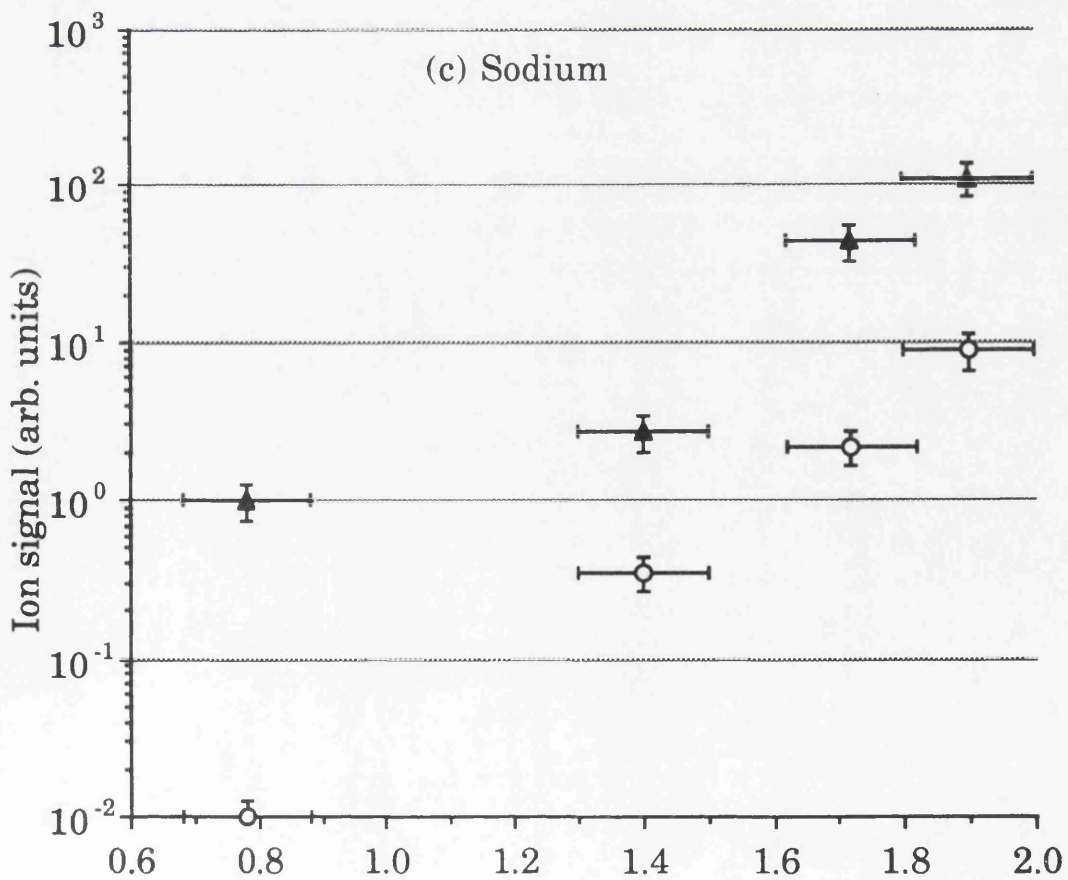
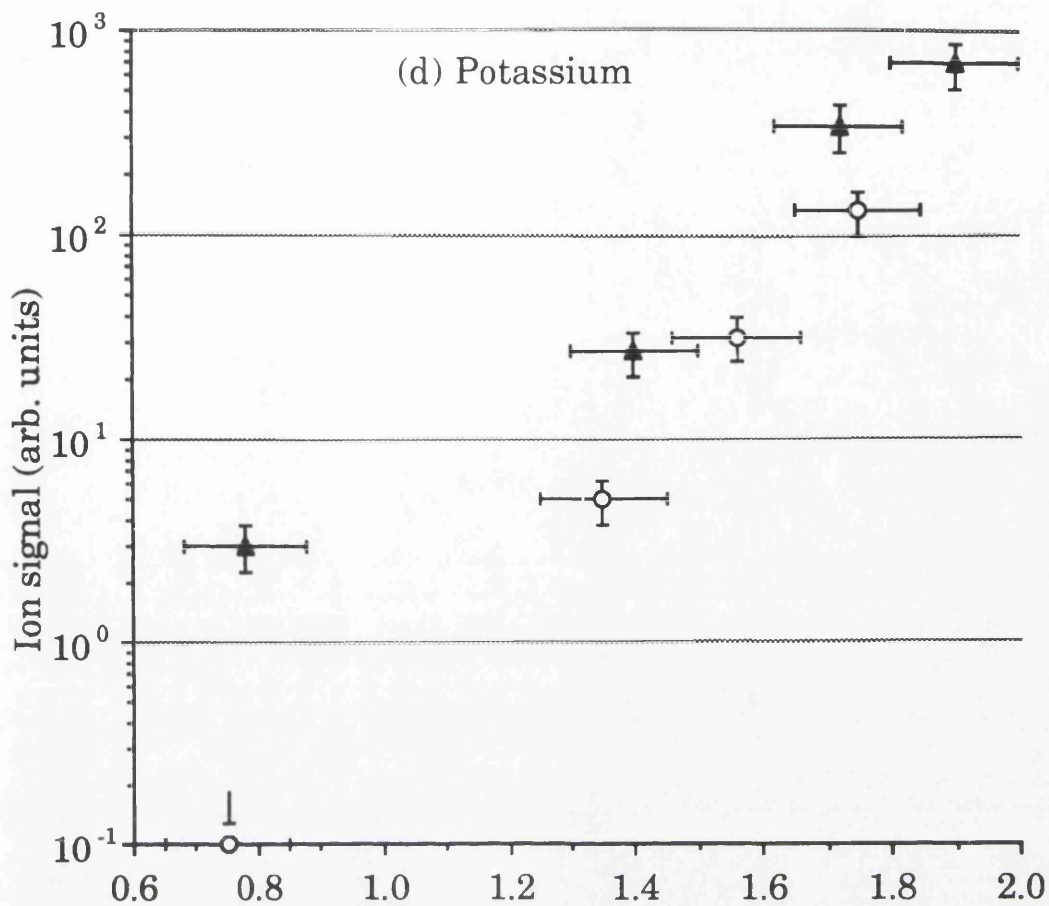


Fig.5.15 Dependence on the dye laser pulse energy of several ion signals (a) Aluminium, (b) Iron, (c) Sodium and (d) Potassium. The sample was a low alloy steel NIST SRM 1263a. In each case a filled symbol signifies that the frequency-doubled wavelength was 308.3nm, which corresponds to a one photon transition in atomic aluminium. An open symbol represents that the wavelength was detuned to 307.5nm. The pulse energy of the ultra-violet beam was kept constant at $7 \pm 3 \mu\text{J}$.



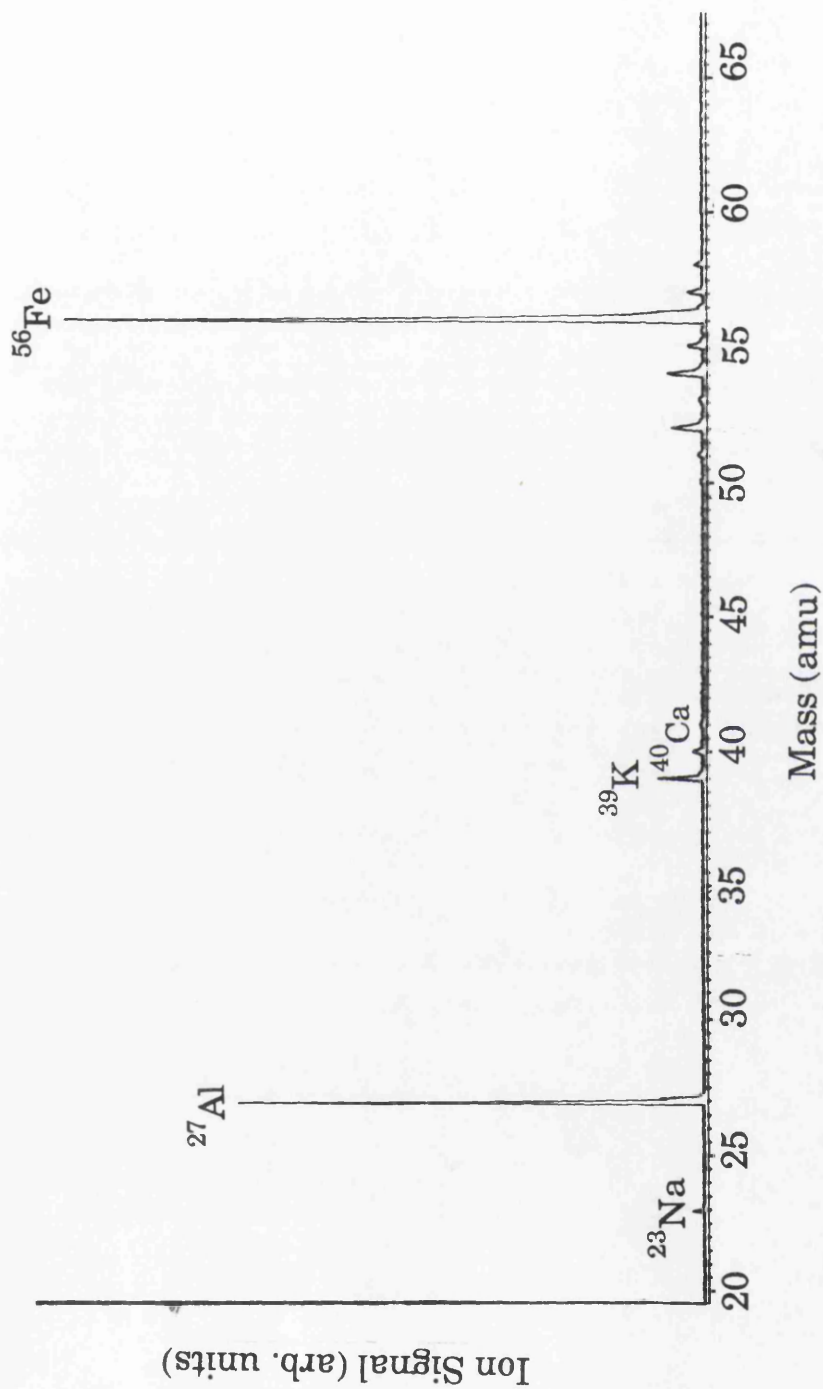


Fig.5.16 Mass spectrum obtained from a low alloy steel SRM 1261a sample. The frequency-doubled wavelength was 308.3nm, which corresponds to a one photon transition in atomic aluminium. The certified concentration of aluminium in the sample is approximately 500ppm.

standards. However, a relative comparison of the peak heights of the Al ion signals from the two standards was made by normalising with respect to the ^{56}Fe peak. From this analysis the aluminium ion signal obtained from SRM 1263a was determined to be five times larger than that obtained from SRM 1261a. This is lower than would be expected if the signal varied in proportion with the aluminium concentration in the sample. However, as mentioned above, it was not possible to exactly reproduce the experimental arrangement for different samples. Also the concentration of Al on the surface may not be constant over the whole sample. Hence, the observed lack of correspondence between the two signal sizes was not considered as unreasonable.

In the RLA experiments described in §5.2, it was observed that excited states were populated. To investigate if this was also the case with this grazing incidence arrangement the ^{56}Fe ion signal was monitored as the laser wavelength was scanned. Two reproducible enhancements in the ion signal were observed at wavelengths of $307.63 \pm 0.04 \text{ nm}$ and $308.47 \pm 0.05 \text{ nm}$, as shown in Fig.5.17. These wavelengths do not correspond to transitions from the ground state, but can be assigned to transitions from states with energies of $\sim 8000 \text{ cm}^{-1}$ above the ground state, as shown in Fig.5.18. It should be possible to monitor ion signals from many excited states of iron. By considering the statistical weights of the states involved it would be possible to determine their relative populations and hence determine the effective temperature of the atoms in the plume, assuming that local thermal equilibrium prevails.

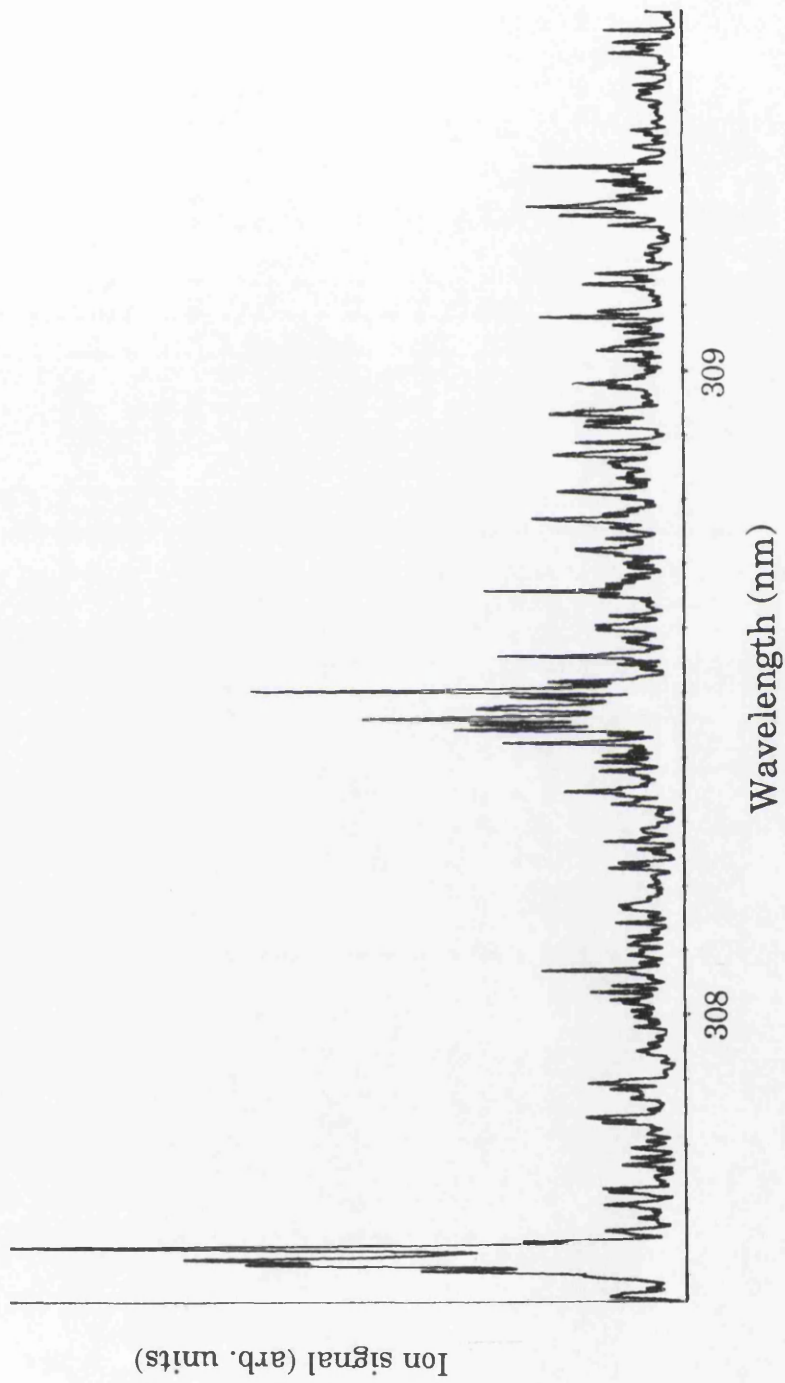


Fig.5.17 ^{56}Fe ion signal from a low alloy steel SRM 1263a sample as a function of the ablation laser wavelength. The enhancements occur at wavelengths corresponding to transitions from the excited states in iron shown in Fig.5.18.

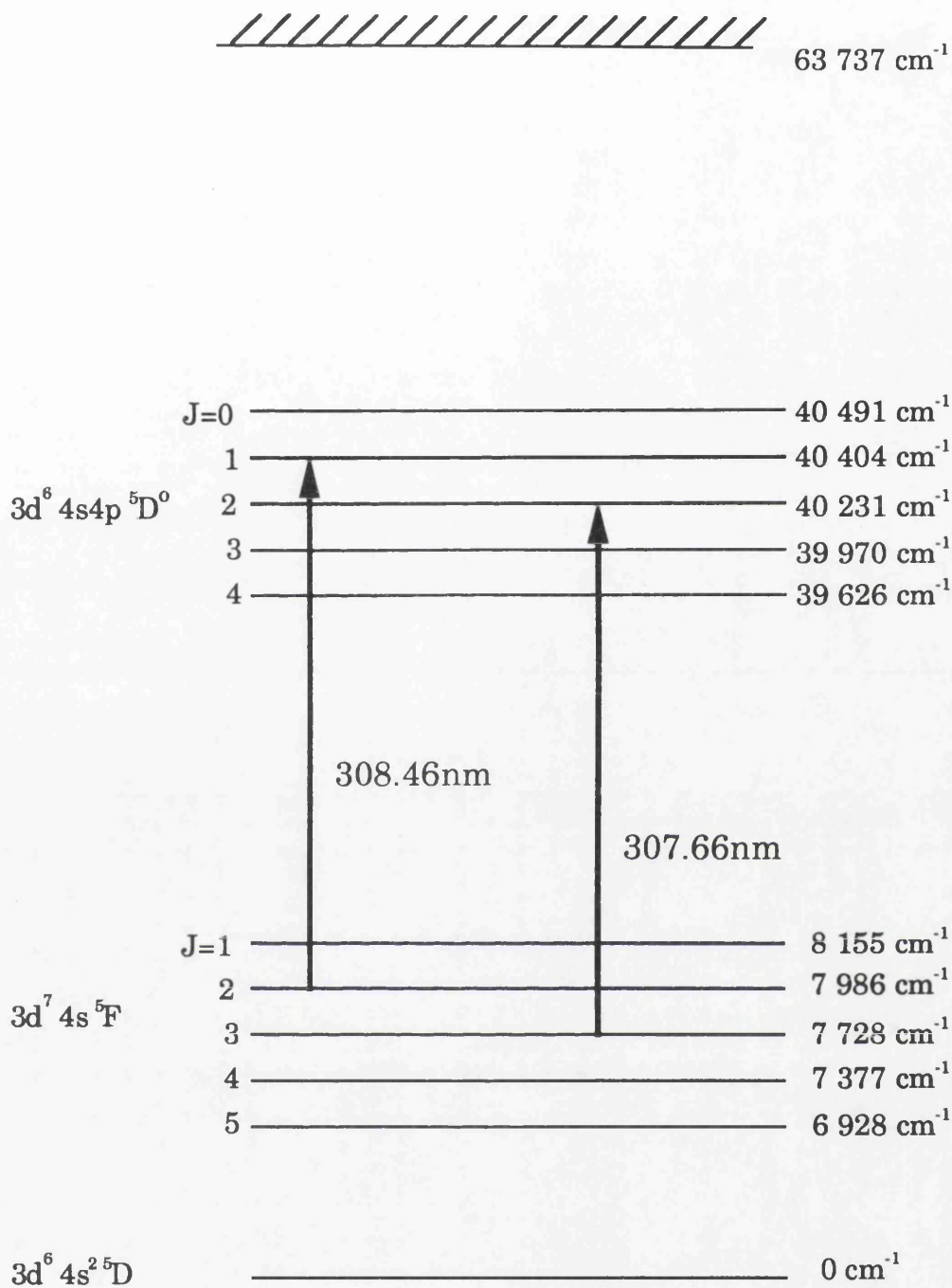


Fig.5.18 Partial Grotrian diagram of iron showing the transitions identified in Fig.5.17

Chapter 6

A comparison of ion sputtering and laser ablation for sample atomisation for RIMS.

§6.1 Introduction

The work reported previously in this thesis has been principally concerned with the interfacing of laser ablation with RIMS for the analysis of species present at relatively high concentrations in a solid sample. In this chapter the addition of an ion gun to the system is detailed, thus allowing ion sputtering to be employed with RIMS. The principles of ion sputtering relative to RIMS will be also be discussed in this chapter. Also reported in this chapter are a series of experiments which were designed to demonstrates a comparison between ion sputtering and laser ablation for trace analysis by RIMS.

§6.2 The Profiling Ion Gun

To allow the utilisation of ion sputtering for sample atomisation a high specification profiling ion gun (Kratos Analytical SB-262) was purchased and interfaced to the existing system. Fig.6.1 is a diagram of the profiling ion gun (PIG), it is a relatively complex system which was specifically designed for profiling applications. The ion beam can be formed from inert gas ions or oxygen ions if a cold cathode assembly was used. The ion beam is of high purity since a Wien filter assembly in the ion beam column allows for multiply charged ions to be removed and a 3° bend in the ion optical column ensures that any neutral species in the beam are not transmitted from the source region to the target. The source region can be electrically isolated up to 15kV, allowing the generation of beams with energies from 500eV to 15keV. The beam can be focused to micron dimensions, the specified spot-size for a 12keV anode potential was 5µm FWHM with a current of 1nA and 125µm for a beam current of 1µA. Therefore, high current densities approaching 10mA/cm² are obtainable.

The construction of the PIG is shown in more detail in the schematic in Fig.6.2. The ions are formed in the source region, which is a Penning

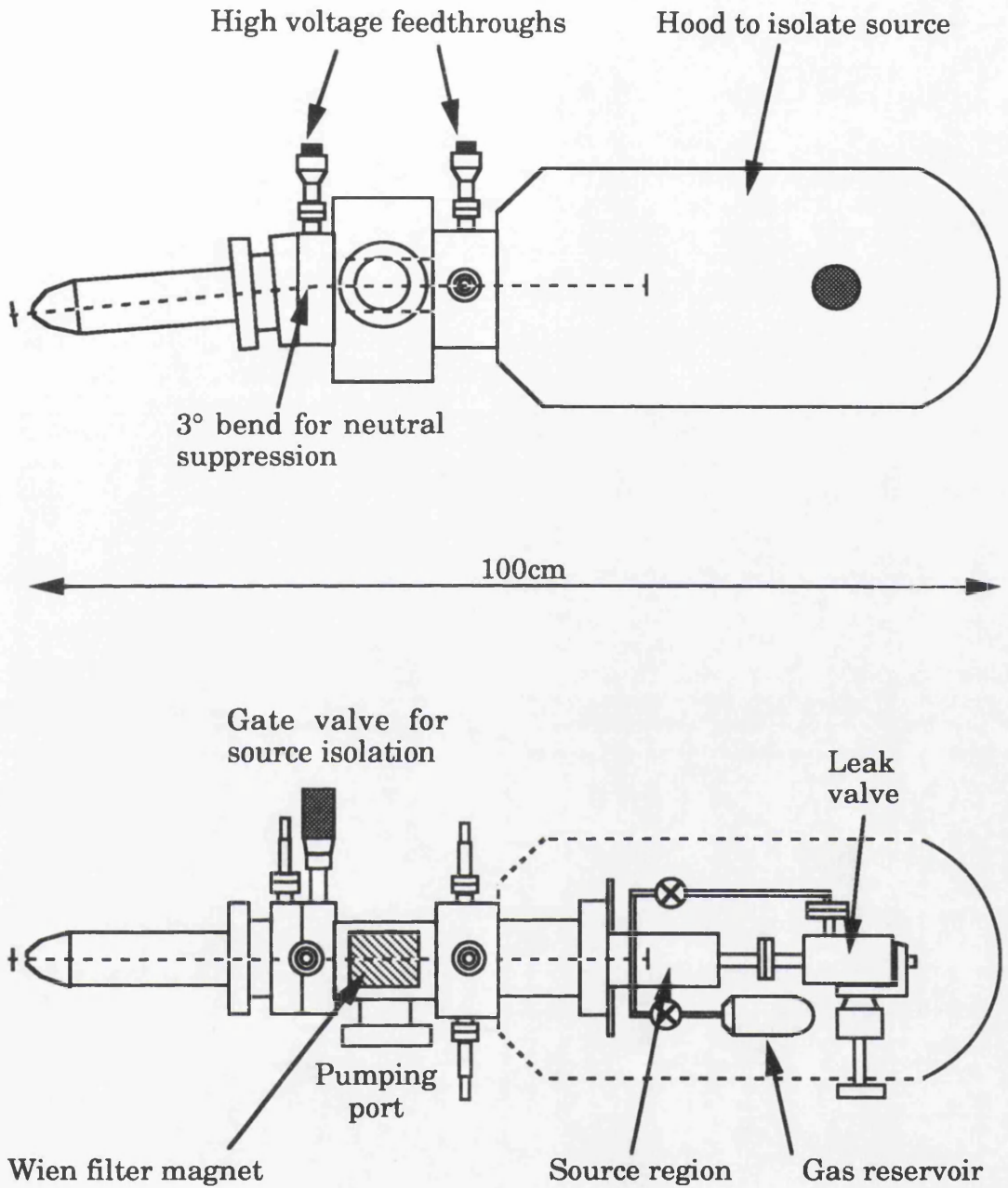


Fig.6.1 Plan view and elevation of the Kratos Analytical profiling ion gun

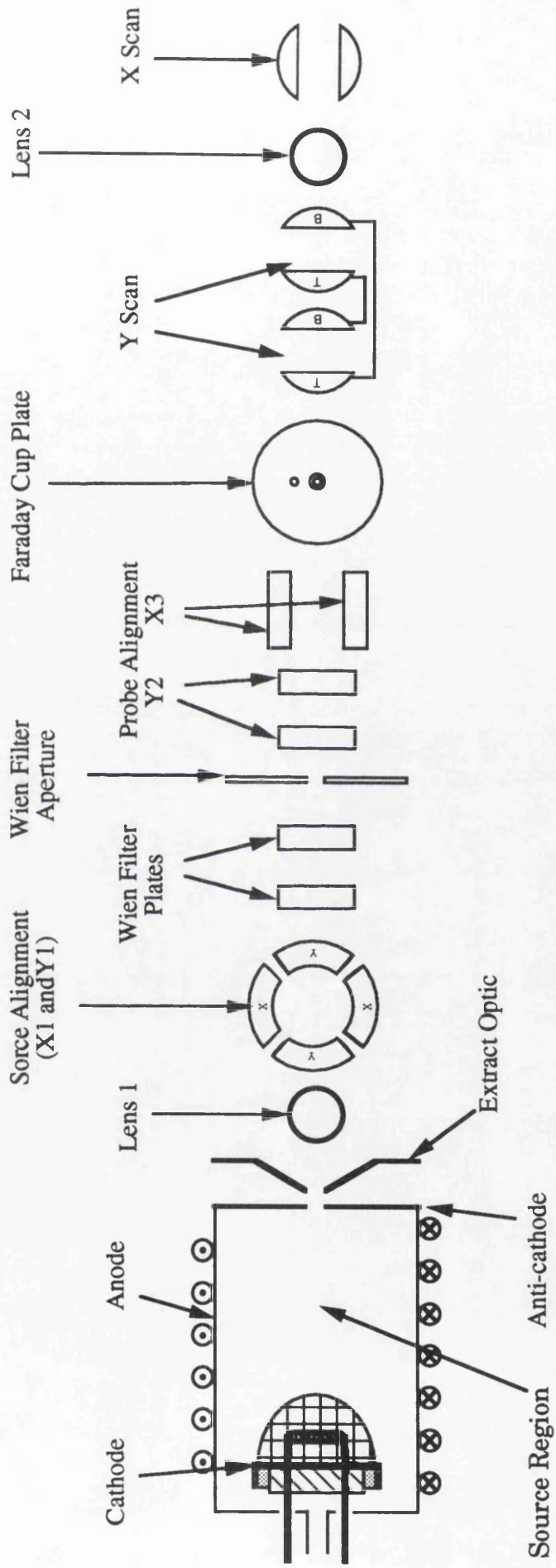


Fig.6.2 Schematic of the layout of the Kratos Analytical Profiling ion gun

source (Sidenius, 1978). Electrons are emitted from a tantalum filament into a pressure of $\sim 10^{-6}$ torr of inert gas. These electrons cause ionisation of the atoms and both the ions and the electrons are confined by the combination of the applied magnetic and electrostatic fields. The extract optic, which is held at a lower voltage than the anti-cathode, projects a field into the source region. This field causes some of the ions close to the anti-cathode to be pulled into the column of the PIG. The source assembly is raised to a high voltage in order to produce ions with the desired kinetic energy. Ions removed from the source region are collimated by a lens in the column and the trajectory of the beam can be adjusted, in order to optimise the transmission through the column, by varying the potentials applied to the next set of plates. The current in the column is monitored by a Faraday cup which is situated on the aperture plate. If the Wien filter is employed then the potential applied across the Wien filter plates is adjusted so that only singly charged ions pass through the aperture undeflected by the magnetic field. The ions are steered around the 3° bend in the column by adjusting the voltages applied to the set of plates directly in front of the Faraday cup plate. Neutral species in the beam are not deflected and are not transmitted past the plate. A series of plates in the nose of the column can have a waveform applied to them to scan the beam across the sample surface. The focusing of the beam onto the sample is accomplished by the lens in the nose of the gun; the voltages on this lens can be increased up to 10kV.

The PIG was incorporated into the system as shown in Fig.6.3. A 57mm extension section was inserted between the port on the main chamber and the flange on the PIG so that the optimum focal distance of 25mm could be obtained between the tip of the gun and the sample stub. A Balzers TPU050 50 litres/second turbo pump and an Edwards EQ80F residual gas analyser were connected to the pumping port on the PIG via a T-piece adapter. The residual gas analyser allowed both the total pressure and the partial pressure of argon in the PIG to be monitored. After baking at 150°C a base pressure of $\sim 10^{-9}$ tor was achieved. The gas handling system of the PIG includes a reservoir which can be charged to a pressure of 3 bar, which provides sufficient argon for over a hundred hours of operation of the ion source. When it became exhausted the reservoir was refilled with research grade argon through a custom made gas line. The limit for

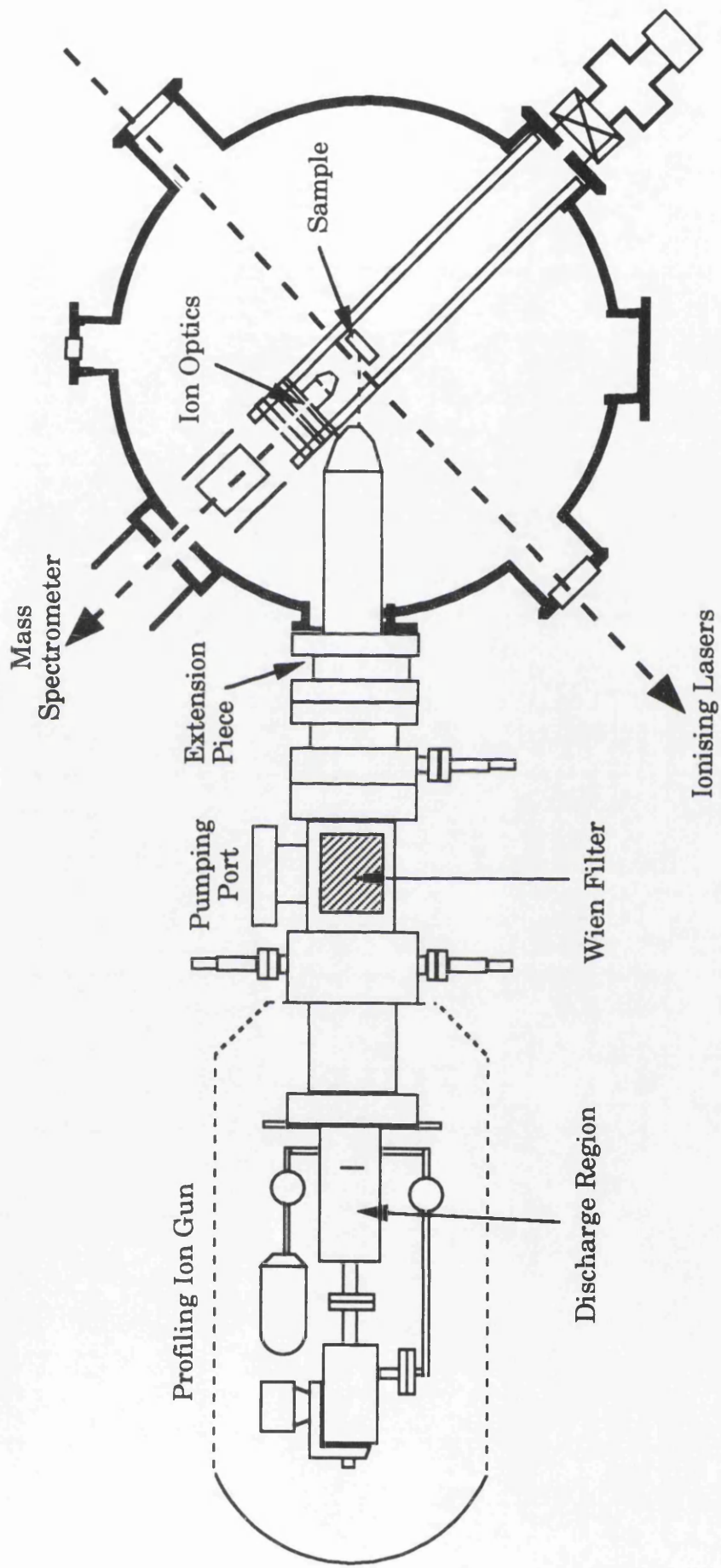


Fig.6.3 The incorporation of the PIG into the RIMS instrument

continuous operation of the PIG was imposed by the finite lifetime of the tantalum filament, which was maximally 50 hours. However, the lifetime could be dramatically reduced if the system was not adequately baked prior to the initial discharge or if the pressure in the discharge region was maintained at too high a level. Due to the expense of the commercially supplied filament assemblies, replacements were constructed in house. These were similar to the commercial assemblies except that they did not have a mess dome surrounding the filament wire. The use of these home-made filament assemblies did not markedly affect either the obtainable discharge current or the filament lifetime.

As mentioned above the optimal working distance for the PIG is 25mm. The ion optics described in Chapter 3 were too large to permit the positioning of the PIG at this distance from the sample stub. Therefore it was necessary to design a new system of optics with a smaller diameter. The system developed consisted of four elements, as shown in Fig.6.4. The first optic is of a conical design, while the others were simply apertured discs. The whole system was constructed from stainless steel and the elements were supported by a ceramic tube. The earthed plate was directly attached to the existing support and deflector plates shown in Fig.3.3. The system was designed with four elements so that voltages could be applied either in the same way as for the previous system, that is with the third optic earthed, or the second optic could be earthed while a voltage was applied to the third optic. In this configuration the second, third and fourth optics operate as an Einzel lens. A simulation of the electrostatic potentials was obtained by using the SIMION3 program, discussed in §4.10.1. Fig.6.5 shows the field contours with the optics configured in the Einzel lens arrangement with -1500 volts applied to the third optic. As was previously the case, the first optic was maintained at ~70% of the voltage of the sample stub in order to ensure that the field gradient in the ionising region was relatively small, ~100V/mm. It can be seen from Fig.6.5 that maintaining the first optic at 1400V ensures that the field between the nose of the gun, which is earthed, and the sample shows no dramatic changes in direction. The angle of incidence of the sputtering ion beam is therefore not markedly affected by the application of voltages to the optics. However, applying a positive potential to the sample stub reduces the kinetic energy of the ion beam. For example, if ions are emitted from the nose of the gun

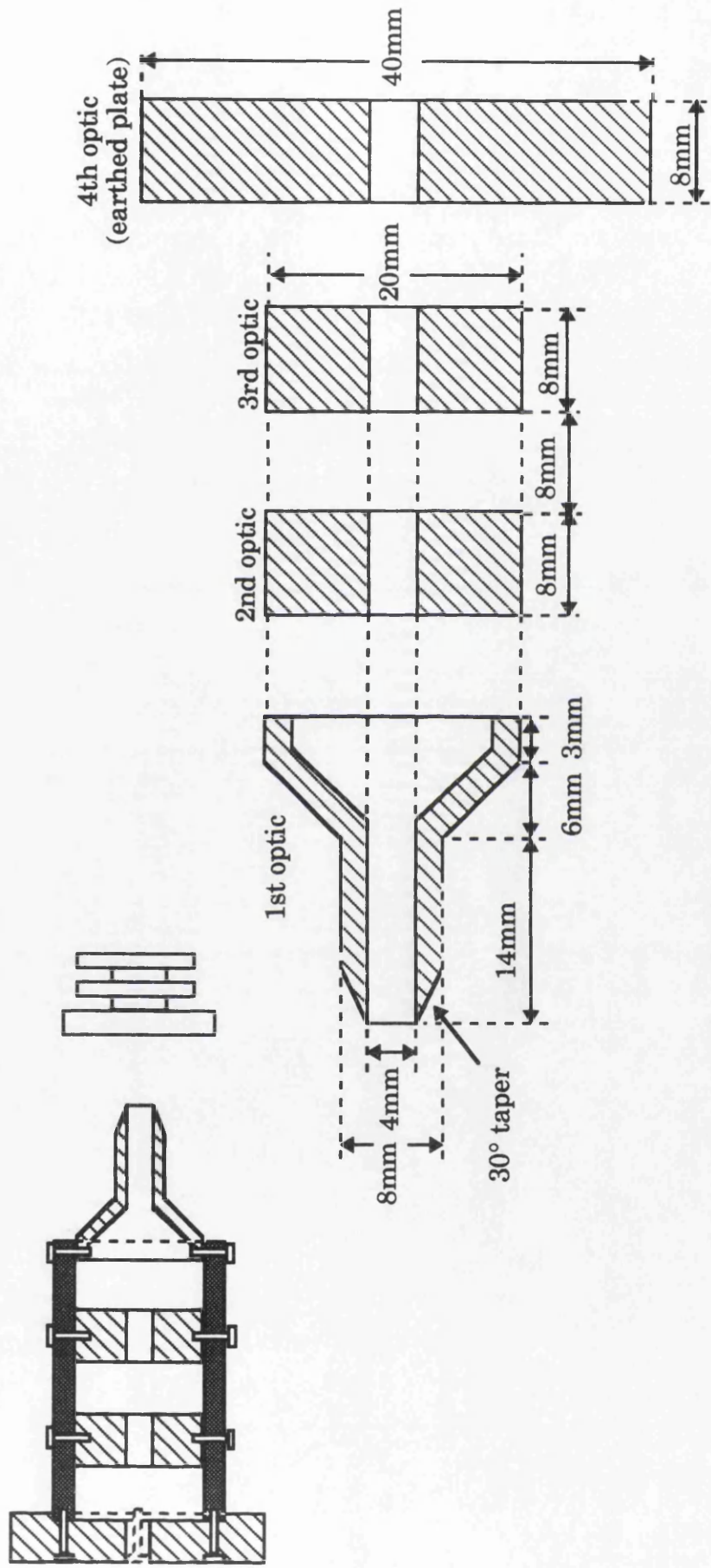
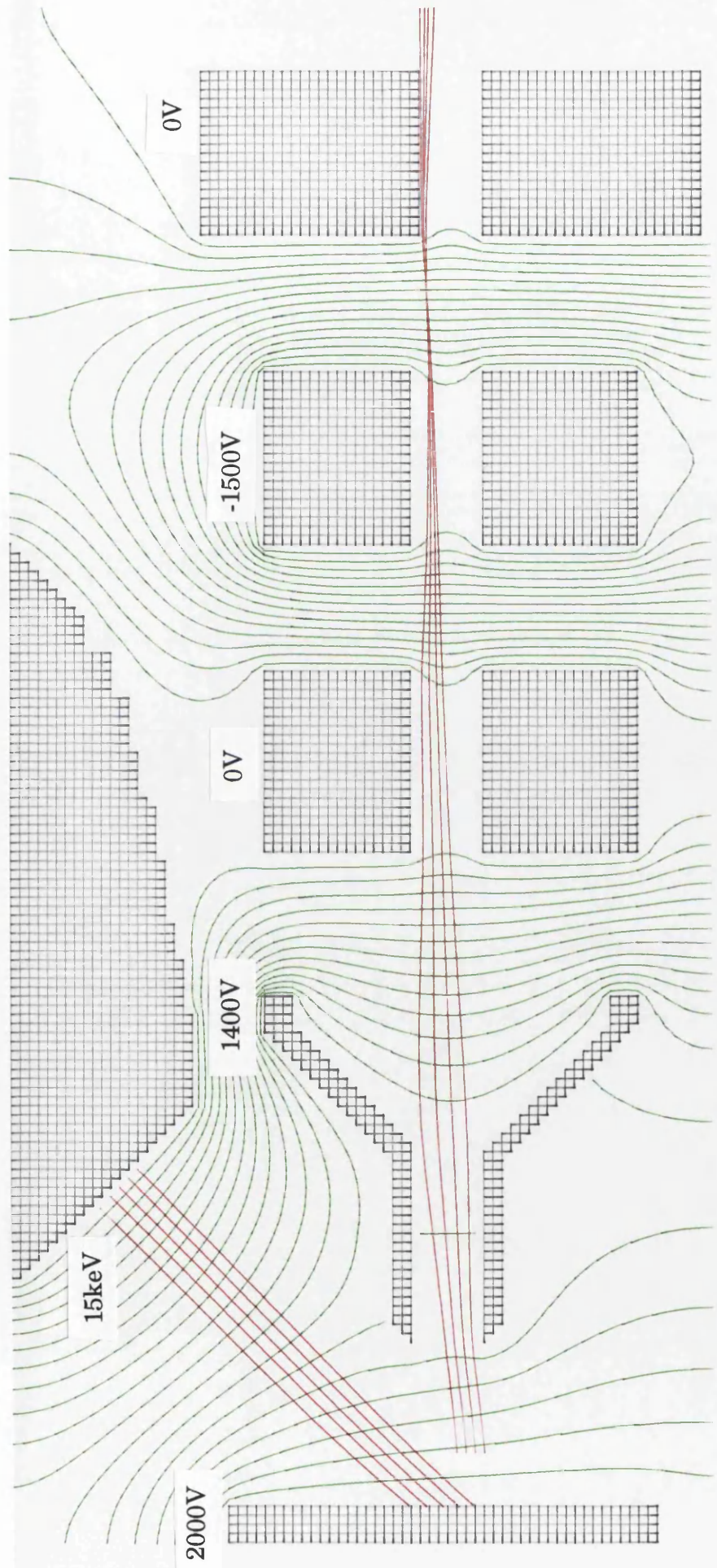


Fig.6.4 A cross-section through the new ion optics, with an insert showing the mounting arrangement

Fig.6.5 SIMION 3 calculation of the potentials generated by the optics shown in Fig.6.4, with the illustrated voltages applied. Equipotentials are shown at 100V intervals. The trajectory of a 15keV ion beam emitted from the ion gun and of ions formed in front of the sample stub are shown.



with a kinetic energy of 15keV they would arrive at the stub with a reduced energy of 13keV after overcoming the potential between the nose of the PIG and the sample stub. The encroachment of the earthed nose of the gun into the otherwise symmetric fields generated by the ion optics causes a pronounced asymmetry in the extraction fields. This is illustrated in Fig.6.5 which is a calculation of the fields in a plane passing through the central axes of the ion optics and the PIG. The asymmetric extraction field causes the ions to be transmitted off the central axis of the ion optics. The transmission of the system could be optimised by applying a voltage to the deflector plates in the plane perpendicular to that of Fig.6.5. It was found that the ion peaks of major species encountered in experiments with laser ablation and subsequent laser ionisation, which could be routinely detected with the original ion optics, were subject to apparent space charge broadening when the new optics were used. This problem was believed to be due to the small size of the aperture through the system, particularly in the nozzle region at the front of the first optic. To overcome this problem the first optic was redesigned and the aperture widened as illustrated in Fig.6.6.

Once the PIG had been positioned in-situ its performance was measured using a Keithley Instruments 610C electrometer to monitor the ion current incident on the sample stub. The stub was biased at a positive potential of 30 volts to prevent thermally liberated low energy electrons from contributing to the recorded current. The PIG was found to generally perform to its specifications, however, the electronics to control the Wien filter did not prove to be reliable and so this facility was not employed for the work reported in this chapter. As the system is not equipped with an electron imaging system it proved difficult to verify that the ion beam was focused to the expected size. A simple method for evaluating the spot-size is to scan the beam across an slit of known width. Such a slit was constructed from two razor blades with a spacing of $200 \pm 15 \mu\text{m}$ and Fig.6.7 shows the dependence of the measured current on the voltage applied to the deflector plates in the nose of the gun. In this manner it was determined that a spot size of $< 50 \mu\text{m}$ FWHM could be obtained at 7kV anode potential and spots of $< 20 \mu\text{m}$ FWHM were achievable with 15kV anode potential. Since the beam current in these experiments were several hundred nano-Amps, these spot-sizes indicate that the PIG was operating

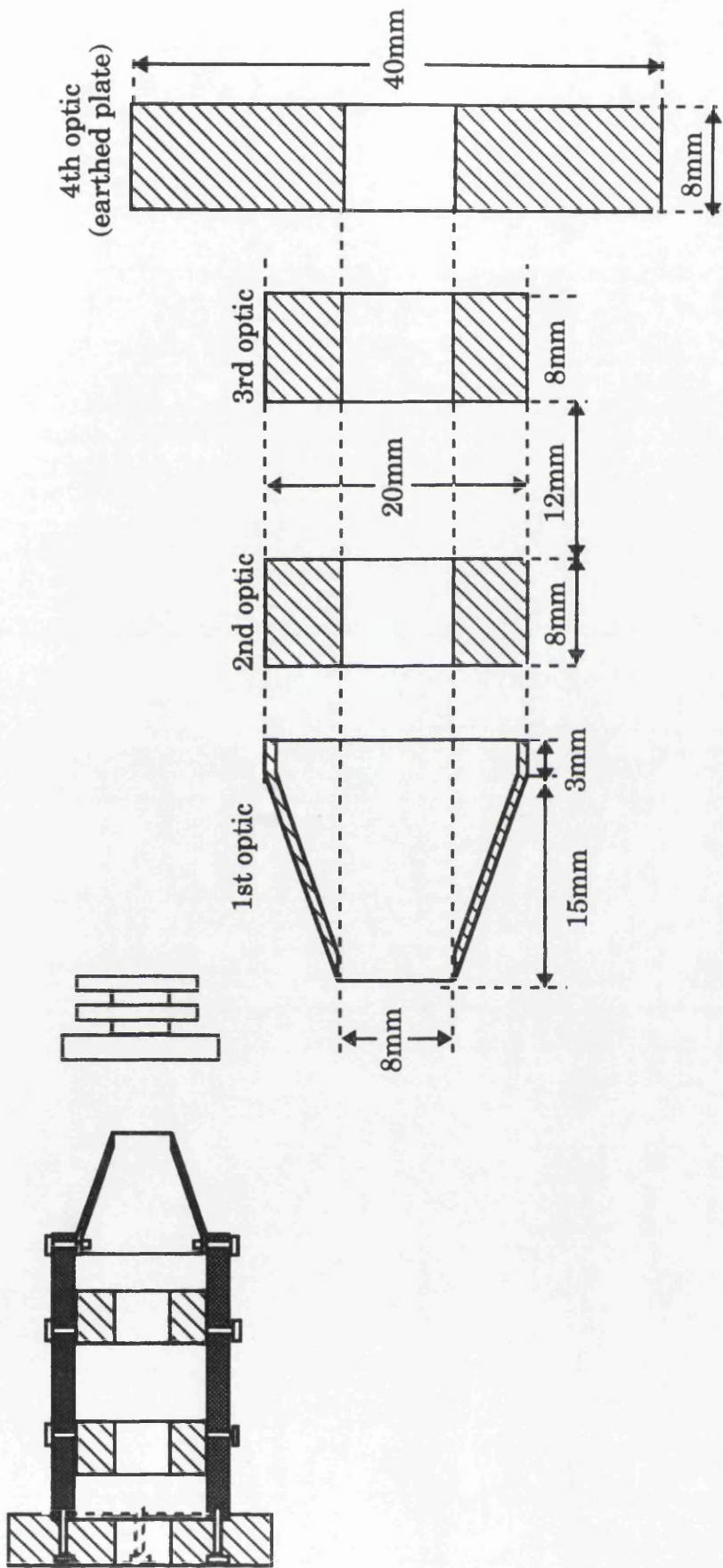


Fig.6.6 A cross-section through the modified ion optics, with an insert showing the mounting arrangement

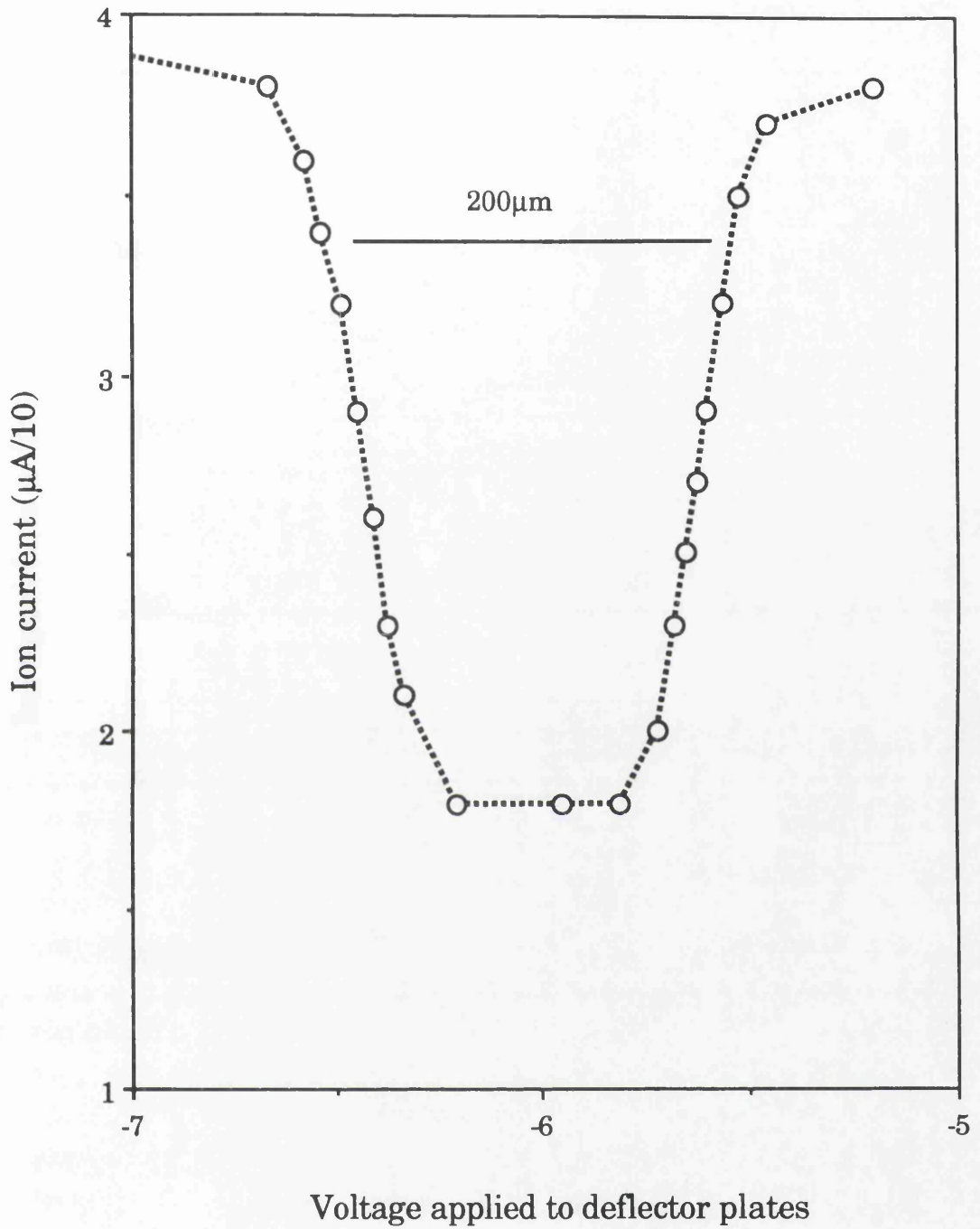


Fig.6.7 Ion current monitored across two razor blades separated by 200μm, as a function of the voltage applied to deflect the ion beam.

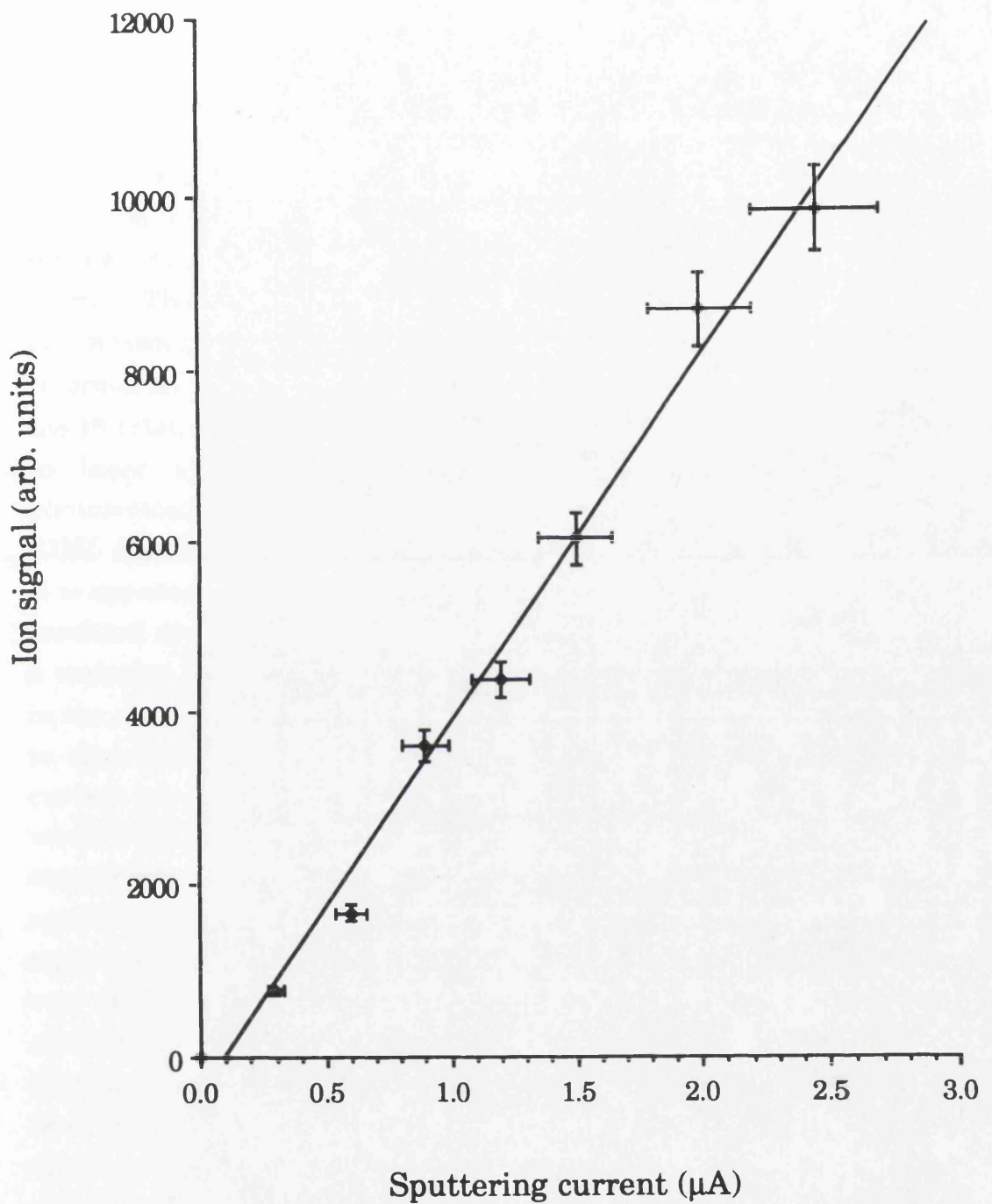


Fig.6.8 Mn RIMS signal as a function of the sputtering ion current. The sample was a Mn foil and the ion beam energy was 15keV.

to specification.

§6.3 Initial studies of ion bombardment with RIMS

In the initial experiments where the PIG was used as a source of atoms for subsequent RIMS detection, a pure Mn metal foil (25 μ m thick, Goodfellow Metals) was studied. The Mn atoms were detected by RIMS using the ionisation scheme discussed later in this chapter. Fig.6.8 shows the dependence of the recorded Mn ion signal on the sputtering ion current. The primary ion beam current was monitored as detailed above. It is apparent that the relationship between the sputtering current and the recorded RIMS signal is of a linear nature. This is in marked contrast to the I^n relationship between ablation laser power and PAI signal observed in laser ablation experiments, for example, in Fig.4.9. If the photoionisation process is saturated then the stability of the recorded RIMS signal is dictated mainly by the stability of the atomisation process. It is apparent, therefore, that if the PIG ion current varies by 10% then the resultant sputtered neutral yield will vary by 10%, whereas, from Fig.4.9, a variation in the ablation laser intensity of 10% would result in a change in the number of liberated atoms by approximately 40%. Hence, if the shot to shot stability of the ablation laser spot intensity and the ion beam current are the same it would be the ion sputtering technique which would result in the most stable RIMS signal. The stability of the PIG ion current was, in fact, found to be very high. Once the system had been operational for over an hour, allowing the temperature of the source region to reach equilibrium, then the monitored current would remain very stable. The sputtering ion current between laser shots was therefore estimated to be constant to better than 1%. In contrast the stability of the ablation laser intensity, when harmonic generation was employed, would be of the order of 5%. A graphic illustration of the increased stability of the signals obtained by employing ion bombardment is in Fig.6.9. This diagram shows the signals obtained as the tunable laser wavelength is scanned over the vicinity of two transitions in atomic manganese. Both spectra have been smoothed by a five step binomial routine. The spectrum acquired using laser ablation is typical of spectra obtained in this way, and although resonant enhancement of the signal is clearly evident, the peak intensities fluctuate more than is the case when ion sputtering was employed. The two spectra were not obtained under identical conditions;

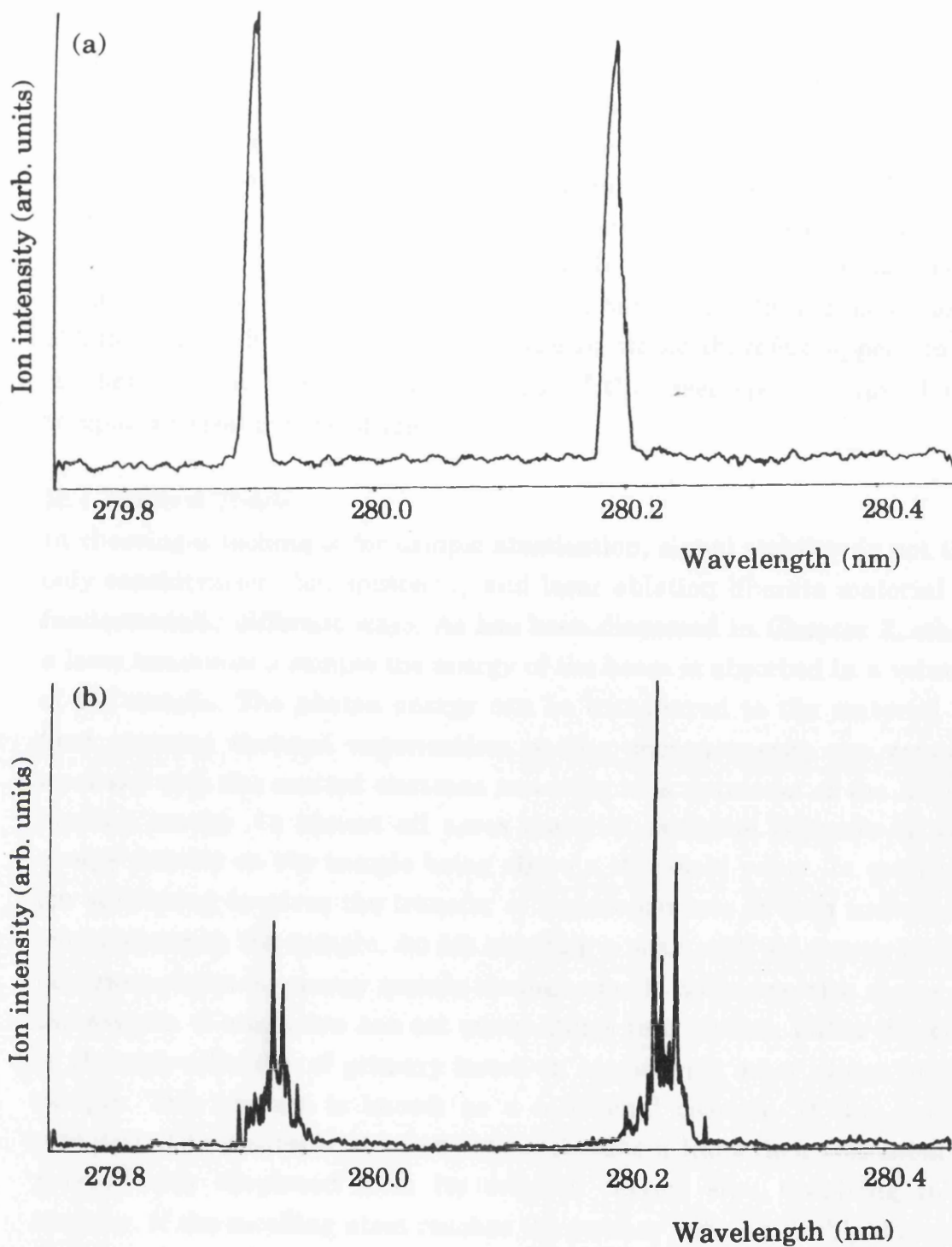


Fig.6.9 Mn RIMS signal as a function of the doubled laser wavelength. The sample was atomised by (a) ion sputtering and (b) laser ablation.

in the ion sputtering experiment the target was a pure metal foil, whereas in the laser ablation case the sample was aluminium with a 1% Mn content. Also, in the laser ablation experiment the photoionisation step was not saturated with the third harmonic of the Nd:YAG. Although these factors may to some extent explain the differences between the two spectra it is nevertheless apparent that the definition of the spectrum obtained with ion sputtering is better than has been obtained using laser ablation on the RIMS system. Ion sputtering would therefore appear to be the better suited atomisation technique if the laser spectroscopy of the sample material is to be studied.

§6.4 Neutral Yields

In choosing a technique for sample atomisation, signal stability is not the only consideration. Ion sputtering and laser ablation liberate material in fundamentally different ways. As has been discussed in Chapter 2, when a laser irradiates a sample the energy of the beam is absorbed in a volume of the sample. The photon energy can be transferred to the material as heat, causing thermal vaporisation, or the photon energy can remain localised with the excited electrons resulting in a reduction of the lattice binding energy. In almost all cases material emission depends on the energy density on the sample being above a threshold value. In contrast, ion sputtering involves the transfer of the momentum of each individual ion to atoms in the sample. An ion entering a solid with an energy in the keV range loses its energy mainly through elastic collisions with atoms in the sample. A single ion can set many atoms into motion, either directly or through collisions of primary knock-on atoms with other atoms in the sample. This process is known as a collisional cascade. If the energy transferred to a sample atom exceeds a threshold limit then this atom is permanently displaced from its original lattice site, resulting in a vacancy. If the recoiling atom reaches the surface with a suitably directed momentum and an energy exceeding the binding potential of the solid then sputtering occurs. As was mentioned in §1.7 a comprehensive theory to explain the sputtering of many materials has been developed (Sigmund, 1969; Benninghoven *et al*, 1987). Only the expressions from that theory which are of direct relevance to the work discussed in this chapter will be detailed. If the sample is monoelemental and monoisotopic with a random surface orientation free from any surface contamination then the sputter

Chapter 6

yield (Y) is given by:

$$Y = \frac{\text{Sputtered target atoms}}{\text{Primary ions}} \quad - \text{Eqn.6.1}$$

$$Y = \frac{0.042[\text{\AA}^{-2}] \alpha S_n[\text{eV} \cdot \text{\AA}^{-2}]}{U_s[\text{eV}]} \quad - \text{Eqn.6.2}$$

where U_s is the surface binding potential of the solid, usually taken as the sublimation energy for most elements, α is a dimensionless factor dependent on the relative masses of the projectile and the target and the angle of the ion beam on the sample. For ion beam energies in the keV range:

$$\alpha \approx 0.15 + 0.13 \left(\frac{M_2}{M_1} \right) \quad - \text{Eqn.6.3}$$

where M_1 and M_2 are the masses of the primary and secondary particles respectively. The term S_n in Eqn.6.2 is the nuclear stopping cross-section for particles of energy E_p . This may be expressed as:

$$S_n = 84.77 \frac{Z_1 Z_2}{(Z_1^{2/3} + Z_2^{2/3})^{1/2}} \frac{M_1}{M_1 + M_2} s_n(\epsilon) \quad - \text{Eqn.6.4}$$

where Z_1 is the atomic number of the incident ion and Z_2 is the atomic number of the sample. $s_n(\epsilon)$ is the reduced stopping cross-section which can be approximated by:

$$s_n(\epsilon) = \frac{\frac{1}{2} \ln(1+\epsilon)}{\epsilon + 0.14\epsilon^{0.42}} \quad - \text{Eqn.6.5}$$

where ϵ is the dimensionless reduced energy, defined as:

$$\epsilon = \frac{32.5 M_2 E_p(\text{KeV})}{(M_1 + M_2) Z_1 Z_2 (Z_1^{2/3} + Z_2^{2/3})^{1/2}} \quad - \text{Eqn.6.6}$$

As an example, consider a 13keV beam of argon ions normally incident on the surface of a manganese metal sample. M_1 is therefore 40 amu and M_2 is 55 amu. The atomic numbers of the two species are 18 and 25.

Substituting these values into Eqn.6.6 gives a value for the reduced energy of 0.138. Using this value in Eqn.6.5 gives $s_n(\epsilon)=0.325$ and, therefore, from Eqn.6.4, $S_n(E) = 1329.5$. Hence, the sputter yield is:

$$Y = \frac{18.36}{U_s \text{ (eV)}}$$

For manganese U_s is $\sim 2.5\text{eV}$ if it is taken simply as the sum of the latent heats of fusion and vaporisation, and hence the sputter yield is 7.3. It is interesting to note that iron, which is only one atomic mass unit heavier than manganese, has a substantially higher latent heat of sublimation, $\sim 4\text{eV}$. This leads to a markedly smaller sputtering yield for the same incident current, ~ 4.5 .

The sputter yield is also dependent on the angle of incidence, θ , of the ion beam with respect to the surface normal. For polycrystalline materials the relationship is given by:

$$\frac{Y(\theta)}{Y(0)} = (\cos \theta)^{-f} \quad \text{- Eqn.6.7}$$

where $Y(0)$ is the sputter yield at normal incidence, which can be calculated from the equations above and f is a constant which depends primarily on the ratio of the masses of the incident and sputtered species. For $M_2/M_1 < 3$ the value of f is approximately $5/3$. Hence, if in the example given above the angle of incidence of the ion beam was increased to 45° , the sputter yield would increase by a factor of 1.8, and at an angle of 60° with respect to the surface normal the sputter yield would be increased by a factor of 3.2. Maxima in the sputter yield are usually observed at around 60° . However, at oblique angles the relationship in Eqn.6.7 breaks down as the reflection coefficient increases until a critical angle is reached where the ions do not have sufficient energy perpendicular to the surface to overcome the potential barrier and all of the ions are totally reflected.

The energy distribution of the atoms liberated by particle sputtering under idealised surface conditions can also be obtained from the theory of Sigmund:

$$\frac{dn}{dE} = \frac{3}{2\pi^2} \frac{\alpha S_n(E_P)}{C_0} \frac{E}{(E+U_s)^{n+1}} \quad - \text{Eqn.6.8}$$

where E_p is the energy of the incident ion, E is the energy of the secondary atom, n is the power law exponent, usually taken to be 2 and C_0 is a constant of the scattering cross-section. This distribution increases linearly at $E \ll U_s$, has a maximum at $E=U_s/2$ and has a E^{-2} dependence for $E \gg U_s$, as has been observed experimentally (Thompson, 1968). Eqn.6.8 can be rearranged into a velocity distribution form (Schorn *et al*, 1987):

$$\frac{dn}{n} = \frac{v^2 \cos \theta}{(v^2 + v_0^2)^3} dv \quad - \text{Eqn.6.9}$$

where v is the velocity of an atom liberated at an angle θ to the surface normal. v_0 is the characteristic velocity which is calculated from the binding energy:

$$v_0 = \sqrt{\frac{2U_s}{M_2}} \quad - \text{Eqn.6.10}$$

It is apparent that the energy distribution of the sputtered atoms is not dependent on either the energy of the incident ion or the sputtering current density. This is in contrast to laser ablation where, as illustrated in Chapter 4, the velocity distribution of the ablated material can be a strong function of the ablation laser power. It is possible to use Eqn.6.9 to evaluate the temporal distribution that would result if the sputtered atoms were ionised by laser beam. Fig.6.10 shows the predicted temporal distribution for a sputtered species of mass 55 amu with the probe laser positioned 3mm from the sample surface, for various values of U_s . It was assumed that all the atoms were emitted normal to the sample surface. Also shown in Fig.6.10 are the distributions calculated from the half-range Maxwell-Boltzmann distribution for characteristic temperatures of 2700K and 5000K. It is apparent that the atoms liberated by ion sputtering are more energetic than those liberated by laser ablation due to a purely thermal mechanism. The distributions in Fig.6.10 were calculated assuming that the atoms were liberated instantaneously from the sample surface. When ion sputtering is combined with RIMS it is not necessary to produce a short pulse of sputtered material. Fig.6.11 shows how the

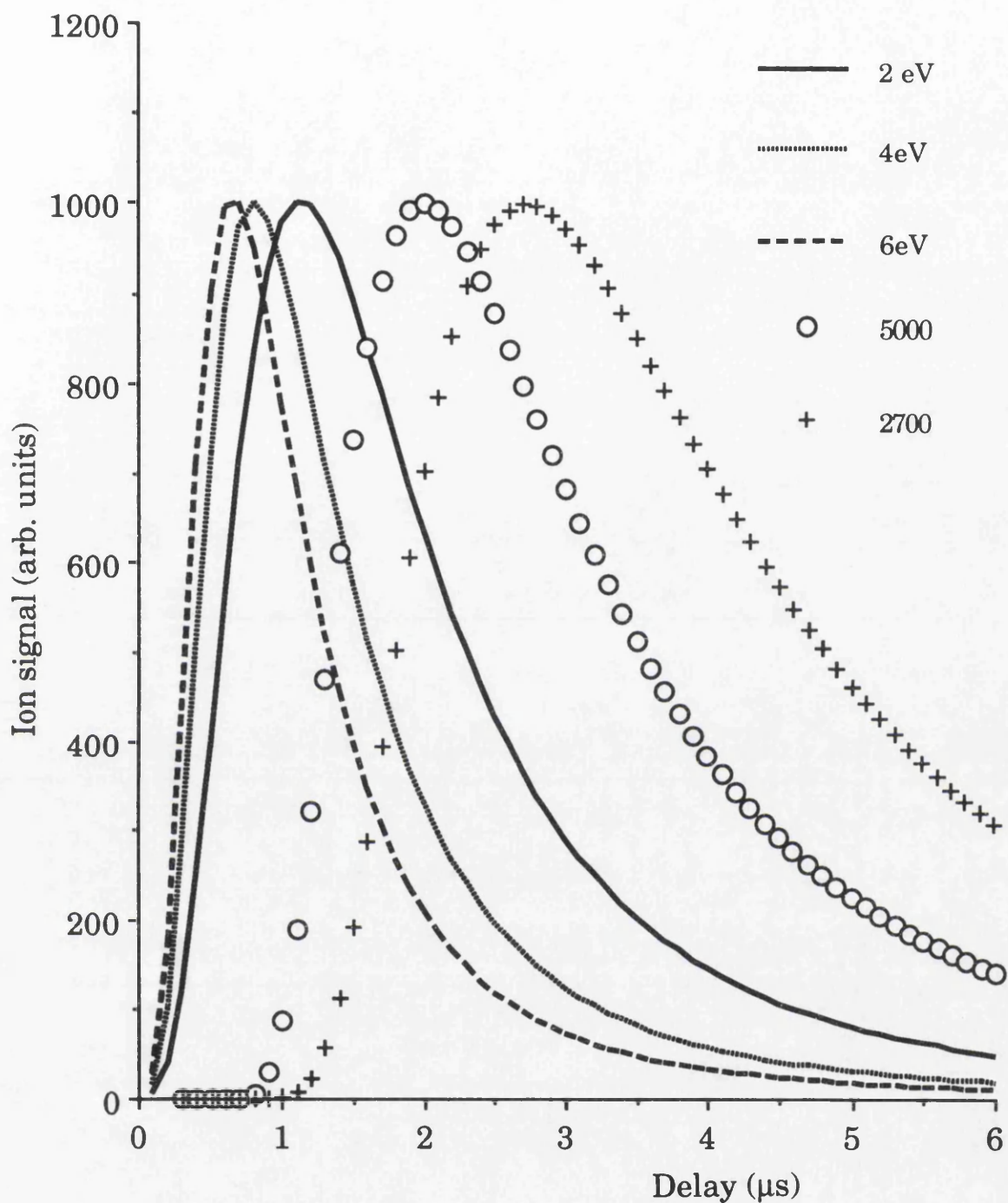


Fig.6.10 Calculation, from Eqn.6.9, of the time-of-flight distribution of Mn atoms sputtered by an infinitesimal short pulse of sputtering ions. A range of surface binding energies are shown. The distance between the target and the detector is 3mm. Also shown is the evaluation of the half-range Maxwell-Boltzmann velocity distribution for manganese for characteristic temperatures of 5000K and 2700K.

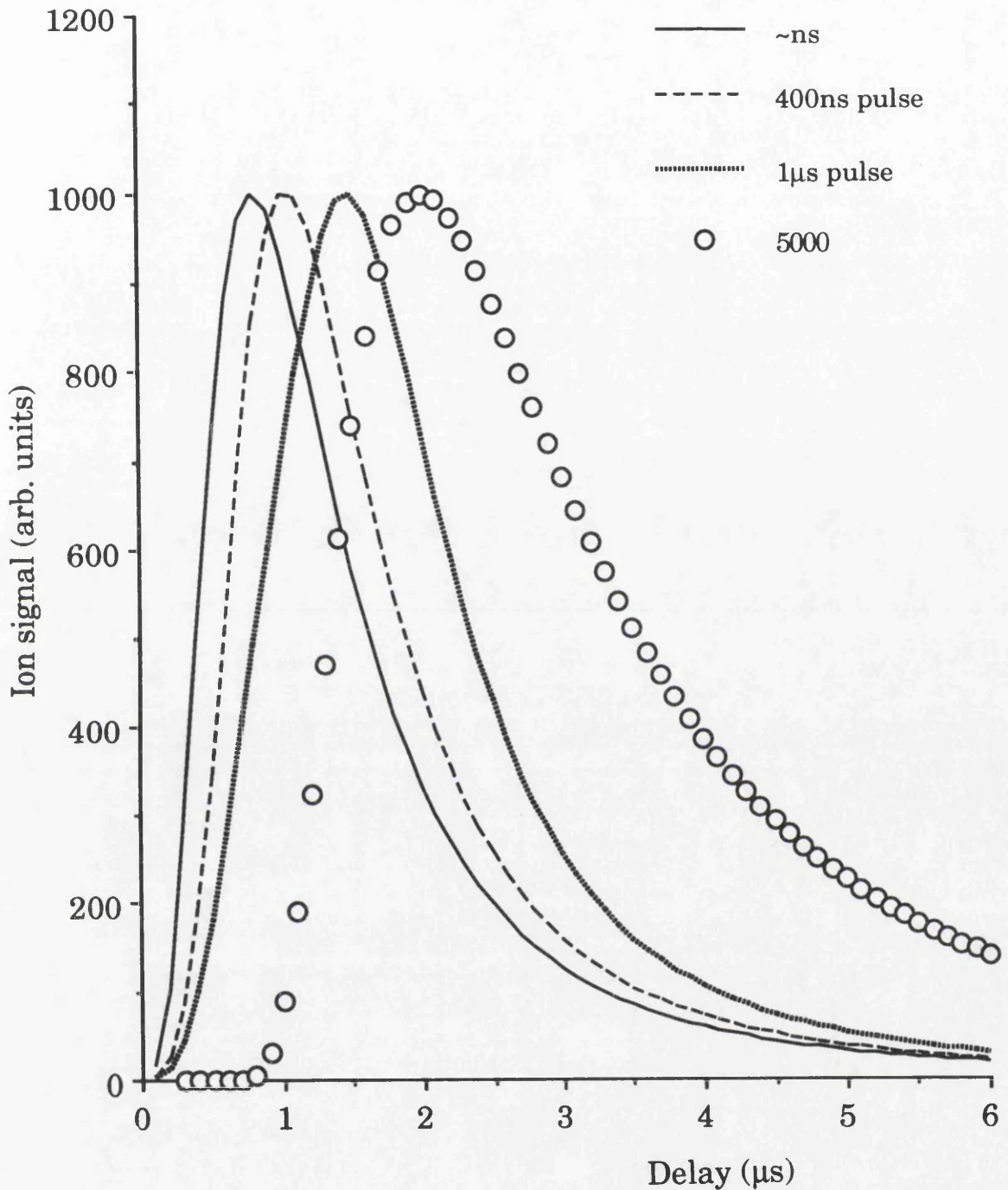


Fig.6.11 Calculation, from Eqn.6.9, of the time-of-flight distribution of Mn atoms sputtered by a pulse of ions, assuming a surface binding energy of 4eV. A range of ion pulse length are shown. The distance between the target and the detector is 3mm. Also shown is the evaluation of the half-range Maxwell-Boltzmann velocity distribution for manganese for a characteristic temperature of 5000K.

calculated temporal distribution is affected if the sputtering beam has a pulse length of $1\mu\text{s}$. It can be seen that as the pulse length is increased the width of the observed temporal distribution becomes significantly broadened, but it is still markedly smaller than the half-range Maxwell-Boltzmann distribution with a characteristic temperature of 5000K . The ion beam of the PIG can be pulsed by applying a pulsed potential to the plates in front of the Faraday cup plates, which would scan the beam across the aperture. Increasing the pulse length therefore increases the number of ions incident on the sample surface, and hence the number of sputtered neutrals. Pulsing the sputtering source is advantageous for the trace analysis of small samples since it increases the amount of the sample that can be analysed by the pulsed RIMS lasers by a factor of $\sim 10^5$ compared with using a continuous sputtering beam. However, in the work reported in this chapter the samples were plentiful and the PIG was not pulsed.

As the neutral yield from ion sputtering can be quantified it is possible to use this technique to determine the amount of atoms liberated by laser ablation. As has been mentioned in Chapter 2, this technique has been applied to studies of ZnS where LIFS was used to monitor the yields from both atomisation methods (Arlinghaus *et al*, 1989b). The same technique was used by Dubreuil and co-workers (1992) where RIMS was used as the probe technique in studies of the laser ablation of metals. In order to elucidate the yields from the ablation process this technique was employed in Glasgow using RIMS as the probe technique and a manganese foil as the sample. Fig.6.12 shows the temporal distribution of the laser ablated Mn atoms, which can be fitted with a half-range Maxwell-Boltzmann distribution with a characteristic temperature of 2700K . This temperature is slightly above the boiling point of Mn (2373K), but as it is considerably below the critical temperature this was taken as indicative of a mainly thermal ablation process. It is interesting to note that the characteristic temperature derived from the temporal distribution of the pure metal is substantially lower than that obtained for Mn present as a minor constituent in a steel sample ($\sim 4500\text{K}$), as illustrated in Fig.4.45. The distribution shown in Fig.6.12 was obtained with a loosely focused probe beam of $\sim 0.5\text{mm}$ diameter. This is not the optimal configuration for determining temporal distributions and the poor fit to the data at low

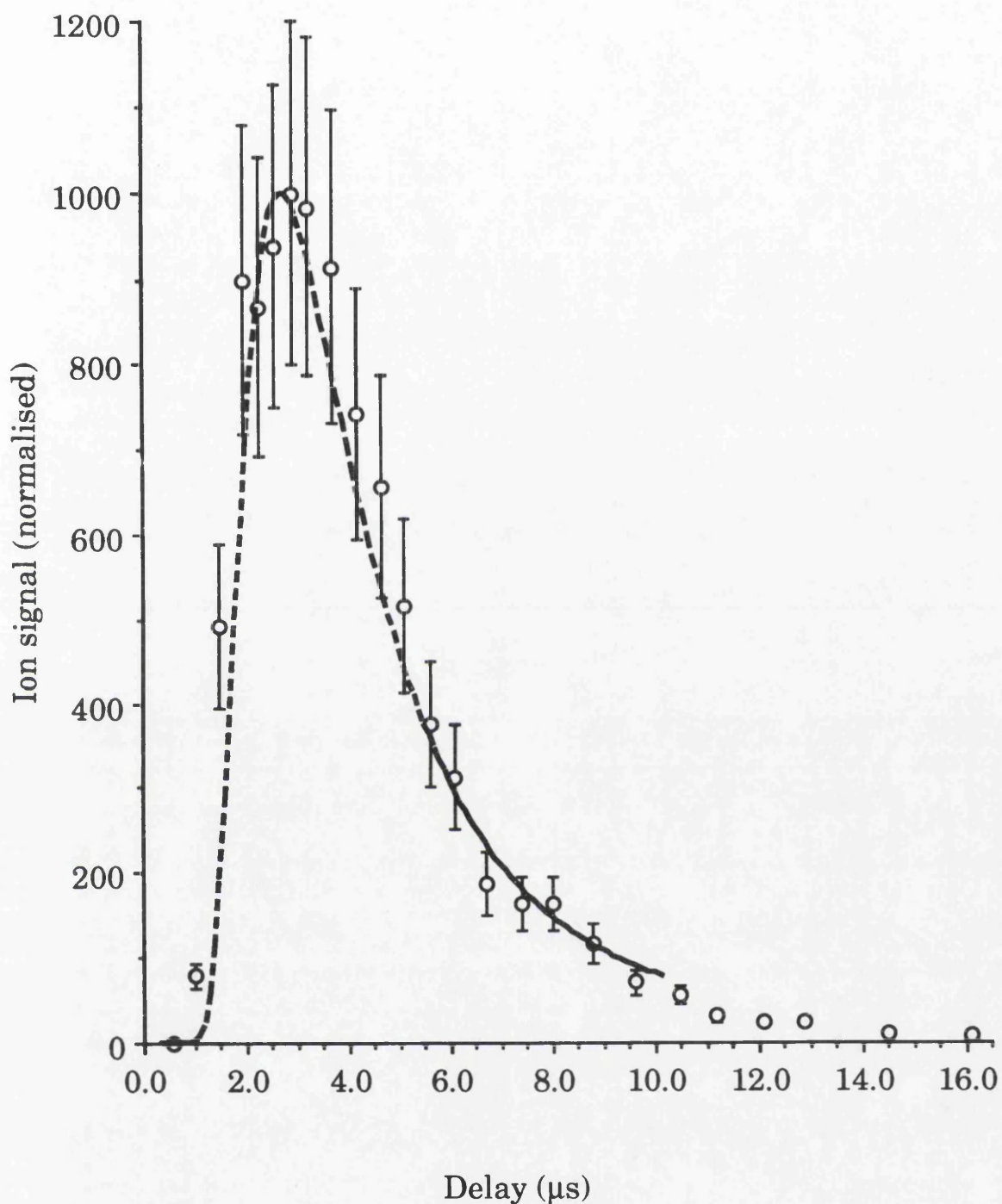


Fig.6.12 Temporal distribution of laser ablated Mn atoms from a pure foil sample. The ablation laser power was 4.5mW and the distance between the target and the detector was 3mm. The data is fitted by the half-range Maxwell-Boltzmann velocity distribution for manganese for a characteristic temperature of 2700K.

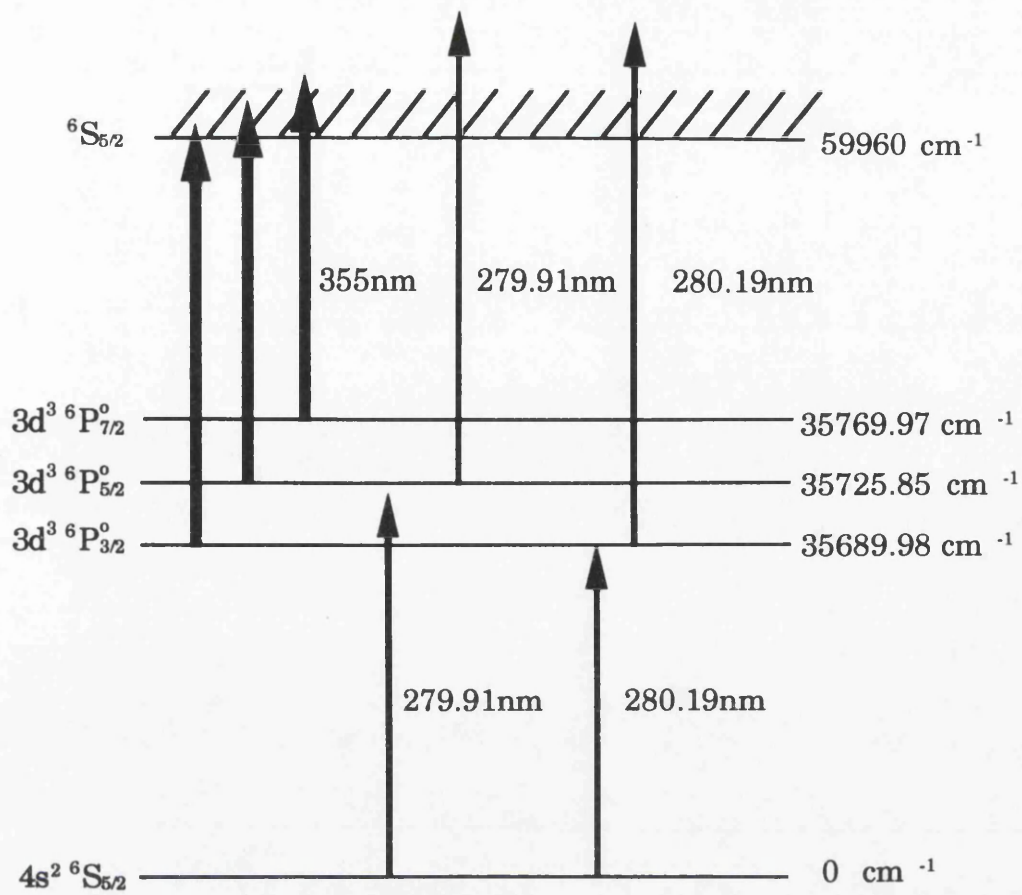
delays was believed to be due to this. In order to ensure that the signals from laser ablation and ion sputtering were of comparable sizes the delay between the firing of the ablating and ionising lasers was set to $16\mu\text{s}$. The signal recorded at this delay is approximately 1% of that recorded at the optimal delay. The RIMS signals resulting from sputtering with a $1\mu\text{A}$ current and a 15kV anode potential and laser ablation with an average power of 4.5mW were monitored. The pulse energy and focal conditions of the RIMS laser beams and the distance between the sample surface and the beam were kept constant throughout the experiment. It was found that the laser ablation initiated RIMS signal averaged from five measurements accumulated from 500 laser shots was 260 ± 50 times larger than the signal resulting from sputtering. If the delay between the ablation laser and the RIMS laser pulse had been optimal, from Fig.6.12, the difference in signals sizes would be $\sim 3\cdot 10^4$. The number of atoms liberated by the ion beam was calculated on the basis that a $1\mu\text{A}$ current is the result of $6.25\cdot 10^{12}$ singly charged ions being incident on the sample each second. From the example cited earlier in this section the sputter yield of Mn for a normally incident 13keV beam is 7.3. This is increased by a factor of 1.8 because the ion beam is incident on the sample at an angle of 45° . The total number of neutral atoms emitted per second is therefore $\sim 8.2\cdot 10^{13}$. The most probable velocity of these atoms in the direction perpendicular to the sample surface is, from Fig.6.10, $3\cdot 10^3\text{m/s}$. The diameter of the ionising laser spot was $\sim 0.5\text{mm}$ and if it is assumed that all the available liberated atoms were interrogated by the secondary beam then the number of atoms available each laser shot is $\sim 1.3\cdot 10^7$. Therefore the number of atoms liberated per shot by the ablation laser is $\sim 4\cdot 10^{11}$. In order to ensure that the ion beam was incident on the centre of the sample stub it was necessary to adjust the manipulator so that the sample was 5mm further from the flight tube than was the case in the previous laser ablation experiments. This resulted in the ablation laser being less strongly focused than had been the case in the previous experiments. The ablation laser spot size was estimated to be $400\mu\text{m}$ diameter. It is possible to calculate the number of atoms in a monolayer of Mn, from the density, to be $1.9\cdot 10^{13}/\text{mm}^2$. From these measurements it would appear that an upper estimate of the laser removal rate is 0.5 monolayers/shot. Although this measurement and analysis are of a provisional nature the results are further illustration that laser ablation can be used to liberate sub-

monolayer quantities of material per shot.

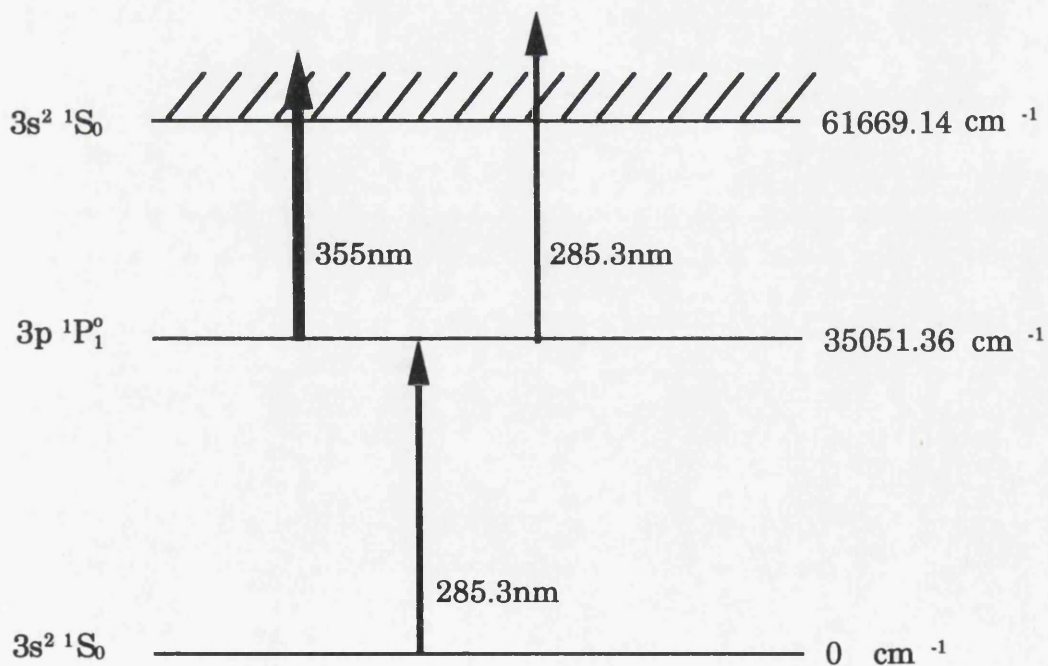
§6.5 Trace analysis of metals using RIMS

In order to allow a comparison between the different sample atomisation techniques discussed in this thesis a set of well characterised aluminium standards were obtained (Alusuisse-Lonza Services AG, Neuhausen, Switzerland). The composition of these samples is shown in Table 6.1. The elements chosen for this investigation were manganese and magnesium, which are present in the standard samples at levels from ppm to 1%. Therefore, the analysis of these elements can illustrate the linearity of the technique and the limits of detection for elements from a complex matrix. Manganese and magnesium have similar ionisation potentials and both elements can be ionised using a simple 1+1 scheme. However, the thermal properties of the two materials are considerably different. The melting point of magnesium (923K) is very similar to that of aluminium (933K), whereas the melting point of manganese (1523K) is substantially higher. The lowest lying excited states of both Mn and Mg are high enough in energy that ultra-violet photons are required to induce the transition from the ground state. However, whereas in the scheme previously discussed for aluminium the photon energy of the undoubled light was sufficient to promote the excited electron into the ionisation continuum, this is not the case for Mn or Mg. As shown in Fig.6.13, ionisation requires the absorption of two ultra-violet photons. Since these photons are produced by frequency doubling of the dye laser output the power available was limited to $\sim 100\mu\text{J}$. In order to saturate the ionisation step it is possible to introduce the higher pulse energy ($>1\text{mJ}$) third harmonic wavelength from the Spectron Nd:YAG laser. The experimental arrangement for combining the beams is shown in Fig.6.14. An obvious disadvantage of introducing a high pulse energy beam of ultra-violet photons into the chamber is that two photon ionisation can be induced in any species which has an ionisation potential below $\sim 7\text{eV}$. However, since the elements under analysis were not liable to isobaric interference this was not considered to be a problem in this case.

The dependence of the Mn ion signal on wavelength has been shown in Fig.6.9. In the work reported subsequently the transition at 280.19nm was used. Fig.6.15 shows the wavelength dependence of the Mg signal which



(a) Mn



(b) Mg

Fig.6.13 RIMS schemes employed for (a) Mn and (b) Mg

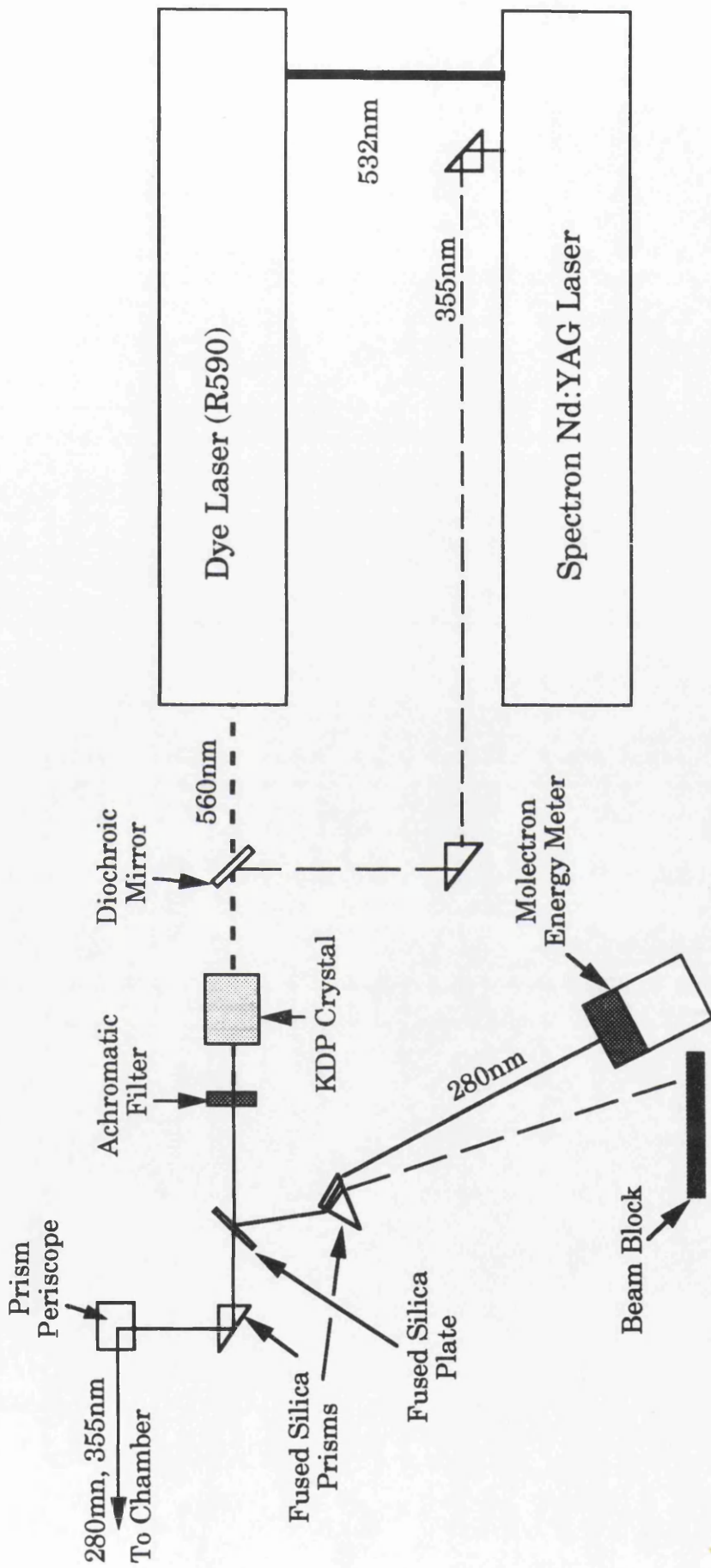


Fig.6.14 Experimental arrangement used to detect trace levels of Mn and Mg

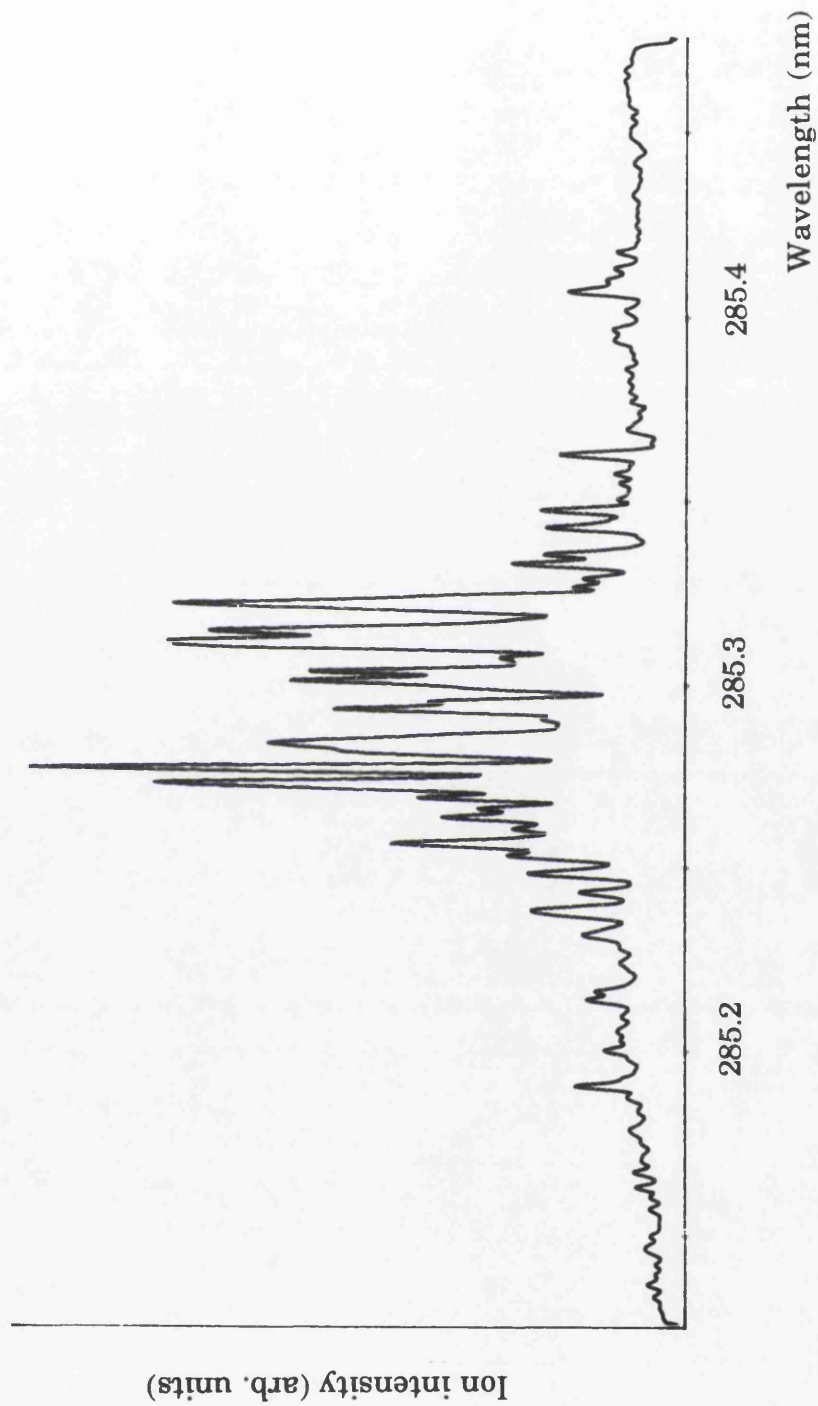


Fig.6.15 ^{24}Mn RIMS signal as a function of the dye laser wavelength. The sample was atomised by laser ablation.

was obtained using only the doubled output from the dye laser. The sample was the aluminium standard 636 and laser ablation was employed. The effect of increasing the RIMS laser power on the Mg ion signal is shown in Fig.6.16. The gradient of this graph is 1 ± 0.2 , this is indicative of the bound-bound transition being saturated and hence, the number of ions depends linearly on the laser power. When the high pulse energy 355nm beam is introduced it is possible to saturate the ionisation process, as is evident in Fig.6.17. In the work reported in this chapter the 355nm wavelength, with a pulse energy of $\sim 1\text{mJ}$, was combined with the tunable beam. Hence the RIMS transitions would be saturated and it is possible to compare signals obtained from samples with different analyte concentrations.

The samples were initially studied using laser ablation coupled with the RIMS schemes detailed above. The samples were all prepared in the same way, discs of $\sim 5\text{mm}$ diameter were cut from the insides of the samples. The surfaces of these discs were roughen with 800 grit SiC paper. They were then immersed in a concentrated sodium hydroxide solution for approximately 30 seconds and were subsequently washed ultrasonically in methanol and finally acetone. From the conclusions drawn from the work discussed in Chapter 4, the second harmonic 532nm wavelength of the Nd:YAG laser was employed for laser ablation. The laser power was constrained so that a large leakage signal was not observed.

Fig.6.18 shows the mass spectra obtained from the 636 standard under the conditions outlined above, with the RIMS lasers tuned to the wavelength of the Mn transition. It is apparent that the dominant peak is from atomic manganese which, from Table.6.1 constitutes 1% of the sample. There are other smaller peaks apparent in this spectra, the one at ~ 27 amu can be attributed to atomic aluminium and the broader peak prior to this is the related leakage signal. There is also a peak observed with a mass of ~ 54 amu, one mass unit smaller than Mn. This section of the spectra is shown in much higher magnification in Fig.6.19. The same peaks were evident with the 144 standard which has a lower concentration of the analyte. When the 117 standard was studied the same peaks were again observed, with markedly different proportions, as shown in Fig.6.20. In this mass spectra, as would be expected, the Mn peak is markedly smaller than those of mass 27 amu and 54 amu. The fact that the ratio between the

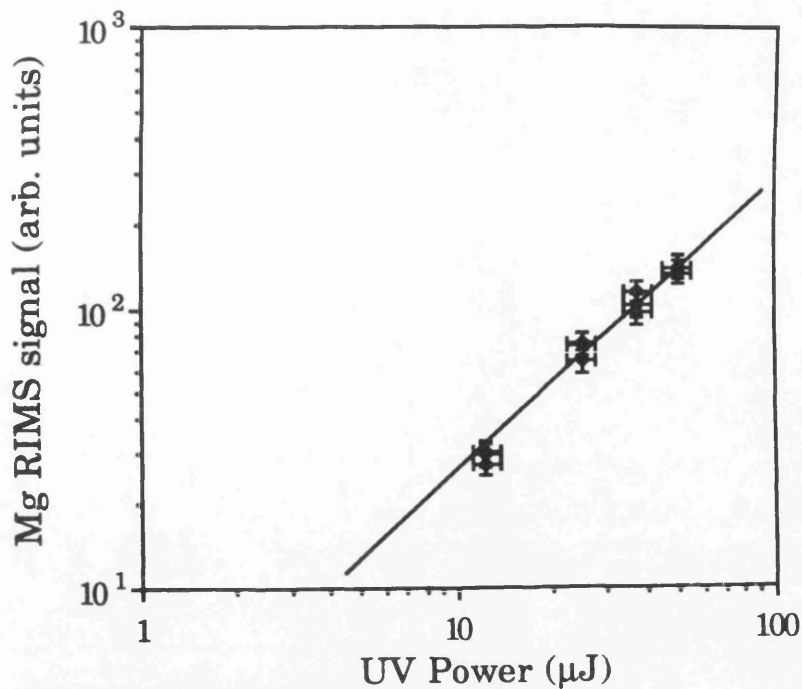


Fig.6.16 Dependence of the Mn RIMS signal as a function of the intensity of the doubled dye laser radiation showing a linear relationship. The sample was atomised by laser ablation.

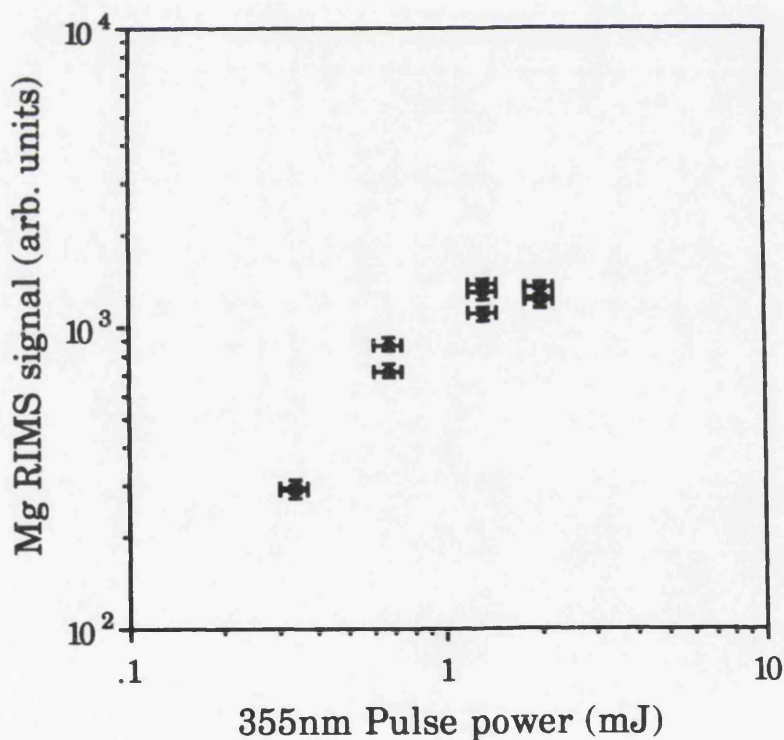


Fig.6.17 Dependence of the Mn RIMS signal as a function of the intensity of the 355nm wavelength radiation, illustrating the saturation of the ionisation process. The pulse energy of the doubled dye laser radiation was $\sim 50\mu\text{J}$.

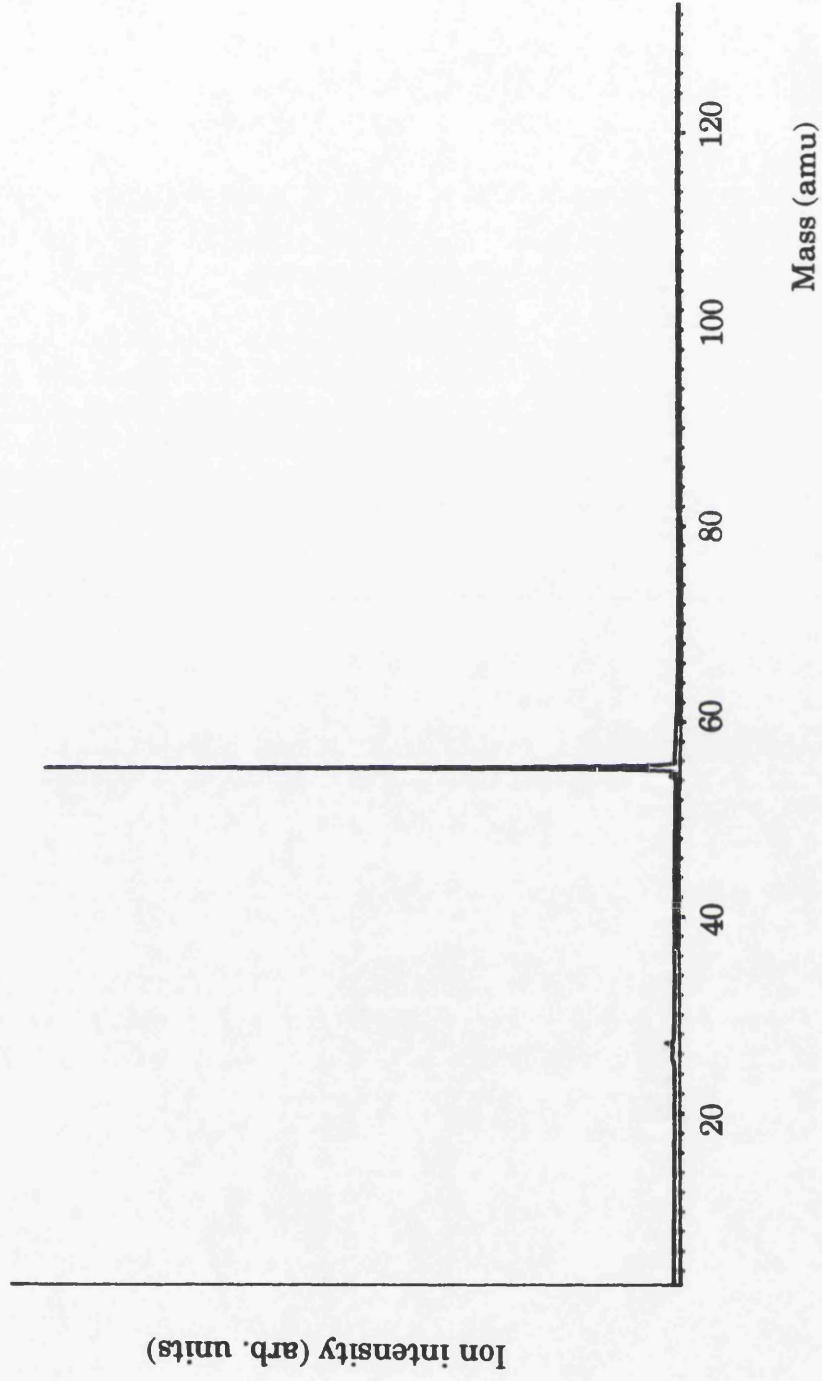


Fig.6.18 Mass spectra from the 636 aluminium standard, atomised by laser ablation with the RIMS lasers tuned to the Mn scheme.

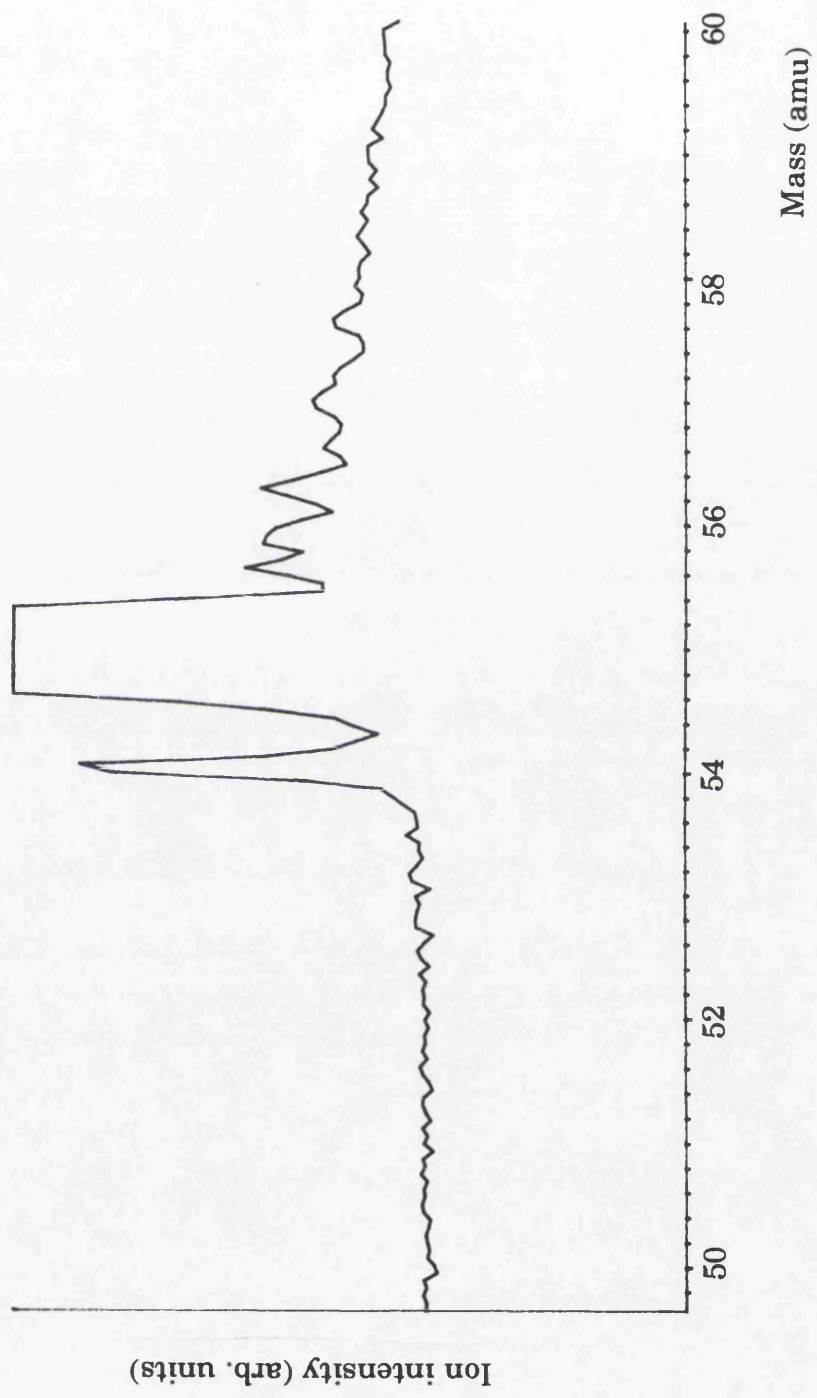


Fig.6.19 A magnified section of the mass spectra from the 636 aluminium standard, showing the peak at ~54 amu.

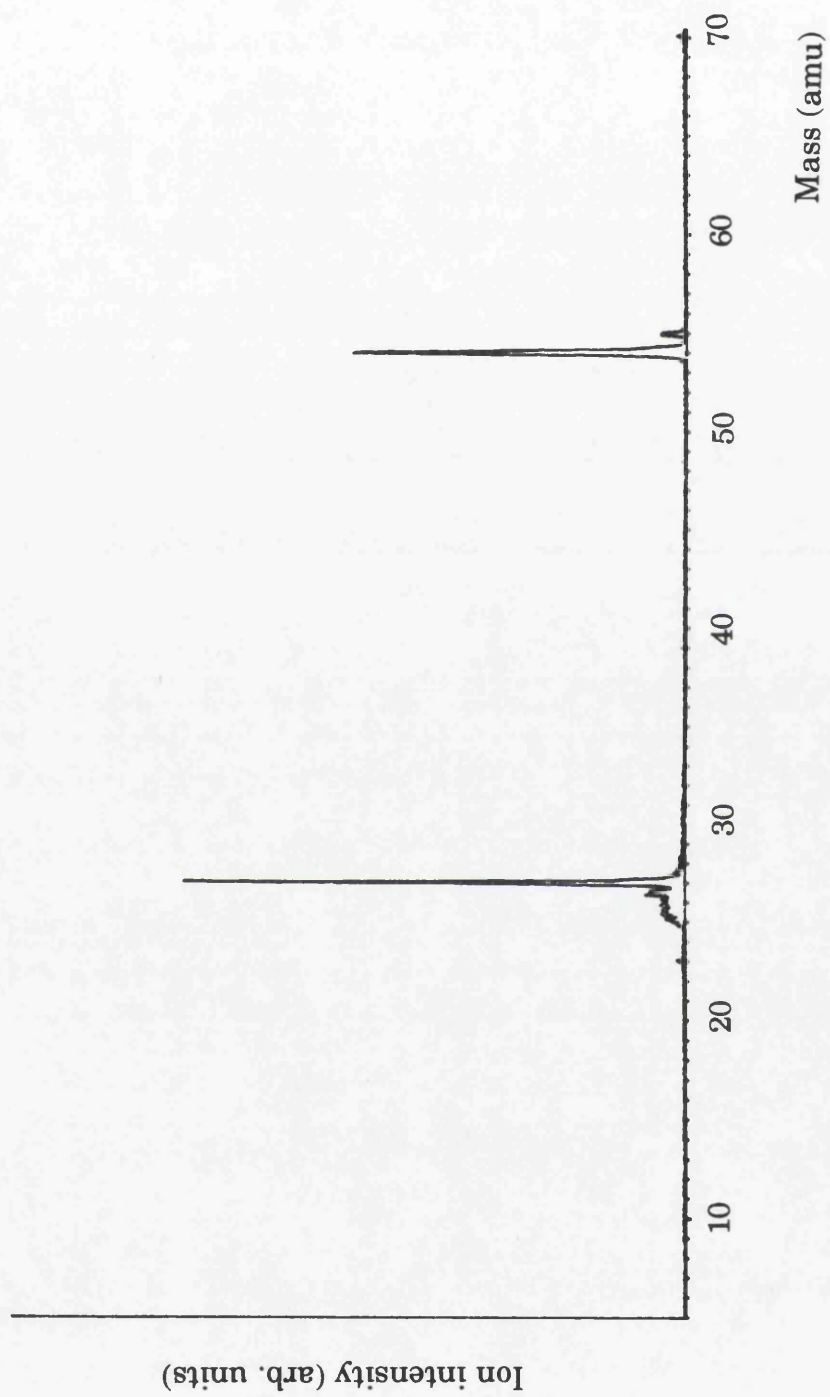


Fig.6.20 Mass spectra from the 117 aluminium standard, atomised by laser ablation with the RIMS lasers tuned to the Mn scheme.

peaks at 27 and 54 amu is approximately constant for the different samples leads to the conclusion that the species of mass 54 amu is a compound of aluminium, the matrix material. It is most probable, therefore, that the peak at mass 54 amu is the aluminium dimer, which is either directly photoionised or produced by the photo-fragmentation of a larger species. The possibility of the formation of cluster species during the laser ablation of aluminium was discussed in Chapter 4. The cluster species of aluminium have been extensively studied in recent years and the ionisation potentials and dissociation energies of clusters Al_n ($n=2$ to 7) have been determined experimentally (Hanley *et al*, 1987). The ionisation potential of the dimer was determined to be between 5-6eV, thus two photon ionisation via two 355nm wavelength photons is possible. Fig.6.21 shows the mass spectra obtained from the 121 standard when only the 355nm wavelength beam interrogated the ablated plume. It is apparent that the 54 amu signal is a factor of two larger than the atomic Al signal. When the same sample was studied using only the doubled dye laser radiation to affect ionisation the resulting spectra was markedly different, as shown in Fig.6.22. In this case the atomic aluminium signal is a factor of four larger than that at 54 amu. It would therefore appear that 355nm wavelength photoionisation of the dimer has an enhanced probability compared with the process at 280.19nm. Fig.6.23 shows a portion of the room temperature LIFS spectrum of the aluminium dimer (Cai *et al*,1991). It is apparent that a 355nm photon can excite an electron from the $\nu=0$ level of the ground state ($X^3\Pi_u$) into the rotationally excited level of the $\nu=5$ level of the $E^3\Sigma_g^+$ valence state. This may explain the enhancement observed in the dimer signal at the 355nm wavelength, compared with the 280.19nm case. It would appear therefore, that the most probable source of the recorded 54 amu signal would be the direct two photon ionisation of neutral dimers. It is not possible from this evidence to determine whether the neutral dimer species are formed directly by the ablation laser or if they are produced by the photo-fragmentation of larger species. In subsequent LAMMS experiments it was noted that the 54 amu signal was consistently below 5% of the size of the atomic aluminium signal. Hence the results discussed above are a graphic illustration of how an accidental resonance, in this case in Al_2 , can lead to a spectra which is not representative of the sample composition. Thus care must be taken in

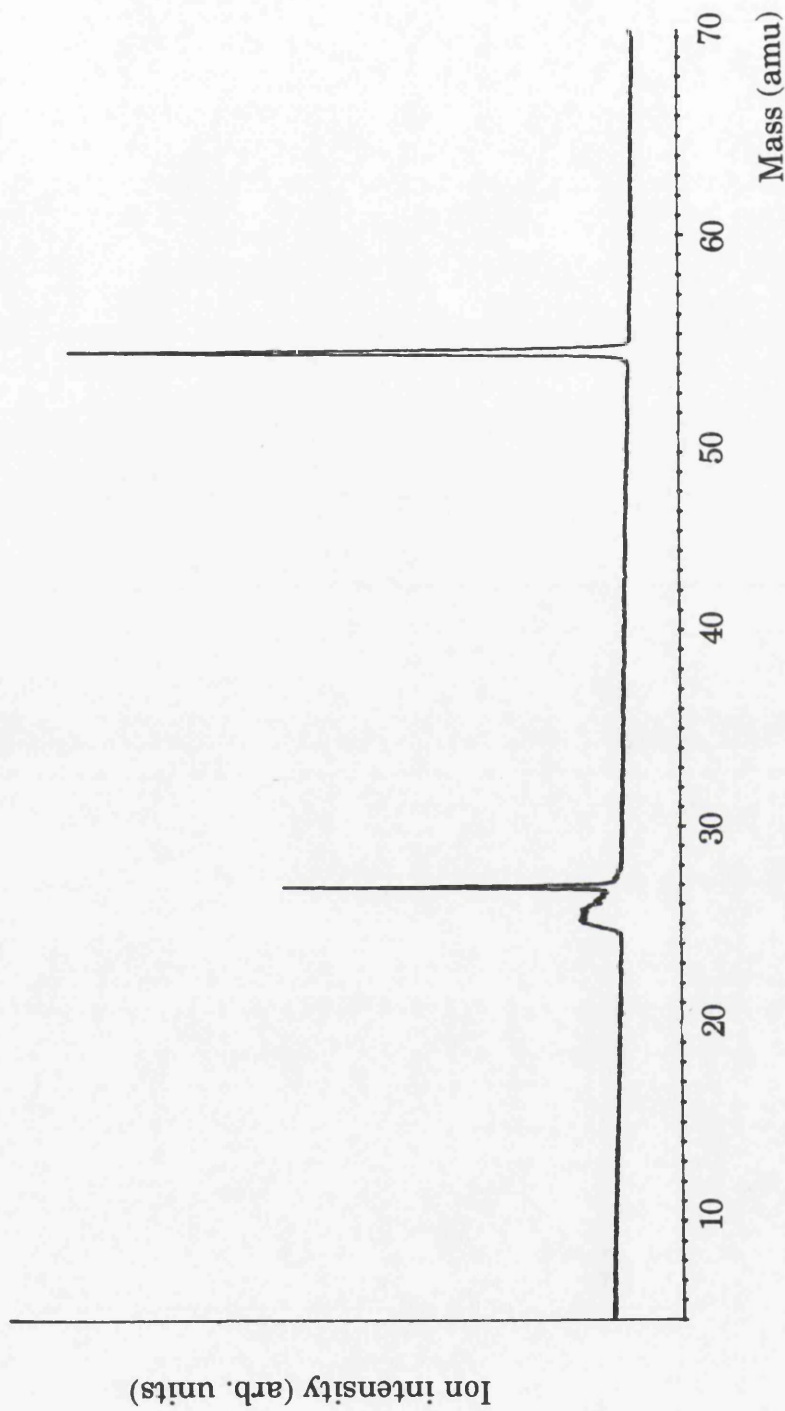


Fig.6.21 Mass spectra from the 121 aluminium standard, atomised by laser ablation. Ionisation was due only to 355nm wavelength radiation. The peak at mass ~54 amu is larger than the aluminium peak.

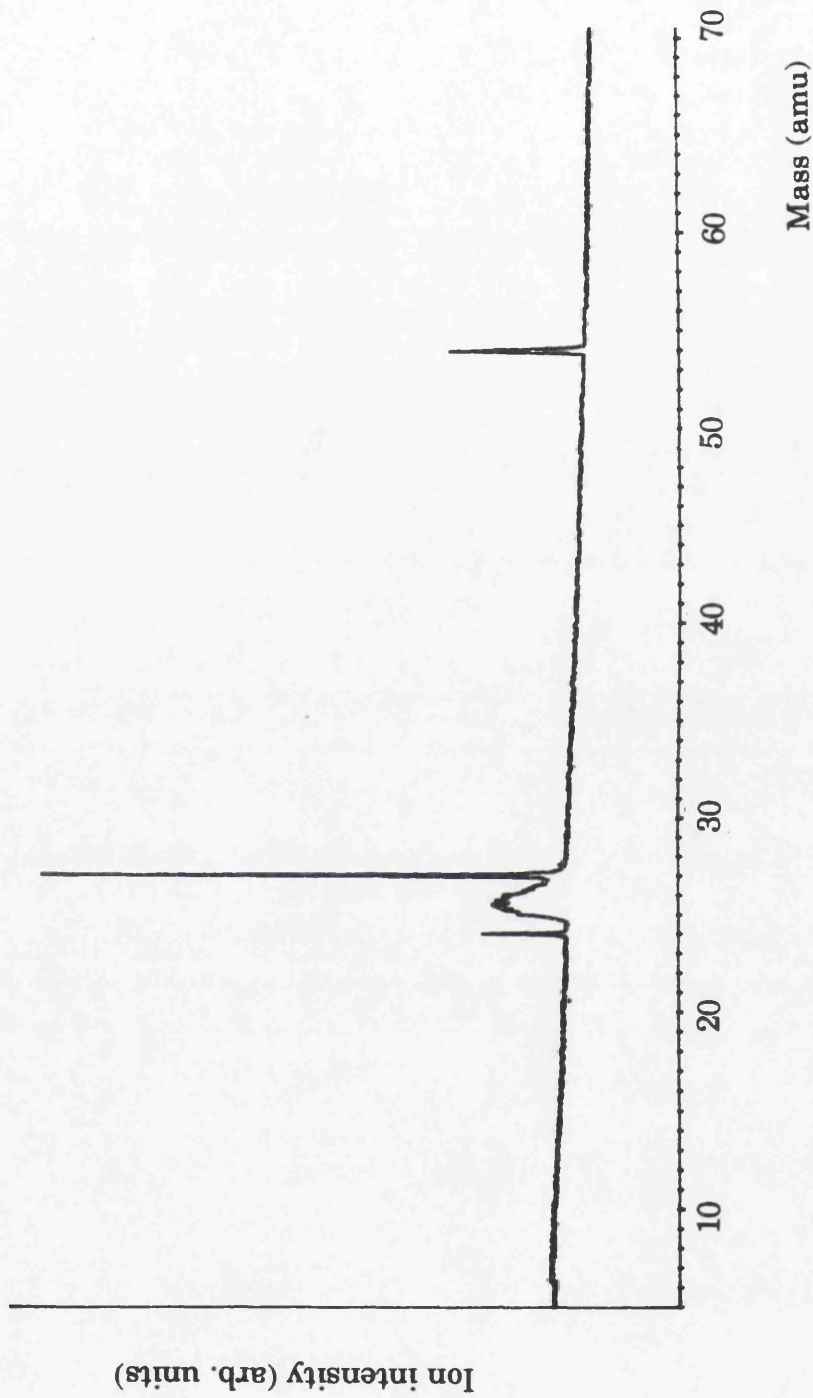


Fig.6.22 Mass spectra from the 121 aluminium standard, atomised by laser ablation. Ionisation was due only to the doubled dye laser radiation. The peak at mass ~54 amu is smaller than the aluminium peak.

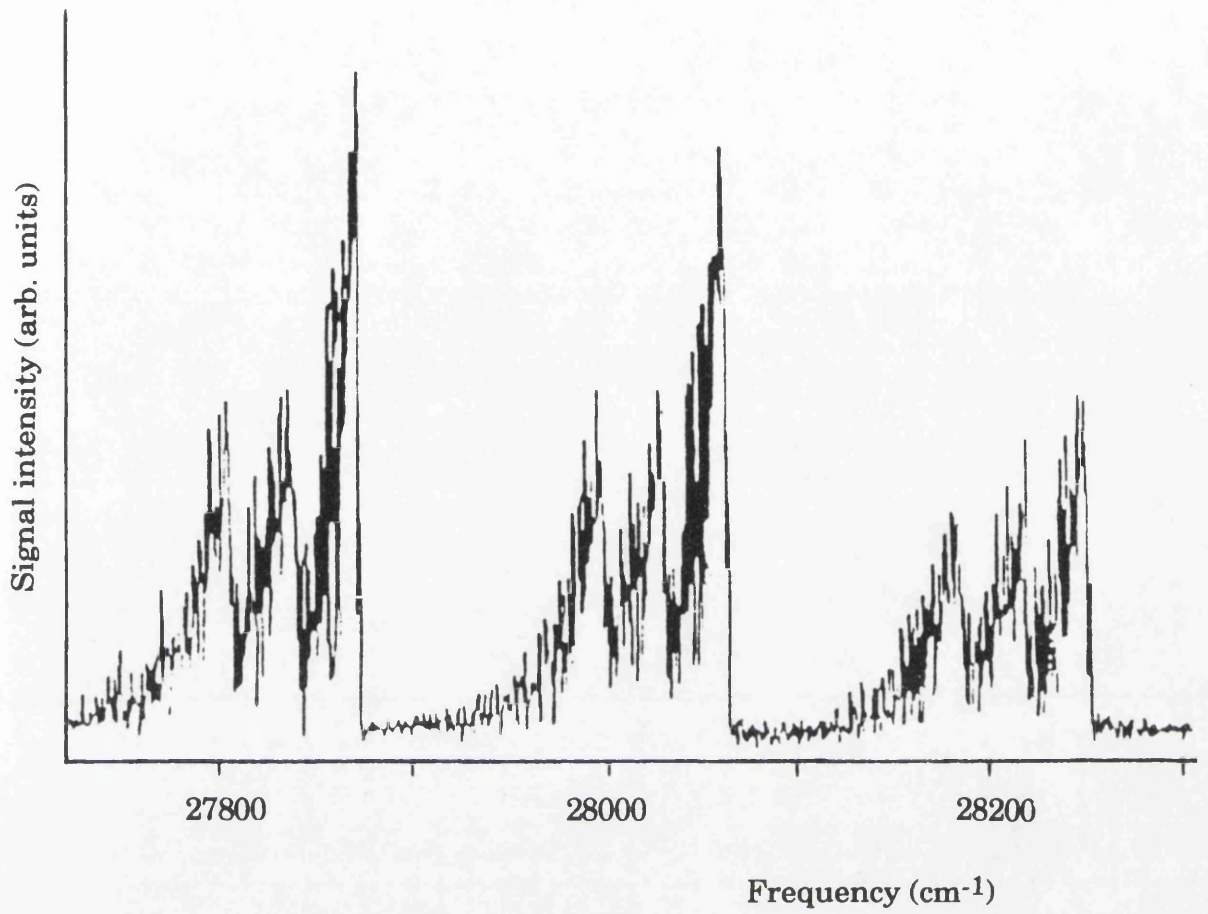


Fig.6.23 Portion of the laser excitation spectrum of Al_2 (Cai *et al*, 1991)

interpreting photoionisation spectra.

When the wavelength of the RIMS laser is tuned to the Mg scheme shown in Fig.6.13(b), the composition of the mass spectra, as expected, becomes dramatically different. Fig.6.24 shows the mass spectra obtained from the 636 standard with the same ablation laser power, 2.5mW, as was used before. When the dye laser wavelength is tuned away from resonances in either Mg or Mn the observed spectrum is dominated by the Al and Al₂ ions, as shown in Fig.6.25. The enhancement in the analyte ion signal obtained when the laser wavelength is tuned to an atomic resonance is of the order of 10³.

In order to compare the analyte signals from the five standard samples each was analysed in turn using the following procedure. The sample was subjected to 1000 laser shots for cleaning prior to the acquisition of data. The section of the mass spectrum containing the analyte peak was then recorded for 30 consecutive runs, each of which was accumulated over 500 laser shots. Since all of the standards were mounted on one sample stub the samples were investigated in ascending order of analyte concentration, in an attempt to reduce any contamination from one sample to another. The recorded RIMS signal plotted against the number of laser shots is shown for Mg in Fig.6.26 and for Mn in Fig.6.27. It is apparent that the RIMS signal decreases as the number of laser shots increases. This is similar to the relationship between manganese signal and the number of laser shots observed for a low alloy steel sample, which has been discussed previously in §4.5.

Due to the design of the data acquisition system a 6.4μs portion of the mass spectrum was recorded for every laser shot. As has been explained previously, it is therefore possible to monitor several species with masses in proximity to that of the analyte. In this particular case it is possible to record the non-resonantly ionised aluminium signal while monitoring the Mg signal. When the timing is adjusted to allow the Mn signal to be recorded the aluminium dimer signal is also obtained. The dependence on the number of laser shots of the aluminium signal obtained in this manner is shown in Fig.6.28, and the relationship for the dimer signal is illustrated in Fig.6.29. It is apparent that both signals exhibit the same

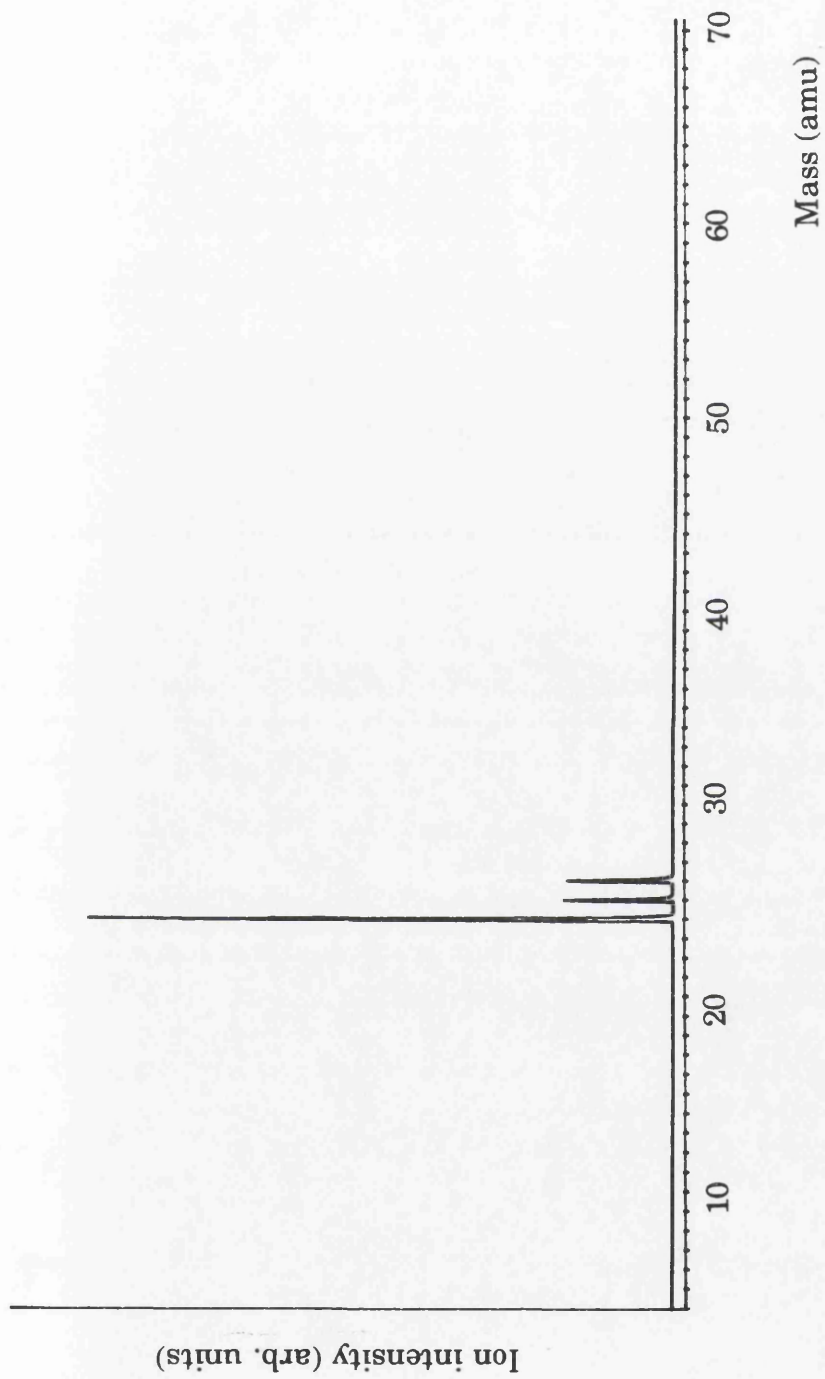


Fig.6.24 Mass spectra from the 636 aluminium standard, atomised by laser ablation with the RIMS lasers tuned to the Mg scheme.

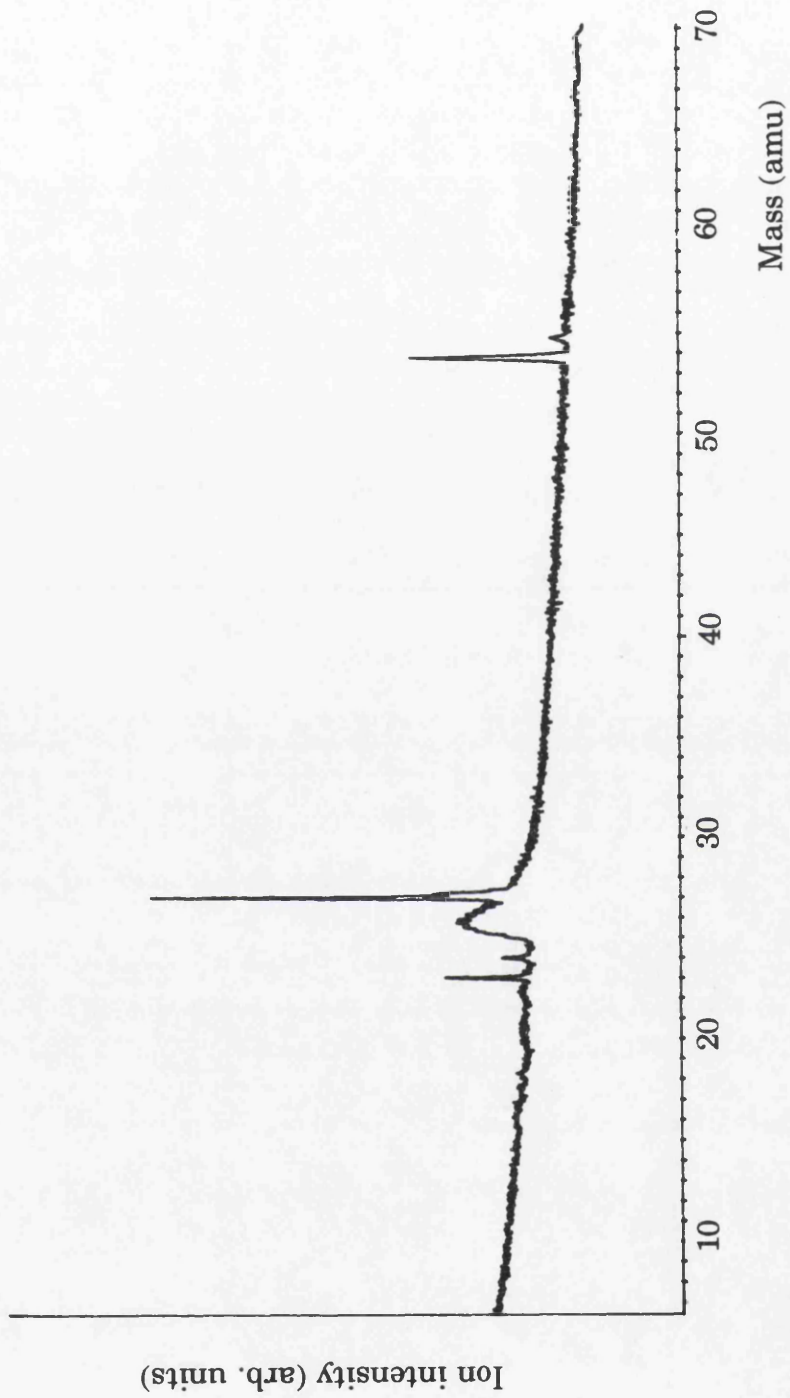


Fig.6.25 Mass spectra from the 636 aluminium standard, atomised by laser ablation. The RIMS laser wavelength was tuned to 565.35nm.

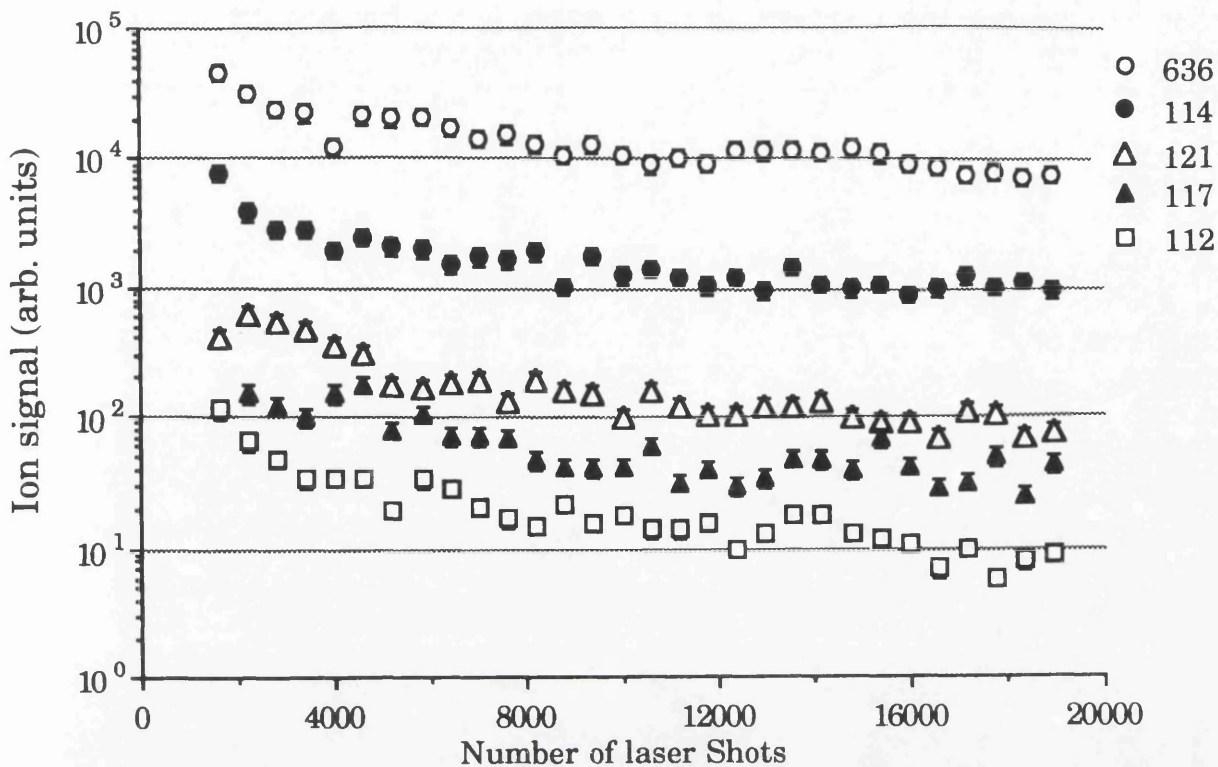


Fig.6.26 Mg RIMS signal from a series of aluminium standards, acquired in 500 shot spectra, as a function of the total number of laser shots. The sample was atomised by laser ablation.

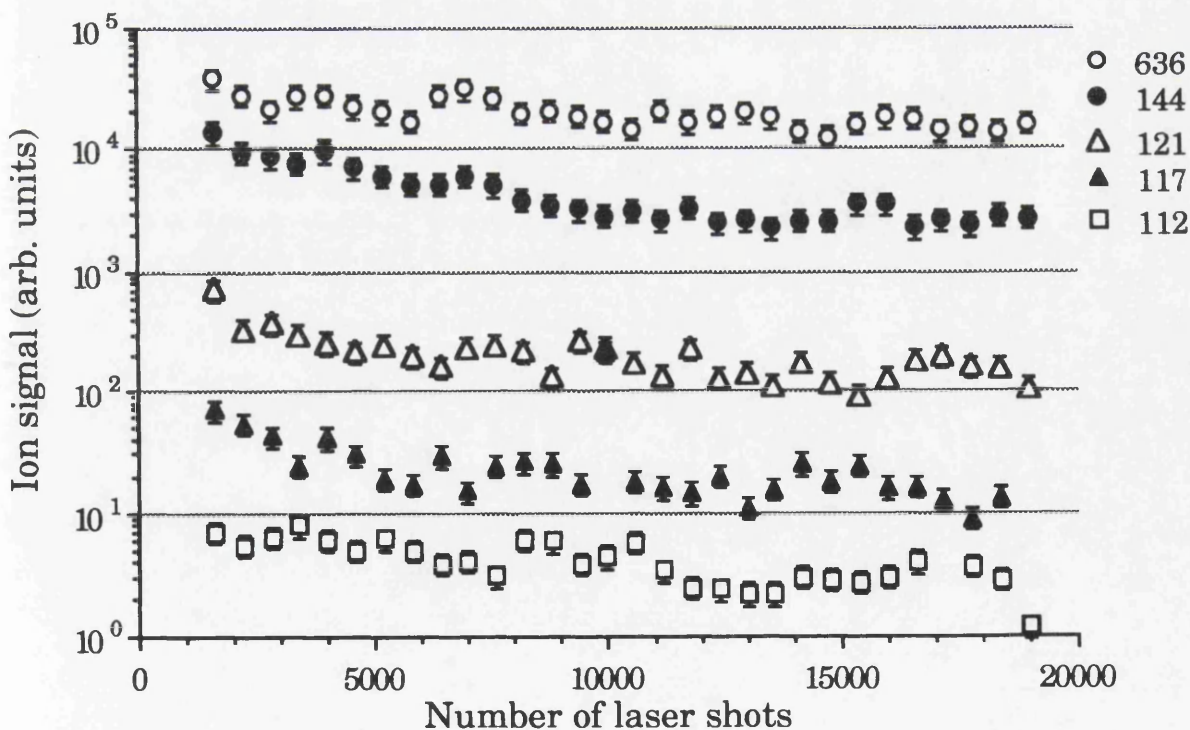


Fig.6.27 Mn RIMS signal from a series of aluminium standards, acquired in 500 shot spectra, as a function of the total number of laser shots. The sample was atomised by laser ablation.

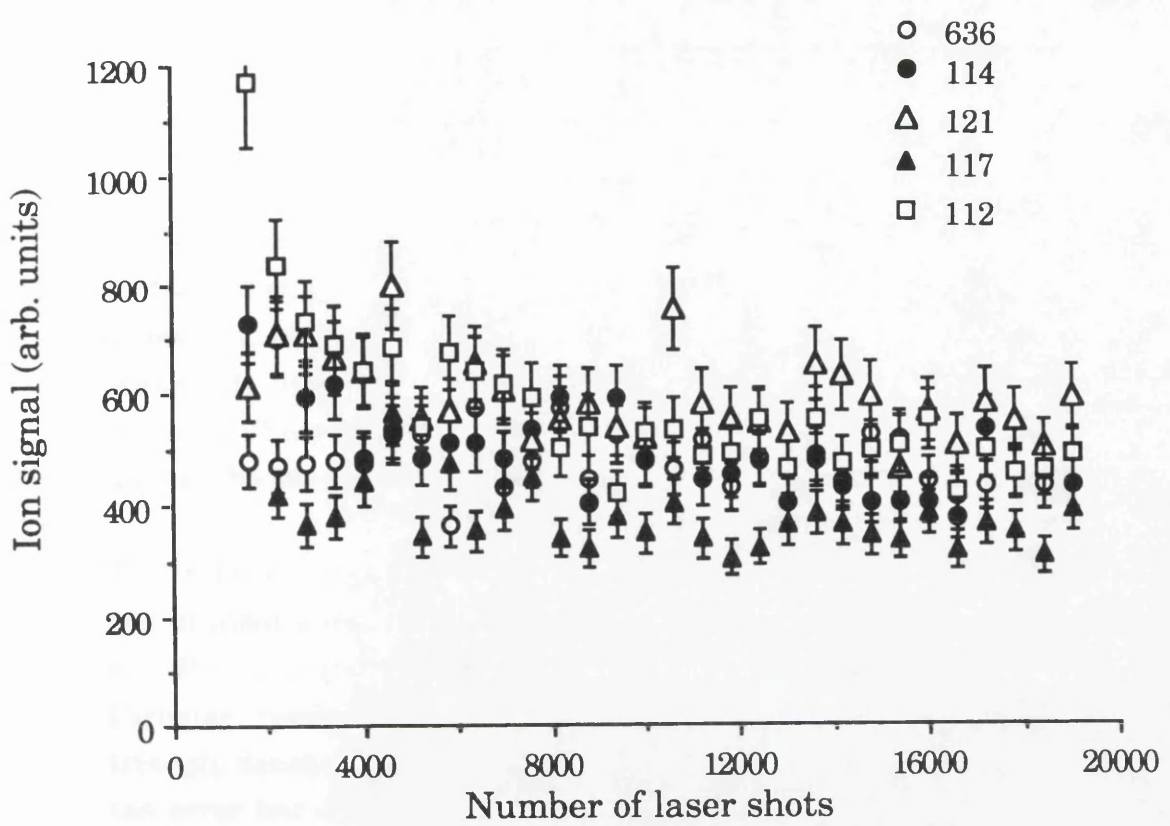


Fig.6.28 Non-resonantly ionised aluminium signal from a series of aluminium standards, acquired in 500 shot spectra, as a function of the total number of laser shots. The RIMS lasers were tuned to the resonance in Mg. The sample was atomised by laser ablation.

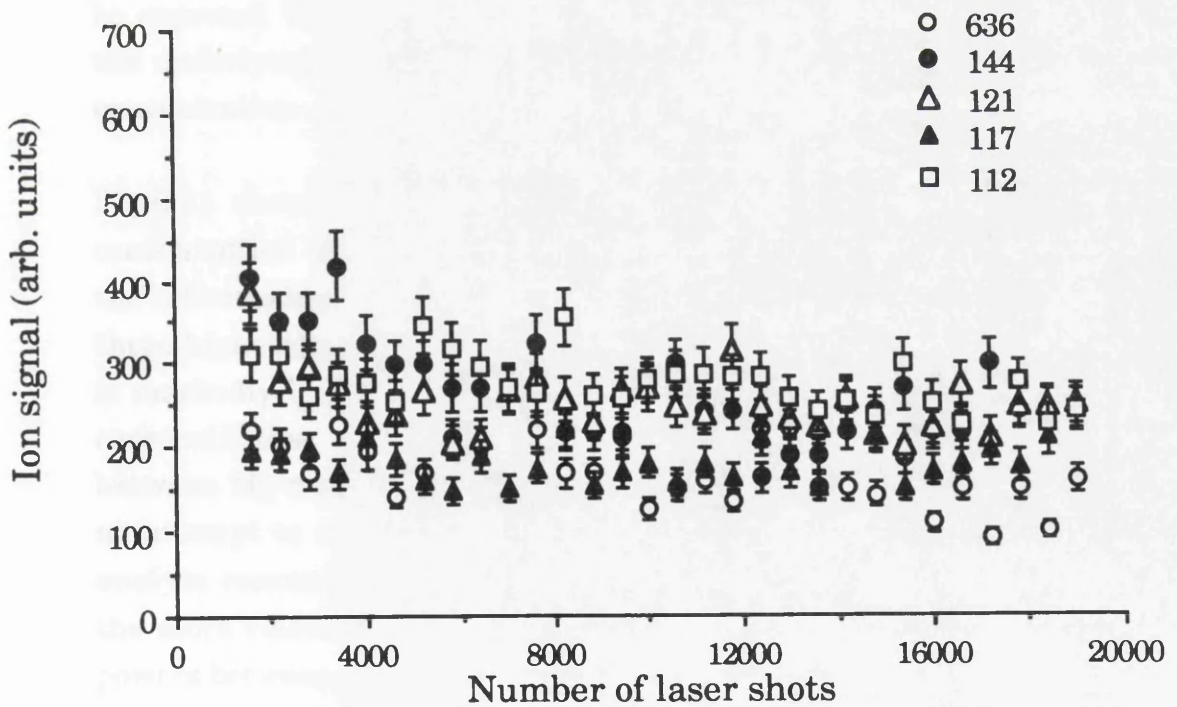


Fig.6.29 Non-resonantly ionised aluminium dimer signal from a series of aluminium standards, acquired in 500 shot spectra, as a function of the total number of laser shots. The RIMS lasers were tuned to the resonance in Mn. The sample was atomised by laser ablation.

general characteristics. Firstly, there appears to be evidence of a decrease in signal with the number of laser shots, although this is not as marked as the order of magnitude decrease observed in the analyte signal in some cases. Secondly, it is apparent that the signals obtained from the five standards vary by approximately a factor of two. Hence the amount of material liberated can be assumed to vary by a maximum of a factor of two during the investigations of the various standards.

The relationship between the RIMS signal and analyte concentration would ideally be linear with gradient of unity. Fig.6.30 shows the plot of certified manganese concentration against the recorded RIMS signal. Circular symbols represents an average of all of the spectra, while a triangle denotes the average of the last ten 500 shot spectra. In both cases the error bar demonstrates the standard deviation of the data. A straight line of unity gradient is shown in Fig.6.31 as a visual aid. It would appear that the relationship between the certified composition and the RIMS signal is as would be expected for the four highest concentration spectra. However, the signal obtained from the standard with the lowest certified concentration, which was at the limit of the signal to noise obtainable with the current arrangement, was an order of magnitude higher than would be expected. It was believed that contamination of the sample surface was the underlying reason for the larger than expected signal from the lowest concentration sample.

Fig.6.31 shows the dependence of the Mg RIMS signal on the analyte concentration of the standard. It is apparent that, as was the case for Mn, the relationship between signal and certified concentration is linear at the three highest concentrations. However, the signal at lower concentrations is markedly larger than would be expected. This was again attributed to contamination of the sample surface. Fig.6.32 shows the relationship between Mg and Mn signal against sample concentration. There has been no attempt to normalise the signals from the two analytes. At the higher analyte concentrations the Mn signal is consistently larger than that of the more volatile Mg. This could be due to a marginal difference in laser powers between the acquisition of the two sets of data. A similar result has been observed by other researchers in a study similar to this one, in which a series of calibrated metal standards were investigated by laser ablation,

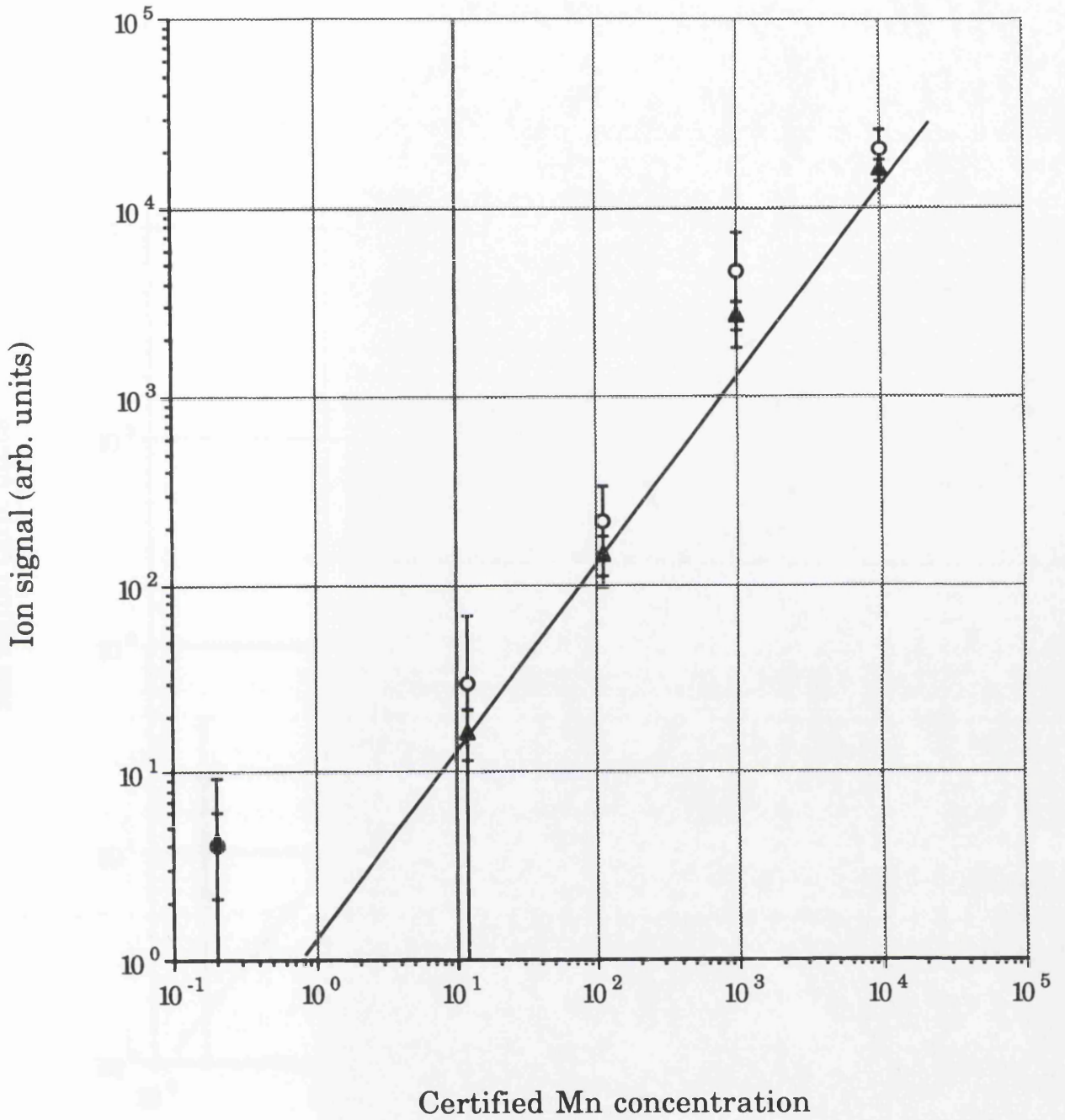


Fig.6.30 Relationship between the Mn RIMS signal and the certified Mn concentration from the series of aluminium standards. The circular symbols shows the average of all thirty spectra from 500 laser shots, while the filled symbol shows the average of the last ten spectra.

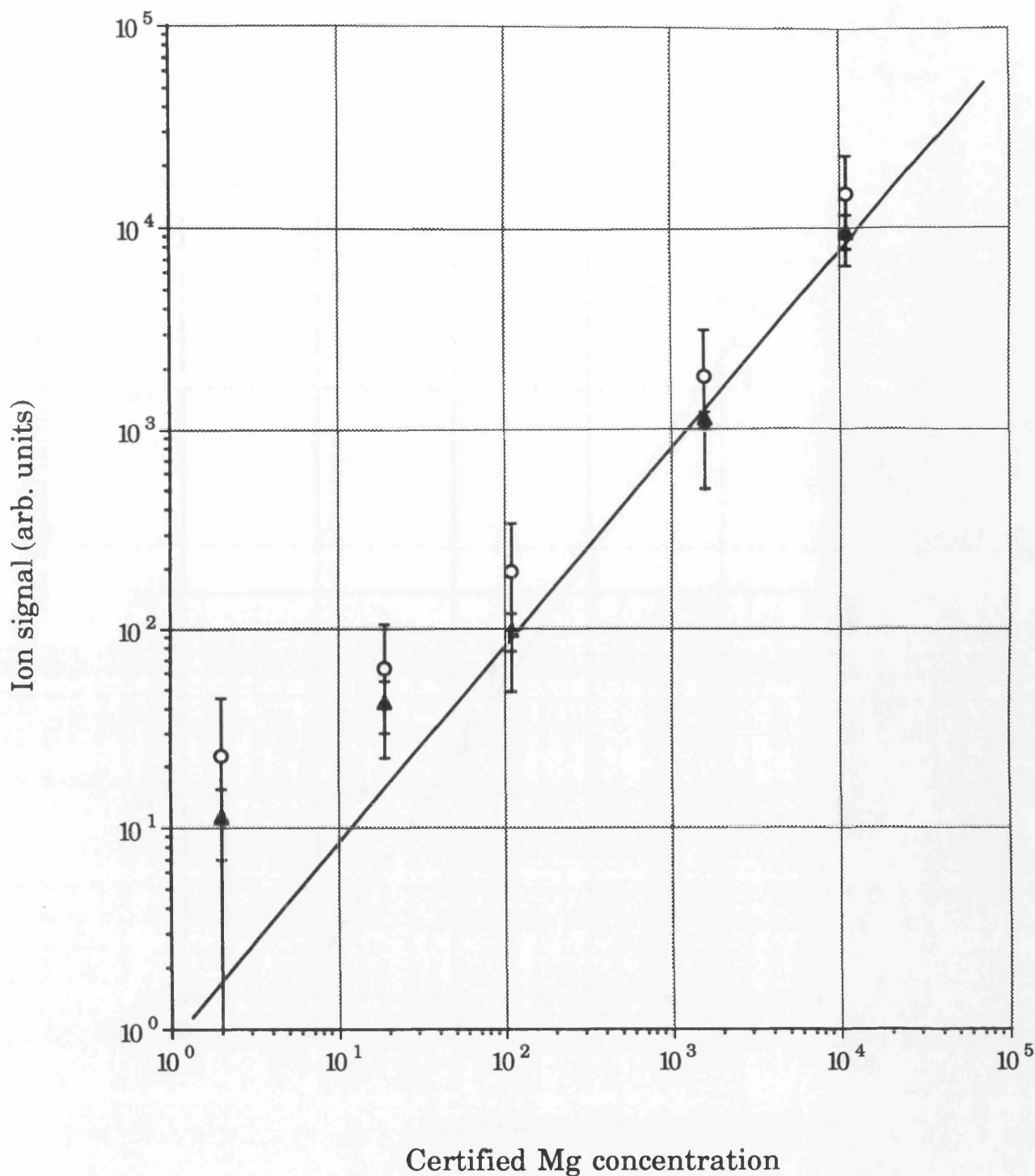


Fig.6.31 Relationship between the Mg RIMS signal and the certified Mg concentration from the series of aluminium standards. The circular symbols shows the average of all thirty spectra from 500 laser shots, while the filled symbol shows the average of the last ten spectra.

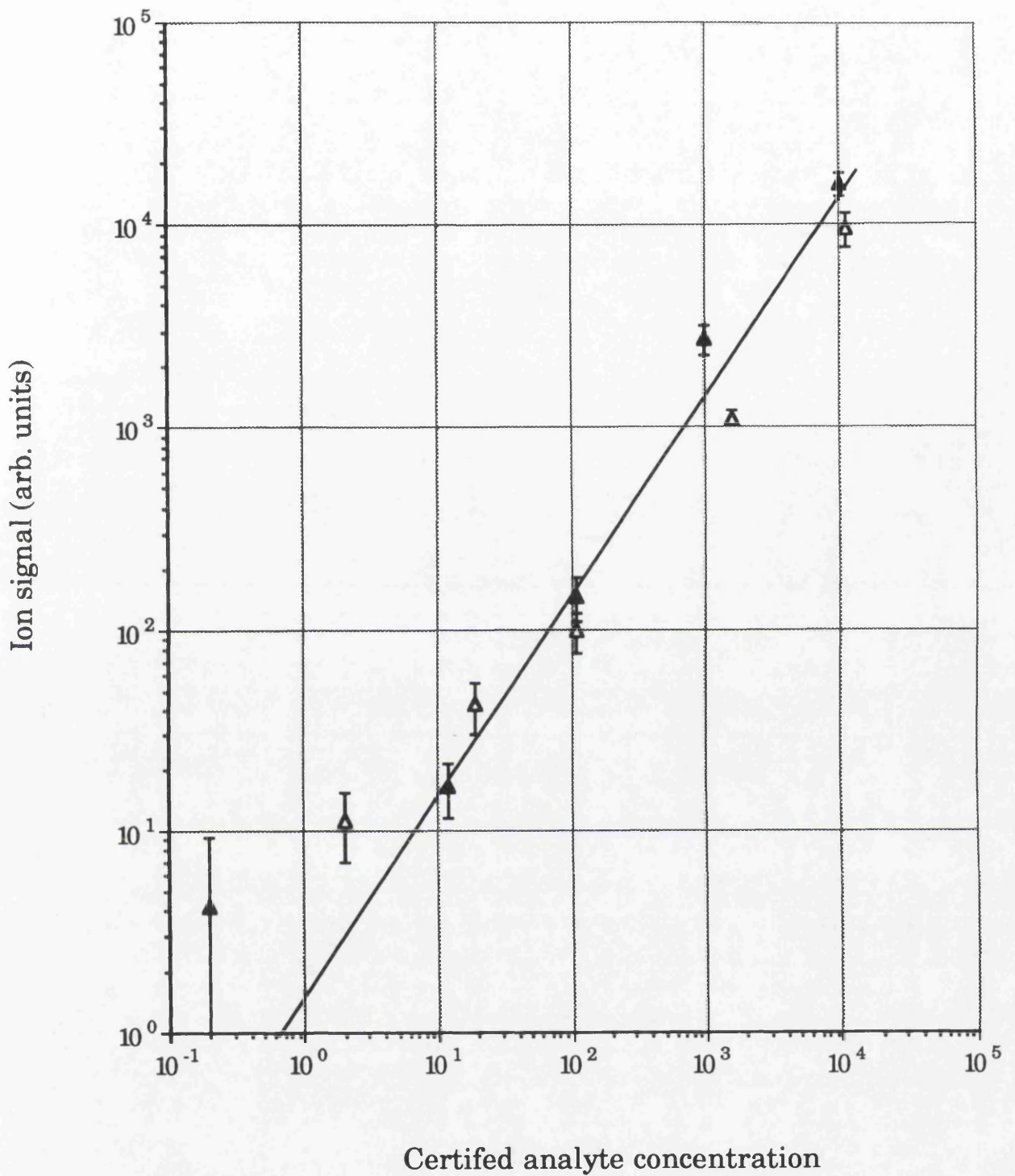


Fig.6.32 Relationship between the RIMS signals for Mg and Mn and the certified analyte concentrations. The outlined symbols are for Mn and the filled symbols are for Mg. The data was acquired from the last ten of thirty spectra.

with the analyte being monitored by recording the fluorescence following laser excitation from the ground electronic state (Quentmeier *et al*, 1990). The fluorescence intensities from different elements, present in the same concentration in an aluminium matrix, were observed to vary by an order of magnitude. However, it was found that the ratios of the LIFS signals from Si, Cr, Mn and Mg were independent of the matrix material and the laser ablation parameters when plotted against the known concentration ratios. This internal standardisation allows for the determination of the concentration of an element in a matrix by determining its ratio with a species of known concentration. This standardisation can be applied to elements in a matrix in which standards are not available since the relationship between the ratios of LIFS intensities and the known analyte concentrations can be determined for a matrix for which standards are available.

In order to attempt to extend this work to other matrices zinc, copper and steel standards containing Mg and Mn were obtained. Due to the possibility of sample contamination having occurred in the experiments discussed above, a more rigorous sample preparation procedure was perceived to be necessary. The samples were each mounted on a separate sample stub to remove the possibility of analyte being transferred from one sample to another during the analysis. Since, at this stage the PIG was not operational it was not possible to employ ion etching of the sample surface. Cleaning of the sample surface with many high power cleaning pulses was not deemed advisable since this can cause dramatic changes to the sample morphology and may also not affect complete removal of the material in the surface layer. It was decided that the best available method for sample cleaning was to use an appropriate acid based etching solution. However, it was found that analysis of sample prepared in this way showed very little relationship between certified analyte concentration and RIMS signal. Therefore, this method of sample cleaning was discontinued and results obtained from these samples will not be discussed.

As has been mentioned in §1.7.2, ion sputtering is a technique widely used for applying RIMS to the microanalysis of solids. It was therefore of interest to investigate the application of the profiling ion gun detailed earlier in this chapter to trace analysis. A portion of the mass spectra

obtained from the Alusuisse-Lonza 636 standard is shown in Fig.6.33. It is apparent that the signal at ~54 amu is not observed.

It proved to be possible to obtain a RIMS signal from the 636 standard with the PIG operated continuously with a current of $3\mu\text{A}$ and a beam energy of 15keV. However, under these conditions the secondary ions created by the sputtering beam form a background to the time-of-flight RIMS signal. Due to this it did not prove to be possible to distinguish a signal for the 144 standard from the background. As has been discussed in §6.4, the neutral yield is $\sim 10^4$ times higher for laser ablation than for sputtering. Therefore the number of analyte atoms interrogated with laser ablation of the 112 sample would be the same as the amount liberated by the ion sputtering of the 144 standard. This was, as mentioned previously at the limit of detection for a 500 shot analysis. Hence it would be expected to be difficult to obtain a signal from the 117 standard, even without interference from the secondary ions. However, it did prove possible to monitor how the signal from the 636 standard depended on the number of laser shots, this is shown in Fig.6.34. It is apparent that the signal does not display the marked dependence on the number of laser shots that was observed with laser ablation. However, in this case since the sputtering is continuous several monolayers would be removed per second. If pulsed sputtering were employed this would not be the case and some enhancement of the analyte yield at the surface due to contamination may be observed.

It would appear, as would be expected, that the laser ablation technique allows for the detection of smaller concentrations of analyte than the ion sputtering technique, in the same number of laser shots. However, the signals obtained from ion sputtering appear to be more reproducible. In order to increase the limits of detection of the system to allow sub ppm analysis it would be necessary to increase the efficiency of ion detection. There are several areas in which enhancements could be achieved. Firstly, employing an optimised Einzel lens should allow a higher ion transmission than the current guide wire arrangement. A second improvement would be the installation of a new detector, which would have a higher gain and would therefore allow ion counting to be employed, as was detailed in §3.4. If the ion beam was pulsed then the interference from secondary ions would be greatly reduced, and the problem could

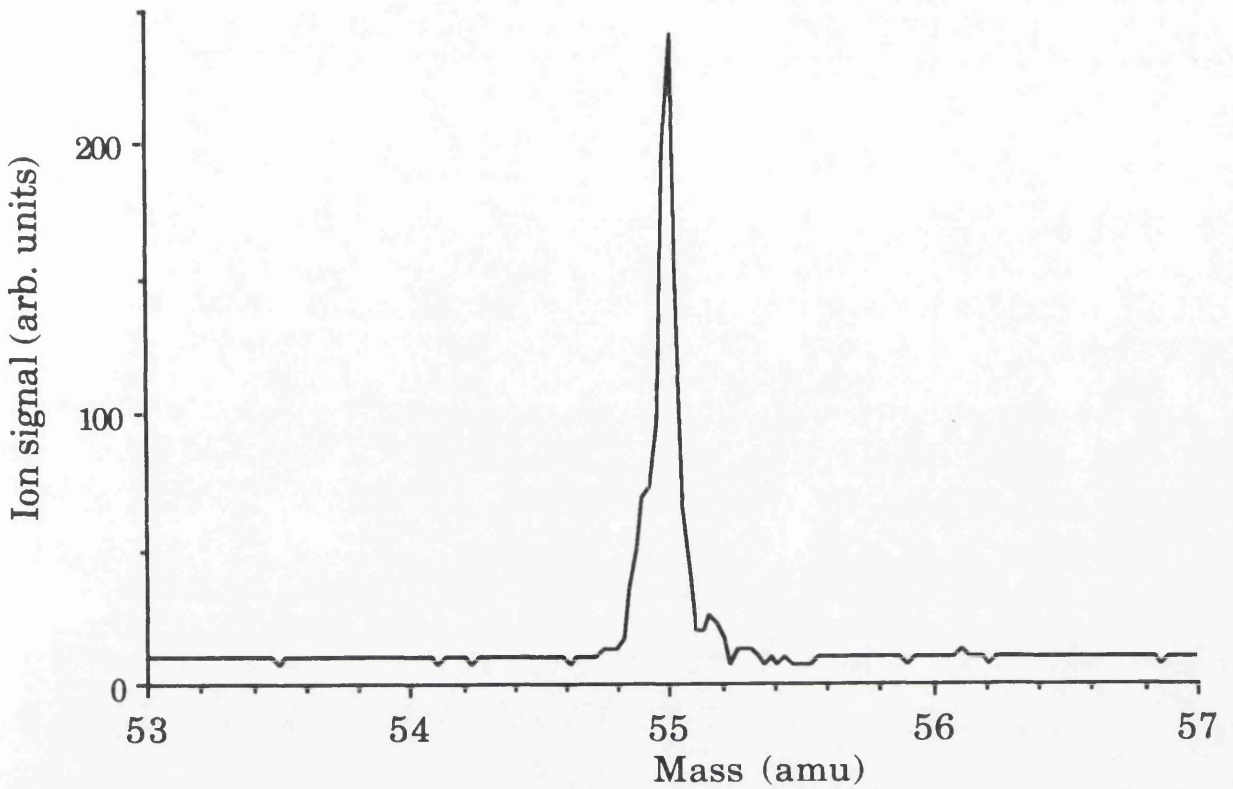


Fig.6.33 A magnified section of the mass spectra from the 636 aluminium standard atomised by ion sputtering. The RIMS laser is tuned to the Mn resonance and the peak at ~54 amu is not apparent.

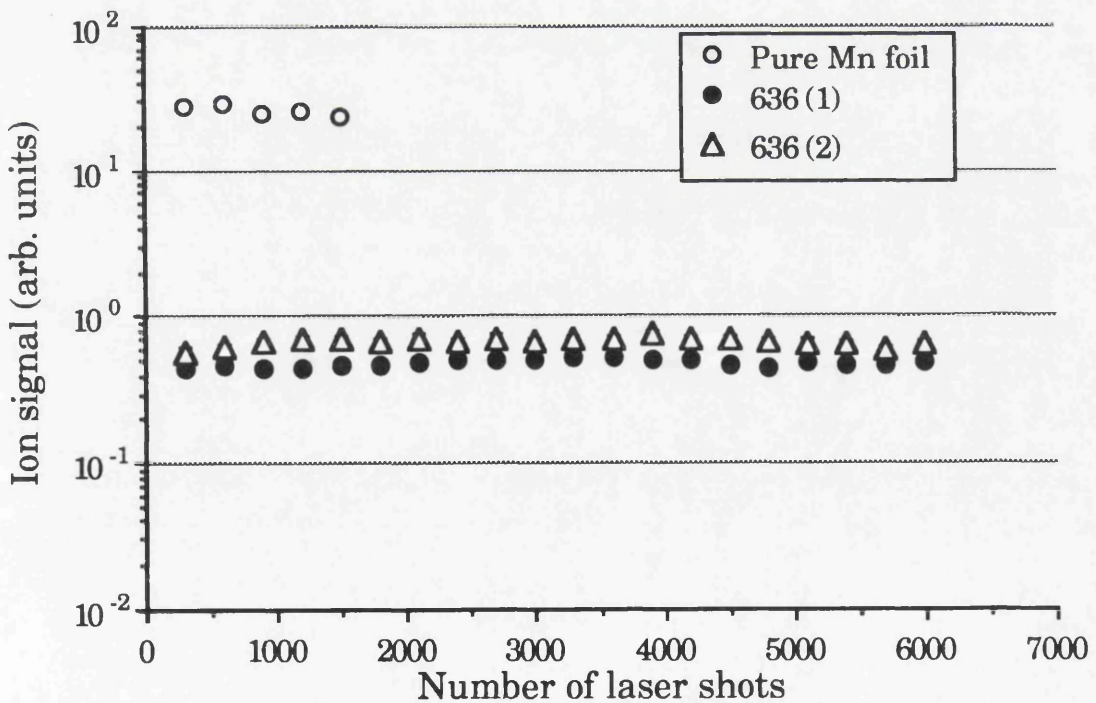


Fig.6.34 Mn RIMS signal from a pure Mn foil and two area from the surface of the 636 aluminium standards, acquired in 250 shot spectra, as a function of the total number of laser shots. The sample was atomised by ion sputtering.

probably be eliminated using the techniques discussed in §4.10. Hence pulsing the PIG would both increase the obtainable detection limit and improve the degree of sample utilisation. If the improvements to increase the transmission of the system were also undertaken it would allow the detection limits of the system to approach those of the established RIMS systems, detailed in §1.7.2.

Chapter 7

§7 Conclusions

In this thesis the possibility of utilising RIMS as a microprobe technique for trace analysis has been detailed. In this final chapter the significant conclusions from the work presented previously will be reviewed and conclusions will be drawn with regards to the prospects of the technique for ultra-trace analysis.

The use of laser ablation for sample atomisation for RIMS was studied in detail in Chapter 4. The technique has many characteristics which make it ideally suited as a sample atomisation technique for RIMS. Specifically, laser ablation causes pulsed atomisation which allows for efficient sample utilisation in combination with the pulsed ionising lasers. However, the pulsed nature of laser ablation also leads to complications in the analysis of samples, because the characteristics of the emitted plume are dependent both on the laser beam parameters and on the sample composition. This is in contrast to ion sputtering where, as can be seen from Eqn.6.9, the properties of the emergent material are independent of both the intensity and the energy of the ion beam. It was apparent for the majority of the samples investigated in Chapter 4 that the observed velocity distribution was a function of both the laser power density and the photon energy. For most of the metal samples studied the velocity distribution could be modelled by a half-range Maxwell-Boltzmann distribution with a characteristic temperature representative of a thermal process. An added complication was seen in the case of aluminium where, in several instances, the velocity distribution was far from that predicted by a thermal half-range Maxwell-Boltzmann distribution. This was attributed to the formation of an oxide layer on the surface, which would have markedly different ablation characteristics than the pure metal. The analysis of several elements present in a steel standard was also reported in Chapter 4. A significant result from those experiments was that the composition of the plume, as represented by the relative sensitivity factors, was not a strong function of the laser power. However, the relative sensitivity factors determined from these experiments deviated

significantly from unity and it was surmised that the plume of material liberated from the sample had a composition related to the thermal properties of the various elements. This would appear to make the quantitative characterisation of compound samples impossible. However, at present the RIMS technique can only be meaningfully applied to one element at a time and since, as was illustrated in §6.5, the RIMS signal produced by laser ablation atomisation appears linear with analyte concentration, this technique may be applicable to the detection of trace levels of a single element in these circumstances.

There appear to be some serious problems that must be addressed in the application of laser ablation for trace analysis by RIMS. Most notably, the behaviour of the analyte signal as a function of the number of laser shots, as discussed in §4.5 and §6.5, illustrates that a more comprehensive knowledge of the processes occurring on the sample surface is required. However, laser ablation does have some considerable advantages over the more established atomisation technique of ion sputtering. The most apparent is that, as illustrated in §6.4, the amount of material liberated by ion sputtering is $\sim 10^4$ times lower than is the case for laser ablation. This was reflected in the determined limits of detection being substantially lower for ion sputtering than was the case for laser ablation. A further advantage of laser ablation, for practical applications, is that the instrumental arrangement is less complex than is required for ion sputtering. This is especially true for non-conducting samples because ion sputtering causes the accumulation of charge on these samples and pulsed electron beams must be incorporated into the system to alleviate the problem. Since photons do not carry electrostatic charge this problem is not encountered when laser ablation is employed for sample atomisation. This is a significant factor in why laser ablation with subsequent laser ionisation, either resonant or non-resonant, has become an established technique in the analysis of organic materials.

In the introduction of this thesis much emphasis was given to the fact that RIMS was a technique which had great potential for routine ultra-trace analysis. However, the technique has still to become widely accepted. The main reason for this would appear to be the instrumental complexity of the technique. In particular, tuneable laser systems are difficult to operate

and maintain and are not easily integrated into stand-alone analysis systems. Although in recent years several alternatives to dye lasers have been proposed, it is not apparent, at present, if any of these systems will provide the 'black box' system which is required if RIMS is to become established as a viable commercial technique. A further difficulty is that for elemental trace analysis, there are an increasing number of established analytical techniques. One particular case is ICP-MS, an established technique for trace analysis of solutions which can be successfully interfaced to solids via several techniques, including laser ablation. The main role for RIMS would therefore appear to be as a SNMS ionisation technique where, as was discussed in §1.7.2, it can both increase the sensitivity of the analysis and reduce the influence of matrix effects. The SIMS systems which have incorporated laser ionisation are almost invariably highly sophisticated and complex systems into which the addition of a laser system does not add too greatly to the total instrumental complexity.

The number of applications of LAMMS have declined markedly, mainly due to the qualitative nature of the process. However, a significant occurrence in recent years has been the commercial exploitation of the MALDI technique, discussed in §5.1. These systems represent one of the fastest growing areas of the mass spectrometry market, currently valued at \$10 million a year and this is expected to increase by ~30% annually. As these systems proliferate the aversion of analysts to laser mass spectrometry techniques may decline. A MALDI system is, in essence, a compact LAMMS system, usually utilising an inexpensive nitrogen laser. There will therefore be a significant increase in the number of systems capable of performing LAMMS analysis and although these instruments have been designed for the determination of molecular weights it would be perfectly feasible to make simple adaptations to allow for the RIMS analysis of solid samples. If the development of diode laser systems, which was discussed in §3.3, results in relatively inexpensive devices which can be applied to RIS, then it can be envisaged that RIMS may become more widespread than is foreseeable at present.

References

- Adrain R S and Watson J, (1984)
Laser microspectral analysis: a review of principles and applications
J. Phys. D: Appl. Phys., 17 pp1915-1940
- AIP Handbook, 1972
American Institute of Physics Handbook, Ed. Gray D E,
Pub. McGraw-Hill Inc. pp6-124 - 6-157
- Alcock C B, Itkin V P, Horrigan M K, (1984)
Vapor-pressure equations for the metallic elements - 298-2500K
Can. Metallurg. Quart., 23, pp309-313
- Allegrini M, Gabbanini C, Moi L and Colle R, (1985)
Cross-section measurement and theoretical evaluation for the energy-transfer collision $Na(3P) + Na(3P) \rightarrow Na(4F) + Na(3S)$
Phys. Rev. A, 32 pp2068-2076
- Ambartzumian R V and Letokhov V S, (1972)
Selective two-step (STS) photoionization of atoms and photodissociation of molecules by laser radiation
Appl. Optics, 11 pp354-358
- Anacker D C and Erskine J L, (1991)
Analysis of microchannel plate response in relation to pulsed laser time-of-flight photoemission spectroscopy
Rev. Sci. Instrum., 5 pp1246-1255
- Anisimov S I, (1968)
Vaporization of metal absorbing laser radiation
Sov. Phys. JETP, 27 pp182-183

- Arlinghaus H F, Calaway W F, Young C E, Pellin M J and Gruen D M,
(1989a)
High-resolution multiphoton laser-induced fluorescence spectroscopy of zinc atoms ejected from laser-irradiated ZnS crystals
J. Appl. Phys., 65 pp281-289
- Arlinghaus H F, Calaway W F, Young C E, Pellin M J, Gruen D M and Chase L L, (1989b)
Analysis of ion-bombarded and laser-irradiated surfaces of ZnS and Zn via two-photon high-resolution laser-induced fluorescence spectroscopy
J. Vac. Sci. Technol., A7 pp1766-1771
- Arlinghaus H F, Spaar M T, Thonnard N, Holloway P, Kabalka G W and Switzer R C, (1992)
Three-dimensional analysis of semiconductors and biological surfaces using SIRIS and LARIS
Resonant Ionisation Spectroscopy 1992, Inst. Phys. Conf. Ser. No.128, pp275-278
- Arrowsmith P, (1987)
Laser ablation of solids for elemental analysis by inductively coupled plasma mass spectrometry
Anal. Chem., 59 pp1437-1444
- Arrowsmith P, (1990)
Applications of laser ablation: Elemental analysis of solids by secondary plasma source mass spectrometry
In "Lasers and Mass Spectrometry", Ed. Lubman D M, Pub. Oxford University Press, New York, pp179-204
- Asaro F, Bekov G I, Belkin R S, Gulevich V M, Khomyakov N G, Kursky A N and Yu Pakhomov D, (1992)
TARIS analysis in biomedical, environmental and geochemical researches
Resonant Ionisation Spectroscopy 1992, Inst. Phys. Conf. Ser. No.128, pp205-208

- Auciello O, Krauss A R, Kingon A I and Ameen M S, (1990)
A critical analysis of techniques and basis phenomena related to deposition of high temperature superconducting thin films
Scanning Microsc., 4, pp203-226
- Bakos J S, Földes I B, Ignác P N and Kedves M Á, (1991)
Investigation of the surface impurity content of silicon samples by resonance ionization spectroscopy
Resonant Ionisation Spectroscopy 1990, Inst. Phys. Conf. Ser. No.114, pp443-446
- Baldwin J M, (1970)
Q-switched laser sampling of copper-zinc alloys
Appl. Spectrosc., 4 pp429-435
- Bechtel J H, (1975)
Heating of solid targets with laser pulses
J. Appl. Phys., 46 pp1585-1593
- Becker C H and Gillen K T, (1984)
Surface analysis of contaminated GaAs: Comparison of new laser based technique with SIMS
J. Vac. Sci. Technol., A3 pp1347-1349
- Becker C H and Gillen K T, (1985)
Can nonresonant multiphoton ionization be ultrasensitive
J. Opt. Soc. Am. B, 2 pp1438-1443
- Beekman D W, Callcott T A, Kramer S D, Arakawa E T, Hurst G S and Nussbaum E, (1980)
Resonance ionization source for mass spectroscopy
Int. J. Mass Spectrom. Ion Phys., 34 pp89-97
- Beekman D W and Callcott T A, (1984)
Laser ablation studies using RIS
Resonant Ionisation Spectroscopy 1984, Inst. Phys. Conf. Ser. No.71, pp143-150

Beekman D W and Thonnard NA, (1989)

Laser ablation as an atomization source for ultratrace element analysis using resonance ionization time-of-flight mass spectrometry

Resonant Ionisation Spectroscopy 1988, Inst. Phys. Conf. Ser. No.94, pp163-166

Bekov G I, Letokhov V S and Radaev, (1985)

Laser photoionization spectroscopy of ruthenium at the level of 1 part in 10^{12}

J. Opt. Soc. Am. B, 2 pp1554-1559

Bekov G I, Kudryavtsev Y A, Auterinen I and Likonen J, (1987)

The laser resonance ionization spectrometer

Resonant Ionisation Spectroscopy 1986, Inst. Phys. Conf. Ser. No.84, pp97-102

Belov M E, Alimipiev S S and Nikiforov S M, (1992)

Laser ablation/ionization analysis of trace elements from bulk materials

Report - Laboratory of Laser Diagnostics, General Physics Institute, 117492 Moscow, Russia.

Benninghoven A, Rüdener F G and Werner H W, (1987)

Secondary ion mass spectrometry: Basic concepts, instrumental aspects, applications and trends

John Wiley and Sons, New York

Berman P R and Robinson E J, (1982)

Combined radiation field-collisional excitation of atoms

Photon-Assisted Collisions and Related Topics, Ed. Rahman N K and Guidotti C, Pub. OPA, Amsterdam, pp15-34

Bialkowski M M, Hurst G S, Parks J E, Lowndes D H and Jellison.Jr, G E, (1990)

Charge emission from silicon and germanium surfaces irradiated with KrF excimer laser pulses

J. Appl. Phys., 68 pp4795-4801

- Bicchi P, Kopystynska A, Meucci M and Moi L, (1990)
Energy-pooling ionization via an autoionizing state in indium
Phys. Rev. A, 41 pp5257-5260
- Bickel G, (1992)
AECL Research - Chalk River, Ontario, Canada
Private communication
- Birge R R, (1983)
One-photon and two-photon excitation spectroscopy
In "Ultrasensitive Laser Spectroscopy", Ed. D S Kliger, Academic
Press, New York
- Borthwick I S, Ledingham K W D and Singhal R P, (1992)
Resonant Laser Ablation - a novel surface analytic technique.
Spectrochimica Acta, 47B pp1259-1265
- Brewer P D, Zinck J J and Olson G L, (1991)
Excimer laser ablation of CdTe
Lecture Notes in Physics 389, "Laser Ablation- Mechanisms and
Applications", Eds. J C Miller and R F Haglund, Jr., pub.
Springer-Verlag, Berlin Heidelberg, pp96-105
- Cai M F, Carter C C, Miller T A and Bondybey V E, (1991)
*Laser excitation and resolved emission spectra of supersonically
cooled aluminium dimer*
Chem. Phys., 155 pp233-245
- Calaway W F, Coon S R, Pellin M J, Young C E, Whitten J E, Wiens R C,
Gruen D M, Stingeder G, Penka V, Grasserbauer M and Burnett
D S, (1992)
*Resonance ionization of sputtered atoms - progress toward a
quantitative technique*
Resonant Ionisation Spectroscopy 1992, Inst. Phys. Conf. Ser.
No.128, pp271-274
- Cannon B D, Bushaw B A and Whitaker T J, (1985)
*Continuous-wave double resonance ionization mass spectrometry
of barium*
J. Opt. Soc. Am., B2 pp1542-1545

- Carslaw H S and Jaeger J C, (1959)
Conduction of heat in solids, 2nd Edn.
Oxford at the Clarendon Press
- Clark N S, (1989)
Laser microprobe mass spectrometry
Chemistry in Britain, 484-488
- Clark A, Ledingham K W D, Marshall A and Singhal R P, (1992)
Resonant ionization spectroscopy of carbon atoms following laser-induced fragmentation of nitro-aromatic molecules
Spectrochimica Acta, 47B pp799-808
- Combis P, Cazalis B, David J, Froger A, Louis-Jacquet M, Meyer B, Nierat A, Saleres A, Sibille G, Thiell G and Wagon F, (1991)
Low-fluence laser-target coupling
Laser and Particle Beams, 9 pp403-420
- Conzemius R J and Capellen J M, (1980)
A review of the applications to solids of the laser ion source in mass spectrometry
Int. J Mass Spectrom. Ion Phys., 34 pp197-271
- Cookson J A, (1987)
Analytical techniques
In "Principles and Applications of High-Energy Ion Microbeams", Ed. F Watt and G W Grime, IOP Publishing, pp21-78
- Cotton F A and Wilkinson G, (1972)
Advanced inorganic chemistry - A comprehensive text, 3rd Ed
Interscience Publishers
- Cowin J P, Auerbach D J, Becker C and Wharton L, (1978)
Measurement of fast desorption kinetics of D₂ from tungsten by laser induced thermal desorption
Surf. Sci., 78 pp545-564
- Crawford J, (1992)
Foster Radiation Lab., McGill University, Montreal, Canada
Private communication

- Dahl D A and Delmore J E, (1987)
The SIMION PC/PS2 user's manual. Version 3.11
Informal Report, Idaho National Engineering Laboratory, EGG-
CS-7233 Rev. 2, November.
- Danielzik B, Fabricius N, Röwekamp M and von der Linde D, (1986)
*Velocity distribution of molecular fragments from
polymethylmethacrylate irradiated with UV laser pulses*
Appl. Phys. Lett., 48, pp212-214
- Demtröder W, (1982)
Laser spectroscopy - Basic concepts and instrumentation
Springer Series in Chemical Physics 5, Springer-Verlag,
Heidelberg
- Devyatykh G G, Gaponov S V, Kovalev I D, Larin N V, Luchin V I,
Maksimov G A, Pontus L I and Suchkov A I, (1976)
*Possible chemical analysis of microscopic regions with a laser
mass spectrometer*
Sov. Tech. Phys. Lett., 2 pp356-357
Translated from Pis'ma Zh. Tekh. Fiz., 2 p906
- Dittrich K and Wennrich R, (1984)
Laser vaporization in atomic spectroscopy
Prog. Analyst. Atom. Spectrosc., 17, pp137-198
- Dreyfus R W, Walkup R E and Kelly R, (1986a)
*Laser sputtering -Part IV: Laser interferometry and laser-
induced fluorescence studies of insulators*
Radiation Effects, 99, pp199-211
- Dreyfus R W, Kelly R and Walkup R E, (1986b)
*Laser-induced fluorescence studies of excimer laser ablation of
Al₂O₃*
Appl. Phys. Lett., 49 pp1478-1450
- Dreyfus R W, Kelly R and Walkup R E, (1987)
Laser-induced fluorescence study of laser sputtering of graphite
Nucl. Instr. and Meth., B23 pp557-561

Dreyfus R W, (1989)

Are laser-ablated monolayers accurately characterized by their ion emission?

Microbeam Analysis 1989, San Francisco Press Inc, pp261-263

Dreyfus R W, (1991)

Cu⁰, Cu⁺ and Cu₂ from excimer laser-ablated copper

J. Appl. Phys., 69, pp1721-1729

Dubreuil B, Gilbert T, Barthe M F and Debrun J L, (1992)

RIMS study of low energy laser sputtering of metal and semiconductor surfaces

Resonant Ionisation Spectroscopy 1992, Inst. Phys. Conf. Ser. No.128, pp265-270

Duckwoth A, Smalley J, Adrian R S and Tozer B A, (1992)

Analysis of laser-ablated solid samples using a small time of flight mass spectrometer

Meas. Sci. Technol., 3 pp596-602

Duncan M A and Rouvray D H, (1989)

Microclusters

Scientific American, Dec. pp60-65

Duncan M and Devonshire R, (1991)

Optogalvanic spectroscopy in commercially available hollow cathode lamps

Inst. Phys. Conf. Ser. No.113, pp207-214

Eastham D A, (1986)

Atomic physics of lasers

Taylor and Francis, London and Philadelphia

Estler R C, Apel E C and Nogar N S, (1987)

Laser mass-spectrometric studies of optical damage in CaF₂

J. Opt. Am., B4 pp281-286

Estler R C and Nogar N S, (1991)

Ablation of high temperature superconductor studied by resonance ionization mass spectrometry (RIMS)

J. Appl. Phys., 69, pp1654-1659

- Fassett J D and Travis J C, (1988)
Analytical applications of resonance ionization mass spectrometry (RIMS)
Spectrochimica Acta, 43B pp1408-1422
- Fearey B L, Tissue B M, Olivares J A, Loge G W, Murrell M T and Miller C M, (1992)
High -precision thorium RIMS for geochemistry
Resonant Ionisation Spectroscopy 1992, Inst. Phys. Conf. Ser. No.128, pp209-212
- Friichnicht J F, (1974)
Laser-generated pulsed atomic beams
Rev. Sci. Instrum., 45 pp51-56
- Fürstanau N, (1981)
Investigation of laser induced damage, evaporation and ionization with homogeneous inorganic target foils
Fresenius Z. Anal. Chem., 308 pp201-205
- Gabbanini C, Gozzini S, Squdrito G, Allegrini M and Moi L, (1989)
Energy-pooling collisions for K(4P) + Rb(5P) and Na(3P) + Rb(5P) hebronuclear systems
Phys. Rev. A, 39 pp6148-6153
- Gathers G R, (1986)
Dynamic methods for investigating thermophysical properties of matter at very high temperatures and pressures
Reports Prog. Phys., 49 pp341-396
- Hanley L, Ruatta S A and Anderson S L, (1987)
Collision-induced dissociation of aluminium cluster ions: Fragmentation patterns, bond energies, and structures for Al⁺² - Al⁺⁷
J. Chem. Phys., 87 pp260-268
- Hansen S G, (1989)
Velocity profiles of species ejected in ultraviolet laser ablation of several polymers examined by time-of-flight mass spectroscopy
J. Appl. Phys., 66 pp3329-3336

- Harnafi M and Dubreuil B, (1991)
Characterization and analysis of the CO₂ laser-induced ablation of lithium target via laser induced fluorescence and absorption spectroscopy of emitted atoms
J. Appl. Phys., 69 pp7565-7571
- Hattori K, Nakai Y and Itoh N, (1990)
Non-linear photo-induced sputtering of GaP for photons of sub-band-gap energies
Surf. Sci., 227 ppL115-L119
- Hergenröder R and Niemax K, (1991)
Continuous wave field ionization laser spectroscopy
Resonant Ionisation Spectroscopy 1990, Inst. Phys. Conf. Ser. No.114, pp133-136
- Hindmarsh W R, (1967)
Atomic spectra
Pergamon Press, Oxford
- Hotop H, Klar D and Schohl S, (1992)
Resonance ionization of metastable rare gas atoms
Resonant Ionisation Spectroscopy 1992, Inst. Phys. Conf. Ser. No.128, pp45-52
- Housden J, Hutt K W and Wallach E R, (1989)
Evolution of ion energy distributions with increasing ion yields in a laser microprobe mass spectrometer (LAMMS)
Micobeam Analysis-1989, San Francisco Press, pp269-272
- Hurst G S, Nayfeh M H and Young J P, (1977)
A demonstration of one-atom detection
Appl. Phys. Lett., 30 pp229-231
- Hurst G S, Payne M G, Kramer S D and Young J P, (1979)
Resonance ionisation spectroscopy and one-atom detection
Rev. Mod. Phys., 51 pp767-819
- Hurst G S and Payne M G, (1988)
Principles and applications of resonance ionisation spectroscopy
IOP Publishing Ltd, Bristol

- Hussla I and Viswanathan R, (1984)
Excimer laser induced ablation of clean and CO-covered polycrystalline copper surfaces: Generation and characterization of high energy copper species
Surf. Sci., 145 ppL488-L492
- Hutt K W, Housden J and Wallach E R, (1989)
Anomalous ion transmission in a laser microprobe (LAMMS): Investigation by high frequency monitoring of the current through the sample/target
Int. J. Mass Spectrom. Ion Pro., 94 pp237-249
- Ichige K, Matsumoto Y and Namiki A, (1988)
Laser-induced desorption from compound semiconductors
Nucl. Instr. and Meth., B33 pp820-823
- Iida Y, (1990)
Effects of atmosphere on laser vaporization and excitation processes of solid samples
Spectrochimica Acta, 45B pp1353-1367
- Izawa Y, Yamanaka T, Tsuchimori N Onishi M and Yamanaka C, (1968)
Density measurements of the laser produced plasma by laser light scattering
Jpn. J. Appl. Phys., 7 p954
- Johansson S A E and Campbell J L, (1988)
PIXE - A novel technique for elemental analysis
John Wiley and Sons, Chichester
- Karas M, Bachmann D and Hillenkamp F, (1985)
Influence of the wavelength in high-irradiance ultraviolet laser desorption mass spectrometry of organic molecules
Anal. Chem., 57.pp2935-2939
- Karas M, Bahr U and Giessmann U, (1991)
Matrix-assisted laser desorption ionization mass spectrometry
Mass Spectrom. Rev., 10 pp335-357

- Kelly J F, Harris M and Gallagher A, (1988c)
Collisional energy pooling for $Sr(5^3P_J) + Sr(5^3P_J) \rightarrow Sr(6^3S) + Sr(5^1S)$
Phys. Rev. A, 38 pp1225-1229
- Kelly R and Rothenburg J E, (1985)
Laser sputtering.
Part III. The mechanism of the sputtering of metals at low energy densities
Nucl. Instr. and Meth., B7/8 pp755-763
- Kelly R and Dreyfus R W, (1988a)
On the effect of Knudsen-layer formation on the studies of vaporization, sputtering, and desorption
Surf. Sci., 198 pp263-276
- Kelly R and Rothenburg J E, (1988b)
Reconsidering the mechanisms of laser sputtering with Knudsen-layer formation taken into account
Nucl. Instr. and Meth., B32 pp341-348
- Kelly R, (1990)
On the dual role of the Knudsen layer and unsteady, adiabatic expansion in pulse sputtering phenomena
J. Chem. Phys., 92 pp5047-5056
- Kelly R and Miotello A, Braren B, Gupta A and Casey K, (1992a)
Primary and secondary mechanisms in laser-pulse sputtering
Nucl. Instr. and Meth., B65 pp187-199
- Kelly R, (1992b)
Personal communication
- Kools J C S, Baller T S, DeZwart S T and Dieleman J, (1992)
Gas flow dynamics in laser ablation deposition
J. Appl. Phys., 71 pp4547-4556
- Kovalev I D, Maksimov G A, Suchkov A I and Larin N V, (1978)
Analytical capabilities of laser-probe mass spectrometry
Int. J Mass Spectrom. Ion Phys., 27 pp101-137

- Krätschmer W, Lamb L D, Fostiropoulos K and Huffman D R, (1990)
Solid C₆₀: a new form of carbon
Nature, 347 pp354-358
- Krönert U, Becker St, Hilberath Th, Kluge H J and Schulz C, (1987)
Resonance ionization mass spectroscopy with a pulsed thermal atomic beam
Appl. Phys., A44 pp339-345
- Land A P, (1990)
Thesis, University of Glasgow
- Land A P, Ledingham K W D, Singhal R P and Towrie M, (1992)
Two-photon resonance enhancement in calcium
Resonant Ionisation Spectroscopy 1992, Inst. Phys. Conf. Ser. No.128, pp99-102
- Lazneva E F, (1991)
Laser induced desorption
Rad. Eff., 115 pp257-284
- Leis F, Sdorra W, Bak Ko J and Niemax K, (1989)
Basic investigations for laser microanalysis: I. Optical emission spectrometry of laser-produced sample plumes
Mikrochim. Acta [Wien], II pp185-199
- Leismann P, Henc-Bartolic V, Rebhan U and Kunze H J, (1984)
Some properties of atomic beams from laser irradiated zirconium
Physica Scripta, 30 pp186-188
- Letokhov V S, (1987)
Laser photoionization spectroscopy
Academic Press, Orlando
- Loudon R, (1973)
The quantum theory of light
Clarendon Press, Oxford
- Mamyrin B A, Karataev V I, Shmikk D V and Zagulin V A, (1973)
The mass-reflectron, a new nonmagnetic time-of-flight mass spectrometer with high resolution
Sov. Phys.-JETP, 37 pp45-48

- Mathews L J, Baxter C S and Leake J A, (1989)
Electron-optical examination of LAMMS craters in transverse section
Microbeam Analysis 1989, San Francisco Press Inc, pp264-268
- Mayo S, Lucatorto T B and Luther G G, (1982)
Laser ablation and resonance ionization spectrometry for trace analysis of solids
Anal. Chem., 54 pp553-556
- McCombes P T, Borthwick I S, Jennings R, Ledingham K W D and Singhal R P, (1991a)
Resonance ionization mass spectrometry applied to the trace analysis of gold
Inst. Phys. Conf. Series No. 113, pp163-168
- McCombes P T, (1991b)
Thesis, University of Glasgow
- McKee J S C and Smith G R, (1989)
Proton microprobes and their applications
Advances in Electronics and Electron Physics: Aspects of Charged Particle Optics, Academic Press Inc., pp93-132
- McLean C J, (1990a)
Thesis, University of Glasgow
- McLean C J, Marsh J H, Land A P, Clark A, Jennings R, Ledingham K W D, McCombes P T, Marshall A, Singhal R P and Towrie M, (1990b)
Resonant laser ablation (RLA)
Int. J. Mass Spectrom. Ion Proc., 96,ppR1-R7
- Moenke-Blankenburg L, (1989)
Laser microanalysis
John Wiley and Sons, New York
- Moore C E, (1971)
Atomic energy levels - As derived from the analysis of optical spectra
Nat. Stand. Ref. Data Service, Nat. Bur. Stand. (US)

- Muller J F, Krier G, Verdun F, Lamboule M and Muller D, (1985)
Ionization of organic crystals with a tuneable dye laser connected to a LAMMA instrument
Int. J. Mass Spectrom. Ion Proc., 64, pp127-138
- Nakai Y, Hattori K, Okano A, Itoh N and Haglund R F Jnr, (1991)
Nonthermal laser sputtering from solid surfaces
Nucl. Instr. and Meth., B58 pp452-462
- Namiki A, Fukano H, Kawai T, Yasuda Y and Nakamura T (1985a)
Temperature dependence of desorption in highly photo-excited CdS
J. Phys. Soc. Japan., 54 pp3162-3167
- Namiki A, Kawai T, Yasuda Y and Nakamura T, (1985b)
Pulsed laser induced desorption in GaAs: A dynamic pulse mass counting study
Jpn. J. Appl. Phys., 24 pp270-273
- Namiki A, Kawai T and Ichige K, (1986)
Angle-resolved time-of-flight spectra of neutral particles desorbed from laser irradiated CdS
Surf. Sci., 166 pp129-140
- Namiki A, Cho S and Ichige K, (1987)
Laser stimulated desorption from compound semiconductors, Dimerization enhanced phase transition
Jpn. J. Appl. Phys., 26 pp39-44
- Namiki A, Katoh K, Yamashita Y, Matsumoto Y, Amano H and Akasaki I, (1991)
Dynamics of laser sputtering at GaN, GaP and GaAs surfaces
J. Appl. Phys., 70 pp3268-3274
- Nicholas M, Pruett J G, Havrilla G J and Bryan S R, (1989)
Laser postionization time-of-flight mass spectrometry with a laser-ablation carrier-gas transport source
Micobeam Analysis-1989, San Francisco Press, pp323-324

- Niemax K and Sdorra W, (1990)
Optical emission spectrometry and laser-induced fluorescence of laser produced sample plumes
Appl. Optics, 29 pp5000-5006
- Nogar N S, Estler R C and Miller C M, (1985)
Pulsed laser desorption for resonance ionization mass spectrometry
Anal. Chem., 57 pp2441-2444
- Nogar N S, Dye R C, Estler R C, Foltyn S R, Muenchausen R E and Wu X D, (1991)
Diagnostic studies of $YBa_2Cu_3O_{7-x}$ laser ablation
Lecture Notes in Physics 389, "Laser Ablation- Mechanisms and Applications", Eds. J C Miller and R F Haglund, Jr., pub. Springer-Verlag, Berlin Heidelberg
- NoorBatcha I, Lucchese R R and Yehuda Z, (1987)
Monte Carlo simulations of gas-phase collisions in rapid desorption of molecules from surfaces
J. Chem. Phys., 86 pp5816-5824
- NoorBatcha I, Lucchese R R and Yehuda Z , (1988)
Anisotropic translational energy distribution due to gas-phase collisions in rapid desorption of molecules from surfaces
Surf. Sci., 200 pp113-134
- O'Keefe A, Ross M M and Baronavski A P, (1986)
Production of large carbon clusters by laser vaporization
Chem. Phys. Lett., 130 pp17-19
- O'Shea D C, Callen W R and Rhodes W T, (1978)
Introduction to lasers and their applications
Addison-Wesley Pub. Co., Massachusetts
- Oakey N S and MacFarlane, (1967)
An electrostatic particle guide for high resolution charged particle spectrometry in intense reactor fluxes
Nucl. Inst. Meth., 49 pp220-221

- Odom R W and Schueler B, (1987)
Thin film microanalysis using laser ablation and laser ionization mass spectrometry
Thin Solid Films, 154 pp1-10
- Odom R W and Schueler B, (1990)
Laser microprobe mass spectrometry: Ion and neutral analysis
In "Lasers and Mass Spectrometry", Ed. Lubman D M, Pub. Oxford University Press, New York, pp103-137
- Okada T, Shibamaru N, Nakayama Y and Maeda M, (1992)
Time-of-flight measurement of particles with laser-induced fluorescence in the plume produced by laser ablation of YBa₂Cu₃O_{7-x} target
Jpn. J. Appl Phys., 31 ppL367-L369
- Olstad R A and Olander D R, (1975a)
Evaporation of solids by laser pulses. I. Iron
J. Appl. Phys., 46 pp1499-1508
- Olstad R A and Olander D R, (1975b)
Evaporation of solids by laser pulses. II. Zirconium hydride
J. Appl. Phys., 46 pp1509-1518
- Palik E D, (1985)
Handbook of optical constants of solids
Academic Press Inc, Orlando, pp429-444
- Pang H and Yeung E S, (1989)
Laser-enhanced ionization as a diagnostic tool in laser-generated plumes
Anal. Chem., 61 pp2546-2551
- Pappas D L, Hrubowchak D M, Ervin M H and Winograd N, (1989)
Atom counting at surfaces
Science, 243 pp64-66
- Parks J E, (1990)
Surface analysis using resonance ionization spectroscopy
In "Lasers and Mass Spectrometry", Ed. Lubman D M, Pub. Oxford University Press, New York, pp37-64

- Pellin M J, Young C E, Calaway W F, Whitten J E, Gruen D M, Blum J D, Hutcheon I D and Wasserburg G J, (1990)
Secondary neutral mass spectrometry using three-colour resonance ionization: osmium detection at the p.p.b. level and iron detection in silicon at the <200 p.p.t. level
Phil. Trans. R. Soc. Lond., A333 pp133-148
- Peugnet C, (1977)
Kinetic temperature measurement of the front surface of a target exposed to an intense pulsed electron beam
J. Appl. Phys., 48 pp3206-3210
- Pospieszczyk A, Abdel Harith M and Stritzker B, (1983)
Pulsed laser annealing of GaAs and Si: Combined reflectivity and time-of-flight measurements
J. Appl. Phys., 54 pp3176-3182
- Prenzel A T, Dehaven J, Johnson E J and Davidovits P, (1977)
Production of neutral atoms by pulsed laser heating
J. Appl. Phys., 48 pp3551-3556
- Price D, (1990)
The resurgence in time-of-flight mass spectrometry
Trends Anal. Chem., 9 pp21-25
- Qu J, Zhou Z, Zhu L and Lin F, (1991)
Laser-induced fluorescence studies of pulsed uranium ablation by a Nd:YAG Q-switched laser
Appl. Phys. Lett., 59, pp271-273
- Quentmeier A, Sdorra W and Niemax K, (1990)
Internal standardization in laser induced fluorescence spectrometry of microplasmas produced by laser ablation of solid samples
Spectrochimica Acta, 45B pp537-546
- Rahman N K and Guidotti C, (1982)
Photon-Assisted Collisions and Related Topics
Pub. OPA, Amsterdam

- Ralston J, Moretti A L, Jain R K and Chambers F A, (1987)
Intermixing of $Al_xGa_{1-x}As/GaAs$ superlattices by pulsed laser irradiation
Appl. Phys. Lett., 50 pp1817-1819
- Ready J F, (1971)
Effects of high power laser radiation
Academic Press, New York
- Rothenburg J E and Kelly R, (1984)
Laser sputtering.
Part II. The mechanism of the sputtering of Al_2O_3
Nucl. Instr. and Meth., B1 pp291-300
- Saloman E B, (1990)
A resonance ionization spectroscopy/resonance ionization mass spectrometry data service. I - Data sheets for As, B, Cd, C, Ge, Au, Fe, Pb, Si and Zn
Spectrochimica Acta, 45Bpp37-83
- Saloman E B, (1991)
A resonance ionization spectroscopy/resonance ionization mass spectrometry data service. II - Data sheets for Al, Ca, Cs, Cr, Co, Cu, Kr, Mg, Hg and Ni
Spectrochimica Acta, 46B pp319-378
- Saloman E B, (1992a)
Status report on the National Institute of Standards and Technology resonance ionization spectroscopy/resonance ionization mass spectrometry data service
Resonant Ionisation Spectroscopy 1992, Inst. Phys. Conf. Ser. No.128, pp67-70
- Saloman E B, (1992b)
A resonance ionization spectroscopy/resonance ionization mass spectrometry data service. III- Data sheets for Sb, Bi, P, Na and Sn
Spectrochimica Acta, 47B pp517-543

- Schorn R P, Bay H L, Hintz E and Schweer B, (1987)
Investigation of partial sputtering of lithium from a binary Al/Li alloy with laser induced fluorescence
Appl. Phys. A, 43 pp147-151
- Schueler B and Odom R W, (1987)
Nonresonant multiphoton ionization of the neutrals ablated in laser microprobe mass spectrometry analysis of GaAs and Hg_{0.78}Cd_{0.22}Te
J. Appl. Phys., 61 pp4652-4661
- Sdorra W, Quentmeier A and Niemax K, (1989)
Basic investigations for laser microanalysis: II. Laser-induced fluorescence in laser-produced sample plumes
Mikrochim. Acta [Wien], II pp201-218
- Selter K P and Kunze H J, (1982)
Analysis of atomic beams produced by laser-induced ablation
Physica Scripta, 25 pp929-932
- Shaw R W, Young J P and Smith D H, (1989)
Diode laser initiated resonance ionization mass spectrometry of lanthanum
Anal. Chem., 61 pp695-697
- Shaw R W, Young J P and Ramsey J M, (1992)
Resonance ionization of rubidium using sequential diode laser-driven transitions
Resonant Ionisation Spectroscopy 1992, Inst. Phys. Conf. Ser. No.128, pp297-300
- Sidenius G, (1978)
Ion sources for low energy accelerators
Nucl. Instru. Meth., 151 pp349-362
- Sigmund P, (1969)
Theory of sputtering. I. Sputtering yield of amorphous and polycrystalline targets
Physical Rev., 184 pp383-416

- Singh R K, Holland O W and Narayan J, (1990)
Theoretical model for deposition of superconducting thin films using pulsed laser evaporation technique
J. Appl. Phys., 68 pp233-247
- Singhal R P, Drysdale S L T, Jennings R, Land AP, Ledingham K W D, McCombes P T and Towrie M, (1991)
Observations on carbon clusters during trace elemental analysis of coal samples by RIMS
Resonant Ionisation Spectroscopy 1990, Inst. Phys. Conf. Ser. No.114, pp185-188
- Sizer T and Raymer M G, (1987)
Atomic collisions in the presence of intense, ultrashort laser pulses
Phys. Rev. A, 36 pp2643-2658
- Spiess G, Roussel F, Carre B, Breger P and Manus C, (1982)
Laser induced ionisation of Na vapour at the $3P_{1/2}$ and $3P_{3/2}$ resonances
Photon-Assisted Collisions and Related Topics, Ed. Rahman N K and Guidotti C, Pub. OPA, Amsterdam, pp199-216
- Srinivasan R, Braren B, Dreyfus R W, Hadel L and Seeger D E, (1986)
Mechanism of the ultraviolet laser ablation of polymethyl methacrylate at 193 and 248nm: laser-induced fluorescence analysis, chemical analysis, and doping studies
J. Opt. Soc. Am., B3 pp785-791
- Sykes D E, (1990).
Dynamic secondary ion mass spectrometry
In "Methods of Surface Analysis", Ed. J M Walls, Cambridge University Press, pp216-262
- Sze S M, (1985)
Semiconductor devices, Physics and technology
Pub. John Wiley & Sons, Inc, New York

- Tang K, Allman S L and Chen C H, (1992)
Laser mass spectrometry for biopolymers
Resonant Ionisation Spectroscopy 1992, Inst. Phys. Conf. Ser.
No.128, pp289-292
- Tembreull R and Lubman D M, (1986)
*Pulsed laser desorption with resonant two-photon ionization
detection in supersonic beam mass spectrometry*
Anal. Chem., 58 pp1299-1303
- Thompson M W, (1968)
*The energy spectrum of ejected atoms during the high energy
sputtering of gold*
Philos. Mag., 18 pp377-414
- Thompson M, Goulter J E and Sieper F, (1981)
*Laser ablation for the introduction of solid samples into an
inductively coupled plasma for atomic-emission spectrometry*
Analyst, 106 pp32-39
- Thompson M, Chenery S and Brett L, (1990)
*Nature of particulate matter produced by laser ablation -
implications for tandem analytical systems*
J. Anal. Atomic Spectrom., 5 pp49-55
- Thonnard N, Parks J E, Willis R D, Moore L J and Arlinghaus H F, (1989)
*Resonance ionization of neutral atoms with applications to
surface science, noble gas detection and biomedical analysis*
Surf. Interface Anal., 14 pp751-759
- Towrie M, Drysdale S L T, Jennings R, Land AP, Ledingham K W D,
McCombes P T, Singhal R P, Smyth M H C and McLean CJ, (1990)
*Trace analysis using a commercial resonant ionisation mass
spectrometer*
Int. J. Mass Spectrom. Ion Proc., 96 pp309-320
- Travis J C, Fassett J D and Lucatorto T B, (1987)
Resonance ionization mass spectrometry
Resonant Ionisation Spectroscopy 1986, Inst. Phys. Conf. Ser.
No.84, pp91-96

- van Vaeck L and Gijbels R, (1989)
Overview of laser microprobe mass spectrometry techniques
Microbeam Analysis 1989, San Francisco Press Inc, pp xvii-xxv
- Verdun F R, Krier G and Muller J F, (1987)
Increased sensitivity in laser microprobe mass analysis by using resonant two-photon ionization processes
Anal. Chem., 59 pp1383-1387
- Vertes A, Juhasz P, De Wolf M and Gijbels R, (1988)
The role of energy deposition processes in the understanding of laser microprobe analysis mechanisms
Scan. Microsc., 2 pp1853-1877
- Vertes A, Juhasz P, De Wolf M and Gijbels R, (1989a)
Hydrodynamic modelling of laser plasma ionization processes
Int. J. Mass Spectrom. Ion Pro., 94 pp63-85
- Vertes A, De Wolf M, Juhasz P and Gijbels R, (1989b)
Threshold conditions of plasma ignition in laser ionization mass spectrometry of solids
Anal. Chem., 61 pp1029-1035
- Vertes A, Gijbels R and Adams F, (1990)
Diagnostics and modeling of plasma processes in ion sources
Mass Spectrom. Rev., 9 pp71-113
- Vickerman J C, (1990)
Static secondary ion mass spectrometry
In "Methods of Surface Analysis", Ed. J M Walls, Cambridge University Press, pp169-215
- von Allmen M, (1987)
Laser-beam interactions with materials - Physical principles and application
Springer Series in Materials Science 2, Springer-Verlag, Berlin Heidelberg

- Walkup R E, Jasinski J M and Dreyfus R W, (1986)
Studies of excimer laser ablation of solids using a Michelson interferometer
Appl. Phys. Lett., 48, pp1690-1692
- Wang H, Salzberg A P and Weiner B R, (1991a)
Laser ablation of aluminium at 193,248 and 351nm
Appl. Phys. Lett., 59, pp935-937
- Wang L, Borthwick I S, Jennings R, McCombes P T, Ledingham KWD, Singhal R P and McLean C J, (1991b)
Observations and analysis of resonant laser ablation of GaAs.
Appl. Phys. B, 53 pp34-38
- Wang L, Ledingham KWD, Singhal R P and McLean C J, (1992)
Laser-induced collisional processes in resonant laser ablation of GaAs.
Appl. Phys. B, 54 pp71-75
- Wedler G and Ruhmann H, (1982)
Laser induced thermal desorption of carbon monoxide from Fe(110) surfaces
Surf. Sci., 121pp464-486
- Wernick S and Pinner R, (1972)
The surface treatment and finishing of aluminium and its alloys.
Fourth Edition, Volume 1, Published by Robert Draper Ltd,
Teddington
- Williams M W, Beekman D W, Swan J B and Arakawa E T, (1984)
Detection of trace elements with resonance ionization and time-of-flight mass spectrometry
Anal. Chem., 56 pp1348-1350
- Winograd N, Zhou Y, Wood M and Lakiszak S, (1992)
Prospects for submicron molecular imaging with ion beams and lasers
Resonant Ionisation Spectroscopy 1992, Inst. Phys. Conf. Ser.
No.128, pp259-264

Wittmaack K, (1993)

Quantitative analysis of solids by SIMS and SNMS

In 'Quantitative microbeam analysis - Proceedings of the 40th
Scottish Universities Summer School in Physics', IOP Publishing,
pp 351-374

Wiza J L, (1979)

Microchannel plate detectors

Nucl. Instr. and Meth., 162 pp587-601

GLASGOW
UNIVERSITY
LIBRARY

GLASGOW
UNIVERSITY
LIBRARY